Coherent Radar Performance Estimation

James A. Scheer and James L. Kurtz

Editors

Artech House
Boston • London

Library of Congress Cataloging-in-Publication Data

Coherent Radar Performance Estimation/James A. Scheer and James L. Kurtz, editors
Includes bibliographical references and index.
ISBN 0-89006-628-0
Coherent Radar. 2. Radar—Interference—Mathematical models.
I. Scheer, Jim, 1944– . II. Kurtz, J. L. (James L.), 1945– .
TK6592.C6C64 1993 92-40716
621.3848—dc20 CIP

ISBN 0-89006-628-0

British Library Cataloging-in-Publication Data

Coherent Radar Performance Estimation
I. Scheer, James A. II. Kurtz, James L.
621.3848

ISBN 0-89006-628-0

685 Canton Street
Norwood, MA 02062

International Standard Book Number: 0-89006-628-0

editors

)716

t of this book may be
including photocopy-
permission in writing

Contents

Preface

The motivation for the publication of this book is the need to pull together information related to predicting the effects of various generic contaminants on the performance of coherent radar systems. Its genesis was in the execution of a Senior Technology Guidance Council (STGC) program at the Georgia Tech Research Institute (GTRI) and the development of a short course on the material. Some of the material in this book is found in other texts and in periodical publications, while some material is not found elsewhere. Derivations are not presented, but results are. The reader is given usable results in the form of equations, graphs, charts, and methods, and given references for the background information. The book presents information that is valuable to a radar system engineer who has the basic understanding of radar technology but needs some advanced information regarding coherent system error sources and their effects on performance. The book could also be used as a text by senior- or graduate-level students in engineering who are studying advanced radar concepts and system evaluation.

The book has three major sections in addition to the introductory chapter (Chapter 1). Section 1 discusses the origin of various contaminants. Chapter 2 presents the definition and an understanding of the concept of phase noise and provides representative examples for various oscillator configurations. Chapter 3 discusses the errors that are possible in I/Q detector networks and the images that can result. Chapter 4 discusses the noise associated with timing jitter. Chapter 5 discusses quantization and saturation effects in A-to-D converters. Chapter 6 discusses the effects of system nonlinearities, in particular for wideband systems, on FFT processing. Chapter 7 discusses the effects of radar motion and motion compensation.

Section 2 includes six chapters that present the effects of the various contaminants from the specific system application's point of view. Chapter 8 discusses MTI systems, including phase noise effects, in addition to some of the more commonly discussed factors. Chapter 9 discusses pulse Doppler systems—again,

Chapter 1
Introduction to Coherent Radar Systems

James A. Scheer
Georgia Institute of Technology

1.1 INTRODUCTION

Radar systems are used to detect targets of interest on the basis of the energy returned to the radar antenna resulting from a transmitted signal that illuminates and returns from the target. In the past, most radars were noncoherent in that they transmitted noncoherent bursts of RF energy and the presence and position of a target were determined from an analysis of the amplitude of the signal returning to the radar from that target. In modern coherent radar systems, the detection is based not only on the amplitude of the signal, but on its phase characteristics as well. The received vector is measured by relating the phase of the received signal to that of a stable reference oscillator in the radar system. The phase relationships are measured and processed over an extended period of time relative to the range delay time, often in the tens or sometimes hundreds of milliseconds. The effects of instabilities in such radar systems in predicting their detection, imaging, and tracking performance is the topic of this book.

1.1.1 Noncoherent Systems

Figure 1.1 is the simplified block diagram of a radar system. The basic components are the transmitter, the antenna, and the receiver. There is usually either a display system or a signal processor, or both. The transmitter generates a highpower microwave signal that is applied to the antenna and radiated. The transmitted signal propagates through space and illuminates a target of interest. Some of this signal is reflected from the target and reradiated back toward the radar. The receiver antenna intercepts some of the received energy and applies it to the receiver for

emphasizing phase noise. Chapter 10 discusses the performance of pulse compression systems; while not in the strictest sense a "coherent" process, the material is included for completeness. Chapter 11 discusses the effects of various contaminants on the stepped frequency waveform for high range resolution and the *inverse synthetic aperture radar* (ISAR) process for high cross-range resolution. Chapter 12 discusses various noise, leakage, and reflection effects on FMCW systems. Chapter 13 presents material associated with range, angle, and Doppler tracking processes implemented in coherent systems.

The final three chapters in Section 3, Testing, provide an overview of testing procedures and methods. Chapter 14 discusses testing for the characterization of phase noise, with examples. Chapter 15 discusses the testing of components and subsystems, such as A-to-D converters and I/Q networks. Finally, Chapter 16 discusses system level testing, emphasizing signal synthesis techniques.

We wish to acknowledge several people who, besides the contributors, were instrumental in the production of this publication. Firstly, it was due to the special efforts on the part of Dr. Josh Nessmith of GTRI, who provided sustained motivation, beginning with the above referenced STGC program, the development of the short course, and the preparation of the publication, that this book was prepared. Contributors not identified as chapter authors are Dr. Jim Echard and Dr. Eric Sjoberg. Lamar Gostin, who said something to the effect that "a book is only as valuable as its index" made us sensitive to the value of a complete index of the material. The artwork, of which we are particularly proud, was prepared primarily by Ms. Phyllis Hinton, with help on Chapters 8 and 9 by Ms. Kay Lindsey, who, as might be expected, had to work with poorly prepared material, submitted with little time to complete. Finally, we are grateful to Georgia Tech Research Institute for giving us additional motivation and support to write this book.

James A. Scheer
James L. Kurtz

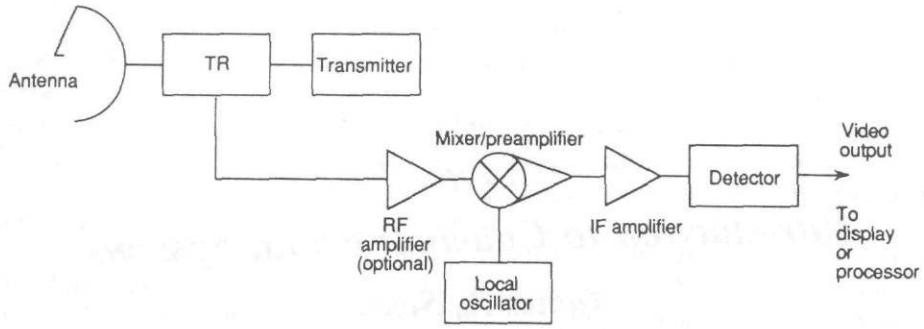

Figure 1.1 Simplified block diagram of a radar system.

(typically) amplification, downconversion, more amplification, detection, and displaying or signal processing, according to the functional requirements of the system.

The original radar systems were noncoherent, in the sense that they transmitted a burst of RF energy and detected the amplitude of that portion of the signal that came back from a target of interest. With such a system the range to the target is estimated by measuring the time it takes for the signal to get to the target and return to the radar. The *radar cross section* (RCS) of the target is estimated by measuring the amplitude of the received signal. The resolution with which such a system can separate two or more targets in range and azimuth is dependent on the transmitted pulse width and the antenna beamwidth, respectively. Today, there is still a place for noncoherent systems, but modern radar technology and system demands require that the systems be coherent. A coherent system can measure the phase of the received signal, as well as the amplitude.

1.1.2 Coherent Systems

Figure 1.2 is the block diagram of a simple coherent radar system. The transmitted signal is derived from a set (two or three or more) of stable oscillators, which serve as the reference for measuring the phase of the received signal. Typically, the received signal is characterized as a vector having an *amplitude* (A) and a *phase* (Φ). The typical coherent radar measures the received vector in terms of the two orthogonal components in the rectangular coordinate system, the *inphase* (I) and the *quadrature* (Q) components of the received vector, rather than the amplitude and phase explicitly.

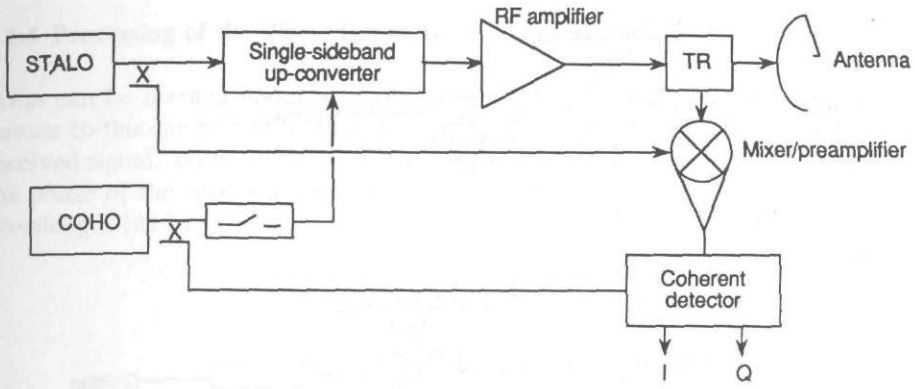

Figure 1.2 Simplified block diagram of a coherent radar system.

1.1.3 I/Q Detection

Figure 1.3 is a block diagram of a typical I/Q detector network. The received signal is applied to a 3-dB power splitter, the two outputs of which are applied to the RF ports of double-balanced mixers. The *local oscillator* (LO) ports are driven by a two samples of the *coherent oscillator* (COHO) signal, the two components being in quadrature. The resulting outputs from the mixers are the inphase and quadrature phase video (baseband) signals representative of the received vector. The relationships between the I and Q components and the amplitude and phase are given by:

$$I = A\cos(\Phi) \tag{1.1}$$

$$Q = A\sin(\Phi) \tag{1.2}$$

Figure 1.4 is a vector representation of the received signal, showing the relationships between the polar coordinate and rectangular coordinate representations. The amplitude (A) and phase (q) can be determined, if desired, from I and Q from:

$$A = \sqrt{I^2 + Q^2} \tag{1.3}$$

$$\Phi = \arctan(Q/I) \tag{1.4}$$

keeping in mind the quadrant to eliminate the ambiguity in the arctan function.

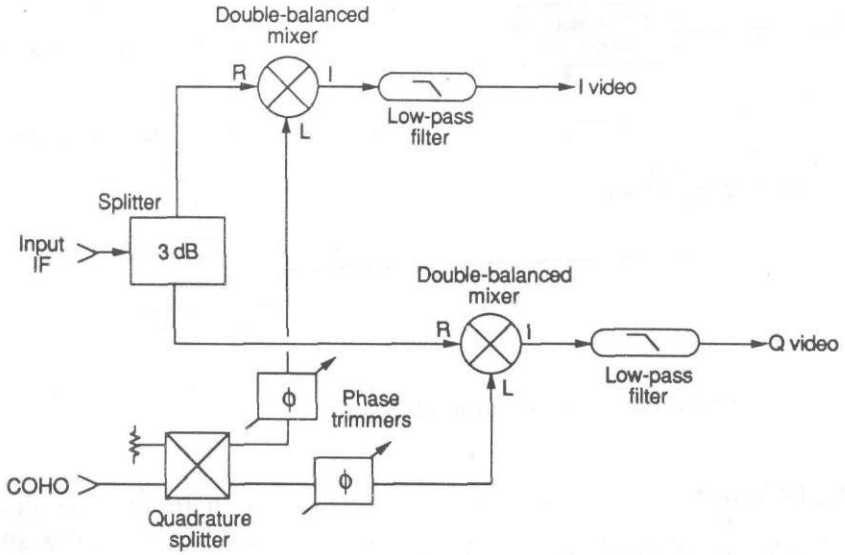

Figure 1.3 Block diagram of a typical I/Q detector network.

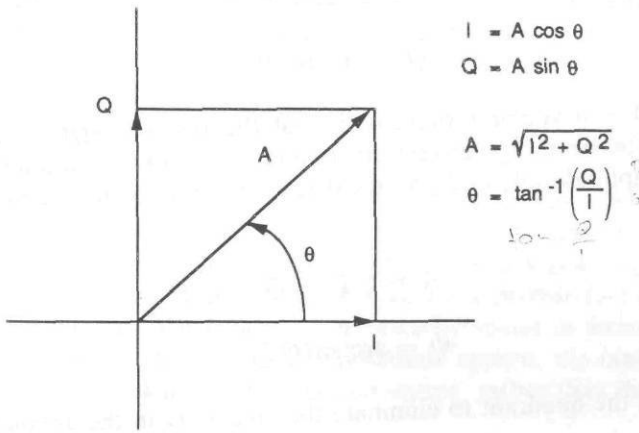

Figure 1.4 Rectangular and polar coordinate system representations of received vector.

1.1.4 Processing of the Phase Information

What can be learned about a target if the phase of the signal is measured? The answer to this can best be appreciated if we explore the nature of the phase of the received signal. Without plowing through the mathematics, it is easy to agree that the phase of the received signal is related to the range to the target (R) and the wavelength (λ) by:

$$\Phi = \frac{4\pi R}{\lambda} = \frac{4\pi FR}{c} \tag{1.5}$$

where:

R is the range to the target,
λ is the transmitted wavelength,
F is the transmitted frequency, and
c is the velocity of electromagnetic propagation.

Several things are worthy to note in this relationship. First, the phase of the received signal is ambiguous for every wavelength of round-trip distance. That is, the radar does not measure the absolute distance to the target, but rather only "knows" the residue of the phase number. Second, the phase of the signal changes linearly with target distance, providing a means to determine that a target is moving and further to measure the velocity of the target. Third, the phase of the received signal changes with wavelength (or frequency), providing a means to measure the range to the target using a special stepped frequency waveform. Techniques to exploit the information available in the signal phase, as well as the effect of contaminants to these processes, are the topics of later chapters of this book.

Evaluation of the first derivative (with respect to time) of (1.5) provides more insight into the value of the phase information in the received signal. As stated, the phase of the received signal is ambiguous for every wavelength of distance to the target. That is, the system cannot tell how many wavelengths there are between the radar and the target, but it can measure fractional wavelength changes. The phase changes with target range according to the following formula.

$$\dot{\Phi} = \frac{4\pi F}{c}\dot{R} \tag{1.6}$$

where:

$\dot{\Phi}$ is the first derivative of phase with time (frequency) and
$\dot{R}$ is the first derivative of target range with time (velocity).

It can be seen that if there is a radial component of velocity of the target, then the distance (R) will be changing, resulting in a changing phase (Φ). The rate of range change (velocity) to the target can be determined by measuring the frequency of rotation of the received vector. The shift in frequency between the transmitted signal and the received signal due to the radial component of the target motion is referred to as the doppler frequency.

If the radar signal processor is designed to filter out signals that do not have this frequency on them and pass target signals that do, then the system can differentiate between moving and stationary targets. If the system is designed to measure the frequency, it can tell how fast the target is moving (radial component).

Further examination of the first derivative of (1.5) reveals the fact that if the frequency of the transmitted signal is not constant, then there is an additional contribution to the apparent doppler frequency related to the target range and the frequency deviation rate, as demonstrated in (1.7).

$$\dot{\Phi} = \frac{4\pi R}{c} \dot{F} \qquad (1.7)$$

where $\dot{F}$ is the rate of change of frequency with time.

The implication here is that target range can be determined from the "synthetic" doppler frequency. In fact, this is true except that for the normal range of values of target range and wavelength and frequency deviation, there is a high degree of ambiguity in the measurement. The concept is useful in providing high resolution images of a target, given that the knowledge of absolute range from this technique is not important.

But sometimes a stepped frequency waveform is employed and the target has motion. In this case, range and range rate are coupled; that is, a portion of the doppler frequency is due to the frequency stepping and a portion is due to the target motion.

$$\dot{\Phi} = \frac{4\pi F}{c} \dot{R} + \frac{4\pi R}{c} \dot{F} \qquad (1.8)$$

The discussion above provides some insight into the uses for coherent radar systemsmeasuring target motion and imaging characteristics. The techniques used for characterizing target motion are commonly categorized as *moving target indication* (MTI) and doppler processing, including *target motion resolution* (TMR) processing. The former of these involves the use of a high-pass filter for suppressing the received signal from stationary targets and clutter, while passing the signal from moving targets. The specific velocity of targets is not determined, but the

fact that the target is moving is. The doppler process provides information regarding the velocity of the target or at least the radial component thereof.

1.2 PROCESSES EMPLOYED—COHERENT SYSTEM APPLICATIONS

There are many operational applications for coherent radar systems. They range from ground-based and shipborne applications to airborne and spaceborne applications. Functions range from search, acquisition, and tracking systems to instrumentation systems for measuring RCS characteristics and imaging targets. Virtually all applications, however, rely on a limited subset of general processing techniques to accomplish their mission. Table 1.1 lists the most basic of the processes employed by coherent systems and the system applications that are related to such processes.

1.2.1 Integration

Integration involves vector-summing of a sequence of received samples to improve the *signal-to-noise ratio* (SNR). Ideally, a nonmoving target will have a constant vector, in terms of phase and amplitude, and a vector sum of n pulses will approach n times the vector amplitude. Noise, which has a random vector phase and amplitude, will not integrate up in the same fashion. The resulting SNR improvement is ideally n. Because of the frequency response of the process, integration is sometimes referred to as low-pass filtering.

Less obvious is the ability to perform the integration process on a signal that has a rotating vector, such as experienced with a moving target or with a moving radar platform. The integration process in such cases can be done by a number of methods. The frequency of the rotating vector can be shifted to (nominally) zero by correcting the phase of the signal on each sample, if the required phase shift is known. This is a form of motion compensation in which the radar signal processor derives the velocity information from a navigation system. Integration can be

Table 1.1
System Applications

Process	*Application*
Integration	Target detection
High-pass filtering	Moving target indication
Fourier transform	Pulse doppler
	High-resolution range profiles
	Synthetic aperture radar
	Inverse synthetic aperture radar

accomplished by performing a fast Fourier transform (FFT). The signal will add vectorially in the doppler bin, which represents its radial component of velocity.

1.2.2 Moving Target Indication

A high-pass filter is sometimes employed to detect moving targets in the presence of stationary clutter. Because the phase of successive received samples changes for a moving target and the phase for stationary clutter does not (except for the hopefully small phase scintillation due to clutter spectrum caused by internal motion), the existence of a moving target can be detected by performing a high-pass filter process. The dc associated with the clutter is canceled, and the fluctuating vector associated with the moving target is passed.

Figure 1.5 shows the frequency response of several configurations of an MTI filter. The filter response is symmetric about the mid-*pulse repetition frequency* (PRF) line and is therefore sometimes only from zero to 1/2 PRF, is shown. In this case the response looks like a high-pass filter. Chapter 8 discusses the operation and performance of MTI systems in detail.

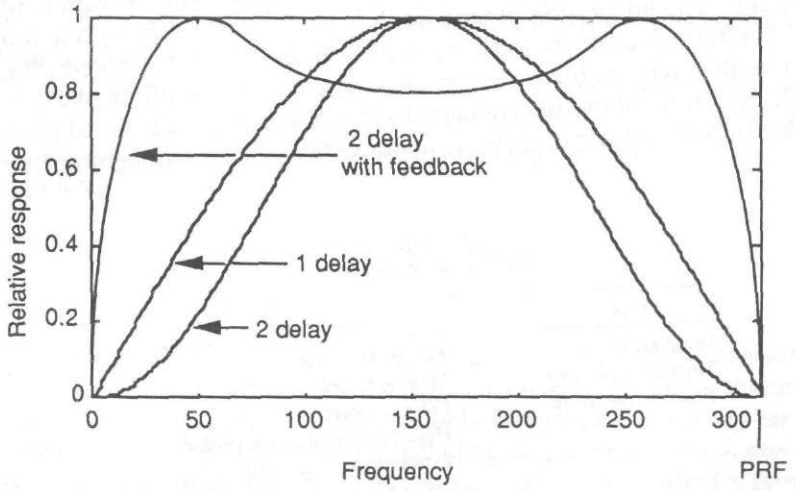

Figure 1.5 Various MTI frequency responses.

1.2.3 Fourier Transform Processing

Whereas an MTI process determines that a target is moving because it has a doppler shift, Fourier processing provides a means for the system to measure the frequency components of the received signal, including stationary and moving targets. In a pulse-doppler application, the radial component of velocity of the moving targets is determined by measuring the doppler frequency. Figure 1.6 shows the output of a hypothetical doppler processor, showing an ideal response from a target having a specific doppler frequency shift, and the sidelobe structure that results from Hamming weighting of the samples before the FFT process is executed.

High resolution spatial imaging of radar target areas can be accomplished by proper processing of the coherent signal. Several approaches to developing a high-resolution profile of the target in the range dimension are used, all requiring a bandwidth wide enough for the resolution desired.

In the simplest case of a pulse transmitted without phase or frequency coding, the range resolution can be determined from:

$$R_r = \frac{c\tau}{2} \tag{1.9}$$

where:

R_r = range resolution (meters), and
τ = pulse length (seconds).

In the more general case, the processed pulse width will be approximately the reciprocal of the signal bandwidth, and the resolution will be:

$$R_r = \frac{c}{2B} \tag{1.10}$$

where

B = bandwidth (Hz).

Some system implementations, such as those in which a narrow pulse is transmitted, require an instantaneous bandwidth equivalent to that needed for the required resolution. Some use an ensemble of pulses, each at a different frequency, developing the required bandwidth over a period of time. In the cases in which an ensemble of pulses, or samples, is processed, some weighting function is applied to the input data before FFT processing. Generally, this process reduces the effec-

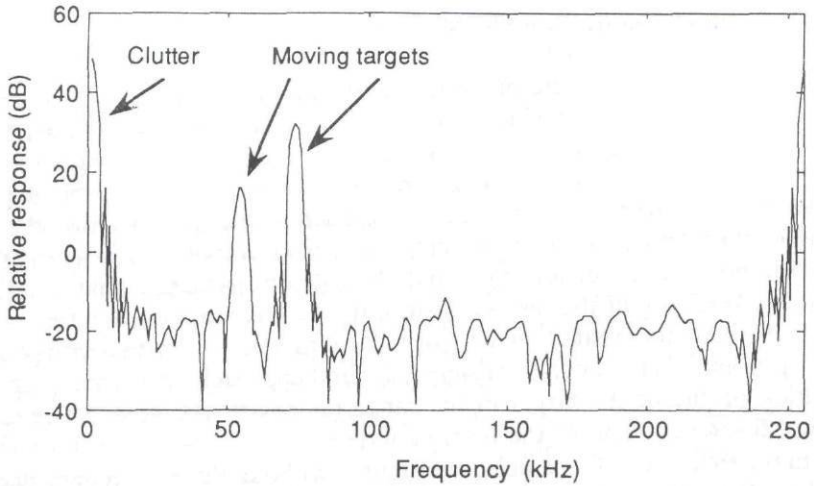

Figure 1.6 Typical FFT response for a pulse-doppler radar.

tive bandwidth an amount dependent on the nature of the weighting function. In general, the lower the sidelobes, the more bandwidth reduction. A rule of thumb for determining the range resolution in such cases is found from:

$$R_r = \frac{1.3c}{2B} \tag{1.11}$$

A more exact figure, however, can be determined if the spreading factor of the particular weighting function being used is known. Harris [1] provides a complete summary of many of the weighting functions typically employed in modern FFT-based signal processing.

1.2.4 Pulse Compression

Some systems use a technique called pulse compression to allow the average power to be increased for a given PRF by transmitting a pulse that is wider than that of a monochromatic pulse consistent with the desired range resolution. The bandwidth is achieved by coding the pulse in frequency (either in a linear or nonlinear ramp or in steps) or in phase, with a sequence of multiple phase subpulses. Often, the pulse is coded with a biphase sequence, using a Barker code or other optimum code. All of these techniques provide the required bandwidth within a single pulse

without the necessity to transmit a narrow pulse and without the requirement that the system be coherent.

1.2.5 Other Coherent Processing Techniques

Several techniques are used for developing the required bandwidth, in addition to transmitting a wideband pulse. In a recently developed application of coherent radar systems, called the *stepped-frequency waveform* (SFWF), the frequency of the transmitter is systematically changed, creating a synthetic doppler on a stationary target [2, 3, 4]. In particular, high-resolution range profiles (range images) of the targets are developed. The stepped-frequency technique is finding its way into the instrumentation radar community, the air-to-ground seeker applications, and airborne pulse-doppler system applications. The large instrumentation systems used in reentry vehicle signature analysis employ a combination of the stepped-frequency and pulse-compression waveforms.

The *frequency-modulated continuous wave* (FMCW) waveform allows for a relatively high average power with a small solidstate transmitter, compared to the average power achievable with a solid-state pulsed system, particularly suitable to seeker applications. Both FMCW and SFWF systems exploit the relationship between received synthetic doppler shifts and target range, though the FMCW system is not a coherent system in the sense that the SFWF system is.

If the target is rotating or the radar is moving so that the target appears to be rotating relative to the radar, the small differences in doppler frequency shift among each of the scatterers on the target provide the means to synthetically establish high crossrange resolution. In the case in which the radar is moving, the process is called *synthetic aperture radar* (SAR), and in the case in which the target is rotating, the process is called *inverse SAR* (ISAR).

Besides high-resolution range processing, high resolution cross-range processing is performed by coherent radars. In airborne applications, SAR technology allows simulation of a long array, providing a narrow effective beamwidth, by collecting successive samples of the target scene as the radar is moved along a known trajectory. The samples are coherently processed to simulate the simultaneous arrival of the received signal by a large focused aperture. In a similar technique, ISAR high-resolution cross-range imaging of a rotating target is achieved by performing an FFT on each high-resolution range cell.

A high degree of understanding of the micromotion of a target can be gained by processing the doppler signals in a fine-grained fashion. Target nutation and the occurrence of subtle events can be detected and accurately timed by close examination of the coherent signal. There are at least two terms used to describe these processes. In the instrumentation radar community, such as White Sands Missile Range in New Mexico, the process is called TMR [5]. In the ballistic missile

defense community, the process is referred to as *phasederived range* (PDR). Detailed examination of the subtle motion of the target requires that the bulk effects of motion be removed from the doppler history by curve-fitting techniques that generate a phase history over relatively long periods of time, often up to a minute. The residual phase changes represent motion of the various target scatterers relative to the target centroid.

1.3 SYSTEM PERFORMANCE ANALYSIS—RADAR SYSTEM MEASURES OF PERFORMANCE

The most basic parameters to use in discussing the detection performance of a radar system are *probability of detection* (P_d) and *probability of false alarm* (P_{fa}). These terms best describe the measure of performance for which most (but not all) radar systems are developed; that is, to detect targets in the presence of interference (noise, for example). There is no closed form analysis to determine the P_d and P_{fa} directly from knowledge of the radar system parameters, but it is relatively straightforward to calculate the *signal-to-interference ratio* (SIR). We need a convenient method for converting the easily derived performance parameters to those specified by the user.

There are two methods for performing this transformation. The purist (or the analyst) may choose to do the transformation analytically. This is done by establishing a threshold level and then integrating the probability density function of the signal resulting from the interference from the threshold level to "+ infinity" to determine the P_{fa} and integrating the probability density function of the target-plus-interference from the threshold to "+ infinity" to determine the P_d. This provides the P_d and P_{fa} for the given threshold level. The procedure is normally repeated for several threshold levels, representing several P_{fa}s. Alternately, if the P_{fa} is known, the appropriate threshold can be determined so that the related P_d can be found.

Many radar texts have curves that summarize the results of the above analysis for popular P_ds, P_{fa}s, and probability functions [6, 7, 8, 9, 10]. Figure 1.7 is an example from [6]. It is a plot of the P_d versus SNR for a family of P_{fa}s. The target is modeled as nonfluctuating, and single pulse detection is used. Although this may not be satisfying for the analyst, the method provides a close (at least first order) approximation of performance at a minimum of effort. Reference [10] provides the most complete set of such curves, calculated for target models 0 through 4, for a wide range of false alarm numbers and number of pulses integrated (noncoherently) from 1 through 10,000.

Random variables are described by their amplitude distribution functions (mean, variance, shape, etc.) and their time history, expressed as the autocorrelation function or the power spectral density. Both forms of random variable

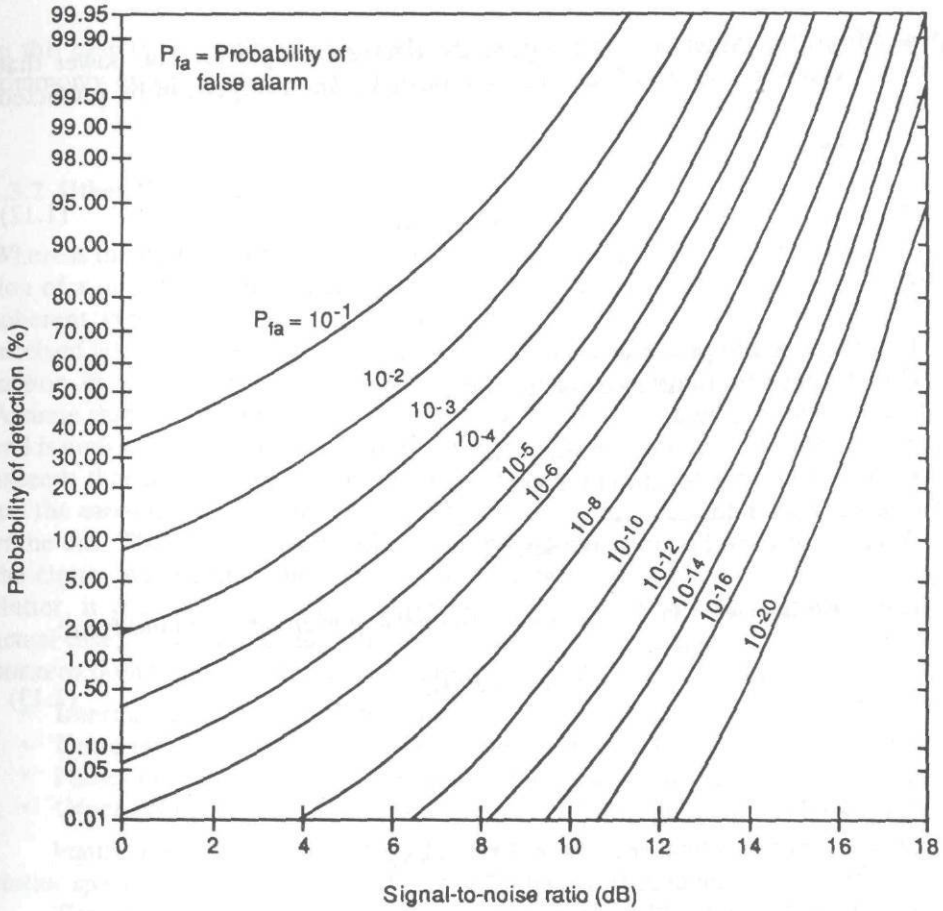

Figure 1.7 Probability of detection versus signal-to-noise ratio (after [6]).

description are required to fully determine the performance of a system in the presence of randomly varying interference. The probability functions are required to perform the P_d, P_{fa} analysis, and the spectrum is required to perform the analysis over the expected range of doppler (or induced-doppler) frequencies.

1.3.1 Thermal Noise

As mentioned above, determining the SIR will lead to the ability to determine the P_d and P_{fa} performance. This typically involves two steps: determining the received

power from the target and determining the interference power. The power that enters a receiver because of the energy reflected from a target can be predicted from:

$$P_r = \frac{P_t G^2 \lambda^2 \sigma}{(4\pi)^3 L_s R^4} \tag{1.12}$$

where:

P_r is the received power in watts,
P_t is the peak transmitted power in watts,
G is the antenna gain,
σ is the target RCS in square meters,
λ is the radar wavelength in meters,
L_s is the system losses, and
R is the range to the target in meters.

If the interfering signal is thermal noise, the noise power can be found from:

$$P_n = k\text{TBF} \tag{1.13}$$

where:

P_n is the noise power in watts,
k is Boltzmann's constant (1.38×10^{-23} W/sK),
T is the system temperature (usually 290 K),
B is the noise bandwidth in Hertz, and
F is the system noise factor.

Dividing (1.9) by (1.10) yields the SNR, applicable to a simple monochromatic pulse:

$$\text{SNR} = \frac{P_t G^2 \lambda^2 \sigma}{(4\pi)^3 \, k\text{TBFL}_s R^4} \tag{1.14}$$

The following expression is applicable to virtually all waveforms, in particular for pulse-compression systems, at the IF processor after the pulse compression process:

$$\text{SNR} = \frac{P_t G^2 \lambda^2 \sigma \tau}{(4\pi)^3 \, k T_0 F L_s R^4} \tag{1.15}$$

In this case the L_s term must include matching filter losses, as well as the other commonly experienced system losses.

1.3.2 Other Contaminants

Whereas the performance of a noncoherent radar system associated with the detection of a target is limited by the presence of thermal noise, the performance of a coherent system is limited by additional factors. The integrity with which the received vector can be described depends on the amplitude and the phase contamination in the system. To make the case, the following example is presented. Assume that a moving target of interest is in the field of view of the radar system and is embedded in a clutter environment where the amplitude of the clutter signal exceeds that of the target in the particular range bin. The coherent radar system has the capability to find the moving target by analyzing the doppler environment in the cell. The moving target will exhibit some doppler frequency component and the clutter will (ideally) not. Although the target amplitude is smaller than the clutter, it will appear in its own doppler bin and therefore be detectable. In the actual case, although the clutter is not moving, it will have spectral components in nonzero doppler bins due to several mechanisms. They are listed here.

- Internal motion of the clutter (natural spectral spread).
- Finite antenna or processing dwell time, limiting doppler resolution.
- Phase noise of the system, creating spectral spread of the stationary clutter.
- Other system contaminants that "spread" the spectrum of the clutter.

Figure 1.8 shows the effect of the spreading of the otherwise well-confined clutter spectrum into the passband of a typical MTI filter.

The effect of coherent system contaminants is not limited to the spectral spreading of clutter. Other effects that dominate the list of performance limitations are image signal generation; mainlobe signal loss, spreading, and frequency shift; and sidelobe increase (integrated and peak). Figure 1.9 shows a hypothetical doppler processor output. The mainlobe and sidelobe structure is annotated with these various features.

Figure 1.10 is a block diagram of a coherent radar system used for developing the ISAR image of a target, showing the potential source of contaminating elements that are discussed further in this book. In the system depicted, the synthesizer is used to develop the SFWF for the high-range resolution, and the target rotation is used to develop the doppler signal for the crossrange resolution. The error sources are denoted by italicized lettering near the components that are likely to introduce the contaminants.

The performance of such modern radar systems and the degree to which the target characteristics can be determined depend on the integrity of the coherent

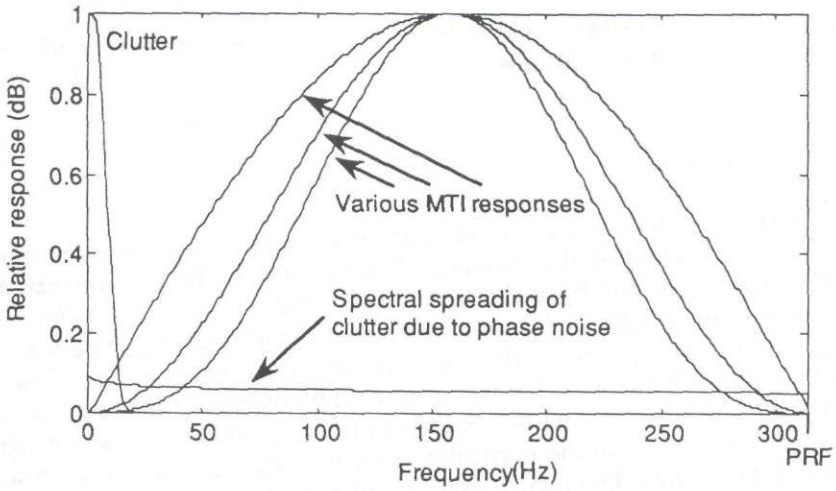

Figure 1.8 Frequency response of a typical MTI filter showing the effect of phase noise spreading the clutter signal across the PRF interval.

structure of the radar system. The performance of these systems is not necessarily limited by thermal amplitude noise, but rather, may be limited by the phase and amplitude effects of errors in the vector detection process.

A noncoherent system detects and processes only the amplitude of the received signal, without regard to the phase. The phase information is lost because (1) usually the phase of the transmitted signal is random and (2) there is no record (or reference) of the transmitted phase. A coherent system, on the other hand, "knows" the phase of the transmitted signal so that it can determine the phase and the amplitude of the received signal.

A moving target can be detected in the presence of a higher level clutter signal because it will exhibit a doppler frequency shift in the received signal, whereas the stationary clutter will not. The objective of the radar processor is to distinguish the sometimes small difference in doppler between a stationary and moving target. The major mechanism by which this detection process is limited involves the elements of the system that spread the spectrum of the stationary clutter into the frequency bins occupied by the target of interest. Because the clutter power is usually very large compared to that of the target of interest, it takes very little spreading of the clutter energy to mask the intended target. In addition to the internal motion (spectrum) of the clutter itself, the factors that cause the clutter power to occupy other than the first doppler bin are described below.

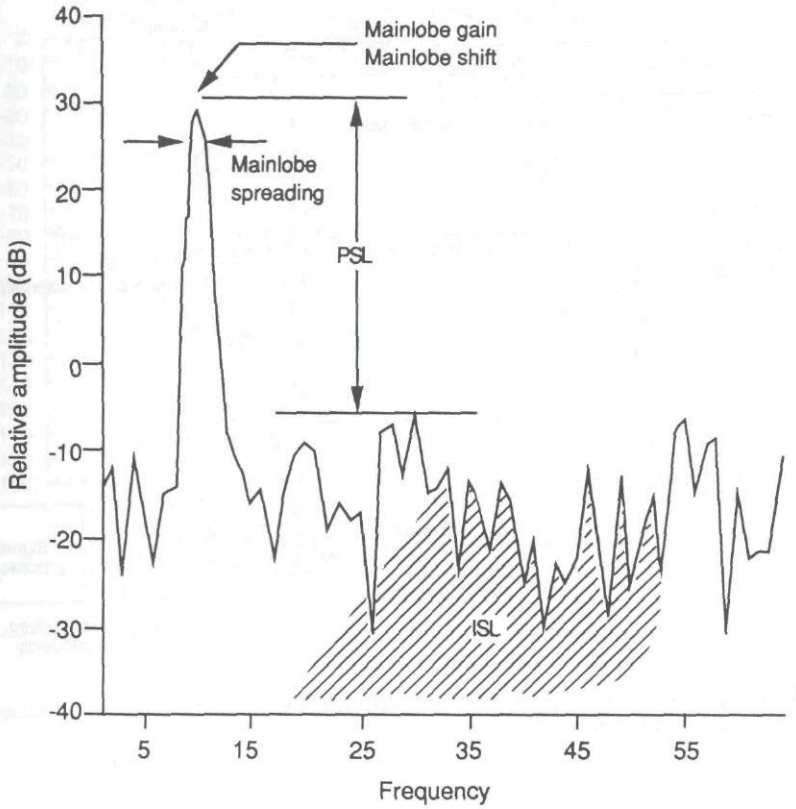

Figure 1.9 FFT response of a single target showing the measures of performance.

Phase Noise

In heuristic terms, phase noise is the characteristic of an oscillator (or amplifier) that relates the phase of the oscillator at a point in time to the phase it would have had if the oscillator were completely stable in phase (or frequency). In most coherent radar systems, the oscillator from which the transmitted signal is derived is the same oscillator that is used for the reference in the coherent detector process. Therefore, the phase error associated with the phase noise of that oscillator is directly responsible for a phase measurement error for any given sample.

Figure 1.11 depicts the phase noise in decibels below carrier in 1-Hz bandwidth as a function of frequency offset for a typical oscillator. Such a curve is normally supplied with an oscillator, as either a measured parameter (preferred) or as a not-to-exceed specification. The vertical axis is usually normalized to present the results

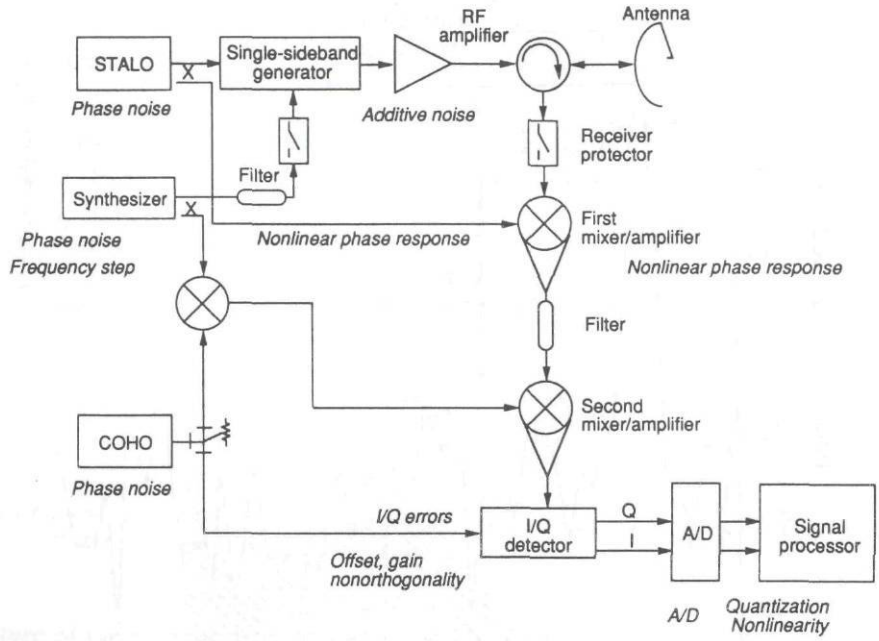

Figure 1.10 Block diagram of a typical coherent radar system showing the sources of contamination (in italicized lettering).

in a 1-Hz bandwidth, even though it is not measured in that bandwidth, nor is it usually used in that bandwidth. The phase noise must be multiplied by the system processing bandwidth in hertz to determine the net noise.

There are two effects that increase the phase noise of the system. If the oscillator signal is multiplied to some higher harmonic frequency, as in many systems, then the phase noise increases by the square of the frequency ratio. Also, if the system is a sampled system, such as with a pulsed radar or *continuous wave* (CW) radar using any received signal sampling, then the phase noise that extends beyond the sample rate (PRF) is folded back into the first PRF interval. The effect of this folding is to increase the phase noise at any offset frequency, as depicted in Figure 1.12. Chapter 2 discusses the methods for describing phase noise and the typical phase noise performance that can be expected from various oscillator configurations. Chapters 8, 9, 11, and 12 describe the effect of phase noise on various system architectures, and Chapter 14 describes the methods for testing oscillators for phase noise.

Phase noise is a measure of the variation of the phase of an oscillator relative to that of an ideal oscillator having a purely sinusoidal signal. The effect of such

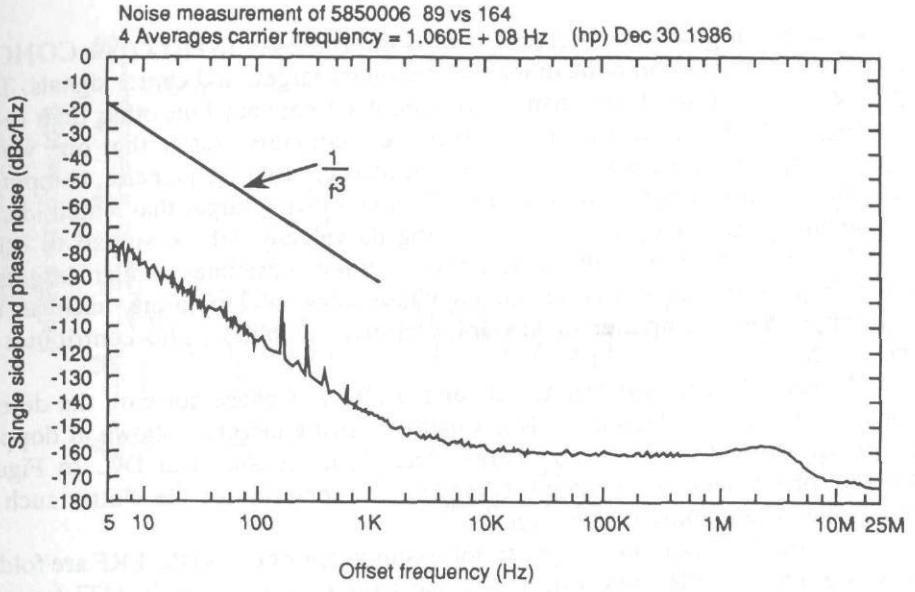

Figure 1.11 Typical phase noise plot.

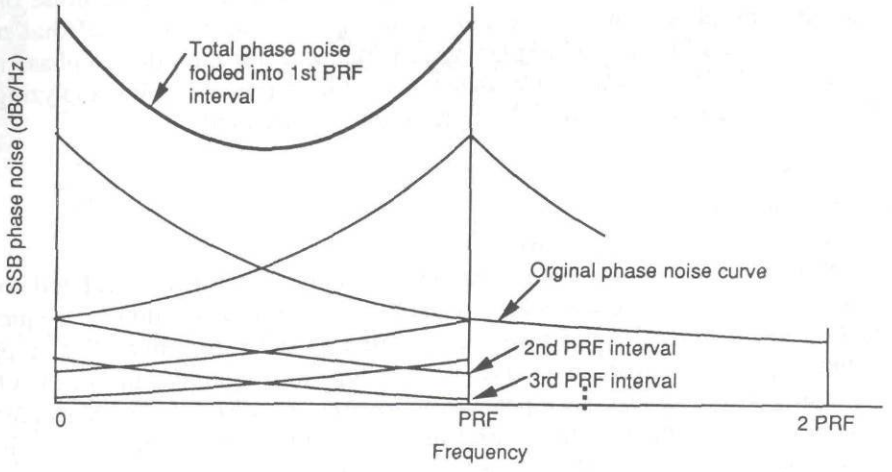

Figure 1.12 Effect of folding the phase noise spectrum.

perturbations in phase in a system's *stable local oscillator* (STALO) or COHO is to induce phase noise onto the otherwise stationary targets and clutter signals. This spreads the spectrum of such signals into doppler frequency bins other than those represented by the ideal signal. For example, stationary clutter that one would expect to appear in the first doppler bin is spread to other frequencies, competing with the targets of interest in those bins. A large moving target that would ideally appear in a single doppler bin representing its velocity will be spread to other bins, likewise competing with the detection of other, sometimes smaller, targets in those bins. The input-to-output added phase noise of amplifiers, such as the transmitter power amplifier or low-noise receiver amplifier, also contributes to this effect.

Figure 1.13 demonstrates the simulated effect of phase noise on the detectability of a target. In Figure 1.13(a), a pair of moving targets is shown at doppler frequencies of 110 and 150 Hz. Large ideal clutter is shown at DC. In Figure 1.13(b), phase noise is simulated, spreading the spectrum of the clutter such to reduce the detectability of the targets.

For low-PRF systems, the phase noise components beyond the PRF are folded to within the first PRF interval. This is most often experienced in MTI (usually low-PRF) systems. In high-PRF systems, the clutter is often range ambiguous; that is, clutter in cells other than that in which the target resides is folded into the target range bin. In medium-PRF systems, both of these effects must be considered in computing the phase noise effects. Finally, a mechanism that reduces the effect of phase noise occurs for targets that are at close range or low-doppler frequencies. If the same oscillator used for the STALO is used as the LO for the down-conversion process, then there is some degree of correlation between the phase noise on the target and the phase noise of the LO, reducing the total influence of that phase noise. A method for determining the improvement factor limit due to phase noise is given in Chapter 8, and in Chapter 9 a complete procedure for analyzing the effects of phase noise on a pulse-doppler radar is presented.

Phase Nonlinearity

In high-resolution imaging radar systems, the range resolution is related to the bandwidth. Target scatterers exhibit a phase rotation as a function of frequency, which allows a means to determine the relative position in range. The stepped-frequency process is sometimes used to develop the required bandwidth. Other techniques often employed are pulse compression and FMCW. These techniques all use a linear frequency sweep, and all assume that a scatterer at a particular range will exhibit a linear shift in phase for a linear frequency shift. Some of the frequency-dependent components in a radar system may not exhibit a linear phase

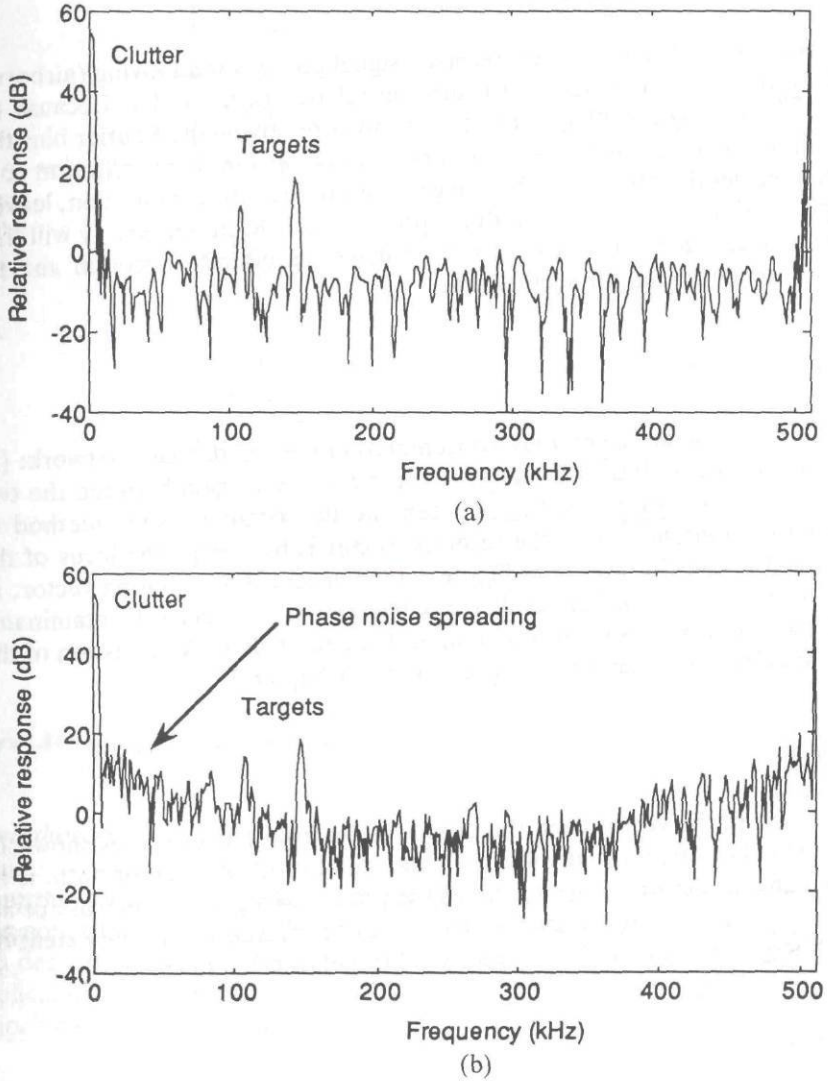

Figure 1.13 (a) Simulated targets in clutter. (b) Effects of phase noise on target detectability.

shift with frequency, most notably a bandpass filter. This nonlinear phase in the system will degrade scatterer amplitude and resolution, displace it from the proper position (doppler bin), and increase the sidelobe level. Chapter 6 discusses the effects of phase nonlinearity on FFT processor performance.

Motion and Motion Compensation

Because the coherent radar detects received signal phase, for a moving (airborne) radar all clutter (as well as targets) is moving relative to the radar. Because the process of eliminating the effects of clutter involves removing the Fourier bins that contain clutter energy, it is necessary to know which bins these are. Motion compensation involves the process of removing phase shift due to radar motion, leaving only target-motion-induced phase shift for processing. The clutter energy will then be in the zero-frequency bin. Chapter 7 discusses the effects of motion and the process for compensating for such effects.

I/Q Errors

Three types of errors are commonly encountered in the I/Q detector network: (1) DC offset of one or both of the channels, (2) imbalance of gain between the two channels, and (3) nonorthogonality between the two channels. One method of representing the time history of the received vector is by tracing the locus of the vector tip as it rotates, as shown in Figure 1.14. For an ideally rotating vector, as depicted in Figure 1.14(a), the result is a circle centered at zero. Contaminants cause a departure from this ideal situation, as discussed below. A discussion of the quantitative effects of these errors is presented in Chapter 3.

DC Offset

A displacement of the vector from the origin results from DC offset, as shown in Figure 1.14(b). The effect of DC offset in either the I or Q channel, or both, is to produce a signal in the zero-doppler bin of the processed signal. In the case of an ISAR image, it places a false scatterer at some range (maybe within the extent of the target) and at the center of rotation of the target in cross-range.

Gain Imbalance

If the gains of the two channels are not identical, resulting in a elliptical vector plot (shown in Fig. 1.14(c)) as opposed to the circular plot, then an image of each scatterer will result. The effect of a 3% gain imbalance in development of an image is about 35.5 dB below the real scatterer. The frequency of the image signal is the complement of the actual signal frequency; that is, the image is as far below the first PRF line as the signal is above it. The ellipse is either horizontally or vertically oriented, depending on the relative gains of I and Q.

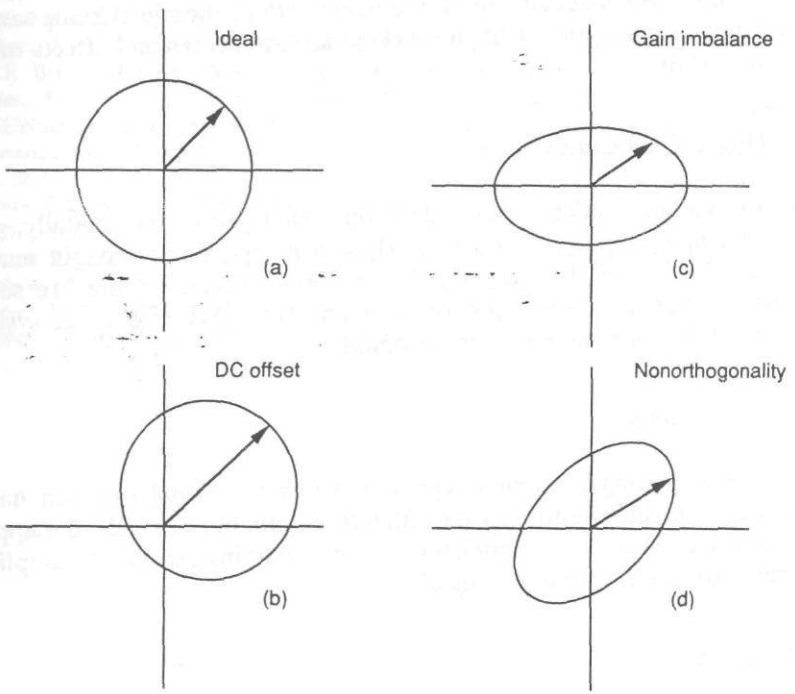

Figure 1.14 Locus plot of ideal target vector and the effects of I/Q errors.

Nonorthogonality

Nonorthogonality also produces an image of each scatterer. The image resulting from nonorthogonality is much the same as for gain imbalance. A nonorthogonality of 3 deg produces an image about 30 dB below the actual signal. Note that the elliptical pattern resulting from the nonorthogonality is oriented at 45 deg from a major axis, as shown in Figure 1.14(d).

Timing Jitter Effects

The performance of most coherent system applications and related processes depends on the fact that the transmitted signal is stable in amplitude and phase on a pulse-to-pulse or sample-to-sample basis. The same stability is required in the signal sampling process. The amplitude of the sampled signal can have a noise component added if there is jitter in the time at which the signal is sampled. The

amplitude of this noise is dependent on the bandwidth of the signal being sampled and the amount of time jitter. Chapter 4 discusses the causes and effects of such jitter in more detail.

Analog-to-Digital Quantization Effects

Because most modern radar systems perform signal processing digitally, these systems must employ *analog-to-digital* (A/D) converters. Some thought must be given to the selection of the proper A/D converter, because there are several mechanisms associated with the process that limit the performance of systems. Chapter 5 discusses these effects in more detail.

Amplitude Quantization

The process of digitizing an analog signal transforms a signal that can have a continuous range of values into a signal with a finite number of levels that approximate its true value. This process imparts a randomly varying error in the amplitude of the signal, equivalent to a noise signal.

Time Quantization

The A/D process occurs at discrete points in time, usually uniformly spaced at a rate sufficient to capture the events that are important to the system process. The sampling of the signal causes potential introduction of contamination in the frequency domain, the most obvious of which is signal aliasing or folding.

Saturation and Signal Dropout

If the signal into the A/D converter is too large relative to "full-scale" of the converter, then a situation equivalent to saturation can occur. On the other hand, if the signal into the converter is so small that no bits are excited, then a condition known as "signal dropout" will occur. Because there is often a wide range of values from the smallest signal to the largest clutter signal, care must be taken in scaling the A/D converter range correctly.

REFERENCES

[1] Harris, F. J., "On the Use of Windows for Harmonic Analysis With the Discrete Fourier Transform," *IEEE Proc.*, Vol. 66, No. 1, January 1978, pp. 51–83.

[2] Wehner, D. R., *High Resolution Radar*, Norwood, MA: Artech House, 1987, pp. 273–339.

[3] Currie, N. C., *Radar Reflectivity Measurement: Techniques and Applications*, Norwood, MA: Artech House, 1989, Chap. 10.
[4] Scheer, J. A., *Principles and Applications of Millimeter Wave Radar*, Edited by N. C. Currie and C. E. Brown, Norwood, MA: Artech House, 1987, Chap. 13.
[5] Nunn, E. C., and P. J. Smith, "Target Motion Resolution Capabilities," Technical Report STEWSID841, U.S. Army White Sands Missile Range, New Mexico, November 1984.
[6] Hovanessian, S. A., *Radar Detection and Tracking Systems*, Norwood, MA: Artech House, 1973, pp. 58.
[7] Eaves, J. L., and E. K. Reedy, *Principles of Modern Radar*, New York: Van Nostrand Reinhold, 1987, pp. 270–277.
[8] Barton, D. K., *Modern Radar System Analysis*, Norwood, MA: Artech House, 1988, p. 62.
[9] Slolnik, M. I., *Introduction to Radar Systems*, 2nd Ed., New York: McGraw-Hill, 1980, p. 28.
[10] Meyer, D. P., and H. A. Mayer, *Radar Target Detection, Handbook of Theory and Practice*, New York: Academic Press, 1973.

Chapter 2
Stability and Stable Sources

George W. Ewell
Georgia Institute of Technology

2.1 STABILITY

In Chapters 8 to 13, some requirements for stability (more correctly, but less frequently, referred to as instability) in a number of applications are outlined. In this section, the concept of stability will be discussed and formalized, and some measures that have been developed to provide analytic descriptions of stability will be presented. This section is largely based on several excellent references [1–5], and the reader is referred to these for additional detail.

A stable signal may be expressed as:

$$(A_o + \epsilon(t)) \sin (\omega_o t + \Delta\phi(t)) \tag{2.1}$$

where:

$\epsilon(t)$ = the amplitude variations, and
$\Delta\phi(t)$ = phase variations in the signal.

In general, $\epsilon(t)$ and $\Delta\phi(t)$ may be random processes, deterministic functions, or some combination of such functions. Of course, if the phase and amplitude in the time domain were completely known, the frequency spectrum of the signal would also be determined. In general, a highly stable signal that exists for an extended period of time would be represented in the frequency domain as a single line in the spectrum, whereas instability in such a signal (or a short observation time) would increase the width of this spectral line. A stable signal may be char-

acterized in either the time or the frequency domain; both types of signal stability characterizations are discussed in the following sections.

2.1.1 Time Domain Representation

If the frequency difference between the frequency of a waveform and a stable reference frequency is plotted as a function of time, a representation as shown in Figure 2.1 might be obtained. If the difference in frequency between such signals is measured using a frequency counter, a measure of the frequency stability would be obtained. If the change in frequency over an interval is defined as Δf, then the fractional stability may be defined as:

$$\frac{\Delta f}{f_o} \tag{2.2}$$

where f_o is the nominal reference frequency.

Measurement intervals might typically range from seconds to days. Representative values of fractional stability for high quality oscillators might be on the order of 10^{-10} to 10^{-13}.

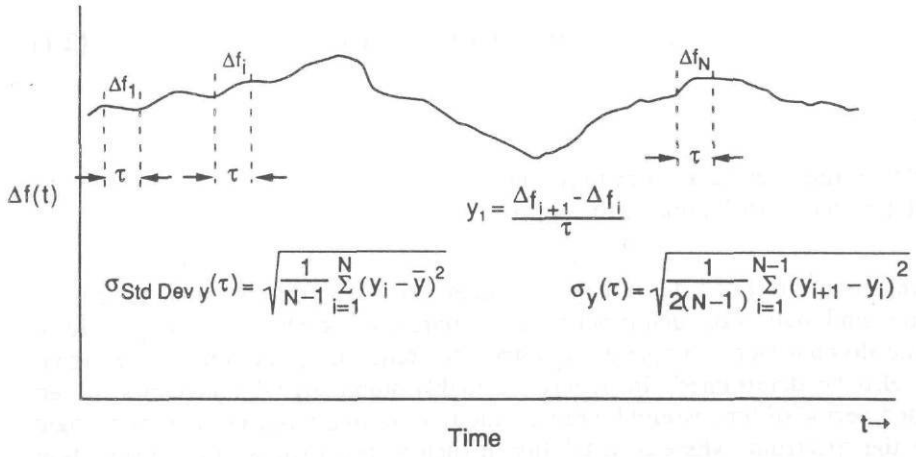

Figure 2.1 Time-domain representation of an unstable signal. Also shown are the calculation intervals for measurement of fractional frequency stabilities y_i. See text for additional details. (After [6].)

The measurement of fractional frequency variations as discussed above has a few fundamental problems, including the fact that such measurements may change with time. To accommodate such a situation, a measure of the fractional frequency stability, called the "Allan variance," has been developed; its square root is defined:

$$\sigma_y(\tau) = \left[\frac{1}{2(M-1)} \sum_{i=1}^{M-1} (y_{i+1} - y_i)^2\right]^{1/2} \tag{2.3}$$

where:

M = the number of points in the measurement,
y_i = the fractional frequency variation of the ith measurement, and
τ = the measurement interval.

Although frequently used, such a measure does not provide information that directly describes other features associated with frequency stability, such as the sideband structure.

2.1.2 Frequency Domain Descriptions

As discussed earlier, information describing the stability of a signal is included in its spectral shape. Of course, both amplitude and phase variations are included in such a description; however, in many cases of interest the effects of amplitude fluctuations are considerably less than the amplitude of the sideband power (or spectral spreading) associated with the phase fluctuations. In such cases, much information concerning the stability of the signal is contained in the spectrum of the received signal.

Considerable insight may be obtained into the relationship of spectral shape to the degree of phase modulation by considering the case for sinusoidal phase modulation of the waveform of (2.1) [7].

$$\Delta\phi(t) = \mu \cos(2\pi f_m t) \tag{2.4}$$

where:

$\mu = \dfrac{\Delta f}{f_m}$ for frequency modulation, and
$\mu = \Delta\phi$ for phase modulation.

The spectrum is given by:

$$S(f) = \frac{A_0^2}{2} \sum_{m=0}^{\infty} J_m^2(\mu)[\cos(-2\pi M f_m t) + \cos(2\pi M f_m t)] \tag{2.5}$$

If μ is small, only $M = 1$ will yield significant sidebands and:

$$J_1(\mu) \approx \frac{\mu}{2}, \quad \text{and} \quad S(f) \approx \left(\frac{A_0^2}{2}\right)\left(\frac{\mu}{2}\right)^2 \tag{2.6}$$

Under these conditions the ratios of carrier power to sideband power, P/P_c, become:

$$\frac{P}{P_c} = -20 \log_{10}\left(\frac{\Delta\phi}{2}\right) \text{ for phase modulation, and}$$

$$= -20 \log_{10}\left(\frac{\Delta f}{2f_m}\right) \text{ for frequency modulation.}$$

The one requirement for these particularly simple relationships to be valid is that the modulation index, μ, be sufficiently small [2]. This is normally satisfied if:

$$\mu < 0.01 \tag{2.7}$$

which in turn implies that the sideband levels be less than:

$$-20 \log\left(\frac{0.01}{2}\right) = -46 \text{ dB} \tag{2.8}$$

relative to the carrier for the above relationships to be valid; [2] suggests an even more stringent criterion.

In almost all instances of interest, the corrupting signal is not sinusoidal, but is a random process that is defined by its power spectral density (or its autocovariance). However, the relatively straightforward results of the above analyses for sinusoidal phase or frequency modulation may often be extended to the case for which the modulating signal is a random variable. This may be accomplished by

approximating the continuous spectrum by a series of sinusoids, each one having amplitude:

$$S(f)\Delta f$$

as illustrated in Figure 2.2 [8].

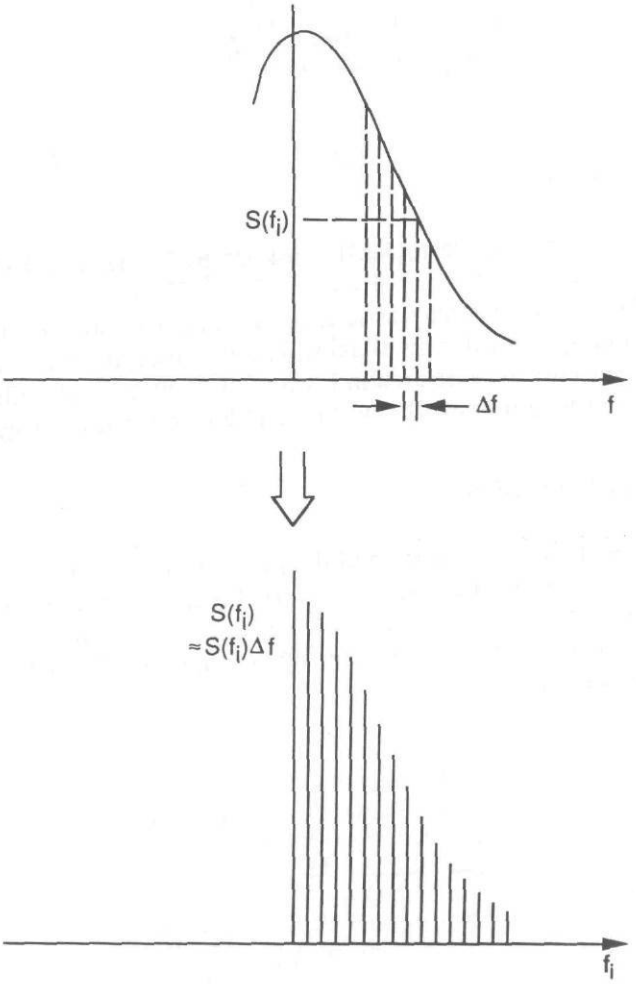

Figure 2.2 Approximation of a continuous spectrum by a series of sinusoids. This approach is often used in phase noise analysis.

A number of spectral-based measures of waveform stability have been developed, the more commonly accepted ones being given in Table 2.1.

Yet another descriptor of frequency stability is residual FM [9]. Residual FM may be defined as the total rms frequency deviation within a specified bandwidth. This is specified over a frequency band from f_a to f_b as:

$$\begin{aligned} \text{res FM} &= \int_{f_a}^{f_b} \sqrt{S_{\Delta f}(f)}\, df \\ &= \int_{f_a}^{f_b} \sqrt{\frac{f^2 S_\phi(f)}{B}}\, df \end{aligned} \tag{2.9}$$

where:

B = the measurement band, $f_b - f_a$.

Typical bandwidths are from 50 Hz to 3 kHz, 300 Hz to 3 kHz, or 20 Hz to 15 kHz.

Phase modulation of signals may arise from a number of sources and may possess different power spectral density shapes. These shapes are often approximated by various power laws as illustrated in Figure 2.3. Figure 2.3 also illustrates the conversion of these spectral shapes between the phase and frequency domains.

2.1.3 Time-Frequency Conversion

Assuming that the power spectral density and the phase of the spectrum are completely known, it is possible in principle to convert this information to the time domain to obtain complete time descriptions of the signals. In a similar manner, there is a conversion possible between time domain descriptions of signals and the frequency domain representations.

Table 2.1
Some Commonly Used Frequency Domain Stability Descriptors and Their Relationships

Descriptor	*Symbol*	*Units*	*Relationships*
Single sideband noise-to-carrier ratio	$L(f)$ or $S(f)$	dBc/Hz	See below
Spectral density of phase noise	$S_\phi(f)$	Radian^2/Hz	For small levels $S(f) = 10 \log_{10} (S_\phi(f)/2)$
Spectral density of frequency fluctuations	$S_{\Delta f}(f)$	Hz^2/Hz	$S_\phi(f) = S_{\Delta f}(f)^2$ $S(f) = 10 \log_{10}(S_{\Delta f}(f)/2f^2)$

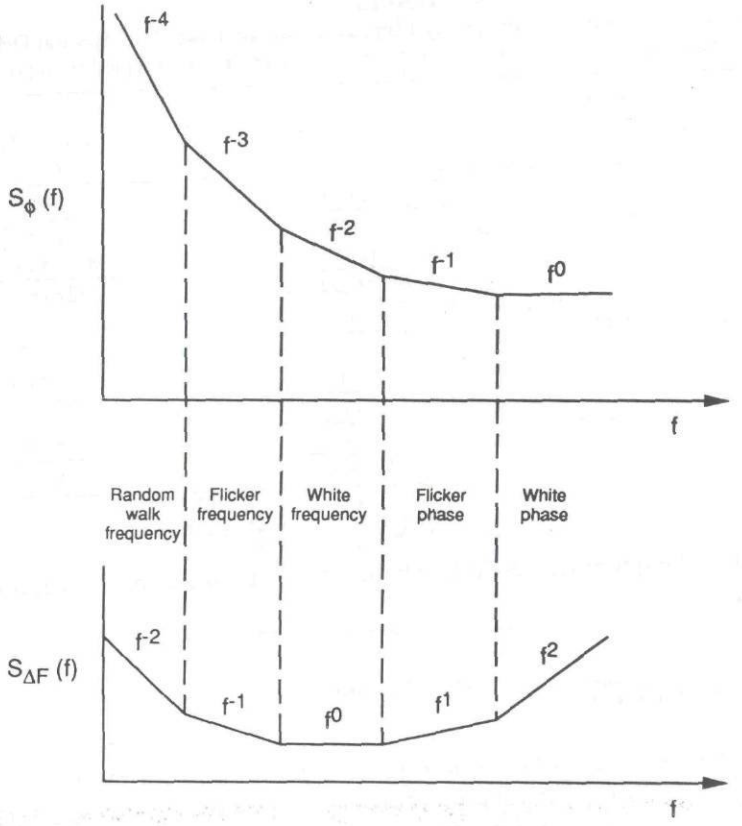

Figure 2.3 Power law dependencies for spectra of phase and frequency changes. See text for details. (After [2, 4].)

In practice, information is usually lost or subsumed into either the time or the frequency domain measurements. This loss of information often prevents direct conversion between the time and frequency domain descriptors of stability. In some instances, however, if knowledge concerning the underlying phase or frequency modulation process is assumed, such conversions may indeed be possible.

Table 2.2 presents the relationships between the time and the frequency domain representations of stability for various power law spectral density dependencies [10]. Because, however, the actual power spectral density may differ from, or be a combination of, several of these power laws, such conversions should be applied with care. The only certain procedure necessitates careful and appropriate

Table 2.2
Conversion from Time Domain to Frequency Domain for Integer Power Law Spectral Densities (f_h is the measurement bandwidth and t is the measurement time.) (Adapted from [10].)

Power Law Dependence, α, of Fractional Frequency Fluctuations, $(S_y(f))$	$S_{\Delta f}(f) = a\sigma_y^2(\tau)$ $a =$	$\sigma_y^2(\tau) = bS_\phi(f)$ $b =$
2	$\dfrac{(2\pi)^2\tau^2 f^2}{3f_h}$	$\dfrac{3f_h}{(2\pi)^2\tau^2\nu_o^2}$
1	$\dfrac{(2\pi)^2\tau^2 f}{1.038 + 3\ln(\omega_h\tau)}$	$\dfrac{[1.038 + 3\ln(\omega_h\tau)]f}{(2\pi)^2\tau^2\nu_o^2}$
0	2τ	$\dfrac{f^2}{2\tau\,\nu_o^2}$
-1	$\dfrac{1}{2\ln(2)\cdot f}$	$\dfrac{2\ln(2)\cdot f^3}{\nu_o^2}$
-2	$\dfrac{6}{(2\pi)^2\tau f^2}$	$\dfrac{(2\pi)^2\tau f^4}{6\nu_o^2}$

measurement of the quantities desired, whether they be time domain or frequency domain descriptors.

2.2 STABLE SOURCES

The generation of a signal of high stability may be a difficult technical challenge, and the difficulties may be increased by additional requirements such as tunability, shock and vibration, temperature extremes, power supply variations, and modulation capabilities, to name only a few. These discussions will center on oscillator-generated phase noise, because this is normally the dominant contributor to the sideband levels. Another source of phase noise, power supply-related phase variations, is not treated, because this is an application-dependent effect.

This chapter briefly discusses some of the generic types of oscillators and gives a simple model for phase noise generation in oscillators. Then, a number of sources are briefly discussed and representative phase noise levels commonly associated with each type of source outlined.

2.2.1 Oscillator Phase Noise Models [1–3, 11]

There are a number of types of oscillators that may be defined as an aid in categorization and analysis. Some of the more commonly used representations are given as Figure 2.4. In each case, the frequency-determining element is a resonant

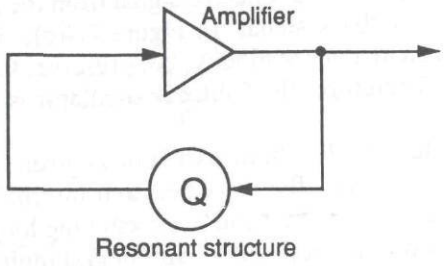

(a) Feedback oscillator

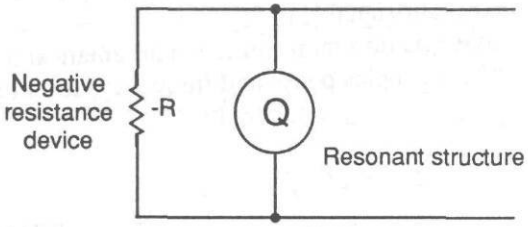

(b) Negative resistance oscillators

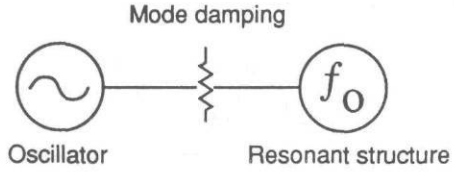

(c) External cavity stabilized

Figure 2.4 Some common representations of oscillator configurations. See text for details.

circuit of some description: a cavity resonator, a lumped constant resonant circuit, a dielectric resonator, or one of a number of other possible resonant structures.

Although they all appear different, all of the oscillator structures of Figure 2.4 may be considered a variant of the feedback oscillator of Figure 2.4(a). In the

configuration of Figure 2.4(b), the reflected signal from the resonant structure may be considered to be a feedback signal. In Figure 2.4(c), the external circuit and the oscillator interact in a manner to modify, but preserve, the feedback mechanism in the basic oscillator. Therefore, the feedback oscillator is the configuration most often analyzed.

A simplified model of a feedback oscillator is given as Figure 2.5, showing the feedback resonant structure, the amplifier, and internal additive phase noise. In any oscillator (1) the loop gain around the oscillating loop will be unity and (2) the net phase shift around the loop will be an integral multiple of 2π. If either of these conditions is not met, the operating conditions of the oscillator must change to establish this condition if oscillation is to continue. Referring to the simplified model of a feedback oscillator given as Figure 2.5 [11], when phase noise in the oscillator is included, then the dispersion relationship of the frequency-determining element is the means by which these phase noise modulations are converted to frequency fluctuations of the output signal [11, 12].

Converting the above concepts into more precise mathematical formulation, the dispersion relationship (which couples phase and frequency) for a tuned circuit is given by:

$$\Delta\phi = 2Qf/f_o \tag{2.10}$$

where:

$\Delta\phi$ = phase variations,
Q = Q of the resonant circuit,
f_o = resonant frequency of the resonant circuit, and
f = frequency of the signal.

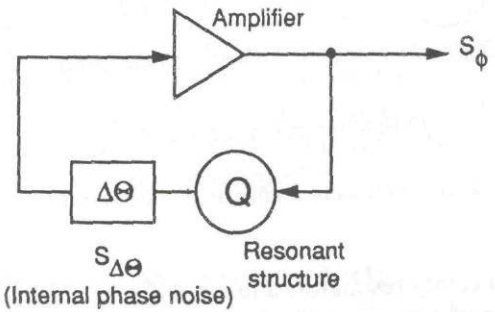

Figure 2.5 Simplified block diagram of a feedback oscillator. The oscillation condition must be that the loop gain is equal to unity and that the phase shift around the loop be an integral multiple of 2π [11].

Also from earlier discussions,

$$S_\phi(f_m) = \frac{S_f(f_m)}{f_m^2} \tag{2.11}$$

where:

f_m = the modulation or offset frequency.

Using the above relationships, the output phase noise may be predicted for various values of f_m. For low frequency offsets, well within the 3-dB bandwidth of the resonant circuit,

$$f_m < \frac{f_o}{2Q}, \quad \text{and} \quad S_\phi(f_m) = \left(\frac{f_o}{2Qf_m}\right)^2 S_{\Delta\phi}(f_m) \tag{2.12}$$

and for high frequencies, the resonant circuit will appear as an open circuit,

$$f_m < \frac{f_o}{2Q}, \quad \text{and} \quad S_\phi(f_m) = S_{\Delta\theta}(f_m) \tag{2.13}$$

An asymptotic expression for the output phase noise is given as [11]:

$$S_\phi(f_m) = \left[1 + \left(\frac{f_o}{2Qf_m}\right)^2\right] S_{\Delta\theta}(f_m) \tag{2.14}$$

This indicates that the phase noise spectrum of the internal noise of the oscillator is modified by (2.14). Typically, the internal phase noise is dominated by $1/f$ noise at low frequencies and by thermal noise at high frequencies. However, more complex variations are possible.

2.2.2 Transistor Oscillators

In the generalized feedback oscillator diagram of Figure 2.4(a) there are two key elements: the amplifier and the frequency-determining element. In many feedback oscillators the active amplifier is a transistor amplifier, either a bipolar or an *field effect transistor* (FET) device. The available noise figure of such transistor amplifiers varies with frequency from approximately 1 dB in the megahertz region to several dB at microwave frequencies. Perhaps as important as the thermal noise described by the noise figure is so-called flicker noise, which dominates at frequencies sufficiently close to the carrier [3, 13].

If a highly stable oscillator is desired, then a high-Q resonant element will be included as the frequency-determining element. In such cases, the oscillators are separately categorized and discussed based on the frequency-determining element. In some cases, such as phase-locked oscillators, the oscillator must be phase-lockable, and relatively low-Q resonant circuits may be employed; again, detailed discussion will be a part of the performance summary in the appropriate section that follows.

2.2.3 Crystal Oscillators

Inclusion of a piezoelectric crystal resonator in the feedback circuit of a transistor oscillator is one means of realizing a resonator for a feedback oscillator of high stability. The detailed characteristics of the crystal resonator are a function of a number of variables, including the source of the crystal, the direction of cut relative to the crystal structure, and the type of mounting of the crystal. Precision oscillators are often contained in temperature-controlled ovens (which may be quite small) and may be vibration isolated from their immediate environment.

An actual measured spectrum of a high-quality crystal oscillator is given as Figure 2.6. Several features are evident in such a representation that deserve brief mention. The first is a general monotonic decrease in phase noise with frequency that is characteristic of many oscillators. The second is the presence of spurious components that exceed this general background level; these components are often associated with power supply frequencies and local vibrations. The third is the leveling off of the phase noise variations at higher frequencies toward a uniform noise floor as predicted in [11]. When discussing spectra of stable oscillators, often only the general background levels are reported, and application-specific spurious components are omitted. This procedure is followed in this chapter.

Figure 2.7 summarizes the performance of a number of crystal oscillators of moderate stability. All of the phase noise spectra have been normalized to a nominal 10-MHz operating frequency. For oscillators operating at other than 10 MHz, this was accomplished by adjusting the reported phase noise by the square of the frequency ratio between 10 MHz and the reported frequency for the oscillator phase noise measurement. Note that although the low frequency noise differs for various oscillators, they all tend to approach a constant noise floor at higher frequencies.

In addition to providing a stable signal at a relatively low frequency, such oscillators are often used as frequency references for phase-locked oscillators or may be frequency multiplied to provide signals into the microwave region.

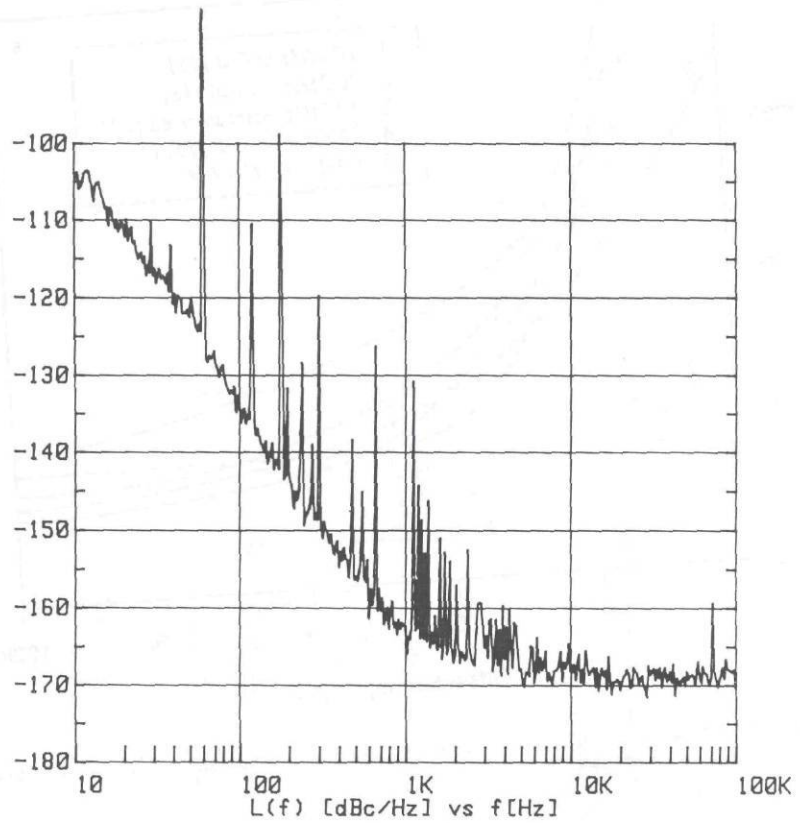

Figure 2.6 Measured phase noise spectrum of a highly stable crystal oscillator operating at a frequency of 100 MHz. Note the presence of line spectra (spurious), which in this case occur primarily at harmonics of the power line frequency. (Courtesy Brightline Corp. [14])

2.2.4 Saw Oscillators [19, 20]

Another frequency-determining element that may be used in a feedback oscillator is a *surface acoustic wave* (SAW) resonator. A schematic diagram of one such device is given as Figure 2.8, and its resultant phase noise is given as Figure 2.9. Considerable care is required to achieve these levels of phase noise [20]; although the upper limit for such a device is on the order of 500 MHz, the signal may be multiplied to X-band frequencies to produce highly stable signals. Also, it is possible to phase-lock these devices to achieve increased long-term stability if desired.

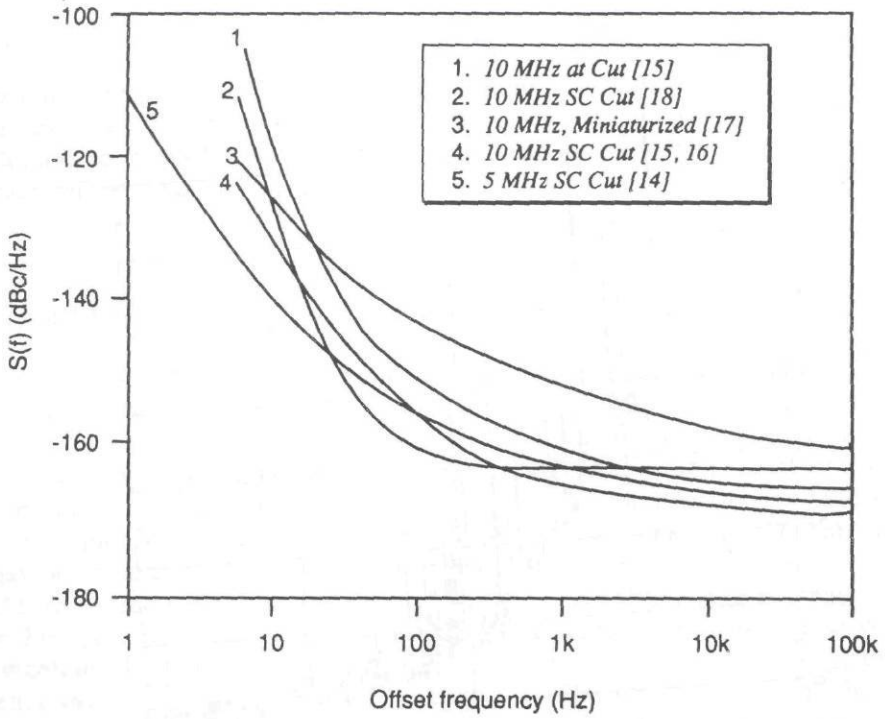

Figure 2.7 Phase noise of a variety of crystal oscillators, all of which have been converted to 10 MHz levels. See text for details.

It is interesting to compare the performance of the 500MHz SAW oscillator with that of the 100-MHz crystal oscillator of Figure 2.6, multiplied to 500 MHz. The multiplication by a factor of five increases the phase noise by 14 dB. Therefore, at 1-kHz offset the -163-dBc/Hz level of the crystal oscillator would correspond to -149 dBc/Hz when multiplied; this would be about 10 dB better than that of the SAW oscillator. The ultimate noise floor of the crystal of about -170 dBc/Hz would correspond to -156 dBc/Hz at 500 MHz, compared to -180 dBc/Hz for the SAW; thus, relative phase noise levels vary with frequency offset. Of course, when comparing sources, factors other than phase noise, such as temperature and vibrational sensitivity, should also be considered.

These SAW oscillators may be quite small. Figure 2.10 is a photograph of a signal source that combines a SAW oscillator with a frequency multiplier and filtering chain.

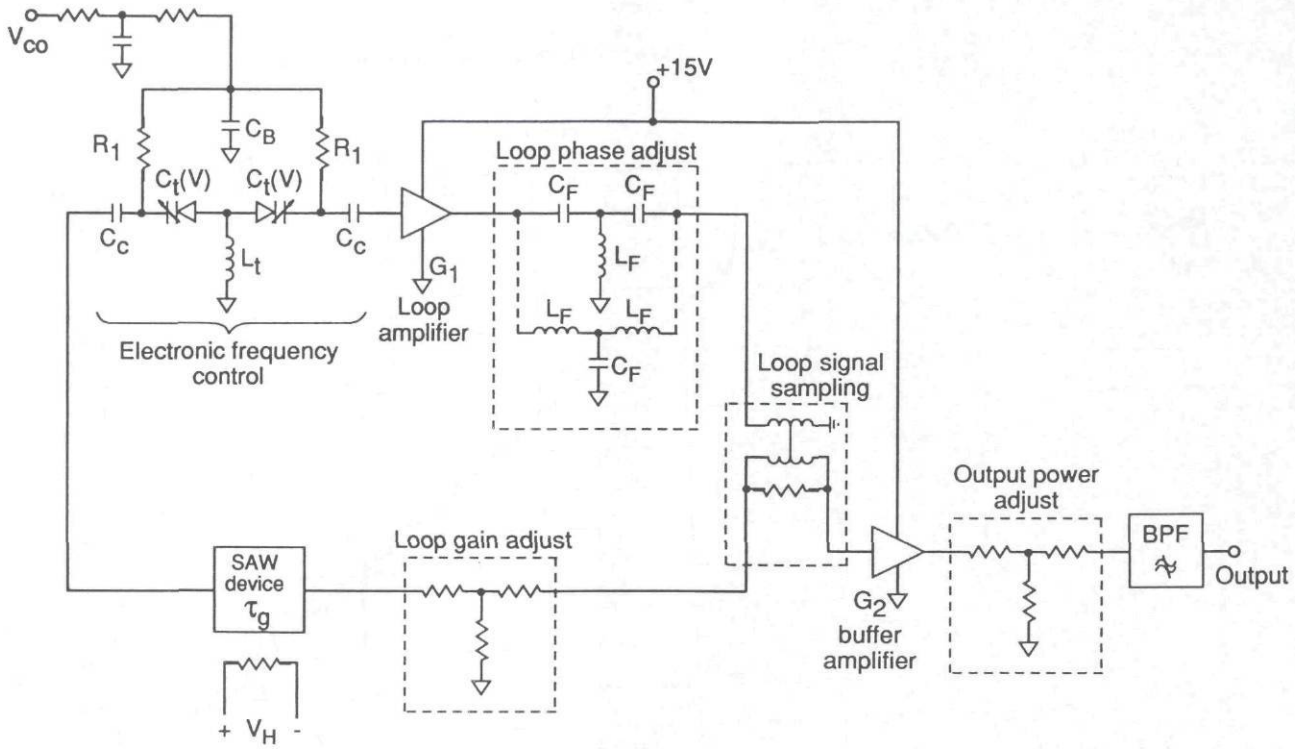

Figure 2.8 Simplified schematic diagram of a UHF SAW oscillator. (Courtesy Raytheon [21])

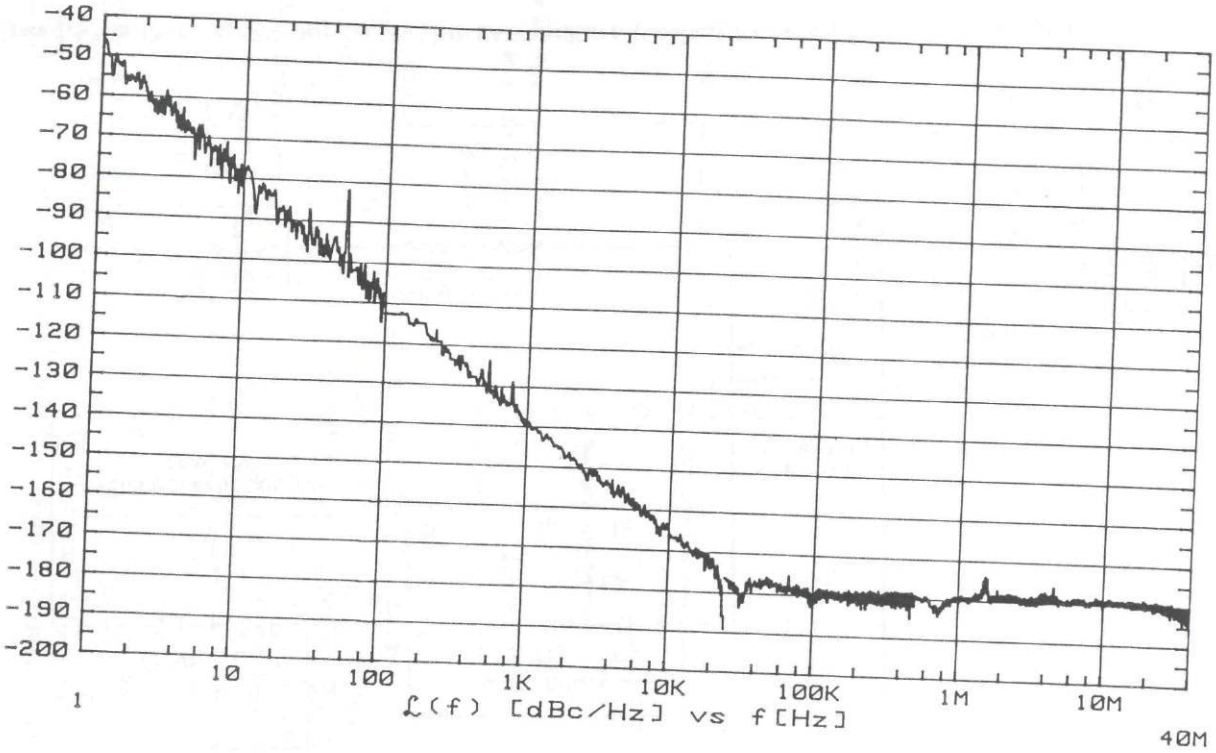

Figure 2.9 Phase noise of the oscillator of Figure 2.8 operating at 500 MHz. (Courtesy Raytheon [21])

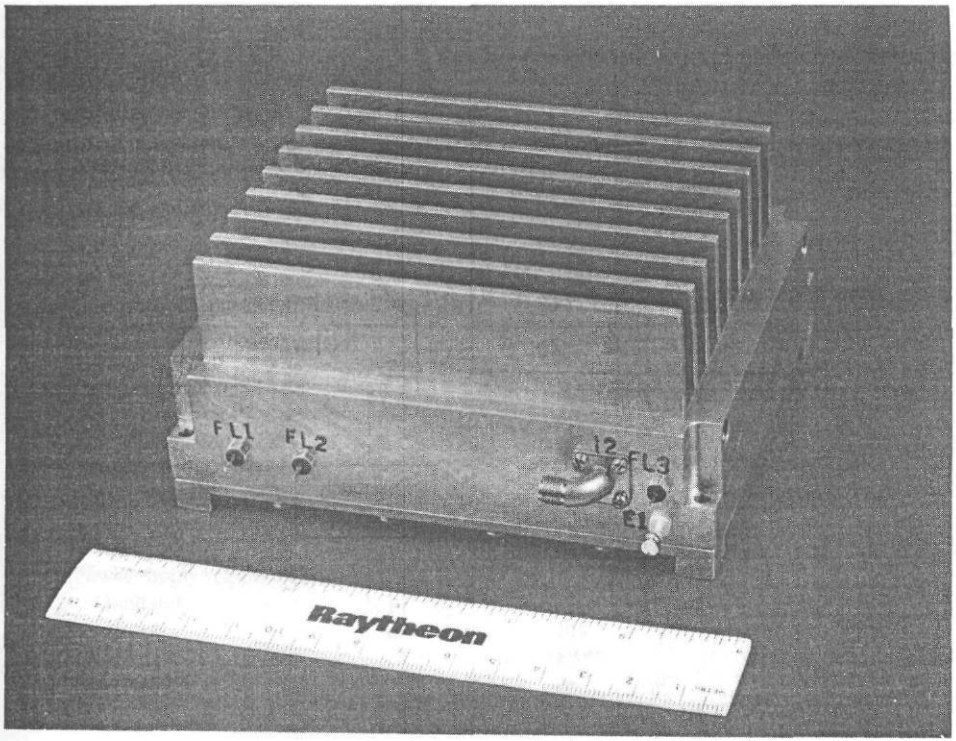

Figure 2.10 Photograph of a SAW oscillator and a frequency multiplier chain. (Courtesy Raytheon [21])

2.2.5 Dielectric Resonator Oscillators

The use of a dielectric resonator in the feedback circuit of a transistor oscillator, as shown in the schematic diagram of a *dielectric resonator oscillator* (DRO) in Figure 2.11, is another method of achieving high stability. The advantage of a dielectric resonator is its high Q relative to its size, permitting small, high-stability oscillators to be fabricated at relatively low frequencies. Because the resonator is small and has a high degree of rigidity, it may be relatively insensitive to shock and vibration.

As with any feedback oscillator, the phase noise levels of the DRO are strongly affected by the Q of the resonator. Conventional designs operate with low-order modes in the resonator and achieve performance similar to that shown in Figure 2.12.

If larger dielectric resonators are used, higher order resonant modes may be utilized, permitting higher Q and enhanced frequency stability. One such device uses an extremely pure sapphire crystal operating in the "whispering gallery" mode

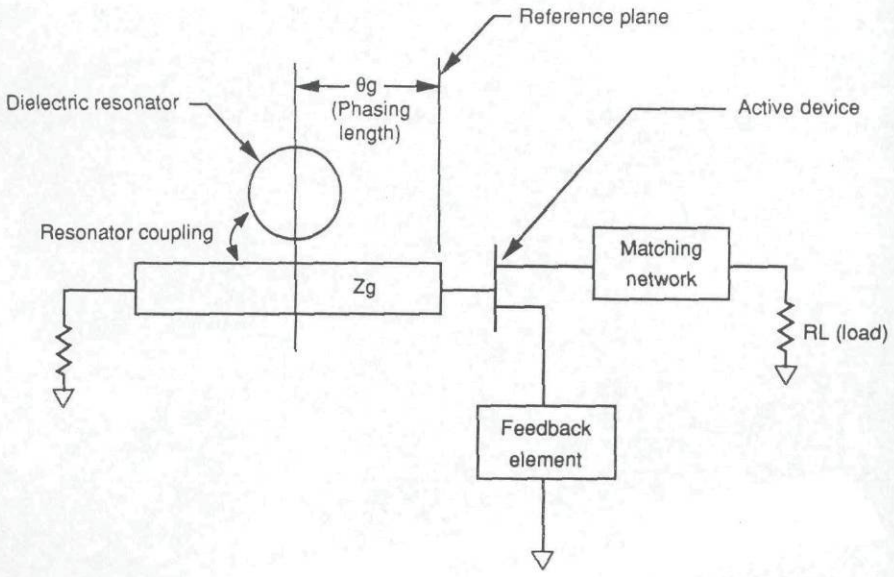

Figure 2.11 Simplified schematic diagram of a DRO. (After [22].)

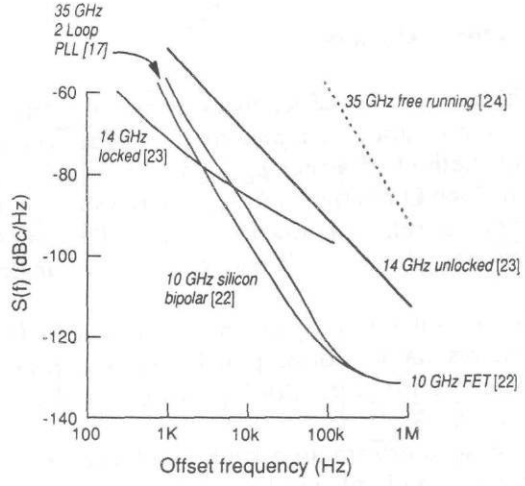

Figure 2.12 Phase noise of some representative DROs.

(a circumferential mode with $N = 19$) [25]. A summary of the characteristics of a similar oscillator is given as Table 2.3, and the phase noise associated with such an oscillator is given as Figure 2.13. Because of the large physical size of the resonator, such units may have substantial temperature and vibrational sensitivity. Nevertheless, these achieved phase noise levels are representative of some of the most stable room-temperature oscillators, regardless of type.

Table 2.3
Characteristics of B-M 5.410.031 Series Oscillators [26]

Parameter	*Value*
Output signal frequency	Any fixed value 2 to 12 GHz
Long-term frequency stability (−30 to 60 C)	2×10^{-4}
Fine frequency control	1×10^{-3}
Phase noise spectral density	−125 dBc/Hz, 1 kHz from carrier
Spurious signals	< −100 dBc
Output impedance	50 ohms
Output power	50 mW
Power supply requirements	
Oscillator	12V at 200 mA
Heater	19V
Mass	6 kG
Dimensions	20 × 17 cm

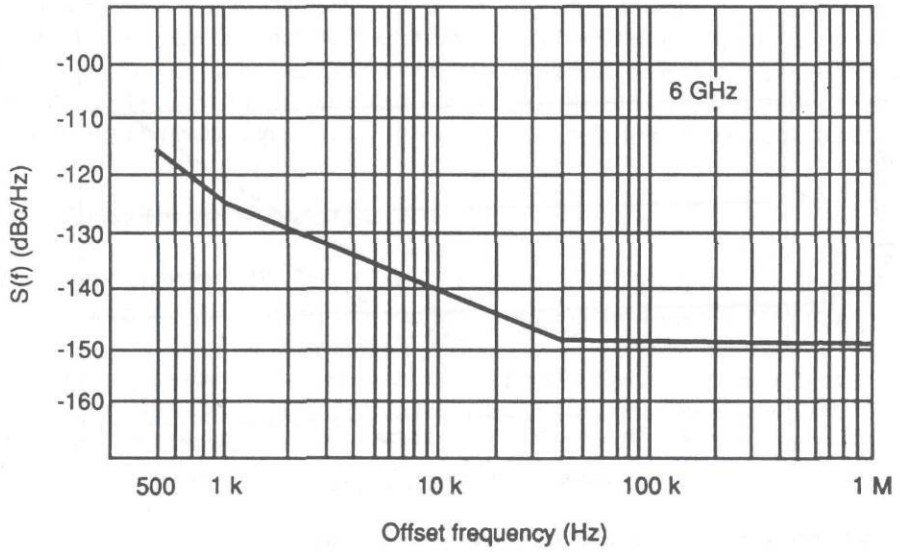

Figure 2.13 Phase noise of an extremely stable Russian DRO operating at 6 GHz. (After [26].)

2.2.6 YIG Oscillators

If a small sphere of *yttrium indium garnet* (YIG) is suspended within a resonant cavity and a magnetic field applied, a tunable resonator is obtained (i.e., the resonant frequency varies with magnetic field). If this tunable resonator is used as the resonant element of an oscillator, a YIG-tuned oscillator is realized. Such oscillators are usually employed where a high degree of tunability is desired, and such devices tend to have relatively high levels of phase noise.

Representative phase noise levels for one series of YIG oscillators are illustrated in Figure 2.14. The high phase noise levels are the price of tunability, and if less tunability is acceptable, somewhat lower phase noise levels may be obtained.

2.2.7 Gunn Oscillators

If a properly biased Gunn diode is placed in a resonant structure (which may be as simple as a length of shorted waveguide with an iris), oscillation may be obtained. The phase noise levels of such devices are relatively high, but if an external sta-

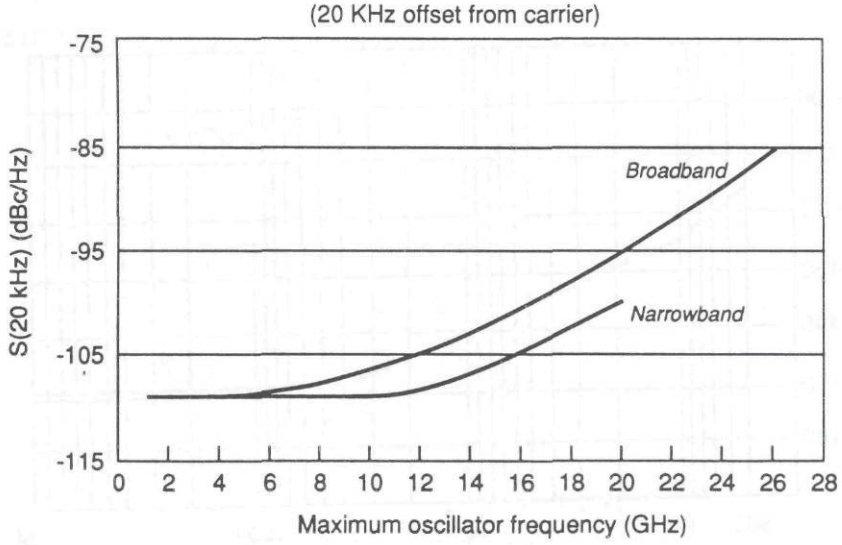

Figure 2.14 Representative phase noise of a family of YIG oscillators, measured 20 kHz from the carrier frequency. (After [27].)

bilization cavity is coupled to the resonator, increased stability may be obtained. The stability of such a Gunn oscillator is given as [28]:

$$\Delta f_{\text{rms}} = \sqrt{\frac{f_o^2 kTB}{Q_L^2 P_c} + \frac{\left(\frac{df}{dv}\right)^2 N}{f_m^{\alpha}}} \tag{2.15}$$

where:

B = bandwidth,
k = Boltzmann's constant,
T = absolute noise temperature,
Q_L = loaded Q,
P_c = carrier power,
N = excess noise constant (typically 1 x 10^{-7}/kHz),
α = 0.6 to 1.2,
df/dv = voltage pushing, and
f_o = output frequency.

Some representative results are given as Figure 2.15. As expected, achieving high values of Q is important, although df/dv may be a limiting factor. It is interesting to note that increasing P_c will reduce Δf, all other factors remaining constant. However, because the noise temperature of amplifiers tends to increase with output power, this needs to be carefully evaluated. Because the levels of phase noise are related to the Q of the stabilization cavity, the use of extremely high Q cavities, such as superconducting cavities, can yield extremely low phase noise levels [32].

2.2.8 Stable Klystron Oscillators

The reflex klystron was one of the first widely used microwave oscillators. The reflex klystron is not particularly stable, but if coupled to a high-Q cavity, a reasonably stable source is obtained [33].

In those cases where high stability is a prime requirement, a two-cavity klystron is often the choice [34]. The stability of a two-cavity klystron may be further enhanced by coupling it to an external high-Q cavity. Figure 2.16 summarizes the phase noise levels achieved with a number of stable klystron oscillators at X-band frequencies. The extraordinarily low values obtained by Mann and Blair [39] and by Golant [35] were obtained using a superconducting cavity as the stabilizing element.

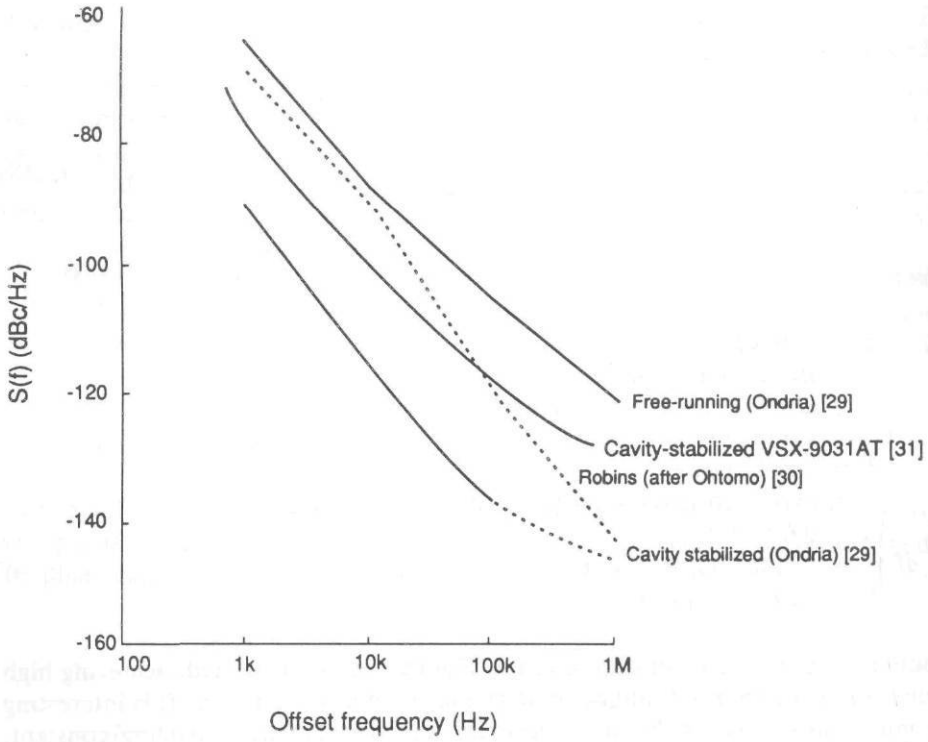

Figure 2.15 Phase noise for a number of X-band Gunn oscillators.

2.2.9 Frequency Multipliers

A stable low-frequency signal may be multiplied to a higher frequency signal using a nonlinear device such as a diode or a varactor to generate harmonics and a selective circuit to select the desired harmonic. In such a frequency multiplication process, the phase noise is increased, and this increase is due to at least two factors.

The first factor that contributes to the increase in phase noise is associated with the inherent increase in the modulation index during the frequency multiplication process. This produces an increase in phase noise by the square of the frequency multiplication ratio, N.

The second factor that contributes to additional phase noise in multipliers is additive phase noise. Figure 2.17 is a plot of additive phase noise for a particular series of commercial frequency multipliers [40].

Figure 2.18 is a block diagram of an oscillator-multiplier chain, using the SAW oscillator described in Section 2.2.4. Figure 2.19 is the phase noise associated

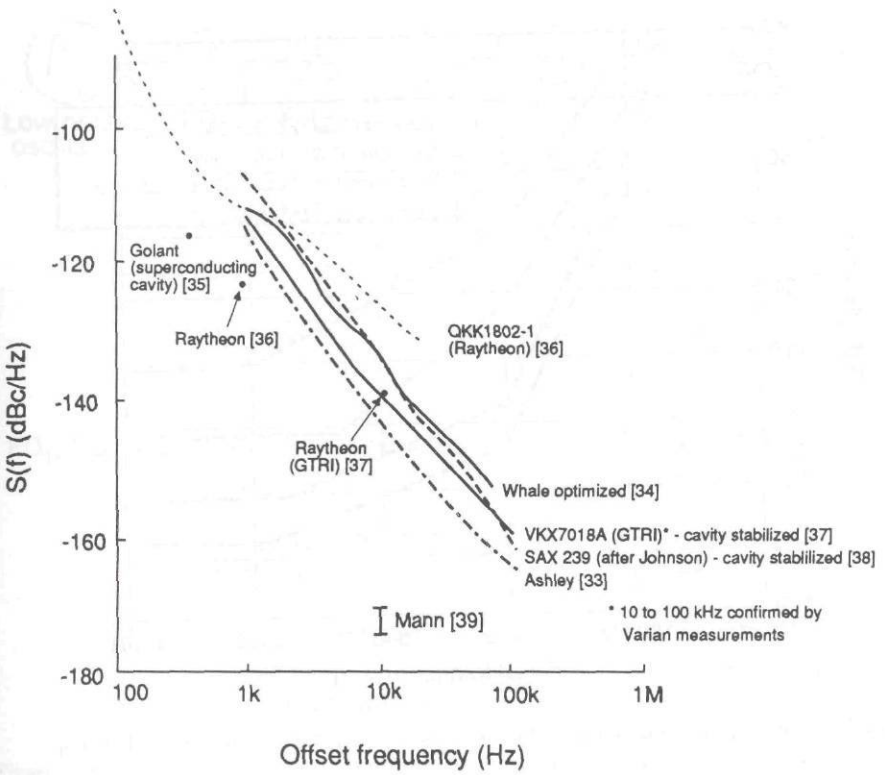

Figure 2.16 Phase noise levels achieved for a number of stable klystron oscillators operating at *X*-band frequencies.

with this oscillator-multiplier combination and evidences excellent stability at *X*-band frequencies.

The use of frequency multiplication provides an excellent method for transferring the excellent long-term frequency stability of low-frequency oscillators to higher frequencies. Unfortunately, the phase noise at higher offset frequencies may become excessive using this approach. The use of a phase-locked oscillator is one way of avoiding such a difficulty.

2.2.10 Phase-Locked Oscillators

As discussed earlier, multiplication of a low-frequency oscillator provides a signal with excellent low-frequency phase noise, but phase noise levels at frequencies far

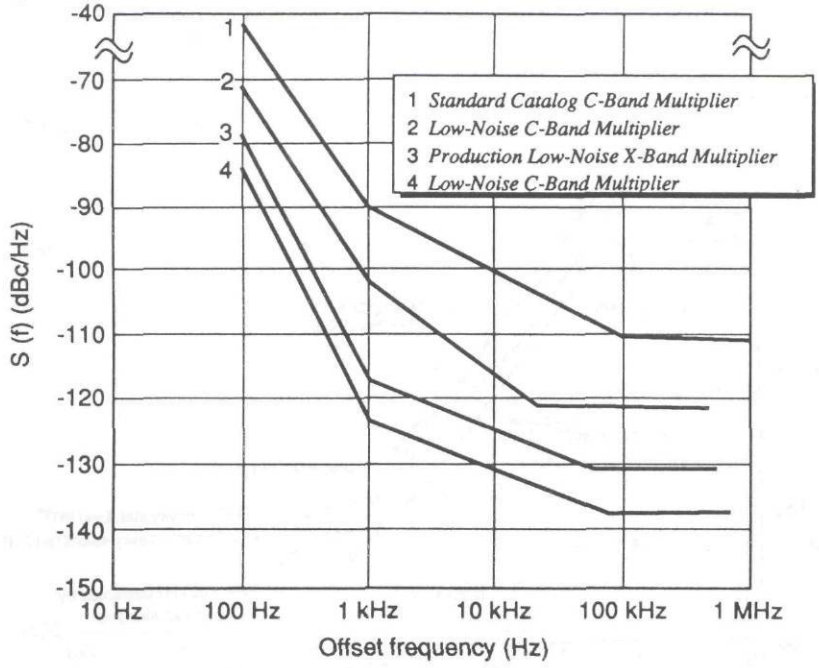

Figure 2.17 Additive phase noise for a number of classes of frequency multipliers. (After [40].)

removed from the carrier may be higher than free-running oscillators operating at these higher frequencies. This is illustrated in Figure 2.20, which shows the phase noise of a crystal oscillator multiplied to *X*-band and the phase noise of a free-running *voltage-controlled oscillator* (VCO) operating in the same frequency range.

Figure 2.20 illustrates that the multiplied frequency exhibits superior phase noise performance close to the carrier, but the VCO has lower phase noise for higher frequency offsets. One way to combine the best phase noise levels of both sources is by phase-locking the two together to form a *phase-locked oscillator* (PLO).

A simplified block diagram of a PLO is given as Figure 2.21. In such an arrangement the stability of the multiplied signal is transferred to the VCO for frequencies within the loop bandwidth of the phase-locking loop. The bandwidth of the loop is often chosen to be approximately equal to the frequency at which the phase noise of the VCO and the multiplied signal are equal. This will produce a composite phase noise spectrum, as shown in Figure 2.20. The degree of peaking of the phase noise curve near the crossover point is a function of the details of the response of the loop.

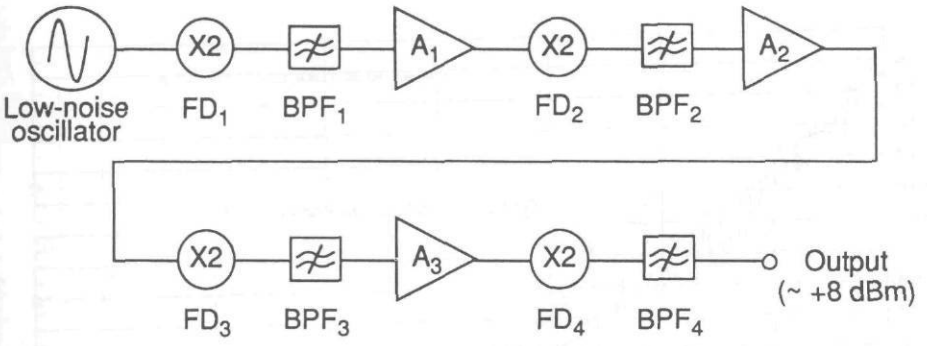

FD_1, FD_2, FD_3 : Watkins - Johnson FD25HC

FD_4 : Watkins - Johnson FD93HC

BPFs : 50% bandwidth, 12 section, tubular bandpass filter

A_1 : Watkins - Johnson A19-1

A_2 : Avantek APG-2001M

A_3 : Avantek APG-4002M

Figure 2.18 Block diagram of a frequency multiplier chain using the SAW oscillator described earlier, which multiplies 500 MHz to 8 GHz. (Courtesy Raytheon [21])

The composite curve of Figure 2.20 is illustrative of an excellent phase-lock loop that has been optimized for low phase noise performance. Other considerations such as operating temperature range, lock-in range, or speed of lock-in may degrade such excellent phase noise levels.

Figure 2.22 gives the phase noise levels for a number of different PLOs of the same general type operating at different frequencies. In general, the higher frequencies exhibit higher phase noise levels. This increase with frequency varies approximately as the square of the frequency, but there are small variations from such ideal behavior.

2.2.11 Direct Digital Synthesis

Recent advances in digital technology have permitted the implementation of direct digital synthesis (DDS) signal sources. Typically, a DDS may be implemented on

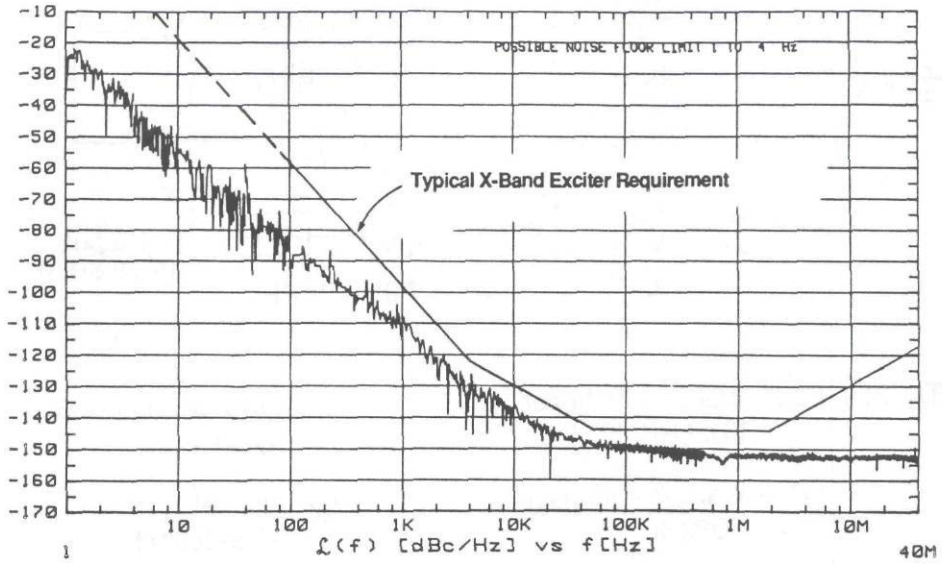

Figure 2.19 Measured phase noise at 8 GHz for the multiplier and oscillator described by Figure 2.18. (Courtesy Raytheon [21])

a single chip and may be configured as shown in Figure 2.23. Such an implementation directly synthesizes the waveform, filters the signal to remove undesired components, and may multiply the signal to a higher operating frequency. Table 2.4 summarizes the specifications of a single-package DDS source.

One of the limitations of a DDS may be spurious responses that are generated by such devices. The levels of such spurious signals are related to the number of bits used to generate the signal components. Representative values are usually given by a rule of thumb that the largest levels are approximately 9 dB/bit, with a floor of approximately 70 dB, regardless of the number of bits. Table 2.5 summarizes the results of digital simulations that support such approximations.

2.2.12 Frequency Conversion

Although not a frequency source, often two signals are combined through a mixing and filtering process to generate a new signal, as shown in Figure 2.24. Such an operation is often used to obtain a tunable or frequency-coded signal. In such an application, a high-frequency signal is mixed with a lower frequency coded or tunable signal; the resulting signal contains the sum and difference signals, as well

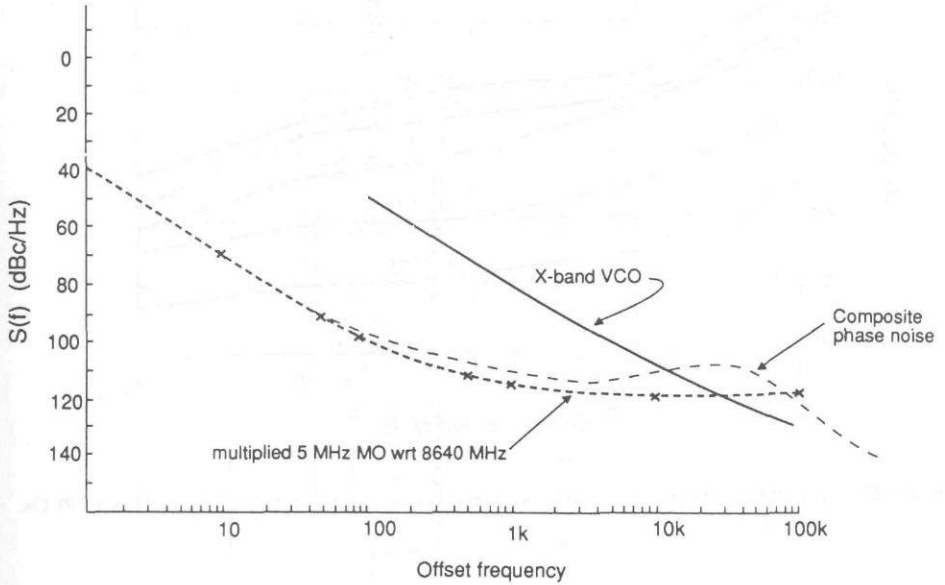

Figure 2.20 Phase noise of a multiplied crystal and a free-running VCO, both at *X*-band frequencies. Also shown is the composite phase noise achieved by phase-locking the VCO to the multiplied crystal output. (After [1].)

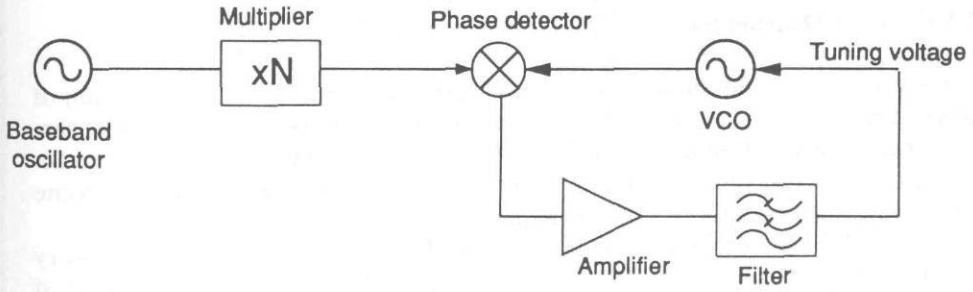

Figure 2.21 Simplified block diagram of a PLO (phase-locked loop).

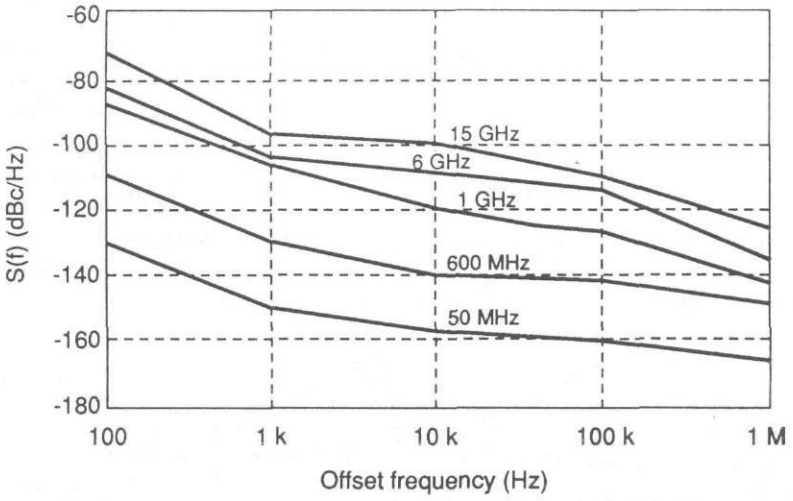

Figure 2.22 Representative phase noise levels as a function of frequency for a commercial line of PLOs. (After [41].)

as both of the original signals. The selected sideband is then selected by filtering of the desired signal.

Special consideration must be given to preserving the desirable phase noise levels during the mixing process. Conversion loss, local oscillator leakage, and distortion are all important considerations in implementing such an approach. The phase noises of the two sources combine at each offset frequency, adding powers if the signals are uncorrelated, and adding voltages if the phase perturbations are derived from the same source.

2.2.13 Noise Degeneration

In instances where the ultimate in noise performance is required, some version of noise degeneration may be used to further improve the low-frequency noise performance of a low-frequency oscillator. A Pound discriminator, the cryogenic-stabilized oscillator of Mann and Blair [39], and the noise degeneration of some CW radars are examples of this technique.

In [45], Banks provides an extreme example of the lengths that are necessary to achieve repeatable low phase noise performance. The system that was developed for CW radar applications is shown in block diagram form in Figure 2.25. The transmitted signal is sampled and applied to a microwave discriminator bridge. The

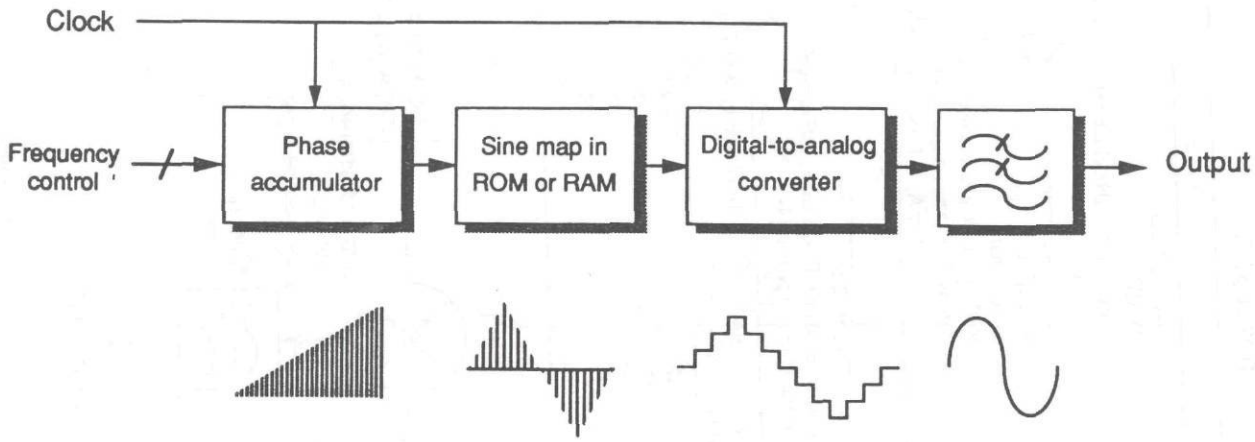

Figure 2.23 Simplified block diagram of a DDS signal source. (After [42].)

Table 2.4
Performance Specifications of a Commercially Available DDS Chip [43]

Parameter	*Value*
Frequency range	Over 11 MHz
Maximum clock rate	25 MHz
Frequency steps	5 mHz at 25 MHz clock rate
Switching speed	< 1 ms
Switching mode	Phase continuous
Output signals	Sine wave, 1 $V_{p\text{-}p}$
Amplitude control	11-bit binary
Phase noise	Reflects clock phase noise
Package	1-in by 1-in ceramic
Power requirements	+5V at 150 mA, −5.2V at 100 mA

Table 2.5
Amplitude of Largest Spurious Response as a Function of the Number of Bits [44]

No. of Bits	*Worst Spur Location (Harmonic Number)*	*Amplitude of Worst Spur (dBc)*
1	3rd	−9.5
2	9th	−18.1
3	19th	−25.5
4	43rd	−34.3
5	45th	−45.9

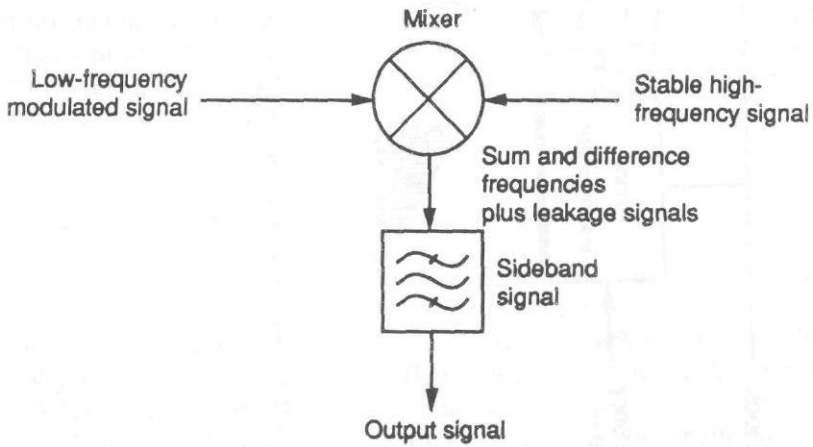

Figure 2.24 Simplified diagram of the mixing process. Mixing of two signals is often used in synthesizers and exciters to tailor signal characteristics to requirements.

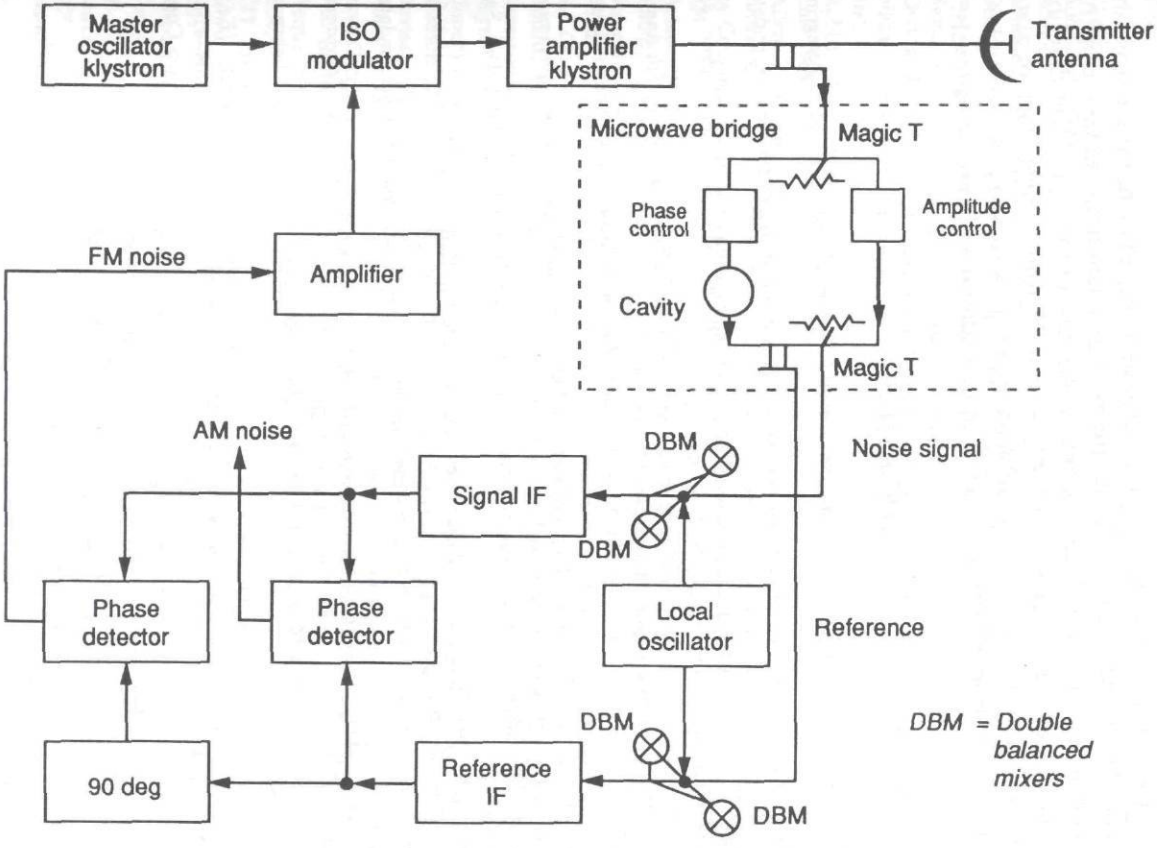

Figure 2.25 Simplified diagram of noise degeneration employed in a CW radar transmitter. (After [45].)

outputs from this bridge are then used to develop AM and FM correction signals that are then applied to appropriate points in the system to correct the distortions in the output.

If extremely low phase noise signals are to be achieved in the face of vibrations and similar disturbances, considerable care must be taken in the design, construction, and maintenance of such equipment. In the case of the equipment described in [45], the microwave bridge was not only machined from a single block of metal, the metal was even chosen for its vibration damping properties in order to minimize microphonic vibration, which could result in degradation in phase noise levels.

REFERENCES

[1] Robins, W. P., *Phase Noise in Signal Sources*, Second Edition, London, UK: Peter Peregrinus Ltd, 1984.

[2["Phase Noise," *Hewlett-Packard RF and Microwave Phase Noise Measurement Seminar*, undated notes.

[3] Parker, T. E., "Characteristics and Sources of Phase Noise in Stable Oscillators," *Proc. 41st Annual Frequency Control Symp.*, 1987, pp. 99–110.

[4] Howe, D. A., et al., "Properties of Signal Sources and Measurement Methods," *Proc. 35th Annual Frequency Control Symp.*, 1981, pp. A 1-A 47.

[5] Rogers, R. G., *Low Phase Noise Microwave Oscillator Design*, Norwood, MA: Artech House, 1991.

[6] Howe, D. A., et al., "Properties of Signal Sources and Measurement Methods," *Proc. 35th Annual Frequency Control Symp.*, 1981, p. A 11.

[7] Schwartz, M., *Information Transmission, Modulation, and Noise*, New York: McGraw-Hill, Section 3–9.

[8] Raven, R. S., "Requirements for Master Oscillators for Coherent Radar," *IEEE Proc.*, Vol. 54, No. 2, February 1966, pp. 237–243.

[9] "Phase Noise," *Hewlett-Packard RF and Microwave Phase Noise Measurement Seminar*, undated notes, p. 23.

[10] Howe, D. A., et al., "Properties of Signal Sources and Measurement Methods," *Proc. 35th Annual Frequency Control Symp.*, 1981, Table 11.1, p. A 36.

[11] Leeson, D. B., "A Simple Model of Feedback Oscillator Noise Spectrum," *IEEE Proc.*, February 1966, pp. 329–330.

[12] Sauvage, G., "Phase Noise in Oscillators: A Mathematical Analysis of Leeson's Model," *IEEE Trans. on Instrumentation and Measurement*, Vol. IM-26, No. 4, December 1977, pp. 408–410.

[13] Montress, G. K., "Residual Phase Noise Measurements of VHF, UHF, and Microwave Components," *Proc. 43rd Annual Symp. on Frequency Control*, 1989, pp. 349–359.

[14] Stone, C. S., Brightline Corp., personal communication, January 1990.

[15] Wenzel Associates, advertisement, *Microwaves and RF*, November 1990, p. 176.

[16] Wenzel Associates, advertisement, *Microwaves and RF*, February 1989.

[17] Ball, Efratom Division, "Ultra Stable, Miniature 10 to 10.23 MHz Crystal Oscillator," *Microwave Journal*, November 1990, p. 191.

[18] Piezo Systems, advertisement, *Microwaves and RF*, April 1987, p. 120.

[19] Montress, G. K., "Extremely Low Phase Noise SAW Resonator Oscillator Design and Performance," *Proc. 1987 Ultrasonics Symp.*, 1987, pp. 47–52.

[20] Parker, T. E., and G. K. Montress, "Low Noise SAW Resonator Oscillators," *Proc. 43rd Annual Symp. on Frequency Control*, 1989, pp. 588–595.
[21] Montress, G. K., Raytheon Research Division, Lexington, MA, personal communication, January 1990.
[22] Ho, C. Y. and T. Kajita, "DRO State of the Art," *Applied Microwaves*, Spring 1990, pp. 69–80.
[23] *Dielectric Resonator Oscillators*, Varian Product Data, 1984, p. 11.
[24] *Solid State Millimeter Wave Sources*, Varian Product Data Sheet.
[25] Abramov, S. L., et al., "A Low-Noise Self-Excited Microwave Oscillator with a Thermally Compensated Disk Dielectric Resonator," *Radiotekhnika*, No. 11, 1988, pp. 81–83.
[26] B-M 5.410.031 Product Data Sheet, NPO "VEGA-M", Moscow, Russia.
[27] Microsource Inc., product data, *Microwave Journal*, July 1990, p. 14.
[28] Sweet, A. A., "Noise in Gunn Oscillators," Ph. D. Thesis, Cornell University, Ithaca, NY, 1970.
[29] Ondria, J. G. and T. R. Turlington, "Feedback Control Analysis of Microwave Oscillator Stabilization with A Transmission Cavity," *G-MTT Int. Microwave Symp. Digest*, May 1970, pp. 166–169.
[30] Robins, W. P., *Phase Noise in Signal Sources*, Second Edition, London, UK: Peter Peregrinus Ltd, 1984, p. 91.
[31] Allen, S., Varian, personal communication, 1989.
[32] Jimenez, J. J., et al., "Attainment of a Low-Noise High-Power and Highly Stable Gunn Oscillator by Coupling to a Superconducting Cavity," *IEEE Proc.*, Vol. 61, No. 1, January 1973, pp. 123–124.
[33] Ashley, J. R., and C. B. Searles, "Microwave Oscillator Noise Reduction by a Transmission Stabilizing Cavity," *IEEE Trans. on Microwave Theory and Techniques*, Vol. MTT-16, No. 9, September 1968, pp. 743–748.
[34] Whale, A. V., "A Klystron Oscillator Having Low Frequency Modulation Sideband Noise," *5th Int. Conf. on Microwave Tubes*, Paris, September 1964.
[35] Golant, M. B., et al., "Klystron Oscillator for The Three-Centimeter Range, Stabilized by a Superconducting Resonator," *Pribory Tekh. Eksper.*, No. 3, 1969, p. 232.
[36] Raytheon product data.
[37] Unpublished measurements by the author at the Georgia Tech Research Institute, 1988.
[38] Johnson, S. L., "Noise Spectrum Characteristics of Low-Noise Microwave Tubes and Solid-State Devices," *IEEE Proc.*, Vol 54, No. 2, February 1960, pp. 258–265.
[39] Mann, A. G. and D. G. Blair, "Ultra-Low Phase Noise Superconducting-Cavity Stabilized Microwave Oscillator with Application to Gravitational Radiation Detection," *Journal Physics D* (GB), Vol. 16, No. 2, February 14, 1983, pp. 105–113.
[40] Frequency Sources, Inc., advertisement, *Microwave Systems News*, Vol. 21, No. 11, November 1982, p. 1.
[41] CTI, Product Data Sheet.
[42] Edwin, A., "Direct-Digital Synthesis Applications," *Microwave Journal*, January 1990, pp. 149–151.
[43] Scitec Electronics Inc., DDS-1 Frequency Synthesizer Data Sheet.
[44] Kerins, W., "Spur Levels in Multiple-Bit DRFMs," *Journal of Electronic Defense*, January 1991, pp. 49–54.
[45] Banks, D. S., "Continuous Wave (CW) Radar," *Electronic Progress*, Vol. 17, No. 2, Summer 1975, pp. 34–41.

Chapter 3
Effects of I/Q Errors

James A. Scheer
Georgia Institute of Technology

As introduced in Chapter 1, the received vector is often detected using a network that detects the component of the received vector that is in phase with the coherent reference oscillator, the I component, and the component that is in quadrature with the coherent reference, the Q component. These two components describe the received vector. The relationships between these two components and the amplitude and phase of the signal are provided in Chapter 1.

There are some errors that can develop from nonideal circuit components in the I/Q detector that affect the radar system performance [1, 2]. These errors can be summarized by the following: gain imbalance between the I and Q components, nonorthogonality between the I and Q components, and dc voltage offset in either the I or Q component or both. This chapter provides a quantified description of the errors that develop from such nonideal components.

3.1 IDEAL I/Q DETECTION

Referring to Figure 1.4, the I and Q outputs of the coherent detector are given by:

$$I = A \cos \Phi$$
$$Q = A \sin \Phi$$

where:

A is the amplitude of the received vector, and
Φ is the absolute phase.

Combining the two in exponential notation yields:

$$Ae^{j\Phi} = A \cos \Phi + Aj \sin \Phi \tag{3.1}$$

For an ideal vector rotating at ω_d, the real component is represented by:

$$A \cos \phi = \frac{A(e^{j\phi} + e^{-j\phi})}{2} = \frac{A}{2} e^{j\omega_d t} + \frac{A}{2} e^{-j\omega_d t} \tag{3.2}$$

the spectrum of which has an $A/2$ component at $-f_d$ and an $A/2$ component at $+f_d$, and the imaginary component is represented by:

$$A \sin \phi = \frac{A(e^{j\phi} - e^{-j\phi})}{2j} = \frac{A}{2j} e^{j\omega_d t} - \frac{A}{2j} e^{-j\omega_d t} \tag{3.3}$$

the spectrum of which has an $-A/2j$ component at $-f_d$ and an $A/2j$ component at $+f_d$.

When the spectra of $A \cos \Phi$ and $Aj \sin \Phi$ are summed, the result is a component of amplitude A at $+f_d$ and 0 at $-f_d$ and an impulse spectrum at f_d. This represents an ideal case, with no I/Q errors, and a perfectly rotating vector.

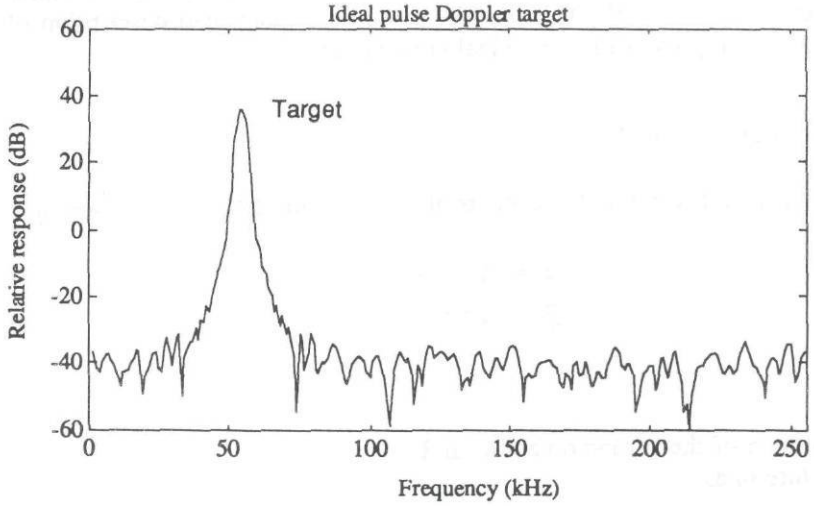

Figure 3.1 Simulated ideal FFT response.

Figure 3.1 shows the FFT response of an ideal vector with no I/Q errors, for a single target at a fixed doppler frequency offset of about 50 Hz.

3.2 GAIN ERROR EFFECTS

If the sine and cosine components have an arbitrarily different gain, denoted by the subscripted amplitude factors, A_c and A_s, then the more general expressions for the two components are:

$$A_c \cos \phi = \frac{A_c(e^{j\phi} + e^{-j\phi})}{2} = \frac{A_c}{2} e^{j\omega_d t} + \frac{A_c}{2} e^{-j\omega_d t} \tag{3.4}$$

which produces a spectral component of $A_c/2$ at $-f_d$, and $A_c/2$ at $+f_d$, and:

$$A_s \sin \phi = \frac{A_s(e^{j\phi} - e^{-j\phi})}{2j} = \frac{A_s}{2j} e^{j\omega_d t} - \frac{A_s}{2j} e^{-j\omega_d t} \tag{3.5}$$

which produces a spectral component of $-A_s/2j$ at $-f_d$ and $A_s/2j$ at $+f_d$.

If the two gains are related by $A_s = A_c(1 + \epsilon)$, then vector summing of the positive frequency $(+f_d)$ component yields an amplitude of $A(1 + \epsilon/2)$ (representing very little error if ϵ is small) and an amplitude of $-\epsilon/2$ at $-f_d$. This is an undesired signal at the image frequency because of the gain mismatch. Figure 3.2 shows the effect of a 3% gain mismatch between the I and Q channels. Given a 256-kHz PRF (sampling frequency), notice that there is a false target (image) at a frequency as far below the sample rate as the real target signal is above zero. In the limit, if the imaginary (or the real) part were to go to zero gain, the FFT would have equal sideband signal levels, as would be the result for a real FFT.

3.3 EFFECT OF NONORTHOGONALITY

Recalling (3.2) and substituting $\Phi = \omega_d t + \alpha$:

$$A \cos \phi = \frac{A(e^{j\omega_d t + \alpha} + e^{-j\omega_d t + \alpha})}{2} = \frac{A}{2} e^{j\omega_d t} e^{j\alpha} + \frac{A}{2} e^{-j\omega_d t} e^{-j\alpha} \tag{3.6}$$

The $A/2e^{+j\alpha}$ and $A/2e^{-j\alpha}$ terms determine the amplitudes and the $e^{j\omega_d t}$ and $e^{-j\omega t}$ terms determine the frequency, giving rise to, when the cos spectrum is added to the j sin spectrum, an amplitude of $(A/2)(1 + e^{j\alpha})$ at $+f_d$ and $(A/2)(1 - e^{-j\alpha})$ at

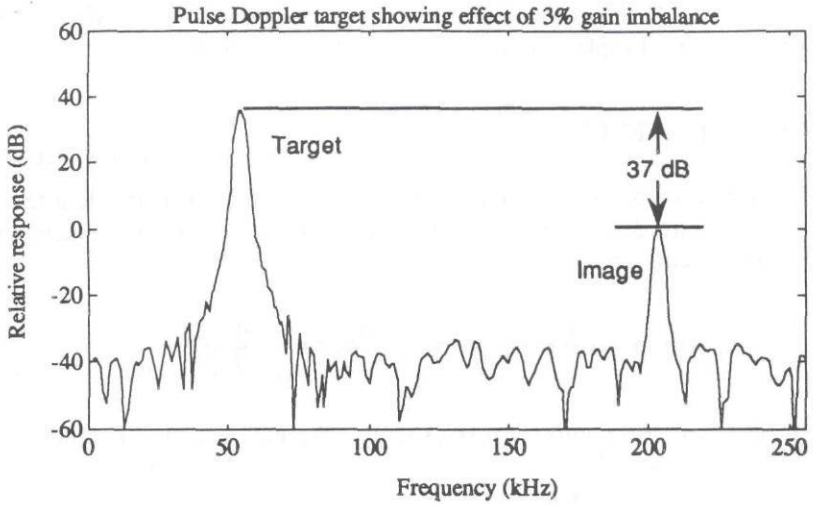

Figure 3.2 Simulated FFT response showing effect of 3% gain imbalance.

$-f_d$. This again represents an undesirable response at the image frequency of $-f_d$. Figure 3.3 shows the effect of a 3-deg nonorthogonality.

3.4 DC OFFSET

In a similar, but less complex fashion, the effect of dc offset in the *I*/*Q* detector will produce a dc term in the frequency response, the amplitude of which is directly proportional to the dc offset level and the number of samples processed. For example, if the dc offset produces a single sample count of 3 with no signal present, and the processor processes 16 pulses (samples), then the resulting dc-related count will be 48, assuming the output is not normalized to the input or some other reference. Figure 3.4 shows the effect of a dc offset in the I channel, the amplitude of which is 3% of the full-scale amplitude. Notice the resulting dc response in the spectral plot.

3.5 QUANTITATIVE EXAMPLES

The effects on the performance of systems due to these errors is to introduce an apparent signal at the processor (FFT) output, whose amplitude depends on the amplitude of the real signal and the degree of imbalance in the detector. The introduction of these unwanted responses will either cause the data processor to

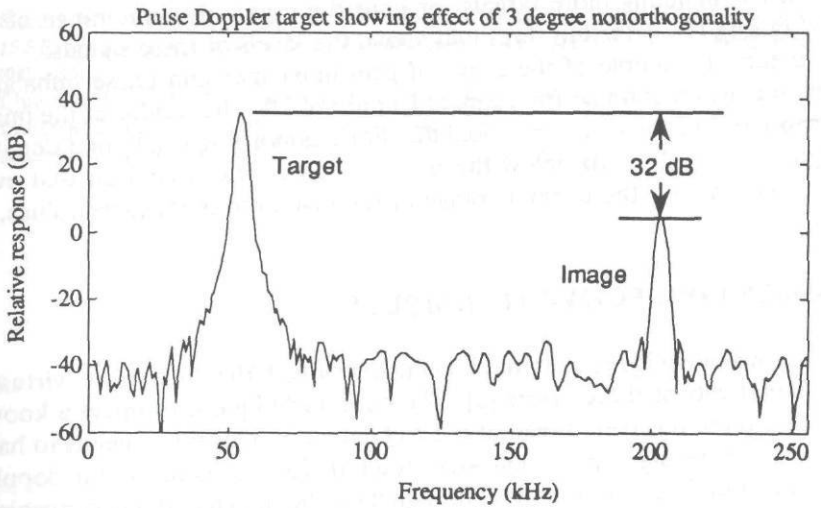

Figure 3.3 Simulated FFT response showing effect of 3-deg nonorthogonality.

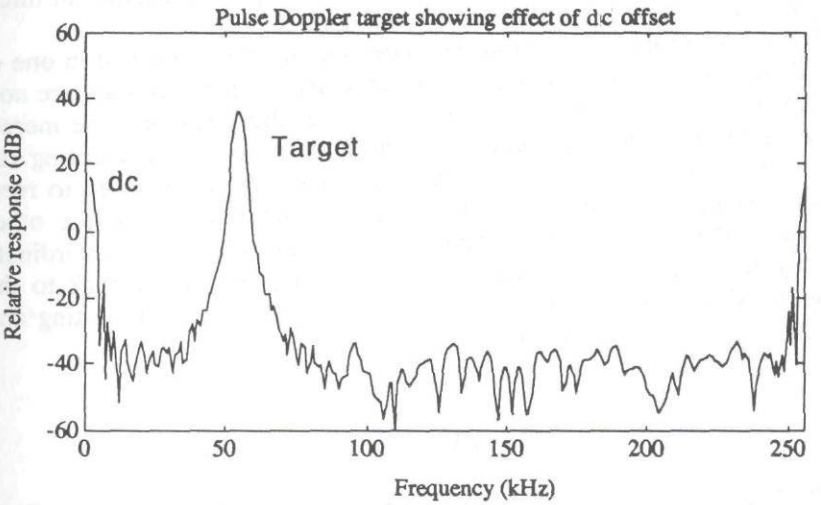

Figure 3.4 Simulated FFT response showing effect of dc offset.

"work" harder, handling more targets, or limit the usable dynamic range of the system by raising the detection threshold above the levels of these signals.

A numerical example of the effect of gain imbalance and phase imbalance (nonorthogonality) shows that for a gain imbalance of 3%, the residue at the image frequency is 0.015 of the peak, or −36.5 dB. For a nonorthogonality of 3 deg, the image signal is only 31.6 dB below the peak response. It can be seen that even modest errors can limit the dynamic range of the system to inadequate values.

3.6 POSSIBLE CORRECTIVE TECHNIQUES

There are some techniques that have been developed that reduce or virtually eliminate the effects of these errors [3]. The basic technique is to inject a known ideal signal into the receiver, ahead of the I/Q detector. This signal needs to have a synthesized doppler signature of known characteristics. For example, the doppler frequency and amplitude are known. The signal can be injected at any convenient time when the processor is not in use, such as at antenna turnaround or between coherent dwells. Depending on the drift expected of the circuits, the correction may not need to be performed very often.

The synthetic signal is processed through the FFT processor and the result is analyzed. A response in the zero frequency bin of either the I or Q component in the output results from a dc offset in the respective I/Q circuit. A response at the image frequency of the injected signal represents a gain imbalance or nonorthogonality, or both. The relative phase of the image signal provides sufficient information to resolve the gain-nonorthogonality ambiguity.

Correction of errors identified in the detectors may be performed in one of several methods. For instrumentation systems in which the received data are normally recorded for offline calibration and processing, the errors may be merely stored in a calibration file. Corrections can be applied to the data during the calibration process. For operational systems, the data may be corrected to reestablish gain balance (by applying a gain correction factor to one or the other channel) and orthogonality (by converting the vector to the spherical coordinate system, applying the phase correction, and reconverting the vector back to the rectangular coordinate system, if desired). Further discussion of the testing and calibration techniques appears in Chapter 16.

REFERENCES

[1] Monzingo, R. A., and S. P. Au, "Evaluation of Image Response Signal Power Resulting From I-Q Channel Imbalance," *IEEE Trans. on Aerospace and Electronic Systems*, Vol. AES-23, No. 2, March 1987, pp. 285–287.

[2] Sinsky, A. I., and P. C. Wang, "Error Analysis of a Quadrature Coherent Detector Processor," *IEEE Trans. on Aerospace and Electronic Systems*, Vol. AES-10, No. 6, November 1974, pp. 880–883.

[3] Churchill, F. E., G. W. Ogar, and B. J. Thompson, "The Correction of I and Q Errors in a Coherent Processor," *IEEE Trans. on Aerospace and Electronic Systems*, Vol. AES-17, No. 1, January 1981, pp. 131–136.

Chapter 4
Timing Jitter Effects

James A. Scheer
Georgia Institute of Technology

The processes associated with a coherent radar system are affected by any jitter in the time at which the received signal is sampled or A/D converted, apart from the time and amplitude quantization effects themselves. As much as the system designer tries to avoid jitter in the timing circuits of a radar system, there inevitably will be some. There are several sources for timing jitter, as listed here:

Clock timing jitter (T_c);

Pulse-forming network timing jitter (T_p);

Transmit delay jitter (T_{tr});

A/D timing jitter (T_{ad}).

Though the timing pulses that are developed to provide the commands for certain events all are usually derived from a common clock, there is some jitter in the relative time at which the various pulses are generated. For example, the common clock that is used to develop all of the timing signals may have some short-term instabilities itself.

The relative times at which various timing pulses are generated can vary, due usually to thermally generated amplitude fluctuations in the logic threshold voltages. There is usually some delay between the time that the transmitter is "told" to transmit and the time that the transmit pulse is actually generated. The sources for this delay are the pulseforming networks (high-power modulator circuits for thermionic (tube type) transmitters) or pulse modulators for the solid-state transmitters. Not only is there some transmit delay, but the delay varies from pulse to pulse. If the circuits that develop the sample timing are such that they "think" that the transmitter developed its pulse at a consistent time, then the sample time will experience the time jitter that is on the transmit pulse. To avoid this situation,

some system designs are such that the transmit RF energy is sampled and detected to provide the reference for the transmit time. In some cases this can reduce the amount of timing jitter on the sampler, but there will always be some uncertainty in this timing technique as well.

When this timing jitter exists, there exists an attendant sample-to-sample variation in the sampled signal amplitude, related to the bandwidth of the signal and the amount of time jitter. If the time jitter is large relative to the rise time of the signal, then there will be a lot of amplitude variation. The spectrum of the amplitude variation is related to the spectrum of the original signal and the distribution of the time jitter.

Figure 4.1 shows the effect of sample timing jitter on the sampled video or baseband signal, demonstrating the generation of amplitude jitter as a result of timing jitter. The amount of amplitude scintillation depends on the location of the sample time relative to the video signal and the slope (related to the bandwidth) of the video. The following discussion relates to the statistical properties of this.

Figure 4.2 depicts several places in the timing diagram of a system at which timing jitter components may occur. The figure demonstrates the jitter in the transmit command, actual transmit delay time due to the pulse-forming network and other circuit elements, the resulting jitter in the received target signal time, and the sampler timing jitter.

Once all of the sources of timing jitter have been identified, the composite timing jitter must be determined. Normally, because the mechanisms for creating the jitter are random, though some may be systematic, the composite timing jitter, δ_t, will be a gaussian random process having zero mean. The composite is found

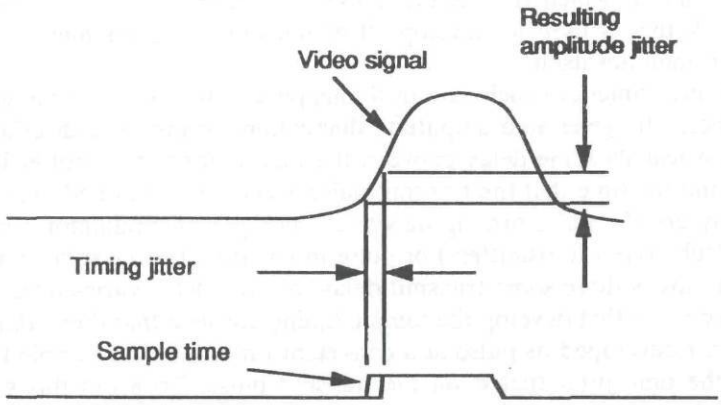

Figure 4.1 The effect of timing jitter on sampled signal amplitude.

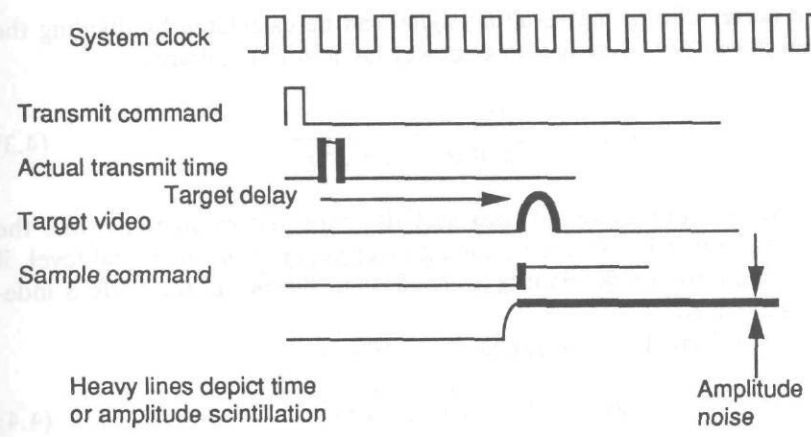

Figure 4.2 Sources of timing jitter in typical radar system timing circuits.

from the individual contributors by combining them in an rms fashion, as given below.

$$\sigma_t^2 = \sigma_{tr}^2 + \sigma_p^2 + \sigma_c^2 + \sigma_{ad}^2 + \cdots \tag{4.1}$$

If a video signal has a signal bandwidth of $B/2$, assuming that the timing jitter is small, as defined by:

$$\delta_t \ll 1/B$$

then the variation in amplitude in the sample process is given by:

$$\delta_A = A\pi B\delta_t \tag{4.2}$$

which, like the timing jitter that causes it, is a zero mean gaussian random variable with standard deviation of $A\pi B\sigma_t$. The assumption of small jitter relative to the video bandwidth is usually valid for radar systems because the timing jitter is normally measured in picoseconds, and video bandwidths seldom exceed a couple of hundred megahertz.

The spectrum of the amplitude noise is the same as that of the timing jitter: white, or "flat." Thus, the effect of sample timing jitter is to add an amplitude variation, or white noise component, to the original signal amplitude.

$$A_s = A + \delta_A$$

The signal-to-noise ratio of the resulting signal can be calculated by dividing the original signal power ($A^2/2$) by the noise power ($A^2\pi^2B^2\sigma_t^2$) yielding:

$$\text{SNR} = \frac{A^2/2}{A^2\pi^2B^2\sigma_t^2} = \frac{1}{2\pi^2B^2\sigma_t^2} \tag{4.3}$$

which, when the A^2s are cancelled, provides the expected result that while the component of noise that is induced by timing jitter depends on the signal level, if timing jitter is the only (or dominant) contributor to the noise, the SNR is independent of signal level.

Expressed in decibels, the result is:

$$\text{SNR} = 10 \text{ Log } (1/2\pi^2B^2\sigma_t^2) \tag{4.4}$$

Figure 4.3 shows the SNR as a function of timing jitter for 10-MHz video bandwidth.

Some timing jitter components are not necessarily gaussian in distribution or white in spectrum. For example, timing jitter that results from power supply variations that will be harmonically related to the ac line frequency may have an amplitude distribution that are not gaussian and a spectrum that is almost certainly not white. The amplitude distribution of the sampled signal will then have a non-gaussian distribution and its spectrum will not be white. Because the total timing jitter, its amplitude distribution, and its spectrum are the result of a combination of components, so will the resulting sampled signal noise characteristics.

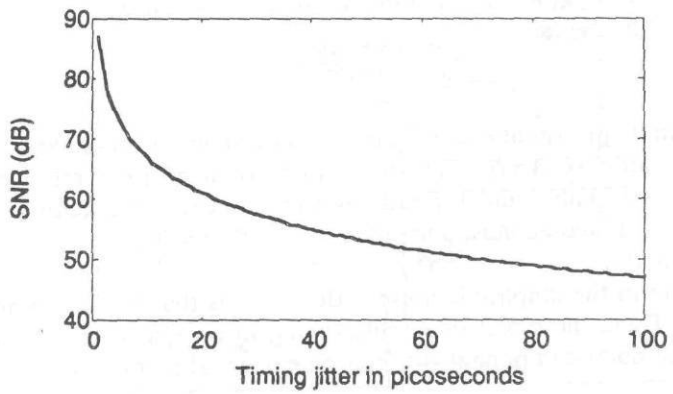

Figure 4.3 SNR versus timing jitter for 10-MHz video bandwidth.

Chapter 5
A/D Conversion Effects

James A. Scheer
Georgia Institute of Technology

5.1 INTRODUCTION

The process of converting the analog signal (usually out of the I and Q detector network) to a digital (binary) representation is performed in the A/D converter. This process, which can be divided into two stages, sampling and amplitude quantization, creates errors in the signal representation in the amplitude and frequency domains. Several effects are inherent in the A/D conversion process. The most salient of these are time quantization, amplitude quantization, timing jitter, and saturation. The effects of timing jitter are discussed in Chapter 4 and will not be repeated here.

5.2 TIME QUANTIZATION AND ALIASING

The original signal $A(t)$ is sampled in the time domain at sampling interval, T, as depicted in Figure 5.1. Figure 5.1 depicts a hypothetical analog signal that is a continuous function of time. The figure depicts the process of sampling the signal at discrete times and the effects of quantization that convert the continuous amplitude of the signal to discrete amplitudes. The time sampling process is depicted by the ensemble of sample times shown on the horizontal axis, and the amplitude quantization is depicted by the discrete amplitude levels shown on the vertical axis. The number of discrete amplitude values that can be developed with an A/D converter having M bits is $2^M - 1$. The voltage value of the least significant bit (E_0) is determined by dividing the total peak-to-peak signal level by the number of quantization levels.

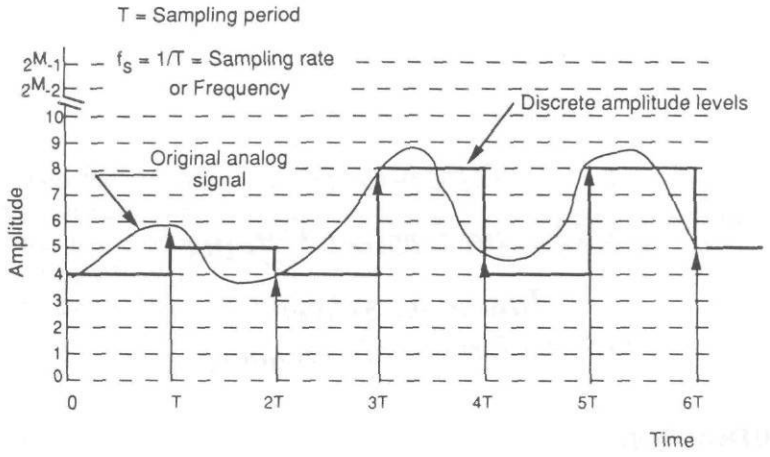

Figure 5.1 Effects of time and amplitude quantization.

$$E_0 = \frac{E_{p-p}}{2^M - 1} \tag{5.1}$$

The spectrum of the original hypothetical analog signal is depicted in Figure 5.2. The time sampling process causes any component of the original signal spectrum in excess of the sampling rate to fold over into the spectral interval between zero and the sampling rate. This effect is often called aliasing and is depicted in Figure 5.3. Unless the system designer has the luxury of a much higher sampling rate (PRF) than the highest frequency component of the original signal, some aliasing of the signal will occur.

Sometimes an anti-aliasing filter is used to band-limit the original signal so that aliasing is prevented. Although this approach eliminates (to a large degree) the aliasing, it suppresses some of the desired information if it existed outside the bandpass of the filter. Obviously, to preserve the entire spectrum of the original signal, an adequate sampling rate must be used so that the appropriate antialiasing filter does not suppress important information.

Often, it is not practical to entirely prevent overlap in the spectrum that repeats itself. Some degree of overlap, or aliasing, is permissible. The amount of aliasing that is experienced is determined by integrating the power in the overlap

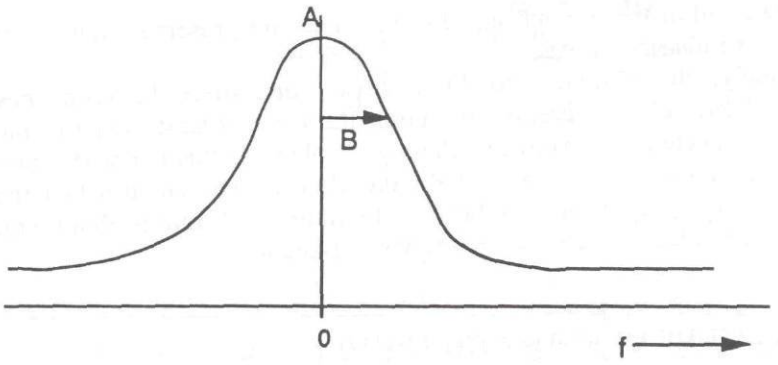

Figure 5.2 Spectrum of original analog signal.

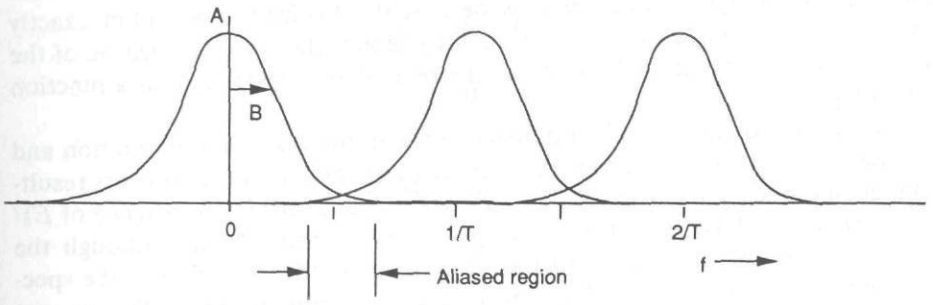

Figure 5.3 Spectrum of sampled signal showing aliasing.

region, which is determined by the sample rate and the original signal spectrum width.

A trade is often required to settle on the errors that are to be allowed and the nature of the errors. At one extreme, a low-pass video (baseband) filter can be employed such that virtually no overlap in the sampled signal is experienced. This will be the case if a narrowband low-pass filter is employed, such that the frequency components that would be aliased (in the absence of the filter) are suppressed to some (arbitrarily) low level, such as -60 or -80 dB. The effect of this is to limit the bandwidth of the signal to be processed, without hope of recovering signals at the high-frequency end of the spectrum. At the other extreme, no filter could be used, such that any spectral component of the signal in excess of one-half the sample rate will be totally aliased or folded into the sampling interval.

In this case, all of the original signal components are preserved, but are contaminated by the aliasing process.

Usually, the optimum condition exists somewhere between these two extremes. Obviously, the desire is to sample the signal at least twice the maximum frequency expected and avoid the aliasing problem. If this is not the case, then often the characteristics of the anti-aliasing filter are chosen such that the error due to loss of signal information beyond the filter bandwidth is about equivalent to the error induced by the aliased signal components.

5.3 AMPLITUDE QUANTIZATION NOISE

Besides sampling the signal in the time domain, the A/D process quantizes the signal in the amplitude domain. The analog signal, which originally has a continuum of values, is quantized to several $(2^M - 1)$ values. There is generally an error associated with this quantization process, because the digitized value seldom exactly represents the true analog value. Figure 5.4(a) depicts the transfer function of the A/D converter and Figure 5.4(b) depicts the related amplitude error as a function of input signal level.

The amplitude error is the difference between the digital representation and the actual analog value. The error is a uniformly distributed random process resulting in an amplitude error between $+1/2\ E_0$ and $-1/2\ E_0$, having a variance of $E_0^2/12$ or a standard deviation of $E_0/\sqrt{12}$. It has been reported that although the spectrum of the error has some structure [1], for most radar applications the spectrum can be considered to be "white" over a few receiver bandwidths. The amount of so-called quantization noise introduced by this mechanism is dependent only on the quantization level associated with the least significant bit and not the level of the signal into the converter.

5.4 SATURATION

If the signal into the A/D converter exceeds the maximum value for which a legitimate digital representation can be determined, then the effects of saturation will be exhibited. The worst case is a condition in which a large (relative to the A/D maximum value) sinusoidal waveform results in saturation severe enough that only two values of the signal are produced. In this case the effect is to develop harmonics of the original signal spectrum. If, for example, the original signal was of the form:

$$S_{in} = A \cos(2\pi t/T) \tag{5.2}$$

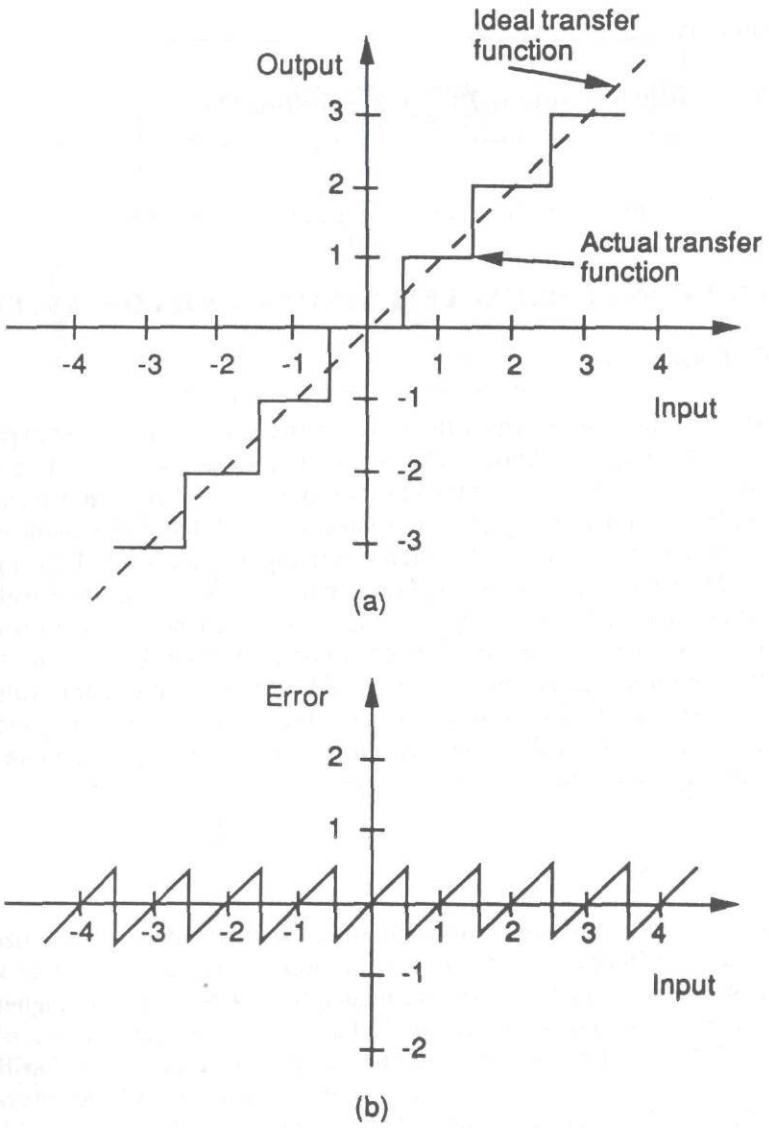

Figure 5.4 A-to-D converter transfer function (a) and related error (b).

and

$$A \gg 2^{M-1} \tag{5.3}$$

then the output is

$$S_{out} = B[\{0.637 \cos(2\pi t/T) - 0.212 \cos(6\pi t/T) + 0.127 \cos(10\pi t/T) - 0.191 \cos(14\pi t/T) + \ldots .] \quad (5.4)$$

resulting in odd harmonics of the original spectrum.

5.5 OPTIMIZATION OF SIGNAL LEVEL INTO AN A/D CONVERTER

5.5.1 Smallest Signal Case

At one extreme is the case in which the signal is the smallest it is ever expected to be (for a given system condition). This is usually the case when receiver noise dominates the signal or the target or the clutter signals (or both) are much smaller than the noise level. Oppenheim [2] has presented a curve relating the quantization noise introduced into a system as a function of the input noise level. This is given as Figure 5.5. The vertical axis is the increase in noise due to quantization (relative to thermal noise), and the horizontal axis is the rms noise (thermal) expressed in quantization levels. The noise increase is held to no more than 1 dB for $\sigma_n > E_0/2$. Obviously, the input signal could be increased arbitrarily above this value to minimize the quantization effects, but increasing the noise level (σ_n) beyond $2E_0$ is beyond the point of diminishing returns. Other effects begin to dominate with arbitrarily large signal levels.

5.5.2 Largest Signal Case

In conflict with the notion of arbitrarily increasing the signal level to minimize the quantization noise effects is the effect of saturation of the A/D converter when using a high signal level. In this case, the higher the signal level, the higher the saturation-related noise. Grey and Zeoli [3] have performed an analysis of the combination of the quantization and saturation effects for a normally distributed signal. Figure 5.6(a) is a plot showing the quantization noise and the saturation noise as functions of k, which is the ratio of the A/D peak level to rms signal level. Figure 5.6(b) is a plot of the composite of the quantization and saturation noise, showing an optimum value of $k = 3.9$ (for an 8-bit converter). Figure 5.7 is a family of plots showing the combination of saturation noise and quantization noise for several quantization bits, from 3 to 10. The results show that there is an optimum value of k (saturation to rms signal level) such that the combination of quantization noise and saturation noise is minimized. The optimum value of k is given in Table 5.1 for values of M from 3 to 10.

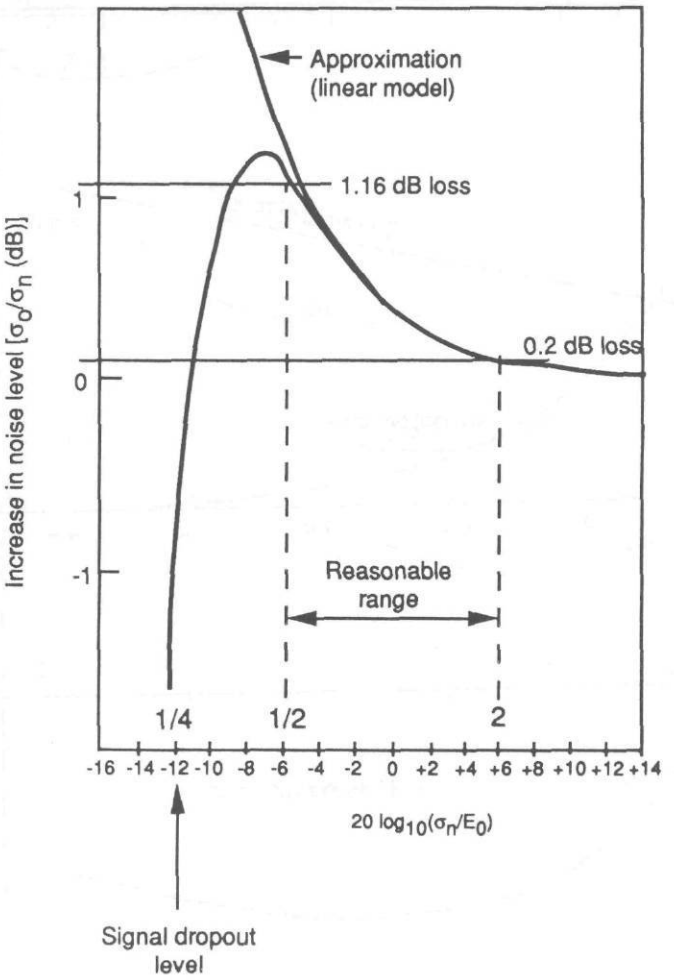

Figure 5.5 Quantization noise introduced by the A/D converted as a function of input noise level. (Adapted from [2].)

5.6 A/D CONVERTER PERFORMANCE MEASURES

5.6.1 Effective Bits

One measure of the performance of an A/D converter is the number of effective bits it produces. Initially, one might think that the number of bits a converter

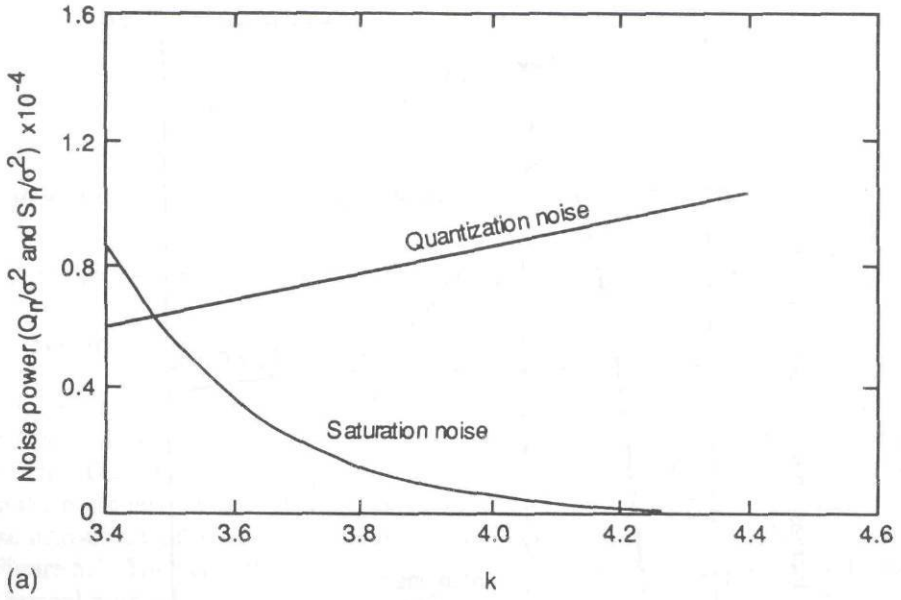

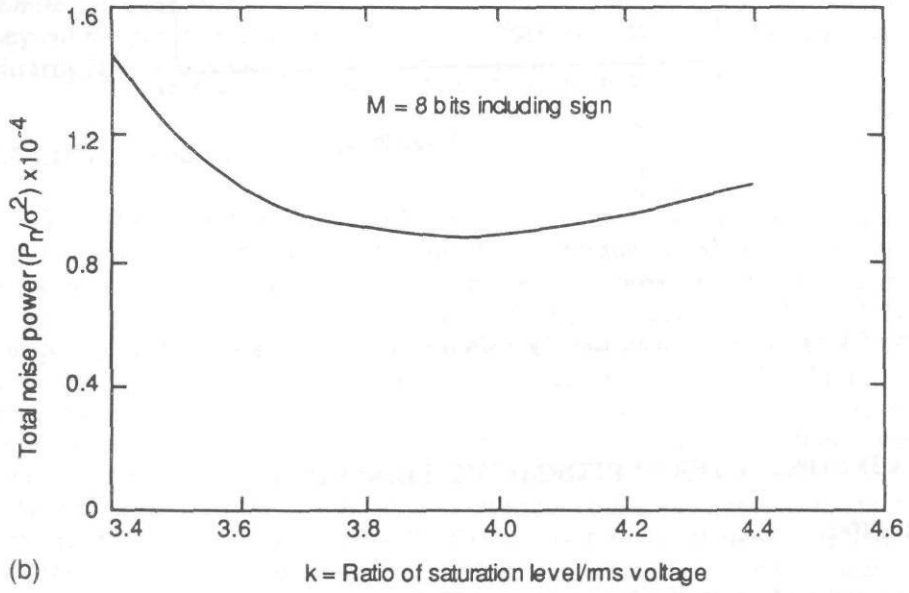

Figure 5.6 Saturation and quantization noise for 8-bit A/D conversion. (Adapted from [3].)

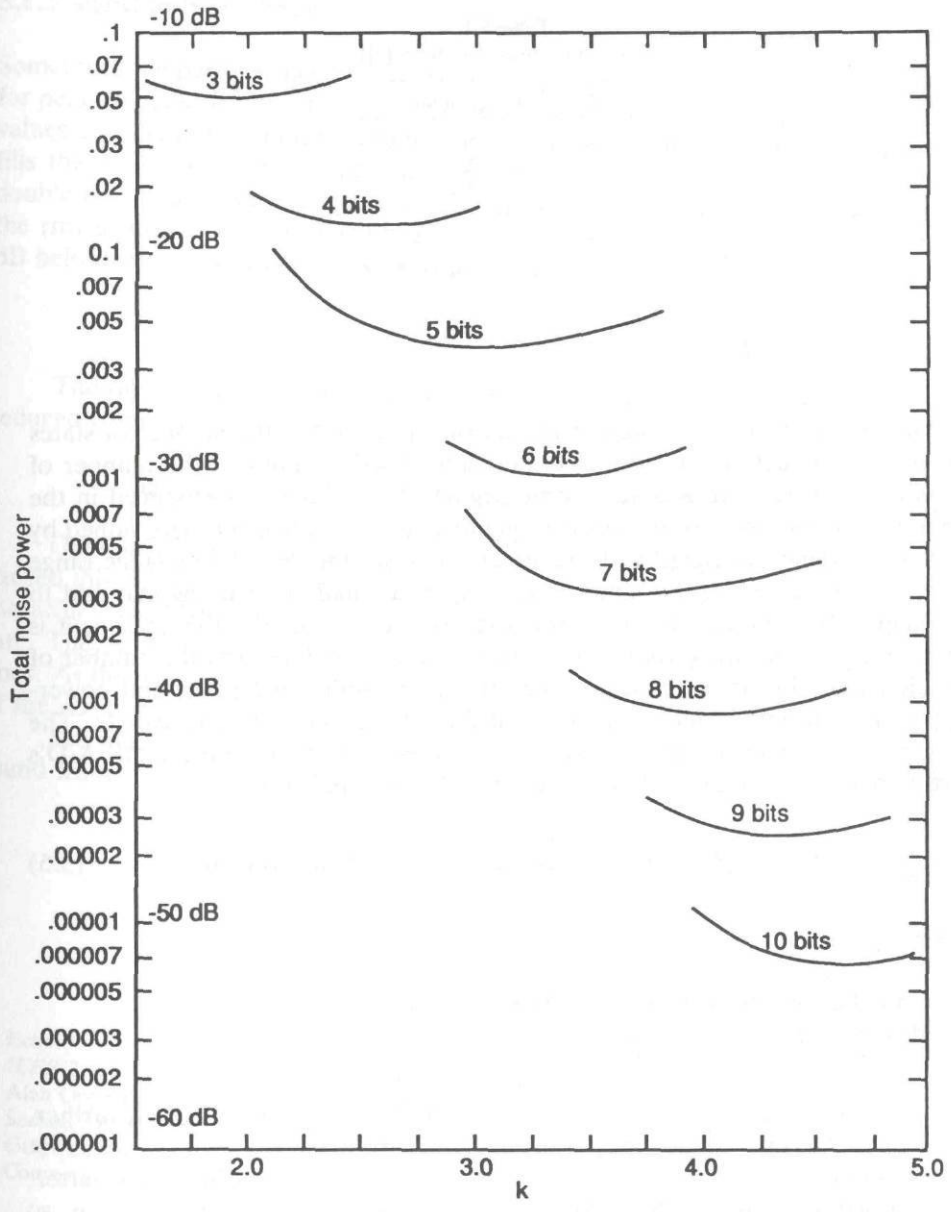

Figure 5.7 Total noise power (saturation and quantization) for 3 to 10 bit A/D conversion. (Adapted from [3].)

Table 5.1
Optimum Value of k (from [3])

M	k (optimum)
3	1.9
4	2.5
5	2.9
6	3.3
7	3.6
8	3.9
9	4.2
10	4.5

produces depends on the design of the converter related to the number of states it converts. Though a converter is usually advertised in terms of the number of states it converts, there is always some degree of noise that is introduced in the converter output. Some of this noise is quantization noise, which is determined by the voltage value associated with the least significant bit, E_0. The dynamic range of an A/D is limited by this value. There are additional noise terms that add to the quantization noise, further limiting the dynamic range. For this reason, it is naive to expect that a converter's performance is predictable from the number of bits alone. Nonlinearities of dc and ac, timing and amplitude jitter, and power-supply-induced noise, among others, contribute to the noise in a converter. The number of effective bits is a more honest representative measure of the A/D's performance. The number of effective bits, M_{eff}, is found from:

$$M_{\text{eff}} = M - \text{Log}_2(\text{measured rms error/ideal rms error}) \tag{5.5}$$

where:

M = number of bits of the converter design, and
the ideal rms error = $E_0/\sqrt{12}$.

The measured rms error is never less than the ideal rms error and, further, usually depends on the frequency of the input signal. As the frequency of the input signal increases, there exists more noise due to the timing jitter in the converter, as described in Chapter 4. Not all of the measured noise is due to timing jitter, so one component of the measured noise is constant with input signal frequency and one component increases. The A/D converter vendors usually supply a table of values of effective bits, or SNR, and sometimes the values are provided for several input frequencies, up to half the sample rate, which is the worst case.

5.6.2 Signal-to-Noise Ratio

Sometimes the performance of a converter is specified in terms of its SNR, either for peak-to-peak signal-to-rms noise or rms signal-to-rms noise. The performance values are given for a sinusoidal input signal, the peak amplitude of which exactly fills the A/D converter voltage range. Because each bit of conversion provides double the voltage range, each bit represents 6.02 dB of dynamic range. Because the rms quantization noise level is $E_0/\sqrt{12}$, the quantization noise level is 10.79 dB below one bit, so the ideal SNR is found from:

$$\text{Signal}_{(\text{pk}-\text{pk})} \text{ to } \text{Noise}_{(\text{rms})} \text{ (ideal)} = 6.02\,M + 10.79 \text{ (dB)} \tag{5.6}$$

The rms signal (for a sinusoid) is the peak-to-peak level divided by $2\sqrt{2}$, (or reduced from the peak-to-peak value by 9.03 dB), so:

$$\text{Signal}_{(\text{rms}-\text{rms})} \text{ to } \text{Noise}_{(\text{rms})} \text{ (ideal)} = 6.02\,M + 1.76 \text{ (dB)} \tag{5.7}$$

Obviously, the measured SNR published by the converter vendor cannot exceed this value and will generally be lower. Most A/D converter vendors supply the achievable SNR for at least one input signal bandwidth and A/D conversion rate. The A/D rate does not influence the noise, but the input signal bandwidth does. As the input signal bandwidth increases, the timing-jitter-related component of the noise increases, decreasing the SNR.

The number of effective bits of an A/D converter, given the SNR, can be found from:

$$M_{\text{eff}} = M - \frac{6.02M + 10.8 - \text{SNR}}{6.02} = \frac{\text{SNR} - 10.8}{6.02} \tag{5.8}$$

REFERENCES

[1] Echard, J.D., and M.L. Watt, "The Quantization Noise Spectrum of a Sinusoid in Colored Noise," *IEEE Trans. on Acoustics, Speech, and Signal Processing*, August, 1991.

[2] Alan Oppenheim, (Ed.), *Applications of Digital Signal Processing*, Englewood NJ: Prentice Hall, Section 5.8, "Analog-to-Digital Converters."

[3] Gray, G. A., and G. W. Zeoli, "Quantization and Saturation Noise Due to Analog-to-Digital Conversion," *IEEE Trans. on Aerospace and Electronic Systems*, January 1971, pp 222–223.

Chapter 6

Nonlinear Effects in Fourier Transform Processing

Mark A. Richards
Georgia Institute of Technology

The Fourier transform is ubiquitous in radar signal processing, where it is used for digital filtering, spectral estimation, and imaging. Filtering applications take advantage of the convolution theorem of Fourier analysis to provide computationally efficient implementations of time-domain digital filtering for pulse compression and uniform doppler filter banks. The spectral estimation applications arise because many radar signal processing tasks reduce to detecting one or more sinusoids in the presence of interference. Examples include detecting plane waves impinging on an array and estimating their angle of arrival, beamforming for array antennas, the related techniques of FMCW and "stretch" wideband pulse compression and range estimation, and certain classes of *automatic target recognition* (ATR) processing. Imaging applications include SAR and ISAR processing, *doppler beam sharpening* (DBS), and high-range resolution processing of frequency-stepped radar data.

In most of these applications, the signal analyzed can be modeled as a sum of sinusoids embedded in noise and clutter. For example, in doppler filtering each moving target produces an individual doppler frequency component, whereas in array processing, the spatial signal across an array at any fixed time instant due to a plane wave is a sinusoid whose frequency is determined by the angle of arrival. In FMCW or stretch processing, scatterers at different ranges appear as different constant frequency components at the mixer output.

Because the Fourier transform is a linear operator, its response to a weighted sum of sinusoids is just the appropriately weighted sum of shifted replicas of the response to a single sinusoid. Consequently, a great deal can be learned about systems implementing each of these radar signal processing algorithms by studying

the response of the system to a single sinusoid. This approach separates algorithm and hardware effects from target and interference phenomenology.

In practice, signals rarely conform to the pure sinusoid ideal. Unintended relative motion between the radar and target can produce linear, quadratic, sinusoidal, or random phase deviations from the ideal signal. Antenna pattern effects, transmitter instabilities, and target fluctuations can introduce amplitude errors as well. Fourier domain sampling effects lead to greatly different responses to apparently similar inputs. Several of these effects are reviewed and summarized in this chapter.

6.1 DISCRETE FOURIER TRANSFORM BASICS

There are several versions of the Fourier transform, depending on whether the signal being analyzed is defined on a continuous or discrete domain and is finite or infinite in extent. The relationship between them is detailed in [1]. Signals of practical concern in modern practice are sampled and finite length. Restricting attention to this case, the *discrete time Fourier transform* (DTFT) and the *discrete Fourier transform* (DFT) are of most concern. Consider a finite length discrete signal $x[n]$, $n \in 0, \ldots, N-1$ obtained by uniform sampling of a continuous signal $x(t)$. Thus, $x[n] = x(nT)$, where T is the sampling interval in the signal domain.[1] The sampling frequency is $f_S = 1/T$. The DTFT of $x[n]$ is a function of a *continuous* Fourier domain variable:

$$X(f) = \sum_{n=0}^{N-1} x[n]\, e^{-j2\pi fn}, \qquad f \in (-0.5, +0.5] \tag{6.1}$$

The DFT of $x[n]$ is a function of a *discrete* Fourier domain variable:

$$X[k] = \sum_{n=0}^{N-1} x[n]\, e^{-j(2\pi/N)nk}, \qquad k = 0, \ldots, N-1 \tag{6.2}$$

Inspection of (6.1) and (6.2) shows that the DFT is obtained by sampling the DTFT in the Fourier domain:

$$X[k] = X(f)\big|_{f=k/N}, \qquad k \in 0, \ldots, N-1 \tag{6.3}$$

[1]The "signal domain" is the domain in which the signal to be Fourier transformed is defined. This is usually, but not always, the time domain. Another example is the space domain in the case of array beamforming. The Fourier transform is said to be defined in the "Fourier domain." This is normally the conventional frequency domain, with units of cycles (or radians) per second; but if the signal is in the space domain, the Fourier domain will be spatial frequency, with units of cycles (radians) per meter.

which shows that the discrete variable DFT used in the actual radar signal processing should be interpreted as a sampled version of the continuous variable DTFT. The frequency variable f is called "normalized frequency." It ranges from -0.5 to $+0.5$ and is related to conventional analog frequency f_a as $f = f_a T = f_a/f_s$. For example, a normalized frequency of 0.1 corresponds to one-tenth the data sampling frequency.

The DFT is normally implemented in practice using the famous FFT algorithm. It is important to realize that the FFT is only an efficient procedure for computing the DFT; it is not a separate transform. Furthermore, "the" FFT is actually a large and growing class of algorithms optimized for different transform sizes, real versus complex data, and so forth. The choice of FFT algorithm is important when considering computational speed and quantization noise. Because each multiplication or addition is a source of roundoff error, their number and ordering is significant. Whether the direct computation of (6.2) or an FFT algorithm is used is irrelevant to consideration of sampling, amplitude error, and phase error effects.

6.2 DFT RESPONSE TO A SINUSOID

Consider a sampled pure complex sinusoid:

$$x[n] = e^{j2\pi f_0 n}, \qquad n = 0, \ldots, M-1 \tag{6.4}$$

Its discrete time Fourier transform is [1]:

$$X(f) = \frac{\sin[\pi(f - f_0)M]}{\sin[\pi(f - f_0)]} e^{-j2\pi(M-1)(f-f_0)}, \qquad f \in (-0.5, +0.5] \tag{6.5}$$

Equation (6.5) is the expected "digital sinc" function. Figure 6.1 plots the magnitude of $X(f)$ for $M = 20$ and normalized frequency $f_0 = 0.25$. The figure also illustrates two of the principal figures of merit for the DTFT response to a sinusoidal input. The *impulse response width* (IPRW) is the width of the mainlobe of the sinc function. Smaller IPRWs indicate finer Fourier domain resolution. The level of the first sidelobe peak relative to the mainlobe peak, or *peak sidelobe level* (PSL), indicates the susceptibility of weak signals to masking by the sidelobes of adjacent strong signals. Not explicitly shown are the gain, which is the ratio of the peak DTFT amplitude to the sinusoidal signal amplitude, and the *integrated sidelobe level* (ISL), which is the total energy in the sidelobes relative to the mainlobe. Another important figure of merit is the *peak shift* (PS), which measures how far the observed peak is from the true sinusoid frequency. PS is zero in Figure 6.1.

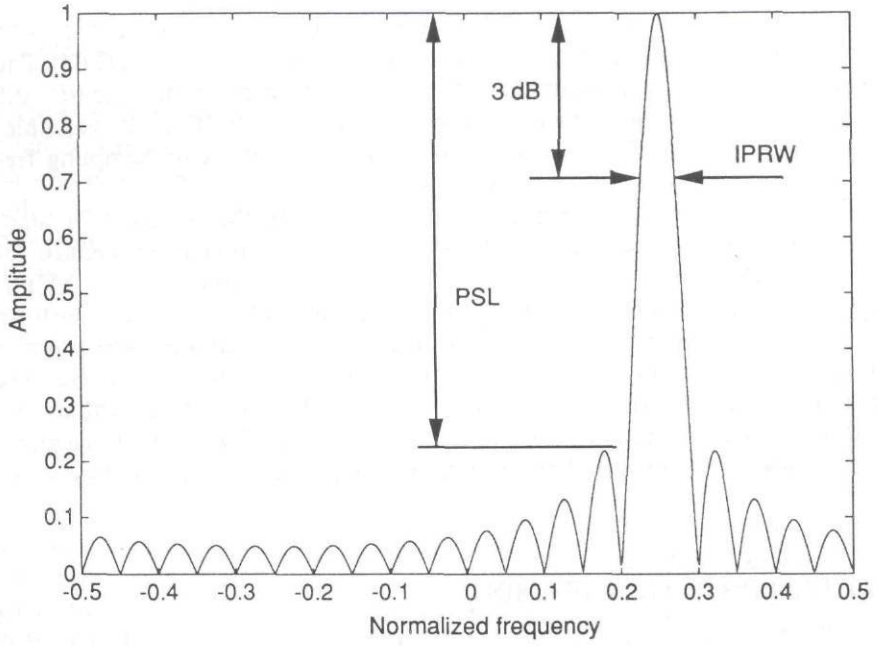

Figure 6.1 The DTFT of a sampled pure complex sinusoid of 20 samples length and normalized frequency 0.25. The definitions of IPRW and PSL are illustrated.

The DFT of $x[n]$ is just a sampled version of the function in Figure 6.1. However, the appearance of a plot of the DFT magnitude depends strongly on where those samples fall on the underlying DTFT sinc function. Figure 6.2 is the magnitude of the 20-point DFT of $x[n]$. With $N = 20$, the DFT sample frequencies are 0.0, 0.05, 0.10, . . . , 0.95 (or equivalently, -0.50 to $+0.45$); therefore, the frequency of the sinusoid exactly matches one of the DFT sample points. When this is true *and* the DFT size equals the sequence length, all the other DFT samples will fall exactly on the zeros of the DTFT sinc function, giving the impulse spectrum of Figure 6.2. In this case, there is no leakage of energy into adjacent frequency bins and no indication of sinc-like sidelobes.

If the DFT size N is larger than the sequence length M (not including any zero padding) *or* if the sinusoid frequency is not equal to a DFT sample frequency, at least some of the DFT samples will not fall on zeroes of the DTFT. The latter case is shown in Figure 6.3, which is the magnitude of the 20-point DFT of a 20-point sinusoidal sequence with frequency 0.275, exactly halfway between two DFT sample points. The DFT samples now fall around the peaks of the sidelobes

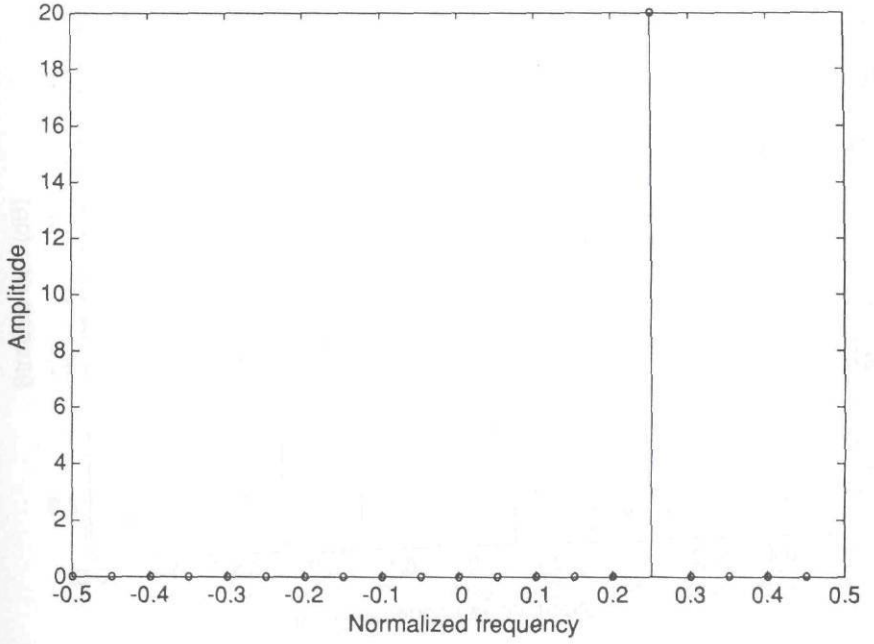

Figure 6.2 The 20-point DFT of a sampled pure complex sinusoid of 20 samples length and normalized frequency 0.25.

rather than at the zeros, resulting in a very different looking plot even though the two signals have identically shaped DTFTs; one is merely shifted on the frequency axis relative to the other. There is no longer a distinct peak; two samples straddling the true peak location each have equal (but lower) amplitude. Finally, the samples away from the peak show energy leakage into other bins, but do not indicate the lobed structure of the underlying sinc function. These graphs illustrate that the Fourier domain sampling by the DFT causes the apparent spectrum to be a strong function of the DFT size relative to the signal length and of the signal frequency relative to the DFT sample frequencies.

The loss of apparent amplitude in the DFT when the sinusoid frequency does not correspond exactly to a DFT sample frequency is called "straddle loss." It is a function of the degree of zero padding used in computing the DFT and the data window used, if any. Straddle loss is greatest if the sinusoid falls halfway between two DFT frequencies and no window is used. Straddle loss is also a weak function of sequence length, but is essentially independent of it for $M \geq 10$, which covers most practical cases. Figure 6.4 illustrates the limiting value of straddle loss as a

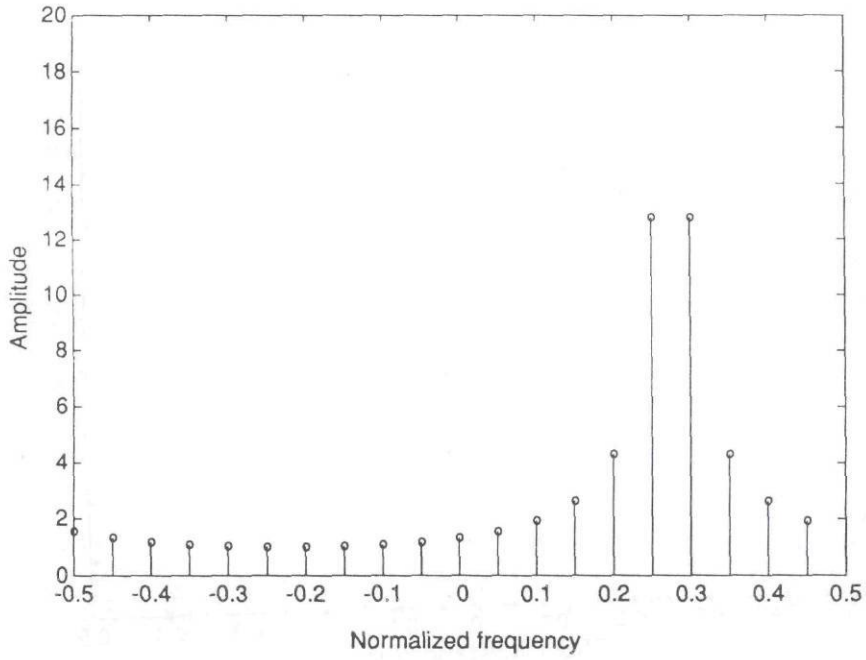

Figure 6.3 The 20-point DFT of a sampled pure complex sinusoid of 20 samples length and a normalized frequency of 0.275.

function of frequency deviation from a DFT sample frequency for the cases of no window and a Hamming window. The peak losses are 3.92 and 1.73 dB, respectively, whereas the average losses are 1.54 and 0.65 dB.

6.3 EFFECT OF DATA ERRORS

Suppose the ideal sinusoidal signal $x[n]$ is contaminated with an amplitude error $a[n]$ and a phase error $\phi[n]$:

$$\tilde{x}[n] = (1 + a[n])e^{j\phi[n]}\, x[n] \tag{6.6}$$

The amplitude and phase errors may each contain any or all of linear, quadratic, sinusoidal, or random components. The errors act as a window function applied to the ideal data. If the errors are fairly smooth, one would expect effects similar to conventional windows: loss of resolution and reduction of peak sidelobes.

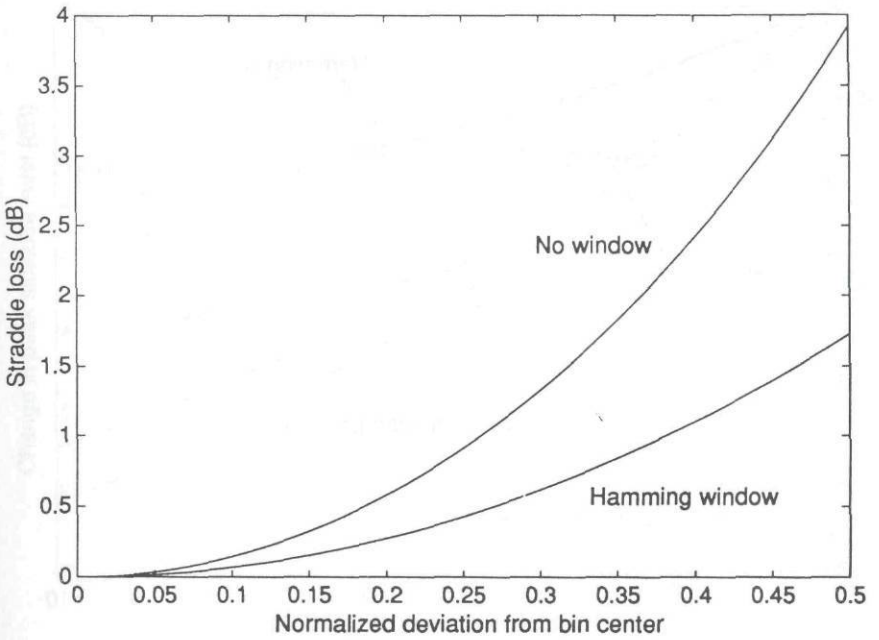

Figure 6.4 Straddle loss for a sinusoidal signal. The average loss is 1.54 dB when no window is used and 0.65 dB when a Hamming window is used.

6.3.1 Amplitude Errors

The DTFT of a sinusoid is relatively insensitive to smooth amplitude errors, which act in a similar way to intentional weighting. One example is antenna beamshape weighting in a mechanically scanning radar. The response from a given target is weighted by the antenna two-way voltage pattern. Figures 6.5, 6.6, and 6.7 illustrate the effect of a symmetric parabolic amplitude taper, which approximates the shape of the mainlobe of a generic antenna pattern. If the data are otherwise unweighted, tapers up to 3 dB cause a gain loss of only about 1 dB, whereas the PSL actually decreases over 2 dB. Resolution is degraded about 5%. If the data are already Hamming weighted, the additional taper has even less effect. In most cases, all three measures vary only slightly with the data sequence length. The exception is the PSL behavior of the longer signals with Hamming windowing, which shows a distinct inflection. Initially, the amplitude of the third sidelobe, which is the largest in the Hamming-windowed response, decreases as in the other cases. At the same time, the smaller first sidelobe is rising. When the edge attenuation exceeds 6 dB, the first sidelobe rises above the third, thereby becoming the new peak sidelobe.

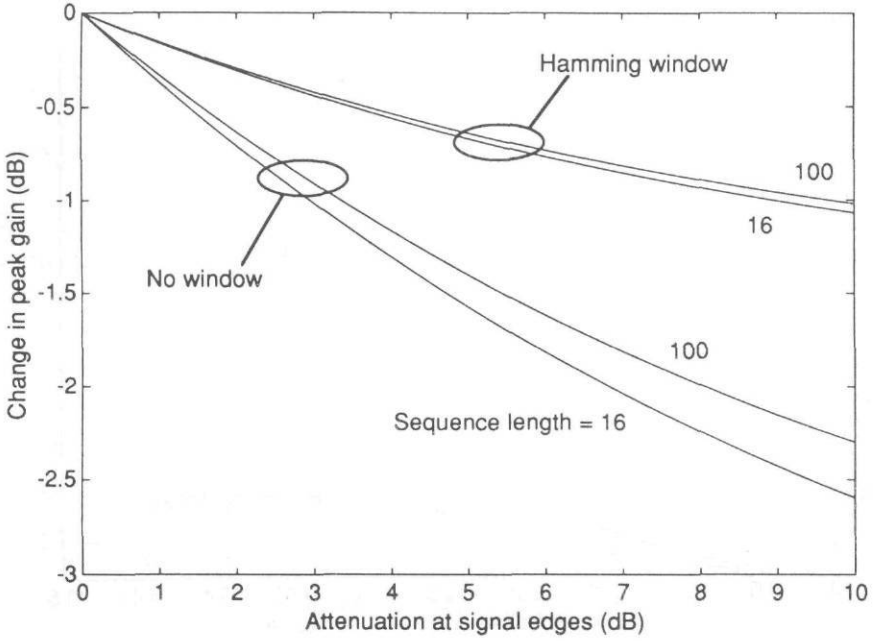

Figure 6.5 Reduction of gain due to parabolic amplitude taper for a sinusoidal input with no window and with a Hamming window. Results are shown for sequence lengths of 16 and 100 samples.

Another common model for some types of systematic amplitude errors is a sinusoidal ripple:

$$\tilde{x}[n] = \{1 + \alpha \sin(2\pi\beta n)\}\, x[n] \tag{6.7}$$

The effect of this amplitude modulation is to create classical "paired-echo" replicas of the principal peak in the DTFT of the distorted signal (provided that the ripple frequency β is large enough to separate the echoes from the mainlobe). The effect is analyzed in many texts (e.g., [2]). If the amplitude of the ripple in decibels is denoted as γ, the amplitude of the paired-echo peaks is (in decibels):

$$\delta = 20 \log_{10} [10^{\gamma/20}/2] \tag{6.8}$$

Figure 6.8 illustrates this relationship. The effect of sinusoidal amplitude ripple is dependent on whether a window is used only in that the normal sidelobes must be low enough for the paired echoes to be evident.

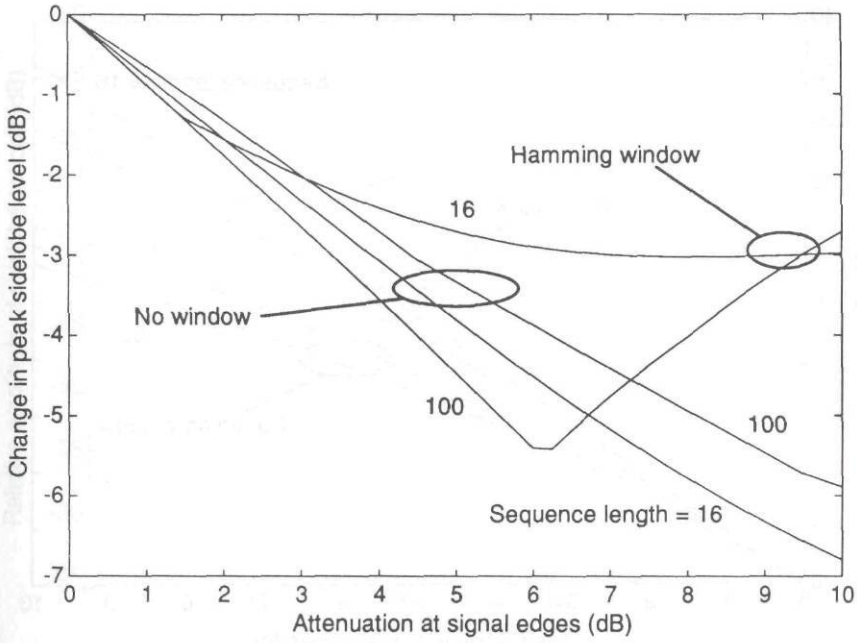

Figure 6.6 Change in PSL due to parabolic amplitude taper for a sinusoidal input with no window and with a Hamming window. Results are shown for sequence lengths of 16 and 100 samples.

6.3.2 Phase Errors

First, consider the effect of a linear phase error:

$$\phi[n] = 2\pi\alpha n \tag{6.9}$$

It is well known that a linear phase shift translates the DTFT [1] on the frequency axis:[2]

$$\tilde{X}(f) = X(f - \alpha) \tag{6.10}$$

The shape of the DTFT does not change. A linear phase added to a sinusoidal

[2]The frequency shift is actually a so-called "circular shift" [1] in which shifted normalized frequencies $f - \alpha$, which fall outside of the range $(-0.5, +0.5]$, are aliased back into that range. Thus, (10) is more correctly written as $\tilde{X}(f) = X((f - \alpha + 0.5)_{1.0} - 0.5)$, where the notation $(\ )_{1.0}$ indicates that the argument within the parentheses is evaluated modulo 1.0.

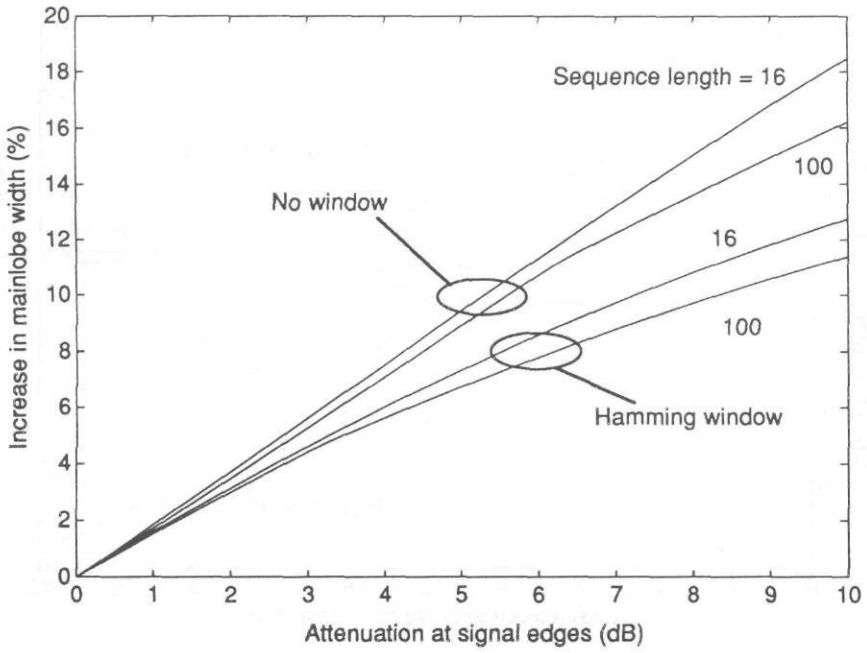

Figure 6.7 Percentage increase in mainlobe width due to parabolic amplitude taper for a sinusoidal input with no window and with a Hamming window. Results are shown for sequence lengths of 16 and 100 samples.

signal effectively changes the frequency, shifting the DTFT on the axis. However, the DFT frequency sampling points remain fixed, so that the points on the DTFT sinc sampled by the DFT change. For example, a linear phase shift with a value of $\alpha = 0.025/2\pi$ applied to the signal used to obtain Figure 6.2 will result in the DFT of Figure 6.3 instead. Straddle losses may be incurred (as might straddle gains), depending on the true and apparent input frequencies.

Quadratic phase errors cause more complex behavior, including mainlobe broadening, sidelobe level changes, and gain reductions. Figures 6.9, 6.10, and 6.11 illustrate the effect of a symmetric phase error function:

$$\phi[n] = \phi_{\max}\left[1 - 4\left(\frac{n}{N-1}\right) + 4\left(\frac{n}{N-1}\right)^2\right] \tag{6.11}$$

This function reaches a maximum of $\phi_{\max}$ at the sequence endpoints $n = 0$ and $N - 1$ and is zero at the sequence midpoint, $n = (N - 1)/2$. The unusual behavior

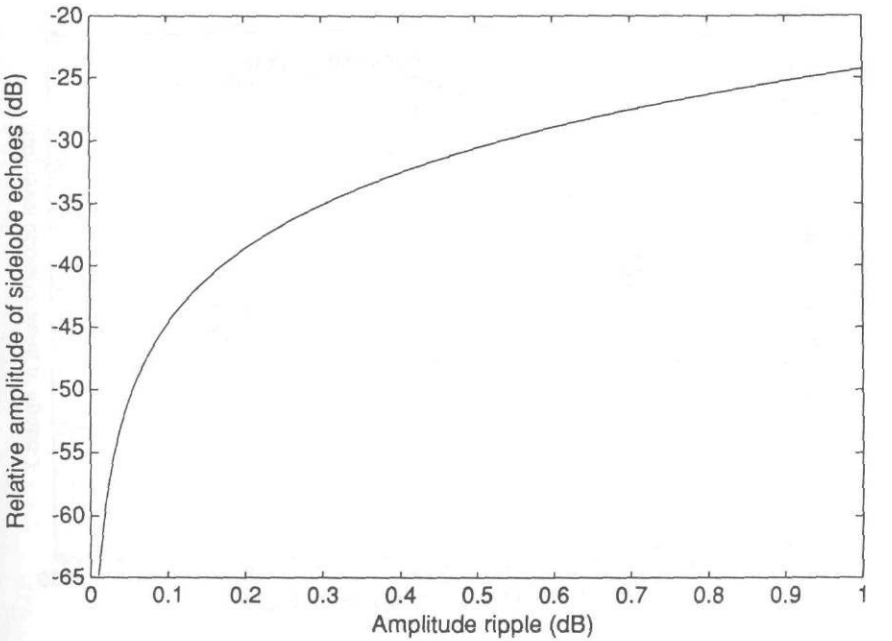

Figure 6.8 Amplitude of paired echoes due to sinusoidal amplitude ripple.

of the PSL seen in Figure 6.10 occurs as follows. The level of the peak sidelobe initially rises. As the error becomes larger, the first sidelobe merges into the broadening mainlobe, losing its identity. The second sidelobe now becomes the largest. Because it is still lower than the first sidelobe had been, the PSL curve drops. Figure 6.10 shows the effect of the first three sidelobes all merging into the mainlobe as the peak phase error reaches 360 deg for the case of Hamming weighting.

The figures of merit of PSL, gain, and resolution become meaningless for sufficiently large quadratic phase errors, because the DTFT response to a sinusoid contaminated by large quadratic phase shifts splits into two distinct peaks. If no window is used on the data, the response splits for phase shifts exceeding about 200 deg. If a Hamming window is used, the DTFT peak does not split until much larger phase shifts of about 2,000 deg accumulate. Figure 6.12 illustrates the central portion of the DTFT for a 100-point sinusoid with a 360 deg quadratic phase shift and no windowing.

Sinusoidal phase ripples create paired echoes, just as do sinusoidal amplitude ripples. Unlike amplitude ripples, phase ripples create a series of harmonic sets of paired echoes. The effect is analyzed in detail in [2]. Generally, the first paired-

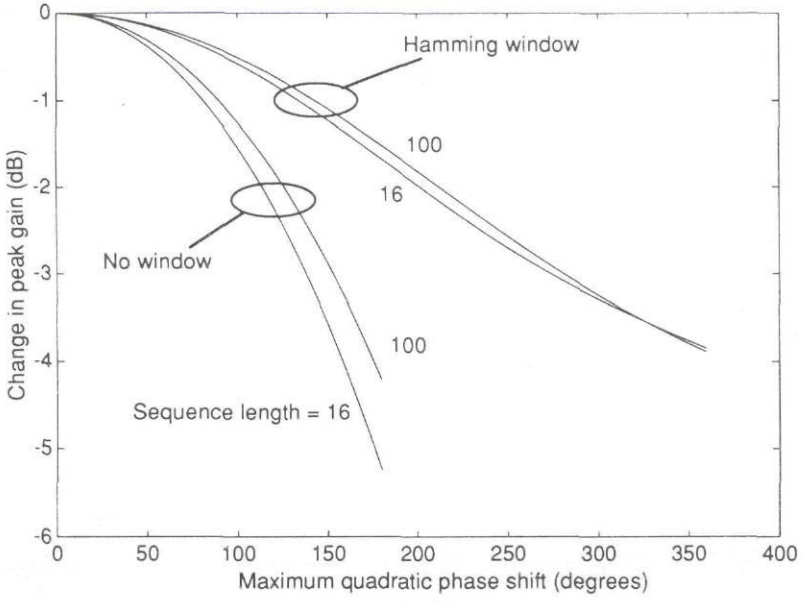

Figure 6.9 Reduction of gain due to quadratic phase error for a sinusoidal input with no window and with a Hamming window.

echo set is the most significant. The relative amplitude of the first echo to the mainlobe of the DTFT response for a phase error given by:

$$\tilde{x}[n] = e^{j\alpha \sin(2\pi\beta n)} x[n] \tag{6.12}$$

is approximately (in decibels):

$$\delta = 20 \log_{10} [J_1(\alpha)/J_0(\alpha)] \tag{6.13}$$

where J_n0 is the Bessel function of the first kind and order n. Figure 6.13 illustrates this relationship.

6.4 SUMMARY

The Fourier transform of a pure sinusoid is a good indicator of the quality of many coherent radar signal processing systems, such as doppler filterbanks, array beamformers, and some types of synthetic aperture imaging systems. Smooth amplitude tapers and quadratic phase errors imposed on the data by uncompensated motion

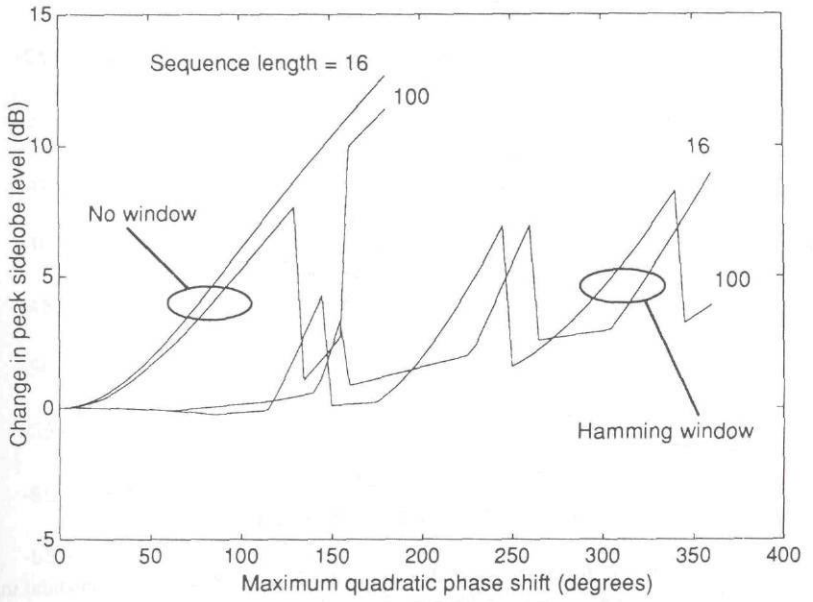

Figure 6.10 Change in PSL due to quadratic phase error for a sinusoidal input with no window and with a Hamming window.

and system errors cause gain losses, sidelobe changes, and resolution losses. Linear phase shifts cause peak shifts. When combined with the sampling effects of the DFT, straddle losses and changes in the apparent sidelobe structure result.

The DFT response to a sinusoid is relatively insensitive to amplitude tapers, which must exceed 3 dB before significant degradation occurs. The gain reduction for unwindowed data is about 1 dB and the mainlobe broadens about 5%. The peak sidelobe actually falls about 2 dB. If the data are windowed with a Hamming or similar function, the gain is reduced only about 0.5 dB.

Quadratic phase errors should be held to less than π radians to avoid excessive degradation. Even with windowing, gain loss reaches nearly 2 db and the mainlobe width increases about 50%. The peak straddle loss of about 3.9 dB (1.7 dB when Hamming windowed) also occurs when the total linear phase shift across the sequence is π. Behavior of the PSL is complex as sidelobes merge into the spreading mainlobe.

Sinusoidal amplitude and phase ripples create paired echo sidelobe responses, similar to antenna grating lobes, in many cases. The echo peaks are about 25 dB below the true peak for 1 dB amplitude ripple and 21 dB down for 10 deg phase ripple.

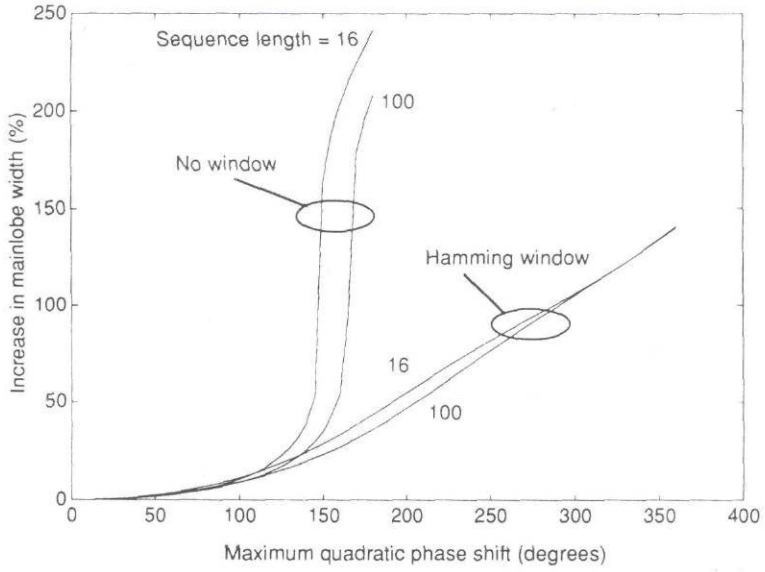

Figure 6.11 Percentage increase in mainlobe width due to quadratic phase error for a sinusoidal input with no window and with a Hamming window.

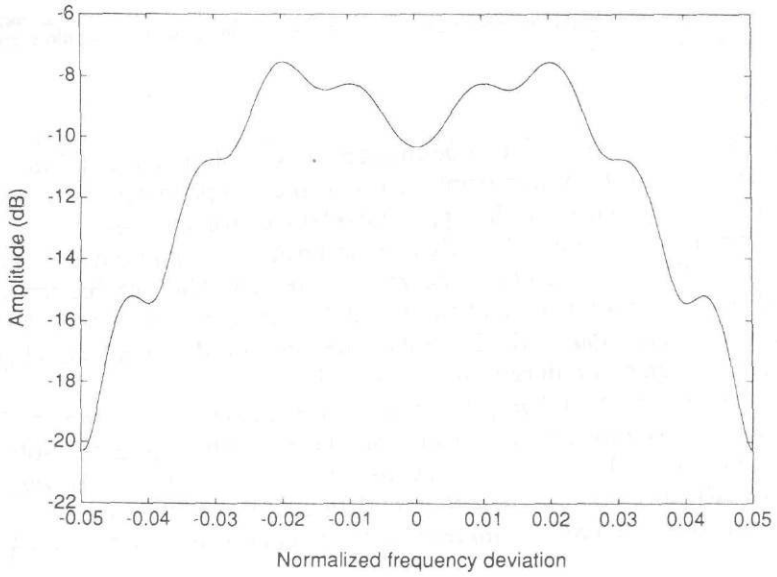

Figure 6.12 Magnitude of the DTFT of an unwindowed sinusoid contaminated with 360 deg of quadratic phase shift. The response has split into two distinct peaks.

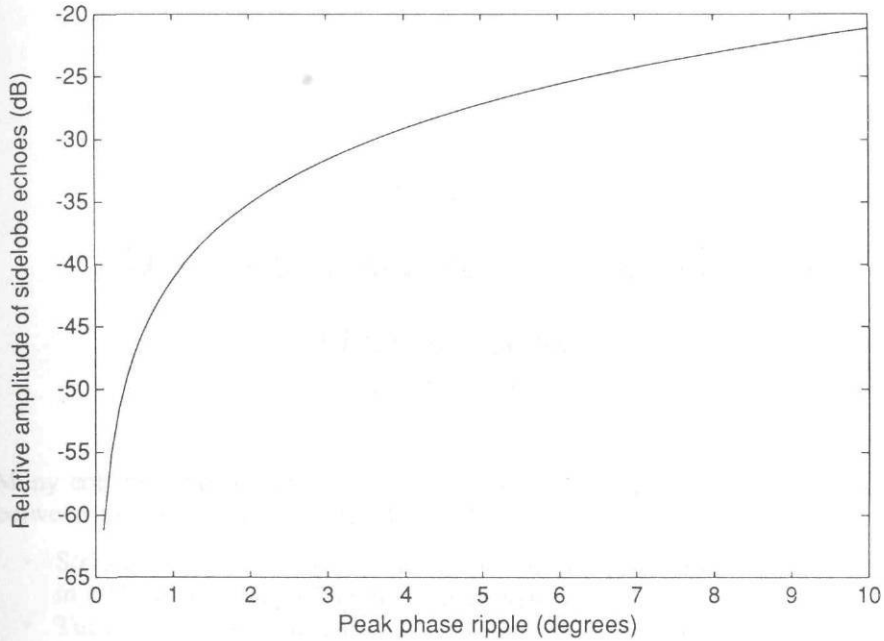

Figure 6.13 Amplitude of paired echoes due to sinusoidal phase ripple.

REFERENCES

[1] Oppenheim, A. V., and R. W. Schafer, *Digital Signal Processing*, Englewood Cliffs, NJ: Prentice-Hall, 1975.

[2] Cook, C. E., and M. Bernfeld, *Radar Signals*, New York: Academic Press, 1967.

Chapter 7
Motion Compensation Fundamentals

Mark A. Richards
Georgia Institute of Technology

Many coherent radar signal processing schemes assume certain relative motions between the radar and its target. Examples include:

- Strip-mapping SAR, where the radar's aircraft platform is assumed to travel in a perfectly straight line at constant velocity;
- Turntable ISAR, where the target rotates at a constant angular rate;
- Doppler beam sharpening, where a constant radial velocity over the dwell time is assumed;
- Frequency-stepped high-range resolution profiles, which assume the target is stationary with respect to the radar.

In practice, the motion between the radar and target does not meet this ideal. For example, even under the best of circumstances turbulence and vibration will cause an aircraft's flight path to deviate from the straight and level, constant velocity ideal of strip-mapping SAR, as shown in Figure 7.1. Motion compensation is the

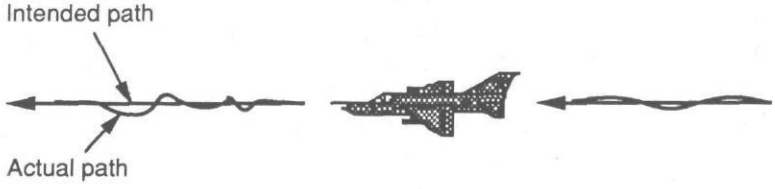

Figure 7.1 Motion compensation corrects for phase errors caused when actual radar-target geometry varies from the intended geometry.

process of correcting for the effect of this unintended motion on the radar signal processing.

7.1 PHASE CORRECTION

Suppose the expected range from the radar phase center to the target at time t is R. Then, the echo received from a constant frequency pulse, after quadrature detection and demodulation to base band, can be represented as:

$$x(t) = A \exp\left[j\left\{2\pi f\left[t - \frac{2R}{c}\right] + \theta\right\}\right] \tag{7.1}$$

where f is the radar frequency and θ is an arbitrary phase offset. All amplitude factors are absorbed into the constant A. If the actual range is instead $R + \Delta R$, then the detected signal will be:

$$\tilde{x}(t) = \tilde{A} \exp\left[j\left\{2\pi f\left[t - \frac{2(R + \Delta R)}{c}\right] + \theta\right\}\right] = \frac{\tilde{A}}{A} x(t) \exp\left[-j4\pi \frac{\Delta R}{\lambda}\right] \tag{7.2}$$

The difference in amplitude for small range deviations is negligible, so that $\tilde{A}/A \approx 1$. Thus, the effect of deviations from the intended geometry is to introduce a phase error into the received data.

As shown in (7.2), small path deviations create large phase changes in the data. A deviation ΔR of one-half wavelength is enough to create a full 360 deg of phase rotation. This is only about 15 cm at L-band, 1.5 cm at X-band, and 1.5 mm at W-band. Thus, motion errors may need to be controlled to very tight tolerances.

Only relative motion errors are normally important. A large bias error ΔR, which is the same for all pulses that are combined in the processing algorithms, will result in the same complex constant multiplying each data sample. This phase offset will factor out of any linear processing, such as doppler filtering, matched filtering, and so forth, and ultimately be removed by the detection process so that it has no effect on the signal processor output. The motion error of significance is the component of ΔR that varies over a *coherent processing interval* (CPI). A CPI is the time interval over which data are collected that are subsequently combined to provide a processed signal. For example, in SAR the "aperture time" is the CPI, whereas in stepped-frequency high-range resolution processing using N frequency steps, it is N times the radar *pulse repetition interval* (PRI).

Because most motion errors vary relatively smoothly, rather than being noise-like, the effect of uncompensated motion is to leave residual linear and quadratic

phase errors in the data, like those described in Chapter 6. These errors, if large enough, will cause response shifts in range and azimuth, gain losses and sidelobe changes, and resolution losses (defocusing). As shown in Chapter 6, the time-varying component of phase variation due to uncompensated motion should be held to 360 deg or less over a CPI.

The major task of motion compensation is to estimate ΔR. A corrected data sequence $\hat{x}(t)$ is then formed:

$$\hat{x}(t) = \tilde{x}(t) \exp\left[+j4\pi \frac{\Delta R}{\lambda}\right] \tag{7.3}$$

The operation of (7.3) restores the phase of the data to that which would have been measured if the relative motion between the radar and target had been ideal. The negligible amplitude variations are not corrected.

7.2 RANGE AND DOPPLER ERRORS DUE TO UNCOMPENSATED MOTION

Some important characteristics of the motion compensation problem can be understood by considering the geometry of the simple case illustrated in Figure 7.2. The radar platform travels in level flight at a constant altitude along the z axis with time-varying velocity $v(t)$. The velocity variation in the z axis is the only deviation

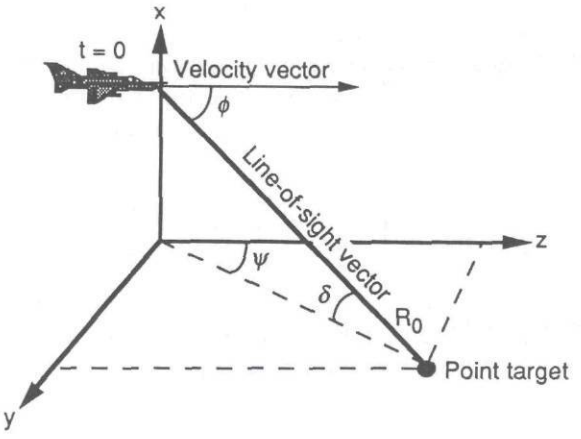

Figure 7.2 Basic geometry of radar mapping scenario.

from perfectly straight, level, constant-velocity flight. We will consider both SAR and DBS processing and determine what motion components must be compensated. A more complete and general analysis is given in [1].

7.2.1 Radar Mapping Geometry

Consider a point scatterer target P located in the y-z earth plane at an initial slant range R_0 at time $t = 0$, and suppose that the squint and depression angles which define the vector from the radar phase center to P are denoted ψ and δ, respectively. The total angle between the *line-of-sight* (LOS) vector and the velocity vector, measured in the plane defined by the two vectors, is the cant angle ϕ. Note that $\cos \phi = \cos \delta \cos \psi$. The target coordinates in the x-y-z coordinate frame are:

$$(x_t, y_t, z_t) = (0, R_0 \cos \delta \sin \psi_t, R_0 \cos \delta \cos \psi) \tag{7.4}$$

The radar coordinates are:

$$(x_r, y_r, z_r) = \left(R_0 \sin \delta, 0, \int_0^t v(\tau)\, d\tau\right) \tag{7.5}$$

The range from the radar to the target as a function of time is:

$$R(t) = \|(x_t, y_t, z_t) - (x_r, y_r, z_r)\| \tag{7.6}$$

Expanding the square root that results from writing out (7.6) explicitly gives [2]:

$$R(t) = R_0 \left\{1 - \cos \phi(\xi) + \tfrac{1}{2} [\sin \phi(\xi)]^2 + \cdots\right\} \tag{7.7}$$

where

$$\xi = \xi(t) = \frac{1}{R_0} z_r(t) = \frac{1}{R_0} \int_0^t v(\tau)\, d\tau \tag{7.8}$$

To get a series that explicitly shows the dependence of the range on velocity, acceleration, and time, we in turn expand ξ in a MacLaurin series:

$$\xi(t) = \frac{v_0}{R_0} t + \frac{1}{2R_0} \dot{v}(0) t^2 + \cdots \tag{7.9}$$

where $v_0 = v(0)$ and $z_r(0) = 0$. Substituting (7.9) into (7.7) and collecting terms gives the desired result:

$$R(t) = R_0 - (v_0 \cos \phi)t + \left\{\frac{(v_0 \sin \phi)^2 - \dot{v}(0)\, R_0 \cos\phi}{2R_0}\right\} t^2 + \cdots \quad (7.10)$$

7.2.2 Effect of Uncompensated Motion in SAR Processing

In analyzing SAR signals, it is usually adequate to approximate $R(t)$ using only terms up through t^2; thus, (7.10) is truncated to the portion explicitly written out. If the platform maintained perfectly straight, level, constant-velocity flight, $\dot{v}(t)$ would be zero. Because the phase of the received signals from a given point scatterer is directly proportional to the range function:

$$\phi(t) = \frac{4\pi}{\lambda} R(t) \quad (7.11)$$

the phase signature of a point scatterer in an idealized SAR mapping situation is the quadratic phase (linear frequency) function:

$$\phi_{\text{SAR}}(t) \cong \frac{4\pi}{\lambda}\left[R_0 - (v_0 \cos\phi)t + \frac{(v_0 \sin \phi)^2}{2R_0} t^2\right] \quad (7.12)$$

The SAR signal processor focuses the image of the point scatterer by matched-filtering the data with a filter having the impulse response $\exp(-j\phi_{\text{SAR}})$.

The signal processor focusing function assumes constant-velocity flight. For the data to focus properly, the motion compensation system must cancel the remaining motion error phase term of (7.10) and (7.11), which is:

$$\phi_e(t) \cong -\frac{2\pi}{\lambda}[\dot{v}(0) \cos \phi]t^2 \quad (7.13)$$

by multiplying the data by the function $\exp(-j\phi_e)$. Because ϕ is the total angle between the radar velocity vector and the LOS vector, $\dot{v}(0) \cos \phi$ is the component of the longitudinal acceleration in the direction of the target, commonly called the LOS acceleration. The LOS accelerations shown in (7.13), unless compensated, will introduce quadratic phase errors in the data. As shown in Chapter 6, these errors in turn will result in loss of gain, resolution, and contrast through broadening of the point target response main lobe and an increase in its sidelobes [1, 3, 4].

Accelerations normal to the LOS do not perturb the phase signature expected by the SAR processor and therefore do not have to be compensated.

Similar analysis shows that uncompensated accelerations in the x (vertical) and y (horizontal) directions also result in quadratic phase errors proportional to their LOS components. The LOS components of uncompensated velocities in the x and y directions produce linear phase errors, which are manifested as beam pointing errors and geometric map distortion. The longitudinal (z) velocity component does not produce an error only because the SAR signal processor mechanization assumes constant velocity longitudinal motion and compensates it as part of the focusing process.

An additional implication of (7.13) is that required motion estimation accuracies become much finer as the imaging resolution is increased. SAR cross range resolution improves in direct proportion to the aperture time T, which is the maximum value of time t that must be considered in the above analysis. If the maximum quadratic phase error is held to some fixed value such as 180 deg, it follows from (7.13) that the accuracy of the estimate of LOS acceleration must be proportional to the square of the resolution.

7.2.3 Uncompensated Motion in DBS Processing

DBS is a simplified form of SAR that uses fine doppler filtering of the returns from a given range bin to separate scatterers at slightly different aspect angles within the physical beamwidth based on their differential doppler shift. Unlike true SAR processing, the aperture time is not increased with range; consequently, the crossrange resolution degrades with range.

The key assumption of the signal processing is that the doppler shift of the echoes from a given target is constant over a CPI. Doppler shift in hertz is related to slant range by:

$$f_D(t) = -\frac{2}{\lambda}\dot{R}(t) \tag{7.14}$$

From (7.10) and (7.14), the doppler shift for a fixed target is seen to be:

$$f_D(t) \cong \frac{2}{\lambda}\left\{v_0 \cos\phi - \left[\frac{(v_0 \sin\phi)^2 - \dot{v}(0) R_0 \cos\phi}{R_0}\right] t\right\} \tag{7.15}$$

The first term of (7.15) is the standard "$2v/\lambda$" doppler shift, projected onto the LOS. It does not vary with time, but does vary with angle ϕ to the target; this is the phenomenon exploited by DBS. The second term, however, represents a linear

doppler frequency drift, equivalent to a quadratic phase error. The DBS processor must compensate this term or suffer a loss of gain and resolution and an increase in sidelobes.

There are two components to the doppler drift. The first is the component of platform velocity orthogonal to the LOS, which can be termed the tangential velocity. This component is present even if the platform exhibits perfect constant-velocity flight. The second is the LOS acceleration. Tangential velocity acts to drift the doppler shift by changing the cant angle ϕ between the velocity vector and the LOS to a given target. LOS acceleration drifts the doppler frequency by directly modifying the radial velocity between the radar and target. Their relative magnitude depends on the encounter geometry, as well as the platform acceleration. For instance, tangential velocity approaches zero for nearly forward-looking DBS, where ϕ may become small.

Both components must be compensated for proper DBS operation. This differs from SAR processing, which did not require motion compensation of the tangential velocity, because the SAR focusing operation assumes constant-velocity forward motion and compensates for the resulting tangential velocity. Also, note that the tangential velocity component varies with range. In general, motion compensation calculations must be carried out separately for each range bin.

7.2.4 Stepped-Frequency Range Profiling

Stepped-frequency radar systems that use the DFT to form high-range resolution profiles assume no relative motion between the radar and target. The effect of a LOS velocity component $v_0 \cos \phi$ is studied in [5], where it is shown that uncompensated LOS velocities introduce both linear and quadratic phase error terms, therefore resulting in both circular shifting of the range profile (due to the linear phase term) and loss of resolution and gain (due to the quadratic term). Consider the quantity:

$$P = \frac{(N \cdot \text{PRI}) v_0 \cos \phi}{\delta R} \tag{7.16}$$

where N is the number of frequency steps and δR is the processed range resolution. Thus, P is simply the target "range walk" (the variation in LOS range over the CPI) normalized to the system range resolution. It is shown in [5] that the number of bins by which the range profile is shifted is $(f_0/B)P$ (where B is the total stepped bandwidth and f_0 is the center of the band of frequencies) and that the quadratic phase error in radians is $2\pi P$. Because the relative bandwidth is usually less than 10%, P must be kept very small to avoid profile shifting. If shifting is tolerable or can be compensated, then P need only be held to about 0.5 to 1. This will result

in quadratic phase errors of 180 to 360 deg. As shown in Chapter 6, the resulting loss of resolution and gain and distortion of the sidelobe structure will be slight.

7.3 MOTION COMPENSATION IMPLEMENTATION

The above discussion shows that velocities and accelerations must be estimated in all three spatial dimensions to determine the correct phase corrections to apply to the radar data. The conventional solution is to use motion sensing instruments such as gyroscopes and accelerometers to estimate position and velocity in three dimensions. The amount and complexity of the instrumentation depends on the resolution required. As shown above, finer resolution requires large improvements in motion estimation accuracy. For example, in [4] it is estimated that velocity errors up to 0.15 m/s can be tolerated for DBS processing at X-band. In [6] a higher resolution X-band SAR is considered and a requirement of 0.3 mm/s is estimated, a decrease by well over two orders of magnitude in the tolerable velocity error.

7.3.1 Conventional Motion Compensation Systems

The most basic approach to instrumenting a motion compensation system is to use the *inertial navigation system* (INS) on board the aircraft to estimate the path deviations. For low-resolution mapping this may be adequate. However, the INS is designed to measure the motion of the aircraft centroid. For correcting radar data, it is the motion of the antenna phase center that is important [1, 3]. Although the nominal position of the antenna relative to the aircraft (the "lever arm") is known, the motion of the antenna gimbal and flexure of the aircraft structure cause the displacement between the INS and the antenna phase center to vary. Because displacements of a small fraction of a wavelength can cause large phase errors, some systems mount additional accelerometers directly on the antenna structure. Although the accelerometer data can solve the gimbal problem, airframe flexure still limits compensation accuracy because of gravity and earth rotation effects [3].

The next step up in complexity replaces the accelerometer triad with an antenna-mounted "strapdown" *inertial measurement unit* (IMU), which combines three gyroscopic channels with the three accelerometers. IMU and INS data are mixed to obtain improved estimates of radar phase center motion. The limiting factor in this configuration is inaccuracy in estimating the attitude of the IMU with respect to local horizontal, which affects the IMU and INS mixing process. The most elaborate configuration uses the same INS and IMU configuration, but implements a "transfer alignment" Kalman filter to optimally align the IMU horizontal reference to that of the INS, thus "slaving" the IMU motion estimates to those of the INS [3, 4, 68]. In some cases, additional position and motion inputs such as

radar-derived velocity estimates, barometric and radar altimeter data, or *global positioning system* (GPS) data may also be used to refine the motion estimates.

Figure 7.3 illustrates a generic example of the fourth motion compensation instrumentation approach. The transfer alignment Kalman filter combines motion and position data from the aircraft INS, the output of the radar's precision doppler velocity measurement mode, and the aircraft altimeter. In a typical sequence [3], the *radar data processor* (RDP) will use data from the INS to provide the IMU with an initial estimate of the transformation from INU coordinates to the local horizontal frame and the aircraft velocity vector in that coordinate frame. Once initialized, the IMU returns data to the RDP, which compensates it for the lever arm displacement between the IMU and INS. The RDP then computes the difference between the INS and IMU attitude and velocity estimates.

These differences become inputs to the Kalman filter, which typically has perhaps 15 to 21 states. For example, the system described in [3] uses the following 21 states:

- Three velocity errors (x, y, and z dimensions);
- Three gyroscope bias errors;
- Three gyroscope scale factors;
- Three each of accelerometer bias and scale factors;
- Three platform misalignment angles;
- Heading error;
- Two tilt angles (x and y dimensions).

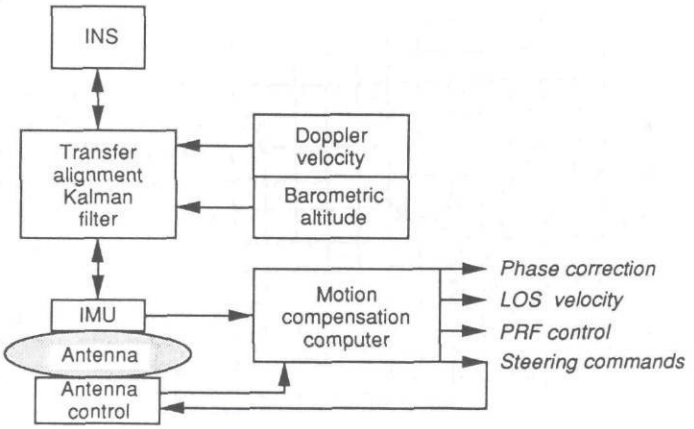

Figure 7.3 Structure of an advanced motion compensation system using both the platform INS and a strapdown IMU. Also included are auxiliary velocity and altitude sensors.

Others may also be used [7]. The Kalman filter outputs are fed back to the IMU, which uses them to correct its velocity and acceleration estimates.

As shown in Figure 7.3, a motion compensation computer uses the corrected IMU data to generate several outputs. Most fundamental is the phase correction function ϕ_e, which is used directly to compensate the phases of the received radar data. Steering commands are fed back to the antenna controller to stabilize the antenna LOS. LOS velocity is used to correct the range gate timing to compensate for range walk, as will be discussed below. Finally, PRF control is used to adjust the interval between pulses so that the spacing of data samples in the along-track dimension ($+z$ in Fig. 7.2) is constant. The motion compensation computations are often carried out in the RDP rather than in a separate processor.

7.3.2 Range Migration

The discussion so far has implicitly assumed that any given scatterer remains within a particular radar range gate during the CPI, but because the radar platform is moving, the range to the target varies during the CPI, as is obvious from (7.10). If the change in $R(t)$ over a CPI is larger than the range resolution, then data from a given scatterer will migrate from one range bin to another during the CPI. This effect must be compensated or the data will not be focused properly in the signal processor.

Range migration has two components: range walk ΔR_w and range curvature ΔR_c. Figure 7.4 illustrates the difference. Range walk results from the second (linear

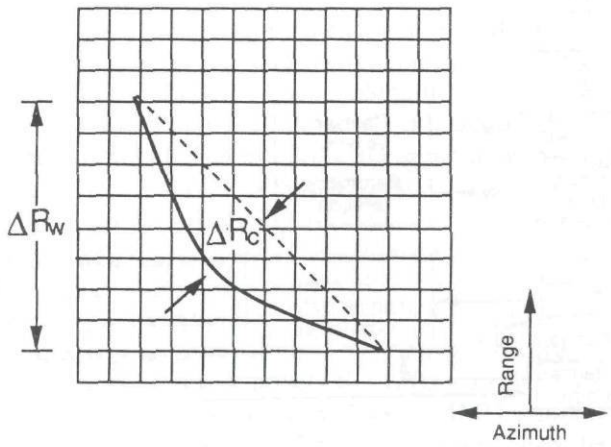

Figure 7.4 Illustration of range walk (ΔR_w) and range curvature (ΔR_c) components of range migration.

in time) term of (7.10). The magnitude of the range walk that develops over a CPI of total duration T is just that term evaluated at time $t = T$ [2]:

$$\Delta R_w = v_0 T \cos \varphi \tag{7.17}$$

Range curvature results from the third (quadratic in time) term. The deviation from the straight line connecting the values of the third term at $t = 0$ and $t = T$ is maximum at $t = T/2$. In the case of constant-velocity flight, this gives a range curvature of:

$$\Delta R_c = \frac{(v_0 T \sin \varphi)^2}{8R_0} \tag{7.18}$$

Range migration can be corrected either by transmitter control or in the signal processor. As shown in (7.17) and(7.18), the amount of migration can be estimated from the same types of LOS and tangential velocity estimates computed by the motion compensation computer for fine phase corrections. For example, a LOS velocity output as shown in Figure 7.3 can be used to adjust the range gate timing so that a given range gate stays fixed at the same absolute position on the ground. The echoes from a given scatterer will then remain in the same range gate throughout a CPI. Alternatively, the range gate timing can be left fixed. Shifting and interpolation of the data in the range dimension can then shift the relative range of the data from successive pulses after the fact in the signal processor [2].

7.3.3 Autofocus

Increasing system resolution rapidly increases motion compensation accuracy requirements. An alternative to increasingly complex conventional motion compensation systems is autofocusing.

Autofocus algorithms use the radar data themselves to aid in estimating the motion parameters needed to focus those same data. At least two distinct approaches have been proposed. The first is the "map-drift" method [9]. In this method, two or more independent images of a scene are formed and then cross-correlated. If the data are well focused, the two images will register and the cross-correlation peak will occur at zero shift. If there are focusing errors, the cross correlation peak will occur away from zero shift. The actual location of the peak can be used to estimate a phase correction to apply to the data. The data can then be refocused. The map-drift method is often applied iteratively.

The second method is the *phase gradient algorithm* (PGA) [9, 10]. This technique assumes the uncompensated phase error is the same for each range bin collected on a given pulse. The phase error is estimated by choosing the brightest

scatterer in each range bin of the focused image, aligning each of them to a common azimuth location, and decompressing the image in azimuth. The phase error function is then estimated from the decompressed image and used to refocus the image. The process is repeated iteratively. According to [9], the PGA generally produces better image quality than the older map-drift methods. Both have similar computational requirements per iteration; however, the PGA method typically requires ten or more iterations versus only two or three for map drift.

REFERENCES

[1] Kirk, Jr., J. C., "Motion Compensation for Synthetic Aperture Radar," *IEEE Trans. Aerospace and Electronic Systems*,Vol. AES-11, No. 3, pp. 338–348, May 1975.

[2] Richards, M. A.,"Synthetic Aperture Processing," Chapter 9 in G. V. Morris, *Airborne Pulsed Doppler Radar*, Norwood, MA: Artech House, 1988.

[3] Kennedy, T. A., "The Design of SAR Motion Compensation Systems Incorporating Strapdown Inertial Measurement Units," *Proc. 1988 IEEE National Radar Conf.*, pp. 74–78.

[4] Oh-hashi, Y., et al.,"Motion Compensation and Effects of Phase Errors in Airborne Synthetic Aperture Radar," *Proc. 1984 IECE Int. Symp. on Noise and Clutter Rejection in Radars and Imaging Sensors*, pp. 615–620.

[5] Einstein, T. H., "Generation of High Resolution Radar Range Profiles and Range Profile Autocorrelation Functions Using Stepped-Frequency Pulse Trains," Massachusetts Institute of Technology Lincoln Laboratory Project Report TT-54, October 18, 1984.

[6] Burns, R. C.,R. M. Schwarz, and J. A. Guffey, "Strapdown Performance Study, Vol. I: Performance Analysis, Simulations, and Improvement Programs," Final Report AFWAL-TR82-1074, Vol. I, U.S. Air Force Avionics Laboratory, July 1982.

[7] Hepburn, J. S. A., et al., "Motion Comepnsation for High Resolution Spotlight SAR," *Proc. IEEE 1984 Position Location and Navigation Symp.* (PLANS '84), November 1984, pp. 59–65.

[8] Bogler, P. L., "Motion-Compensated SAR Image ISLR," *IEEE Trans. on Geoscience and Remote Sensing*, Vol. GE25, No. 6, November 1987, pp. 871–878.

[9] Otten, M. P. G., "Comparison of SAR Autofocus Algorithms," *Proc. Military Microwaves 1990*, pp. 362–367.

[10] Ghiglia, D. C., and G. A. Mastin, "Two dimensional phase correction of synthetic-aperture-radar imagery," *Optics Letters*, Vol. 14, No. 20, October 15, 1989, pp. 1104–1106.

Chapter 8
MTI Systems

Robert R. Kerr
Georgia Institute of Technology

8.1 INTRODUCTION

The *IEEE Standard Dictionary of Electrical and Electronics Terms* defines *moving target indication* (MTI) as [1]: "A technique that enhances the detection and display of moving radar targets by suppressing fixed targets. Doppler processing is one method of implementation." Although other methods of MTI processing exist, the most common configurations in modern radars employ doppler processing through the use of time-delay cancelers at low-to-medium PRF.

This chapter examines several system parameters that affect the MTI performance of coherent radar systems employing time-delay cancelers. These parameters may limit the suppression of fixed targets by effectively corrupting the transmitted and received radar signal spectra, causing a portion of the energy reflected from fixed targets to generate corresponding receiver signals that fall within the doppler frequency passband of the time-delay canceler.

Before presenting performance considerations, two sections are included in reference to coherent MTI systems. Section 8.2 presents the hardware architecture of two common coherent MTI systems at the block diagram level and includes the time domain response of simple time-delay cancelers. Section 8.3 reviews the spectral performance of time domain cancelers and defines terms associated with the performance evaluation of MTI systems.

Section 8.4 reviews the clutter spectrum spreading effects of various system parameters of MTI radars. For scanning radar systems with mechanically steered antennas, the chief performance-limiting factor is usually the scanning modulation caused by the continuous motion of the antenna beam past varying targets and clutter. With the use of electronically steered phased-array antennas that afford

the movement of the antenna beam in discreet angular steps, the target illumination can be controlled such that this effect is reduced. However, other system parameters place limitations on the further improvement of MTI clutter rejection. Probably the least well understood of these is the effect of signal source phase noise. The analysis of this effect will be emphasized here.

Section 8.5 presents example performance calculations for three different coherent MTI systems.

8.2 MTI SYSTEM ARCHITECTURE

8.2.1 MTI Block Diagram

Figure 8.1 presents a block diagram of a single delay (two pulse) time-delay clutter canceler.

The canceler takes advantage of the fact that radar echoes from targets with finite radial velocity relative to the radar's position exhibit a change in the relative phase of the transmitted and received pulses from one pulse to the next, whereas the relative phase of transmitted and received pulses reflected from fixed targets remains stable over the same period. By synchronously detecting the received pulses, using a reference signal that maintains a fixed phase relationship with the transmitted pulses, the detected signal amplitude due to moving targets changes from one pulse to the next, whereas the signal amplitude due to fixed targets remains constant. Cancellation of the fixed target echoes is achieved by subtracting the detected signal amplitudes of sequential pulses. In modern radar systems, this is accomplished by subtracting the digitized receiver video using samples taken one PRI apart.

The response of time-delay clutter cancelers to moving targets varies with the target's radial velocity. For a target at range R_0 and a transmitted wavelength l, the resulting signal at the input to the canceler at time t is described by the equation:

$$A_i(t) = A \sin (2\pi f_d t + \Theta)$$

where

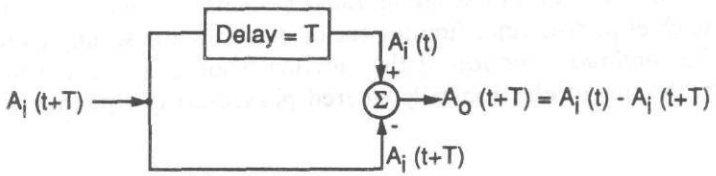

Figure 8.1 Single delay canceler block diagram.

A_i = the amplitude of the uncanceled signal,
f_d = the doppler frequency, and
Θ = the phase shift due to range at time t, relative to the radar's reference oscillator = $4\pi R_0(t)/\lambda$

The signal one PRI (time T) later is:

$$A_i(t + T) = A \sin [2\pi f_d(t + T) + \Theta]$$

The resulting output from the canceler is:

$$\begin{aligned} A_o(t + T) &= A_i(t) - A_i(t + T) \\ &= -2A \sin(\pi f_d/f_r) \cos [2\pi f_d(t + 1/2f_r) + \Theta] \end{aligned} \tag{8.1}$$

where $f_r = 1/T$ = the PRF.

Equation (8.1) describes a sine wave at the doppler frequency whose amplitude depends on the ratio of the doppler frequency to the PRF. If the doppler frequency is any integral multiple of the PRF, the response goes to zero. Maximum response occurs at integral plus one-half (0.5, 1.5, 2.5, etc.) doppler-to-PRF ratios. The output-to-input signal power ratio versus the target doppler-to-PRF ratio is plotted in Figure 8.2

The target radial velocities corresponding to the integral doppler-to-PRI ratios are termed "blind speeds" and are given by:

$$V_{\text{blind}} = \lambda n f_r/2 \tag{8.2}$$

where n = an integer.

It is important to note that, depending on the relationship of f_d, f_r, and Θ in the argument of the cosine term of (8.1), it is also possible to have "blind phases" where the instantaneous response to a moving target is zero even though the target's radial velocity is not equal to a blind speed. Blind phases can be eliminated by using a second receiver channel and canceler whose detection reference signal is phase-shifted by 90 deg. The technique is equivalent to the I and Q detection process described in Chapter 1. The output signal powers of the two quadrature channels are added to maintain the receiver response at the maximum corresponding to the particular doppler-to-PRF ratio.

8.2.2 Coherent-on-Receive Systems

The system block diagram of a coherent-on-receive radar system with quadrature MTI clutter cancelers is shown in Figure 8.3. This type of system is used when the

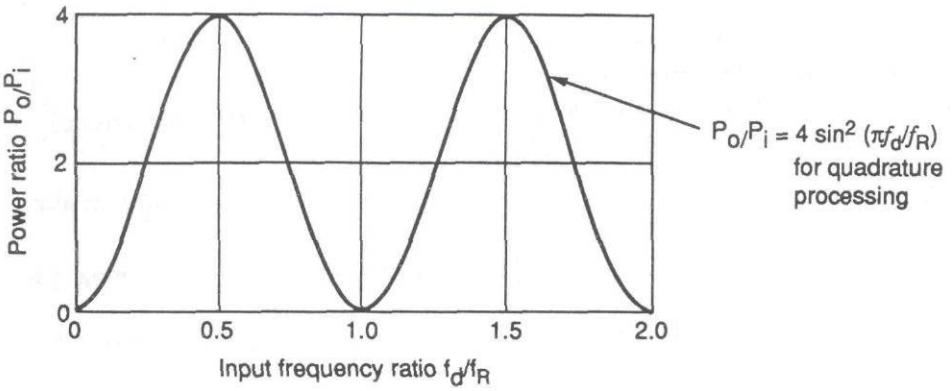

Figure 8.2 Power response of single delay canceler.

transmitter consists of a pulsed-power oscillator, such as a magnetron. Pulsed oscillators exhibit a random shift in the phase of the transmitted carrier from one transmitted pulse to the next. This phase shift must be compensated in the receiver before the time-delay canceler so that sequential echoes from fixed targets will cancel. The solution in this instance is the use of continuous local oscillators to down-convert both the transmitted and received signals to the receiver IF frequency and to detect both the transmitted and received IF signals using quadrature processing. The local oscillators, LO1 and LO2 in Figure 8.3, are phase stable over a period that is long relative to the PRI and serve to generate a phase reference for the transmitted signal. Using digital processing, the detected reference phase of each transmitted pulse is subtracted from the phase of the received signal during the subsequent PRI. The phase-compensated received signal can then be processed by the time-delay canceler.

A disadvantage of coherent-on-receive systems is that they cannot be used to cancel ambiguous range clutter. Clutter echoes from beyond the unambiguous range are not phase-compensated in the receiver and therefore do not cancel. When the unamibiguous range extends to the major part of the detection range of the radar or when the antenna beam does not directly illuminate substantial ground clutter at ambiguous ranges, this is generally of decreased importance, but even under these conditions ambiguous clutter may be significant if the radar's environment contains ducted propagation paths with substantially decreased range loss. And, as system-transmitted power, PRF, and receiver sensitivity are increased, the target masking effects of ambiguous clutter returns become more severe.

Often, the coherent-on-receive technique is implemented as a modification to existing noncoherent pulsed systems in which transmitter intrapulse phase sta-

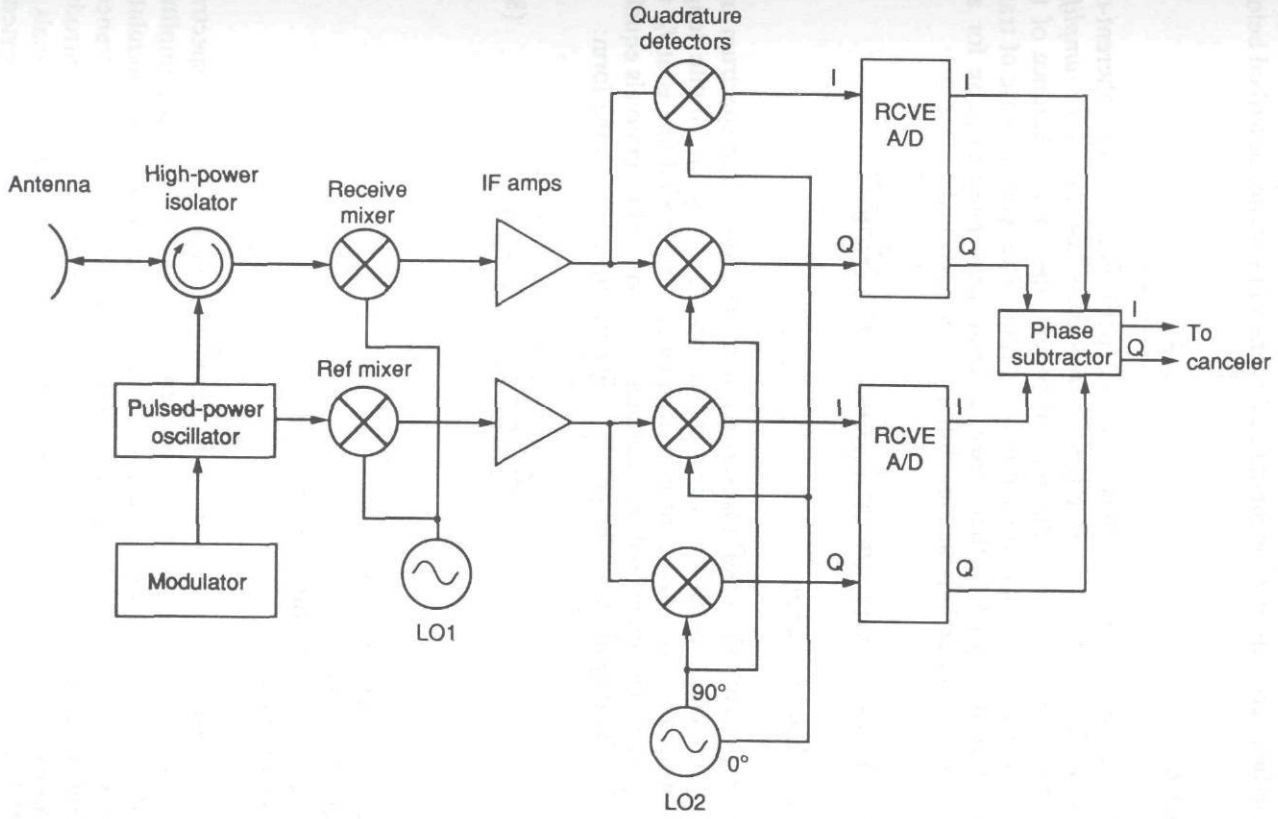

Figure 8.3 Coherent-on-receive MTI system.

bility was not a concern during design. In such cases the MTI performance is not expected to be as good as that for continuously coherent systems, described below.

8.2.3 MOPA

A system architecture that exhibits improved performance over coherent-on-receive, particularly in higher PRF systems, is the *master-oscillator-power-amplifier* (MOPA) type of Figure 8.4 In this type of system, the phase coherence of the transmitted signal extends over the entire pulse train. The relative phase of transmitted and received signals is therefore a constant from pulse to pulse for any particular fixed range, and ambiguous clutter can be cancelled.

8.3 DEFINITION OF MTI SPECTRAL PERFORMANCE

8.3.1 Radar Signal Spectrum

Figure 8.5 represents the ideal positive frequency portion of the spectrum of a continuous, noiseless, coherent carrier signal modulated by an infinite length sequence of pulses of constant repetition frequency. The central line is at f_0, the carrier frequency. The individual spectral lines are separated by intervals equal to the PRF, f_R. The magnitude envelope of the spectral lines follows the form:

$$E(f) = \frac{A\tau \sin(\pi\tau|f - f_0|)}{2T(\pi\tau|f - f_0|)} \tag{8.3}$$

where:

A = peak carrier amplitude,
f_0 = carrier frequency,
$T = 1/f_R$ = pulse repetition period, and
τ = pulse duration.

Unfortunately, real carrier and pulse modulator signals are not so spectrally perfect as that required to produce the spectrum in Figure 8.5. Phase and amplitude noise of the carrier signal and finite duration and timing jitter of the modulating signal cause the spectral lines to spread into bell-shaped curves. Other extraneous modulation of the transmitter interference sources within the system may introduce spectral spreading or spectral lines offset from the carrier. When such signals are transmitted by a radar, reflected from targets and clutter, and down-converted by the receiver, the spectral lines are broadened further by several clutter-spreading

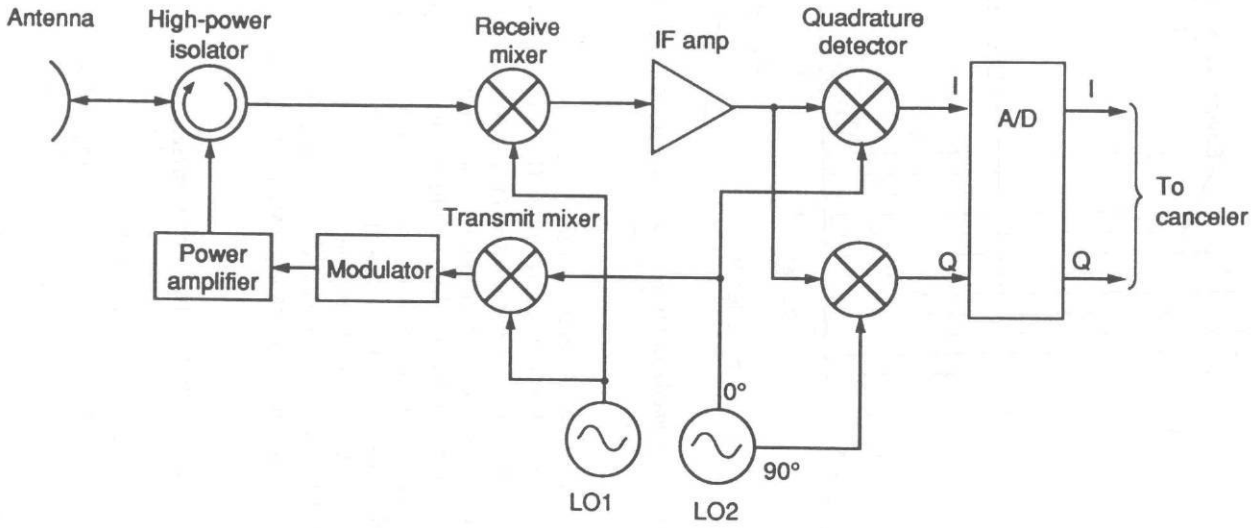

Figure 8.4 MOPA coherent MTI system.

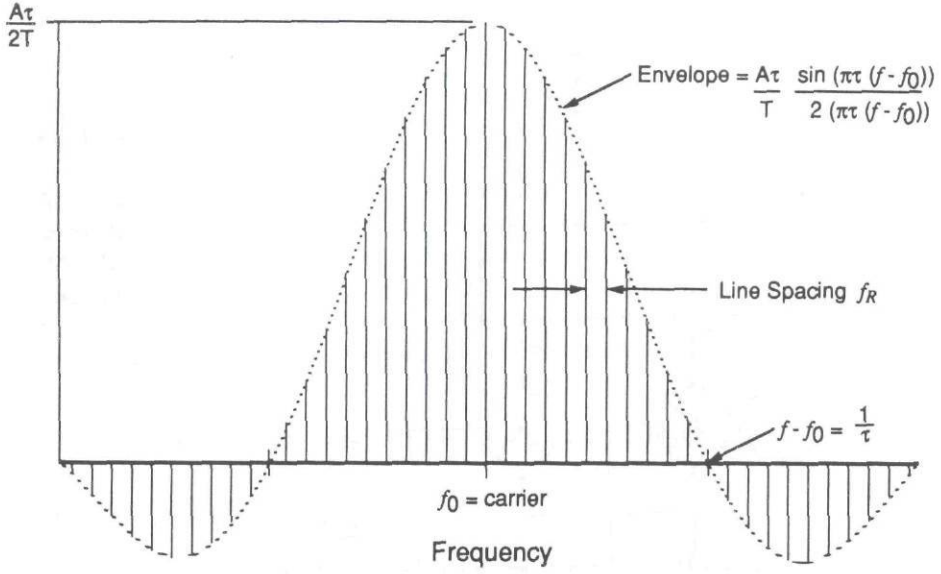

Figure 8.5 Ideal spectrum of a carrier modulated by pulse sequence of infinite length.

effects, including clutter motion, antenna scanning, and receiver local oscillator noise. The resulting signal spectrum at the receiver IF might look something like that of Figure 8.6. (The number of spectral lines shown is reduced for clarity.)

An ideal clutter filter would have an attenuation spectrum that exactly reduced the clutter harmonic spectrum to the level of amplified thermal noise at the filter input, while providing zero attenuation at other frequencies. However, the variability of clutter signal conditions that a typical radar encounters makes this a difficult, if not impossible, design goal to define. Instead, clutter filters are usually designed to have a fixed frequency response that represents a compromise given the anticipated clutter environment and radar system hardware capability.

8.3.2 Delay Canceler Clutter Filter Spectral Performance

The single delay canceler described in section 8.2 has clutter rejection notches of narrow spectral width at frequencies that are integral multiples of the PRF. When a signal spectrum such as that of Figure 8.6 is applied to this filter, a considerable output power, termed "clutter residue," results, because of the portion of the clutter spectrum lying outside the rejection notches. The clutter residue may mask the presence of small amplitude targets of interest; thus, it is desirable to tailor

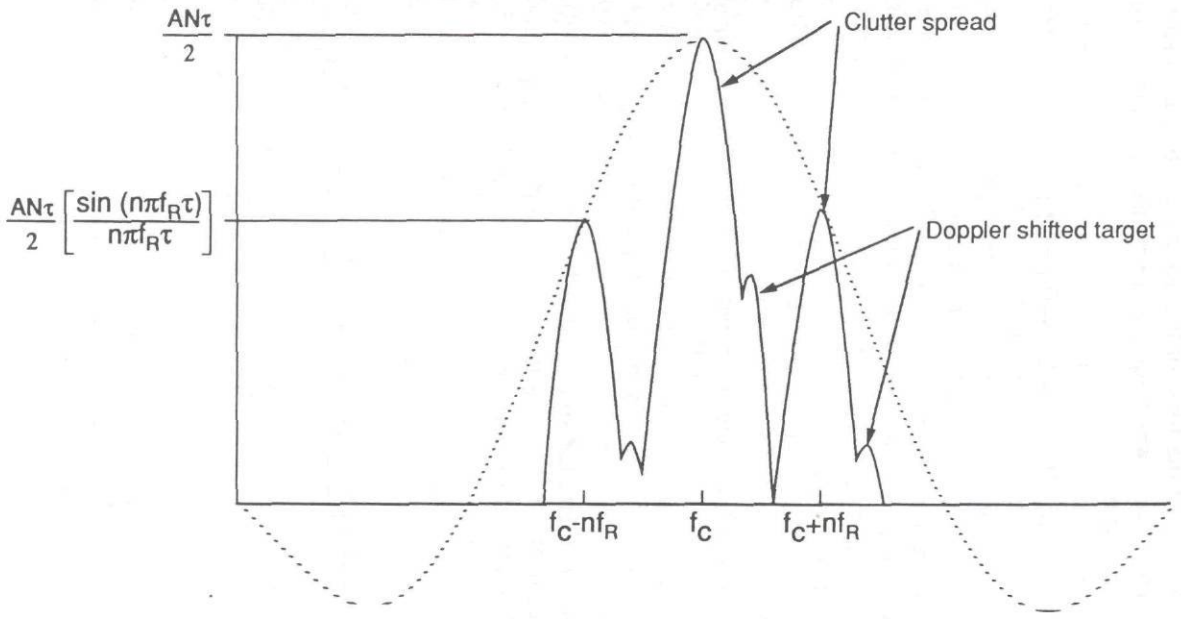

Figure 8.6 Spectrum of a radar signal with clutter spreading and a doppler-shifted target. Several PRF lines have been omitted for clarity.

the spectrum of the rejection notches to increase attenuation of the clutter power spectrum.

Single delay cancelers of the form of Figure 8.1 can be cascaded to obtain a broader rejection notch. The power frequency response of a number of cascaded delay cancelers is of the form:

$$[S_o/S_i]_n(f_d) = 2^{2n} \sin^{2n}(\pi f_d/f_r) \tag{8.4}$$

where:

S_o = Output signal power,
S_i = Input signal power,
n = number of cascaded cancelers,
f_d = doppler frequency, and
f_r = PRF.

The gain of the n delay canceler response of (8.4) averaged over all doppler frequencies is:

$$[S_o/S_i]_n(\text{avg}) = 1 + n^2 + [n(n-1)/2!]^2 + [n(n-1)(n-2)/3!]^2 + \cdots 1 \tag{8.5}$$

An identical response to cascaded single delay cancelers can be obtained with a transverse filter as in Figure 8.7, where the delay outputs are amplitude-weighted with binomial coefficients before being input to a summing network:

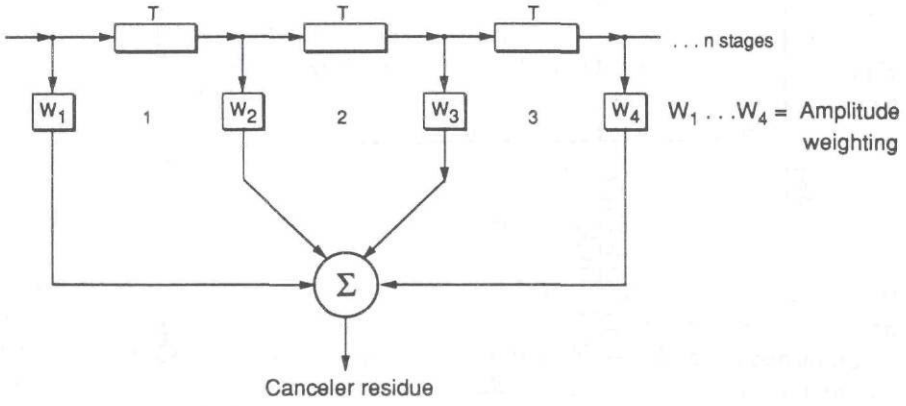

Figure 8.7 Transverse filter.

Coefficients of $(1 - x)^n$:

$n = 1$: 1, −1

$n = 2$: 1, −2, 1

$n = 3$: 1, −3, 3, −1

Other more complex cascaded delay cancelers are possible using weighted feedback and feedforward summations to further control the steady-state frequency response of the filter. However, when feedback is employed in time-delay cancelers, the transient response amplitude and decay time at the canceler output is increased over that of nonfeedback cancelers using the same number of input-to-output delays and operating at the same PRF. Thus, the use of feedback sets a limitation on the maximum antenna angular scan rate for search radars. Also, the use of feedback becomes impossible with step-scanned phased array antennas, if the feedback configuration exhibits infinite impulse response.

Another method of controlling the frequency response of radars employing time-delay cancelers, termed "PRF stagger," sequences two or more slightly different PRIs in the transmitted pulse train. The purpose of PRF stagger is to eliminate nulls in the frequency response (blind speeds) over a range of doppler frequencies equal to several harmonics of the base PRFs used. The frequency response characteristic obtained varies with the number and duration of the various PRIs and the type of canceler used. Design tradeoffs control the passband frequency response flatness versus clutter attenuation limits. Because the time delay(s) of the clutter canceler must be actively staggered to match the transmitted PRI sequence, PRF stagger has the disadvantage that it cannot be used to cancel ambiguous clutter. Clutter echoes from beyond the unambiguous range will arrive with PRIs that do not match those of the time-delay canceler and will not be attenuated. PRF stagger also reduces clutter cancellation relative to a nonstaggered system when using a binomialweighted cancelers.

Figure 8.8 illustrates the frequency response of a PRF stagger system clutter canceler employing two PRIs of ratio 0.65 : 1 and a three-pulse (two-delay) canceler with binomial weighting. The response of an unstaggered system is plotted (artificially suppressed by 20 dB for visual clarity) also for comparison.

As the transmitted PRF is increased, the clutter cancellation limitations of PRF stagger increase in importance because of the increased effects of ambiguous range clutter. These limitations can be overcome by transmitting bursts of different constant PRF waveforms, instead of changing the PRI from one pulse to the next. "PRF diversity" systems independently process the echo returns from each of a sequence of two or more constant PRF waveforms by changing the receiver clutter canceler time delays to match the PRI of each PRF. The independent responses are then integrated to fill in the blind speed doppler frequency ranges or eclipsed range intervals (or both). In order to cancel clutter echoes from any range ambiguity, each constant PRF burst must have sufficient duration for the receiver to

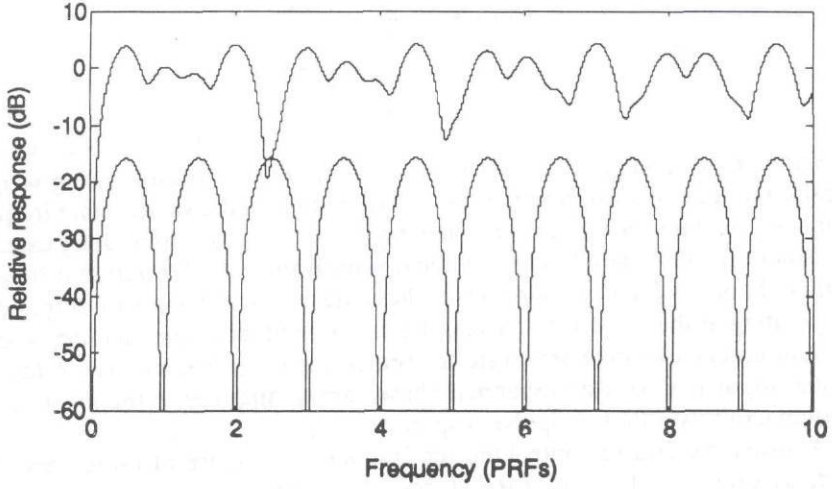

Figure 8.8 PRF stagger system frequency response.

process echoes from the radar's maximum detection range, and the receiver output must be blanked, following each change of transmitted PRF, for an interval long enough to allow the first maximum range echoes from the new PRF to pass through the clutter canceler's time delays.

8.3.3 Definition of Terms Associated With MTI Performance

Several terms are used to describe clutter filter performance [1]:
Clutter Attenuation: "The ratio of clutter power at the canceler input to clutter residue at the output, normalized to the attenuation for a single pulse passing through the unprocessed channel of the canceler."
Clutter Residue: "The clutter power remaining at the output of a moving target indicator system. *Note:* It is the sum of several (generally uncorrelated) components resulting from radar instabilities, antenna scanning, relative motion of the radar with respect to the sources of clutter and fluctuations of the clutter reflectivity."
MTI Improvement Factor: "The signal-to-clutter ratio at the output of the clutter filter divided by the signal-toclutter ratio at the input of the clutter filter, averaged uniformly over all target radial velocities of interest."
Subclutter Visibility: "The ratio by which the target echo power may be weaker than the coincident clutter echo power and still be detected with specified detection and false alarm probabilities. Target and clutter powers are measured on a single pulse return and all target radial velocities are assumed equally likely."

8.4 CLUTTER IMPROVEMENT PERFORMANCE LIMITATIONS FOR COHERENT MTI SYSTEMS

It is desirable to predict the clutter improvement performance of MTI radar systems in order to determine the system parameters required for particular applications. In general, the parameters governing clutter improvement performance that are under the control of the radar designer are those of the radar system itself: antenna beam scan modulation, signal source phase noise, radar platform motion, PRF stagger, and so forth. Any spectral spreading imposed by the nature of the surrounding clutter environment contributes to the degradation of clutter improvement. Initial performance comparisons between radar systems are often made using the system-imposed clutter improvement, with actual clutter statistics considered for specific applications.

The information needed to find the clutter improvement limit is the power spectrum of the received signal at the input to the clutter canceler and the stability of the canceler timing and gain. For echoes restricted to a particular range, the input spectrum will be a reduced amplitude version of the transmitted spectrum, modified by the effects of antenna beam motion, and of amplitude and phase distortion in the receiver. Multiplication of this spectrum by the canceler response ((8.5) for systems employing binomial-weighted cancelers) gives the clutter residue, which can be used to calculate the clutter improvement.

Many clutter spectral spreading mechanisms are modeled in terms of their clutter velocity distributions in order to obtain results that are independent of the operating frequency of the radar. Calculations are greatly simplified if the distributions can be approximated as gaussian, which can be represented by a single parameter, σ, the standard deviation. Conversion from the standard deviation of the velocity distribution to that of the power density spectrum is made by (8.6):

$$\sigma_c = 2\sigma_v/\lambda \tag{8.6}$$

where:

λ = radar operating wavelength, meters,
σ_v = clutter velocity spectrum standard deviation, meters/second, and
σ_c = clutter power spectrum standard deviation, hertz.

The net mean standard deviation due to the action of several different statistically independent mechanisms can be determined as the square root of the sum of the squares of the independent standard deviations:

$$\sigma = [\sigma_1^2 + \sigma_2^2 + \sigma_3^2 + \cdots]^{1/2} \tag{8.7}$$

The calculation of clutter improvement limits for systems employing binomial-weighted cancelers is extensively covered in the literature. Following the development of [2], the improvement factors for gaussian clutter spectra for binomial cancelers with one, two, and three delays, preceded by linear processing, can be found as:

$$I_1 = [1 - \exp(z^2/2)]^{-1} \tag{8.8(a)}$$

$$I_2 = [1 - (4/3)\exp(-z^2/2) + (1/3)\exp(-2z^2)]^{-1} \tag{8.8(b)}$$

$$I_3 \approx (4/3)\, z^6 \tag{8.8(c)}$$

where:

$z = (2\pi\sigma_v)/V_b = (2\pi\sigma_c)/f_R$
f_R = PRF, hertz,
σ_v = clutter velocity spectrum standard deviation, meters/second,
σ_c = clutter power spectrum standard deviation, hertz, and
$V_b = V_{\text{blind}}$ (8.2), meters/second.

It can be intuitively understood that the clutter improvement (I) is a function of the ratio z, (8.8), by recalling that I is defined (Sec. 8.3.3) as the signal gain to clutter gain power ratio averaged over the frequency range $f = -f_R$ to $f = +f_R$. The ratio z is a measure of the extent to which the clutter spectrum is spread outside the rejection notch into the passband of the canceler.

For clutter spreading mechanisms that are statistically independent and random from pulse to pulse, the individual clutter residues can be combined to arrive at the resulting system clutter improvement limit as:

$$I_s = [(1/I_x) + (1/I_1) + (1/I_2) + \cdots]^{-1} \tag{8.9}$$

where:

I_s = system clutter improvement limit,
I_x = limit imposed by clutter spectrum standard deviation for an x delay canceler, and
I_1, I_2 = individual clutter improvement limits.

Table 8.1 [3] presents clutter improvement limits due to several radar system instabilities.

The remainder of this section reviews several parameters that affect the received clutter spectrum and presents models for their individual effects on the

Table 8.1
Instability Limitations

Pulse-to-Pulse Instability	*Limit on Improvement Factor*
Transmitter frequency	$I = 20 \log[1/(\pi \Delta f \tau)]$
Receiver LO frequency	$I = 20 \log[1/(2\pi \Delta f T)$
Transmitter phase shift	$I = 20 \log(1/(\pi \Delta f T)]$
Pulse timing	$I = 20 \log[\tau/(\sqrt{2}\Delta t \sqrt{B\tau})]$
Pulse width	$I = 20 \log[\tau/(\Delta PW \sqrt{B\tau})]$
Pulse amplitude	$I = 20 \log(A/\Delta A)$
A/D jitter	$I = 20 \log[\tau(J\sqrt{B\tau})]$
A/D jitter with pulse compression following A/D	$I = 20 \log[\tau/(JB\tau)]$

where:

Δf = interpulse frequency change,
τ = transmitted pulse length,
T = transmission time to and from target,
$\Delta\phi$ = interpulse phase change,
Δt = time jitter,
J = A/D sampling time jitter,
$B\tau$ = time-bandwidth product of pulse compression system (Bt = unity for uncoded pulses),
ΔPW = pulse-width jitter,
A = pulse amplitude, volts, and
ΔA = interpulse amplitude change.

clutter improvement. A more extensive analysis of the effects of signal source phase noise is presented.

8.4.1 Antenna Scan Modulation

When the radar antenna beam is scanned in angle, the number of pulses reflected from a particular target is limited by the antenna angular beam width and scan rate. This is effectively a truncation of the transmitted pulse train, and therefore, the reflected signal power spectrum has some of its energy distributed into sidebands around the PRF harmonic lines.

Figure 8.9 shows the positive frequency portion of the voltage frequency spectrum of a coherent signal modulated by a constant PRF pulse sequence of N pulses. The envelope of the peak amplitudes at the PRF harmonic frequencies is similar to (8.3), following a $\sin(x)/x$ curve, but has amplitude proportional to N:

$$E(N, f) = \frac{A\tau N \sin(\pi\tau|f - f_0|)}{2(\pi\tau|f - f_0|)} \tag{8.10}$$

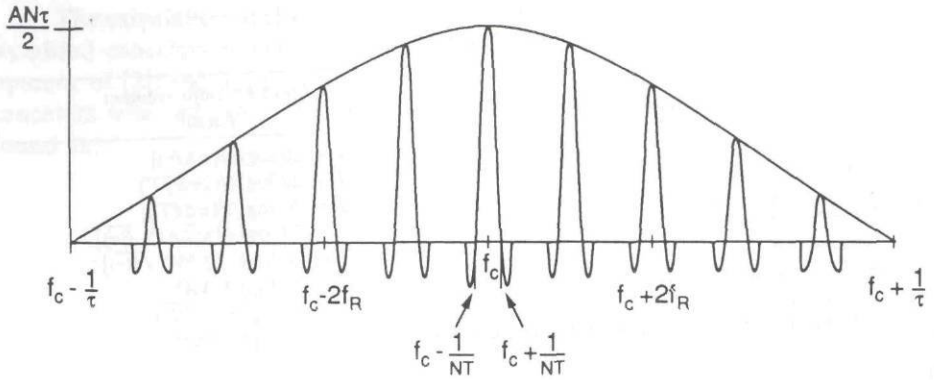

Figure 8.9 Voltage frequency spectrum of coherent signal modulated by a sequence of N pulses.

where:

$E(N, f)$ = envelope amplitude,
A = peak carrier amplitude,
f_0 = carrier frequency, hertz,
N = number of pulses in time domain sequence, and
τ = pulse duration, seconds.

The spectral lines also have a $\sin(x)/x$ form centered about the PRF harmonics:

$$F(f+) = \frac{E(N, f)\sin(\pi NT(f - f_0 \pm nf_R))}{(\pi NT(f - f_0 \pm nf_R))} \tag{8.11}$$

where:

$E(N, f)$ = envelope amplitude (8.5),
f_0 = carrier frequency, hertz,
N = number of pulses in time domain sequence,
n = nth PRF harmonic sideband, $n = 0$ for central spectral line,
$T = 1/f_R$ = pulse repetition period, seconds, and
τ = pulse duration, seconds.
$\pm$ = Applies to upper (+) and lower (−) PRF harmonic sidebands.

Figure 8.9 and (8.11) show that the spectral line width is inversely proportional

to the number of pulses in the sequence. For antenna beam scanning, a more rigorous spectral formulation includes amplitude weighting of the time domain pulses according to the two-way radiation pattern of the antenna. From [3], the clutter power spectrum standard deviation for a gaussian pattern is:

$$\sigma_c = 0.265\, f_R/N \tag{8.12}$$

where:

f_R = PRF, and
N = number of pulses on target between the one-way 3-dB points of the antenna pattern.

The result of (8.12), although derived for a gaussian pattern, is essentially independent of the actual radiation pattern.

8.4.2 Amplitude Limiting

From [2] many radar receivers lack sufficient dynamic range necessary to accommodate large clutter and small target signals simultaneously. This limitation may be imposed by linearity or thermal noise limitations in the analog circuitry, insufficient clutter attenuation in the clutter cancelers, or the number of bits of resolution of the A/D converters. To avoid saturation of the receiver circuitry during signal peaks, amplitude-limiting circuitry is employed, usually in the IF circuitry where analog saturation occurs first as signal amplitude increases because of the signal gain of preceding stages.

The limiting process introduces nonlinear distortion of the clutter spectrum, which tends to spread into the doppler passband of the canceler as the input signal level to limiting level (the signal level at which the circuit begins to clamp the signal amplitude) increases. Figure 8.10 shows how a gaussian clutter spectrum spreads for several values of clutter signal to limit level ratio. Figure 8.11 shows the clutter improvement limits for one, two, and three delay binomial cancelers with and without limiting for varying z (8.8). It is shown that hard limiting reduces the clutter improvement performance of two and three delay cancelers to that of a one delay canceler with no limiting.

8.4.3 A/D Noise

The receiver A/D converter imposes limitations on the signal dynamic range. If the input signal is so large that the A/D saturates, a nonlinear process similar to IF amplitude limiting occurs, spreading the clutter spectrum and degrading the

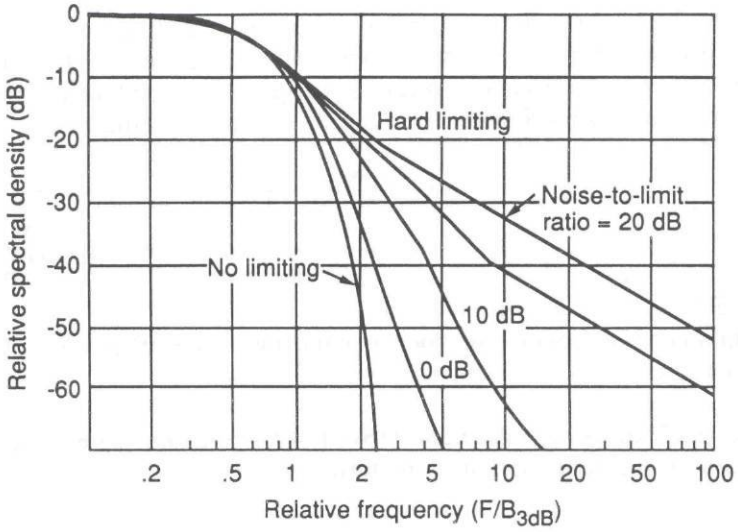

Figure 8.10 Spectral spreading caused by limiting.

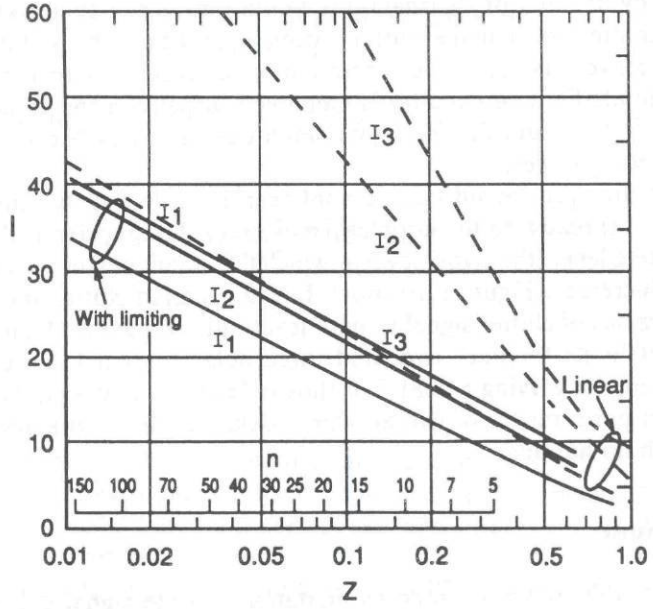

Figure 8.11 MTI improvement factor for linear and limiting processors.

improvement factor. If the input signal is too small, the quantization of the A/D introduces noise that places a fixed limit on the clutter improvement:

$$I_q = 0.75(2^m - 1)^2 \tag{8.13}$$

where:

I_q = quantization noise clutter improvement limit, and
m = number of A/D converter bits.

This limitation is independent of the number of delays in the canceler.

8.4.4 Timing Jitter

From [4] Figure 8.12 illustrates the effect of pulse timing jitter on a time-delay clutter canceler. Fixed-length pulses are assumed to have independent timing error jitters about the correct PRI. If pulse (a) is the canceler input at time t and pulse (b) is the input at time $t + T$, where the canceler delay is T, the output (c) follows from (8.1), showing intervals at the leading and trailing edges of the pulses that are not canceled.

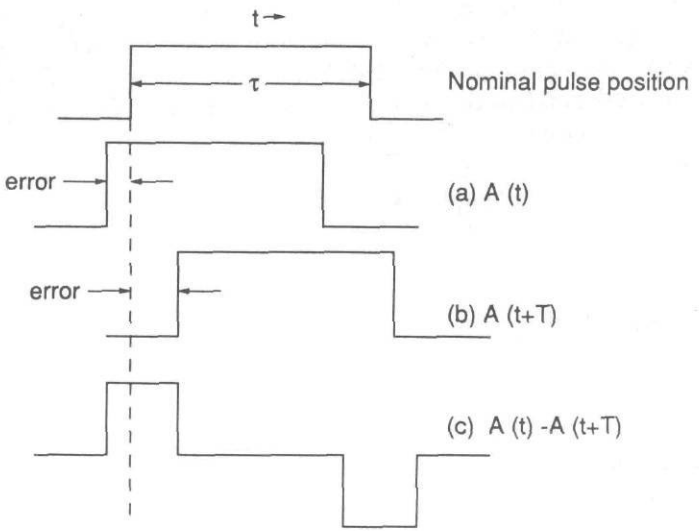

Figure 8.12 Pulse-to-pulse timing jitter.

Assuming the post canceler processing contains a lowpass filter matched to the pulse length t, the clutter improvement limit for one and two delay binomial cancelers with pulse position jitter is approximately:

$$I_1 = I_2 = \tau^2/(2\sigma_\epsilon^2) \tag{8.14}$$

where:

τ = pulse duration, and
σ_ϵ = standard deviation of the pulse leading edge time error.

Similarly, pulse *width* timing jitter causes a clutter improvement limit:

$$I_1 = I_2 = \tau^2/(\sigma_\delta^2) \tag{8.15}$$

where σ_δ = standard deviation of the pulse duration time error.

8.4.5 PRF Stagger

As mentioned in Section 8.3.2, PRF stagger degrades the clutter improvement when binomial weight cancelers are used. PRF stagger causes distortion of the clutter spectra of scattering elements (external clutter, scan modulation, signal source phase noise), generating clutter residues at doppler frequencies near harmonics of the average PRF divided by the number of staggered PRIs used. From (8.3) the clutter improvement limit for a PRI stagger system employing binomial weighted cancelers (independent of the number of canceler delays) in conjunction with antenna scan modulation is:

$$I = 20 \log[(2.5N)/(\gamma - 1)] \text{ (dB)} \tag{8.16(a)}$$

where:

γ = maximum PRI ratio, and
N = number of pulses on target between the one-way 3-dB points of the antenna pattern.

For PRF stagger in conjunction with an independent clutter velocity spectrum, the clutter improvement limit is:

$$I = 20 \log[(0.33\ \lambda f_R)/((\gamma - 1)\sigma_v)] \text{ (dB)} \tag{8.16(b)}$$

where:

f_R = average PRF,
γ = maximum PRI ratio, and
σ_v = rms clutter velocity standard deviation.

Most of the clutter canceling performance of fixed PRF systems employing binomial cancelers can be regained in PRF stagger systems by employing complex, or time-varying, weights in the cancelers to compensate for the uneven sampling intervals of PRF stagger. This added complexity is justified only if PRF stagger is the dominant mechanism limiting system clutter improvement.

8.4.6 Phase Noise

In Chapter 2 a thorough examination of the sources of phase noise is presented, with typical values for various oscillator configurations and frequency bands summarized.

When, as in an MOPA configuration MTI radar transmitter, the signal source signal is pulse-modulated by a fixed PRF, the resulting spectrum is the convolution of the CW source spectrum with the line spectrum of the pulse train. Each of the pulse train spectral lines is spread by the phase noise spectrum of the CW source. This process is illustrated in Figure 8.13.

The frequency range of interest for clutter improvement calculations in a constant PRF MTI system is the interval between central spectral line centered at $f_0 \pm f_R$ and the first PRF lines centered at $f_0 f_R$. In Figure 8.13 it can be seen that all the PRF harmonic clutter spectra contribute to the noise density in this interval by virtue of the frequency extent of their sidebands.

From [5] the normalized transmitted phase noise power density spectrum can be expressed as the summation of the phase noise power densities due to the sidebands of each of the PRF harmonic clutter spectra lying within the transmitted bandwidth:

$$S_T(f_0 + f_d) = S(f_d) + \sum_{i=1}^{i=N} [[E(f_0 + if_R)/E(f_0)]^2 \cdot [S(f_0 + if_R + f_d) + S(f_0 + if_R - f_d)]] \tag{8.17}$$

where:

$E(f)$ = spectral amplitude envelope (8.3),
f_d = doppler frequency, hertz,

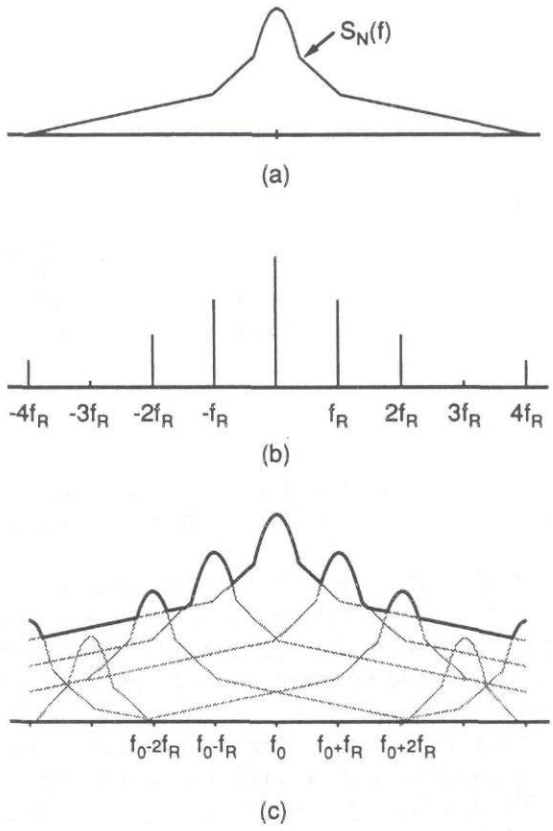

Figure 8.13 Convolution of CW source phase noise spectrum with modulating pulse train line spectrum. (a) CW source phase noise spectrum; (b) modulating pulse train line spectrum; (c) resulting transmitted spectrum.

f_0 = transmitter carrier frequency, hertz,
f_R = PRF,
N = *number of PRF harmonics within the transmitted bandwidth (ssb), and*
$S(f)$ = normalized signal source power density spectrum.

In (8.17) the first term on the right side represents the phase noise at offset from the carrier f_d due to the noise sidebands of the central spectral line. Inside the brackets of the summation the first factor is a normalizing ratio; the first term of the second factor represents the phase noise at f_d due to the noise sidebands of the spectral lines at $f < f_0$; the second term of the second factor represents the

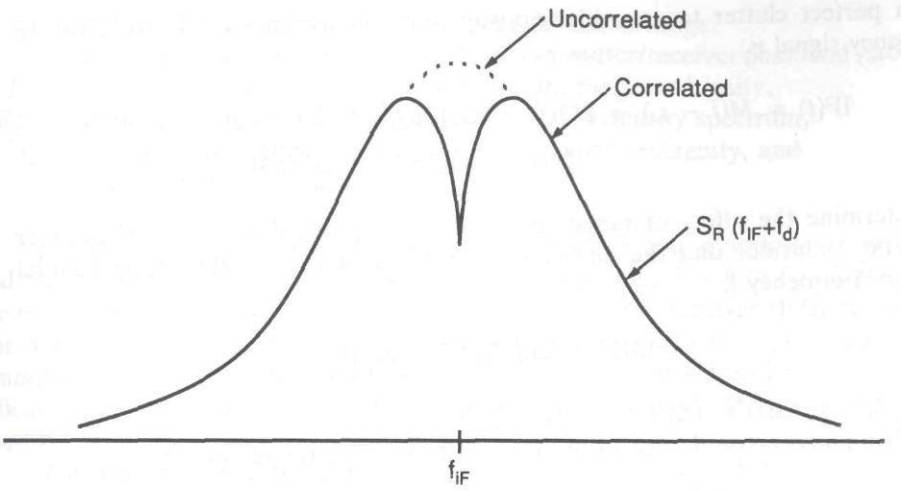

Figure 8.14 Effect of range correlation on received phase noise power density spectrum.

phase noise at f_d due to the noise sidebands of the spectral lines at $f > f_0$. If $S(f)$ for the signal source is known from measurements, (8.17) can be used to find the total phase noise power density over the desired doppler frequency range. In translating this to arrive at the received spectral power density, the effects of returns from ambiguous ranges and of range correlation must be considered.

In coherent systems the phase errors of the transmitted signal are correlated with those of the receiver LO at any given instant, because they are derived from the same source or are phase-locked (Sec. 8.2). For short ranges, where the time interval of the two-way range delay between transmission and reception is short, these phase errors remain correlated to some extent and tend to cancel. This effect is beneficial because it reduces the effect of phase noise on short range clutter, and it effectively attenuates the received phase noise power density spectrum at very low frequencies.

From [5, 6] consider a signal source with phase error (t):

$$M(t) = \cos[2\pi f_0 t + \phi(t)]$$

If the phase error contribution of the IF offset oscillator is small, the coherent receiver LO signal is:

$$\mathrm{LO}(t) = \cos[2\pi(f_0 - f_{if})t + \phi(t)]$$

For a perfect clutter target with two-way range delay time t_d, the receiver IF frequency signal is:

$$\mathrm{IF}(t) = M(t - t_d) - \mathrm{LO}(t) = \cos[2\pi f_{if}t + \phi(t - t_d) - \phi(t)]$$
$$\mathrm{IF}(t) = \cos[2\pi f_{if}t + \Delta\phi(t_d)]$$

To determine the effect of range correlation at a particular range and doppler frequency, consider that the master oscillator is phase-modulated by sinusoidal signal of frequency f_m:

$$M(t) = \cos[2\pi f_0 t + \phi(t)]$$

where $\phi(t) = (\Delta(t) = (\Delta f/f_m)\cos[2\pi f_m t]$

The phase error change for a target with two-way range delay t_d is:

$$\Delta\phi(t_d) = (\Delta f/f_m)[\cos(2\pi f_m t) - \cos(2\pi f_m t - t_d)]$$
$$= -2(\Delta f/f_m)[\sin(\pi f_m t_d)\sin(\pi f_m(t - t_d)]$$

For small $\Delta\phi$, the voltage sidebands at offset frequency f_m are given by:

$$F(f) = 2(\Delta f/f_m)\sin|\pi f_m t_d|$$

The peak value of the power of the phase modulation sidebands at frequency f_m for range t_d is:

$$S(f) = 4\sin^2|\pi f_m t_d| \tag{8.18}$$

A received signal spectrum centered at the receiver IF frequency, representing the sum of the average clutter powers received from each range ambiguity within the radar detection range, can now be determined from the transmitted spectrum:

$$S_R(f_{if} + f_d) = \sum_{i=0}^{i=M} (\tau/T)Pc_i\{[S(f_0 + f_d)\cdot 4\sin^2|\pi f_d t_{di}|]$$
$$+ \sum_{j=1}^{j=N} [[\sin(\pi\tau jf_R)]/(\pi\tau jf_R)]^2\cdot[[S(f_0 + jf_R + f_d)\cdot 4\sin^2|\pi(jf_R + f_d)t_{di}|] \tag{8.19}$$
$$+ [S(f_0 + jf_R - f_d)\cdot 4\sin^2|\pi(jf_R - f_d)t_{di}|]]\}$$

where:

f_d = doppler offset frequency,
$1/T$ = PRF,

M = number of range ambiguities in radar detection range,
N = number of PRF spectral harmonics in transmitter/receiver passband (ssb),
Pc_i = average clutter power return from the ith range ambiguity,
$S(f)$ = normalized signal source phase noise power density spectrum,
t_{di} = two-way range time delay to clutter in the ith ambiguity, and
τ = transmitted pulse width.

Equation (8.19) includes the effects of signal source phase noise on transmit and receive and can be evaluated over the frequency range $f = 0$ to $f = f_R$ to get the ssb power density spectrum of the received signal at the receiver IF frequency. For most MTI systems, where relatively low PRFs are employed, (8.19) can be simplified because the clutter returns from ambiguous ranges are of reduced significance. In most cases only the unambiguous range interval ($M = 0$ in (8.19)) need be considered.

When the received signal is converted from IF to baseband, the lower and upper sideband spectral noise components fold over each other. The ssb power density must be increased by 3 dB to obtain the baseband power spectral density at the input to the canceler.

The ssb power spectrum (+ 3 dB) from (8.19) applied to the normalized clutter canceler response, (8.4) and (8.5), and averaged over the range $f = 0$ to $f = f_R$ gives the clutter improvement due to phase noise of the signal source for a binomial canceler.

8.5 EXAMPLE CALCULATIONS OF MTI SYSTEM CLUTTER IMPROVEMENT PERFORMANCE

This section provides the results of several example calculations of the effects of phase noise on MTI system clutter improvement performance. Example 1 is for a relatively generic, but short-range, relatively high PRF MTI radar.

Example 1: MOPA System With Continuously Scanned Antenna

System parameters:
Antenna beamwidth = 3.0 deg.
Antenna scan rate = 360 deg/s.
Transmitted pulsewidth = 100 ns.
Average PRF = 7.5 kHz.
Range to clutter of interest = 40 km.
Receiver bandwidth = 7.0 MHz.
Clutter canceler = two delays with binomial weighting.
Master oscillator phase noise power density spectrum:
SSB phase noise at f_d = 10 kHz = −120 dBc;

$1/f_d^3$ slope for $f_d < 1$ kHz;
$1/f_d^2$ slope from 1 kHz to 31 kHz;
Zero slope for $f_d > 31$ kHz.

MTI improvement limitation due to scan modulation:
Number of pulses per beamwidth (bw):

$$N = \frac{7500 \text{ Hz}}{360 \text{ deg/s}} \times 3.0 \text{ deg/bw} = 62.5$$

Clutter power spectrum standard deviation due to scan modulation (8.12):

$$\sigma_c = 0.265 f_R/N = 31.8$$

MTI improvement limit for two-delay canceler (8.8):

$$z = (2\pi\sigma_c)/f_R = 26.641 \times 10^{-3}$$
$$I_2 = [1 - (4/3)\exp(z^2/2) + (1/3\exp(-2z^2)]^{-1}$$
$$= 3.972 \times 10^6 = 65.9 \text{ dB}$$

MTI improvement limitation due to master oscillator phase noise (8.19):
Two-way range delay to clutter:

$$t_{di} = \frac{40 \text{ km}}{150 \text{ m}/\mu\text{s}} = 266 \ \mu\text{s}$$

Number of spectral harmonics in receiver ssb bandwidth:

$$N = (7.0 \text{ MHz}/2)/7500 \text{ Hz} = 466.6$$

Using $P_{ci} = 1$ to obtain a carrier-normalized received noise power density spectrum, and summing over a single range ambiguity containing the clutter of interest, a computer calculation of (8.19) using the given system parameters is shown in Figure 8.15. The resulting output noise power spectral density for a two-delay canceler is also shown. The MTI improvement limit due to master oscillator phase noise is the ratio of these two curves, averaged over the range $f_d = 0$ to $f_d = 1$ PRF. The calculated result for this case is:

$$I_2 = 63.6 \text{ dB}$$

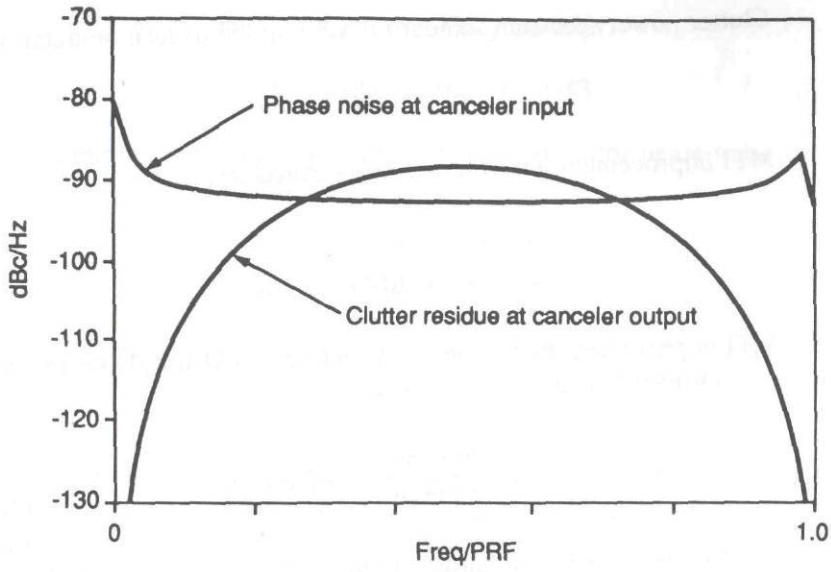

Figure 8.15 Calculated phase noise for Example 1.

Example 2: Medium-Range and Long-Range, Low-PRF MOPA Systems

Example 2 is for two cases, a medium-range, low-PRF MOPA system with continuously scanned antenna and a longrange version of the same system, with a slower antenna scan.

Case 1 system parameters:
Antenna beamwidth = 3.0 deg.
Antenna scan rate = 135 deg/s.
Transmitted pulsewidth = 1 ms.
PRF = 500 Hz.
Range to clutter of interest = 100 km.
Receiver bandwidth = 700 kHz.
Clutter canceler = two delays with binomial weighting.
Master oscillator phase noise power density spectrum:
Same as Example 1.
MTI improvement limitation due to scan modulation:
Number of pulses per beamwidth:

$$N = 11.1$$

Clutter power spectrum standard deviation due to scan modulation:

$$\sigma_c = 11.93$$

MTI improvement limit for two-delay canceler:

$$z = 149.9 \times 10^{-3}$$
$$I_2 = 4.041 \times 10^3 = 36.1 \text{ dB}$$

MTI improvement limitation due to master oscillator phase noise:
Two-way range delay to clutter:

$$t_{di} = \frac{100 \text{ km}}{150 \text{ m}/\mu\text{s}} = 667 \ \mu\text{s}$$

Number of spectral harmonics in receiver ssb bandwidth:

$$N = (700 \text{ kHz}/2)/500 \text{ Hz} = 700$$

Figure 8.16 shows the computer-calculated phase noise power density spectra at the canceler input and output for this case. The calculated improvement limit due to master oscillator phase noise is:

$$I_2 = 62.3 \text{ dB}$$

The parameters of Case 1 result in a system for which MTI improvement is substantially limited by antenna scan modulation. If the antenna scan rate is reduced or the system PRF is increased, the MTI improvement performance will approach the limit set by the master oscillator phase noise performance. If the scan-limited performance is suitable to the particular application, the system cost could be reduced by using a less stable frequency source.

Case 2: Using the parameters of Case 1 with the following modifications:
Antenna scan rate = 20 deg/s.
Range to clutter of interest = 250 km.
MTI improvement limitation due to scan modulation:
Number of pulses per beamwidth:

$$N = 75$$

MTI improvement limit for two-delay canceler:

$$I_2 = 8.24 \times 10^6 = 69.2 \text{ dB}$$

MTI improvement limitation due to master oscillator phase noise:
Two-way range delay to clutter:

$$t_{di} = \frac{250 \text{ km}}{150 \text{ m}/\mu\text{s}} = 1.67 \text{ ms}$$

The calculated improvement limit due to master oscillator phase noise is:

$$I_2 = 59.7 \text{ dB}$$

Case 2, with reduced antenna scan rate and increased range to clutter, the low-PRF system MTI improvement limit is set by the master oscillator phase noise performance. Also note in comparing Figures 8.16 and 8.17 that the effect of range decorrelation on received phase noise approaches 10 dB at very low doppler frequencies.

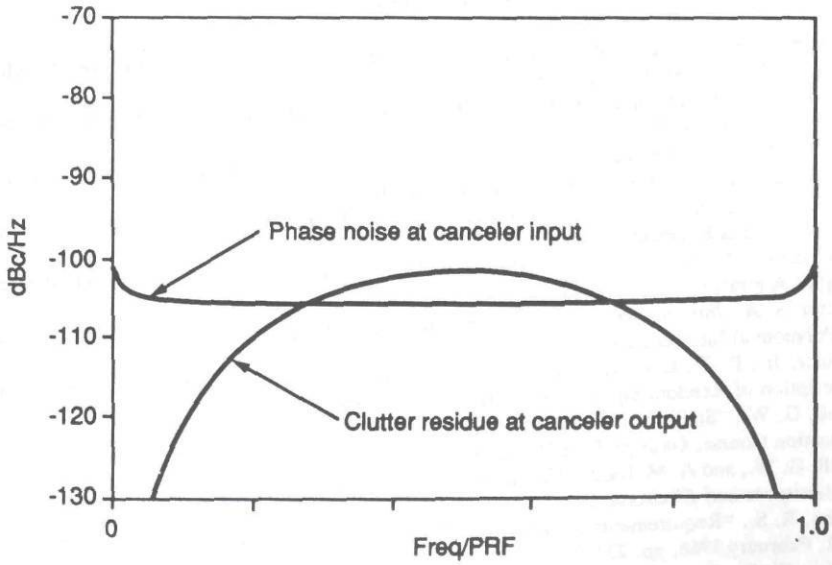

Figure 8.16 Calculated phase noise for Example 2, Case 1.

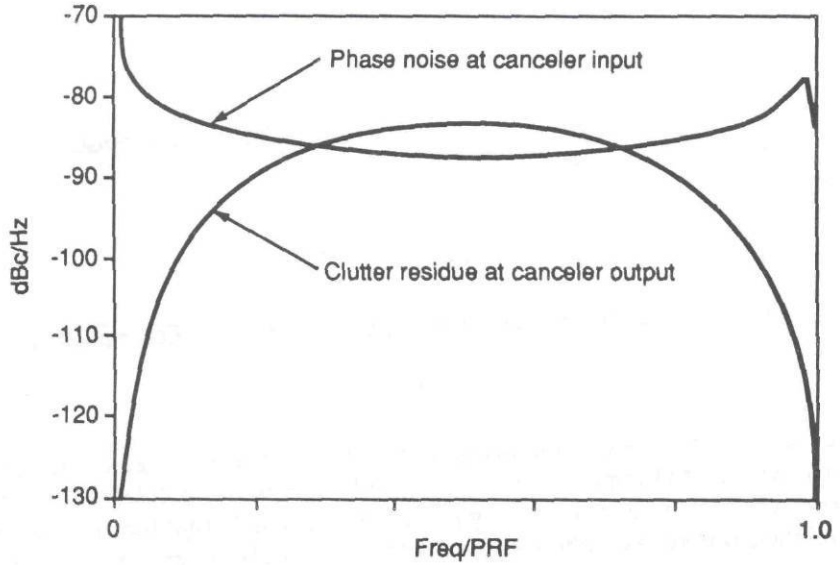

Figure 8.17 Calculated phase noise for Example 2, Case 2.

REFERENCES

[1] Nathanson, F. E., J. P. Reilly, and M. N. Cohen, *Radar Design Principles*, Chapter 9, "Moving Target Indicators (MTI)," McGraw-Hill, 1991.

[2] Barton, D. K., *Modern Radar System Analysis*, Section 5.3, "Moving Target Indication," Norwood, MA: Artech House, 1988.

[3] Skolnik, M. I., *Radar Handbook*, second edition, Chapter 15, "MTI Radar," authors W. W. Shrader and V. GregersHansen, McGraw-Hill, 1990.

[4] *IEEE Standard Dictionary of Electrical and Electronics Terms*, third edition, Institute of Electrical and Electronics Engineers, Inc., 1984.

[5] Stimson, G. W., *Introduction to Airborne Radar*, Chapter 16, "Spectrum of a Pulsed Signal," Hughes Aircraft Company, 1983.

[6] Tretter, S. A., *Introduction to Discrete Time Signal Processing*, Chapter 3, "Data Reconstruction by Polynomial Interpolation and Extrapolation," John Wiley, 1976.

[7] Peebles, Jr., P. Z., *Communication System Principles*, Chapter 4, "Statistical Concepts and the Description of Random Signals and Noise," Addison Wesley, 1976.

[8] Ewell, G. W., "Stability and Clutter Effects," Material for Coherent Radar Systems Continuing Education Course, Georgia Tech Research Institute, 1991.

[9] Ewell, G. W., and A. M. Bush, "Constrained Improvement MTI Radar Processors," *IEEE Trans. on Aerospace and Electronic Systems*, Vol. AES-11, No. 5, September 1975, pp. 768–780.

[10] Raven, R. S., "Requirements on Master Oscillators for Coherent Radar," *Proc. IEEE*, Vol. 54, No.2, February 1966, pp. 237–243.

[11] Robins, W. P., *Phase Noise in Signal Sources*, Peter Perigrinus, Ltd., on behalf of the Institution of Electrical Engineers, 1982.

[12] Emerson, R. C., "Some Pulsed Doppler MTI and AMTI Techniques," Rand Corporation Report R-274, March 1954, pp. 11–24.

[13] Prinsen, P., "Elimination of Blind Velocities of MTI Radar by Modulating the Interpulse Period," *IEEE Trans. on Aerospace and Electronic Systems*, Vol. AES-9, No. 5, September 1973, pp. 714–724.

[14] Ward, H. R., "The effect of bandpass limiting on noise with a Gaussian spectrum," *Proc. IEEE*, Vol. 57, No. 11, November 1969, pp. 2089–2090.

Chapter 9
Pulsed Doppler Radar

Melvin L. Belcher and Guy V. Morris
Georgia Institute of Technology

9.1 OVERVIEW OF PULSED DOPPLER RADAR

The term doppler radar refers to any radar that is capable of measuring the shift between the transmitted frequency and the frequency of reflections received from objects. Doppler radars are used most often to discriminate between the return from a desired target, often moving, and that from undesired objects, usually ground clutter, often not moving. The topics discussed in this chapter include:

1. Types of pulsed doppler;
2. Range and doppler ambiguities;
3. Clutter-limited versus noise-limited performance;
4. An example of dynamic range requirements calculation;
5. Distribution of clutter in the range-doppler map.

9.1.1 Types of Pulsed Doppler Radar

Table 9.1 defines the three waveforms used in pulsed doppler radar. Each of the waveforms possesses significant differences in performance. The optimum choice is dependent on the operational requirements of the radar. Many radars are required to operate over a sufficiently wide range of conditions such that one single waveform is not acceptable. Many modern radars are "multimode"; that is, they can function using two or more of the waveforms shown.

Table 9.1
Definition of Pulsed Doppler Radar Modes

Mode	*Range*	*Velocity*
Low-PRF	Unambiguous	Usually ambiguous
High-PRF	Highly ambiguous	Unambiguous
Medium-PRF	Ambiguous	Ambiguous

Low-PRF Radars

Low-PRF (LPRF) radars are defined as radars with a PRF sufficiently low that range is unambiguously measured. The transmitted pulse travels to and from the maximum range of interest during the interpulse period, before the transmission of the next pulse. The unambiguous range, R_u, is calculated using:

$$R_u = \frac{c}{2\text{PRF}} \tag{9.1}$$

where c = speed of light.

High-PRF Radars

High-PRF (HPRF) radars are defined as radars with a PRF sufficiently high that all target velocities of interest are unambiguously measured. The maximum doppler shift that can be unambiguously measured is given by:

$$f_{d\max} = \text{PRF} = \frac{2fV_u}{c} \tag{9.2}$$

where f = transmitter frequency, and V_u = total closing velocity.

A typical X-band (9 GHz) airborne radar operating in a mach 2 aircraft might have a PRF of 250 kHz to ensure detection and unambiguous velocity measurement of a similar high performance target. From (9.1), we can see that the corresponding unambiguous range is only 600 m (2,000 ft). Therefore, a target at a range of 150 km (80 nmi) would be highly ambiguous in range.

Medium-PRF Radars

Medium-PRF (MPRF) radars are defined as radars with a PRF that produces ambiguities in both range and doppler. Medium PRF seems to combine the worst

features of both high- and LPRF radars. However, we will show later in this chapter that MPRF is often the best choice of waveform for airborne radar.

Table 9.2 presents some typical parameters for the three modes of pulsed doppler radars.

9.1.2 Range and Velocity Ambiguities

The equations for unambiguous velocity, V_u, and unambiguous range, R_u, are both functions of the PRF and, therefore, cannot be independently chosen. It can be easily shown that R_u and V_u are related by:

$$R_u V_u = \frac{c\lambda}{4} \tag{9.3}$$

For X-band radars, $R_u V_u = 2.5 \times 10^6$ m^2/s or 2.5×10^7 ft^2/s. Figure 9.1 is a plot of (9.3). The choice of PRF for a given mode determines the operating point on the hyperbola and thus the ambiguity characteristics. Assume that the shaded area represents the operational radar requirements for maximum velocity and range of interest. If the entire shaded area were below the hyperbola, then it would be possible to choose a single PRF that provides both unambiguous and range. However, the shaded area shown is representative for air-to-air radar requirements. Three points are highlighted on the curve. One shows the highest value of PRF that permits LPRF operation. A second depicts the lowest value of PRF that permits HPRF operation. In the domain between the HPRF and LPRF points, ambiguities exist in both range and velocity. We have defined this domain as MPRF operation.

Table 9.2
Typical Pulsed Doppler Radar Parameters

	Airborne Multimode			*Ground-based*	
Parameter	*Low-PRF*	*Medium-PRF*	*High-PRF*	*Low-PRF*	*High-PRF*
Frequency band	X	X	X	S	S
PRF, kHz	1	10	250	1	20
Unambiguous range, km (nmi)	150 (80)	15 (8)	0.6 (0.3)	150 (80)	7.4 (4)
Unambiguous velocity, m/s (ft/s)	15 (50)	150 (500)	3,800 (12,500)	50 (164)	1,000 (3,280)
Compressed pulse width, μs	1	1	1.3	1	1
Pulse compression ratio	13	13	1	1	1
Duty factor	0.013	0.13	0.33	0.001	0.02

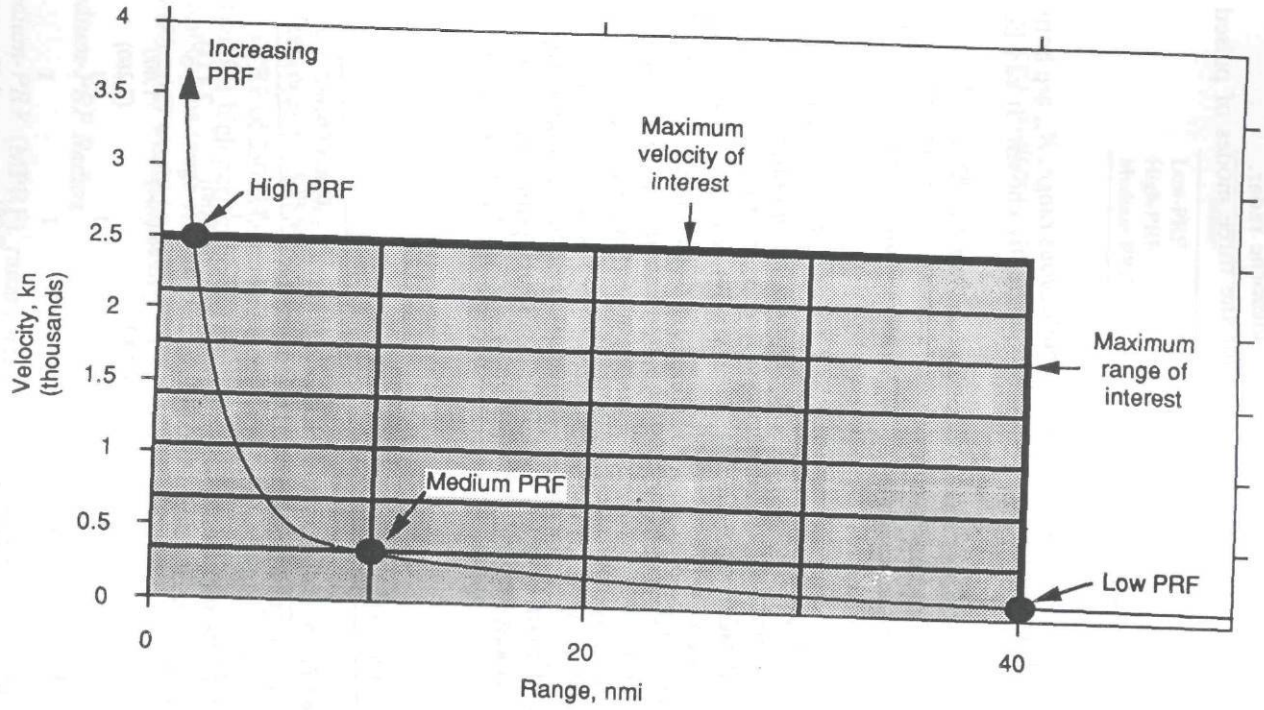

Figure 9.1 Unambiguous range versus unambiguous velocity.

The third point indicates a typical MPRF. In general, there are range and velocity blind zones at integer multiples of R_u and V_u, depicted by the heavy horizontal and vertical lines of Figure 9.1. Targets appearing in each of the "window panes" of Figure 9.1 (i.e., not in one of the blind zones) will be detected, but the measured range and velocity will be ambiguous. Additional measurements using other MPRFs are necessary to resolve the ambiguity [1].

9.1.3 Fundamentals of Doppler Radar Performance Estimation

The detection process for a pulsed radar without doppler processing is illustrated in Figure 9.2(a). The output of the receiver is amplitude detected and sampled at each range of interest. The samples for each range cell resulting from several consecutive pulses are integrated to improve the signal-to-noise ratio (SNR). Detection occurs when the signal at the range gate containing the target is sufficiently larger than its neighboring range gates. The most commonly used performance measure of a radar is the detection capability in a purely noise environment. Typically, one would start by establishing the output signal-to-noise ratio $(\text{SNR})_o$ necessary to provide the required probability of detection and false alarm rate, using detection curves or analytic closed-form expressions [2, 3]. Then the required single pulse signal-to-noise ratio $(\text{SNR})_{sp}$ is determined using $(\text{SNR})_o = N_i\,(\text{SNR})_{sp}$, where N_i is the integration gain. The integration gain for the ideal integrator equals N_p, the number of pulses integrated. The loss due to imperfect integration is usually accounted for by adding an integration loss to the other losses in the radar range equation. Finally, the radar range equation is used to calculate the range at which the required $(\text{SNR})_{sp}$ will be achieved.

The detection process for a doppler radar is shown in Figure 9.2(b). The amplitude detector is replaced by a synchronous detector that retains the coherent phase information by extracting the inphase and quadrature video components for each range cell. The additional block, doppler processing, requires the accumulation of samples from several transmitter pulses and must be performed on each range cell. Doppler processing separates the clutter from the target and provides coherent processing gain, ideally equal to the number of pulses processed coherently, N_{pc}. The complete output of the doppler processor is a range-doppler map. Noncoherent processing gain can also be provided. The additional processing gain is ideally equal to the number of doppler processor outputs noncoherently integrated. Thus, the total number of pulses processed $N_c = N_{pc}N_{pi}$. The detection process consists of comparing the target range-doppler cell with its neighbors.

Because doppler radars are most often employed to provide detection in a clutter environment, the receiver output contains the signal, clutter, noise, and possibly other interference powers, represented as S, C, N, and I, respectively. The interfering power within the target range-doppler cell or in the neighboring

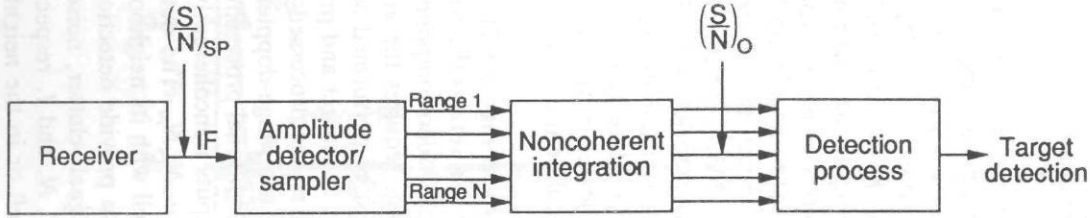

(a) Noncoherent radar

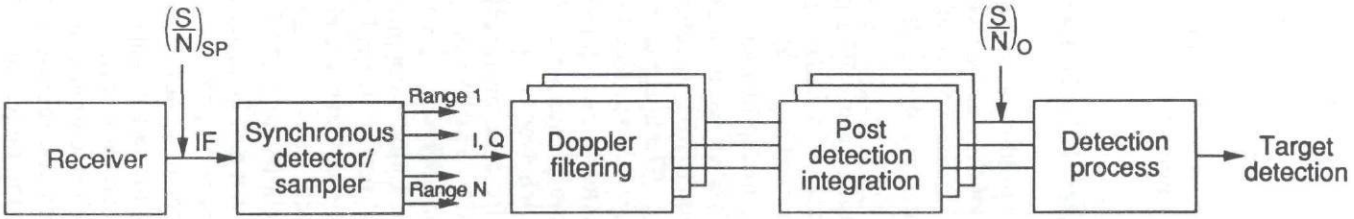

(b) Doppler radar

Figure 9.2 Radar detection process.

cell used to establish the detection threshold may be noise alone or may be dominated by residual ground clutter or other interference depending on the scenario and the waveform. Therefore, an accurate performance estimation is best achieved by computing the S, C, N, and I powers individually and understanding their contribution in each cell of the range-doppler map. In subsequent paragraphs, we will explore the conditions in which the performance can be adequately estimated assuming noise-limited performance and when the system is noise-limited.

9.1.4 Clutter Distribution in Range and Doppler

Distribution of Clutter in Range

Determining the total clutter power at each range cell is useful in establishing the dynamic range requirements and the requirements for clutter attenuation within each range cell. The total clutter power, normalized with respect to the peak transmitter power, as a function of range can be calculated from:

$$\frac{P_c(R)}{P_t} = \frac{\lambda^2 G(\phi)^2 \sigma_c}{(4\pi)^3 R^4} \tag{9.4}$$

where:

$G(\phi)$ = antenna gain,
R = actual slant range to the ground, and
σ_c = RCS of clutter.

The clutter cross section is given by:

$$\sigma_c = R\Delta\theta\left(\frac{c\tau}{2\cos\epsilon}\right)\sigma^0 \tag{9.5}$$

where:

$\Delta\theta$ = antenna beamwidth,
τ = transmitter pulse width, and
σ^0 = clutter backscatter coefficient.

The clutter power versus range plots for a ground and an airborne radar shown in Figure 9.3 were made using the so-called "constant gamma" assumption

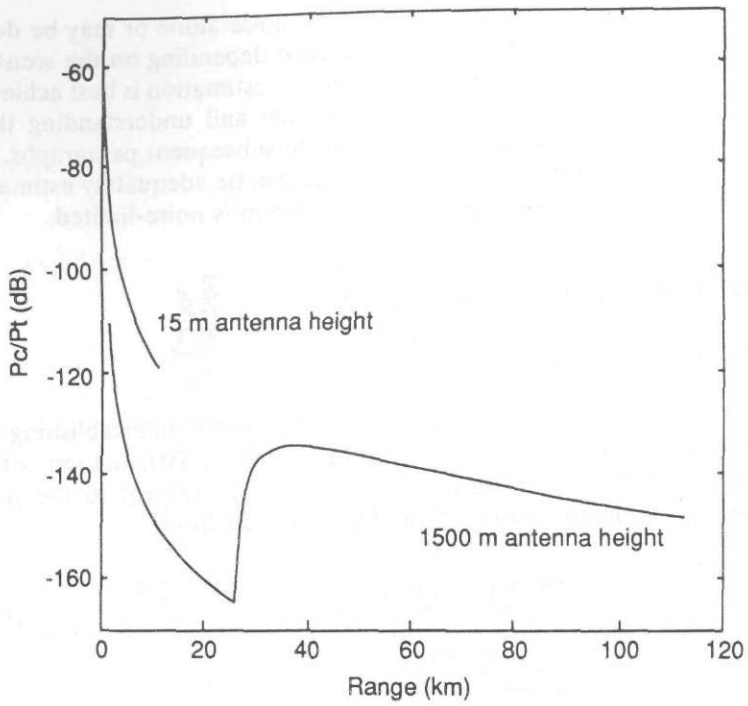

Figure 9.3 Clutter power versus range.

($\sigma^0 = \gamma \sin \epsilon$, where ϵ is the depression angle) and pointing the boresight of the radar antenna at the radar horizon.

Note that the sidelobe clutter of the ground radar is greater in magnitude, but the *mainlobe clutter* (MLC) of the airborne radar extends to far greater ranges.

Distribution of Clutter in Doppler

For stationary, ground-based radars, the doppler distribution of the clutter is determined by the motion of the individual components of the clutter within the range cell; for example, foliage motion due to wind. One useful empirical approximation for the clutter spread, derived from data collected by Lincoln Laboratory at L- and X-band [4], is given by:

$$\mathrm{RCS}_r(V_c) = -50\, k_c |V_c| \tag{9.6}$$

where:

RCS$_r$ = relative RCS in decibels,
V_c = the doppler velocity of the clutter in m/s, and
k_c = 0.7 for strong 10- to 20-kn winds and 2.5 for moderate 5- to 10-kn winds. The doppler spread is usually less than 1 m/s.

For airborne radars, the doppler spread is dominated by the spreading caused by the aircraft motion. The true doppler shift of a clutter element is given by:

$$f_d = \frac{2V_a \cos \phi}{\lambda} \tag{9.7}$$

where:

V_a = aircraft velocity,
ϕ = angle between the velocity vector and the LOS, and
λ = transmitter wavelength.

Figure 9.4 shows an idealized HPRF clutter spectrum. The clutter from all ranges is collapsed into a single range cell. In the limiting case, a clutter patch on the radar horizon directly in front of the aircraft has an apparent closing rate equal to the aircraft velocity, V_a; that is, the angle ϕ is approximately zero. Similarly, a clutter patch on the radar horizon directly behind the aircraft will appear to be

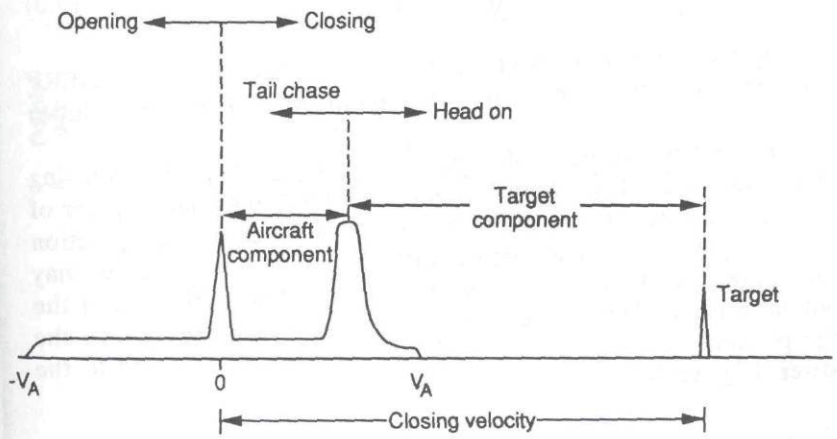

Figure 9.4 HPRF radar clutter spectrum.

opening at the aircraft velocity, at $-V_a$. In theory, all apparent velocities between V_a and $-V_a$ can be present. The strength of each spectral component depends on the effective RCS of the ground and the antenna gain at each of the LOS angles. Two large peaks are shown in the spectrum. The one at zero velocity is called the "altitude line," because it is dominated by the return from directly below the aircraft. In actual radar systems, the component at zero velocity may be the result of direct leakage between the transmitter and the receiver. The second large peak shown in the spectrum corresponds to the pointing angles of the main beam of a high gain antenna; this is called "mainlobe clutter."

Figure 9.4 also relates the regions of the spectrum to the relative heading of the target. The radar is closing on all targets that have a velocity on the right side of zero. The distance from zero to the peak of MLC is the radar contribution to the total closing rate. The target component extends from the peak of the MLC to the target return. If the total closing rate is greater than the radar contribution, then the target is moving toward the radar. Such encounters are often referred to as nose-on or head-on. The clutter-free region above V_a provides the greatest detection sensitivity.

Even though the clutter returns from many ranges are collapsed into the doppler cell in a HPRF radar, it is instructive to examine the zones on the ground that contribute to each doppler cell. Obviously, the shortest slant range from which a ground can be received is the point directly below the aircraft, whose range is the altitude of the aircraft, h_a. For a plane earth illustration, the boundary of the clutter region, f_{de}, can be expressed as a function of the slant range, R:

$$f_{de} = \frac{2V_a}{\lambda}\sqrt{1 - \left(\frac{h_a}{R}\right)^2} \tag{9.8}$$

Figure 9.5 depicts the contributions from the various ranges to the total HPRF clutter spectrum. Equation (9.8) is plotted as the boundary of the sidelobe clutter region.

The true range and true doppler of each clutter component calculated using (9.2) does not depend on the PRF. However, the apparent range and doppler of the target and its position relative to mainlobe and sidelobe clutter is a function of the PRF. For example, targets that are in a clutter-free region in one mode may be immersed in clutter for other waveforms. A complete characterization of the clutter distribution in each of the rangedoppler cells is necessary to estimate the detection range performance. The clutter power in each cell, normalized to the transmitter power, is given by:

$$\frac{P_c(f_{da}, R_a)}{P_t} = \frac{\lambda^2 G(\phi)^2 \sigma_c}{(4\pi)^3 R^4} \text{ modulo PRF, modulo } R_u \tag{9.9}$$

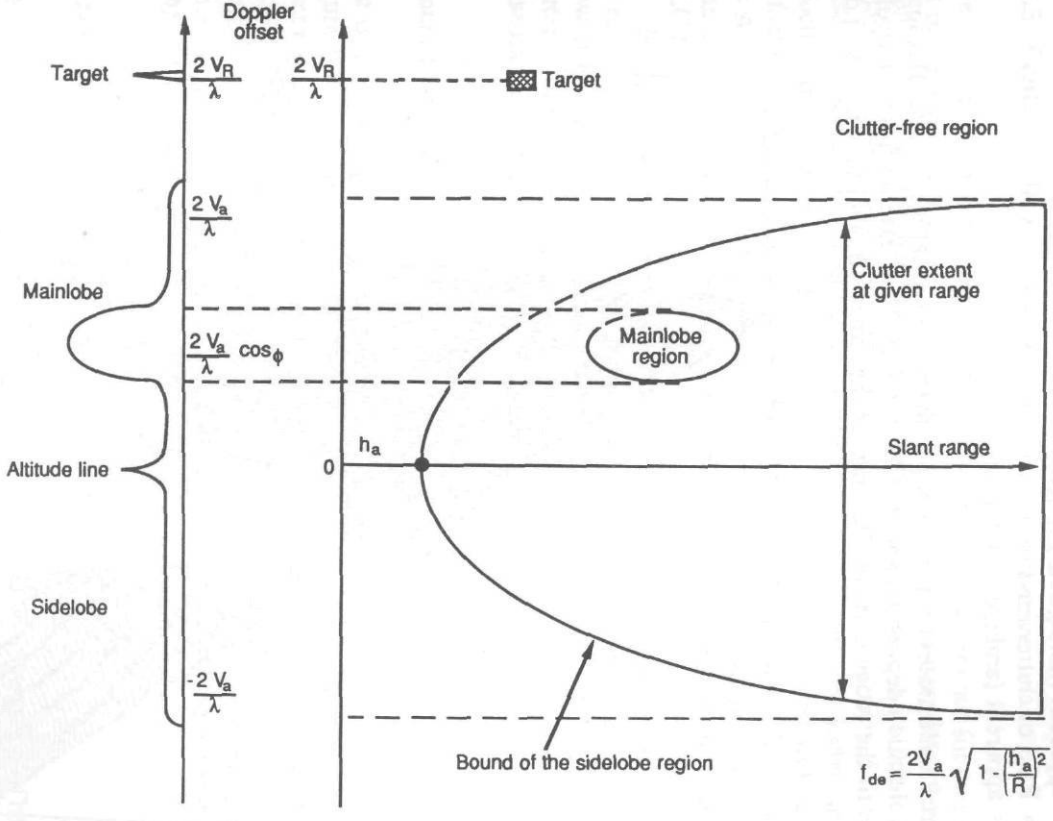

Figure 9.5 Clutter contributions from various ranges.

where:

$G(\phi)$ = antenna gain,
R = actual slant range to the ground,
R_a = apparent (ambiguous) range,
σ_c = RCS of clutter, and
f_{da} = apparent (ambiguous) doppler.

Figure 9.6 illustrates the range-doppler map for a typical MPRF case. Because of the low-elevation depression angle of the antenna, MLC extends from relatively near range to the radar horizon. Because of the range ambiguity, MLC extends

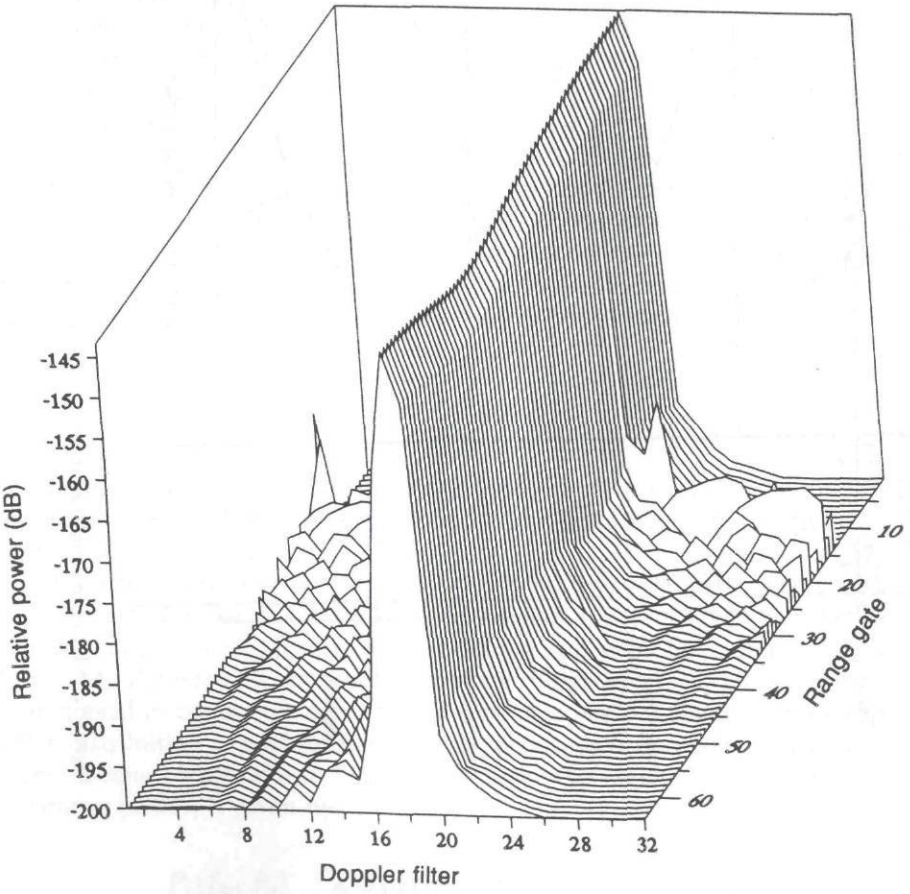

Figure 9.6 Typical MPRF range-doppler map.

throughout the apparent range interval. The PRF is less than the doppler spread of clutter, and the doppler ambiguity causes sidelobe clutter to be present throughout the doppler space.

9.1.5 Clutter-Limited Versus Noise-Limited Performance

One of the most important aspects of establishing the requirements for or estimating the performance of a pulsed doppler radar is a clear understanding of the interference environment that the target return must compete with for detection. Whether the competing environment in the range-doppler vicinity of the target is noise or residual clutter depends on the radar mode and the radar and target velocities in the ideal case. In the practical case, the environment will be affected by factors such as transmitter spectral purity, antenna sidelobes, the resolution of the A/D converter, and the precision of the digital processing (e.g., the ability to form a doppler filter at the target frequency that has adequate rejection at the MLC frequency).

Noise-limited performance can truly exist only in doppler regions where clutter cannot be present, but calculations for a particular system and scenario may show that the sidelobe clutter is below the noise level. If the level of sidelobe clutter competing with the target is not negligible, then the common gaussian noiselimited performance estimation techniques are not appropriate.

Ground-Based Radar

The true (unambiguous) clutter regions of a ground-based radar are depicted in Figure 9.7. The ambiguities introduced by the radar PRF must be examined to determine if any regions of noise-limited performance actually exist. Simplistic calculations of the boundaries of MLC can be made assuming a smooth curved earth. A more accurate estimate requires a detailed knowledge of the terrain and varies with antenna pointing angle. The doppler extent can be estimated using (9.6).

Airborne Radar

The airborne clutter regions were defined previously in Figure 9.5. The center frequency of MLC can be calculated from (9.7). The spectral width of MLC can be estimated using:

$$\Delta f_{\text{mlc}} = \left[\frac{2V_a}{\lambda} \sin \phi\right] \Delta\phi \tag{9.10}$$

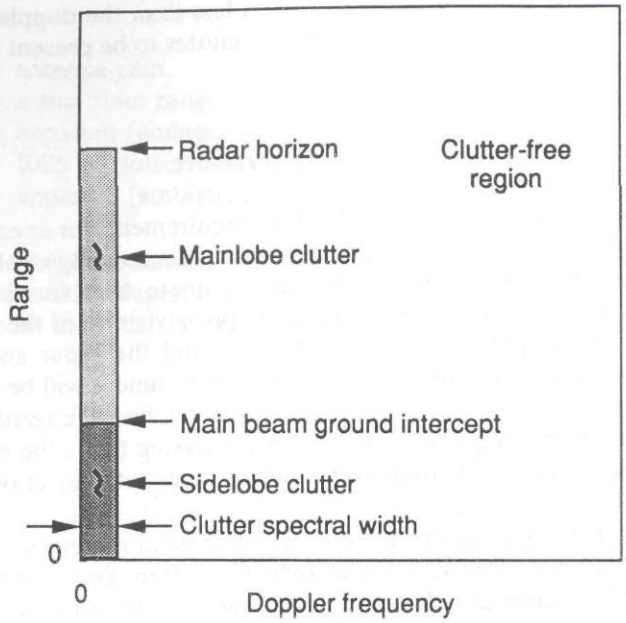

Figure 9.7 Ground-based radar clutter regions.

where $\Delta\phi$ = null-to-null antenna beamwidth or 2.5 times the 3dB beamwidth, and the other terms are as previously defined.

In general, the HPRF waveform is the only one that provides a true clutter-free region when waveform ambiguities are taken into account.

9.2 COHERENT PERFORMANCE DEGRADATION

9.2.1 Performance Degradation Due to Imperfect Coherence

The pulse doppler radar performance estimation procedure presented in Section 9.1.3 effectively assumes perfect coherence. In practice, system coherence is imperfect as measured in terms of the two-way system frequency response. The two-way system frequency response denotes the return from a nonfluctuating target as a function of doppler frequency. The system frequency response should be defined over a frequency extent corresponding to the doppler passband of the radar system.

From linear system theory, the two-way system frequency response can be calculated as the Fourier transform of the cumulative convolution of the time-

domain impulse responses of all the stages in the transmit and receive chain. The system frequency response is referenced to baseband so as to implicitly incorporate frequency conversion because perfect coherence implies a stable frequency-reference source. For a system with perfect coherence, the system frequency response is largely determined by the product of the MTI frequency response (if used) and the nominal doppler filter response, given that the CPI is on the order of or greater than the inverse of the filter bandwidth.

In practice, estimation of the system frequency response must also consider nonlinearities in the transmit and receive chain and instability in the frequency conversion reference sources. Nonlinearities, such as limiting, generally broaden the spectral extent of strong signals such as clutter returns. Reference source instability effectively broadens the associated spectrum and introduces sidebands. Receiver frequency conversion can readily be represented as time-domain multiplication corresponding to frequency-domain convolution. The resulting impact on system performance is depicted in Figure 9.8, which illustrates how CW/HPRF carrier instability results in broadening the MLC across frequency and generating associated sidebands that can degrade target detection performance in nominally clear doppler regions.

Radar system coherence is sometimes characterized in terms of the associated spectral linewidth. This can be defined as the bandwidth of the two-way frequency response achieved by coherently integrating over an extended CPI. This definition assumes that no amplitude weighting is used to control doppler sidelobes because the weighting has the effect of broadening the spectral bandwidth. The necessary CPI duration must be empirically defined by noting that increasing the CPI beyond this point results in no significant reduction in the reference return doppler bandwidth (due to radar source instability). In the limit, the two-way frequency response of a perfectly coherent radar system should converge to a frequency-domain impulse function as the CPI increases to infinity.

System-level performance degrades in three principal areas due to imperfect coherence.

1. The duration of coherent integration is constrained to approximately the inverse of the spectral linewidth. This minimum doppler filter bandwidth constraint limits the noise-limited sensitivity, as well as clutter rejection capability of the radar system. Doppler filters with less bandwidth than this value will reject signal components.
2. Contiguous extraneous sidebands will raise the effective interference floor of the radar system.
3. Discrete extraneous sidebands may appear as false targets so as to degrade search and track performance of the radar under some conditions.

Extraneous contiguous and discrete sidebands will generally only degrade radar performance in a clutter-dominated environment. The sidebands associated

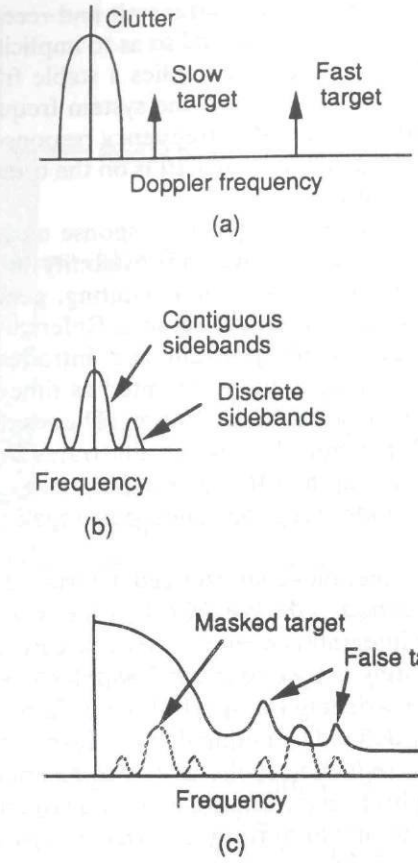

Figure 9.8 Effect of reference source instability on MLC return.

with MLC returns will tend to mask slow-moving targets that otherwise would be resolved from the clutter in doppler. Sideband-induced performance degradation is sometimes termed "self clutter" in that the radar generates this interference in otherwise nominally clutter-free doppler regions.

In most pulsed doppler radar system applications, extraneous sidebands are of more concern than spectral linewidth broadening. Sideband suppression rather than the spectral mainlobe width generally determines clutter-limited target detection performance.

The limiting factor on coherent integration interval may be the decorrelation interval of the target itself. The composite return of a complex target such as an aircraft will possess a finite bandwidth due to the fluctuating interaction among

individual scatterers caused by rotational and translational motion of the aircraft. Reported data indicate that this skin-return bandwidth at X-band should be less than 100 Hz in practice, so CPIs of at least 10 ms are readily achievable [5]. This effect is independent of engine modulation returns that are generally doppler-resolved from the airframe return.

9.2.2 Source Instability and Spurious Signal Generation

Sources and characterization of coherence degradation are addressed in Chapter 2. The effects of these instabilities on surface-based and airborne pulsed doppler radar operation are described below.

A notional pulsed doppler transmit and receive chain is depicted in Figure 9.9, along with principal sources of coherence degradation. Note that the frequency and timing reference source introduces two-way errors that are common to both the transmit and receive chain. In contrast, degradation effects introduced by the transmitter and receiver front end are present on only a single path. One-way degradation effects are independent in terms of estimating the composite two-way frequency response.

As described subsequently, common extraneous *phase modulation* (PM) is suppressed from short-range clutter at small doppler frequency offsets. Spectral components that are highly correlated between the transmit and receive chain are removed by the down-conversion process. Essentially, components that are common to the transmit and receive paths cancel out because down conversion only passes the difference-frequency terms. Correlation of spurious signal components is maximized by minimizing the time offset (range delay) and frequency offset (doppler offset) between the clutter return and the receiver LO output.

Extraneous PM generally dominates *amplitude modulation* (AM) in the system spurious sidebands. The dominance of phase noise over spurious AM components is due to the present of hard-limiter nonlinearities in the transmitter and frequency synthesis chain that convert AM to PM. The transmitter is operated in saturation for maximum efficiency so that spurious input AM is suppressed. The LO reference frequency sources are generally generated by frequency multiplication of HF and VHF sources such as a crystal oscillator. Frequency multipliers essentially consist of hard limiters with filtering and amplification circuitry so as to pass only specific harmonics of the input.

Antenna

Coherence is degraded within the antenna by any phenomenon that results in phase center wander over the CPI. Transmission and reception through a mechanically scanning antenna results in broadening of the system spectral response if the

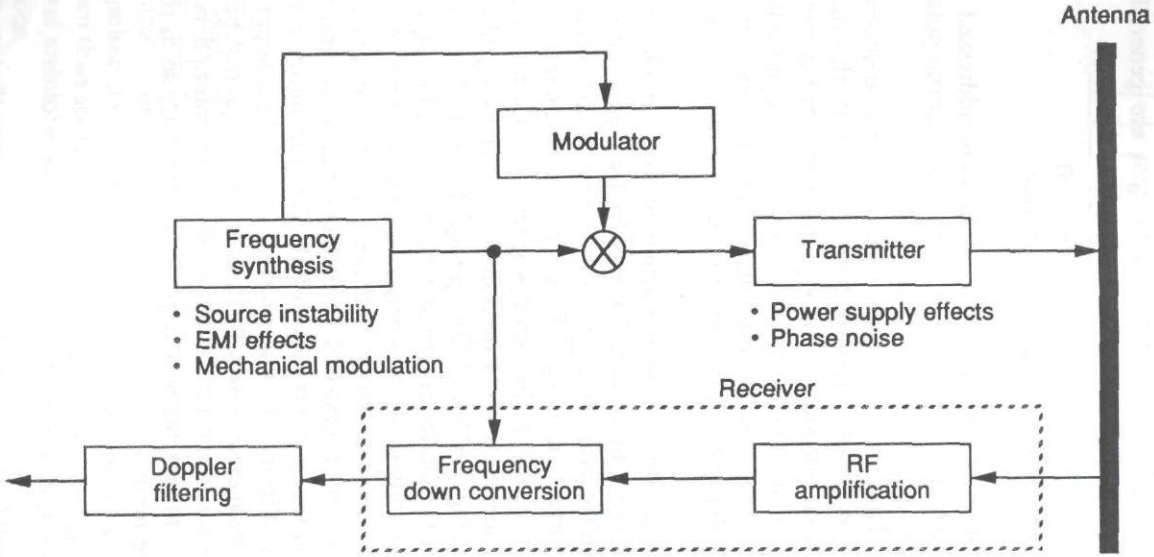

Figure 9.9 Sources of spurious modulation in a radar system.

antenna phase center is not perfectly centered on the axis of rotation. In contrast, fixed phased arrays remain scanned to a single beam position over a given CPI so that there is no associated spectral broadening other than that imposed by platform motion.

Receiver

Frequency Synthesis. The reference LO is often the principal source of contiguous-sideband phase noise. As demonstrated in Chapter 2, phase noise magnitude generally increases with increasing oscillator frequency. The LO frequency is much greater than the master oscillator frequency, so it can generally be presupposed to dominate phase noise performance.

Frequency multiplication increases the power of the spurious phase noise sidebands relative to the carrier by approximately the square of the frequency multiplication factor. Each frequency multiplication factor of 2 will increase the input phase noise sidebands by about 6 dB. Hence, a 1024X frequency multiplier used to convert from 10 MHz to 10.24 GHz would increase the extraneous PM sidebands by at least 60 dB. Two additional sources of degradation are (1) additive noise imposed by the multiplier and (2) vibration effects as described below.

Receive-Chain Nonlinearities. Nonlinearities in the receive chain seriously degrade performance in clutter-dominated environments. A fundamental goal of coherent radar receiver design is to prevent nonlinearities or at least limit their effects to doppler bands where targets are not present.

The principal sources of receive-chain nonlinearities are (1) amplifier saturation and (2) spurious mixing products associated with down conversion. The fundamental concern is that large signal capture effects and masking sidebands associated with strong clutter returns and *electronic countermeasure* (ECM) signals will degrade detectability of weaker target returns that are located in the nominally clutter-free doppler region.

Amplifier saturation is of particular concern in land-based MPRF and HPRF pulsed doppler applications because ambiguous range operations preclude *sensitivity time control* (STC). STC is used in LPRF radar to reduce the receiver gain inversely with range to prevent limiting that might otherwise be associated with strong near-in returns. *Automatic gain control* (AGC) can be implemented on a range-gate-by-range-gate basis for MPRF operation.

Limiting broadens the spectrum of strong signals such as clutter returns so as to obscure nominally clear doppler regions. In pulse doppler radar design, it may be necessary to sacrifice receiver front-end noise figure in order to achieve the required dynamic range. Dynamic range requirements are particularly stressing in ground-based radar applications. The clutter power may be more than 20 dB

greater than that typically encountered in airborne radar applications [6]. Figure 9.3 also illustrates the ground- versus airborne-radar return signal strength. Receiver dynamic range requirements have historically constrained development of ground-based HPRF radar systems.

As addressed in Chapters 3 through 5, other sources of spurious signals in the receive chain include I/Q imbalance, timing jitter, and nonlinear A/D converter operation. Any spectral component generated by harmonic or intermodulation effects manifests as a spurious signal if it is in the doppler band potentially occupied by targets. In stationary ground-based radars, the principal MLC is confined to near-zero doppler so that spurious signal components can be referenced relative to the radar carrier frequency. (Unless otherwise noted, it is assumed that MLC is composed primarily of surface scatterer returns, as this is generally a much more significant MLC source than volumetric clutter such as rain.) The range of possible MLC bandwidths and frequency offsets relative to the target doppler band must be considered in assessing spurious signal impacts on performance of airborne radars.

Analog MTI is often required before digitization and subsequent doppler filtering to meet system-level dynamic range requirements. Analog MTI is used to suppress MLC such that the clutter residue can be accommodated by the dynamic range of the A/D converters. In airborne applications, it is necessary to track the MLC center frequency and adjust the MTI notch center-frequency accordingly. MLC suppression can be implemented by inserting an appropriate frequency-offset in the down-conversion chain of the radar receiver so that the MLC is kept centered in the fixed MTI notch response. In practice, the MLC center frequency can be calculated in real-time as indicated in (9.1), from knowledge of the platform velocity, antenna pointing direction, and radar wavelength.

Transmitter

With advances in low-phase-noise reference sources, there is increasing interest in other portions of the radar system, such as the transmitter. The contiguous sideband contribution of the transmitter can be partially characterized by its associated noise figure such that:

$$\frac{S}{N_\theta} = \frac{P_{in}}{N_{oi} F_t} \tag{9.11}$$

where:

S/N = *power spectral density* (PSD) of extraneous sidebands referenced to carrier peak as function of frequency offset from the carrier,
P_{in} = transmitter drive signal power,

N_{oi} = transmitter input noise level, and
F_t = transmitter noise figure.

It follows that phase noise is minimized in the transmit and frequency synthesis chain by using the maximum signal drive levels achievable within the linear operating regime of the device.

Solid-state active-array transmitters can theoretically achieve lower transmit noise floors than conventional tube radar transmitters. In solid-state active arrays, each element is driven by a separate transmit and receive module containing a transmit amplifier, receiver amplifier, attenuation and receiver protection, phase shifter, and control circuitry. In addition to often possessing low individual transmit noise figures relative to a high-power tube amplifier, the phase noise generated by each module is statistically independent. Assuming identical mean phase noise output, the extraneous sidebands are suppressed by the number of independent noise sources because they do not contribute to the coherent antenna pattern.

For a 2,000-module solid-state array suitable for airborne intercept applications, module-level amplitude and phase error would be suppressed about 33 dB relative to modulation components common to the entire array. The limiting factor in solid-state array performance should generally be spurious signals imposed by the exciter, frequency synthesizer, or power supply, because the resulting spurious signal components will be common to all the modules driven by those sources [7, 8].

A solid-state array driven by a single power supply will impose the mean power supply fluctuation response at each module. Spurious modulation that is highly correlated among the individual elements will receive the full spatial gain of the antenna. Hence, achievement of enhanced subclutter visibility depends on the power supply performance, as well as that of the transmit and receive modules. Development of low-weight, well-regulated switching power supplies has been as important as module technology development in meeting airborne pulsed doppler radar performance requirements.

Power supply effects may be the limiting factor in suppressing spurious signals in both tube and solid-state transmitters. Transportable and airborne radar weight limitations favor compact power supplies. There is a corresponding tradeoff among power supply regulation to suppress spurious signal generation and filtering to suppress leakage supply leakage versus weight.

Mechanical and Microphonic Effects

The crystal oscillator is generally the most sensitive stage in the coherent frequency synthesis chain to vibration. In addition to the nominal phase noise contribution characteristics, mechanical and microphonic modulation imposes spurious modulation on the reference frequency output because of the piezoelectric characteristics

of quartz crystals. Other sources of spurious signals under vibration include power and signal line connectors.

The sensitivity of a quartz crystal oscillator to various environmental factors is summarized in Table 9.3. The degree of required environmental isolation required is determined by the spurious signal suppression and long-term stability requirements of the specific application.

Spurious signal suppression can degrade significantly when the receiver is subjected to strong vibration and acceleration environments. This problem is of particular concern in two applications: (1) airborne or missile-seeker radars and (2) gun fire control systems. However, some spurious signal generation in benign environments may occur because of such sources as cooling fan vibration.

The airborne environment leads to a level of vibration that affects the phase noise of an oscillator. Vibration sources include flight-induced airstream interaction

Table 9.3
Quartz Crystal Oscillator (From [20])

Parameter	*Typical value*	*Best value*	*Basic Mechanism*	*Shielding Mechanism*
Stability 1 s floor	10^{-11} 10^{-12}	10^{-13} 10^{-13}		
Aging, per day	10^{-10}	10^{-12}	changes in the quartz crystal	none
Retrace	10^{-9}	10^{-12}	changes in the quartz crystal	none
Temperature (per K)	10^{-10}	10^{-12}	crystal lattice property	controlled oven and dewar
Acceleration (per g)	10^{-9}	10^{-10}	crystal mounting and lattice property	none
Barometric (0 to 1 atmosphere)	10^{-10}	none	crystal enclosure and mounting	normally none (sealed case)
Humidity (0 to 100%)	10^{-9}	none	electronics and convective cooling	normally none (sealed case)
Magnetic (per gauss)	10^{-11}	none	none	none
Radiation (per krad)	upset plus temporary and permanent worsening of the drift rate		changes in crystal lattice (upset mostly a thermal effect)	radiation shield around resonator and/or oscillator

and the aircraft engines. Fire control radars that are collocated with a gun system are subject to extreme vibration when the weapon is in operation. Airborne intercept radars combine both airborne environment and gun fire control. Mechanical isolation of the gun from the vibration-sensitive subsystems of the radar system represents a significant mechanical engineering challenge. Crystal isolation mounts designed for use in airborne environments provide in excess of two orders of magnitude of vibration effects suppression. Other measures are generally also required to reduce mechanical modulation susceptibility.

Even with adequate mechanical vibration damping, a reference crystal in an airborne system is still subject to acceleration forces imposed by aircraft maneuvering. Crystal sensitivity in terms of frequency stability relative to imposed acceleration is on the order of 10^{-9}/g. Modulation of the reference frequency signal with a compensation signal derived from an inertial measurement unit monitoring acceleration forces can reduce this source of degradation at the cost of increased complexity [9, 10]. Also, reference oscillators based on other technologies inherently less sensitive to vibration and acceleration forces are under development.

Airborne Vibration Environment

One source of phase noise is the vibration environment. The mechanisms for coupling mechanical motion into electrical noise signals include (1) the piezoelectric properties of the crystal oscillators used to generate the various local oscillators, (2) loose cable connections or other fluctuations in RF transmission lines, and (3) antenna vibration. A typical jet engine aircraft environment is shown in Figure 9.10(a) [11]. Most current requirements are stated in terms of the PSD of random vibration. To establish requirements for doppler radar components, it might be helpful to convolve the curve of Figure 9.10(a) with the doppler filter bandwidth to determine the total vibration acceleration at each frequency. Figure 9.10(b) is an example based on Figure 9.10(a) and a doppler filter bandwidth of 100 Hz.

If the aircraft is armed, the vibration environment when the gun is firing can be much more severe. The requirements are a function of the radar equipment location relative to the gun, the type of gun, and other factors. The vibration spectrum contains large spectral lines at harmonics of the gunfire rate [12].

9.2.3 Diagnosis of Spurious Signals

Specialized laboratory equipment, such as high-resolution, high-dynamic-range spectrum analyzers, and environment simulation facilities, such as vibration tables, are generally necessary during system development. *Built-in test* (BIT) techniques with relatively modest peculiar test support equipment requirements have proven successful for routine maintenance operations [13].

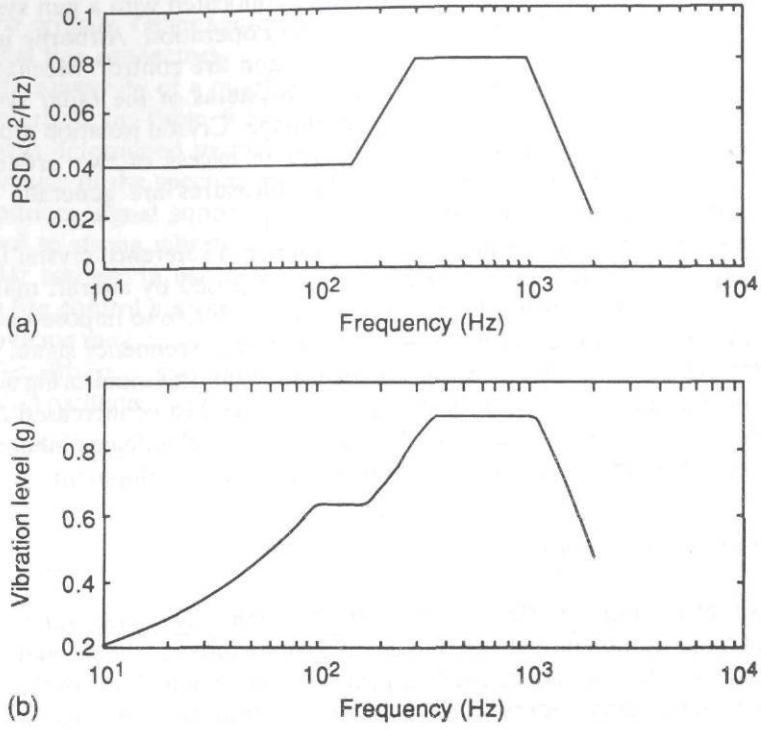

Figure 9.10 Jet aircraft vibration environment. (a) MIL-STD-810 power spectral density (PSD) versus frequency. (b) Vibration level in 100 Hz bandwidth versus frequency.

Identification of the source of spurious signals in coherent radar systems can be difficult. A common troubleshooting approach is to sequentially examine system RF, IF, video, and timing outputs and correlate spurious signal characteristics with radar modes. Onsite and flightline testing applications may attempt to exploit BIT capability. The receiver and signal processor of a pulsed doppler radar essentially constitute a high-resolution spectrum analyzer, so this approach can be very useful with two restrictions:

1. The signal under test and the reference signal will be derived from the same reference source with very little relative time delay, so that common phase noise will be suppressed as described in section (9.3).
2. Static testing will not duplicate environmental effects associated with such applications as airborne intercept radar systems.

Injected test signals must be of sufficient magnitude so as to emulate MLC return effects on the receive chain. As indicated in Table 9.4, the spurious signals

Table 9.4
Selected Spurious Signal Characteristics

Possible Source	*Variability with PRF*	*Spectral Characterization*
Frequency source instability	PRF independent	Contiguous sidebands
IM of PRF harmonic and carrier leakage	Observed on single PRF	Narrowband, constant frequency
IM of MLC with PRF line	PRF dependent	Dependent on MLC spectrum
Microwave gating circuit oscillation	Changes as PRF changes	Random spectral lines
Vibration/acceleration	PRF independent	Source and IM interaction dependent

that appear in the radar passband may well be *intermodulation* (IM) products of strong signals outside the doppler band associated with target returns. The spectral characteristics cited in Table 9.4 are generally associated with the injection of sinusoidal test signals. The effect of MLC doppler spread associated with moving platform operation can be investigated by varying the input test signal across a suitable bandwidth.

In some cases, target effects may induce apparent spurious signals. During testing of the AN/APG-66 F-16 airborne intercept radar, a phenomenon termed skinless sidebands was observed [14]. These returns were determined to originate from stationary idling aircraft. The associated aircraft body return was rejected by MLC suppression, but the engine modulation produced radar detections. Jet engines will generally produce such sideband returns at multiples of the product of the number of engine turbine blades and the engine-shaft rotation rate ([1], Chap. 16).

9.3 PULSE DOPPLER PERFORMANCE ESTIMATION

9.3.1 Phase Noise Modeling

Phase noise can be modeled as a spurious phase modulation, $\theta(t)$, imposed on a sinusoidal signal at a given doppler frequency, as depicted in Figure 9.11. The sinusoidal signal corresponds to a specific doppler offset frequency. The subscripts depicted in Figure 9.11 denote that $\theta(t)$ corresponds to the spurious PM contributions of the transmitter ($\theta_t(t)$), transmit-chain exciter ($\theta_{et}(t)$), or receive-chain exciter ($\theta_{er}(t)$). This model does not include the LO signal components explicitly but models their composite phase noise in terms of $\theta_{et}(t)$ and $\theta_{er}(r)$. The doppler

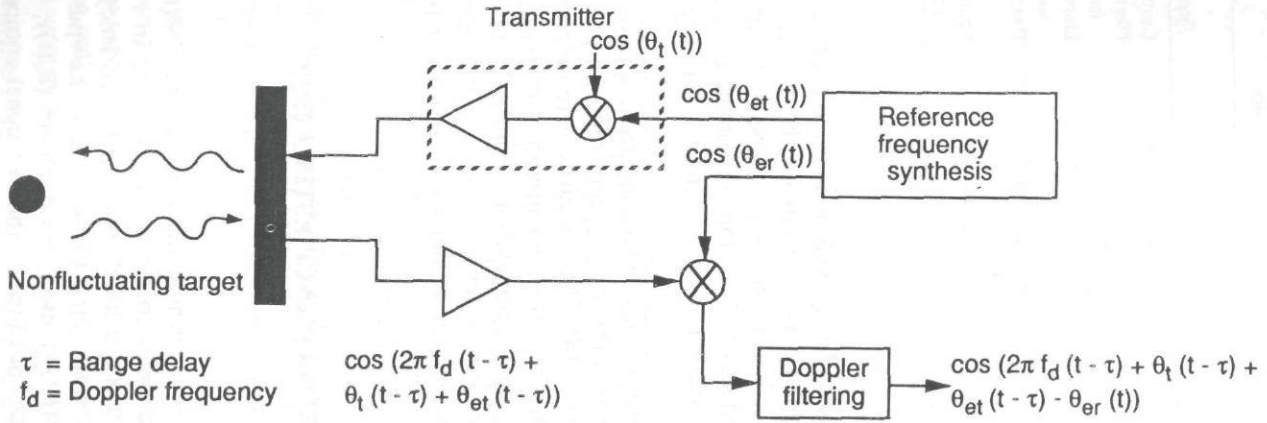

Figure 9.11 Model of phase noise effects.

filter output, $d(t)$, can be represented using complex notation to denote the difference-product operation of the frequency down conversion such that:

$$d(t) = e^{j[2\pi f_d(t-\tau)+\theta_t(t-\tau)+e\theta_t(t-\tau)]}e^{-j\theta_{er}(t)} = e^{j2\pi f_d(t-\tau)}e^{j[\theta_{et}(t-\tau)}e^{-\theta_{er}\theta_t(t-\tau)} \quad (9.12)$$

where:

f_d = doppler frequency, and
τ = range delay.

Raven has addressed the issue of common phase noise cancellation for the case of discrete sinusoidal PM [15]. Robins has extended this formulation so as to treat contiguous sidebands as effectively composed of an ensemble of sinusoidal PM terms [16]. This approach provides a useful means for approximately estimating correlated phase noise residue associated with common phase noise. Mainlobe clutter leakage into a nominally clutterfree doppler region is characterized by this SSB magnitude.

In this case, one can represent the spurious PM at the output of the doppler filter as:

$$\theta(t) = m\cos(2\pi f_m t) \quad (9.13)$$

where:

m = modulation coefficient, and
f_m = modulation frequency.

For $m < 0.1$ radians, the resulting sideband magnitude of a transmit-only or receive-only PM sinusoid can be closely estimated as $20\log(m/2)$ with the sidebands centered at the carrier frequency with an offset of f_m from the carrier frequency for one-way phase noise such as $q_t(t)$. The resulting sideband magnitude is depicted in Figure 9.12. The spurious phase modulation coefficient must be held to less than 0.1 deg to suppress the sideband to 60 dB below the carrier.

The effects of the transmit and receive correlation associated with the frequency reference signal can be considered by defining $\theta_{et}(\tau) = \theta_{er}(\tau) = \theta(\tau)$ and $\theta_t(\tau) = 0$, so that the doppler filter output is given by:

$$d(t) = e^{j[2\pi f_d(t-\tau)+m\cos(2\pi f_m(t-\tau))]}e^{-j[m\cos(2\pi f_m t)]} = e^{j2\pi f_d(t-\tau)+jm\sin(2\pi f_m(t-\tau/2))2\sin(\pi f_m\tau)} \quad (9.14)$$

The last term $(2\sin(\pi f_m\tau))$ is the so-called transmit-receive correlation factor. The correlation factor is a nonlinear function of the product of the clutter range delay and the targetclutter doppler offset. The spurious sidebands of short-range

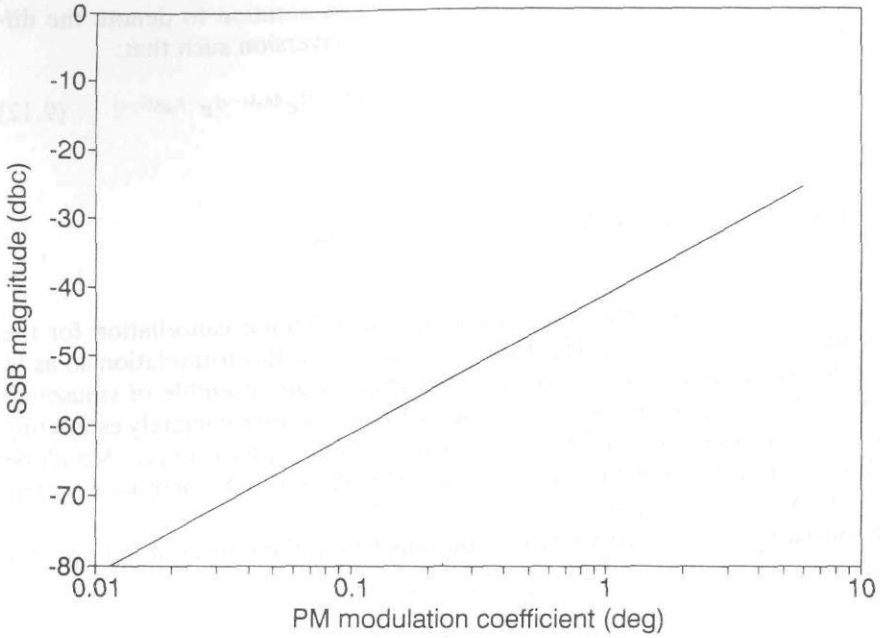

Figure 9.12 Single-sideband magnitude of sinusoidal phase modulation.

clutter returns at small doppler offsets will be suppressed significantly by the difference-mixing inherent in superheterodyne receiver operation. The resulting correlation suppression for a surface-based stationary radar is depicted in Figure 9.13 as a function of clutter range for several target doppler frequencies. Obviously, as the clutter range and target doppler offset from the clutter increases, the correlation factor varies from complete cancellation to a maximum theoretical gain of 6 dB when the transmit and receive PM are in phase. Over a wide span of clutter range and range rate, the average value of the correlation factor is 3 dB.

9.3.2 Phase Noise Effects on Pulse Doppler

Pulse doppler radars perform time-domain sampling so that there is corresponding frequency-domain aliasing, as described in Section 9.1.2. The replicated spectra are spaced at the radar PRF. Clutter contributions from the aliased MLC spectra must be summed to calculate the clutter power in a given range-gate and doppler-filter output.

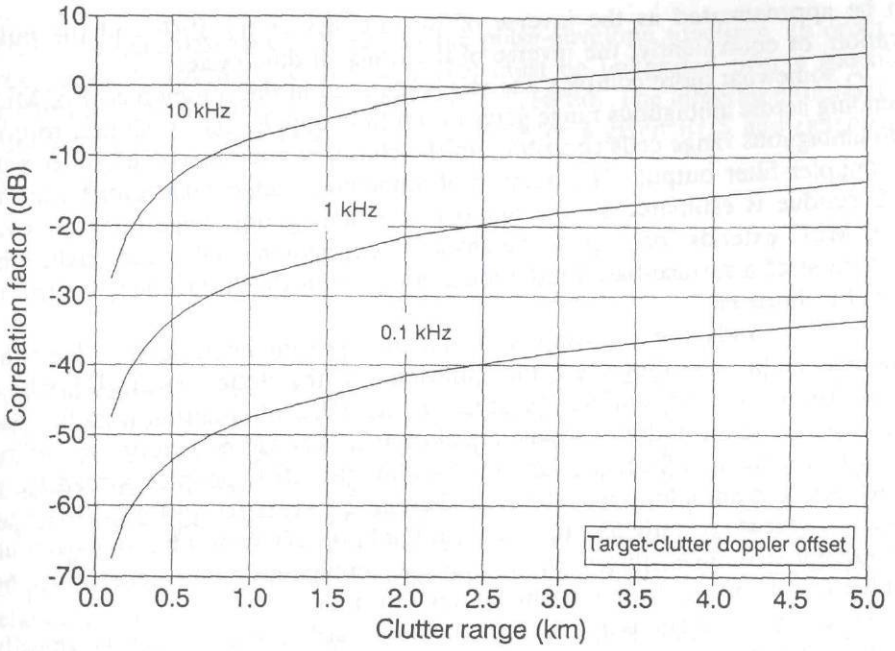

Figure 9.13 Two-way phase noise cancellation.

The spectrum of a point-scatterer pulse-doppler return can be characterized as:

$$H(f) = DT_0 \,\mathrm{PUL}\left(\frac{f}{1/\tau}\right) \sum_{i=-\infty}^{+\infty} W\left(\frac{f + i\,\mathrm{PRF}}{T_0}\right) \approx DT_0 \sum_{i=-N_d/2}^{N_d/2} W\left(\frac{f + i\,\mathrm{PRF}}{T_0}\right) \tag{9.15}$$

where:

D = the transmit duty cycle,
$W(fT_0)$ = the Fourier transform of the weighting applied over the CPI of duration T_0, and
$\mathrm{PUL}(f\tau)$ = the Fourier transform of the envelope of the pulse of duration t.

In the absence of pulse-envelope weighting, $\mathrm{PUL}(f)$ is given by $\sin(\pi f)/(\pi f)$. The effective doppler passband is on the order of the inverse of the pulse duration. It follows that the number of significantly contributing doppler ambiguities, N_d,

can be approximated as the inverse of the product of the PRF and the pulse duration, or equivalently, the inverse of the transmit duty cycle.

A somewhat more complex analysis is required in the common case of MLC extending across ambiguous range gates or multiple doppler filters. Clutter returns from ambiguous range cells contribute to the clutter residue in a given range-gate and doppler-filter output. The number of ambiguous range cells contributing to MLC residue is estimated by the number of unambiguous range intervals over which MLC extends for a given beamwidth, depression angle, and PRF. The intersection of a surface-based radar's mainbeam with the surface may extend to the clutter horizon.

Airborne radars may operate with sufficient grazing angle so as to limit the number of ambiguous range cells that contribute to the clutter return ([1], Chap. 15). Unlike a stationary surface-based radar, the MLC of an airborne radar may be distributed across multiple doppler resolution cells because of clutter spreading imposed by radar platform motion. At X-band, the MLC doppler spread for a ground-based radar is less than 100 Hz, whereas the MLC return for an airborne intercept radar is typically less than several kilohertz. The contributions from all MLC-occupied doppler filters, as well as the ambiguous range cells, must be included in computing the composite clutter return.

MLC is not ambiguous in frequency; however, airborne radar MLC is typically distributed among adjacent doppler filters. Sideband contributions must be summed across MLC-occupied doppler filters relative to the doppler filter containing the target.

$S(f)$ may effectively be substituted for sinusoidal PM to examine the effects of common phase noise cancellation. Two-way phase modulation at a given frequency is suppressed by the correlation factor in (9.14). The doppler frequency offset of the clutter from the doppler filter containing the target can be closely approximated by the target doppler frequency for the case of a stationary radar platform.

The composite spectrum of stationary radar MLC can be represented as a summation over ambiguous range gates and aliased phase noise spectra such that:

$$P(f) = D \sum_{i=-\infty}^{+\infty} P_{ci} \left[S(f)(2 \sin(\pi \tau_{di} f))^2 + \sum_{j=-\infty}^{+\infty} \mathrm{PUL}\left(\frac{f}{1/\tau}\right)^2 \cdot S(f + j\,\mathrm{PRF})(2 \sin(\pi(f + j\,\mathrm{PRF})\tau_{di}))^2 \right] \tag{9.16}$$

where P_{ci} is the average clutter power from the ith range ambiguity [17]. Here, range cells are referenced to the target range. The summations' bounds are constrained, as noted above, by the range extent of significant clutter returns and the

effective doppler passband imposed by the pulse-envelope spectrum. In order to assess radar detection performance, (9.16) must be integrated over a specified doppler filter to calculate the associated clutter residue. The integrated summation is divided into the target power, P_t, calculated for a given RCS and range such that:

$$\frac{S}{C} = \frac{P_t}{\int P_c(f)\, df} \tag{9.17}$$

The operations of (9.16) and (9.17) must generally be solved through a computer program because of the numerical complexity of the summation and integration. Such a simulation can be used to compute the composite S/C as a function of target RCS, range, and doppler frequency. Approximations for estimating required phase noise suppression performance is described in the next subsection.

Equation (9.16) applies to the case of two-way phase noise. It can be readily adapted to the case of one-way spurious modulation by simply replacing the correlation factor with 1.

The clutter and waveform interaction for the stationary radar case is depicted in Figure 9.14, in terms of the corresponding range-doppler ambiguity surface. The two-way frequency response of the radar system is convolved with the PRF lines of the pulse-train spectrum and weighted by the pulse envelope spectrum. The two-way frequency response should incorporate the weighting effects applied in the signal processor over the CPI so as to suppress the nominal doppler sidelobes. This effect is sometimes neglected in assessing phase noise performance impacts, because the spurious signal sidebands are not significantly suppressed by weighting.

In airborne HPRF radar operation, the composite clutter return is essentially collapsed into a single range gate. As a result, spectral sideband suppression requirements are more severe than associated with MPRF operation, which divides the mainlobe range clutter up among multiple range cells.

9.3.3 Approximate Estimation of Phase Noise Effects

As noted above, the MLC sideband contribution defined in (9.17) must be summed in range and integrated in frequency for each clutter-contributing ambiguous range cell. However, simplified calculations are sometimes suitable for initial performance assessment as described below.

$S(\phi)$ may be approximated as constant over a given doppler filter. Hence, the integration of $S(\phi)$ may be approximated as the product of the doppler bandwidth and $S(\phi)$ evaluated at the midpoint of the filter. This expression may be

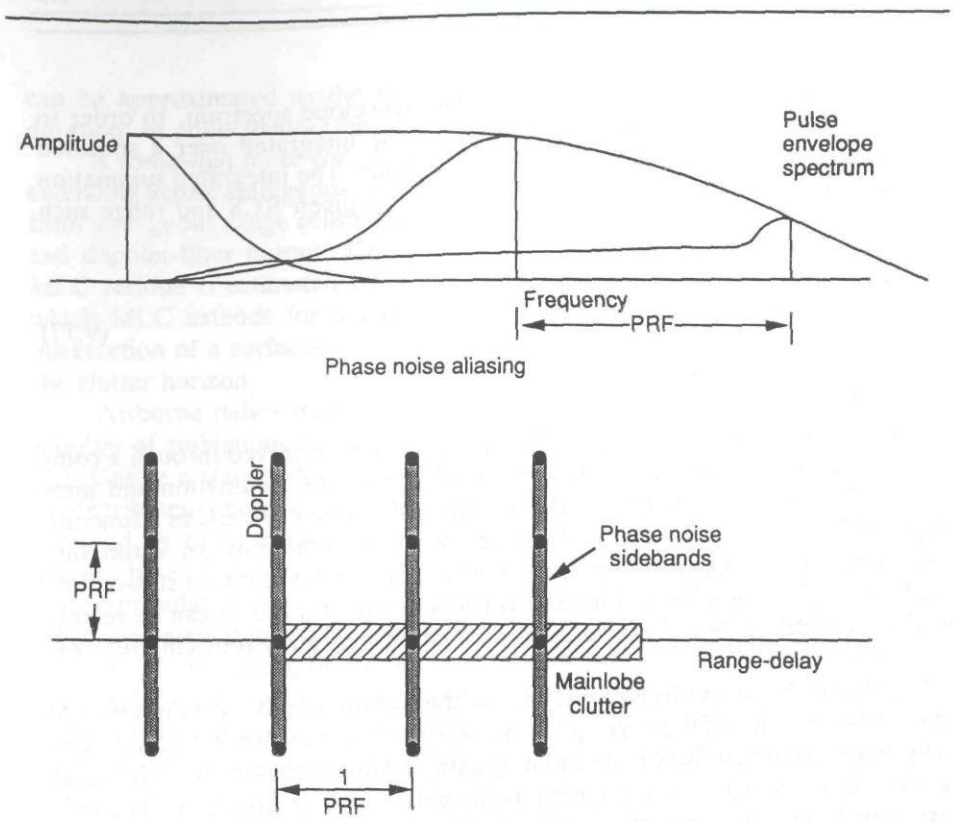

Figure 9.14 Pulse-doppler ambiguity folding.

further simplified by assuming that the spurious sideband magnitude of far-out doppler ambiguities can be approximated by a constant PSD value, S_o.

The effect of the two-way correlation factor can be approximated by taking the mean value of 3 dB. Because of the long ranges associated with the airborne scenario, this approximation is often appropriate for airborne radar applications. In groundbased radar applications, however, one should generally take a more rigorous approach and consider the cancellation of shortrange clutter returns in estimating detection performance against slow-flying targets. Otherwise, the radar capability may be significantly underestimated.

Subject to use of the average value of the correlation factor, the double summation of (9.16) may be replaced with the signal-to-mainlobe-clutter ratio $(S/C|_{mlc})$. $S/C|_{mlc}$ is typically calculated early in the radar design and analysis process to provide an indication of dynamic range requirements.

The composite signal-to-interference ratio (S/I) needed at the output of a doppler filter containing a target is established by the system probability of detection

and false alarm rate requirements. The interference is the sum of the noise and clutter return residue. For example, a representative required composite signal-to-clutter ratio ($S/C|_{rqd}$) of 18 dB is assumed. The resulting S/I would be 15 dB, assuming equal noise and clutter power residue. For purposes of analysis, assume that the target is approaching with a sufficient range-rate such that its return is in the nominally clear doppler region of the radar system. The only significant clutter is the residue attributable to extraneous sidebands of the MLC return.

The single-sideband phase noise suppression in decibels below carrier in 1 Hz bandwidth (dBc/Hz) can then be specified as a function of the doppler offset for stationary clutter such that:

$$S(f_{os}) = -\frac{S}{C}\bigg|_{reqd} - 10\log(B_d) + \frac{S}{C}\bigg|_{mlc} - 3 \tag{9.18}$$

Evaluating this expression for a doppler filter bandwidth of 500 Hz and $S/C|_{mlc}$ of -80 dB results in a requirement for -128 dBc/Hz at the offset frequency from the carrier equal to the target doppler. Phase noise suppression requirements become more stressing as the minimum target range-rate at which detection is required decreases because there is a corresponding decrease in f_{os}.

9.3.4 Numerical Example—Airborne Radar, HPRF Waveform

This example illustrates how stability requirements can be derived from system performance requirements. Specifically, we consider how to determine the reference oscillator stability requirements necessary to ensure that MLC does not degrade detection performance more than 0.5 dB, given the following conditions:

Radar: $V_a = 300$ m/s, $h_a = 5{,}000$ m, $\Delta\Theta_b = 2.5$ deg, $f_t = 9.6$ GHz, PRF = 300 kHz, $\tau = 1$ μs, $\sigma^0 = -20$ dB, doppler filter bandwidth (including the broadening effects resulting from doppler sidelobe control weighting) = 150 Hz, and SNR = 15 dB required for detection in the absence of MLC noise sidebands.

Target: V_t is between 300 and 600 m/s directly toward the radar, $R_t = 100$ km, $h_t = 100$ m, $\sigma_t = 5$ m^2.

Step 1. Calculate the total MLC power. The power can be calculated by summing all the power from all the ambiguous range and doppler cell using (9.9). Alternatively, the clutter cross section may be estimated as follows. Assuming a flat earth and that the antenna is pointed at the target, the antenna depression angle is 2.81 deg. The 3-dB (6-dB two-way) antenna elevation pattern subtends depression angles from 1.56 to 4.06 deg, which correspond to ranges from 184.8 to 70.6 km, respectively. The ambiguous range projected on the earth's surface is given by $c/$

(2 PRF cos Γ) and for a 300-kHz PRF is approximately 500 m. Therefore, there are 226 ambiguous ranges that contribute to MLC within the 3-dB pattern. The clutter cross section at the target range is calculated using (9.5) and multiplied by 226, which yields $\sigma_c = 62$ dBsm (dB relative to 1 square meter). Therefore, $S/C = -57$ dB. The MLC geometry is shown in Figure 9.15.

Step 2. Calculate the spectral location of the target relative to MLC and the number of MLC doppler ambiguities contributing phase noise at the target doppler using (9.16). Assuming a rectangular pulse, PUL($f\tau$) is of the form sin x/x, with a bandwidth of approximately 1 MHz. The number of PRF lines may be estimated as the inverse of the duty factor. Therefore, the 300kHz PRF will have three spectral lines within the 3-dB bandwidth. Using (9.7), the target doppler is found to be in the range 38.4 to 57.6 kHz. Similarly, the center of MLC corresponding to the three PRF spectral lines are as shown in Table 9.5.

Step 3. Estimate the phase noise suppression required. In the absence of phase noise effects, the target doppler is in the clutter-free region and competes only with receiver noise. The $5m^2$ target produces a $S/N = 15$ dB, exceeds the detection threshold, and is detected. It is desired that the cumulative contribution of the three MLC sidebands is such that when the target is detected at $S/(N + C) = 15$ dB, the S/N = 15.5 dB. In other words, the maximum degradation is 0.5 dB. Therefore, $S/C_{rqd} = 24.6$ dB.

One possible specification approach would allow the central spectral line to contribute all the allowable clutter power and place more stringent requirements on the outer sidebands so that they contribute negligibly to the total. Another possible specification is to divide the allowable contribution equally between the three sidebands. From PUL($f\tau$) above, the total power of the three PRF sidebands of MLC is calculated to be 4 dB higher than the central spectral line. This latter method will be used in this simple example. Therefore, a $S/C_{rqd} = 28.6$ dB will be used. Finally, using (9.18) we have:

$$S(f_{os}) = -28.6 - 21.8 - 57 - 3 = -110.4 \text{ dBc/Hz}$$

This requirement must be met in the relative spectral regions where target returns are expected that span from 19.2 to 561.6 kHz, as shown above. Also remember that the requirements must be achieved when the radar is subjected to the vibration environment of Figure 9.10.

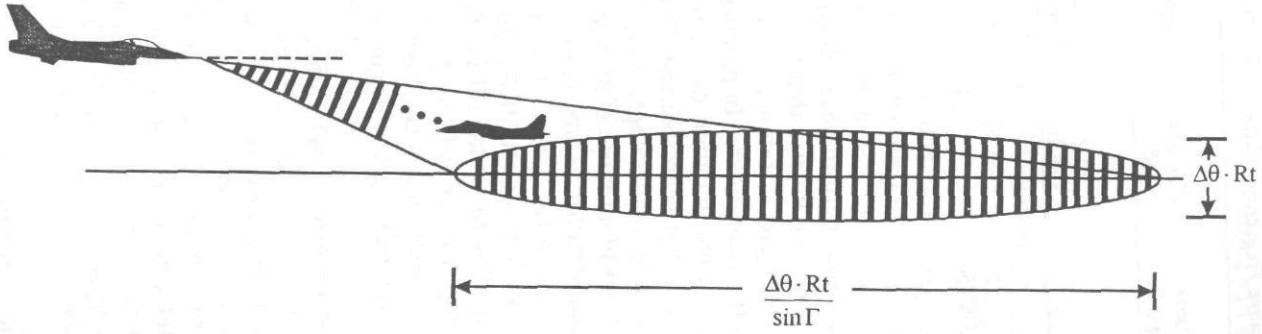

Figure 9.15 Target/clutter geometry.

Table 9.5
Relative Frequency of MLC

	Frequency relative to f_0, kHz	*PUL(f_T), dB*	*Frequency separation of target, kHz*
f_{mlc}	19.2	0	19.2 to 38.4
f_{mlc} + PRF	319.2	−1.5	−280.8 to −261.6
f_{mlc} − PRF	−280.8	−1.2	−580.8 to −561.6

9.4 FILL PULSE REQUIREMENTS

9.4.1 System Performance Issues

Most discussions of pulsed doppler radar performance effectively presuppose the absence of transient effects. This condition implies that (1) the composite clutter return present in each ambiguous range gate is stationary in a statistical sense over the CPI and (2) there are no filter transient effects. In practice, the clutter-return stationary requirement implies that at the initiation of coherent integration, the return from the maximum-range clutter has been received. This condition is often characterized as clutter fill in that each input sample collected from successive pulses should be the sum of the full set of all-range clutter returns.

These steady-state performance conditions are reasonably well met by a mechanically scanning pulsed doppler radar operating at a constant PRF. As described in the following subsection, changing the PRF requires an initialization period prior to coherent processing to allow for clutter fill and filter transient decay. In general, a phased-array pulse doppler radar will require a similar initialization period whenever the beam position is electronically scanned, even when operating at the same synchronized PRF, because the spatial origin of the clutter returns may have changed significantly.

Steady-state performance is established by transmitting a series of fill pulses that do not contribute to coherent integration gain. As a minimum, an adequate number of fill pulses must be transmitted at the onset of the dwell to satisfy clutter fill requirements. Additional fill pulses may be required to establish system stability at the onset of the CPI. Filter transient effects associated with MTI operation or infinite impulse response doppler filtering must be allowed to decay before outputting doppler-filtered data for subsequent detection processing. This ringing is in response to the step input of a strong signal to a filter. In addition, MPRF radars may require AGC settling time to allow the range-gate gains to be established for each dwell.

The fill-pulse period, T_{fill}, required for initialization before beginning coherent processing is sometimes termed burn time in phased-array applications. The fill

time is effectively the period of the dwell that does not contribute to improving S/N. The corresponding loss, L_{fill}, can be denoted in decibels as:

$$L_{\text{fill}} = 10 \log \left(\frac{T_{\text{fill}} + \text{CPI}}{\text{CPI}} \right) = 10 \log \left(\frac{T_{\text{dwell}}}{\text{CPI}} \right) \tag{9.19}$$

where T_{dwell} is the composite length of the CPI and the fill time. Barton has noted that 1 ms is a typical fill time for a ground-based radar [18]. A fill time of 1-ms duration corresponds to almost 1-dB loss for a 5-ms dwell and decreases to less than 0.5-dB loss for a 10-ms dwell.

Clutter fill requirements also dictate that receive operations be terminated upon cessation of the transmit pulse train. Otherwise, doppler filtering performance will significantly degrade as it will not be based on a full N samples of the strong near-in clutter return.

9.4.2 Clutter Fill

Weighting techniques for doppler sidelobe suppression include Hamming and Taylor tapers. In general, mainlobe broadening and S/N loss increase with increasing degree of sidelobe suppression. Sidelobe reduction through weighting is ineffective against spurious sidebands because they effectively represent separate signal components from the nominal return.

To achieve the nominal performance afforded by an N sample taper, it is necessary to have N samples of the signal being processed. Otherwise, the taper is incomplete, as indicated by an aperture fill of less than unity in the following pair of figures. An ensemble of frequency responses associated with 40-dB Taylor weighting truncated in the time domain is depicted in Figure 9.16. Maximum sidelobe suppression as a function of weighting aperture fill is depicted in Figure 9.17 for commonly used Taylor weights. Note that the sensitivity to truncation increases with the degree of nominal spectral sidelobe suppression.

As stated above, it is necessary to allow adequate time from the onset of a dwell to obtain N returns from every clutter range cell of interest to obtain the full benefits of an N-point sidelobe suppression weighting. N is typically the length of the FFT used to implement a bank of doppler filters for each ambiguous range cell. To determine maximum possible clutter range of interest, one must estimate the range at which clutter returns fall below the noise floor referenced to the doppler filter output.

The range extent of discernable surface clutter observed by a ground-based radar can be less than 50 km, corresponding to a clutter fill time of about 330 μs. However, prominent geographic features (such as mountains) and ducting prop-

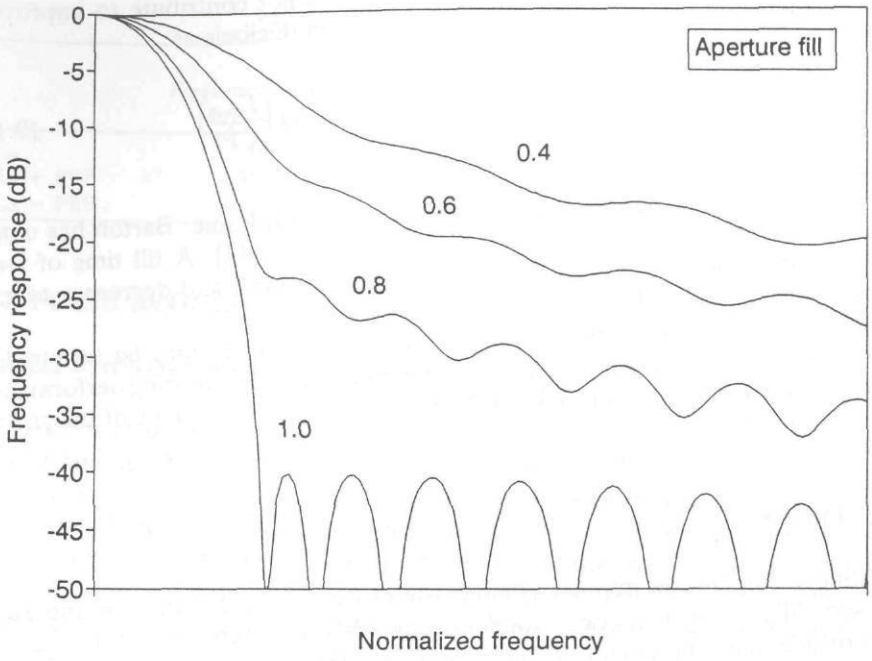

Figure 9.16 Truncation effects on -40-dB Taylor weighting performance.

agation may extend the maximum clutter range of interest significantly beyond this value. Volumetric clutter, such as chaff, may be also produce significant returns from well beyond the nominal horizon-limited range.

Airborne radar operation must essentially accommodate all-range clutter returns. Just as high altitude extends LOS range against airborne targets, so does it extend the horizon-limited surface clutter range. Long-range airborne early warning radars operating in LPRF are sometimes said to possess "over-the-horizon" capability to denote that their noise-limited detection range is further than the maximum significant-clutter range. (This term should not be confused with the operation of true over-the-horizon radar systems that operate in the HF band, 3 to 30 MHz, to extend their range beyond the LOS horizon.) In contrast, less sensitive airborne intercept radars will typically encounter significant clutter returns even at their maximum noise-limited range.

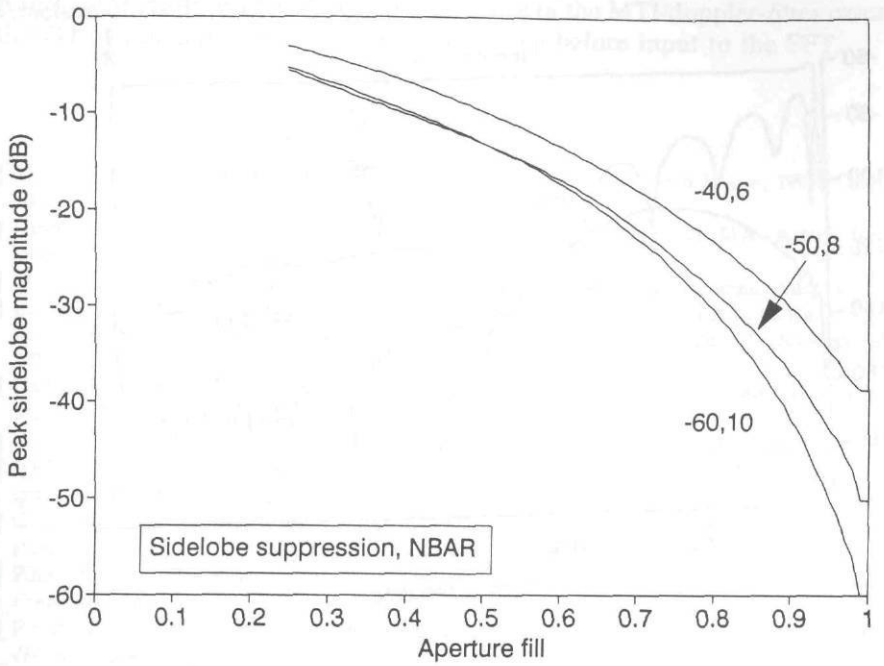

Figure 9.17 Peak sidelobe suppression degradation due to weighting truncation.

9.4.3 Filter Transient Effects

The sudden introduction of a strong signal into an analog filter will produce a transient response termed ringing. This effect is particularly significant in radar systems that use doppler filtering with relatively long time constants. Figure 9.18(a) depicts an example of an analog-MTI/digital-doppler-filter response for a ground-based radar system. The mean clutter input power, front-end MTI response, and composite FFT clutter output are depicted as a function of time over the dwell duration.

Fletcher and Burlage have suggested an initialization technique to reduce ringing effects associated with infinite impulse response filters [19]. Essentially, their approach consists of initializing the filter with the estimated steady-state filter response based on knowledge of the filter transfer function and measurement of the received power from the leading edge of the CPI.

A simple technique used in with analog MTI is simply to delay input from the MTI to the doppler filter until after the filter settling time has been attained.

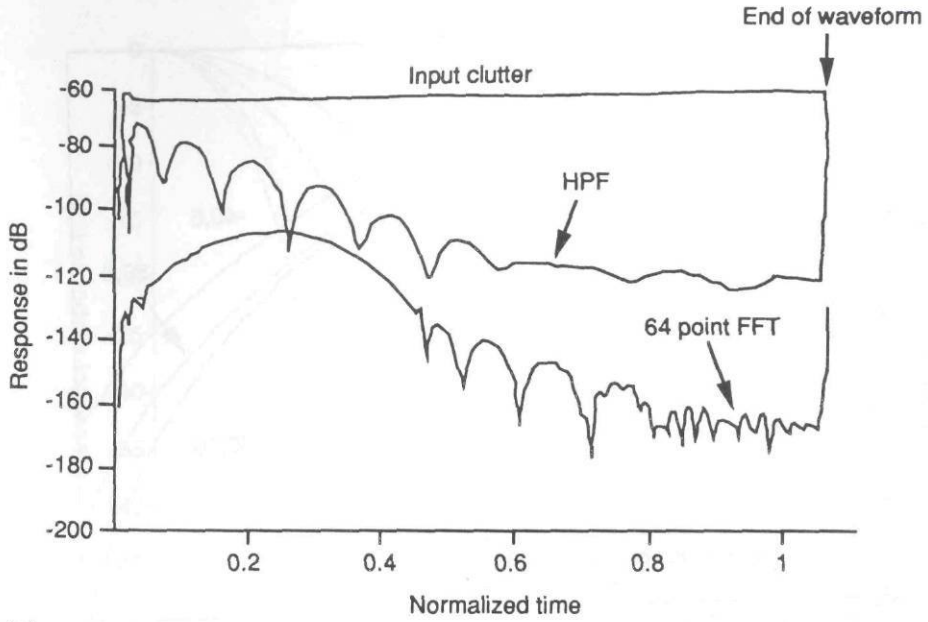

(a)

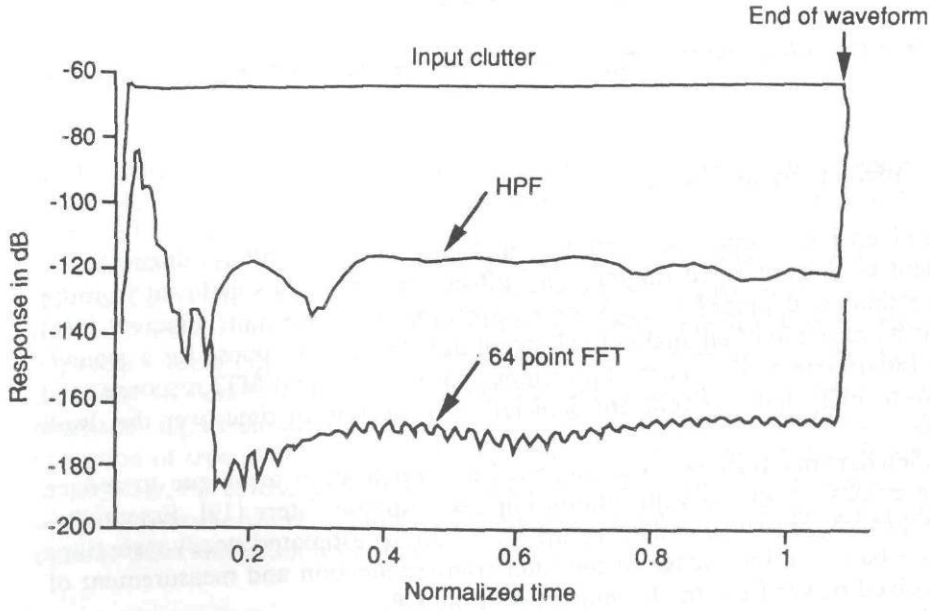

(b)

Figure 9.18 Transient response of filter (a) without initialization and (b) with initialization (from [21]).

Figure 9.18(b) illustrates the settling performance of the MTI/doppler-filter cascade with MTI output gating to allow transient settling before input to the FFT.

REFERENCES

[1] Morris, G. V., *Airborne Pulsed Doppler Radar*, Norwood, MA: Artech House, 1998, Chapters 10 and 11.

[2] Hovanessian, S. A., *Radar Detection and Tracking Systems*, Norwood, MA: Artech House, 1973.

[3] Meyer, D. P., and H. A. Mayer, *Radar Target Detection*, New York: Academic Press, 1973.

[4] Billingsley, J. B., and J. F. Larrabee, "Measured Spectral Extent of L- and X-Band Radar Reflections from Wind-Blown Trees," Lincoln Laboratory, Massachusetts Institute of Technology, ESD-TR-86-153, February 1987, pp. 14–20.

[5] Nathanson, F. E., *Radar Design Principles: Signal Processing and the Environment*, New York: McGraw-Hill, 1969.

[6] Barton, D. K. *Modern Radar System Analysis*, Norwood, MA: Artech House, 1988.

[7] Iglehart, S. C., "Noise and Spectral Properties of Active Phased Arrays," *IEEE Trans. on Aerospace and Electronic Systems*, Vol. AES-11, No. 6, November 1975.

[8] Gostyukhin, V. L., "Spectral Characteristics of Active Phased Antenna Arrays," *Izvestiya VUZ. Radioelektronika*, Vol. 30, No. 2, 1987 (translated by Allerton Press, 1987).

[9] Filler, R. L., "The Acceleration Sensitivity of Quartz Oscillators: A Review," *41st Annual FrequencyControl Symp.*, 1987.

[10] Rosati, V. J., "Suppression of Vibration-Induced Phase Noise in Crystal Oscillators: An Update," *41st Annual Frequency Control Symp.*, 1987.

[11] MIL-STD-810E, Method 514,4, Vibration, 14 July 1989.

[12] MIL-STD-810E, Method 519.4, Gunfire Vibration, 14 July 1989.

[13] Gray, M., et al., "Stability Measurement Problems and Techniques for Operational Airborne Pulse Doppler Radar," *IEEE Trans. on Aerospace and Electronic Systems*, Vol. AES-5, No. 4, July 1969.

[14] Ringel, M. B., D. H. Mooney, and W. H. Long, "F-16 Pulse Doppler Radar (AN/APG-66) Performance," *IEEE Trans. on Aerospace and Electronic Systems*, Vol. AES-19, January 1983.

[15] Raven, R. S., "Requirements for Master Oscillators for Coherent Radar," *IEEE Proc.*, Vol. 54, No. 2, February 1966 (reprinted in *CW and Doppler Radar*, Vol. 7 of *Radars*, D. K. Barton, editor, Norwood, MA: Artech House, 1978.

[16] Robins, W. P., *Phase Noise in Signal Sources*, Peter Peregrinus Ltd, 1982.

[17] Ewell, G. E., "Stability and Clutter Effects," *Coherent Radar System Performance*, Georgia Institute of Technology Short Course Notes, Atlanta, GA, 1991.

[18] Barton, D. K., *Modern Radar System Analysis*, Norwood, MA: Artech House, 1988.

[19] Fletcher, R. H., and D. W. Burlage, "An Initialization Technique for Improved MTI Performance for Phased Arrays," *IEEE Proc.*, December 1972.

[20] From H. Hellwig, "Environmental Sensitivities of Precision Frequency Sources," *IEEE IM-39*, April 1990.

[21] Budge, M. C., Personal communication, Pynetics Inc., 1992.

Chapter 10

Pulse Compression Waveforms and Error Effects

James L. Kurtz
Scientific Research Corporation

10.1 INTRODUCTION

This chapter will begin with a review of pulse compression waveforms, matched filter concepts, and frequency and time domain relationships. Linear and nonlinear frequency modulation waveforms and phase modulation waveforms will be described, along with pulse compression characteristics of those waveforms. Techniques for the generation and processing of coherent pulse compression waveforms will be presented. Both active and passive waveform generation and processing techniques will be described.

The remainder of the chapter will concentrate on error effects in pulse compression waveforms. Amplitude and phase error effects, as well as time-delay and frequency error effects, will be described. Techniques for estimating the effects of different types of errors on pulse compression system performance will be given. Several examples of error effects on pulse compression system performance will be given.

10.2 PULSE COMPRESSION WAVEFORMS

The choice of a radar waveform will affect radar performance in terms of range, doppler, and angle measurements, as well as the radar system's detection performance. For example, a short CW pulse of timelength t_p will allow range resolution of $\Delta R_p = ct_p/2$. Therefore, targets that are closer in distance than ΔR_p cannot be easily "resolved" or separated, because the returns will overlap. The important

parameter for range resolution is signal bandwidth; thus, a CW pulse has an effective bandwidth $B_p = 1/t_p$. The effective bandwidth for a CW pulse waveform is the bandwidth of the pulse spectrum (a function of the form $\sin(\pi f t_p)/(\pi f t_p)$) at the 4-dB points. By making a CW pulse timelength shorter, or the effective bandwidth larger, range resolution is improved. However, the amount of energy contained within the pulse diminishes as the timelength shortens. Coherent radar systems are often employed in order to improve the radar system's detection performance; therefore, it is often important to select a waveform that improves or optimizes target detection. Thus, whereas a single frequency or CW pulse waveform may be sufficient in terms of a parameter measurement (i.e., range resolution), certain types of coded waveforms provide good range resolution and an additional potential advantage of improved detection performance.

Pulse compression waveforms are coded waveforms that allow a radar to use a long pulse (in time) to transmit more radiated energy than a CW pulse and, simultaneously, to obtain the range resolution of a short CW pulse. As we will see, the effective bandwidth of the pulse compression waveform still determines the range resolution obtainable. Improved detection in pulse compression is achieved by the proper filtering or processing of the received signal.

10.2.1 Concept and Characteristics of Matched Filter Receiver

Once a radar waveform is selected, it is important that the radar receiver and signal processor operate on the waveform in a way that optimizes performance. Often, the detected *signal-to-noise ratio* (SNR) is used as a measure of performance for assessing a coherent radar's receiver and signal processor performance under a given set of conditions. Therefore, we should examine what type of receiver processing will optimize SNR.

A network whose frequency response function maximizes the output peak-signal-to-mean noise (power) ratio is called a "matched filter" [1]. Consider the receiver frequency response function to be $H(f)$, which is the amplitude and phase response of the receiver in the frequency domain. If $H(f)$ is wide compared to the signal, extraneous noise is introduced into the receiver; this will result in lower output SNR. On the other hand, if $H(f)$ is too narrow, significant signal energy is lost and this is not optimum either. There is an optimum bandwidth (more exactly a frequency response) for which the SNR is maximum. For a rectangular pulse of width t_p, the effective bandwidth is $1/t_p$, and the receiver should be matched to the pulse by having this bandwidth (approximately). This simple inverse time and bandwidth relationship is not sufficiently precise for other waveforms, in general, and a more precise requirement can be established.

Matched Filter Frequency Response

Suppose $x(t)$ is the radar transmit waveform, then:

$$X(f) = \int_{-\infty}^{\infty} x(t) e^{-j2\pi ft}\, dt \tag{10.1}$$

which is the voltage spectrum (Fourier transform) of the input signal $x(t)$. When the noise is stationary with uniform spectrum (i.e., white noise), the linear, time-invariant filter response that maximizes the output peak-signal-to-noise (power) ratio is [2]:

$$H(f) = G_{mf} X^*(f)\, e^{-j2\pi ft_d} \tag{10.2}$$

where:

$X^*(f)$ = complex conjugate of $X(f)$,
t_d = fixed value of time delay at which the signal is observed to be maximum, and
G_{mf} = constant equal to maximum filter gain (assume unity).

Interpretation and Characteristics of the Matched Filter Receiver

There are several observations that can be made regarding the matched filter:

1. The frequency-response function of the matched filter is the conjugate of the received waveform, except for a phase shift of $e^{-(j2\pi ft_d)}$.
2. The phase shift represents a constant time delay, which is required to make the filter physically realizable.
3. The impulse response of the matched filter can be found by the inverse Fourier transform [2]:

$$\begin{aligned} h(t) = x_r(t) &= \int_{-\infty}^{\infty} H(f)\, e^{-j2\pi f}\, df \\ &= G_m x(t_d - t) \end{aligned} \tag{10.3}$$

where:

G_m = arbitrary gain constant,
$x(t)$ = the input signal, and
$x_r(t)$ = the time domain response of the matched filter.

Matched Filter Impulse Response

The impulse response of the matched filter can be found by the inverse Fourier transform and is given by (10.3). This equation can be interpreted as follows: the impulse response of the matched filter is the image of the received waveform; that is, it is the same as the received signal run backward in time, starting from time t_d [2]. This result is significant, in that, once a transmit waveform is selected, the matched filter for that waveform can be determined. This will prove valuable for the determination of pulse compression matched filter functions.

Cross-Correlation and Autocorrelation

The output of the matched filter will be proportional to the cross-correlation of the input signal plus noise and a delayed replica of the input signal. If the noise is minimal, then the output will be the autocorrelation of the input. The cross-correlation is given by the equation [2]:

$$R(t) = \int_{-\infty}^{\infty} x(\lambda)\, y(\lambda - t)\, d\lambda \tag{10.4}$$

where $x(t)$ is the input signal and $y(t)$ is the receive filter time function. If the receive filter is the matched filter, it can be shown that the time response output of the filter, $y_m(t)$, is:

$$y_m(t) = R(t - t_d), \tag{10.5}$$

that is, the matched filter output is the cross-correlation between the received signal, corrupted by noise, and a replica of the transmit signal. As noted above, if noise is minimal, the filter output becomes the autocorrelation of the transmit waveform. As an example, the autocorrelation of a rectangular pulse of width T will be triangular in shape with the peak of the autocorrelation greater than unity. Whereas the peak output is increased, the autocorrelation is broadened to width $2T$.

The correlation process in pulse compression results in an increase in the amplitude of the time domain response at the output of the matched (or correlation) filter and a simultaneous reduction in noise, due to the filtering or processing. A pulse compression waveform, which actually consists of a coded transmit waveform (for example, coded in frequency or phase) and a corresponding receiver filter that is matched to that transmit waveform, is an example of a matched filter pair. Therefore, pulse compression waveforms have a processing gain or improvement in SNR (as compared to unmatched filters or waveforms).

Signal Processing Gain and Mismatch Loss

Consider a radar with a CW pulse of width t_p. The effective bandwidth associated with this pulse, B_p, is approximately $1/t_p$ (the 4-dB bandwidth of the pulse spectrum). For pulse compression waveforms, the timelength of the transmit pulse may be expanded and the bandwidth of the waveform kept large (by coding the waveform within the pulse). With the CW pulse, the product of the pulse width and the bandwidth is unity, but for a pulse compression waveform, this product can be much larger. The product $T_w B$, where T_w is the pulse width of the transmit pulse, and B is the coded pulse bandwidth, is called the "pulse compression ratio" or "time-bandwidth product" and relates to the amount of processing gain achievable with the pulse compression waveform. In pulse compression systems, the SNR at the output of the receiver is optimized, because the receiver "matches" the bandwidth (more precisely, the spectrum) of the transmit waveform and eliminates excess noise at the output, while at the same time, there is an increase in the peak signal output from the receiver because of the matched filter properties. There is an improvement in SNR at the receiver matched filter output with a matched signal input to the receiver as compared to a CW input. For a more complete discussion of the mathematical basis for matched filter optimization of SNR, see [1, 2].

The processing gain for most pulse compression waveforms, in decibels, is given by the relation 10 log $(T_w B)$. For FM pulse compression, T_w is the expanded pulse timelength and B is the coded bandwidth. For large time-bandwidth products $(T_w B)$, the processing gain and improvement in SNR (compared to a CW signal input) can be significant (i.e., for $T_w B = 100$, the processing gain is 20 dB; for $(T_w B) = 1{,}000$, the processing gain is 1,000 or 30 dB). Time-bandwidth products between 100 and 1,000 are reasonable to achieve with currently available pulse compression generation and processing techniques.

In practice, pulse compression systems do not achieve the theoretical processing gain or SNR improvement expected from the calculated time-bandwidth product. The difference between the actual signal processing gain or SNR improvement and the theoretical is called "mismatch loss," usually measured in decibels

(not to be confused with mismatch loss due to impedance or *voltage standing wave ratio* (VSWR) effects).

10.2.2 Linear FM Chirp Waveform Characteristics

Linear frequency modulation (LFM) pulse compression waveforms use a frequency-modulated transmit waveform, where the frequency changes linearly across the transmit pulse; such a waveform is often referred to as a "chirp" waveform. The modulation can be achieved by either analog or digital techniques and can be continuous or nearly continuous. A paper by Klauder [3] discusses some detailed aspects of chirp waveforms. Some of the basic characteristics of the LFM waveform will be discussed here. The transmit waveform is generated with a frequency versus time characteristic such as the one shown in Figure 10.1(a), with a resulting time domain waveform shown in Figure 10.1(b). As shown in the figure, there is a linear frequency versus time characteristic for this waveform (frequency ΔF over time T_w). The time waveform for the chirp is characterized by a quadratic phase and can be expressed as:

$$x_t(t) = \text{rect}(t/T_w)\, e^{j2\pi(f_c t + \alpha t^2)} \tag{10.6}$$

where f_c is the carrier frequency, and:

$$\text{rect}(t/T_w) = \begin{cases} 1, \text{ if } |t/T_w| < 1/2 \\ 0, \text{ if } |t/T_w| > 1/2 \end{cases} \tag{10.7}$$

and α is a quadratic phase constant. The phase of the waveform is $\phi(t) = 2\pi(f_c t + \alpha t^2)$. For an LFM, an approximately rectangular transmit spectrum will result. As described above, the time-bandwidth product for the LFM waveform is the product of T_w times B.

The matched filter, or pulse compression network, for the transmit waveform shown in Figure 10.1 is shown in Figure 10.2. The result of processing the transmitted chirp in this network is to collapse it into a narrow time pulse as shown in Figure 10.2. The pulse width of the "compressed pulse" is inversely proportional to the chirp bandwidth, $B = \Delta F$. Notice that the compressed pulse has a characteristic $\sin(\pi Bt)/(\pi Bt)$ form; therefore, the first-time sidelobe is 13.2 dB below the mainlobe.

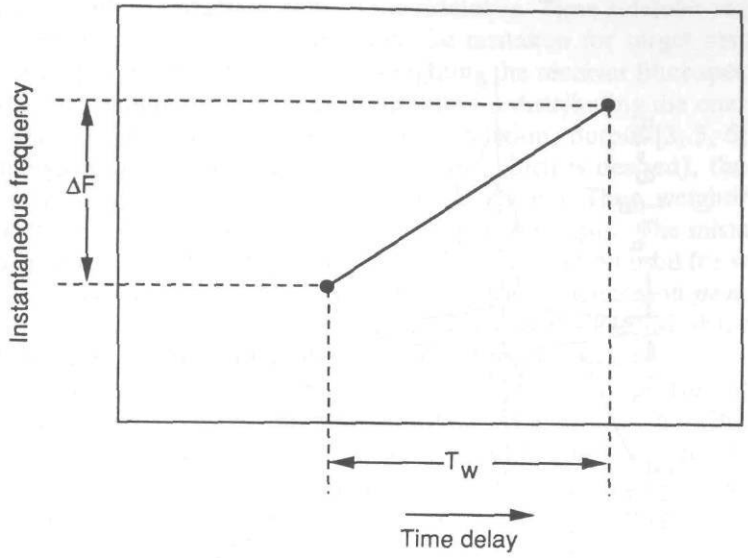

(a)

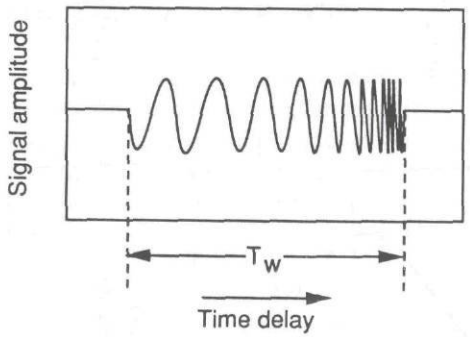

(b)

Figure 10.1 Linear FM chirp characteristics (transmit) (from [4]). (a) Transmitted chirp frequency versus time delay characteristic. (b) Transmitted pulse waveform.

10.2.3 Weighting Functions

An LFM waveform with a uniform or flat amplitude frequency response on the compression filter (i.e., the matched filter) will result in relatively high time sidelobes (-13.2 dB) for the compressed pulse, or the $\sin(\pi Bt)/(\pi Bt)$ time domain characteristics. Frequency domain amplitude weighting on the compression filter

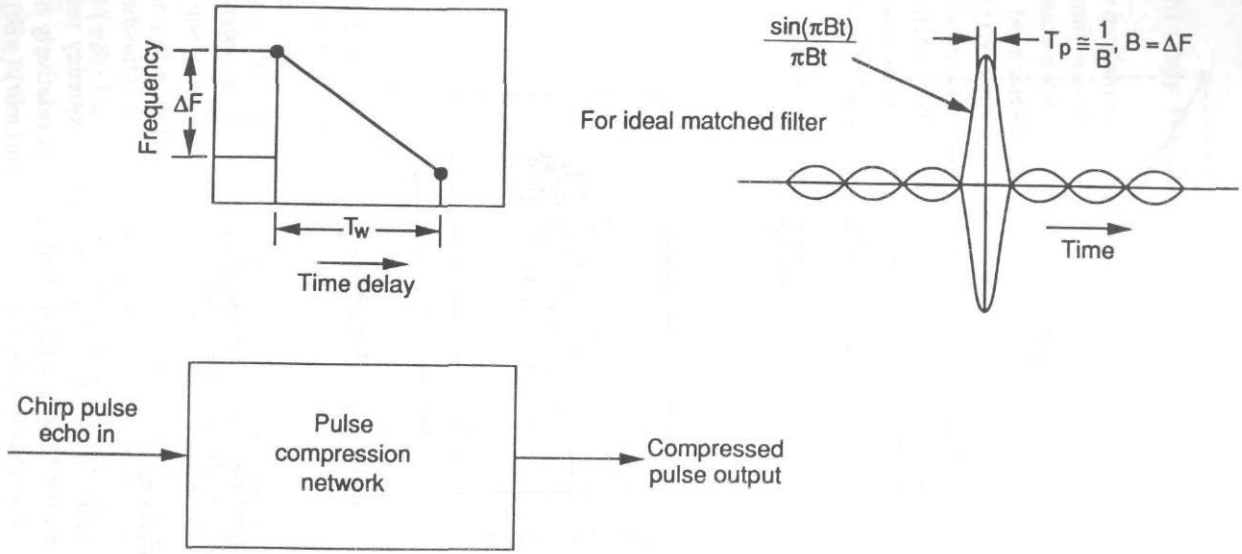

Figure 10.2 Linear FM pulse compression network and output characteristics [From 4].

spectrum will result in reduction of the time sidelobes. Time sidelobe reduction is important, because high time sidelobes may be mistaken for target responses at the receiver output. However, amplitude-weighting the receiver filter spectrum has the effect of broadening the compressed pulse and redistributing the energy in the time sidelobes of the compressed pulse (autocorrelation) output [3, 5, 6].

Although weighting reduces time sidelobes (which is desired), the receiver spectrum is no longer "matched" to the transmit spectrum. Thus, weighting results in a mismatch loss or a reduction in the signal processing gain. The mismatch loss usually ranges from 1 to 2 dB and is dependent on the function used for weighting. Table 10.1 [6] shows the effects of different weighting functions on *peak sidelobe level* (PSL), pulse widening (compared to the inverse of the bandwidth), mismatch loss, and the effects of the weighting functions on sidelobe falloff.

Differences between the transmitter and the receiver spectra (other than intentional weighting), which are error effects, will also have an effect on the performance of the pulse compression system. In some cases, the effects of these errors will be similar to the effects of weighting; that is, the sidelobes, pulse width, and mismatch loss will be effected. Error effects will be examined in more detail in later sections of this chapter.

10.2.4 Nonlinear FM Pulse Compression Waveforms

Nonlinear frequency modulation (NLFM) is another type of pulse compression waveform that achieves low time sidelobes and minimal mismatch loss by utilizing FM modulation to provide the desired amplitude spectrum and the sidelobe level with amplitude weighting of the receive spectrum. By design, the transmit spectrum is "matched" to the receive spectrum for NLFM; therefore, there is theoretically no mismatch loss. In practice there is often several tenths of 1 dB mismatch loss, due to the inability to realize exact waveforms.

Table 10.1
Weighting Functions (from [6])

Weighting Function	*Peak Sidelobe*	*Pulse Widening*	*Mismatch Loss (dB)*	*Sidelobe Falloff*
$k + (1 - k)\cos^n(\pi f/B)$				
Hamming ($k = 0.08$, $n = 2$)	−42.8	1.47	−1.34	$1/t$
Hanning cosine-squared ($k = 0$, $n = 2$)	−32.2	1.62	1.76	$1/t$
Cosine-pedestal ($k = .24$, $n = 2$)	−30.3	1.25	0.74	$1/t$

It is possible to implement a nonlinear FM waveform with a symmetrical frequency versus time waveform or a asymmetrical frequency versus time waveform (about $T_w/2$). An example of a asymmetrical frequency versus time characteristic is shown in Figure 10.3. A symmetrical waveform simply has a mirror image versus time characteristic about the $T_w/2$ point of the pulse. The symmetrical waveform design is more tolerant to doppler shift frequency errors than the asymmetrical waveform.

10.2.5 Pulse Compression Phase-Shift-Keyed Waveforms

Phase-shift-keyed (PSK) waveforms can also be used in pulse compression systems. To generate a PSK transmit pulse, a long pulse of duration T is divided by n subpulses of width T_c. Each subpulse is "coded" in phase by 0 or π (for example). The compression filter is the time inverse of this coded waveform (i.e., the matched filter). The subpulses, each T_c wide, are referred to as "chips" (quite often the terms chip and bit are used interchangeably when referring to the subpulses of PSK-coded waveforms). Barker codes, for example, can be used to modulate a

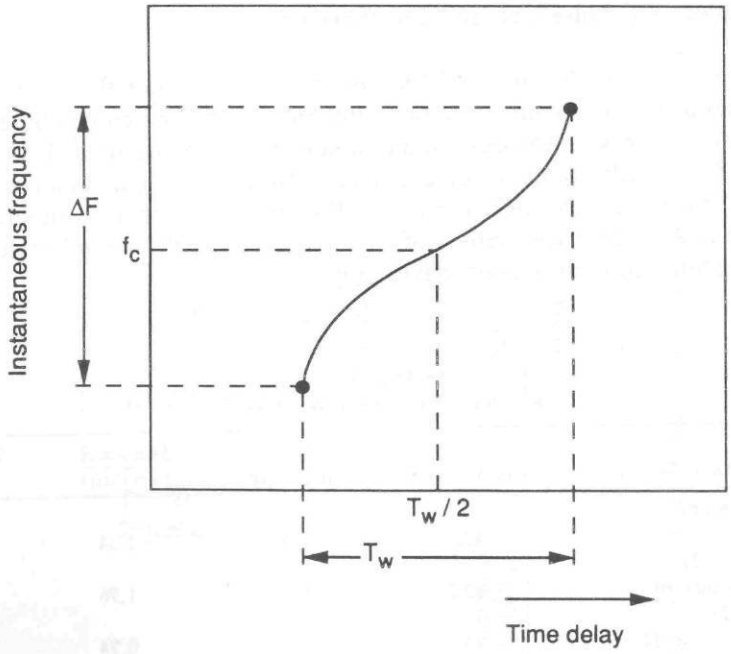

Figure 10.3 Asymmetrical nonlinear FM frequency versus time waveform.

carrier and are one example of a PSK waveform. Figure 10.4 shows a compressed pulse as it would appear for a carrier modulated with a code of n-chips, such as a Barker code.

Barker codes and pulse compression systems that use these codes have the following characteristics:

1. Sidelobes are at a voltage level 1, with peak of level n, where n is the number of bits or chips.
2. Only certain length codes work.

Characteristics of Barker codes (i.e., chip coding and sidelobe levels) for codes of length 2, 3, 4, 5, 7, 11, and 13 are given in several references [5, 6]. Sidelobe levels range from -6 dB to -22.3 dB for codes of length 2 to 13, respectively. When Barker codes are used to modulate a carrier, the spectrum exhibits a $\sin(x)/x$ shape where the first null in the spectrum is equal to the $1/T_c$.

Maximal Length Codes

There also exists a set of long binary codes, known as *pseudorandom* (PN) codes or sequences, that are relatively easy to generate with shift registers, have good sidelobe properties, and can be obtained with mathematical algorithms [5, 6]. Of particular interest are the codes that are maximal length, because these codes have the properties mentioned and also do not repeat until after $2^n - 1$ pulses (or chips), where n is the number of stages in the shift register used to generate the sequence. Figure 10.5 shows the shift register connections for obtaining a maximal-length

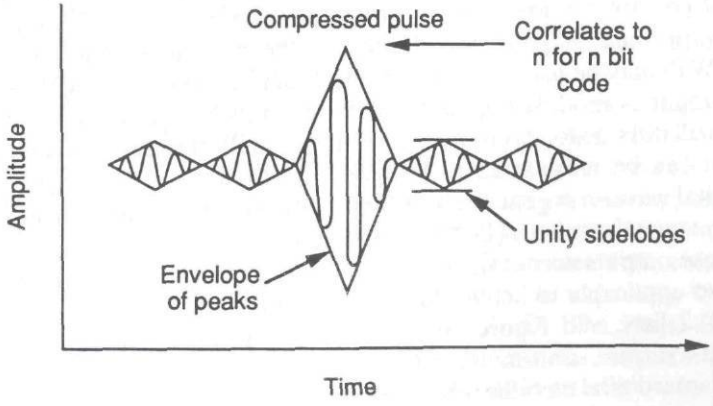

Figure 10.4 Compressed pulse for an n-chip PSK waveform.

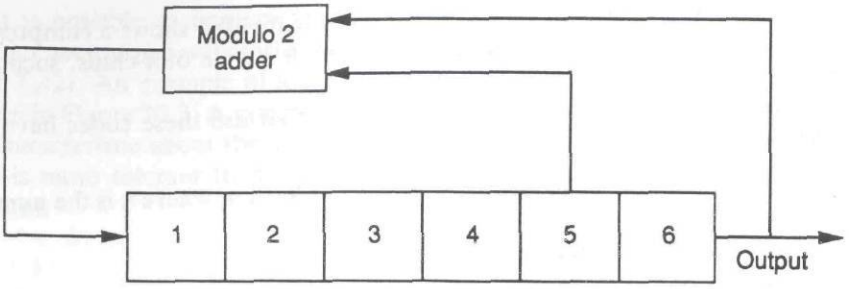

Figure 10.5 Six-bit shift register for generating a pseudorandom linear recursive sequence of length 63.

sequence of length 63. Maximal-length sequences with lengths of 7 to 2,047 are obtainable by using 3- to 11-stage shift registers, respectively, with the appropriate feedback [5, 6].

10.3 COHERENT PULSE COMPRESSION WAVEFORM GENERATION AND PROCESSING

Pulse compression waveforms can be generated by several techniques to realize coherent pulse compression systems. Table 10.2 lists some of the more common active and passive pulse compression waveform generation techniques. Active generation techniques often involve the modulation of a signal source (either analog or digital), whereas passive techniques utilize delay lines, or filters, to realize the coded waveforms by varying the phase versus time or frequency of a carrier signal.

Figure 10.6 shows some active generation techniques for LFM waveforms. NLFM waveforms can be generated by most of the same techniques. A *traveling wave tube* (TWT) may be used to serrodyne (frequency modulate) a CW RF signal applied at its input by modulating the helix (for example). Various types of voltage controlled oscillators exist at frequencies from VHF through *millimeter wave* (MMW), that can be modulated to frequency modulate the oscillator's output. Recently, digital waveform generation techniques have become more available; for example, *direct digital synthesis* (DDS) components allow the generation of variable frequency/phase outputs according to the input digital control word(s). DDS techniques are also applicable to active PSK waveform generation.

Table 10.2 lists, and Figure 10.7 shows, techniques for implementation of waveforms with *surface acoustic wave* (SAW) delay line devices. Figure 10.7(a-c) shows pairs of interdigital metallic transducers that would be mounted on the surface of piezoelectric material, such as quartz. In each figure, the transducer on the left is excited with an electrical signal and the transducer fingers are spaced at $\lambda_s/2$,

Table 10.2
Active and Passive Pulse Compression Waveform Generation Techniques

	FM	*PSK*
ACTIVE	Serrodyning (TWT)	Active PSK generators
	Voltage-controlled oscillators	Switched-line phase shifters
	Digital synthesis (double integration for quadratic phase)	Digital synthesis
PASSIVE	Dispersive delay lines (generation/compression)	
	Surface acoustic wave delay lines	Same as FM
	Folded-tape meander lines	
	Charge-coupled delay lines	

where λ_s is the wavelength of the input signal based on a surface wave velocity of propagation V_s for the piezoelectric material. This electrical signal causes a surface wave to propagate to the transducer on the right. Because the left transducer, in each case shown here is a wideband transducer (i.e., the transducer propagates a wide range of signal frequencies), the transducer on the right will respond to the input signal energy if properly designed. The output transducer also consists of interdigital finger pairs with spacing of fingers at the peaks of the desired output impulse response. Thus, in Figure 10.7(a) the finger pair spacing varies in a manner that creates an LFM chirp (impulse response), and in Figure 10.7(b) the finger pairs reverse polarity at the appropriate points corresponding to phase reversals needed for a PSK code. Lastly, Figure 10.7(c) shows how amplitude weighting can be realized by varying the overlap of the interdigital fingers. The interdigital fingers in Figure 10.7(c) are shown with finite width, which will be the actual case in any of the three sets of SAW transducers shown.

Processing of the transmit pulse compression waveform by the receiver can be done with some of the same techniques shown in Table 10.2, and specifically, with the SAW devices shown in Figure 10.7. SAW devices, which are actually transversal filters, can readily be designed to have an impulse response required to match (i.e., correlate) the transmitted waveform. Figure 10.8 is a block diagram of an LFM coherent radar system employing SAW devices. The coherent LO is pulsed with a narrow pulse, which in turn excites the SAW expander. The expander output is up-converted to RF using the radar STALO. The single-sideband up-converter is gated by the switch and input to the transmitter, which may be a solid state or tube device. Usually, the transmitter output is operated near saturation, maintaining a flat amplitude transmit pulse. After down-converting the receive signal to the COHO frequency, a SAW compressor (matched filter) is used for

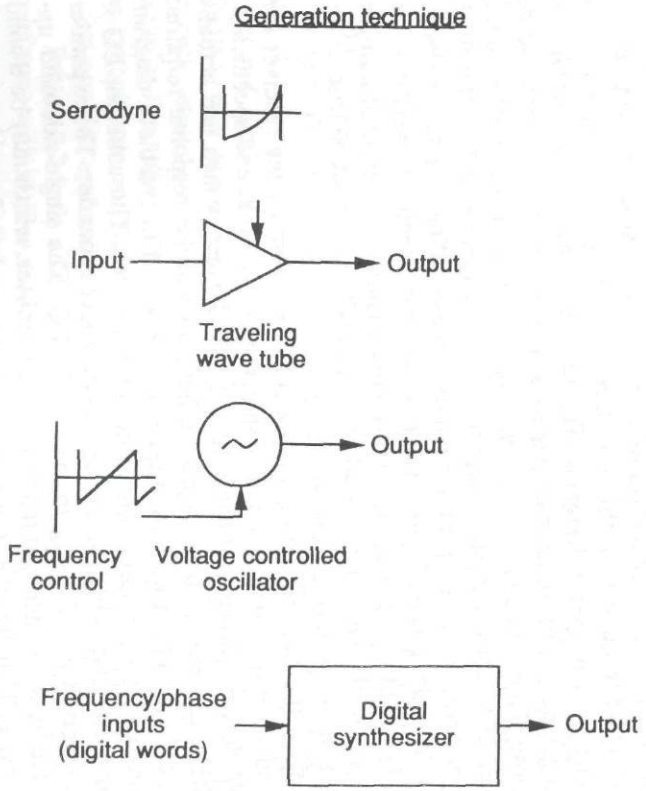

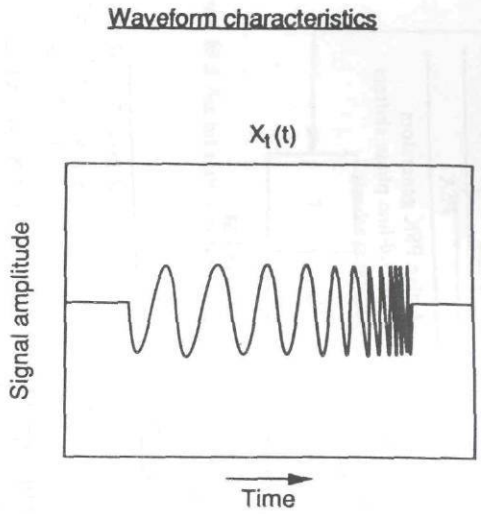

The phase of the waveform $X_t(t)$ is

$$\phi(t) = 2\pi\left(f_c t + \alpha\frac{t^2}{2}\right)$$

f_c = Carrier frequency

α = Quadratic phase constant

Figure 10.6 Linear FM pulse compression active generation.

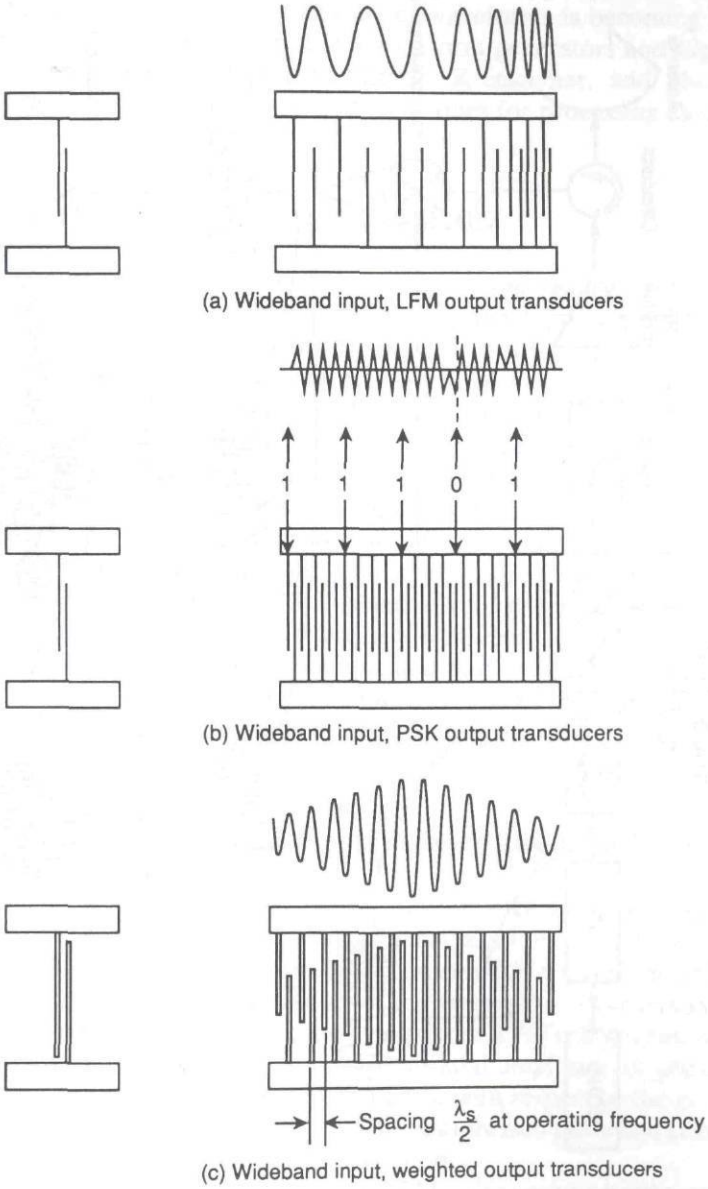

Figure 10.7(a-c) Examples of pulse compression SAW devices.

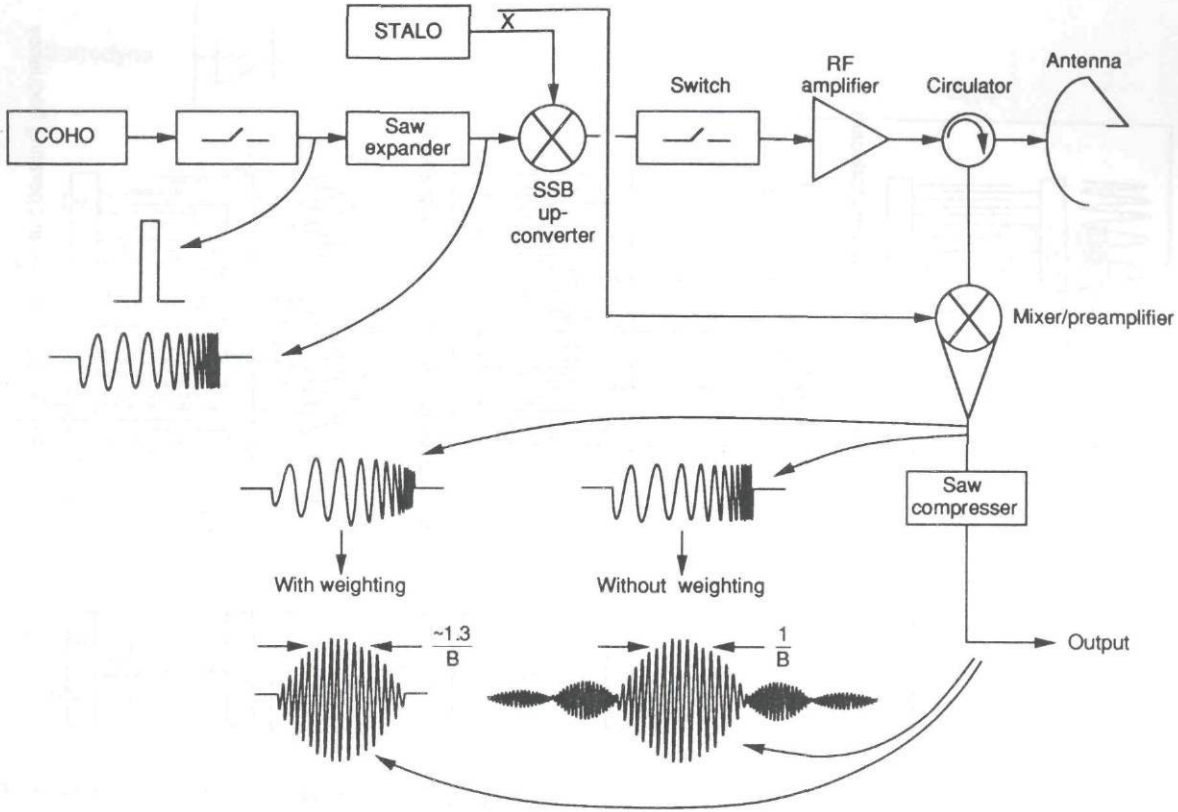

Figure 10.8 Block diagram of LFM pulse compression radar system (from [4]).

obtaining the compressed pulse. The figure shows the compressor output as it would appear for two cases: no weighting and amplitude weighting.

Other techniques exist for the generation and processing of pulse compression waveforms. Digital generation and processing of waveforms is becoming increasingly common with the availability of digital waveform generators and high-speed A/D converters and similar components. Lewis, Kretschmer, and Shelton [7] describe many digitally generated codes and techniques for processing those codes digitally.

10.4 ERROR EFFECTS IN PULSE COMPRESSION

In a pulse compression radar system, distortions in the radar's transmitter or receiver components, the transmission media, or signal processing can cause reduced performance. This reduced performance depends on the nature of the distortion. As we will see, distortions or errors in pulse compression systems usually manifest themselves in three ways: increased compressed pulse PSL, reduced SNR, and broadening of the compressed pulse mainlobe. Increased sidelobes can result in false target detections, whereas reduced SNR improvement causes reduced target detection performance. Wider compressed pulse widths degrade range resolution. Errors can also cause other effects such as time shifts in the compressed pulse. We will consider some of the more common error effects in LFM and PSK pulse compression systems and techniques for quantitatively estimating the effects of these errors. Many of the error effects addressed in this chapter for pulse compression waveforms affect the time-domain compressed pulse response similarly to the way the same errors affect the frequency domain response of a sinusoidal tone. See Chapter 6, "Nonlinear Effects in Fourier Transform Processing," for that discussion.

10.4.1 Linear FM Pulse Compression Amplitude and Phase Error Effects

Amplitude and phase errors, in either the transmit or receive pulse compression waveforms, are common errors. For example, sinusoidal amplitude errors can occur in the receive filter transfer function (usually the transmit LFM waveform amplitude is maintained flat by limiting or saturation in the transmitter). Sinusoidal phase errors may be caused by phase ripple in the bandpass of TWTs, klystrons, or other transmitter components. A primary effect of sinusoidal amplitude or phase error on pulse compression systems is increased sidelobes, with respect to the mainlobe. Loss in SNR improvement and broadening of the compressed pulse can also occur, depending on the nature of the sinusoidal distortion.

Sinusoidal amplitude and phase errors in LFM pulse compression waveforms can be analyzed by using the Fourier transform pair relationships. Klauder and

others [5, 8, 9] have developed a "paired-echo" theory that shows the effects of sinusoidal amplitude and phase errors in pulse compression waveforms. For this analysis, it is assumed that the spectrum, $G(f)$, of the transmit time function, $g(t)$, is contained within the frequency interval ($-B/2$ to $+B/2$), where B is the bandwidth in hertz. If a band-limited waveform is passed through a network that has either sinusoidal amplitude or phase distortions in the frequency response, the output time response will contain paired echoes about the major response. Paired-echo analysis is based on a Fourier series analysis of the distorting network's amplitude and phase versus frequency functions. Thus, the amplitude function and resulting distortions are expressed in terms of a_o and a_1, which are the dc and first harmonic Fourier coefficients of the network's amplitude response. Similarly, b_o and b_1 are the dc and first harmonic Fourier coefficients of the network's phase response (i.e., only one sinusoidal term of the Fourier series is considered). It can be shown (for small errors; i.e., $b_1 < 0.5$ radians) that the relative amplitude of the paired echoes is $a_1/(2a_o)$ for zero phase ripple and $b_1/(2b_o)$ for zero amplitude ripple (i.e., for no other errors in either case).

FM Pulse Compression Amplitude Error Effects

If either the transmit or receive pulse compression filter spectrum experiences a cosine amplitude variation over the pass band, this will create symmetrical paired echoes in the time domain, in addition to the main signal $g(t)$, where the (error-free) shape of $g(t)$ is determined by the error-free spectrum, $G(f)$. For n cycles of ripple across the bandwidth of $G(f)$, the time echoes are replicas of the main signal, delayed and advanced from it by n/B seconds and scaled in amplitude by $a_n/2$, where a_n is the amplitude of the error modulation. This relationship can be used to approximate the effects of amplitude error across the expanded pulse. Figure 10.9 shows the effects of amplitude distortion on the time response.

Paired-echo theory and the Fourier series relationship can also be used to explain the effects of weighting. Consider uniform (spectrum) amplitude weighting across chirp bandwidth B. In this case the Fourier transform relationship indicates that the time domain response will be a $(\sin \pi Bt)/(\pi Bt)$ function (also called a "sinc" function), with high (-13.2 dB) time sidelobes. Duality can be used to show that a rectangular time response results in a $(\sin x)/x$ shaped spectrum.

Other amplitude tapers can also be analyzed by paired-echo theory. For example, using $n = 1$ (1 cycle of ripple, on a pedestal), paired-echo theory shows that three time displaced and weighted "sinc" functions occur. Low time sidelobes are obtainable by the proper choice of the weighting. Similar techniques can be used to select the coefficients for weighting functions, such as Taylor weighting.

Paired-echo theory is valuable to obtain insight into the effects of sinusoidal amplitude error on pulse compression system performance. Using paired-echo

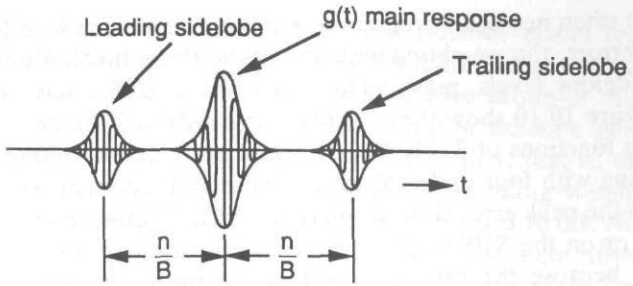

		Responses		
		Leading sidelobe	Main response	Trailing sidelobe
Amplitude ripple:	a_n	$\frac{a_n}{2} g\left(t + \frac{n}{B}\right)$	$a_o\, g(t)$	$\frac{a_n}{2} g\left(t - \frac{n}{B}\right)$
Phase ripple:	b_n	$\frac{b_n}{2} g\left(t + \frac{n}{B}\right)$	$b_o\, g(t)$	$\frac{b_n}{2} g\left(t - \frac{n}{B}\right)$

Figure 10.9 Paired-echo responses for n amplitude or phase ripples across bandwidth B (after [5]).

theory, sidelobes can be predicted for sinusoidal amplitude ripple across the chirp bandwidth, where a_1 is the peak value of the sinusoidal error and a_o is the dc component. When additional weighting is applied to the received filter, a simple application of paired-echo theory to provide a quantitative measure of sidelobe level is not always accurate. A more accurate prediction of sidelobe level for weighted LFM receive filters can be obtained by actual inverse Fourier transform of the receive filter amplitude and phase function to obtain the envelope of the compressed pulse. This approach is quite accurate for the case of high time-bandwidth product waveforms, because, in this case, the pulse compression spectra are nearly rectangular (without any amplitude weighting).

The three weighting functions shown in Table 10.1 have been analyzed by taking the inverse Fourier transform of the receiver filter function for different sinusoidal errors. These weighting functions are representative of what might be used in an actual pulse compression system (although by no means optimum weighting functions), in terms of weighting to achieve a particular sidelobe level. For example, weighting to achieve more than 40-dB reduction in sidelobe level (Hanning weighting) is rarely employed, because sidelobes below 40 dB are difficult to achieve in practice because of error effects. On the other hand, at least 30-dB

sidelobe level is often necessary, requiring weighting consistent with that sidelobe level. With no errors, the weighting with any of the three functions of Table 10.1 results in the sidelobe levels, pulse widths, and loss in SNR shown in the table. The plots in Figure 10.10 show the effects of sinusoidal amplitude error on each of the weighting functions of Table 10.1. Each of the plots in Figure 10.10 shows the error resulting with four cycles of sinusoidal amplitude error across the chirp bandwidth, with the peak error shown. There will be little effect on the compressed pulse mainlobe or on the SNR improvement as long as there are more than four cycles of error, because the primary effect of the sinusoidal error is to reduce sidelobe levels. The results will be nearly the same as long as there are more than two cycles of amplitude error; less than two cycles of errors causes the sidelobe to occur within the compressed pulse mainlobe, and the effect will be to broaden the mainlobe.

Other types of amplitude error can also be predicted by inverse Fourier transform of the error function superimposed on the weighting function. Consider the quadratic amplitude error that is zero at the left edge of the pulse and maximum

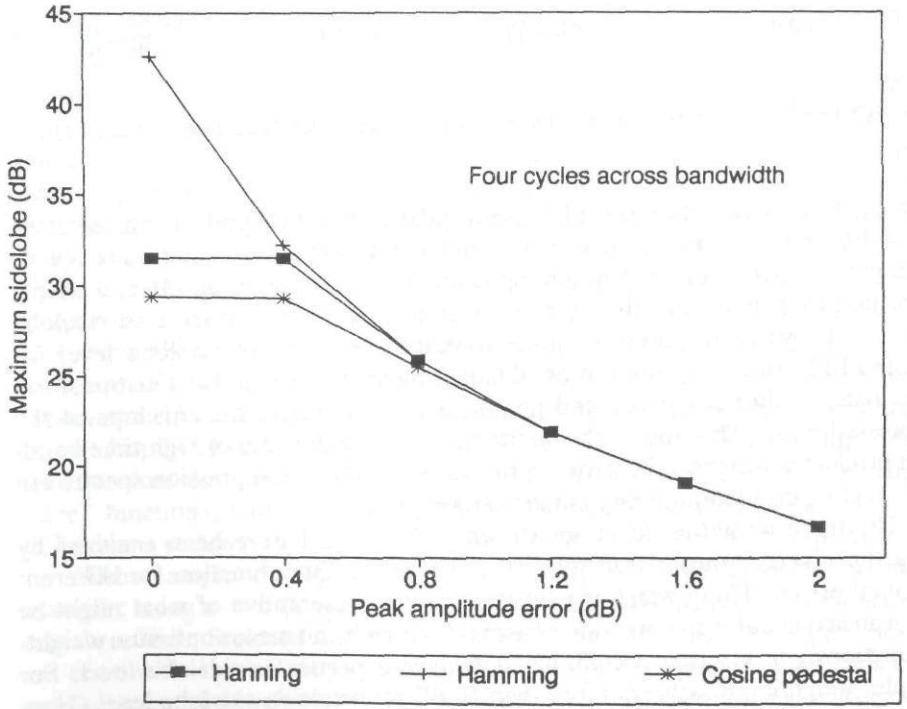

Figure 10.10 Mainlobe to maximum sidelobe versus peak sinusoidal amplitude error.

at the right edge. Figure 10.11 is a plot of peak sidelobe errors resulting from quadratic amplitude error across a Hanning-weighted LFM spectrum. Such quadratic amplitude error could be due to transmitter tube droop or improperly set sensitivity time control. The amount of degradation in sidelobe performance is similar for the other two weighting functions of Table 10.1; that is, the error-free sidelobe levels will approach the same level as for Hanning weighting, as the magnitude of the quadratic amplitude error increases toward 10 dB. Note that only six points are plotted in Figure 10.11 and connected by straight lines in order to show the trend in sidelobe degradation; intermediate points on the curves will not be at exactly the sidelobe levels shown. It is typical to observe additional compressed pulse broadening and loss in SNR improvement with quadratic amplitude error. The pulse broadens by about 5%, and an additional 4 dB in amplitude loss is observed at 10-dB quadratic amplitude error. The results for amplitude errors in pulse compression waveforms (the compressed pulse response) are very similar to the effects of those errors on the frequency domain response of a sinusoidal tone. Refer to Chapter 6 for further discussion of these effects.

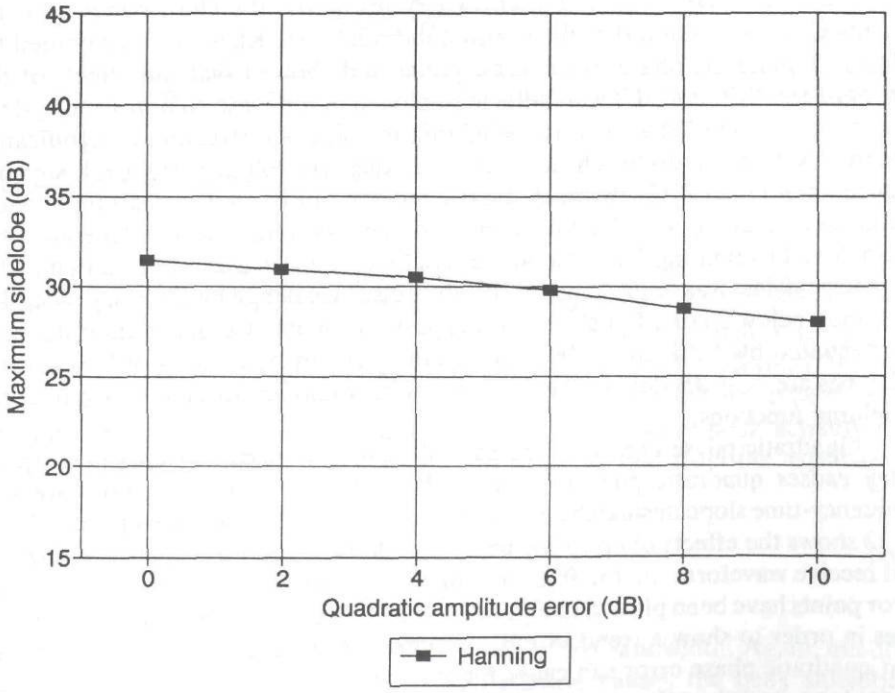

Figure 10.11 Mainlobe to maximum sidelobe versus quadratic amplitude error.

Linear FM Phase Error Effects

Ideally, for the matched filter case, the spectrum of the compression filter (or processor) matches the expansion filter or waveform generator in a pulse compression system. Usually, the amplitude of the expanded pulse is limited (i.e., flattened) for transmission and the design of the compressor should account for the flat amplitude of the expanded pulse. However, phase errors (or phase differences between the expansion and compression filter) can cause sidelobes just as amplitude errors do. Paired-echo theory can also be used to show the effects of phase error across frequency. For example, n cycles of phase ripple across the chirp bandwidth will have the effect on sidelobes shown in Figure 10.9. The quantitative sidelobe level can be predicted by paired-echo theory if no other errors exist and no additional amplitude weighting is employed.

Sinusoidal phase error effects on LFM waveforms with the weighting functions of Table 10.1 have been analyzed and are shown in Figure 10.12 for the case of four cycles of phase ripple across the chirp bandwidth. The sidelobe levels shown are approximately the same for more than two cycles. As with sinusoidal amplitude errors, the primary effect of sinusoidal phase error of more than two cycles is to raise sidelobe levels. With less than two cycles across the chirp bandwidth, the mainlobe will broaden rather than raising the sidelobes. Klauder [3] examined the effects of quadratic phase error in his paper and showed that the effects of this error are greatly reduced if weighting is employed in the pulse compression system. His analysis showed that with no weighting the sidelobe structure is significantly distorted with a quadratic phase error of 45 deg. At 360 deg, the peak signal is reduced more than 7 dB, the peak breaks into two pulses, and the 3dB pulse width increases by a factor of 10. On the other hand, if heavy weighting to reduce sidelobes is employed (weighting for about 40-dB sidelobes), his analysis showed that at 180 deg the peak loss was reduced by 1.5 dB, the pulse broadened by 40%, and sidelobes remained below 38 dB. For the same weighting with 360 deg phase error the peak is attenuated by 4 dB, the 3-dB pulse width increases by a factor of 2.3, and the sidelobes are $>$ 36 dB down. These latter results would be typical for most practical weighting functions.

Quadratic phase errors can be caused by long waveguide runs (linear group delay causes quadratic phase) in the path of the pulse compression system or frequency-time slope mismatch between the transmit and receive waveforms. Figure 10.13 shows the effects of up to 360 deg of quadratic phase error, between transmit and receive waveform, on the PSL for Hanning weighting. Note that only six phase error points have been plotted in Figure 10.13 and those points connected by straight lines in order to show a trend in PSL. Chapter 6 discusses some of the anomalies that quadratic phase error can cause for the frequency domain response of a sinusoidal tone, and the effects are similar for the compressed pulse response. That is,

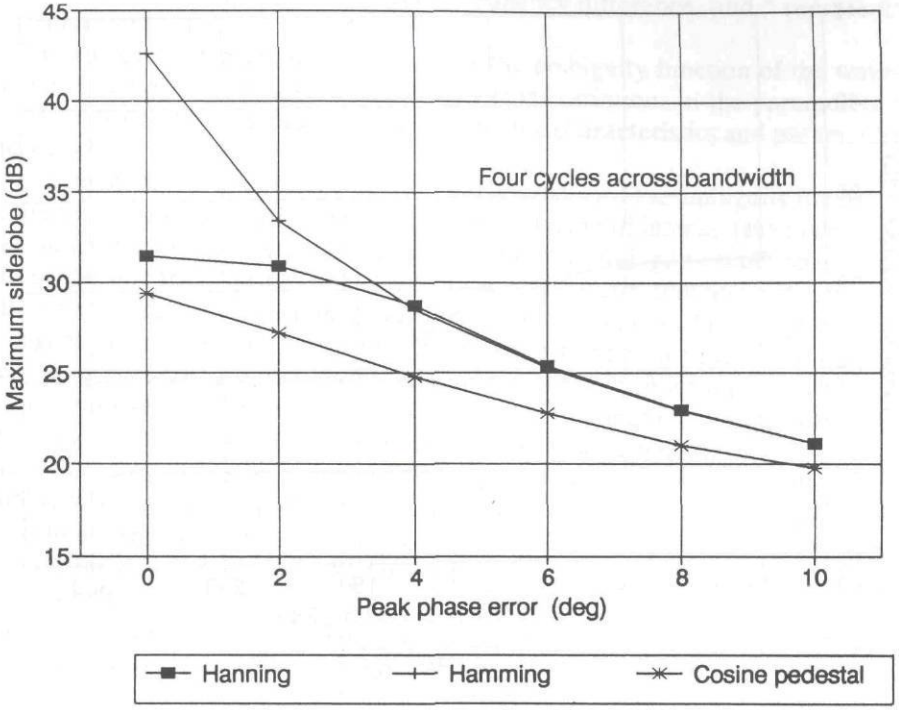

Figure 10.12 Mainlobe to maximum sidelobe versus peak sinusoidal phase error.

the plot of sidelobe level versus quadratic phase error will not be strictly monotonic because the first sidelobe will merge into the mainlobe and the peak sidelobe becomes the second sidelobe, which is at a lower level (see Chap. 6 for this discussion). Nevertheless, Figure 10.13 shows the trend in sidelobe level. It is important to note that quadratic phase shift acts like a frequency mismatch between the transmit and receive waveforms; thus, the compressed pulse peak actually shifts in time. The value of this time shift, τ_e, may be calculated from the expression:

$$\tau_e = \frac{\phi_{\text{error}}}{\pi B} \tag{10.8}$$

where ϕ is the quadratic phase error and B is the chirp bandwidth. Again, quadratic phase error for the other two weighting functions causes the peak sidelobe to approach the same level as that for the Hanning weighting function.

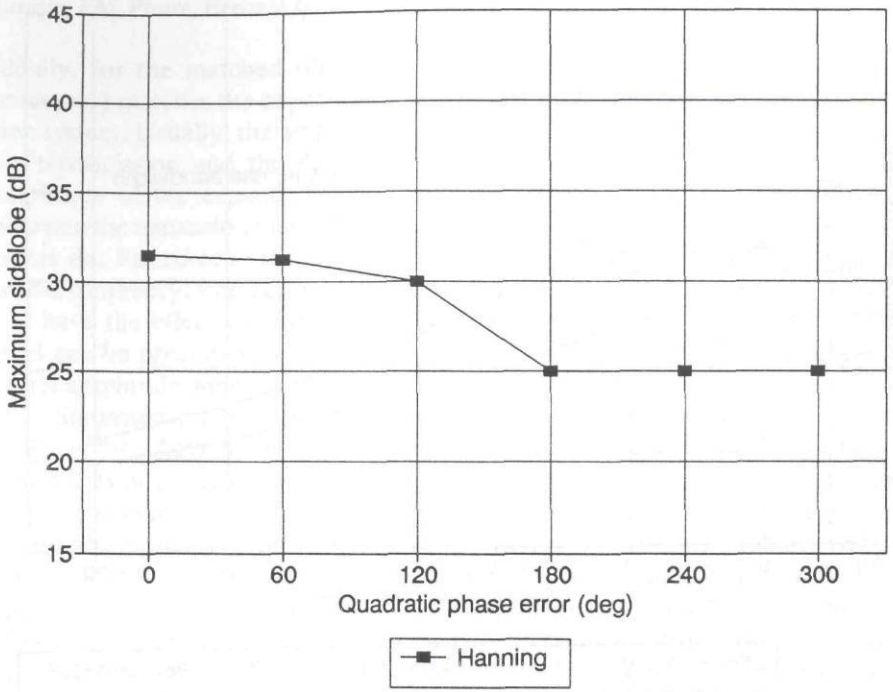

Figure 10.13 Mainlobe to maximum sidelobe versus quadratic phase error.

10.4.2 Ambiguity Functions

It is helpful to discuss the concept of ambiguity functions before discussing frequency and time-delay error effects in pulse compression waveforms. Ambiguity functions were introduced by Woodward [10] and have been examined for specific waveforms by other authors [2, 5, 11]. A radar waveform's ambiguity function can provide a great deal of information about the radar's performance in terms of range or doppler resolution. What is of more interest here is what information the waveform ambiguity function tells us regarding the effects of frequency or time-delay errors (or both) between the transmit and receive waveforms.

One definition of the ambiguity function is obtained from the cross-correlation of a doppler-shifted version of the transmit waveform and an unshifted version of that waveform. Therefore, the cross-correlation can be written (after rearranging terms) as:

$$\chi(\tau, fd) = \int_{-\infty}^{\infty} x(t)x^*(t - \tau)e^{j2\pi f_d t}\, dt \tag{10.9}$$

where τ is the time delay, f_d is the doppler frequency difference, and * represents the complex conjugate.

The absolute value squared of $\chi(\tau, f_d)$ is the ambiguity function of the waveform. The function defines a surface resulting from variations in the parameters τ and f_d. The shape of this surface is dependent on the characteristics and parameters of the waveform.

Although we will not examine all the characteristics of the ambiguity function, there are several characteristics of these functions that are of interest (the interested reader may refer to the references for more details on ambiguity functions). One of the properties that can be deduced from the ambiguity function definition is that the total energy in the response over the entire frequency-delay (range) plane, for a signal of fixed energy, is fixed. Therefore, attempts to reduce the energy content in an particular region lead to increased energy in other regions. Thus, if we try to improve or optimize a waveform's resolution capabilities to very narrow regions (e.g., around the region $\tau = 0$ and $f_d = 0$), the remaining energy will be spread into the sidelobes. If we set $\tau = 0$ or $f_d = 0$ in (10.9), then we will obtain the ambiguity function response along the f_d-axis or the time-delay axis, respectively. Along the f_d axis, the ambiguity function is proportional to the spectrum of $x^2(t)$; along the time delay axis the ambiguity function is the autocorrelation function of the modulation $x(t)$.

It can be shown that the square root of the ambiguity function for a chirped-pulse waveform is [11]:

$$\chi(\tau, f_d) = (|1 - |\tau|/T_w|) \frac{\sin[\pi(\alpha\tau + f_d)(Tw - |\tau|)]}{[\pi(\alpha\tau + f_d)(Tw - |\tau|)} \tag{10.10}$$

for $|\tau| < T_w$, and $\chi(\tau, f_d) = 0$, for $|\tau| > T_w$, where T_w is the chirp pulse width, α is the chirp slope in hertz per second, τ is the delay relative to the origin, and f_d is the doppler shift due to a moving target or other frequency difference between transmit and receive waveforms.

Several things can be determined from the chirped-pulse ambiguity function. First, the ambiguity surface will extend from $-T_w$ to T_w in range delay and from minus infinity to plus infinity in doppler. Time-delay errors (with no doppler shift) will cause the ambiguity function to fall off according to $(1 - |(\tau)/T_w|)$, so that there is a null in the zero doppler range response at $\tau = T_w$. At zero delay, the doppler frequency response is a $\sin(x)/x$ function (where x is a function of doppler). However, a feature of the chirped-pulse ambiguity function is its range-doppler coupling. That is, a doppler shift produces a range-delay shift in the response. As doppler increases, the response output peak will change in delay and will peak above a line defined by $f_d = -\alpha\tau$, extending from the origin of the f_d, τ coordinates. The result of this effect is that a chirped-pulse waveform can tolerate considerable doppler shift before it completely decorrelates, although there will be a range-

delay shift corresponding to the doppler. Figure 10.14 is a plot of the amplitude loss of a chirped pulse waveform as a function of doppler shift (calculated for a moderate time-bandwidth product chirp waveform). Note that a frequency shift of 0.5 B is required for 6 dB of amplitude loss.

A PSK waveform, such as a 13-bit Barker code, will result in a sharp ambiguity function near the origin. The zero range-delay doppler response will fall off as $\sin(x)/x$, where the first null equals $1/T_e$, and T_e is timelength of the envelope of the 13-bit PSK time waveform. The range-delay resolution is equal to the timelength of 1 bit. We will discuss frequency, time, and phase delay errors for PSK waveforms in more detail in a later section.

The above discussion has been limited to a consideration of the ambiguity function of a single pulse with certain pulse compression coding characteristics, in order to consider the effects of errors. However, it is interesting to note that when a sequence of pulse waveforms is transmitted at a given PRF, significant responses at multiples of the PRF can occur if there is a frequency difference between the transmit and receive waveform corresponding to a multiple of the PRF. These are "ambiguous" responses that can be plotted similarly to the ambiguity function surface. The references noted above can be consulted for more insight into these effects.

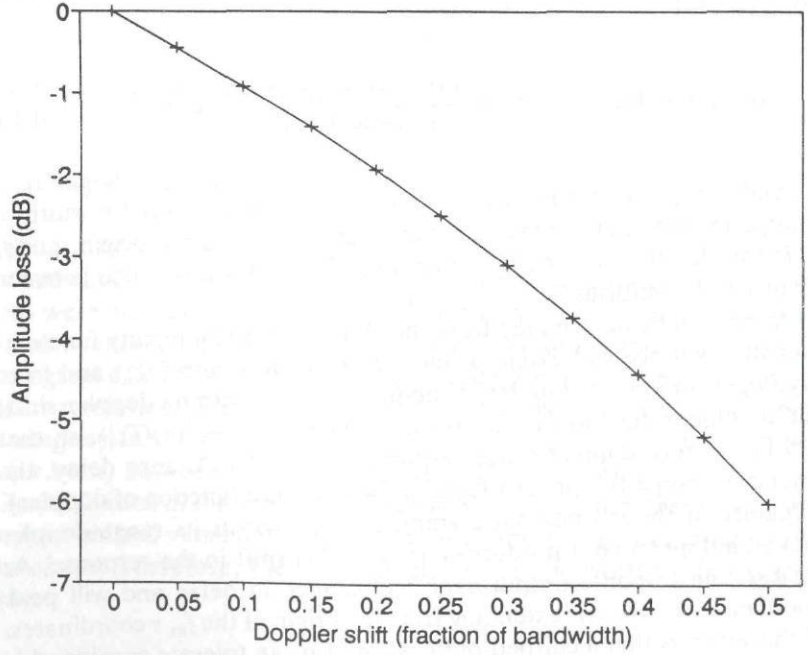

Figure 10.14 Amplitude loss of chirp pulse with doppler.

10.4.3 Frequency Error Effects in Linear and Nonlinear FM Pulse Compression

Frequency errors between the transmit and receive pulse compression filters may occur because of hardware or target effects. Hardware effects include drifts or instabilities in the LOs or differences in the transmit and receive LOs. Target effects, such as target movement, will cause a doppler (frequency) shift on the receive waveform, with respect to the transmit waveform. Regardless of the cause, frequency errors between the transmit and receive pulse compression waveforms result in four effects for LFM. Similar effects hold for asymmetrical NLFM.

1. The compressed pulse width broadens from the nominal (error-free) value as the frequency error (difference) increases.
2. There is a loss in correlation of the pulse compression system.
3. There is a time shift (delay or advance) in the compressed pulse peak. Recall that a significant effect in LFM waveforms is that of range-doppler coupling, meaning that doppler errors will cause a shift in time delay of the compressed pulse.
4. The time sidelobes (PSL) of the compressed pulse increase.

These effects can be predicted by the ambiguity function of the chirped-pulse waveform (see (10.10)). Figure 10.15 shows a plot of (10.10) for a chirped-pulse waveform along the time-delay axis, for different amounts of doppler shift.

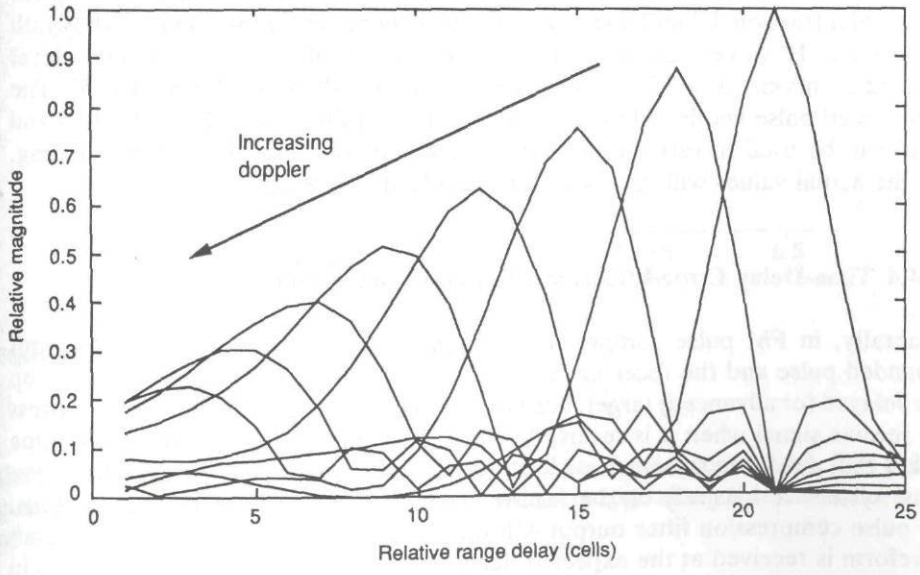

Figure 10.15 Delay shifts due to doppler frequency shifts.

Although this ambiguity function is plotted for a chirp of relatively low time-bandwidth product ($BT = 8$), the effects of doppler are similar on higher time-bandwidth waveforms. The largest autocorrelation response (at range bin 25) in Figure 10.15 is the response for zero doppler shift. Note that as the doppler shift increases, the time delay of the peak shifts (to the left), the correlation decreases, sidelobes increase, and the correlation response broadens. In this plot, a frequency shift of $1/T_w$, where T_w is the pulse width of the chirp, causes a delay shift in the autocorrelation response to the position of the null in the autocorrelation response for zero doppler.

Frequency errors (differences) in LFM pulse compression systems cause the compressed pulse to shift linearly; for example, a frequency error of 10% of the bandwidth causes a 10% shift in the delay of the compressed pulse peak. The effects of the delay of the compressed pulse depend on the sign of the frequency error ($+/-$) and the transmit chirp direction (frequency versus time) according to Table 10.3.

Amplitude loss with doppler shift was plotted in Figure 10.14. At a doppler frequency difference of 50% of the chirp bandwidth, the correlation has decreased by 6 dB. At a frequency difference of 100% of the chirp bandwidth, the correlation response is zero. The compressed pulse width will increase as doppler frequency difference increases, as shown in Figure 10.16 (this plot is based on calculation at several discrete doppler frequencies). Note that doppler frequency shift causes the pulse width to increase. Larger time-bandwidth pulse compression waveforms allow for lower sidelobes initially (without frequency errors), and the sidelobe level for a particular fractional doppler shift will remain lower than for lower time-bandwidth waveforms. However, as doppler shift approaches 0.5 B, the sidelobe level approaches about 13 to 15 dB, regardless of the time-bandwidth product [5]. The compressed pulse width will broaden with doppler shift as well. Figures 10.14 and 10.16 can be used to estimate amplitude loss and compressed pulse broadening, but the actual values will vary with time-bandwidth product.

10.4.4 Time-Delay Error Effects in FM Pulse Compression

Generally, in FM pulse compression systems, time delay between the transmit expanded pulse and the receiver matched filter (compressor) will simply show up as a delayed (or advanced) target, because the pulse compression filter will compress the receive signal when it is received. Thus, it is important to determine the time delays that exist in a system in order to determine the true time delay of targets. Some system designs rely on the receive signal arriving at a particular time; thus, the pulse compression filter output will fully compress (correlate), if the transmit waveform is received at the expected delay time. In this case, unwanted delays in

Table 10.3
Frequency Error Effects on Compressed Pulse in Linear and Nonlinear FM Pulse Compression

	Frequency Difference	
Transmit Chirp Direction	*Positive*	*Negative*
Down-swept chirp	Compressed pulse delayed	Compressed pulse advanced
Up-swept chirp	Compressed pulse advanced	Compressed pulse delayed

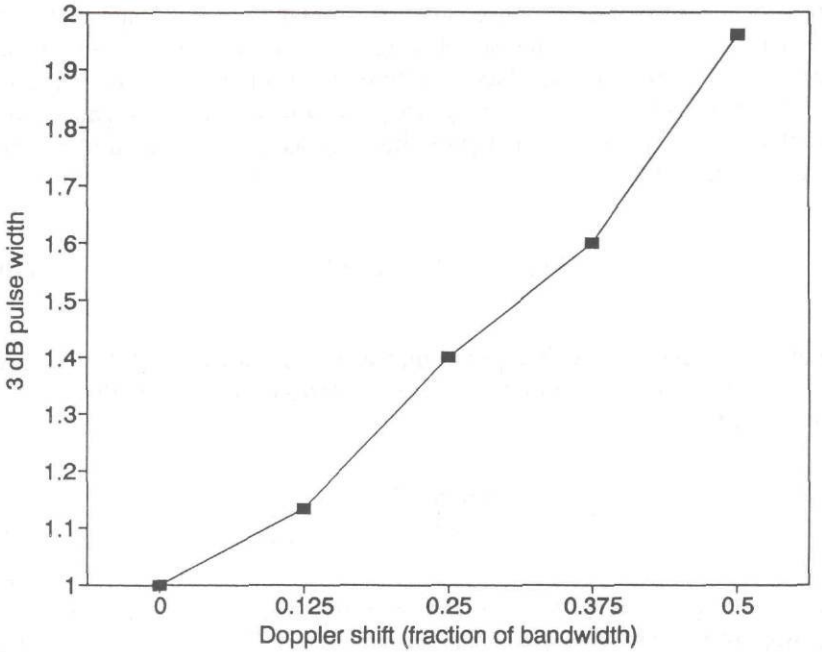

Figure 10.16 3-dB compressed pulse width versus doppler.

the receive signal will cause the output to not fully compress (correlate). The pulse compression filter output will follow the expected output along the time-delay axis of the ambiguity diagram, for this case.

If dispersive delays occur between the expanded pulse and the compressor, those dispersive delays will have the effect of shifting and decorrelating the compressed pulse, in a manner analogous to frequency errors above. Sometimes dispersive equalization is employed to correct the frequency versus delay response of the expander to improve correlation in the compressor. Usually, however, if the expanded pulse spectrum is well matched to the compressor spectrum, then extraneous dispersive delays are to be avoided.

10.4.5 Frequency, Phase, and Time-Delay Error Effects in PSK Waveforms

Bell and Claiborne [12] show that the correlation response of PSK waveforms can be expressed in terms of a response function similar to the ambiguity function, (10.9). For PSK waveforms, some simplifying observations can be made to determine the effects of frequency, phase, or time-delay error on peak correlation. Because PSK time waveforms are made up of piecewise uniform segments of the same timelength, it is possible to examine the response function around $\tau = 0$ and show that it reduces to:

$$\chi(0, f_d) = \int_{-\infty}^{\infty} |x^2(t)|^2 \, dt \tag{10.11}$$

For signals with rectangular envelopes (which is the case for most PSK waveforms) of duration T, it can be shown that the autocorrelation function for the main peak (i.e., for $\tau = 0$) is:

$$\chi(0, f_d) = \frac{\sin(\pi f_d T)}{(\pi f_d T)} = \frac{\sin(\pi \Delta)}{(\pi \Delta)} \tag{10.12}$$

where Δ = total phase error in wavelengths. Table 10.4 shows the value of Δ for certain losses in peak correlation. Equation (10.12) or Table 10.4 can be used to estimate the correlation loss due to total phase, or frequency, or time-delay errors in PSK waveforms.

Note that the term Δ in (10.12) can be written as $(N\phi)$ where N is the total length of the PSK waveform (number of cycles) and ϕ is the fractional phase error. Thus, we can write:

$$\chi(\tau, \phi) = \frac{\sin(\pi N \phi)}{(\pi N \phi)} \tag{10.13}$$

where ϕ, the fractional phase error, can be due to fractional frequency or time errors, that is:

$$\phi = \frac{\Delta F}{F} \text{ or } -\frac{\Delta T}{T}$$

In PSK waveforms, small errors will most commonly effect the compressed pulse peak by reducing correlation loss. Equation (10.12) or Table 10.4 can be used to estimate the effects of fractional phase error (frequency or time) on correlation. If the PSK code has very low sidelobes (without errors), then sidelobes may increase significantly; however, a change in peak amplitude is usually the most significant effect.

Table 10.4
Loss in Correlation Peak Versus Error in Wavelengths

Error in Wavelengths Δ	*Loss (dB)*
0.25	1
0.48	3
0.59	6
0.75	10
0.84	15
0.92	20

PSK Waveform Errors: An Example

Figure 10.17 shows an example of a PSK waveform with 200 chips, a center frequency of 84 MHz, a 5.25-MHz chip rate, and 16 cycles/chip. Note the number of cycles per chip is f_o/(chip rate), where f_o is the carrier frequency.

The total number of cycles, N, for this waveform is 3,200 (200 × 16). Using (10.12), it can be seen that a fractional error of about 150 ppm error causes 3-dB correlation loss, and 80 ppm error causes 1-dB correlation loss. These fractional errors could be due to any error that affects total phase (i.e., frequency or time). For example, 1-dB correlation loss could be caused by 6,720 Hz = ((80 10^{-6}) (84 MHz)) frequency error, whereas 3-dB correlation loss would result from 12,600 Hz = ((150 10^{-6})(84 MHz)) frequency error.

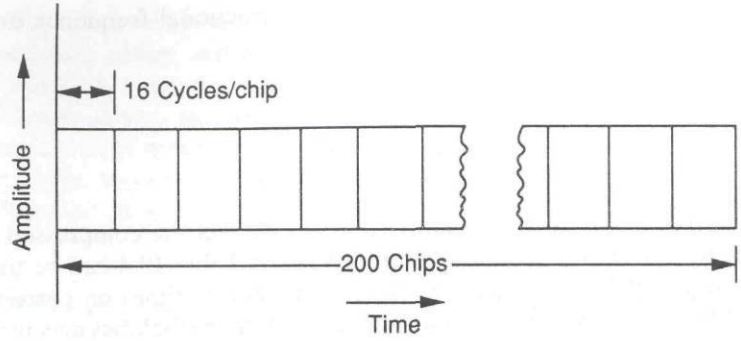

Figure 10.17 PSK waveform errors—example of 200-chip, 16 cycles/chip PSK waveform.

10.5 EXAMPLES OF PULSE COMPRESSION COMPONENT ERROR EFFECTS

10.5.1 Traveling Wave Tube Transmitter Error Effects

TWT amplifiers are frequently used as the final stage (or sometimes as a driver stage) in a transmitter chain for coherent radar designs. The TWT is used in a MOPA configuration, where the transmit waveforms are generated with very stable sources and then up-converted to RF using STALOs at the appropriate carrier frequency. Pulse compression waveforms are often used in such a configuration, with the pulse compression expanded pulse chirp being generated at low intermediate frequencies, either with active generation techniques, SAW devices, or some other technique, as previously discussed. The IF waveform generation is usually quite error free; that is, unwanted amplitude and phase distortions are not appreciably introduced in the low frequency signal generation stages. On the other hand, the final transmitter stages often introduce appreciable errors that determine the ultimate pulse compression system performance.

The following example examines the error effects introduced by the TWT amplifier section of a transmitter designed for use with a millimeter wave instrumentation radar. In the example, it is assumed that an expanded pulse of approximately 10 μs timelength with a 200-MHz chirp bandwidth is employed. A block diagram of the TWT section of the transmitter, along with the modulator and power supply is shown in Figure 10.18. The TWT used in the example is the Hughes 982HA (a 95-GHz, air-cooled tube). The chirp waveform derived from the exciter at RF is input to the TWT at a sufficient drive power level to saturate the output (the normal TWT mode of operation is in saturation).

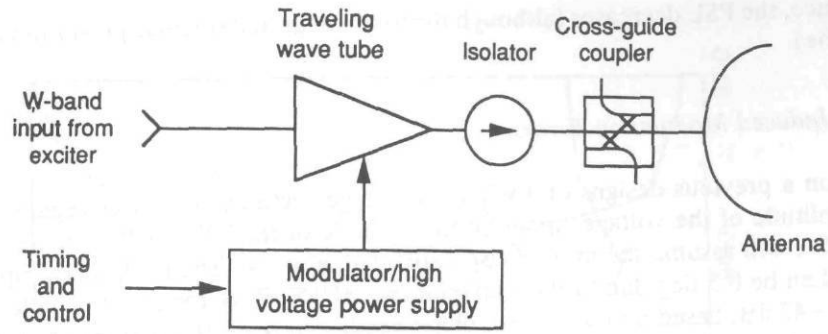

Figure 10.18 Transmitter block diagram.

The TWT will introduce both phase and amplitude distortions in the transmitter; therefore, these distortions must first be estimated and their effects on the pulse compression waveform calculated. Distortions can be introduced by the TWT *high-voltage power supply* (HVPS) and modulator, by the TWT insertion phase and gain characteristics, and by reflections due to antenna VSWR. The amounts of distortion due to each of these effects can be estimated, and the individual results combined in a rms fashion to obtain an estimate of the composite LFM response and range sidelobe performance.

In a TWT the cathode voltage fluctuations will have a significant effect on the amplified waveform. The following sections assume that the TWT cathode voltage sensitivity is approximately 0.25 deg/volt and that the TWT phase sensitivity is much greater than the amplitude sensitivity. The latter is true for most TWT transmitters, because a high-gain TWT typically exhibits higher phase sensitivity than amplitude sensitivity.

The results of the paired-echo analysis discussed in Section 10.4 can be used to calculate the effects of amplitude and phase distortions on the range sidelobe performance of the pulse compression waveform.

AM: Paired-echo sidelobe level below peak = 20 log $(AM/2)$, where AM = peak amplitude ripple in percent/100.

PM: Paired-echo sidelobe level below peak = 20 log $(E\phi/2)$, where $E\phi$ = peak phase ripple in radians.

As previously discussed, the paired-echo analysis assumes that the distortion signals are at singular frequencies, which forces all of the energy in the range sidelobes into a pair of echoes symmetrically located around the main response (for each distortion signal). If the phase or amplitude distortion is random in nature or spread out spectrally, then the energy in the sidelobes is spread out in time,

and hence, the PSL decreases (although the total integrated sidelobe power remains the same).

HVPS-Induced Modulation Errors

Based on a previous designs of TWT high-voltage sections and series regulators, the amplitude of the voltage ripple on the cathode of the TWT will be about 1V to 2V. We will assume the more conservative value of 2V. The peak phase ripple would then be 0.5 deg due to the ripple on the HVPS. Peak range sidelobe levels will be -47 dB, based on the 0.5-deg phase ripple estimate. It is assumed that the series regulator pulse response will be linear and hence will not degrade the pulse compression waveform to any great extent. Note that this ripple is not synchronous to the PRF and will therefore show up on a pulse-to-pulse basis, limiting clutter rejection performance to -41 dB (i.e., 20 log $1/E\phi$), if, for example, a two-pulse MTI canceler were employed. It must be emphasized that the phase ripple cited for this example is not representative of ripple in other transmitters or coherent radar systems.

TWT-Induced Modulation Errors

This section describes an analysis of the phase and amplitude modulation errors that might be added to the signal by the TWT itself. TWT insertion phase and output power are not constant with frequency, even in TWTs at lower frequency bands where tighter control of internal reflections is easier to implement because of larger physical structures.

TWT-Induced Amplitude Error

Swept-frequency amplitude data are available for the Hughes 982HA S/N 1 (the first air-cooled version). The data available are plots of output power versus frequency (see Fig. 10.19), but do not include plots of insertion phase versus frequency. It can be seen from Figure 10.19 that the output power varies as a function of frequency. This variation can be as much as 10% to as little as 1% for a 200-MHz deviation. This corresponds to range sidelobe level limitations of -26 dB (worst case, 10% power variation) to -46 dB (best case, 1% power variation).

TWT-Induced Phase Error

The TWT insertion phase data were derived from Figure 10.19. It is assumed that the output power variations are due to a principal reflection inside the TWT (in

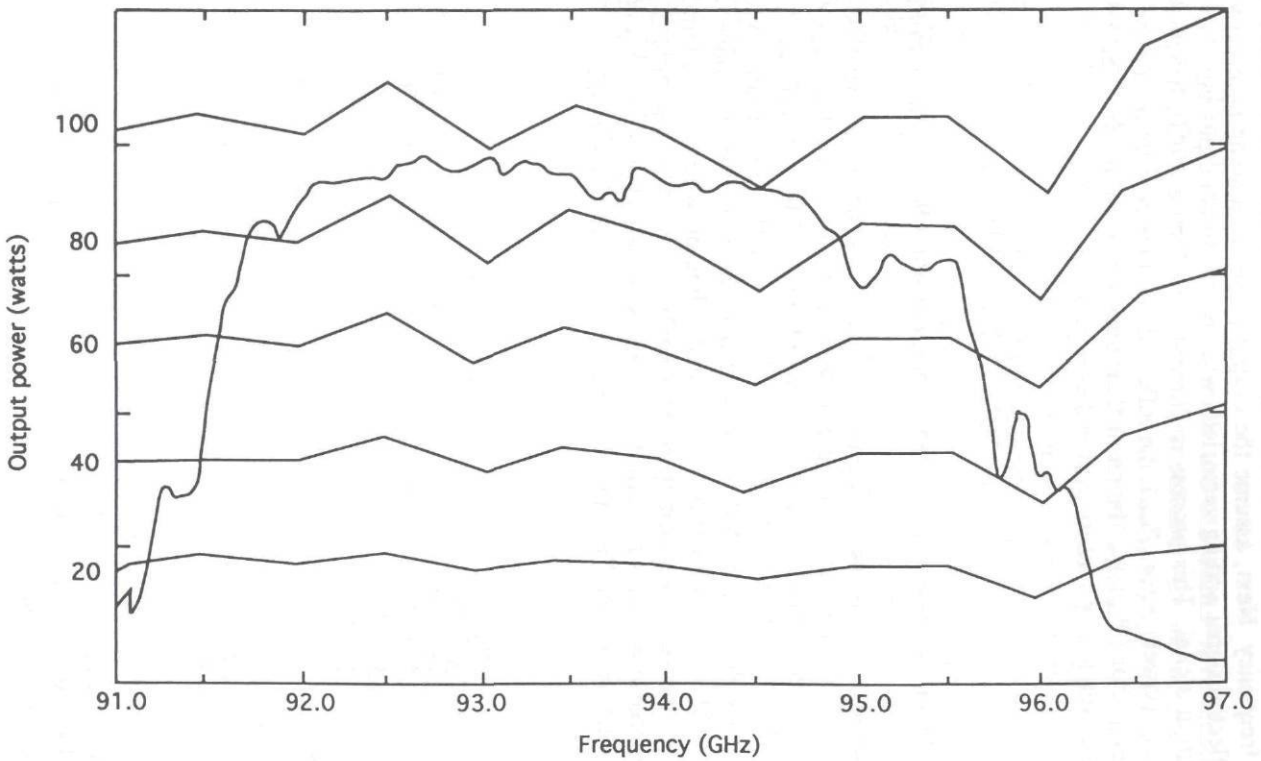

Figure 10.19 Plots of actual saturated power versus frequency for Hughes 982H TWT.

actuality, it is at the output of the device), and the phase of this reflected signal varies with frequency. Next, assume the output power is at some nominal value, with this reflected signal adding vectorially with the nominal output signal to form the total output signal. This process is illustrated in Figure 10.20, in which the nominal output power vector (P_{nom}), the reflected power vector (P_{ref}), and the total output power vector (P_{out}) are shown in their vectorial relationship. The relative insertion phase angle is ϕ and its peak value is given by:

$$\phi_{peak} = +/- \arctan(\text{Pref/Pnom}) \tag{10.14}$$

and occurs when P_{nom} and P_{ref} are at right angles to each other, as shown in Figure 10.20.

From data taken on the 982HA S/N 1 over the band of frequencies from 93 GHz to 95 GHz, the maximum peak power of 100W occurred at 94.5 GHz, and the minimum peak power of 83.6W occurred at 93.6 GHz. Therefore, $P_{nom} = (100 + 83.6)/2 = 91.8$W, and $P_{ref} = (100 - 83.6)/2 = 8.2$W. Substituting into the above equation yields $\phi_{peak} = 5$ deg, meaning that the TWT can introduce up to 5 deg of phase shift across a chirped pulse, depending on where in the band the chirp is placed. Because the output power variation can be as high as 10% and as low as 1% (approximate ratio of P_{ref} to P_{nom}), the nominal range of expected sidelobe levels due to the change in TWT insertion phase is -26 dB to -46 dB.

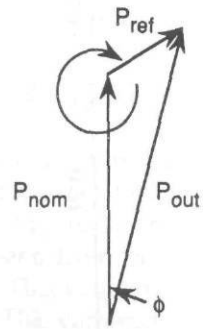

P_{ref} rotates and adds vectorially to P_{nom} to form P_{out}, the total output power. ϕ is thus the relative angular phase shift.

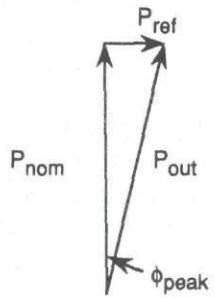

ϕ_{peak} occurs when P_{ref} and P_{nom} are at right angles to each other.

Figure 10.20 Vectorial relationship between foreword and reflected waves in a TWT.

VSWR-Induced Modulation Errors

Both phase and amplitude modulation errors are introduced by reflections due to antenna VSWR. These errors are especially troublesome at millimeter wavelengths where antenna VSWR is somewhat harder to control than at lower frequencies. The antenna VSWR for this application is approximately 1.7 to 1. The analysis is also different depending on whether an isolator is used at the output of the TWT. Figure 10.21 illustrates the principal reflections that occur in both cases. The case that includes the isolator is drawn with the isolator directly connected to the output of the TWT, with any additional waveguide runs being after the isolator to the antenna; the reasoning for this approach will be given in the section on VSWR-induced phase error. This connection scheme, however, affects the calculation of amplitude errors. The results of this analysis should show whether or not an isolator is necessary to keep antenna VSWR from degrading the pulse compression range sidelobes.

VSWR-Induced Phase Error

Under mismatched conditions, the amount of phase error across the pulse is a function of the chirp bandwidth. If Δf is the change in frequency that results in a phase shift of $\lambda/2$ (where λ is the wavelength), then Δf is given by [13]

$$\Delta f = (f\lambda_o^2)/(2S\lambda_g) \tag{10.15}$$

where λ_o is the mean operating wavelength, f is the mean operating frequency, S is the length between mismatches (length of waveguide run), and λ_o is the guide wavelength. At 95 GHz (f), λ_o is 0.3158 cm, and λ_g is given by:

$$\lambda_g = \lambda_o/\sqrt{(1 - (fc/f)^2)} \tag{10.16}$$

which calculates to 0.403 cm in this case (for a cutoff frequency, fc, of 59.01 GHz for WR-10 waveguide). Using S of 1 ft or 30.48 cm, Δf calculates to 386 MHz. The proposed chirp bandwidth is on the order of 200 MHz, so the results of this analysis may be conservative.

Reed [13] has developed equations and plots of the phase deviation versus VSWR for two equal or two unequal mismatches (in this case the TWT output VSWR equals the antenna VSWR), which can be used to estimate the phase deviation due to VSWR. Reed showed the phase deviation, ϕ, to be:

$$\phi = \pm \arctan [(Z - 1)^2/\sqrt{(8Z(Z^2 + 1))}] \tag{10.17}$$

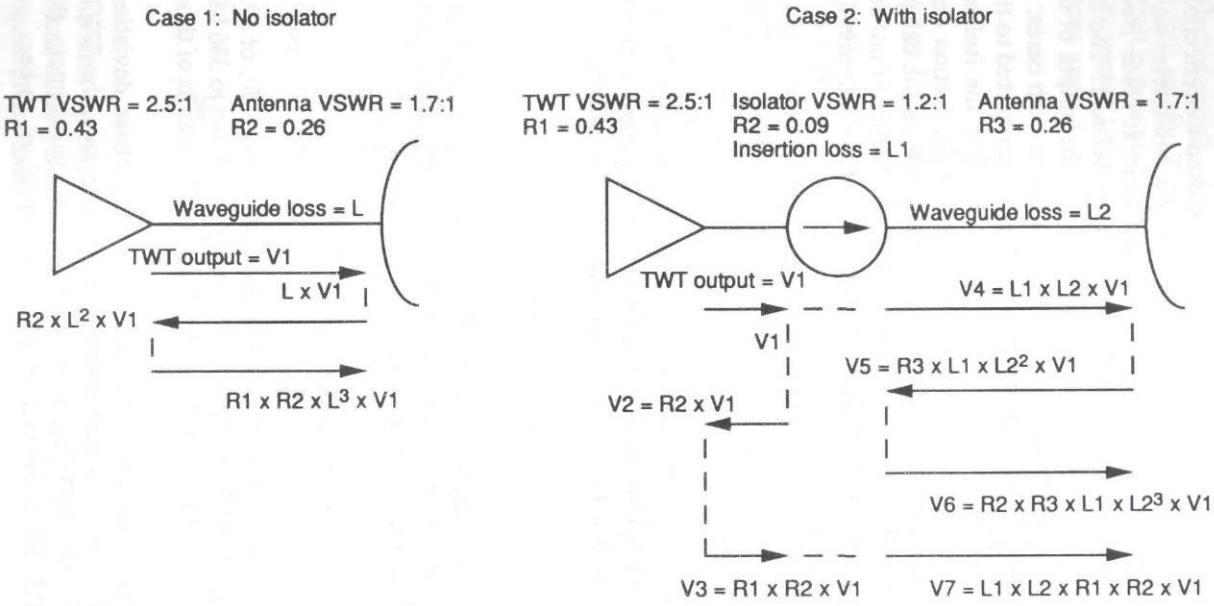

Figure 10.21 Wave reflections due to VSWR mismatches.

where Z is the VSWR and ϕ is the amount of phase shift due to the mismatch. We can used this equation to find the effects of TWT and interfacing components VSWR on phase.

From a technical report and as a result of work done by Hughes on the 982H TWT development program [14], a plot of input and output reflectances showed that the output reflectance averaged about 20% across the frequency band of interest, which corresponds to a VSWR of 2.5 to 1. For the case of no isolator, the source Z is 2.5 and the load Z is 1.7. Because Reed's equal VSWR case cannot be used directly to find ϕ, an assumption is made that the load and source Z can be transformed to be equal and equivalent to the operational scenario, in which case the equation can be used. The voltage reflection coefficient R_1 corresponding to a VSWR of 2.5 to 1 is 0.43, and R_2 is 0.26 for a VSWR of 1.7 to 1. Multiplying these reflection coefficients together results in an R_1 R_2 value of 0.1118. If the VSWRs were the same and hence the Rs were the same, then R_2 would equal 0.1118 and hence R would be 0.334, which corresponds to a VSWR of 2 to 1. Using $Z = 2$ in (10.17) yields $\phi = 6.4$ deg (0.1117 radians), which limits range sidelobe performance to -25 dB (without using an isolator).

If an isolator is used, then the problem can be broken up into two parts: one that takes into account the mismatch between the TWT and the isolator, and one that takes into account the mismatch between the isolator and the antenna. The equation for Δf has an S term in the denominator; therefore, making S small (short waveguide run) makes Δf large, which has the effect of decreasing the phase shift due to a mismatch. If the isolator is placed right on the output of the TWT, the phase shift due to the TWT-to-isolator interface will be virtually eliminated (in this case, for $S = 1$ cm, $\Delta f = 11.75$ GHz, the maximum phase shift for a 200-MHz chirp is about 0.2 deg, which corresponds to a limit of -55 dB on sidelobe performance). The primary mismatch is then between the isolator (VSWR of 1.2 to 1 nominal) and the antenna (VSWR of 1.7 to 1). For this case, ϕ is approximately 1.3 deg (0.0227 radians), which limits range sidelobe performance to -38.9 dB (using an isolator).

VSWR-Induced Amplitude Error

Referring to Figure 10.18, two separate cases must be analyzed to determine the effects of VSWR: one that includes the isolator and one that does not. In the subsequent discussions, it should be noted that signals, losses, and reflection coefficients are voltage terms, not power terms.

Without an isolator, the problem is fairly straightforward. If the output of the TWT is denoted as V_1, then the signal reaching the antenna is $L \times V_1$, where L is the insertion loss of the waveguide between the TWT and the antenna. The signal reflected from the antenna back to the TWT is $R_2 \times L^2 \times V_1$, where R_2 is

the reflection coefficient of the antenna. The signal reflected off of the TWT output and back out to the antenna is $R_1 \times R_2 \times L^3 \times V_1$, where R_1 is the reflection coefficient of the TWT output window. For 1 ft of waveguide, the insertion loss is about 1 dB (for a voltage loss L of 0.89). For R_1 of 0.43 (VSWR of 2.5 to 1) and R_2 of 0.26 (VSWR of 1.7 to 1), the error signal at the output is 0.0788, which corresponds to a range sidelobe level of 28 dB (without an isolator).

With the isolator in place, two major reflections need to be accounted for: one between the TWT and the isolator and the other between the isolator and the antenna. If V_1 is the output of the TWT, then the portion of this signal reaching the antenna is $V_4 = L_1 \times L_2 \times V_1$. The portion of this signal that reflects off of the antenna and reaches the circulator is $V_5 = R_3 \times L_1 \times L_2^2 \times V_1$. The portion of V_5 that reflects off of the circulator and reaches the antenna is given by $V_6 = R_2 \times R_3 \times L_1 \times L_2^3 \times V_1$. Assuming virtually no loss between the TWT and the isolator, the signal reflected off of the isolator and back to the TWT is $V_2 = R_2 \times V_1$. The signal reflected off of the TWT output back to the isolator is then $V_3 = R_1 \times R_2 \times V_1$. The portion of this signal that reaches the antenna is then given by $V_7 = L_1 \times L_2 \times R_1 \times R_2 \times V_1$. Therefore, the total error signal that reaches the antenna is $V_6 + V_7 = V_1 \times L_1 \times L_2 \times R_2 \times (L_2^2 \times R_3 + R_1)$. For the values of the various reflection coefficients and losses as given in Table 10.5, the error signal calculates to 0.0492, which corresponds to a range sidelobe level of -32.2 dB.

Summary of Transmitter-Induced Modulation Errors

Table 10.6 summarizes the transmitter-induced modulation errors discussed in the preceding sections.

The above individual error components must be combined to estimate the total overall range sidelobe level. Unless something is known about the modulation frequency of the individual error signals, the individual error sources should be combined in the worst case scenario; that is, all PSLs adding in time and in phase.

Table 10.5
Values of Reflection Coefficients and Insertion Losses for Calculation of VSWR Effects

Parameter	*Description*	*Value*
R_1	TWT output reflection coefficient (VSWR = 2.5:1)	0.43
R_2	Isolator reflection coefficient (VSWR = 1.2:1)	0.09
R_3	Antenna reflection coefficient (VSWR = 1.7:1)	0.26
L_1	Isolator insertion loss (0.3-dB power loss)	0.966
L_2	Waveguide insertion loss (1-dB power loss for 1 ft)	0.89

However, additional detail can be deduced for the VSWR amplitude error; namely, its period and hence its frequency. The period will be on the order of several nanoseconds (the time it takes for the signal to reflect off of the antenna, then off of the isolator, and back out to the antenna). This corresponds to a modulation frequency of about 500 MHz (this estimate does not even have to be that close, as will be seen). From paired-echo theory [3, 15], the time separation Δt between the main signal and a time sidelobe resulting from an error modulation of frequency f_m is given by:

$$\Delta t = f_m \times T \times t \tag{10.18}$$

where T is the uncompressed pulse width and t is the compressed pulse width. If T is 10 μs, the time separation between the main signal and the signal resulting from VSWR amplitude error is more than 1,000 compressed pulse widths, which is extremely far away from the main signal. It is therefore assumed that this error source will not add in time with the other error sources (for which a similar analysis is not practical). Table 10.7 summarizes the individual cases (best and worst case TWT characteristics with and without an isolator). In reality, the remaining errors may not add in this worst case manner, so that the total sidelobe level performance predictions in Table 10.7 can be considered worst case numbers.

As can be seen from Table 10.7, under only one case is the peak range sidelobe level below 30 dB, which is a typical design goal. This is the case for which an isolator is used and the chirp is strategically placed within the passband of the TWT characteristic. However, because the numbers in Table 10.7 are only estimates, some form of range sidelobe correction should be incorporated into the design. Error correction will be discussed in the next section.

Table 10.6
Summary of Individual Transmitter-Induced Modulation Errors

Source of Error	*Type of Error*	*Sidelobe Level Limitation*
HVPS	Phase	−47 dB
TWT	Phase	−26 dB (worst case)
TWT	Phase	−46 dB (best case)
TWT	Amplitude	−26 dB (worst case)
TWT	Amplitude	−46 dB (best case)
VSWR	Phase	−38.9 dB (with isolator)
VSWR	Phase	−25 dB (without isolator)
VSWR	Amplitude	−32.2 dB (with isolator)
VSWR	Amplitude	−28 dB (without isolator)

Table 10.7
Summary of Range Sidelobe Performance Due to Transmitter Modulation Errors

Scenario	*Total Peak Range Sidelobe Level*
Best case TWT phase and amplitude, no isolator	−23.0 dB
Best case TWT phase and amplitude, with isolator	−31.8 dB
Worst case TWT phase and amplitude, no isolator	−15.9 dB
Worst case TWT phase and amplitude, with isolator	−18.7 dB

Correction Techniques for Range Sidelobe Suppression

The goal for the range sidelobe level is −30 dB; because the best case value from Table 10.7 is −31.8 dB, some form of correction may be required or desirable. According to Cook and Bernfield [15], when the path delay through the high-power chain (in this case the TWT, isolator, waveguide, and cross-guide coupler) is small compared to the period of the highest frequency component to be corrected, then intrapulse error correction is feasible. In this design, the delay through the TWT is approximately 1.4 ns, so the delay through the entire path will be estimated at 3 ns. A period of 3 ns corresponds to a frequency of 333 MHz. This should be high compared with HVPS- and TWT-induced errors, but will not be higher than VSWR-induced amplitude errors because the period of those errors is also a function of the path delay (distance between reflection points). From Table 10.6, it can be seen that the VSWR-induced errors, particularly the amplitude error, is the single worst source of errors in the transmitter. Because closed-loop correction will not alleviate the problem, some other correction scheme needs to be considered.

A more comprehensive correction scheme would consist of measuring the distortion signal, storing the information as a calibration, and predistorting the signal in the waveform generator to compensate for the errors. This scheme can correct for errors that occur in the entire signal generator and high power transmitter signal path, not only the transmitter errors discussed in this section. The implementation of this technique can become cumbersome if unlimited frequency diversity is allowed; therefore, only a limited number of distinct center frequencies (perhaps five) should be considered for such a correction scheme. This limits the number of possible calibration points that must be measured and stored. It also allows for proper placement of the chirp waveform within well-behaved sections of the TWT gain characteristic, which minimizes TWT-induced errors. This type of capability can be designed into the radar, but does not have to be exercised if

the system sidelobe level is sufficient at a particular center frequency and operating bandwidth.

10.5.2 Surface Acoustic Wave Device Errors

When selecting or specifying SAW devices for passive generation or matched filtering of pulse compression waveforms, the radar designer should be aware of the types of errors that can be introduced. Things to consider in SAW pulse compression filters, which potentially contribute to performance limits, include impedance matching and VSWR errors, amplitude and phase errors due to surface wave device reflections, temperature effects, and device orientation and other mechanical effects.

Impedance matching the SAW filter is almost always desirable because the device input and output transducers are not matched to 50 ohms or other standard impedance. Therefore, matching networks are usually employed to match the transducers nominal characteristic impedance to that of adjacent components. Although the impedance matching network may be provided by the manufacturer, care should be taken to ensure that the matching network does not limit the device bandwidth or introduce unwanted amplitude and phase distortions. Once the device has been nominally matched (to some VSWR) over the operating bandwidth, then (10.17) and the techniques described above for transmitter-VSWR-induced errors may be used to estimate phase errors. Similarly, the amplitude reflection technique can be used to estimate VSWR-related amplitude errors.

Amplitude and phase errors due to surface wave reflections are always present in SAW devices, to some degree, but are usually beyond the radar designer's control. Nevertheless, it is worthwhile to recognize these errors will exist and, in some cases, make plans for corrections. The basic mechanism for these errors are reflections that occur at each of the interdigital fingers on the SAW device. These reflections cause a fraction of the surface wave energy not to be transferred to the electrical load, as designed, and consequently, the waveform is distorted. The reflections can also cause phase errors by combination of the reflected waves with the forward traveling surface wave. More surface wave energy or signal level is lost to reflections as the surface wave travels longer distances across a surface wave transducer. Consequently, the output waveform response will typically fall off in amplitude (in time), corresponding to the distance the surface wave has traveled over the coded transducer.

This gradual amplitude falloff (often several decibels) can be corrected by external filters that weight the filter amplitude versus time or frequency (or both) or by iteration of the SAW device design. The latter empirical approach is often taken, but at considerable cost because the entire device must be refabricated.

Fortunately, phase errors caused by reflections are usually less severe, and to some degree, those errors are randomized by the multiple interdigital finger reflections. Often, if the gross amplitude errors (falloff) are corrected, sidelobe levels of at least 30 dB can be obtained with SAW device pulse compression systems. If sidelobe levels much below this are required, techniques to reduce reflections or correct for the effects of the reflections (or both) must be taken. Reducing reflections in the devices themselves involves materials and processing techniques that reduce or cancel reflections at the interdigital fingers (these techniques are left to the SAW device designers). If digital pulse compression techniques are used in combination with SAW device expanded pulse generation, external corrections can sometimes be made by measuring the phase and amplitude of the SAW device and applying digital corrections to the phase and amplitude.

Temperature also effects the performance of SAW devices, because both the surface wave velocity and the piezoelectric substrate size changes with temperature. The effect is to change the phase or delay of the waveform. One material, called ST Quartz (which refers to a particular orientation of the material), is often used for SAW devices because it has a zero temperature coefficient near room temperature. The main effect of delay change with temperature can be approximated by a quadratic equation, and several authors [12] report the temperature coefficient of delay for ST Quartz as:

$$\Delta t/t = -3.13 \times 10^{-8} \Delta T^2$$

where $\Delta t/t$ is the relative change in delay and ΔT is the change in temperature (from room temperature). Knowing the temperature change, this relation can be used to estimate the amount of time shift in SAW device waveform due to temperature. Compensation or correction for temperature effects may necessitate putting the SAW device and associated components in a thermalcontrolled environment. Small heater devices are often mounted near the SAW device to maintain the device temperature more nearly constant as the surrounding temperature changes.

Other mechanical effects can also affect the performance of SAW device pulse compression systems by causing certain errors. These mechanical effects include orientation of the surface wave piezoelectric crystal with respect to the metalized transducers and stress or vibration of the SAW device. In general, SAW device designers and manufacturers will design and orient the SAW transducers on materials in such a way that the effects of orientation are minimized; these effects are further described in reference [12]. Stress of the surface wave crystal material also must largely be taken care of by the designer or manufacturer, and this usually consists of mounting the device on some material to absorb some of the stress and thermal expansion or compression of the mounting base. It is important, however, that the radar designer place the SAW filters in an environment

that will minimize stress and vibration. Vibration can cause the effective carrier frequency to be modulated, much like the effects of phase noise and therefore limit the performance of the SAW device filter.

REFERENCES

[1] North, D. O., "An Analysis of the Factors Which Determine Signal/Noise Discrimination in Pulsed-Carrier Systems," RCA Laboratories Tech. Report PTR-6C, June 25, 1943, reprinted in *Proc. IEEE* Vol. 51, No. 7, July 1983, pp. 1016–1027.

[2] Skolnik, M. I., *Introduction to Radar Systems*, Second Edition, Chapters 10 and 11, New York: McGraw Hill, 1980.

[3] Klauder, J. R., A. C. Price, S. Darlington, and W. L. Albersheim, "The Theory and Design of Chirp Radars," *Bell System Technical J.*, Vol. 39, July 1960, pp. 745–808.

[4] Currie, N. C., *Radar Reflectivity Measurement Measurement: Techniques and Applications*, Chapter 10, Norwood, MA: Artech House, 1989.

[5] Skolnik, M. I. (Ed.), *Radar Handbook*, Chapter 10, "Pulse-Compression Radar," by E. C. Farnett and G. H. Stevens, Second Edition, New York: McGraw Hill, 1990, Fig. 10.17.

[6] Eaves, J. L., and E. K. Reedy, *Principles of Modern Radar*, Chapter 15, New York: Van Nostrand Reinhold Company, 1987.

[7] Lewis, B. L., F. F. Kretschmer Jr., and W. W. Shelton, *Aspects of Radar Signal Processing*, Chapters 1 and 2, Norwood, MA: Artech House, 1986.

[8] Wheeler, H. A., "The Interpretation of Amplitude and Phase Distortion in Terms of Paired Echoes," *Proc. IRE*, Vol. 27, June 1939, pp. 359–385.

[9] Burrow, C. R., "Discussion on Paired Echo Error Analysis," *Proc. IRE*, Vol. 27, June 1939, pp. 384.

[10] Woodward, P. M., *Probability and Information Theory, with Applications to Radar*, New York: McGraw Hill, 1953.

[11] Wehner, D. R., *High Resolution Radar*, Chapter 4, Norwood, MA: Artech House, 1987.

[12] Matthews, H., (editor), *Surface Wave Filters*, Chapter 7, "Phase Code Generators and Correlators," by D. T. Bell and L. T. Claiborne, New York: John Wiley and Sons, 1977.

[13] Reed, J., "Long Line Effects in Pulse Compression Radar," *Microwave Journal*, Vol. 4, 1961.

[14] Davis, J. A., "3.2 Millimeter Wave Transmitter Tube," ERADCOM Report No. DELET-TR-78-3015-F, February, 1983.

[15] Cook, C. E., and M. Bernfeld, *Effect of Distortion in Matched Filter Signals; An Introductions to Theory and Application*, Academic Press, 1967, pp 366–412.

Chapter 11
Stepped-Frequency and ISAR Imaging Systems

Teddy L. Lane
Georgia Institute of Technology

11.1 INTRODUCTION

Over the past few years the applications for imaging or multidimensional high-resolution radar systems have expanded greatly. This has been primarily due to the improvements in both the waveform generation and the signal processing needed to support the radar imaging technology. Applications of radar imaging include (1) diagnostic methods for determining and modifying target signatures, (2) development of target detection, discrimination, recognition, and classification techniques, (3) improvements in radar target detectability, and (4) diagnostic methods to support the physical and medical sciences.

In this chapter a technique for developing *two dimensional* (2D) radar images is described, along with the major factors both internal to the radar system and external that limit the theoretical performance. The imaging technique involves the combination of two high-resolution processes: (1) development of a *high-range resolution* (HRR) profile in slant range, using a discrete frequency-coded waveform (stepped-frequency waveform), and (2) the development of a high-resolution profile in crossrange using an *inverse synthetic aperture radar* (ISAR) technique.

The following sections of this chapter provide an overview of the theory associated with the two high-resolution processes and will discuss the important contaminating effects that degrade the resolution and image quality. The effects of several of the contaminants on resolution and image quality are shown through simulations throughout the chapter.

11.2 STEPPED-FREQUENCY WAVEFORM

There are several ways to achieve HRR, such as *frequency-modulated CW* (FMCW), short pulse, linear frequency-modulated (LFM) pulse compression, and *stepped-frequency waveform* (SFWF) (pulse-to-pulse, discrete frequency coding) pulse compression. Each of these processes has limitations, depending on the particular application; the range resolution in all cases, however, is determined by the total radar bandwidth; that is:

$$\Delta R = K\left(\frac{c}{2B}\right) \tag{11.1}$$

where:

ΔR = the range resolution along the radar-target line of sight LOS,
K = a constant determined by signal processing effects and is equal to or greater than unity,
c = the propagation velocity, and
B = the total radar bandwidth.

Because of the technology and the flexibility associated with the SFWF, many systems are using this process to achieve high- and ultra-high-range resolution. Using this waveform, instrumentation systems have been developed that provide range resolution on the order of a few centimeters, and operational systems with tens of centimeters of range resolution are under development. Other HRR waveforms cannot typically provide comparable resolution performance because of technology limitations dealing with requirements for high data conversion rates or high system linearity.

An example of a SFWF pulse train is shown in Figure 11.1. As shown, the SFWF consists of a sequence of pulses (wave packet) transmitted with fixed, uniform, pulse-to-pulse frequency change. Each pulse within the packet is relatively wide (i.e., narrow instantaneous bandwidth), and the total radar bandwidth is determined by the frequency step size (ΔF) and the number of frequency steps within the packet (N). Thus, the resulting radar bandwidth is $N \times \Delta F$, and the resulting range resolution after processing is:

$$\Delta R = K\left(\frac{c}{2N\Delta F}\right) \tag{11.2}$$

For example, the uncompressed pulse width may be on the order of hundreds

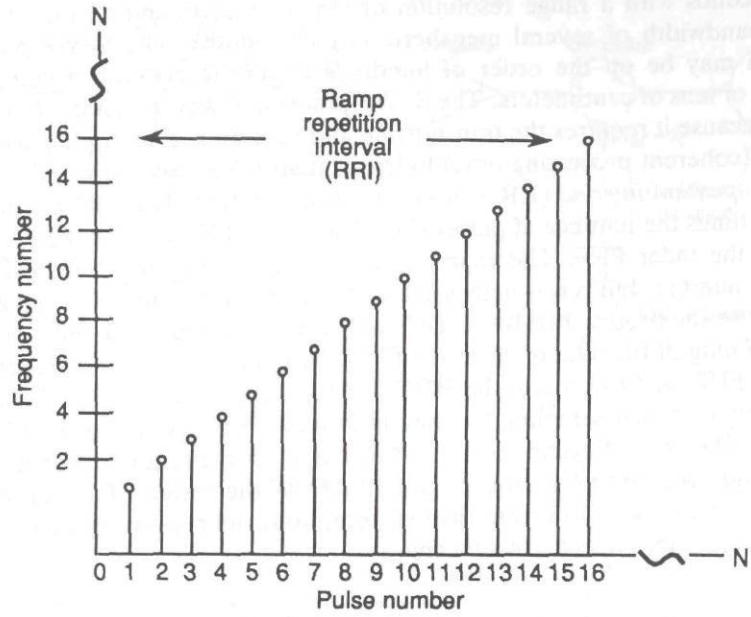

(a) Complete waveform packet

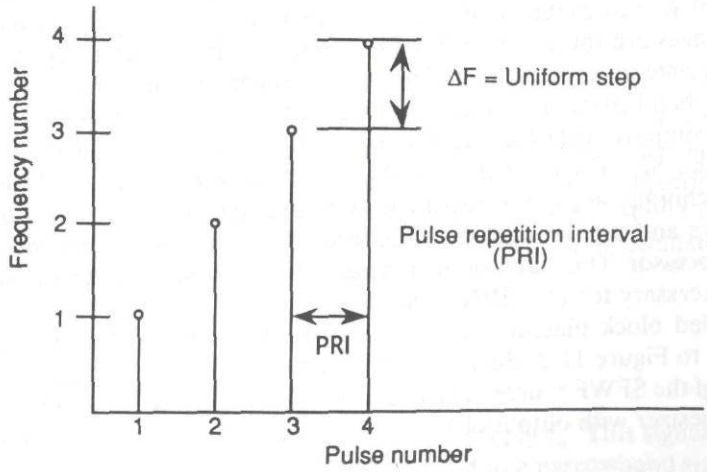

(b) Relationship between frequency and pulse numbers.

Figure 11.1 Stepped-frequency waveform showing relationship between PRI, ΔF, and RRI.

of nanoseconds with a range resolution of tens of meters and an instantaneous receiver bandwidth of several megahertz (1/pulse width). The SFWF-processed bandwidth may be on the order of hundreds of megahertz with a compressed resolution of tens of centimeters. The SFWF process, however, is not a single-look process, because it requires the transmission and reception of multiple pulses. The total time (coherent processing time) to transmit an HRR waveform is denoted as the *ramp repetition interval* (RRI) shown in Figure 11.1(a). The RRI is simply the radar PRI times the number of pulses (i.e., RRI = $N \cdot$PRI), where the PRI is the inverse of the radar PRF. The example shown is for a 16-pulse wave packet. N can be any number, but it is usually selected to be an integer power of 2 (i.e., 128, 256), because the process involves a DFT of the data. If N is not an integer power of 2, zero filling of the data input to the DFT is accomplished, and in general, the size of the FFT used to process the HRR is double the data size (i.e., $N_{fft} > 2N$). This technique of over sampling the data improves the resolution of the FFT (not the HRR). The actual determination of N is based on the required step size (ΔF) and the total processing bandwidth ($B = N\Delta F$) of the system. For many applications, the time required for transmission, reception, and processing the waveform is a major limitation in using this technique.

11.2.1 SFWF Radar Configuration

The hardware implementation of the SFWF involves a fairly simple change to a typical coherent pulsed radar discussed in the section on short pulse waveform. The major changes are the addition of a fast, coherent, frequency stepped source with the appropriate up-conversion and down conversion circuitry and the requirement for a wideband front end (transmitter and receiver). The latter requirement is necessary to support all HRR waveforms regardless of the technique. A major advantage of the SFWF over both the short pulse and the typical LFM pulse compression technique lies in the narrowband processing, which greatly simplifies the data capture and provides a high SNR through a narrowband matched filter receiver and processor. The major disadvantage lies in the time required to generate the N pulses necessary for the HRR processing.

A simplified block diagram of a coherent SFWF radar is shown in Figure 11.2. Referring to Figure 11.2, the major change from a simple short pulse system is the addition of the SFWF source. The heart of the system is the coherent stepped-frequency synthesizer with output of f_{syn}, where f_{syn} is stepped at the PRF rate and is given by:

$$f_{syn_i} = f_0 + i\Delta F \tag{11.3}$$

where $i = 0, N - 1$.

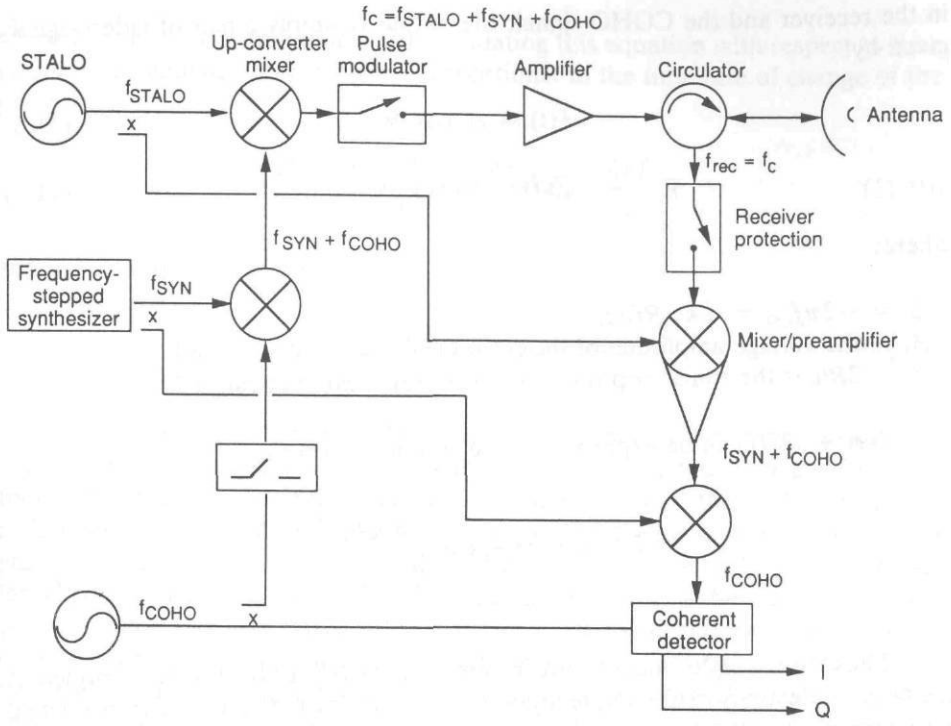

Figure 11.2 Simplified block diagram of an SFWF radar.

The output of the synthesizer provides an LO drive to the second mixer in the receiver and is also mixed with a sample of the fixed frequency coherent oscillator (f_{coho}). Following this up conversion, the signal is up-converted to the final transmitted frequency by mixing with a sample of the stable local oscillator (f_{stalo}). The final output frequency f_c is the sum of the three oscillators; two fixed frequencies and one stepped given by:

$$f_{c_i} = f_{coho} + f_{stalo} + f_{syn_i} \tag{11.4}$$

On receive, the input signal frequency is simply f_{c_i}. This signal is first mixed with the fixed STALO and then down-converted to a narrowband signal by mixing with a sample of the synthesizer. The final stage in the process is coherent detection. This is usually accomplished through an I/Q detector (alternatively, direct sampling may be feasible) providing both amplitude and phase (complex data) to the processor. The signals into the I/Q detector are the IF output from the second mixer

in the receiver and the COHO signal; the output is simply a pair of video signals given by:

$$I_i(t) = A_i \cos \Phi_i \tag{11.5}$$

$$Q_i(t) = A_i \sin \Phi_i \tag{11.6}$$

where:

$\phi_i = -2\pi f_{c_i} t_0 = -4\pi R f_{c_i}/c$,
A_i = the voltage amplitude of the ith return, $i = 0, N-1$, and
$t_0 = 2R/c$ is the round-trip time to a scatterer located at range R.

$I_i(t) + Q_i(t)$ can be expressed in the complex form as:

$$\begin{aligned} I_i + jQ_i &= A_i \exp\left[j\left(\frac{4\pi R f_{c_i}}{c}\right)\right] \\ &= A_i e^{j\Phi_i} \end{aligned} \tag{11.7}$$

Thus, the sampled quadrature mixer outputs (I/Q) are discrete samples of the target reflectivity in the frequency domain. This information is then transformed into a series of range-delay reflectivity values through the inverse DFT to form the range (time) domain HRR profile:

$$\text{IDFT} = H_l = \frac{1}{N}\sum_{i=0}^{N-1} [A_i e^{j\Phi_i}]\left[\exp\left(j\,\frac{2\pi l i}{N}\right)\right] \qquad 0 \le l \le N-1 \tag{11.8}$$

11.2.2 Stepped-Frequency HRR Process

As described in the above paragraphs, the SFWF technique obtains high-range resolution information by generating a phase shift by means of a change in frequency of the transmitting radar. This phase shift is a function of the frequency step size and the range to the target. The resultant information is processed to create a corresponding time-delay profile (HRR profile) of the frequency domain response of the target return. Examining this process more closely, for a single scatterer at range R, the phase response, Φ, in radians is given by:

$$\Phi = 2\pi\left(\frac{2R}{\lambda}\right) = 2\pi\left(\frac{2Rf_c}{c}\right) \tag{11.9}$$

where f_c is the carrier frequency. Differentiating this equation with respect to time results in a frequency shift, which is proportional to the time rate of change of the phase:

$$\frac{d\Phi}{dt} = \frac{4\pi}{c}\frac{d(Rf_c)}{dt} = \frac{4\pi R}{c}\dot{f}_c + \frac{4\pi f_c}{c}\dot{R} \tag{11.10}$$

and the total frequency shift, f_t, is:

$$f_t = \frac{1}{2\pi}\frac{d\Phi}{dt} = \frac{2R}{c}\dot{f}_c + \frac{2f_c}{c}\dot{R} \tag{11.11}$$

It is important to note that the resulting frequency shift consists of two components: the first term due to the phase change associated with changing the transmitted frequency and the range to the scatterer (Note: this is the CHANGE in frequency and NOT the carrier frequency), and the second term due to the phase change associated with a change in range between the radar and the target for a fixed carrier frequency. This latter frequency shift is the classical doppler frequency shift due to relative velocity between the radar and the target and will be denoted as f_d. The frequency shift described by the first component is due to the SFWF and will be referred to as the *induced phase shift* (IPS) frequency and will be denoted as f_{ips}. As an example, if the range to the target is 3 km and the change in frequency is 10 MHz, the frequency shift due to the first term is 200 Hz, regardless of the carrier frequency or the velocity. The second term contribution depends on the carrier frequency and the closing velocity between the radar and the target. For a 10 GHz carrier frequency and a closing velocity of 100 m/s, the second term yields a doppler shift of 6.67 kHz. As discussed later, contributions from this second term will corrupt the HRR profile and must be compensated for in the processing.

If the relative velocity between the target and the radar is negligible (or is removed in the processing) and the frequency f_c is changed by ΔF, the expression can be approximated by:

$$f_t = f_{\text{ips}} = \frac{2R}{c}\frac{\Delta F}{\Delta t} = \frac{2R}{c}\cdot \text{PRF}\cdot \Delta F \tag{11.12}$$

where the rate of change $(1/\Delta t)$ is the radar PRF. The HRR data are generated using fixed, known frequency steps to produce a known phase change on a pulse-to-pulse basis. This phase change may be considered a synthetic doppler, resulting in scatterer response in the frequency domain. Thus, high-range resolution that is inversely proportional to the processed bandwidth is achieved by sampling the

amplitude and phase (or alternatively, the in-phase and quadrature-phase components) of the wide pulse echoes and processing the frequency domain data into time (range) information through a DFT.

To graphically show the effects of varying the waveform parameters and the various contaminants, a computer simulation was developed using MATLAB. Numerous image examples are provided throughout this chapter that simulate the amplitude response (in decibels) of single and multiple scatterers in range and crossrange (FFT bin location) using the SFWF and ISAR processing. In the examples, the scatterer RCS in square meters and location in meters are indicated in the figure captions. Table 11.1 lists the major waveform parameters used in the examples unless noted differently in the figure caption.

Table 11.1
Simulation Parameters

Parameter	*Value*
N (number of pulses)	64
FFT size	$2N = 128$
ΔF (frequency step size)	10 MHz
PRF (pulse-to-pulse)	10 kHz
SNR (single pulse)	40 dB
Window (weighting)	Hamming

Examples of HRR profiles generated using a computer simulation of the SFWF are shown in Figure 11.3(a–c). The HRR profiles simulated in Figure 11.3 are for three scatterers with varying RCS and range separation, as indicated in the figure captions. With a waveform of 64 pulses at 10 MHz/step, the total bandwidth is 640 MHz or approximately 0.34m range resolution with processing losses (for Hamming, $K = 1.33$). As noted in Figure 11.3(a), the 1 m^2 scatterer is not resolvable with a range separation of 0.1m. Increasing the separation to 0.34m, as shown in Figure 11.3 (b), indicates the presence of another close-in scatterer, and increasing the RCS of the third scatterer to 10 m^2, as in Figure 11.3(c), the two are resolvable. The latter is shown as an example of the definition of minimum range resolution: the ability to resolve two scatterers of equal RCS with a null separation of 3 dB.

11.2.3 Range Ambiguities in SFWF

Because the HRR profile is generated through an induced phase shift, there will exist ambiguous frequencies, depending on the range to the target. The frequency responses will always lie between 0 Hz and the radar PRF (i.e., will "fold over").

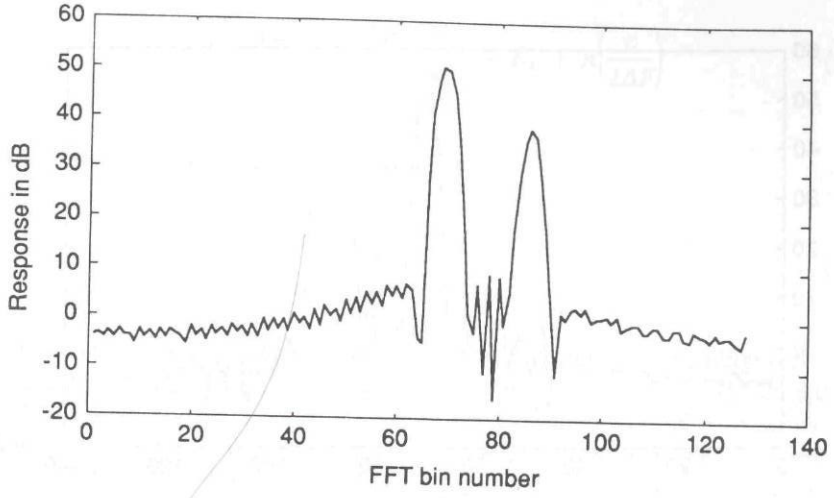

Figure 11.3(a) Example of HRR profile for three scatterers demonstrating SFWF range resolution. Scatterers are located at 908m (100 m^2), 910m (10 m^2), and 910.1m (1 m^2). Scatterers two and three are not resolved due to bandwidth.

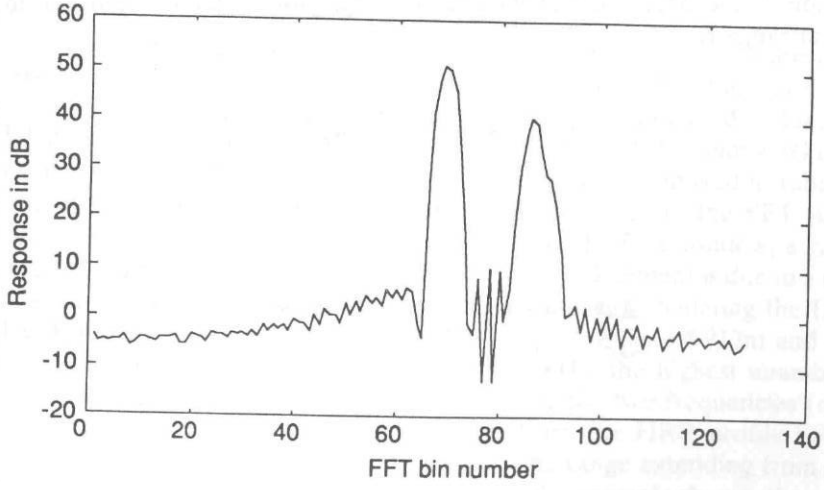

Figure 11.3(b) HRR profile for three scatterers demonstrating SFWF range resolution. Scatterers are located at 908m (100 m^2), 910m (10 m^2), and 910.34m (1 m^2). Scatterer three is barely "resolvable," because of bandwidth and RCS values.

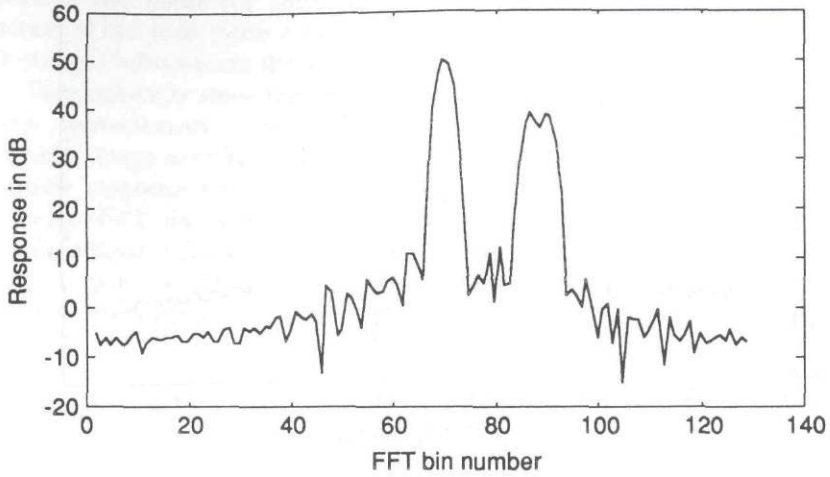

Figure 11.3(c) HRR profile for three scatterers demonstrating SFWF range resolution. Scatterers are located at 908m (100 m^2), 910m (10 m^2), and 910.34m (10 m^2).

The unambiguous range associated with the SFWF process can be determined by examination of the phase (ϕ_i) of the received echo for frequency step i from a scatterer at range R_o:

$$\Phi_i = 2\pi f_{c_i} t_o = \frac{4\pi}{c} f_{c_i} R_o \tag{11.13}$$

then:

$$\frac{\Delta\Phi}{\Delta F} = \frac{4\pi[f_{c_{i+1}} - f_{c_i}]}{[f_{c_{i+1}} - f_{c_i}]} \frac{R_o}{c} = \frac{4\pi R_o}{c} \tag{11.14}$$

or:

$$R_o = \frac{\Delta\Phi}{\Delta F}\left(\frac{c}{4\pi}\right) \tag{11.15}$$

Ambiguities will exist for $\Delta\Phi = \Delta\Phi + n2\pi$; that is:

$$R = \frac{(\Delta\Phi + n2\pi)}{\Delta F}\left(\frac{c}{4\pi}\right) = R_o + n\left(\frac{c}{2\Delta F}\right) \tag{11.16}$$

and the unambiguous range, R_u, is given by:

$$R_u = \frac{c}{2\Delta F} \tag{11.17}$$

For the case of the doppler radar, the ability to measure unambiguous velocity is limited by the PRF; that is, for a 100 kHz PRF, dopplers of 10 kHz, 110 kHz, and 210 kHz all show up as 10 kHz measured doppler (doppler = $2Fv/c$). In a similar fashion, the SFWF is ambiguous in range, limited by the frequency step size. For a ΔF of 10 MHz (R_u = 15m), a scatterer (target) located at 1,210m will appear at the same location in the FFT window as a target located at 10m, 25m, 40m, and so forth. Therefore, the range to individual scatterers is not available in the processed HRR profiles, only relative range position of the scatters contained in the received pulse. The range to the individual scatterers that make up the target is determined by range gating on the target (time-delay measurement). Once the target is under range track, the location in range of the individual scatterers is determined from the composite accuracies of the range measurement to the first scatterer location and the processed HRR profile.

An example of the ambiguous range windowing is shown in Figure 11.4 for the three scatterers in the previous simulation. In Figure 11.4(a) the scatterers are located in range such that the proper range alignment is maintained and scatterers are in the same ambiguous window, where n = 60 in (11.16) (window 60 extends from 900m to 915m). In Figure 11.16(b) the scatterers have moved in range such that the last scatterer now appears as the "first" scatterer in the FFT (the last scatterer has "wrapped" around and is misaligned in the FFT window; a range of 916m has the same FFT bin location as 901m). This misalignment is due to a change in the scatterer IPS associated with the change in range. Calculating the IPS frequency from (11.12) will give values of 608 kHz for a range of 912m and 610.67 kHz for a range of 916m. Because the PRF is 10 kHz, the highest unambiguous frequency shift that can be measured is 10 kHz and the two frequencies (ranges) are aliased as 8 kHz and 670 Hz, respectively. Thus, the HRR profile FFT bins are associated with a frequency shift and range, the range extending from 0 to $c/2\Delta F$ and the IPS frequency from 0 to the PRF. For the example shown, the number of FFT bins is $2N$, where N is the number of pulses. Thus, the FFT resolution is $1/2N$ or 78 Hz for the PRF of 10 kHz and 0.117m for an R_u of 15m. The actual resolvable frequency and range are both proportional to $1/N$, where N is the number of pulses (156 Hz and 0.23m, respectively; prior to processing losses).

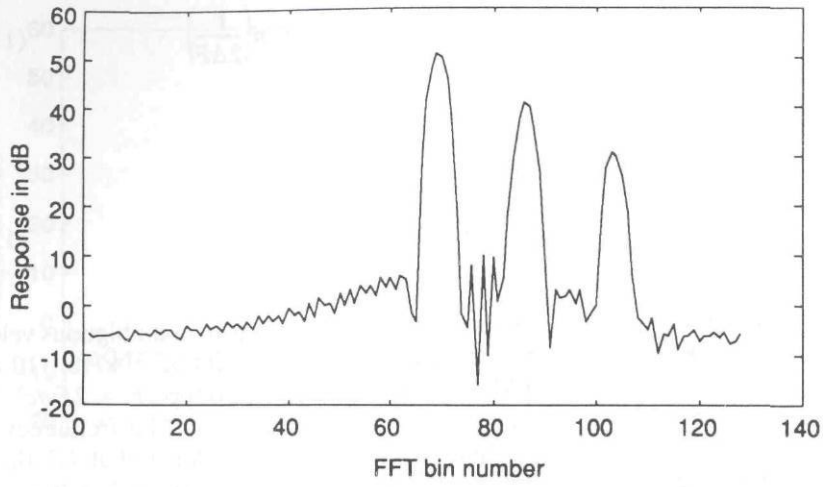

Figure 11.4(a) HRR profile for three scatterers demonstrating SFWF range ambiguity. Scatterers are located at 908m (100 m^2), 910m (10 m^2), and 912m (1 m^2).

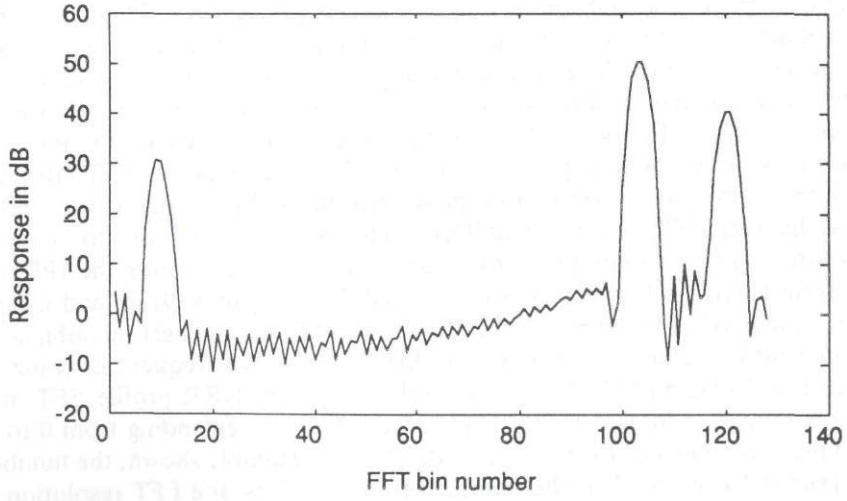

Figure 11.4(b) Example of HRR profile for three scatterers demonstrating SFWF range ambiguity. Scatterers are located at 912m (100 m^2), 914m (10 m^2), and 916m (1 m^2). The scatterer located at 916m is aliased and appears in the FFT bin corresponding to 901m.

11.2.4 Selection of ΔF

The frequency step size is a major parameter in the SFWF, because it determines the ambiguous range window and the number of pulses required to generate the HRR ($B = N\Delta F$), and it is a major factor in determining the RRI ($N \cdot$PRI). In many applications the frequency step size recommended is approximately equal to one-half the inverse of the pulse width. In an air-to-air application (or in any application where there are no contributing scatterers located outside of the target dimensions, such as an indoor anechoic chamber) the requirement for selecting the frequency step size is determined by the target maximum extent in range. If we denote the target maximum extent as E, then the maximum ΔF permitted is simply that change necessary to cause a 180-deg phase change over the length E. This is given by:

$$\Delta\Phi = 2\pi\left(\frac{E\Delta F}{c}\right) \leq \pi \tag{11.18}$$

or:

$$\Delta F \leq \frac{c}{2E} \tag{11.19}$$

For a 10m target, the frequency step must not exceed 15 MHz. If exceeded, the HRR profile will alias. Because the range resolution is determined by the total bandwidth, the frequency step size is usually selected to be as large as permitted (without aliasing) to minimize the number of steps (N). As E increases (longer targets), the maximum step size allowable decreases, resulting in an increase in the number of frequency steps required to maintain the same range resolution.

Additionally, the pulse width must be large enough to encompass the target extent: $\tau \geq 2E/c$. Thus:

$$\Delta F \leq \frac{1}{\tau} \tag{11.20}$$

If the target is "isolated," the pulse width can be much greater than the target and the frequency step size is selected using (11.19). For example, for a 10m target, a ΔF of 15 MHz can be used, but τ can be greater than 67 ns, say 500 ns. This flexibility for selecting the step size and pulse width allows the use of a more narrow receiver bandwidth, improving the SNR achievable. This flexibility, however, is not always an option. In most cases, the relationship between the frequency step size and the pulse width is more restricted.

With a ΔF of 15 MHz, the FFT window is also 10m, and therefore, the target will completely "fill" the FFT window. In most cases, this is not a desirable situation because it will, in general, not be possible without additional processing to separate the "front" from the "rear" of the target when aliasing occurs. Even for the ideal isolated target case, it is usually advisable to select the frequency step size such that $\Delta F < c/2E$.

If, however, the target scenario contains surrounding "targets" (i.e., clutter close in to the target or the pulse width is less than the target extent), then a more appropriate selection, as discussed in [1], would be $\Delta F = 1/2\tau$. This selection is based on several factors, including the level of the surrounding targets or clutter, the pulse shape, and the range sample timing. An example of pulse width and frequency step size selection is shown in Figure 11.5 for six scatterers. In Figure 11.5(a, b) the pulse width is matched to the total target extent and $\Delta F = 1/\tau$. The scatterers fill the entire FFT window, and as indicated in Figure 11.5(b), when aliasing occurs it is not possible to determine the correct order of the scatterer locations. By selecting the pulse width to match the target and $\Delta F = 1/2\tau$, as in Figure 11.5 (c, d), the target occupies one-half of the FFT window and when aliasing occurs, the target "edges" (front and back) are easily determined. For this reason and to reduce the contamination of the HRR profile by scatterers located close in to the target, a conservative and generally recommended selection for frequency step size is then:

$$\Delta F \leq \frac{1}{2\tau} \tag{11.21}$$

11.2.5 Dynamic Range-Weighting Functions

Because the response of the compressed SFWF process is a $\sin(x)/x$ shape, filtering or weighting of the DFT process is often employed to reduce the range (time-delay) sidelobes. For example, if no weighting is used, the compressed response will generate a sidelobe only 13 dB down from the main response, thus limiting the ability to detect any close-in scatterer with an RCS 13 dB below the RCS of the main scatterer. Alternatively, the sidelobe response represents a false target return if greater than 13 dB dynamic range is desired. Thus, weighting functions are commonly used to provide sidelobe suppression (and thereby increase the dynamic range of the HRR profile).

Weighting will result in reduced sidelobes at the expense of a reduction in peak response, as well as a reduction in resolution of the FFT bin response. Typically, Hamming or Hanning weighting is employed. Hamming weighting will result in sidelobes that are 43 dB below the mainlobe peak, but will cause an increase in

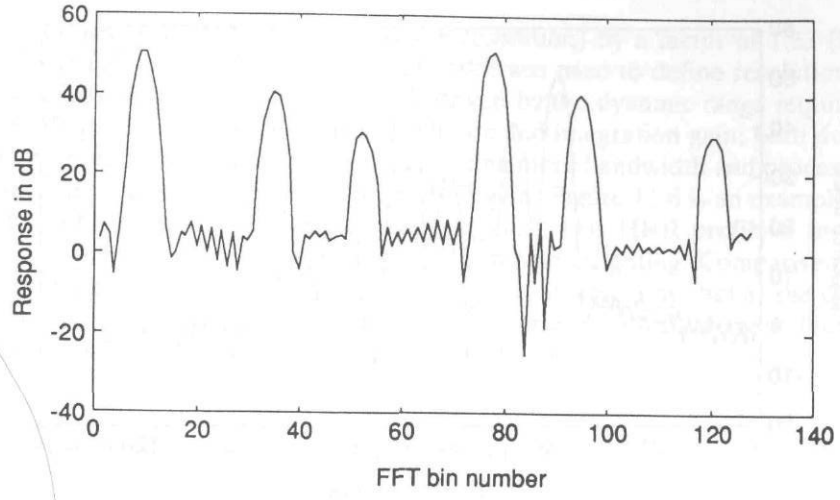

Figure 11.5(a) Nonaliased HRR profile for six scatterers with $\Delta F = 20$ MHz and $\tau = 50$ ns ($\Delta F = 1/\tau$).

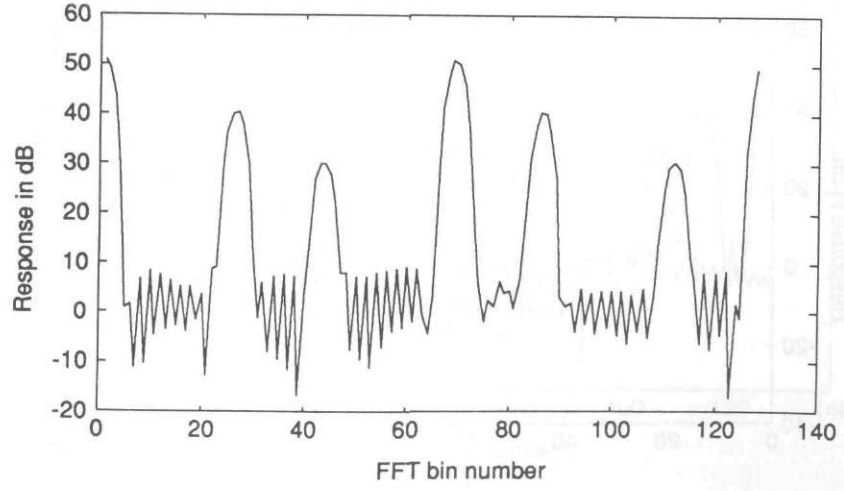

Figure 11.5(b) Aliased HRR profile for six scatterers with $\Delta F = 20$ MHz and $\tau = 50$ ns ($\Delta F = 1/\tau$).

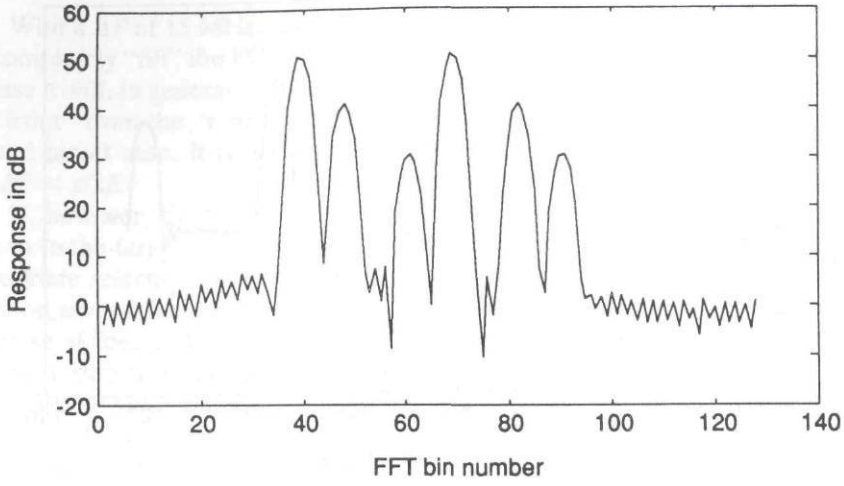

Figure 11.5(c) Nonaliased HRR profile for six scatterers with $\Delta F = 10$ MHz and $\tau = 50$ ns ($\Delta F = 1/2\tau$).

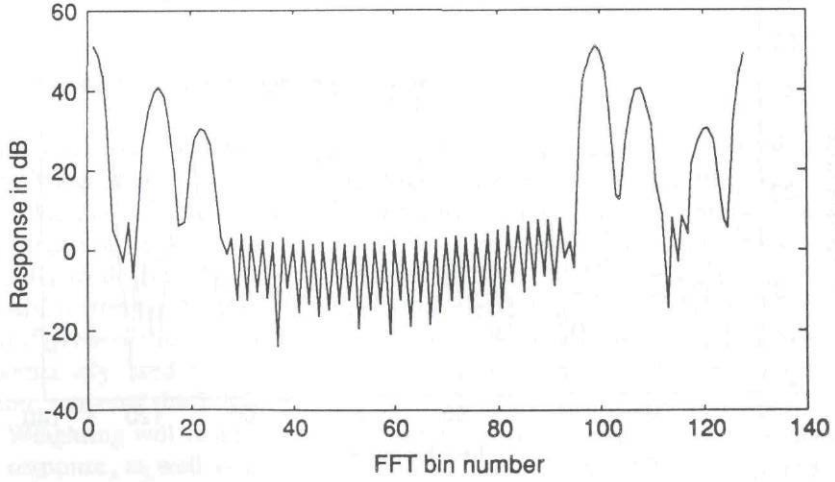

Figure 11.5(d) Aliased HRR profile for six scatterers with $\Delta F = 10$ MHz and $\tau = 50$ ns ($\Delta F = 1/2\tau$).

mainlobe response (reduction in effective resolution) by a factor of 1.33 (i.e., $K = 1.33$ in (11.1)). In (11.1) the -4-dB width was used to define resolution (i.e., $\Delta R = c/2B$). The choice of weighting is driven by the dynamic range required for the HRR profile. The tradeoff is in resolution and integration gain; both decrease with improvements in sidelobe levels, requiring more bandwidth and processing to achieve the preweighted resolution and FFT gain. Figure 11.6 is an example of an HRR profile with no weighting function applied. This HRR profile is the same data as that in Figure 11.3(c), which used Hamming weighting. Comparison of the two shows better resolution ($\Delta R = 0.23$m) without weighting, but at the expense of sidelobe levels. In the simulations provided throughout this chapter, Hamming weighting is always applied unless otherwise stated.

11.2.6 Effects of Radial Velocity on the SFWF

If the operational scenario is dynamic with a relative radial velocity between the radar and the target, then the radial-velocity-induced doppler term in (11.11) is not negligible and, if not compensated for, will result in degradation of the HRR profile data. This relative radial velocity will cause a "shift" (also referred to as a range offset) of the HRR profiles and, if great enough, will result in attenuation and dispersion of the compressed returns. Because of these effects, it is usually necessary to perform velocity compensation of the stepped-frequency data. The

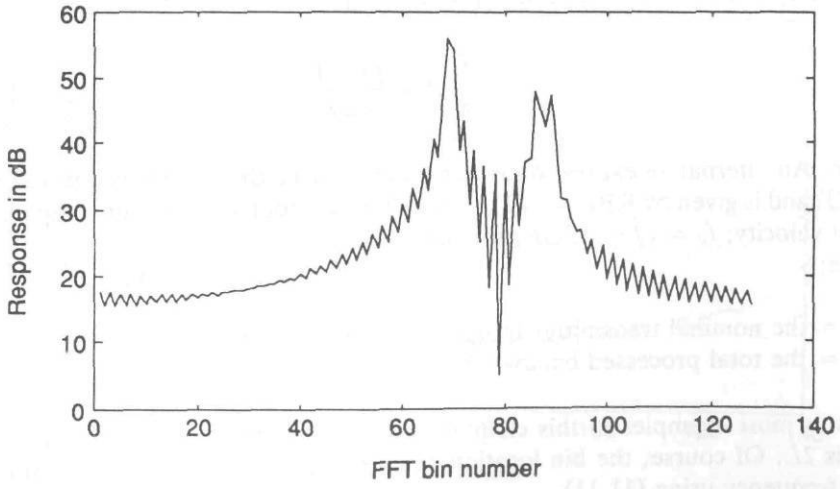

Figure 11.6 HRR profile with rectangular weighting on FFT demonstrating the increase in resolution and sidelobe levels. Same waveform parameters as in Figure 11.3(c).

required accuracy for velocity compensation is a function of the application, as well as the required range resolution. This accuracy requirement is discussed in the following paragraphs and is based on the theory and approach presented by T. H. Einstein on HRR processing using SFWFs [1].

Einstein defines a dimensionless parameter P that relates the radial target motion over the time duration of the SFWF to the resolution of the profile:

$$P = \frac{v_r NT}{\Delta R} \tag{11.22}$$

where:

v_r = the radial velocity between the radar and target (closing velocity),
NT = the duration of the SFWF or RRI, and
ΔR = the processed range resolution.

This is the ratio of how far the target moved with respect to the range resolution cell during the integration time. For all velocities with magnitude greater than zero, this represents a mismatch in the DFT (which acts like a matched filter), resulting in attenuation and dispersion of the HRR profile. Figure 11.7 (from [1]) shows the effect for $P = 0$, 3, and 6.

In addition to the attenuation and dispersion that will result in a reduction in range resolution and SNR, the uncompensated radial velocity will shift the HRR profiles by L FFT bins, where L is given by [1]:

$$L = \frac{\hat{f}_c}{B} P = \frac{\hat{f}_c v_r NT}{B\Delta R} \tag{11.23}$$

(Note: An alternative expression is *range bin error* (RBE), which is equivalent to (11.23) and is given by RBE $= NTf_d$, where f_d is the doppler due to uncompensated radial velocity; $f_d = (\hat{f}_c v_r)/(B\Delta R)$ for $\Delta R = c/2B$.)
where:

$\hat{f}_c$ = the nominal transmitter frequency (center frequency), and
B = the total processed bandwidth.

If, as in most examples in this chapter, the FFT size is $2N$, then the number of bins is $2L$. Of course, the bin location can also be determined by calculating the total frequency using (11.11).

Examples of the effects of velocity are shown in the simulation plots of Figure 11.8(a–c). The examples in Figure 11.8 are for the simulation of Figure 11.4(a)

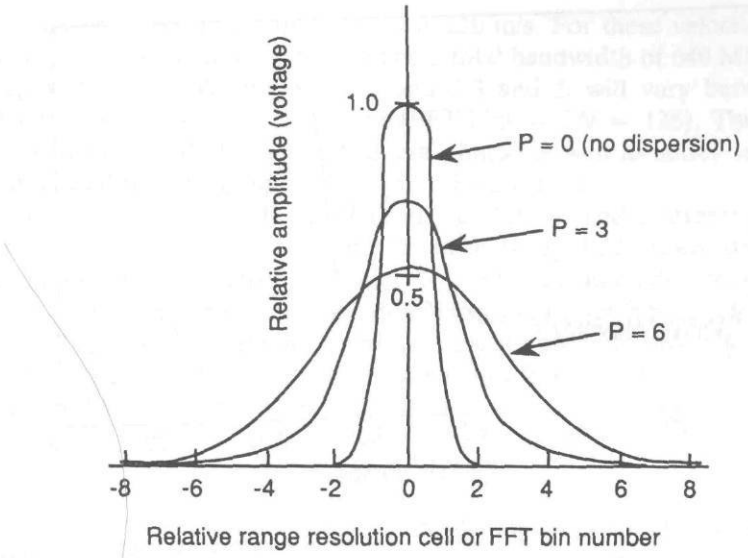

Figure 11.7 Attenuation and dispersion of the HRR profile of a single point scatterer target due to uncompensated relative radial velocity (from [1]).

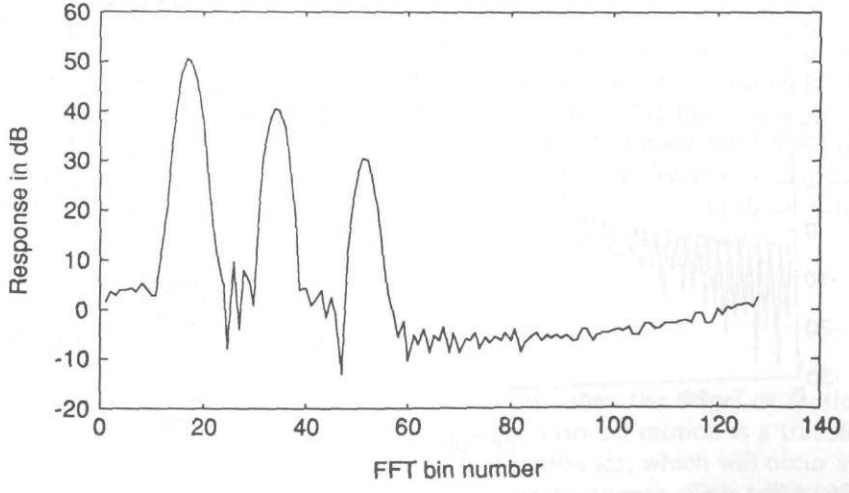

Figure 11.8(a) Effect of radial velocity on the HRR profile. Same waveform parameters as in Figure 11.4(a) with radial velocity of 25 m/s added.

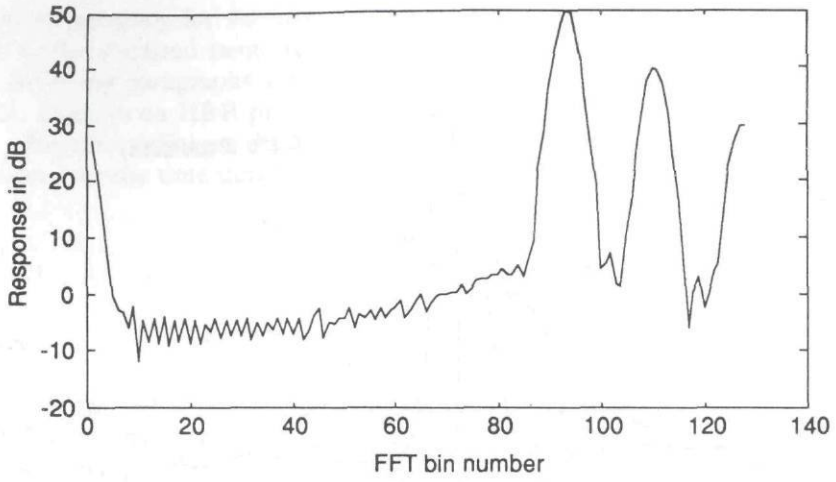

Figure 11.8(b) Effect of radial velocity on the HRR profile. Same waveform parameters as in Figure 11.4(a) with radial velocity of 50 m/s added.

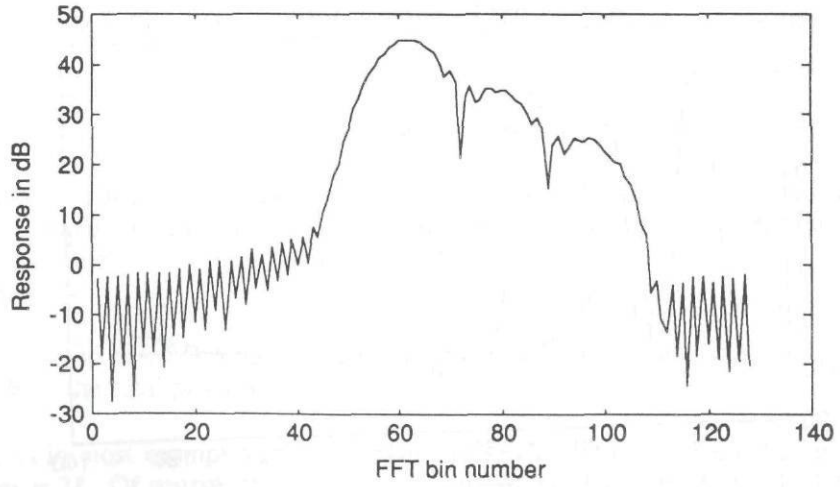

Figure 11.8(c) Effect of radial velocity on the HRR profile. Same waveform parameters as in Figure 11.4(a) with radial velocity of 250 m/s added.

with radial velocities added of 25, 50, and 250 m/s. For these velocities and for a nominal carrier frequency of 35 GHz and a total bandwidth of 640 MHz (10 MHz, 64 steps), P will vary between 0.53 and 5.3 and L will vary between 29 and 290 HRR cells or 58 to 580 FFT bins (FFT bins = $2N$ = 128). Thus, the HRR profile will shift and wrap around several times, as well as suffer serious loss in resolution and peak response, as shown in Figure 11.8.

Obviously, the loss in signal level, resolution, and scatterer alignment is unacceptable and velocity compensation must be applied. Then, the question is what amount of velocity compensation is needed to maintain accurate scatterer absolute position and minimize the attenuation and dispersion effects due to radial velocity. Typically, to maintain accurate scatterer absolute position, we want the range shift to be less than one-half of a resolution bin (Einstein uses 1 bin). Setting $L < 1/2$ and solving for v_r gives:

$$v_r < \frac{c}{4NT\hat{f}_c} \tag{11.24}$$

which for the above example results in about 0.33 m/s (1 ft/s). Thus, a velocity error of ± 0.33 m/s, or about 0.1% velocity error at 250 m/s closing velocity, will give a shift in the HRR profile of ± 0.5 of a resolution cell. Note that this result is dependent on the carrier frequency and NT (RRI), which is the number of frequency steps in the waveform times the PRI (1/PRF). A higher PRF will relax the velocity compensation requirement, as will fewer frequency steps. Additionally, the velocity compensation as stated above will reduce the P factor to 0.007, or approximately zero with no dispersion or attenuation of the compressed pulse.

If the shifting of scatterer locations is not a major concern, then compensation may be relaxed to a level needed to maintain a reasonable match for the FFT process; that is, maintaining a minimal acceptable level of main-level attenuation and dispersion (P factor). A good rule of thumb here is to keep $P < 2$. Because most SFWF systems have fractional bandwidths less than 10% ($\hat{f}_c/B > 10$), this criterion also places a manageable limitation on velocity compensation.

11.2.7 Sinusoidal Motion Effects

Sinusoidal motion can be a result of either vibrations on the target or motion of the radar platform. In either case, the effect of sinusoidal motion is a transfer of energy from the primary scatterer response into sidebands, which will occur at the scatterer frequency plus or minus the modulation frequency. This effect can be easily modeled using the geometry in Figure 11.9. In this case the radar platform

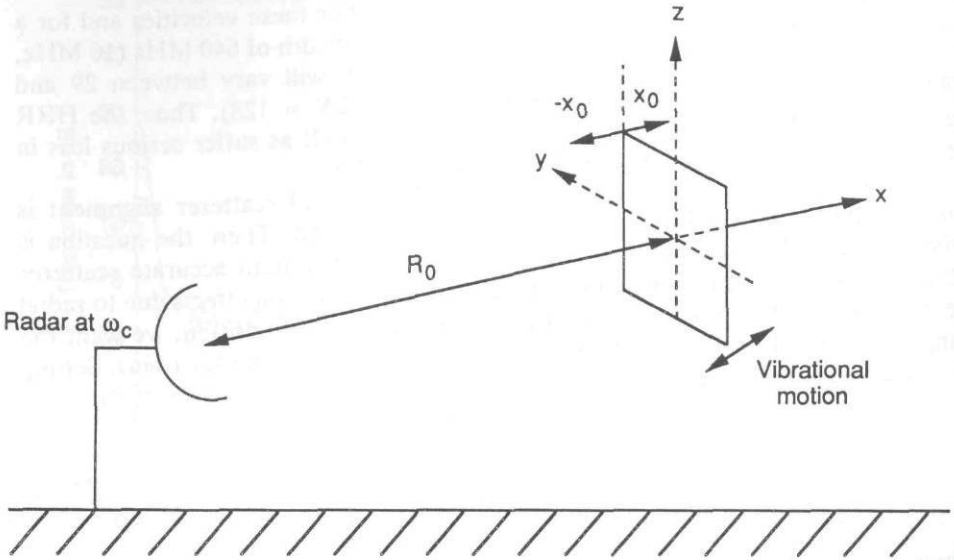

Figure 11.9 Geometry associated with the sinusoidal motion between the measurement radar and a vibrating target (scatterer).

is stationary with a sinusoidal motion induced on the scatterer (flat plate). The time displacement of the scatterer about R_0 is given by:

$$x = x_0 \sin(2\pi f_m t) \tag{11.25}$$

where x_0 is the peak amplitude and the f_m is the modulation frequency. The velocity (v) is then:

$$\frac{dx}{dt} = v = 2\pi f_m x_0 \cos(2\pi f_m t) \tag{11.26}$$

and the doppler due to the sinusoidal motion is given by:

$$f_d = \frac{2f_c}{c}\left[2\pi f_m x_0 \cos(2\pi f_m t)\right] \tag{11.27}$$

where f_c is the carrier frequency. It can be shown that the received signal is given by:

$$e(t) = E \sin[2\pi f_c t + \delta \sin(2\pi f_m t)] \tag{11.28}$$

where the modulation index δ is defined as $\delta = 4\pi x_0/\lambda$.

The equation for the received signal can be expanded into a Bessel function:

$$\begin{aligned} e(t) = {} & EJ_0(\delta) \sin(\omega_c t) \text{ (carrier)} \\ & + EJ_1(\delta)[\sin(\omega_c + \omega_m)t - \sin(\omega_c - \omega_m)t] \text{ (1st sideband)} \\ & + EJ_2(\delta)[\sin(\omega_c + 2\omega_m)t + \sin(\omega_c - 2\omega_m)t] \text{ (2nd sideband)} \\ & + EJ_3(\delta)[\sin(\omega_c + 3\omega_m)t - \sin(\omega_c - 3\omega_m)t)] \text{ (3rd sideband)} \\ & + \cdots \end{aligned} \tag{11.29}$$

from which the sideband power with respect to the primary signal can be calculated. For example, if $f_m = 10$ Hz, $x_0 = 15$ mm, and $\lambda = 3$ mm (100 GHz), then $\delta = 0.06$. Therefore, $J_1\ (0.06) = 0.03$, or 3% of the carrier voltage is in the first sideband. Thus, the ith sideband power (SBP_i) with respect to the main response (primary signal) in decibels is:

$$\text{SBP}_i = 20 \text{ Log}[J_i(\delta)] \tag{11.30}$$

and for the above first sideband power:

$$\text{SBP}_1 = 20 \log(0.03) = -30 \text{ dB}$$

Figure 11.10 illustrates the effect on the HRR profile for a single scatterer under three different conditions with the modulation index, modulation frequency, and radar PRF as variables. Note that the radar frequency is always 100 GHz.

In the first example, Figure 11.10(a), there is no apparent effect of the sinusoidal motion on the image, even though the modulation index is relatively large ($\delta = 0.6$). This is because the sideband modulation frequency is well below the frequency resolution of the SFWF samples (N). Recall that the frequency shift or doppler resolution (Δf_d) is $1/T$, where T is the integration time, and in the context of this discussion, T is equal to $N \times$ PRI. Thus, Δf_d is simply the PRF divided by the number of SFWF pulses. In Figure 11.10(a), $\Delta f_d = 10$ kHz/64, or approximately 156 Hz. Because the modulation frequency is 20 Hz, this doppler will not be resolved. In Figure 11.10(b), the PRF has been reduced to 500 Hz with a frequency

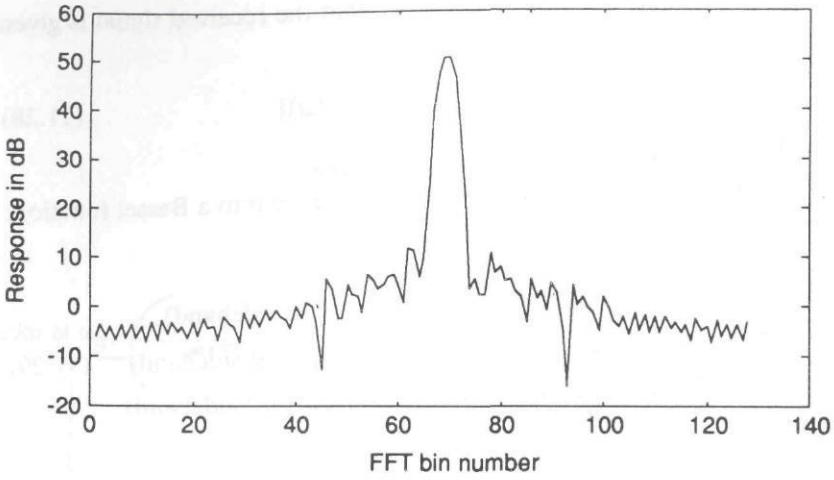

Figure 11.10(a) Effect of sinusoidal motion on the HRR profile for a single scatterer (100 m^2) located at 908m. PRF = 10 kHz, f_m = 20 Hz, and δ = 0.6.

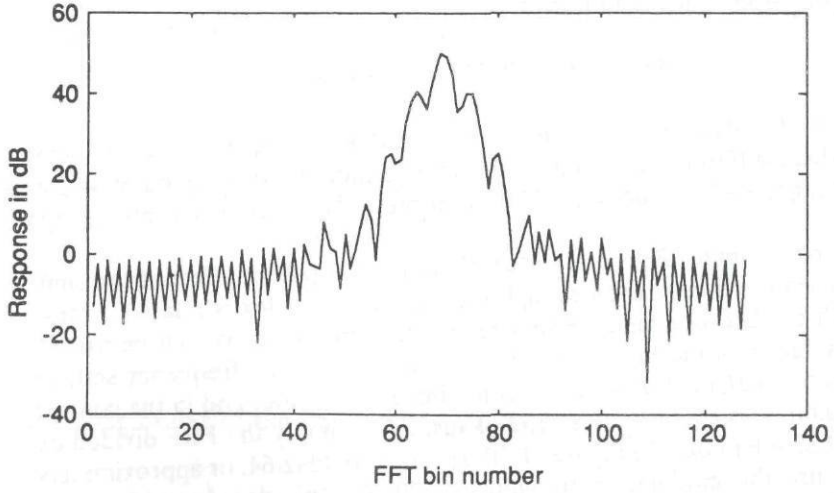

Figure 11.10(b) Effect of sinusoidal motion on the HRR profile for a single scatterer (100 m^2) located at 908m. PRF = 0.5 kHz, f_m = 20 Hz, and δ = 0.6.

resolution of 7.8 Hz. As noted, considerable power is now in the first (20 Hz) and second sidebands (40 Hz), with a dramatic effect on the HRR profile. Figure 11.10(c) is a more realistic example with a modulation index of 0.06. As calculated using the Bessel function above, the sidelobe levels are 30 dB down from the main response.

The example in Figure 11.10(d) is provided to show resolution effects for both the number of samples and the FFT size. The data in Figure 11.10(d) were calculated using a 128 pulse SFWF and a *matched* 128-point FFT. In this case the resolution is PRF/128 or 4 Hz. Also note that the resolution in Figure 11.10(c) is less (one-half); even though the FFT size is the same, the sample size is not. The latter, the number of pulses in the SFWF, determines the compressed data resolution. The FFT size determines the display resolution.

11.2.8 Effects of I/Q Errors on SFWF

If the system design uses conventional I/Q detection, then the HRR profile will be contaminated if any imbalance exists in the I/Q quadrature phase or gain. Additionally, if there exists any dc offset, a dc level will occupy the 0 Hz bin (split between bins 1 and N). The imbalance in the phase and gain will manifest itself as images at the negative of the frequency. Thus, "mirror" images will appear in the HRR or ISAR profiles (shown later). These image "artifacts" not only corrupt

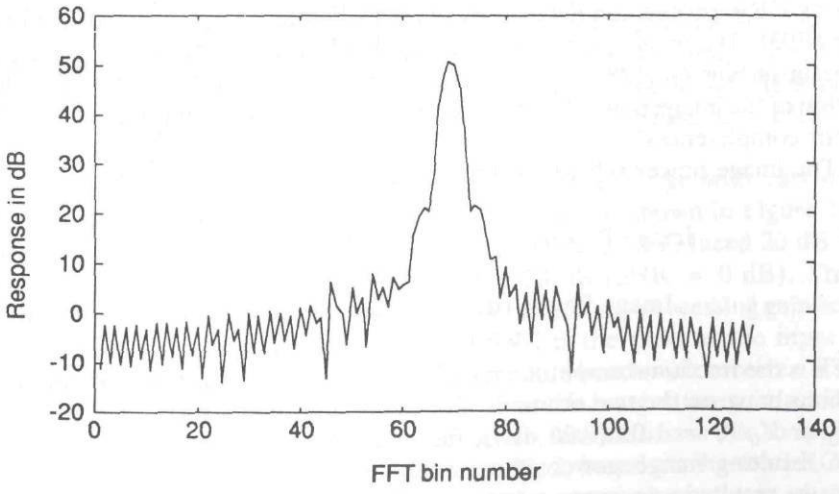

Figure 11.10(c) Effect of sinusoidal motion on the HRR profile for a single scatterer (100 m^2) located at 908m. PRF = 0.5 kHz, f_m = 20 Hz, and δ = 0.06.

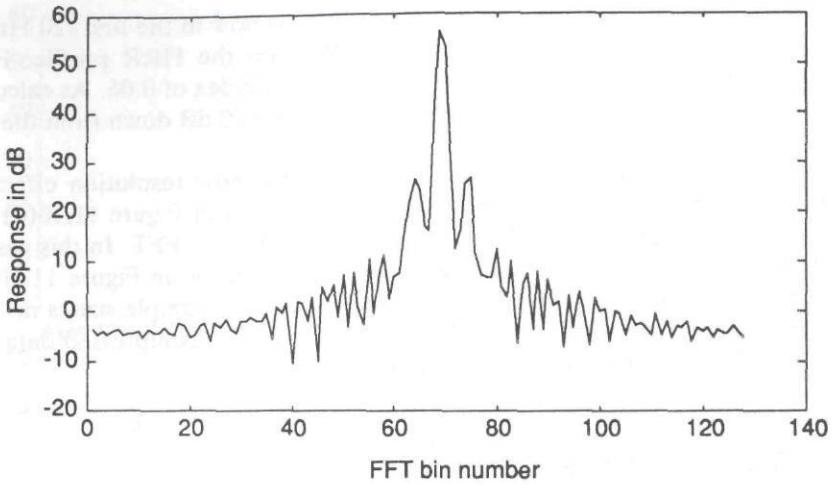

Figure 11.10(d) Effect of sinusoidal motion on the HRR profile for a single scatterer (100 m^2) located at 908m. PRF = 0.5 kHz, f_m = 20 Hz, and δ = 0.06. In this example the FFT size equals the number of pulses processed (FFT size = N = 128).

the actual image, but can also mask smaller scatterers located in the mirror-image bins. An example of these effects is shown in Figure 11.11, where a gain imbalance of 3%, a phase imbalance of 5 deg, and a dc offset of 0.1 is simulated for the three-scatterer HRR profile simulated previously in Figure 11.4(a) located in bins 68, 85, and 103). The images are approximately 32 dB down from their main response and occur at bins 60 (128 − 68), 43 (128 − 85), and 25 (128 − 103). The determination of the image power has been discussed in previous chapters and is repeated here for completeness.

The image power relative to the primary response is given by:

$$\text{Image Power (dB, amplitude)} = 10 \log (\epsilon^2/4) \tag{11.31}$$

$$\text{Image Power (dB, phase)} = 10 \log (\vartheta^2/4) \tag{11.32}$$

where ϵ is the fractional amplitude imbalance (V_I/V_Q) and ϑ is the phase imbalance in radians between the two channels. For example, if there is a 3% gain imbalance (V_I/V_Q or V_Q/V_I = 1.03 (0.26 dB)), the fractional amplitude imbalance is 0.03, with a resulting image power of approximately −36.5 dB. A 3-deg (0.05 rad) imbalance results in an image power of −31.7 dB. Because the effect is additive in power, if both imbalances exist simultaneously, the total image power is −30.5 dB.

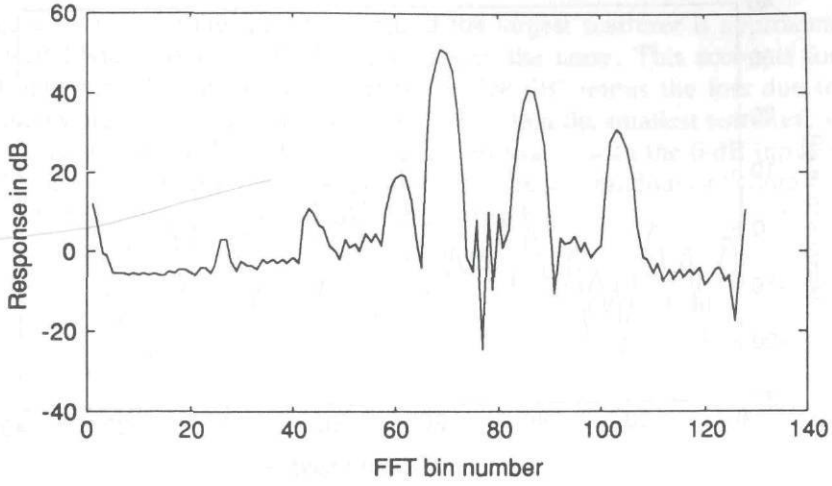

Figure 11.11 Effects of I/Q errors on the HRR profile. Same waveform parameters as in Figure 11.4(a), with I/Q gain imbalance of 0.03, phase imbalance of 0.05 rad, and dc offset of 0.1. Note mirror images of the three scatterers.

11.2.9 Thermal Noise and Phase Noise Effects

Both thermal and phase noise have been discussed extensively in previous chapters. Both contaminants reduce the dynamic range of the images and are additive, as are all effects that reduce the peak response and increase the "noise floor." In this section several examples are provided as to the effects on the SFWF HRR profiles. In addition, a simple expression is provided to estimate the phase noise contribution to the HRR process.

Figure 11.12(a, b) shows examples of the SFWF image with varying SNR (thermal noise levels). Again, the baseline simulation is shown in Figure 11.4(a), which was produced with a 40-dB SNR. Figure 11.12(a) is reduced 20 dB (20-dB SNR) and Figure 11.12(b) is reduced another 20 dB (SNR = 0 dB). The SNR specified is the preprocessed SNR and does not include any processing gain achieved with the SFWF process. The preprocessed SNR is the ratio at the input to the coherent detection stage, assuming a matched filter bandwidth receiver. The processed SNR is simply the preprocessed SNR plus the integration gain achieved by means of the coherent integration of the N pulses, less the losses due to application of a weighting function. Also, the SNR is specified, based on the total RCS of all scatterers in the pulse. To simplify this example, a noncoherent sum of the RCS of the individual scatterers is used. Thus, the individual scatterer SNR exhibited in the HRR profiles is normalized by the RCS sum of all the scatterers. Examination

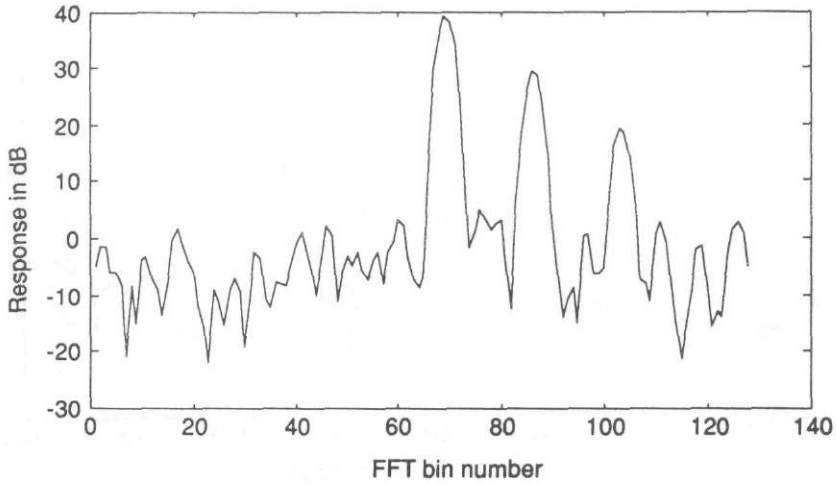

Figure 11.12(a) Effect of thermal noise (SNR) on the HRR profile. Same waveform parameters as in Figure 11.4(a), with SNR = 20 dB.

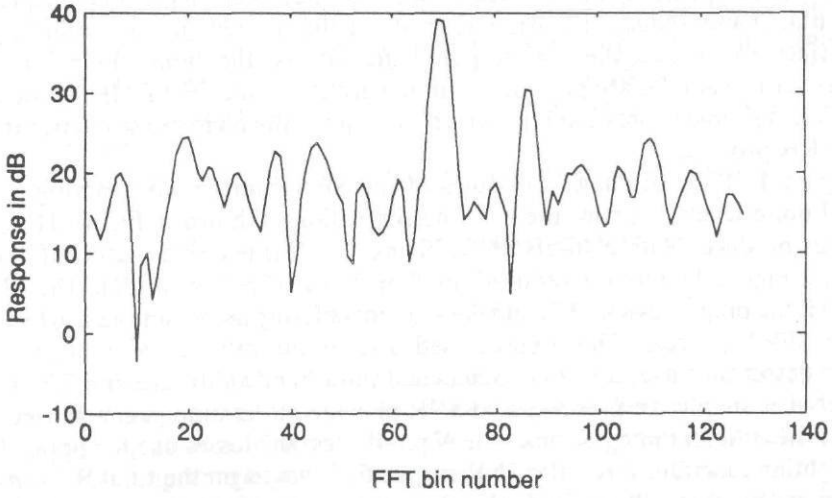

Figure 11.12(b) Effect of thermal noise (SNR) on the HRR profile. Same waveform parameters as in Figure 11.4(a), with SNR = 0 dB.

of Figure 11.12(a, b) indicates the peak of the largest scatterer is approximately 37 (20-dB SNR) and 17 dB (0-dB SNR) above the noise. This accounts for the 17-dB gain with the integration of 64 pulses (18 dB) minus the loss due to the Hamming weighting of approximately 1 dB. Note that the smallest scatterer, which is 20 dB down from the largest, is no longer detectable with the 0-dB input SNR.

Figure 11.13(a–c) shows examples of the effects of random or "white" phase noise, where the level of the phase noise is given by:

$$\rho \approx \frac{\sigma_\phi^2}{N} \tag{11.33}$$

where:

ρ = the desired side lobe level,
N = the number of pulses, and
σ_ϕ = the rms phase noise.

Figure 11.13(a) is provided as a baseline for the addition of phase noise and shows two scatterers of equal RCS (10 m^2), with an input SNR of 20 dB. White noise with an rms of 0.358 and 1.13 radians is added and the effect shown in Figure 11.13(b, c). From the above equation and from the simulations, the two levels of

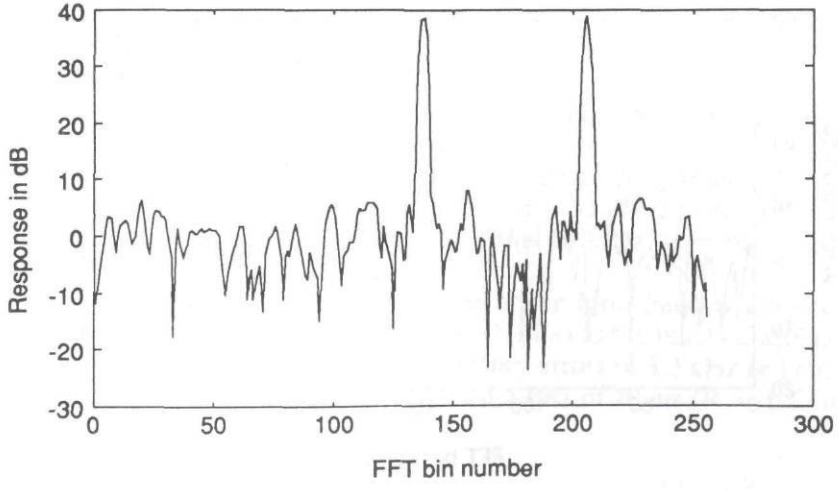

Figure 11.13(a) HRR profile for two 10-m^2 scatterers located at 908m and 912m. N = 128, FFT = 256, SNR = 20 dB, and rms phase noise of 0 rad.

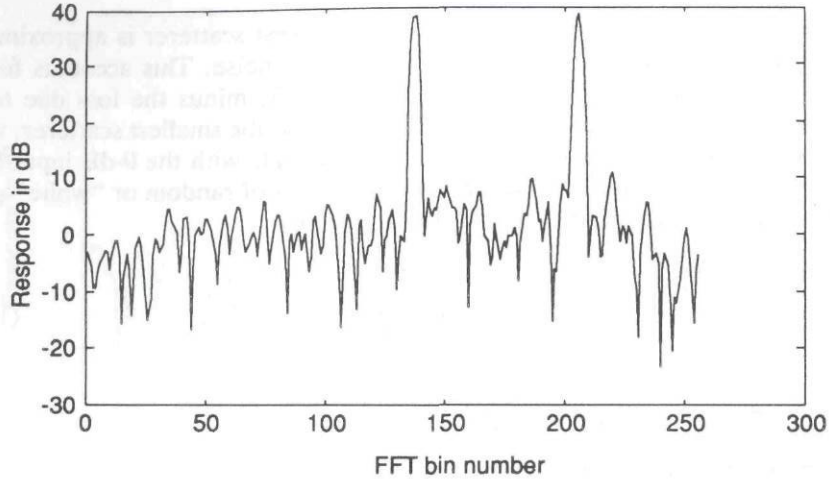

Figure 11.13(b) Effect of phase noise on the HRR profile for the two scatterers in Figure 11.13(a). N = 128, FFT = 256, SNR = 20 dB, and rms phase noise of 0.36 rad.

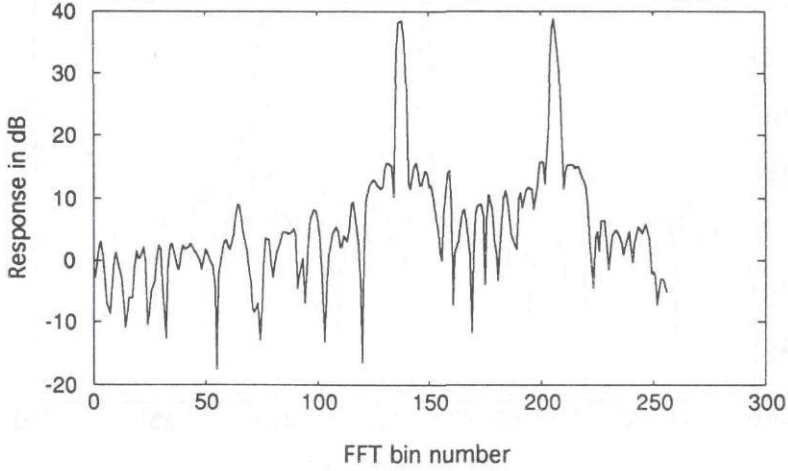

Figure 11.13(c) Effect of phase noise on the HRR profile for the two scatterers in Figure 11.13(a). N = 128, FFT = 256, SNR = 20 dB, and rms phase noise of 1.13 rad.

phase noise result in a noise level of approximately −30 dB and −20 dB, respectively.

11.2.10 Effects of Nonuniform Frequency Step on SFWF

In the generation of the HRR profiles using the SFWF, it was assumed that the frequency step size was uniform (i.e., $f_i = f_0 + \Delta f$, $(i = 0, N - 1)$). In general, this is not the case and small nonuniformities in the frequency step will occur. The random frequency errors will result in an increase in phase noise, which manifests itself in a reduction of SNR, which will be a function of range. The SNR reduction occurs as both a reduction in peak response (loss in FFT integration gain) and increased null responses. This, of course, also results in a loss in system dynamic range because of the increase in the noise floor. In this section an expression is presented that relates the rms frequency error to the operational range, number of pulses processed, and the peak maximum allowable sidelobe level. Simulations are provided that demonstrate the effect on the HRR image.

If we let f_k be the ideal kth frequency transmitted, then $f_k = f_0 + k\Delta f$. If the kth actual transmitted frequency is denoted f'_k, where $f'_k = f_k + E_k$, where E_k is the deviation from the ideal, it can be shown that:

$$|E_k| \leq \frac{1}{2\pi t_{\max}} \sqrt{\frac{\rho N}{3}} \tag{11.34}$$

where:

$t_{\max}$ = the PRI,
N = the number of frequency steps, and
ρ = the maximum peak sidelobe level (close in peak noise level).

Thus, the ΔF accuracy needed is a function of range ($R_{\max} = ct_{\max}/2$), N, and sidelobe level desired. For example, for a PSL of −30 dB, t of 10 ms ($R = 1.5$ km), and $N = 128$, $|E_k| < 3{,}291$ Hz. If the ΔF is 10 MHz, then the percentage error is 3,291/10 MHz or 0.03%.

Figure 11.14 illustrates the effects of the nonuniform frequency step on the HRR profile of a single scatterer, with Figure 11.14(a) as the baseline with no step error. Figure 11.14(b, c) corresponds to frequency errors of 3.3 kHz and 6.6 kHz, respectively, for $\Delta F = 10$ MHz, $N = 128$, and a PRI of 10 ms ($R = 1.5$ km).

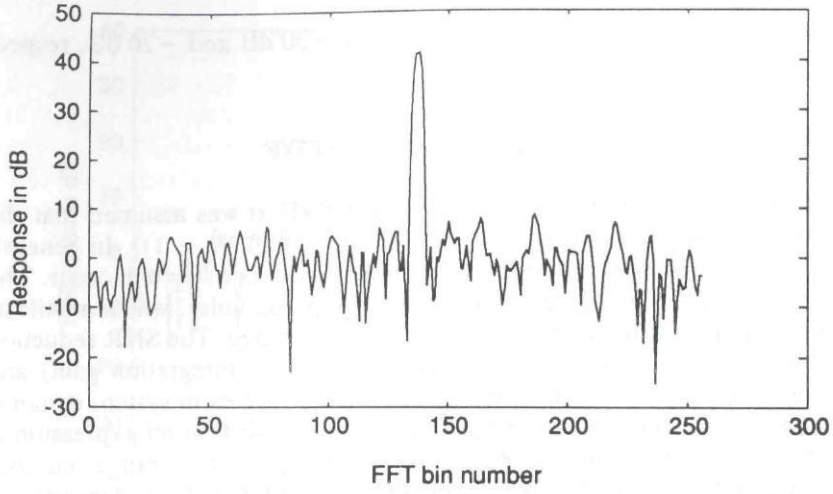

Figure 11.14(a) HRR profile for a single scatterer located at 1,493m. N = 128, FFT = 256, SNR = 20 dB, PRI of 10 ms, and frequency deviation of 0 Hz.

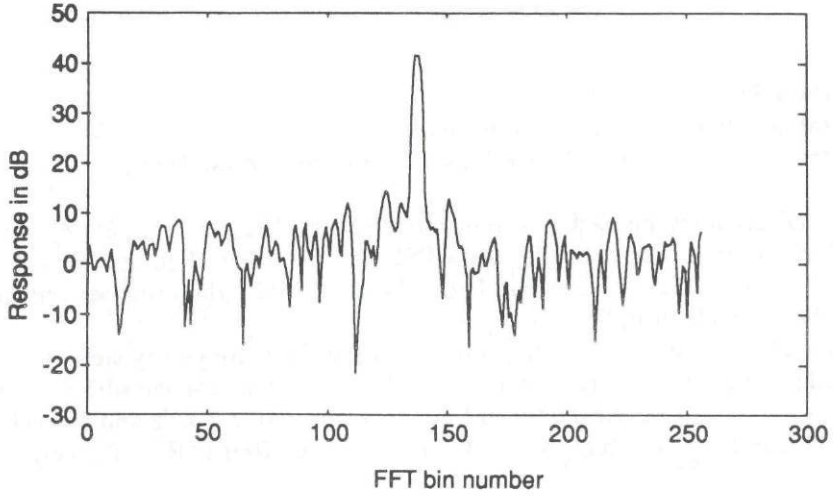

Figure 11.14(b) Effect of nonuniform ΔF on the HRR profile for a single scatterer located at 1,493m. N = 128, FFT = 256, SNR = 20 dB, PRI of 10 ms, and frequency deviation of 3.3 kHz.

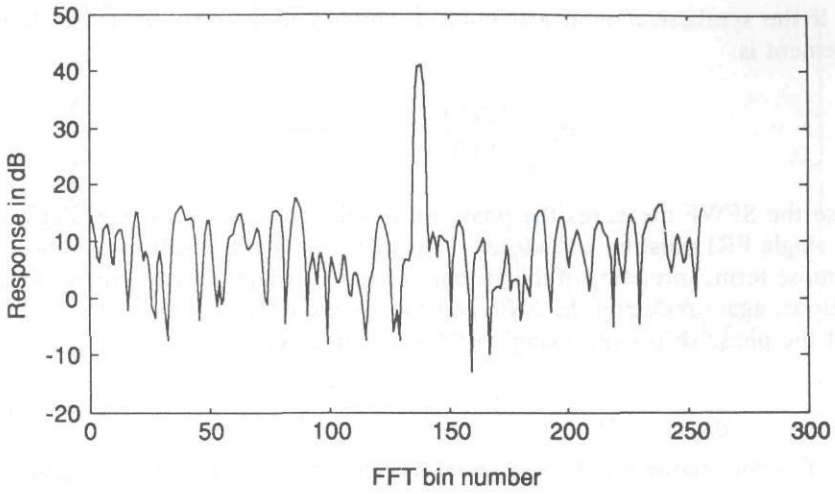

Figure 11.14(c) Effect of nonuniform ΔF on the HRR profile for a single scatterer located at 1,493m. N = 128, FFT = 256, SNR = 20 dB, PRI of 10 ms, and frequency deviation of 6.6 kHz.

11.2.11 Frequency (Phase) Stability Requirements

In examining the frequency stability requirements, there are two key issues: the frequency stability required for the step size accuracy (random frequency error), and the frequency stability required on a pulse-to-pulse basis (short term stability). Both must be examined to determine the final requirements placed on the frequency sources. In most cases, the frequency synthesizer is the source of frequency instabilities (both random and pulse-to-pulse). With few exceptions, the synthesizer is the only source that is being stepped or swept; all other frequency sources are generally fixed frequency and as such can be made extremely stable.

The random frequency error issue as discussed above can be viewed as a frequency stability requirement. If the major source of the nonuniform frequency step is the synthesizer, then the required frequency stability in parts per million (p/m) is given by:

$$\delta f_s = \frac{|E_k|}{f_s} \tag{11.35}$$

where f_s is the nominal frequency of the synthesizer and δf_s is the frequency synthesizer stability in parts per million. Using the above example for frequency rms

error, if the synthesizer is at a nominal frequency of 2 GHz, then the stability requirement is:

$$\delta f_s = \frac{3291 \text{ Hz}}{2 \text{ GHz}} = 1.6 \text{ p/m}$$

Because the SFWF measures the phase on a pulse-to-pulse basis, the phase drift over a single PRI must be considered. This phase drift will result in an additional phase noise term, spreading of the primary response (mainlobe) and increasing the noise floor, again reducing the SNR and the system dynamic range.

If the phase drift over a single PRI is denoted $\Delta\Phi$, then:

$$|2\pi\delta f_i t| \leq \Delta\Phi \tag{11.36}$$

where δf_i is the frequency stability over one PRI and t is the PRI, then the synthesizer stability in parts per million is given by:

$$\delta f_s \leq \frac{|\delta f_i|}{f_s} = \frac{\Delta\Phi}{2\pi f_s t} \tag{11.37}$$

Again, using the above example, the frequency stability for a nominal 2 GHz frequency, a PRI of 10 ms, and a phase drift of $\pi/4$ radians (rule of thumb) is 6 p/m. In general, as in this example, the stability requirement for the SFWF process (random frequency error) is the more strict requirement, which must be applied in specifying the system performance.

11.2.12 Polarization Isolation Effects

Many of the high-resolution applications require (or desire) the collection of polarimetric HRR signature data. A polarimetric system generally switches the transmit polarization on a pulse-to-pulse basis between two orthogonal polarizations and simultaneously receives two orthogonal polarizations. The latter requires two separate receiver channels, resulting in signal leakage between the channels with a loss in polarization "purity." In many cases, the system uses a single antenna for transmission and reception and this causes additional isolation problems. If adequate isolation between the two channels is not maintained, the signals will contain returns from both polarization fields. In the case of ultrawideband systems, maintaining high channel isolation is not always possible and contamination of the HRR profile will occur.

An example of this effect is shown in Figure 11.15, where the ideal returns (infinite polarization isolation) for the target of interest is given in Figure 11.15(a,

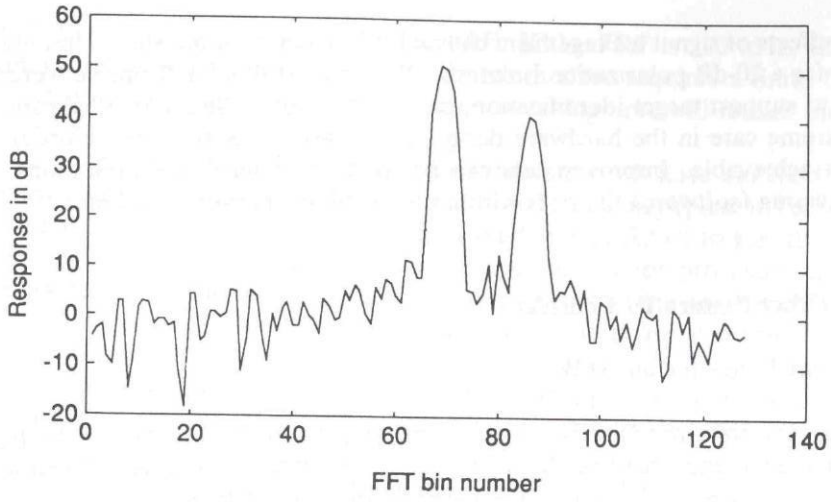

Figure 11.15(a) Channel A ideal response (infinite polarization isolation) HRR profile of two "polarization A" type scatterers located at 908m (100 m^2) and 910m (10 m^2).

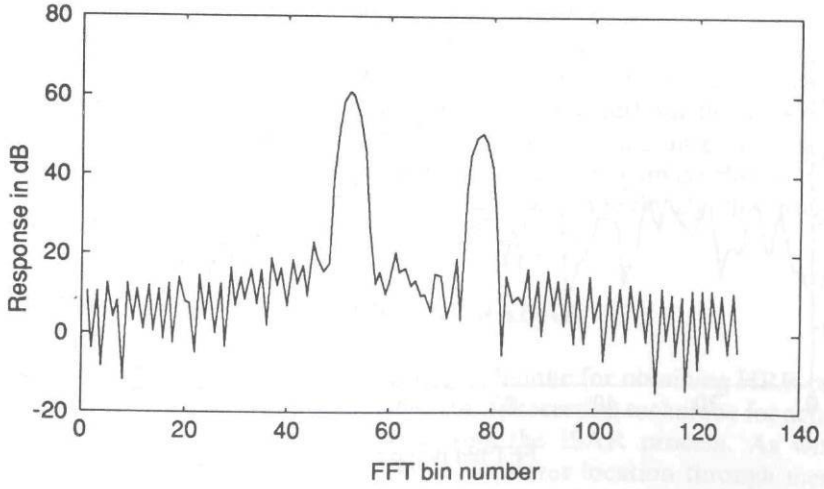

Figure 11.15(b) Channel B ideal response (infinite polarization isolation) HRR profile of two "polarization B" type scatterers located at 906m (1,000 m^2) and 909m (100 m^2).

b). The effects of signal leakage from channel B to channel A are shown in Figure 11.15(c) for a 20-dB polarization isolation. Obviously, if this HRR profile were to be used to support target identification, care must be exercised in its application. With extreme care in the hardware design, polarization isolation on the order of 30 dB is achievable. Improvements can be made over hardware limitations by postprocessing (software) the data with a polarization calibration technique.

11.2.13 Other Factors To Consider

PRF Versus Range for the SFWF

An additional point needs to be made concerning the SFWF technique. As in all coherent radars, the phase of the signal is measured by comparing the received signal to a sample of the transmitted signal. In a coherent pulsed system, the frequencies are all fixed; phase can be measured over several pulses (depending on system drifts and scenario). In the SFWF the frequency of the synthesizer is changing on a pulse-to-pule basis, and in order to measure the phase, the received signal must be compared to the transmitted signal on a pulse-to-pulse basis. This restricts the SFWF to operating at a maximum range consistent with having only one pulse "in the air" at one time. Or, said another way, the maximum range for

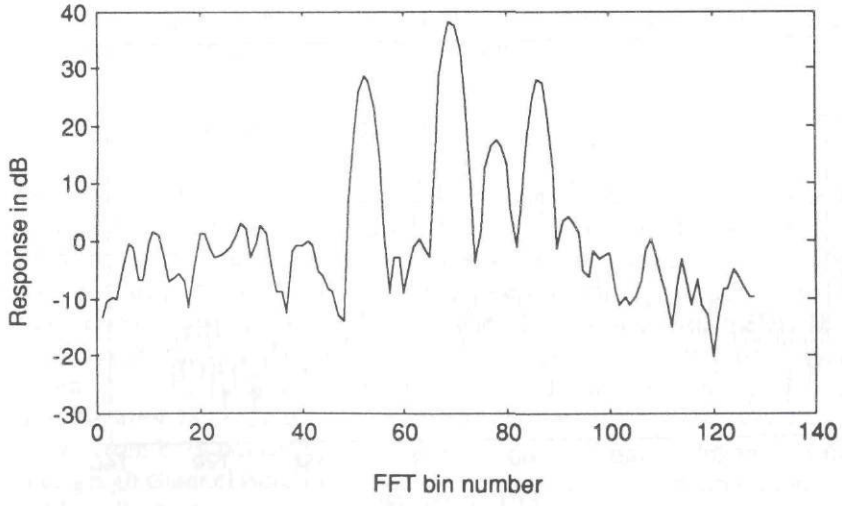

Figure 11.15(c) Channel A HRR profile of two "polarization A" type scatterers located at 908m (100 m^2) and 910m (10 m^2), and "leakage" of two "polarization B" type scatterers located at 906m (1,000 m^2) and 909m (100 m^2) for 20-dB polarization isolation.

SFWF HRR operation is limited by the PRF. If the PRF is 100 kHz, then the maximum range is 1,500m. In actuality, the synthesizer requires a finite time to step to the next frequency and stabilize. This switching time will reduce the maximum range an additional amount.

At longer ranges the frequency of the synthesizer will have switched before receiving and processing the previously transmitted frequency (pulse). Techniques for working around this are to have several synthesizers (LOs) to sort the pulses in the air or measure the transmitted phase and store it for processing on each pulse. Switching back to the previous synthesizer frequency will not in itself suffice, unless the synthesizer is designed to return to the same phase as it was when the pulse was transmitted.

This latter problem is a major disadvantage for applications that require high PRFs and reasonable imaging ranges. Note that going to lower PRFs will increase the RRI factor, resulting in a more stringent velocity compensation. Additionally, if the closing velocities are significant, going to a lower PRF could result in the target experiencing range walk during the HRR processing interval.

SNR Gain of the SFWF Process

Because of the narrowband process associated with the SFWF, a gain in SNR is achieved over that of a short pulse system with the same range resolution. This SNR gain is simply the ratio of the instantaneous receiver bandwidth of the equivalent short pulse system to the instantaneous receiver bandwidth of the SFWF system. Assuming equal range resolution, the short pulse system must have a bandwidth equal to the total processed bandwidth of the SFWF system (i.e., $N\Delta F$). For a matched filter bandwidth receiver, the instantaneous bandwidth of the SFWF is determined by $1/\tau$, where $\tau = 1/2\Delta F$. Thus, the bandwidth for the SFWF system is $2\Delta F$ and the resulting SNR gain is simply $N/2$. Assuming an equal number of processed samples for both systems, additional integration gain is achieved through the coherent integration of the N pulses. As mentioned previously, this integration gain will be reduced by the use of weighting functions.

11.3 INVERSE SYNTHETIC APERTURE RADAR

The previous sections described a processing technique for obtaining HRR profiles using the SFWF. The following sections discuss a processing technique for achieving high- or ultra-high-crossrange resolution using the ISAR process. As with the SFWF, the ISAR technique also determines scatterer location through measurement of frequency shifts. The SFWF generates a frequency shift through a known phase change (frequency) on a pulse-to-pulse basis and requires that the target be nearly stationary (or velocity corrected) during the RRI. The ISAR process mea-

sures scatterer location in crossrange as a result of the frequency shift (doppler) due to relative radial motion between the measurement radar and the scatterers on the target and requires that the transmitted phase be nearly constant (fixed frequency) over the processing interval consisting of multiple RRIs. Thus, both techniques are multiple pulse processes, with the ISAR technique requiring a fixed frequency measurement of a nonstationary target and the SFWF technique requiring a sweep frequency measurement of a stationary target. By proper selection of the measurement parameters, the two processes can be combined to generate 2D images of the target with resolutions on the order of centimeters.

11.3.1 ISAR Crossrange Process

The crossrange resolution obtained in ISAR is dependent on the ability to measure the doppler frequency of a scatterer (or scatterers) that is rotating with respect to the radar LOS. Consider the case of two scatterers located on a rotating target as shown in Figure 11.16. For this example, neither the radar nor the target have translational motion and the radar LOS is in the same plane as the scatterer (0 deg depression angle). The target rotates at a fixed angular rate of ω rad/sec about an axis perpendicular to the LOS. A single point scatterer at a crossrange distance from the center of rotation, r_c, will have an instantaneous velocity toward the radar given by $v = \omega r_c$. The resulting doppler frequency is given by:

$$f_d = 2\omega r_c \frac{f_c}{c} \tag{11.38}$$

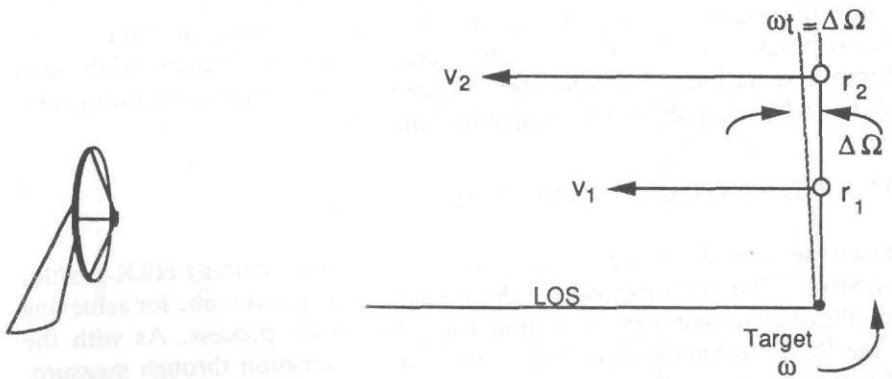

Figure 11.16 ISAR crossrange resolution for a two scatter case.

where f_c is the carrier frequency and c is the propagation velocity. Now, consider two point scatterers in the same slant-range cell, separated by Δr_c. As shown in Figure 11.16, the targets will have velocities $v_1 = \omega r_1$ and $v_2 = \omega r_2$, with a velocity difference of $\omega \Delta r_c$ and a corresponding frequency difference of:

$$\Delta f_c = 2\omega \frac{\Delta r_c f_c}{c} \tag{11.39}$$

If Δf_d is the radar doppler resolution obtainable, then:

$$\Delta r_c = \frac{c \Delta f_d}{2\omega f_c} \tag{11.40}$$

is the crossrange resolution obtainable in the slant-range cell. Similarly, because doppler resolution is approximately $1/T_i$, where T_i is the coherent integration time, then:

$$\Delta f_d = \frac{1}{T_i} = \frac{1}{M \times \text{PRI}} \tag{11.41}$$

where M is the number of pulses processed and:

$$\Delta r_c = \frac{c}{2\omega T_i f_c} = \frac{\lambda}{2\omega T_i} = \frac{1}{2} \frac{\lambda}{\Delta\Omega} \tag{11.42a}$$

where λ is the wavelength and $\Delta\Omega$ is the angle moved during the integration time.

As with the SFWF, a discrete Fourier transform is used to convert the M time samples collected in the range cells into a frequency spectrum and weighting functions are applied to improve the dynamic range (reduce time sidelobes). Thus, the crossrange resolution is broadened by the application of a window-weighting function. As discussed previously, Hamming weighting will cause a broadening of the resolution cell by a factor of 1.33 times the unweighted cell resolution width; that is:

$$\Delta r_c = K \frac{\lambda}{2\Delta\Omega} = \frac{1.33\,\lambda}{2\Delta\Omega} \tag{11.42b}$$

An example of a crossrange ISAR profile is shown in Figure 11.17. In this example, three scatterers are located at -4m (1 m^2), 0m (10 m^2), and $+4$m (100 m^2), where the 0 is the center of rotation, negative ($-$) is left of the center of rotation, and positive ($+$) is to the right of the center of rotation. The doppler convention used

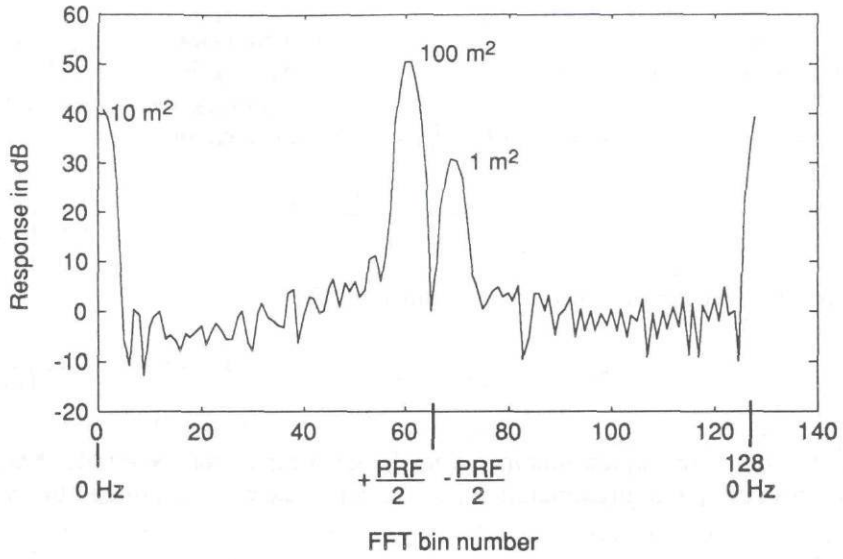

Figure 11.17(a) Example of an ISAR profile for three scatterers for "unshifted" doppler. Scatterers are located at -4m (1 m^2), 0m (10 m^2), and $+4$m (100 m^2), where negative crossrange is to the left of the center of rotation, zero is center, and positive is to the right.

in the example is that approaching velocities will result in a positive doppler. Also, note that because both approaching and receding velocities are generated as the target rotates about the center, positive doppler frequencies are in FFT bins 1 to 64 and negative frequencies in FFT bins 65 to 128.

Because the center scatterer experiences no doppler shift (there is no velocity vector towards the radar), the compressed pulse response shows up in the dc bins of the FFT window, as in Figure 11.17(a). Because the zero doppler in the ISAR is located at the center of the target, a shift in the FFT is usually applied to the data so that zero doppler is in the center of the FFT, negative frequencies to the left of center, and positive frequencies to the right of center, as in Figure 11.17(b). Figure 11.17(c) demonstrates the ISAR crossrange resolution at 10 GHz for one scatterer located at -4m (1 m^2) and two scatterers approximately 0.2m apart (10-m^2 scatterers located at 3.8m and 4m) with a rotation rate of 0.1 rad/s, a PRF of 60 Hz, and 64 pulses (M). For this example, the ISAR resolution is equal to $60/64 = 0.94$ Hz, for a crossrange resolution of 0.14m ((11.40), without weighting). As with the previous simulations, Hamming weighting is used (weighted resolution is 0.2m) and the FFT size is $2M$ for higher display resolution. Also, as with the SFWF simulations, the SNR is the sum of the single pulse SNR (40 dB) plus the

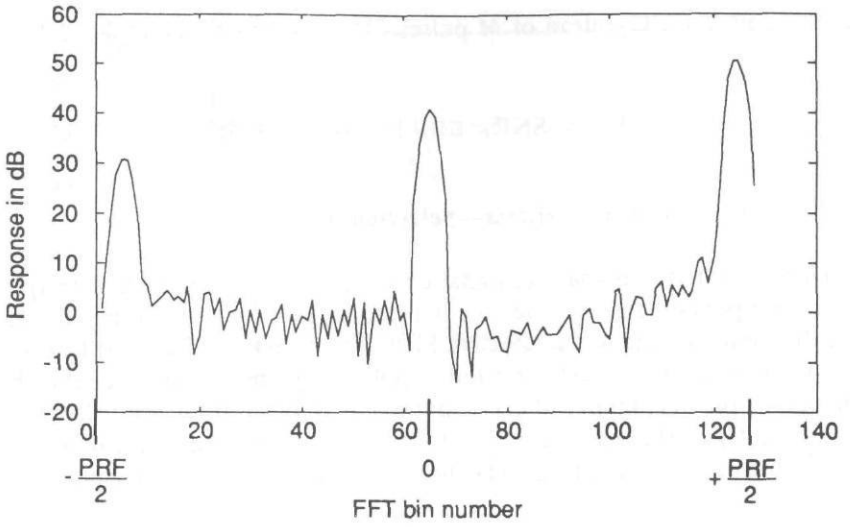

Figure 11.17(b) Example in Figure 11.17(a) with FFT "shift" applied to data.

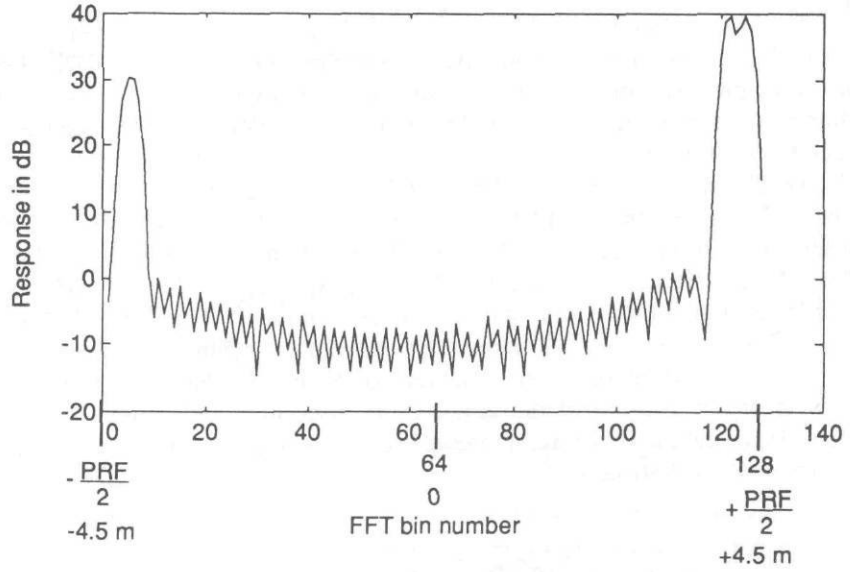

Figure 11.17(c) ISAR profile showing crossrange resolution. Scatterers are located at -4m (1 m^2), $+3.8$m (10 m^2), and $+4$m (10 m^2). $F = 10$ GHz, PRF = 60 Hz, $\omega = 0.1$ rad/s.

integration gain for integration of M pulses ($M = 64$ in this example). Thus the SNR is:

$$\mathrm{SNR}_{64} = \mathrm{SNR}_1 + 10\log(64) = 58\ \mathrm{dB}$$

11.3.2 Crossrange Sampling Criteria—Selection of PRF

Nyquist sampling requires that the signal be sampled at twice the highest expected frequency component (i.e., at twice the highest doppler frequency). For the ISAR process the sampling rate is the effective PRF. The effective PRF must be selected to be at least twice the highest expected doppler frequency. That frequency being determined by the maximum radial component of velocity of the scatterers located on the target where the maximum radial velocity is associated with the maximum crossrange dimension of the target (farthest scatterer from the center of rotation). Thus:

$$\mathrm{PRF}' \geq 2f_{d(\max)} = \frac{4f_c}{c}\omega r_{c(\max)} \tag{11.43a}$$

where PRF′ is the effective PRF associated with a given fixed frequency in the waveform. For a fixed-polarization, fixed-frequency radar, PRF′ = PRF. For a polarization-agile radar or a stepped-frequency radar, PRF′ = PRF/n, where n is the number of pulses in the waveform. For a fixed polarization, $n = N$, the number of frequency steps in the SFWF.

In the example of Figure 11.17(b), the FFT bins are associated with doppler frequencies that extend from −PRF′/2 (−30 Hz) to +PRF′/2 (+30 Hz), for a total frequency spread of 60 Hz. For a rotation rate of 0.1 rad/s, frequency of 10 GHz, and the +4m crossrange, the maximum doppler frequency is (11.38) +26.7 Hz. A scatterer located at +6m would have a doppler frequency of +40 Hz and would alias as −20 Hz (10 − 30 Hz). The result of this undersampling is shown in Figure 11.18, where the 100 m^2 scatterer is moved to +6m. Obviously, undersampling results in incorrect location of the scatterer in crossrange and could mask other scatterers. If we define W_c as the unambiguous crossrange window for ISAR processing, then $W_c = 2\,r(\max)$:

$$W_c = 2r_{c\max} = \frac{c\ \mathrm{PRF}'}{2\omega f_c} = \frac{M\lambda}{2\omega T} \tag{11.43b}$$

where T (the coherent processing time for the ISAR resolution of Δr_c) = M PRI′ = M/PRF′, and M is the number of ISAR waveforms processed (number of fixed frequency time samples).

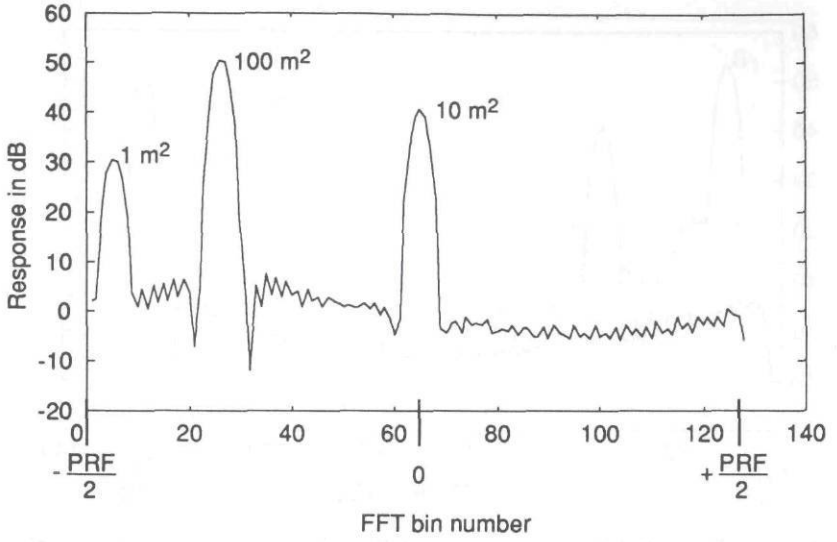

Figure 11.18 ISAR profile with undersampled crossrange. Scatterers are located at -4m (1 m^2), 0m (10 m^2), and $+6$m (10 m^2). F = 10 GHz, PRF = 60 Hz, ω = 0.1 rad/s.

11.3.3 Effects of Errors on ISAR Imaging

In general, the various errors discussed in the SFWF section also apply to the ISAR image process with the same effect on the image quality. As an example, Figure 11.19(a) is an ISAR simulation of two scatterers located at -2m (10 m^2) and at $+4$m (100 m^2), with an SNR of 40 dB. Figure 11.19(b) is the same ISAR image for a 3% gain and 3-deg phase imbalance I/Q error (image power -31.7 dB) and a dc offset of 0.1. Note that in the shifted FFT, the dc offset appears as a scatterer response in the center FFT bins (zero doppler bin). Figure 11.19(c) includes the I/Q errors as well as a phase noise of 0.4 rad. Additional examples will be discussed in the following section on 2D imaging.

11.4 SFWF AND ISAR IMAGE PROCESS (2D IMAGES)

In the 2D target image process discussed in this chapter, the image is constructed using the SFWF in the range dimension and the ISAR process in the crossrange dimension. If N steps of ΔF hertz are taken in the waveform, the downrange resolution is given by:

$$\Delta r_d \sim \frac{c}{2N\Delta F} \tag{11.44}$$

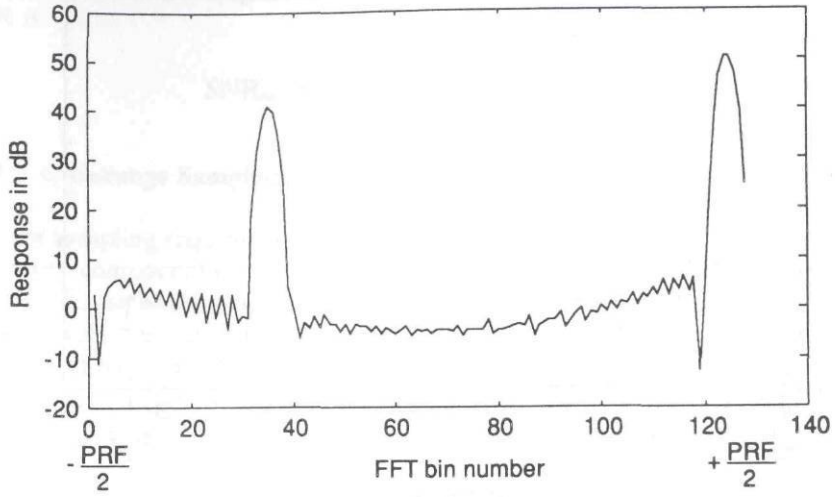

Figure 11.19(a) ISAR profile for two scatterers with 40dB SNR. Scatterers are located at -2m ($10\ m^2$) and $+4$m ($100\ m^2$). $F = 10$ GHz, PRF = 60 Hz, $\omega = 0.1$ rad/s.

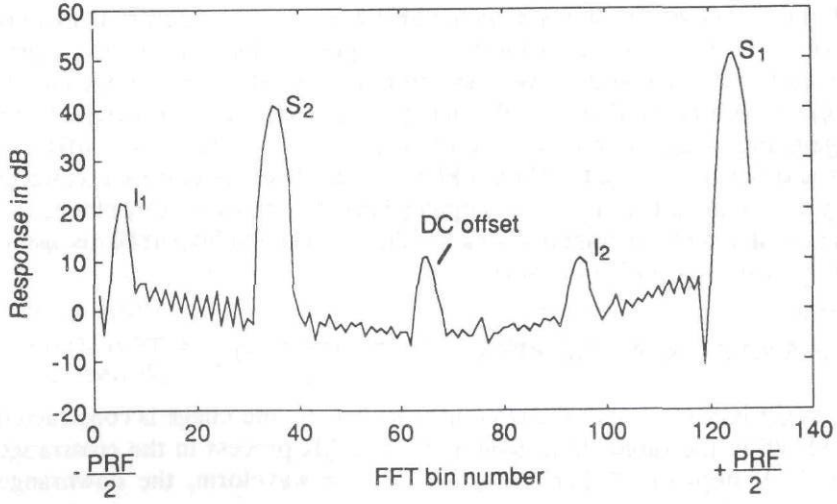

Figure 11.19(b) Example in Figure 11.19(a) with I/Q imbalance (3%, 3 deg, 0.1 dc offset). Note that *S* is the scatterer, *I* is the image.

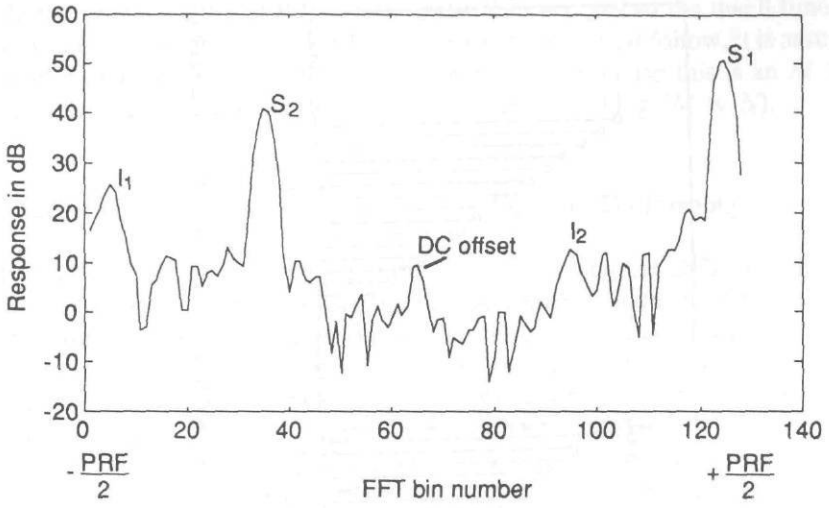

Figure 11.19(c) Same as example in Figure 11.19(b) with 0.4 rad of phase noise added.

and in the same fashion as above, an unambiguous range window can be defined as:

$$W_d = N\Delta r_d = \frac{c}{2\Delta F} \tag{11.45}$$

To obtain crossrange resolution, time-domain reflectivity in each downrange cell must be converted to the frequency domain (doppler) data. Thus, two transforms are required to obtain the ISAR image in downrange and crossrange. For an SFWF, N pulses occur for one waveform. During these N pulses, it is assumed that there is only a small viewing angle change. One way to look at the 2D (SFWF-ISAR) process is that for each of the N pulses of the waveform, a range profile is defined. There are considered to be M such range profiles that define the image. The synthetic range cells can then be transformed by a DFT on a range cell basis (with M complex values in each range cell) to obtain target doppler information for each range cell. The N pulses and the M profiles therefore define range windows in the downrange and crossrange dimensions.

Figure 11.20 is an example of the SFWF-ISAR waveform, showing M waveforms (M fixed-frequency samples), each containing N step frequency pulses. In the example, $M = 4$ and $N = 16$. Thus, the entire process requires $M \times N$ pulses, with a total coherent processing time of T_i. Figure 11.20 shows an $M \times N$ waveform

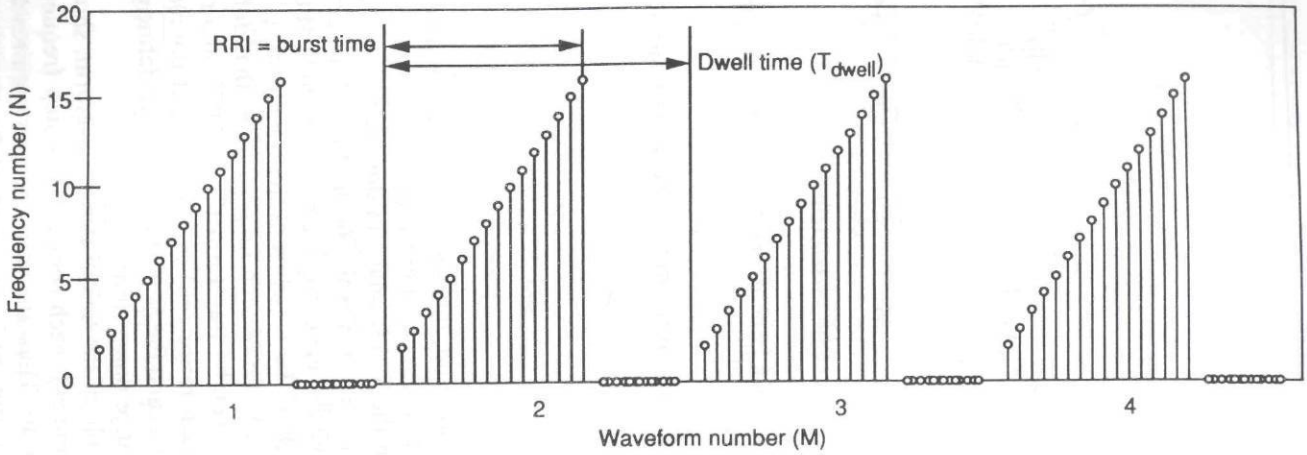

Figure 11.20 Frequencies of successive pulses in the SFWF, showing definitions of burst and dwell times. Each SFWF is processed to form one of M HRR profiles used in generating the ISAR profiles.

with idle time between the SFWF bursts. If the RRI is equal to the dwell time (no idle time), then T_i is simply $M \times N$ PRI. In the derivations that follow, it is assumed that the idle time is zero. It should also be noted that because this is an $M \times N$ pulse process, the integration gain of the 2D process is 10 log $(M \times N)$.

11.4.1 Target Radial (Translational) Velocity Effects on 2D Imaging

Usually, an ISAR image uses many downrange profiles, and the DFT of each range cell is taken to obtain the crossrange target measurement. In developing the downrange resolution equation, it was assumed that no target radial velocity existed. If a radial or translational velocity exists between the radar and the target, the scatterers in each range cell will move between subsequent profiles. This means the scatterers will not be aligned from profile to profile if translational motion exists.

We will follow the terminology derived in Wehner [2], who defines two effects of translational velocity: "range walk" and "range offset." The term range walk implies range changes from profile to profile. As has been discussed, the SFWF has a velocity-induced range error, which is range offset. This range offset is a result of the range-doppler coupling inherent in the SFWF. Range walk will accumulate from profile to profile, whereas range offset is constant, for a constant radial velocity. Range walk will result in "range cell migration," meaning that scatterers will migrate to different cells on successive profiles.

Range offset has already been discussed with the resulting equation (11.23):

$$L = \frac{\hat{f}_c}{B} P = \frac{\hat{f}_c v_r NT}{B\Delta R} \tag{11.46}$$

Recall that:

L = the number of bins shifted,
$\hat{f}_c$ = center frequency,
v_r = target velocity,
N = the number of frequency steps,
T = the PRI,
B = the total bandwidth ($B = N\Delta F$), and
ΔR = the range resolution ($\Delta R = c/2B = c/2N\Delta F$).

Range walk is simply how many resolution bins the scatterer moved during the processing time, or stated differently, the ratio of the change in range during the processing time ($\delta R = v_r t$) over the range resolution (ΔR). The number of bins

"walked" over several waveforms (M) because of the target velocity is denoted by L_w and is given by:

$$L_w = \frac{\delta R}{\Delta R} = \frac{v_r MNT}{\Delta R} \tag{11.47}$$

The total number of range cells shifted, N_t, is therefore:

$$N_t = \frac{\hat{f}_c v_r NT}{B\Delta R} + \frac{v_r MNT}{\Delta R} \tag{11.48a}$$

which can be rewritten as [6]:

$$N_t \sim \left[\frac{2(NT)}{c} f + \frac{2M(NT)N\Delta F}{c}\right] v_r \tag{11.48b}$$

The first term is due to range offset; the second term is the range walk. Range walk usually results in more severe distortion of the ISAR image than range offset. This is somewhat to be expected because the integration time for M profiles is M times that for a single profile. Both effects can be minimized by applying velocity compensation as discussed in the SFWF.

11.4.2 Target Angular Velocity Effects

Range-Doppler Interaction

For the case of no translational velocity (only target angular velocity), a range-doppler interaction will also occur. To avoid contamination of the HRR process, the doppler frequency induced by the radial component of the angular velocity (target rotation) must be less than the IPS frequency resolution of the HRR process. If not, then the location of the scatterers in the HRR profile will shift because of the rotational doppler within the HRR cells and range smearing will occur. If we require that the doppler induced by the angular velocity is less than one-half of an HRR IPS frequency bin resolution, then:

$$\frac{2f_c \omega r}{c} < \frac{1}{2}\Delta f_{ips} = \frac{1}{2}\frac{2\Delta R}{c}\Delta F \times \text{PRF} = \frac{\text{PRF}}{2N} \tag{11.49}$$

or:

$$\omega \leq \frac{1}{2} \frac{C \times \text{PRF}}{ENf_c} \tag{11.50a}$$

where $2r = E$, the target length. As an example, if the target is 10m long and the measurement radar is operating at 35 GHz with a PRF of 10 kHz and 128 frequency steps, the maximum rotation rate is 0.033 rad/s, or approximately a 3min revolution. This assumes (as have all equations) that the radar is in the plane of rotation. If not, the equation(s) must be modified by the appropriate angle function so that the correct magnitude of the velocity vector in the direction of the radar is used; that is:

$$\omega \leq \frac{1}{2} \frac{C \times \text{PRF}}{ENf_c \cos(\psi)} \tag{11.50b}$$

where ψ is the radar pointing depression angle.

Cell Migration Due to Rotation

Another concern for the measurements is the effect of the distortion caused by the angular rotation of the target. This distortion is due to the quadratic phase variation caused by the circular motion of the scatterers as they rotate; that is, the velocity component towards the radar is not constant. This, in combination with the FFT process, results in movement of the scatterers in image space (cell migration) and blurring occurs. The blurring is more severe as the wavelength increases, the target length increases, and the resolution (range and crossrange) cell is reduced.

Cell migration can occur in both the downrange and crossrange dimensions. Consider a target of longest (length) dimension E rotating about its center $E/2$. If the downrange resolution is Δr_d, then it can be shown that the maximum number of range cells moved in T_i ($T_i = N \times M \times \text{PRI}$) is:

$$N_d = \frac{E\omega T_i}{2\Delta r_d} \tag{11.51}$$

In like manner the number of crossrange cells migrated in T_i can be found:

$$N_c = \frac{E\omega T_i}{2\Delta r_c} \tag{11.52}$$

where N_c is the maximum number of crossrange cells that is moved in T_i and Δr_c is the crossrange resolution. For equal downrange and crossrange resolution (i.e.,

$\Delta r_d = \Delta r_c$), the requirement on T_i to prevent cell migration is the same in each dimension, and the number of cells migrated, N_m, is given by:

$$N_m = \left(\frac{E}{2\Delta r}\right)(\omega T_i) \tag{11.53}$$

Using (11.42), N_m may be written:

$$N_m = \left(\frac{E}{2\Delta r}\right)\left(\frac{c}{f_c}\right)\left(\frac{1}{2\Delta r}\right) \tag{11.54}$$

where f_c is the center frequency. This shows that the number of migration cells is inversely proportional to frequency and resolution and directly proportional to target length. To prevent any image blurring, N_m must be less than one.

Using the results derived in (11.50) and the above, an upper bound can be given for the number of waveforms that can be processed (M) before focusing is required ($N_d < 1$):

$$M \leq \frac{4\Delta r_d}{\lambda} \tag{11.55}$$

The above equations are for the scatterers located at the outer edge of the target ($r = E/2$) and for maximum motion in the downrange and crossrange direction (occurs at the cardinal angles). Thus, the amount of image blurring is a function of the scatterer radius and the angle that the scatterer moves through during the processing time. Assuming the worst case, if E is 10m, f_c is 10 GHz, and the image resolution is 0.3m, N_m is 0.8 and cell migration will not occur. For resolutions much better than 0.3m, cell migration will occur and cell realignment may be necessary to prevent unacceptable blurring of the data. One method of correction is polar reformatting. Polar reformatting is a resampling technique to correct for cell migration or "focus" the image. Various techniques for focusing the image are discussed in several of the references.

11.4.3 Effects of Errors on SFWF-ISAR (2D) Imaging

Figure 11.21 shows a series of 2D images where the downrange resolution is generated through a SFWF and the crossrange through ISAR processing. The images are for two point scatterers: (1) a 1 m^2 scatterer located at a range of 158m and a crossrange of -1m (1m to the left of the center of rotation) and (2) a 10 m^2 scatterer at 160m and 2m to the right of the center of rotation. For both the

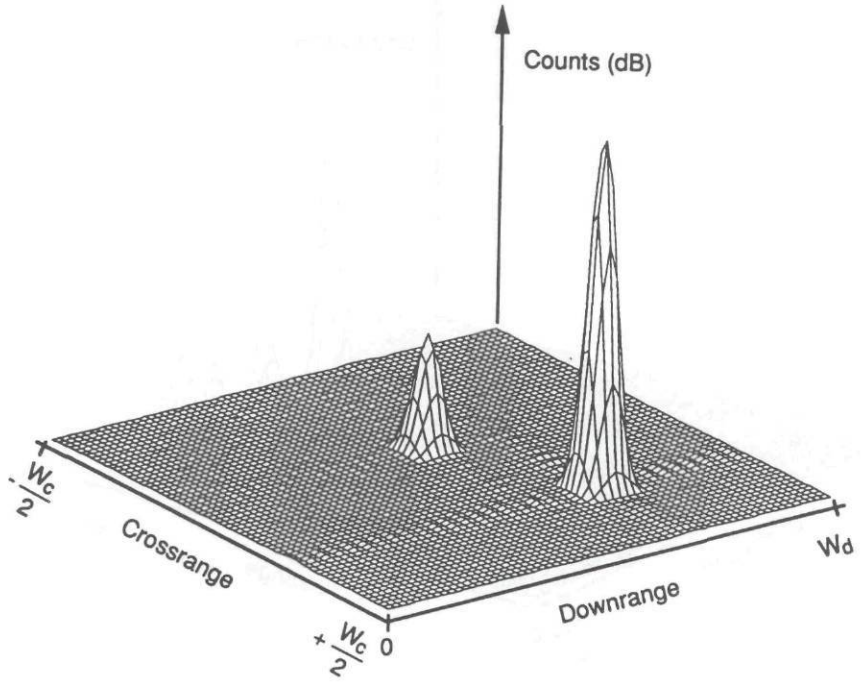

Figure 11.21(a) Example of a 2D image of two scatterers located at (crossrange/downrange) −1m/158m (1 m^2) and +2m/160m (10 m^2). F = 95 GHz, PRF = 2 kHz, ω = 0.01 rad/s, ΔF = 10 MHz, and $N = M = 32$, with 64-point FFT in both dimensions.

downrange and crossrange processing, a 64-point FFT is used, consisting of 32 samples and 32 zero fill to improve display resolution. The radar frequency is 95 GHz and the rotation rate is 0.01 rad/s with a radar PRF of 2 kHz.

In generating the downrange profiles, 32 frequencies are used with a 10 MHz step size. Therefore, the downrange resolution is approximately 0.6m after weighting. The unambiguous downrange window is 15m (150m to 165m) with an unambiguous frequency of 0 to 2 kHz. Each FFT bin represents 0.23m or 31 Hz. In generating the crossrange profiles, 32 HRR profiles are processed with an effective PRF of 62.5 Hz; thus, the unambiguous crossrange window is 9.8m with a crossrange resolution of 0.41m after weighting. Each crossrange FFT bin represents 0.153m or 0.98 Hz.

The effects of dc offset and I/Q errors are shown in Figure 11.21(b). Note that the dc bins are the end bins in downrange and in the center for the crossrange

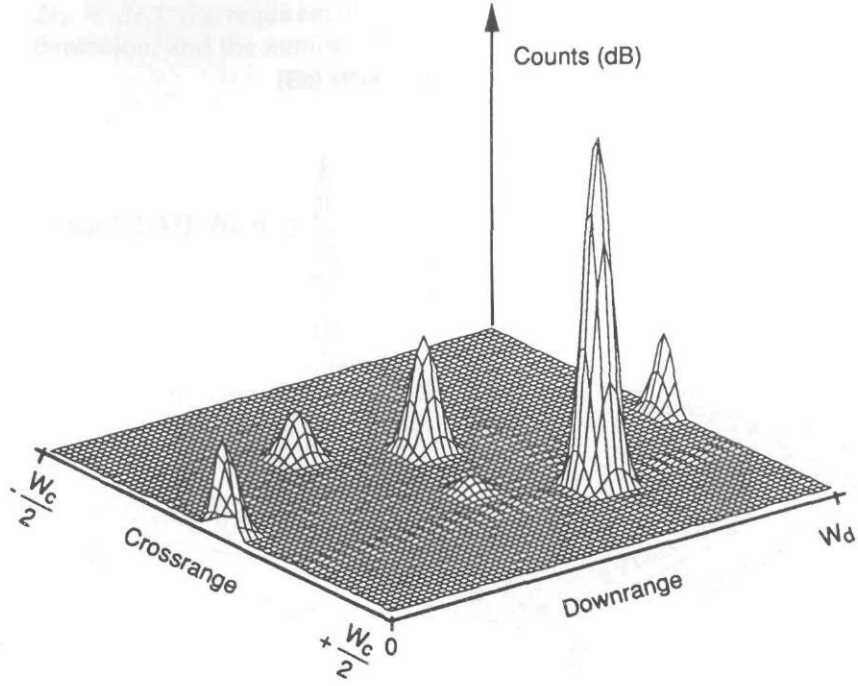

Figure 11.21(b) Same as example in Figure 11.21(a), showing effects of I/Q errors. Note dc offset appears as a scatterer in zero FFT bins (center of ISAR, ends of HRR).

(zero doppler). Also note that the images are mirror images with the mirror plane along the diagonal of the 2D image.

Figure 11.21(c) shows the effects of translational velocity on the images of Figure 11.21(a). Note that the images have shifted in both downrange and crossrange and that attenuation and dispersion of the main response has occurred.

The last example is an example of the effects of sinusoidal motion on the image process. Figure 11.21(d) is due to a sinusoidal frequency of 10 Hz, which shows up only in the crossrange dimension. Increasing the frequency to 300 Hz now effects both the downrange and crossrange profiles, demonstrating the sensitivity of the 2D process to the sinusoidal motion in crossrange. This, of course, is due entirely to the frequency resolution associated with each process. Because the unambiguous crossrange is 62.5 Hz (+/− 31.25 Hz), the sidelobes due to the modulation frequency are aliased several times in crossrange position.

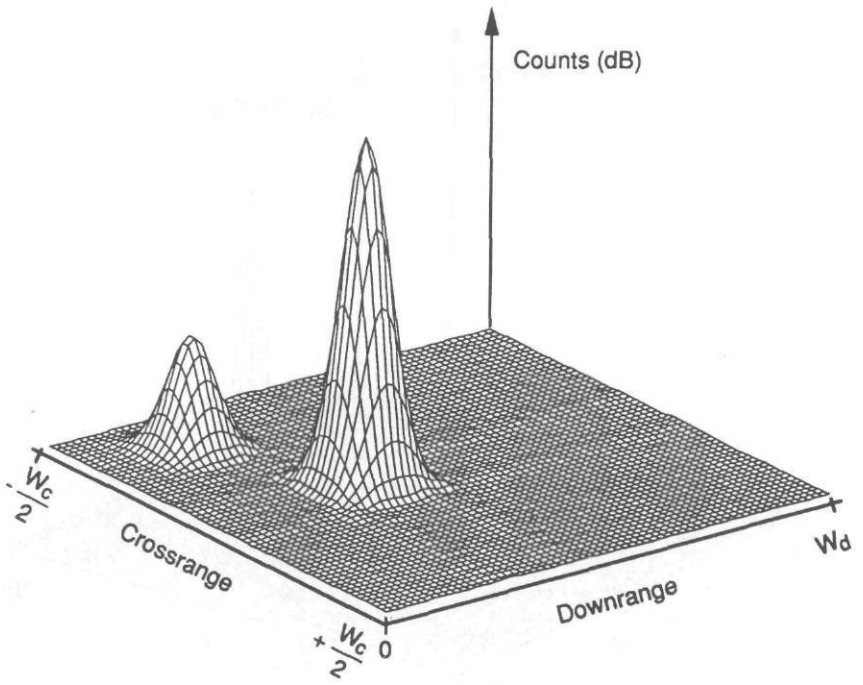

Figure 11.21(c) Same as example in Figure 11.21(a), showing the effects of a translational velocity of 5 m/s on the image.

11.5 SUMMARY

In this chapter we have provided an overview of the SFWF for generating high downrange resolution and inverse synthetic aperture processing for generating high crossrange resolution. When used in combination, high-quality, ultrahigh 2D images are produced of a target's RCS. Throughout the chapter numerous examples of the effects of both internal and external factors on the image quality were presented, along with pertinent equations and simulations. With proper attention to these factors the collector and the user of both one- and two-dimensional images will acquire the proper understanding of the limitations of the SFWF and ISAR data.

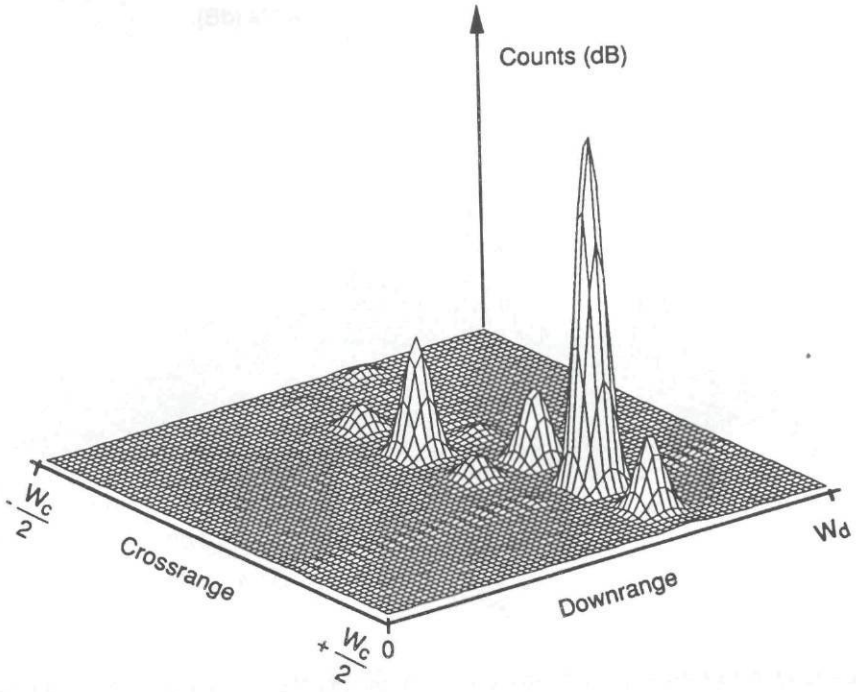

Figure 11.21(d) Same as example in Figure 11.21(a), showing the effects of sinusoidal vibration on the image. Modulation frequency is 10 Hz with 100-mm displacement.

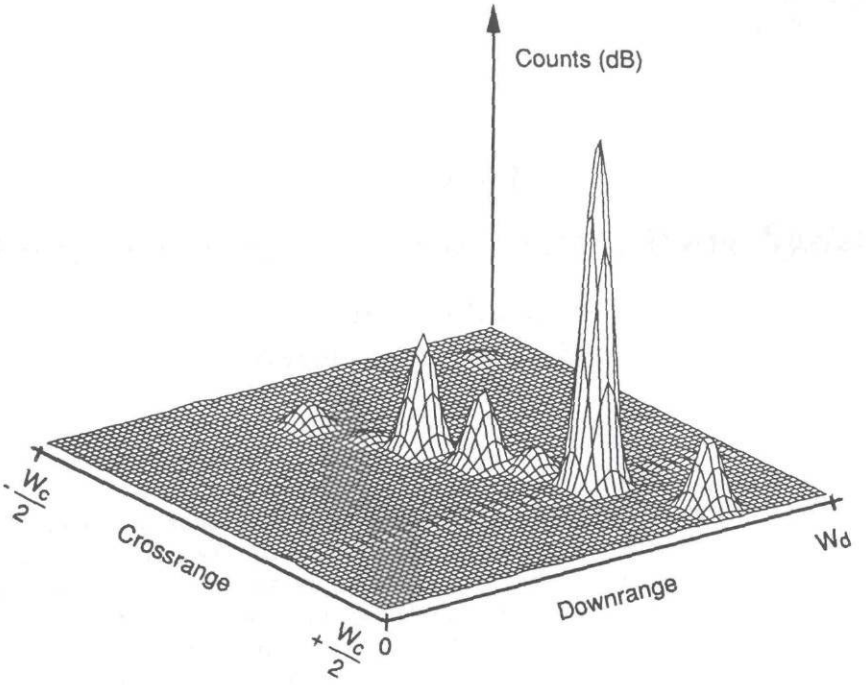

Figure 11.21(e) Same as example in Figure 11.21(a), showing the effects of sinusoidal vibration on the image. Modulation frequency is 200 Hz with 100-mm displacement.

REFERENCES

[1] Einstein, T. H., "Generation of High Resolution Radar Range Profiles and Range Profile Auto-Correlation Functions Using Stepped-Frequency Pulse Trains," Massachusetts Institute of Technology, Lincoln Laboratory, Project Report TT-54, October 18, 1984.

[2] Wehner, D. R., *High Resolution Radar*, Norwood, MA: Artech House, 1987, pp. 273–339.

Chapter 12
Frequency-Modulated Continuous Wave Systems

Samuel O. Piper
Georgia Institute of Technology

12.1 INTRODUCTION

This chapter presents techniques for predicting the performance of FMCW radar systems in terms of sensitivity and range resolution, with consideration of important contaminating effects. Sensitivity and range resolution are key components of the SNR and signal-to-clutter ratio, which determine the overall radar system performance. The sensitivity prediction includes the effect of internal reflections and leakage, considering the effects of phase noise in addition to thermal noise. The range resolution prediction includes the limits due to transmit bandwidth and coherent processing interval and the degradation due to frequency sweep nonlinearities.

This chapter is organized into four sections. This introduction is followed by the qualitative presentation of FMCW waveform tradeoffs in Section 12.2. Then the sensitivity and range resolution prediction techniques are presented with quantitative examples in Sections 12.3 and Section 12.4, respectively.

This discussion emphasizes the homodyne FMCW radar configuration as shown in Figure 12.1. Here, the LO signal is coupled from the transmit signal. This avoids the need for a separate LO. The resulting cost and volume savings make the homodyne FMCW radar configuration attractive for low-cost systems such as in smart munitions. The examples in this chapter are representative for smart munitions applications, but FMCW radar is also used for ground penetration radar, indoor RCS ranges, and other short-range applications.

This chapter concerns linear FMCW radar waveforms such as the sawtooth and triangle FMCW waveforms shown in Figure 12.2. Sinusoidal FMCW waveforms are used in radar altimeters and doppler navigation systems, but they are not appropriate for applications that require resolving multiple targets in range.

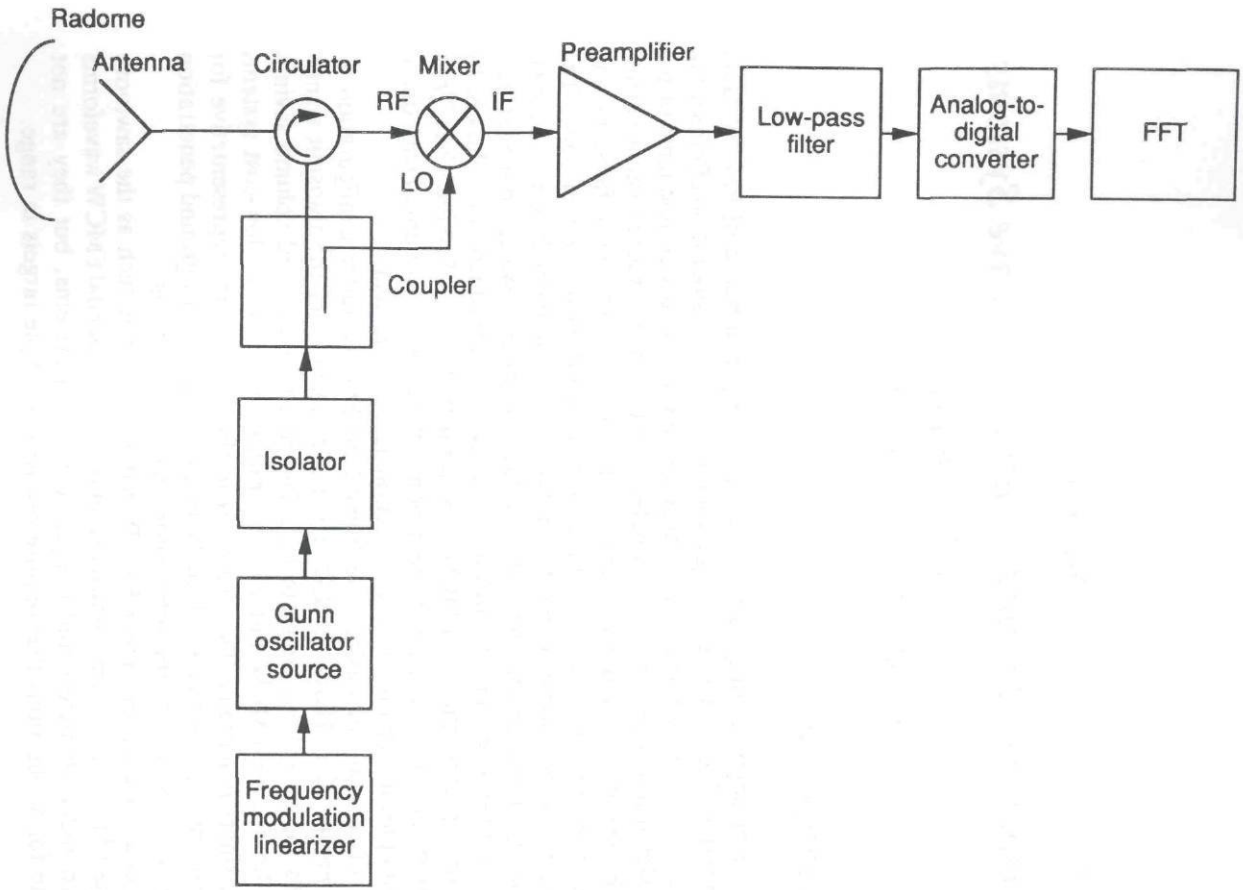

Figure 12.1 Block diagram of homodyne FMCW radar front end.

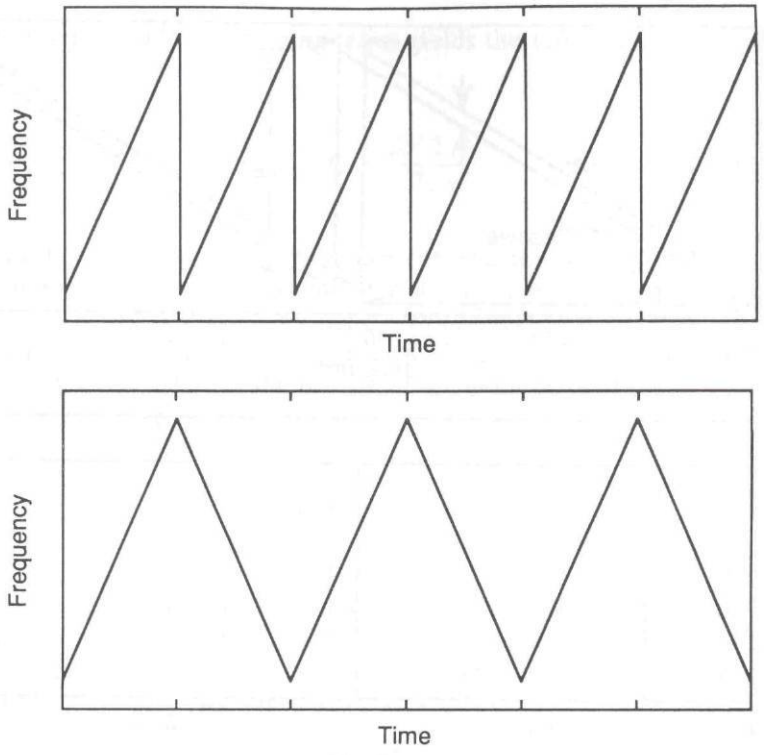

Figure 12.2 Frequency as a function of time for sawtooth and triangle waveforms.

12.2 FMCW WAVEFORM DESIGN TRADEOFFS

Figure 12.3 shows the transmit and receive frequency as a function of time for a sawtooth waveform, along with the resulting beat frequency output of the homodyne mixer, which is the difference in frequency between the transmit and receive waveforms.

Note in Figure 12.3 that the frequency deviation ΔF and modulation period T_m form a triangle similar to that formed by the beat frequency f_b and the transit time delay t_d. This relationship between the frequency deviation, modulation period, beat frequency, and transit time is called the FMCW equation:

$$\frac{f_b}{t_d} = \frac{\Delta F}{T_m} \tag{12.1}$$

where:

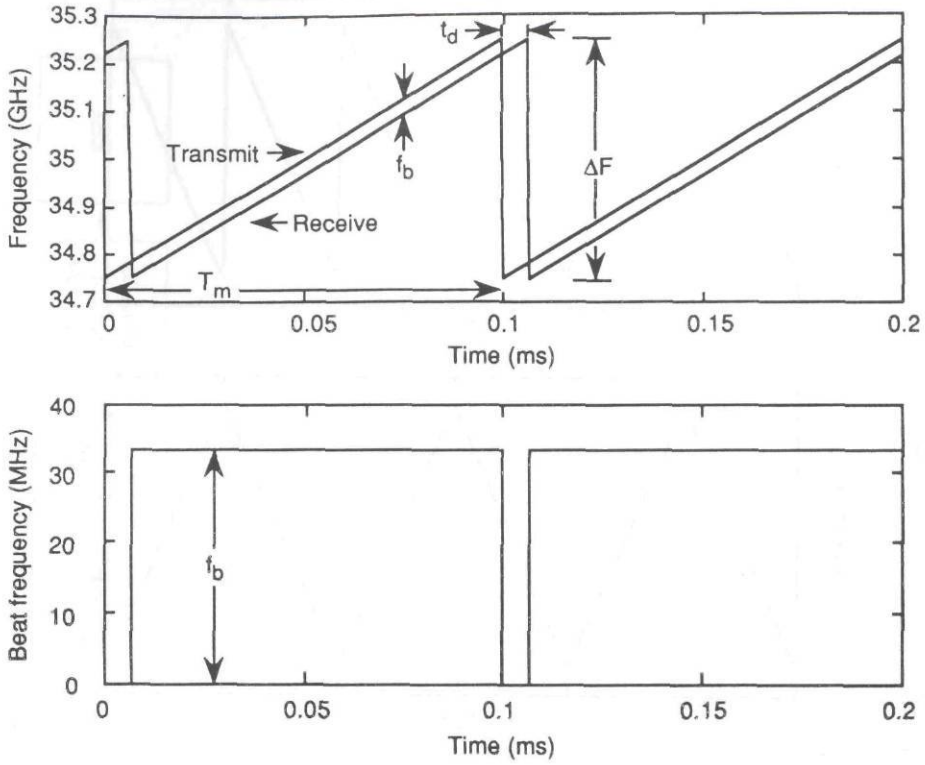

Figure 12.3 Transmit and receive frequency as a function of time showing beat frequency.

f_b = beat frequency,
t_d = round trip propagation time delay,
ΔF = frequency deviation, and
T_m = modulation period.

The round trip propagation time t_d is given by:

$$t_d = 2\,R/c \tag{12.2}$$

where:

R = range to target, and
c = propagation velocity = 3.0×10^8 m/s.

Substituting for t_d and rearranging terms yields the following expression for beat frequency:

$$f_b = \frac{\Delta F\, 2\, R}{T_m c} \tag{12.3}$$

Note that beat frequency is linearly proportional to the frequency deviation and to the range and inversely proportional to the modulation period. For the example in Figure 12.3, with 500-MHz frequency deviation, 0.1-ms modulation period, and 1-km range, the resulting beat frequency is 33.3 MHz. For the sawtooth waveform the modulation period T_m is the inverse of the modulation frequency f_m. Thus, the FMCW equation can also be written:

$$f_b(\text{sawtooth}) = \frac{\Delta F\, 2\, f_m R}{c} \tag{12.4}$$

The equation for the magnitude of the beat frequency for triangle wave modulation includes an additional factor of 2 in the numerator because the period of the triangle wave, including both upsweep and downsweep, is twice that of the sawtooth wave for the same frequency slew rate.

$$f_b(\text{triangle}) = \frac{\Delta F\, 4\, f_m R}{c} \tag{12.5}$$

For moving targets the doppler effect will shift the frequency of the received signals. The doppler frequency shift f_d is given by:

$$f_d = \frac{2\, Vf}{c} \tag{12.6}$$

where:

f_d = doppler frequency shift,
V = target velocity relative to the radar, and
f = nominal radar frequency.

For high-velocity targets and high-frequency radars this doppler frequency shift is significant. At 35 GHz, for example, the doppler frequency shift is 233 Hz/

(m/s). For moving targets the beat frequency for an FMCW sawtooth waveform that sweeps up in frequency is given by:

$$f_b = \frac{-\Delta F 2R}{T_m c} + \frac{2Vf}{c} \tag{12.7}$$

Here the beat frequency depends on both range and velocity. The waveform must be modified to have two frequency slew rates or slopes in order to resolve this range-doppler coupling. The triangle waveform with alternate up and down frequency sweeps is a common choice. For the triangle waveform, range is linearly proportional to the difference in the upsweep and downsweep beat frequencies, and velocity is proportional to the sum of the beat frequencies. For the triangle waveform, the upsweep and downsweep beat frequencies are given by:

$$f_b(\text{triangle, upsweep}) = \frac{-\Delta F 4R}{T_m c} + \frac{2Vf}{c} \tag{12.8}$$

and:

$$f_b(\text{triangle, downsweep}) = \frac{\Delta F 4R}{T_m c} + \frac{2Vf}{c} \tag{12.9}$$

So that range is given by:

$$R = \frac{T_m c}{8\,\Delta F}\left(f_{b(\text{downsweep})} - f_{b(\text{upsweep})}\right) \tag{12.10}$$

and velocity is given by:

$$V = \frac{-c}{4f}\left(f_{b(\text{downsweep})} + f_{b(\text{upsweep})}\right) \tag{12.11}$$

FMCW Waveform Tradeoffs

Choosing the FMCW waveform parameters for a given application requires careful attention to numerous tradeoffs. Table 12.1 summarizes the tradeoffs in decreasing and increasing the frequency deviation, modulation period, and beat frequency [1].

Decreasing the frequency deviation reduces the RF bandwidth over which the antenna and other front-end components must maintain low VSWR and other performance. The RF source bandwidth can often be traded off in favor of higher

Table 12.1
FMCW Waveform Tradeoffs

Waveform Parameter	*Reasons To Decrease*	*Reasons To Increase*
Frequency deviation	Narrower bandwidth RF components Higher power sources available Lower source phase noise	Finer ideal range resolution Lower radiated power spectral density Increase beat frequency
Modulation period	Increase beat frequency Avoid interference with conical scan and other modulations	Increase coherent processing interval Increase effective processed transmit bandwidth and power Better range and doppler resolution Narrower bandwidth linearizer
Beat frequency	Narrower bandwidth range bin filters Less beat frequency bandwidth required to cover given range swath Greater source phase noise correlation	Lower FM noise at greater separation from carrier

output power and lower phase noise. Increasing the frequency deviation offers finer ideal range resolution, lower radiated power spectral density, and increased beat frequency.

Decreasing the modulation period will also increase the beat frequency. Decreasing the modulation period increases the modulation frequency, helping to avoid interference with any conical scan demodulation, automatic gain control, or other internal processing control loops. Increasing the modulation period increases the coherent processing interval and both the effective processed transmit bandwidth and power. The longer coherent processing interval offers the potential for finer receiver frequency resolution and consequently finer range and doppler resolution, as described in Section 12.4. Increasing the modulation period decreases the modulation frequency and the required bandwidth for the frequency sweep linearity compensation circuitry [2].

The FMCW beat frequency signal is processed with narrowband filters to form the range resolution bins. For lower beat frequencies the receiver bandwidth required for each range bin filter is less for a given range resolution, as is the total receiver bandwidth required to cover a given range swath. For lower beat frequencies the phase noise of the transmit and receive signals is more correlated. This acts to reduce phase noise effects and improve sensitivity. At higher beat

frequencies, the lower FM noise of the carrier acts to improve receiver sensitivity. These contributors to system noise are analyzed in Section 12.3. For higher beat frequencies a given doppler shift corresponds to a smaller apparent shift in range.

Covering a slant range swath requires a bank of beat frequency filters in the receiver. For longer modulation periods the beat frequency may be low enough for direct A/D conversion and range bin filtering with FFT techniques. This permits convenient application of weighting functions to reduce range sidelobes. The A/D converter and digital processing must have wide dynamic range because radar returns from near and far ranges are present simultaneously. For a 1-ms modulation period, with 500-MHz frequency deviation and 1-km range, the beat frequency is 3.3 MHz, requiring a digital sampling rate of at least twice that frequency, or 6.7 MHz, to satisfy the Nyquist criterion. For a 0.1ms modulation period the beat frequency is 33.3 MHz, which is less convenient for sampling and digital processing. For higher beat frequencies the range bin filtering can be realized with analog filter banks. This approach may require gating to eliminate transients due to the change in beat frequency at the end of the transmit frequency sweeps.

12.3 SENSITIVITY IN FMCW RADAR

Because the FMCW radar transmits and receives simultaneously, a major challenge is isolating the received signal from the transmit signal, which may be more than 120 dB greater than the receive signal. The FMCW radar designer may achieve some of the isolation with separate transmit and receive antennas, with a circulator that isolates the transmit and receive signals that are traveling in different directions, or with different polarizations on transmit and receive. The choice is guided by the required sensitivity, available antenna aperture, and cost. Additional isolation results from modulating the transmit frequency to produce a frequency difference between the transmit and receive waveforms. The sensitivity of an FMCW homodyne radar is usually not limited by the thermal noise in the receiver, but by other more powerful contaminating internal noise components [3]. The signal-to-interference ratio and thresholding technique determine the detection performance for the radar. Received signal power is determined by calculation, using the radar equation. This section provides a methodology for determining the interference noise power.

Table 12.2 gives the total noise power at the mixer preamplifier output in a 1-kHz bandwidth for a simple 35-GHz FMCW homodyne radar, including components due to thermal noise, circulator leakage, antenna reflections, and mixer LO leakage. Here, the antenna reflection dominates the other components and determines the total noise power. Figure 12.4 illustrates these noise components in the radar front end. The following subsections present the detailed calculation of the noise components at 3.3 MHz, corresponding to the beat frequency for a

Table 12.2
Total System Noise Power and Noise Components

Noise Component	*Power at Mixer Preamplifier Output (in 1-kHz bandwidth)*
Thermal noise	−116.5 dBm
Antenna reflection	−102.9 dBm
Circulator leakage	−129.1 dBm
Mixer LO leakage	−151.3 dBm
Total noise power	−102.9 dBm

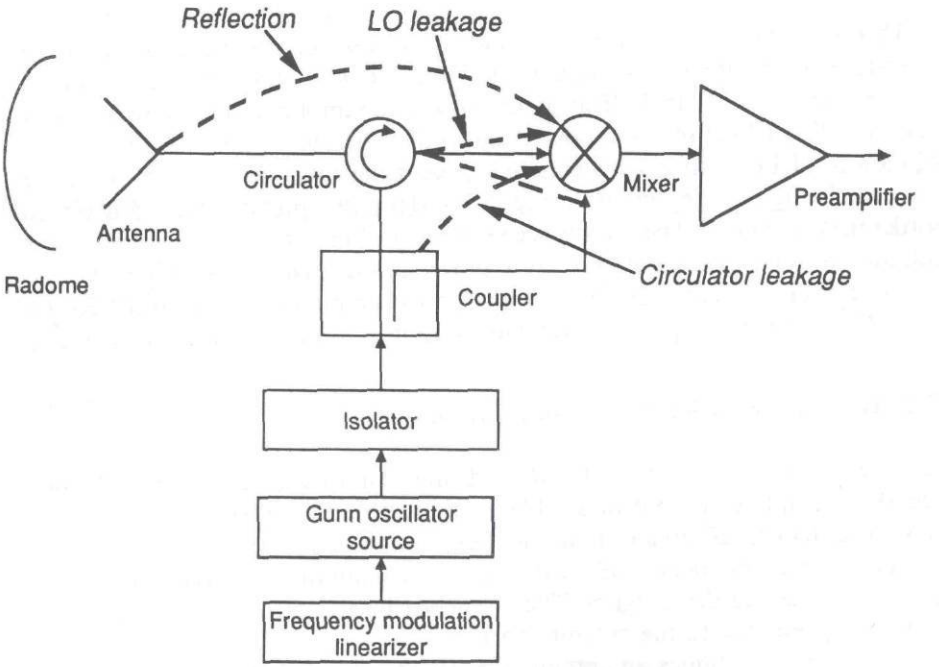

Figure 12.4 Reflection and internal noise components.

sawtooth waveform with a 500-MHz frequency deviation, 1 ms modulation period, and 1km target range. This example is based on current discrete component technology [4].

12.3.1 Thermal Noise

The thermal noise power referenced to the antenna port is given by:

$$N = kTBFL_r \tag{12.12}$$

where:

k = Boltzmann's constant = 1.38×10^{-23} W/(Hz·K)
T = reference temperature = 290K,
B = bandwidth,
F = noise figure, and
L_r = receiver losses [5].

This assumes that the antenna points at an absorbing surface and that the temperature of the RF components is 290K. Table 12.3 shows that the thermal noise component is −116.5 dBm at the mixer preamplifier output in a 1-kHz bandwidth. The 1-kHz receiver noise bandwidth is based on the ideal frequency resolution available with a 1-ms coherent processing interval. The 7.5-dB single sideband noise figure is representative for a 35-GHz mixer preamplifier using silicon Schottky barrier diodes. The 0.8-dB receiver loss is due to the insertion loss of the circulator. In order to compute the noise power at the mixer preamplifier output, the noise power referenced to the antenna port is amplified by the 20-dB RF-to-IF gain, G_p, of the mixer-preamplifier combination, less the 0.8-dB circulator loss.

12.3.2 Antenna Reflection FM Noise Power Calculation

Table 12.4 shows the calculation of −102.9 dBm FM noise due to antenna reflection at the IF preamplifier output in a 1-kHz bandwidth at 3.3-MHz beat frequency. This is more than 13 dB greater than the thermal noise component. The 25.5-dBm source power is attenuated 0.5 dB by the isolator and another 0.5 dB by the coupler that provides the LO drive signal. The circulator insertion loss is 0.8 dB, so that 23.7 dBm is presented to the antenna port.

This example assumes an antenna VSWR of 1.3:1. From Saad [6], the ratio of reflected power P_r to incident power is equal to:

$$\frac{P_r}{P_i} = \left(\frac{\text{VSWR} - 1}{\text{VSWR} + 1}\right)^2 \tag{12.13}$$

where:

Table 12.3
Thermal Noise Power Calculation

Symbol	*Description*	*Value*	*Value (dB)*
k	= Boltzmann's constant	= 1.38×10^{-20} mW/(Hz·K)	= −198.6 dBm/(Hz·K)
T	= Reference temperature	= 290K	= 24.6 dBK
B	= Receiver noise bandwidth	= 1 kHz	= 30.0 dBHz
F	= System noise figure (single sideband)	= 5.6	= 7.5 dB
L_r	= Receiver losses	= 1.2	= 0.8 dB
G_p	= Mixer preamplifier RF to IF gain	= 100	= 20.0 dB
L_r	= Receiver losses	= 0.83	= −0.8 dB
N	= Noise power at the mixer preamplifier output		−116.5 dBm

Table 12.4
Antenna Reflection FM Noise Power Calculation

Noise Power Calculation Component	*Value*
Source power (355 mW)	25.5 dBm
Isolator insertion loss	−0.5 dB
Total loss for 20-dB LO coupler	−0.5 dB
Circulator insertion loss	−0.8 dB
Antenna power reflection coefficient (1.3:1 VSWR)	−17.7 dB
Circulator insertion loss	−0.8 dB
FM noise power density at 3.3 MHz	−115.0 dBc/Hz
Phase noise correlation factor (3.3 MHz, 0.333 ns)	−43.1 dB
Range bin bandwidth (1 kHz)	30.0 dBHz
Mixer preamp RF-to-IF gain	20.0 dB
Antenna reflection FM noise power at 3.3 MHz	−102.9 dBm/1kHz

P_r = reflected power, and
P_i = incident power.

Thus, the reflection from a 1.3 VSWR is 17.7 dB less than the incident power. The reflected signal experiences another 0.8dB insertion loss in passing through the circulator to the mixer input. The nominal beat frequency is 3.3 MHz for the 500-MHz frequency deviation, 1-ms modulation period, and 1-km range. At that offset from the carrier a representative value for the single sideband FM noise is approximately −115 dBc/Hz for varactor-tuned Gunn diode oscillators.

Using the same source to transmit and receive a signal reduces the effect of the source's phase noise because the noise of the received signal is correlated to the transmitted signal [7]. This phase noise correlation factor K^2 depends on the offset frequency from the carrier and the delay between the transmit and receive signals. For the FMCW homodyne radar the carrier offset is the beat frequency f_b. For the antenna reflection the delay t_r is the difference between the source-to-mixer LO port path and the source-to-antenna-reflection-to-mixer RF port path.

$$K^2 = 2 \cdot [1 - \cos(2\pi f_b t_r)] \tag{12.14}$$

Because

$$\sin^2 \alpha = \frac{1}{2}(1 - \cos 2\alpha) \tag{12.15}$$

then

$$K^2 = 4 \sin^2(\pi f_b t_r) \tag{12.16}$$

or

$$K^2 \cong 4(\pi f_b t_r)^2, \text{ for small products of } f_b \text{ and } t_r \tag{12.17}$$

This example assumes that the delay is 0.333 ns, corresponding to 100-mm freespace path length difference between the path from the source to the mixer LO port and the path from the source to the antenna reflection to mixer RF port. This yields a correlation factor $K^2 = -43.1$ dB.

Lower beat frequencies result in both greater FM noise power density and greater phase noise correlation. The phase noise correlation factor is approximately proportional to the square of the beat frequency for the internal reflection and leakage signals. This is because the product of f_b and t_r is small. Over regions where the source FM noise follows a 20-dB/decade slope, these effects will approximately cancel one another, resulting in approximately constant noise power as a function of beat frequency. Figure 12.5 shows the phase noise correlation and the FM noise power density as a function of beat frequency from 0.33 MHz to 3.3 MHz. The phase noise correlation is shown for a 0.333-ns delay. The FM noise power density follows the 20-dB/decade slope over this region.

As discussed in Chapter 2, the FM noise closer to the carrier may follow a 30-dB/decade slope resulting in greater noise for lower beat frequencies. Adjusting

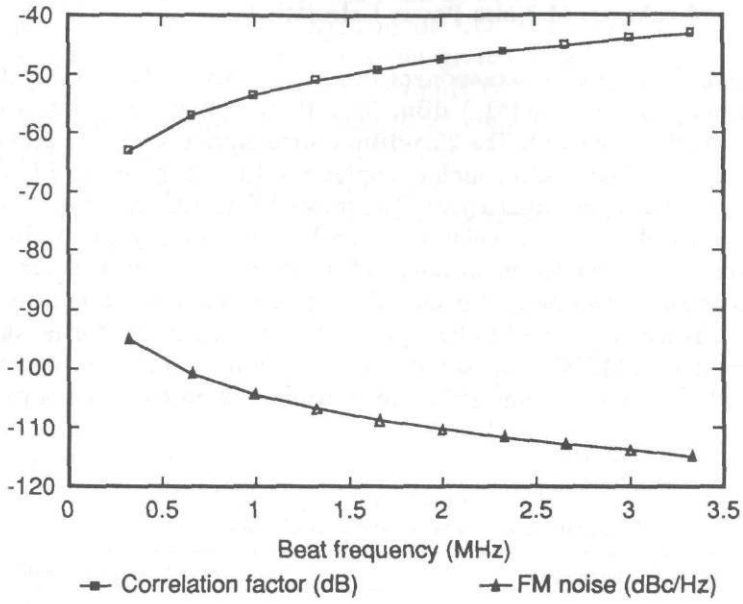

Figure 12.5 Phase noise correlation factor and FM noise power density as a function of beat frequency.

the LO path length to match the strongest reflected signal path will improve the phase noise correlation and reduce the reflected noise component. This technique will be less effective for applications such as radome reflections when the antenna scanning results in changing distance to the reflection. This will also increase the path and decrease the phase noise correlation for other reflected signals and internal leakage signals.

12.3.3 Circulator Leakage

As illustrated in Table 12.5, the FM noise power due to circulator leakage is −129.1 dBm in a 1-kHz bandwidth at the mixer preamplifier output. This is more than 12 dB below the thermal noise component. This noise component is due to power that leaks in the opposite direction than the circulator polarity, directly into the mixer preamplifier input. Here, the FM noise power density is the same as for the antenna reflection calculation. The phase noise correlation factor is lower than for the antenna reflection because a shorter 0.1-ns (30-mm) path length difference is assumed.

12.3.4 Mixer LO Leakage FM Noise Power Calculation

Table 12.6 shows that the noise component due to the mixer LO leakage at the mixer preamplifier output is −151.3 dBm in a 1kHz bandwidth. This is over 35 dB less than the thermal noise. The 25.5-dBm source output power is attenuated 0.5 dB by the isolator. The 20-dB coupler couples 5.0 dBm to the mixer LO port, to satisfy the LO drive level requirement. The mixer RF to LO isolation is 20 dB so that −15 dBm leaks to the circulator. A VSWR of 1.3:1 is assumed for the interface between the mixer RF input port and the circulator, which corresponds to a −17.7 dB power reflection coefficient. The phase noise correlation factor for this mixer LO leakage is assumed to be equal to that for the circulator leakage.

This homodyne FMCW radar sensitivity prediction example illustrates the importance of a low VSWR antenna and radome to minimize reflected noise power,

Table 12.5
Circulator Leakage FM Noise Power Calculation

Noise Power Calculation Component	*Value*
Source power (355 mW)	25.5 dBm
Isolator insertion loss	−0.5 dB
Total loss for 20-dB LO coupler	−0.5 dB
Circulator isolation	−35.0 dB
FM noise power density at 3.3 MHz	−115.0 dBc/Hz
Phase noise correlation factor (3.3 MHz, 0.1 ns)	−53.6 dB
Range bin bandwidth (1 kHz)	30.0 dBHz
Mixer preamp RF to IF gain	20.0 dB
Circulator leakage FM noise power at 3.3 MHz	−129.1 dBm/1kHz

Table 12.6
Mixer LO Leakage Noise Power Calculation

Noise Power Calculation Component	*Value*
Source power (355 mW)	25.5 dBm
Isolator insertion loss	−0.5 dB
Coupling for 20-dB LO coupler	−20.0 dB
Mixer RF to LO isolation	−20.0 dB
Circulator power reflection coefficient (1.3:1 VSWR)	−17.7 dB
FM noise power density at 3.3 MHz	−115.0 dBc/Hz
Phase noise correlation factor (3.3 MHz, 0.1 ns)	−53.6 dB
Range bin bandwidth (1 kHz)	30.0 dBHz
Mixer preamp RF to IF gain	20.0 dB
Mixer leakage FM noise power at 3.3 MHz	−151.3 dBm/1kHz

the need for a circulator with high isolation to minimize leakage noise, and the value of low LO to RF mixer leakage and low LO drive requirements. In a highly integrated transceiver, such as microwave integrated circuits, the short path lengths improve the phase noise correlation. In an FMCW system with separate antennas there will be no noise component due to antenna reflection, and the coupling between the antennas will take the place of the circulator leakage. For applications with a high VSWR antenna or radome, the interrupted FMCW technique may be used to overcome the effect of reflected noise, while realizing other advantages of the FMCW waveform [8].

12.4 RANGE RESOLUTION

This section presents techniques for predicting the range resolution for a linear FMCW homodyne radar, including how the ideal range resolution is degraded by both the reduction in effective processed transmit bandwidth, or the equivalent reduction in coherent processing interval, and the frequency sweep nonlinearities.

12.4.1 Ideal Range Resolution

For any radar waveform the ideal range resolution ΔR_0 is linearly proportional to time resolution ΔT and inversely proportional to the bandwidth of the transmit waveform ΔF, as given below:

$$\Delta R_0 = \frac{c\Delta T}{2} = \frac{c}{2\Delta F} \tag{12.18}$$

where:

ΔR_0 = ideal range resolution,
ΔT = time resolution, and
ΔF = bandwidth of the transmit waveform.

For example, 500-MHz bandwidth corresponds to time resolution no less than 2 ns and range resolution no less than 0.3m. The frequency deviation is ordinarily held constant in linear FMCW waveforms.

12.4.2 Effective Processed Transmit Bandwidth

For a homodyne FMCW radar the overlap between the transmit and receive frequency sweeps is reduced by the delay of the receive signal due to the round trip

propagation time to the target t_d, as shown in Figure 12.3. The reduction in overlap degrades the range resolution. The range resolution degradation may be analyzed in terms of the reduction in effective processed transmit bandwidth or in terms of the decrease in the coherent processing interval. For the sawtooth waveform, the overlap reduction results in a reduced effective processed transmit bandwidth $\Delta F'$:

$$\Delta F' = \Delta F - \frac{\Delta F}{T_m} t_d = \Delta F\left(1 - \frac{t_d}{T_m}\right) \tag{12.19}$$

and degraded range resolution ΔR:

$$\Delta R = \frac{c}{2\Delta F\left(1 - \dfrac{t_d}{T_m}\right)} \tag{12.20}$$

Table 12.7 summarizes the transit time effect on effective processed transmit bandwidth and range resolution. For 500-MHz frequency deviation and 1-ms modulation period, the 1-km range with 6.7-ms transit time reduces the effective processed transmit bandwidth by 3.3 MHz. The effective processed transmit bandwidth may be further reduced by the doppler shift for very-high-velocity targets that shifts a portion of the receive signal bandwidth outside of the receive RF bandwidth.

Normally the modulation period will be at least 5 times the transit time for the maximum range so that the effective processed bandwidth is at least 80% of the total bandwidth. This will also keep the loss in effective processed transmit power less than 1 dB. For an FMCW radar with a separate sweeping LO that delays the start of the demodulating sweep by the propagation time, this loss due to the propagation time will be negligible. Of course, a separate highly linear LO adds complexity and the phase noise correlation described in Section 12.3 will not apply.

Table 12.7
Effective Processed Transmit Bandwidth and Range Resolution

	Frequency	*Time*	*Range*
Total frequency deviation	500.0 MHz		
less product of 6.7 μs transit time and 500 MHz/ms frequency sweep rate	−3.3 MHz		
Effective processed transmit bandwidth	496.7 MHz		
which implies ideal time resolution		2.01 ns	
and ideal range resolution			0.302m

12.4.3 Constant Modulation Period

For a homodyne FMCW radar that maintains constant frequency deviation and constant modulation period, the beat frequency between the transmit and receive waveforms is linearly proportional to the range to the target. Thus, this radar's range resolution is limited by the frequency resolution of the receiver. For a directly tuned source, such as a varactor-tuned Gunn diode oscillator, the transmit signal will be coherent during the frequency sweep, but not necessarily from sweep to sweep. Thus, the coherent processing interval is equal to the FM period, less the propagation time. This limits the minimum receiver frequency resolution to the inverse of that coherent processing interval. Rearranging terms from (12.3):

$$R = \frac{T_m c}{\Delta F2} f_b \tag{12.21}$$

So range resolution ΔR is given by:

$$\Delta R = \frac{T_m c}{\Delta F2} \Delta f_b \tag{12.22}$$

where Δf_b = beat frequency resolution.

Because the beat frequency resolution of the receiver is inversely proportional to the modulation period less the round trip propagation time [9], or:

$$\Delta f_b = \frac{1}{T_m - t_d} \tag{12.23}$$

then the range resolution is given by:

$$\Delta R = \frac{cT_m}{2\Delta F} \frac{1}{T_m - t_d} \tag{12.24}$$

This expression for range resolution is equivalent to (12.20), which was derived in Section 12.4.2. Table 12.8 shows how the transit time affects the coherent processing interval and the range resolution.

Figure 12.6 shows the interrelationships between the FMCW parameters with a quantitative example. The parameters shown along the right side of the figure are the independent parameters. The processing interval limited range resolution is inversely proportional to the coherent processing interval with a proportionality constant equal to the propagation velocity divided by twice the frequency slew

Table 12.8
Coherent Processing Interval and Range Resolution

	Frequency	*Time*	*Range*
Sweep modulation period		1000.0 μs	
less 6.7 μs transit time		6.7 μs	
Coherent processing interval		993.3 μs	
which implies ideal frequency resolution	1,007 Hz		
and ideal range resolution			0.302m
at 3.3-MHz/km frequency to range ratio.			

rate. For the example in Figure 12.6, the ideal range resolution is 0.3m and the processing interval limited range resolution is 0.302m. The effect of frequency sweep nonlinearities is analyzed in Section 12.4.5.

While performing the Fourier transform process, weighting to reduce the frequency sidelobes will broaden the receiver frequency resolution and therefore the range resolution. The minimum receiver range bin bandwidth is also limited by the target acceleration and jerk. For example, at 35 GHz for a receiver matched to the 3.3-kHz nonlinearity bandwidth, acceleration relative to the radar greater than 14.3 m/s^2 will result in smearing the target return over multiple frequency resolution bins.

12.4.4 Constant Beat Frequency

A homodyne FMCW radar with constant frequency deviation can operate with a constant beat frequency by adjusting the modulation period in direct proportion to the range. This requires a frequency discriminator to measure the beat frequency and a control loop to maintain the proper modulation period, along with a compensating frequency sweep linearizer with variable period. This configuration is associated with relatively high beat frequencies and receivers with banks of analog filters. Here, the radar receiver range bin frequency filters correspond to a fixed percentage of the range to the target. Thus, at close range the range resolution is finer in absolute terms than at long range. This is moderated somewhat by the practical problems associated with maintaining good frequency sweep linearity at high modulation frequencies and also by the theoretical limit for range resolution. From (12.22):

$$\Delta R(\text{constant } f_b) = \frac{c\Delta f_b T_m}{2\Delta F} \tag{12.25}$$

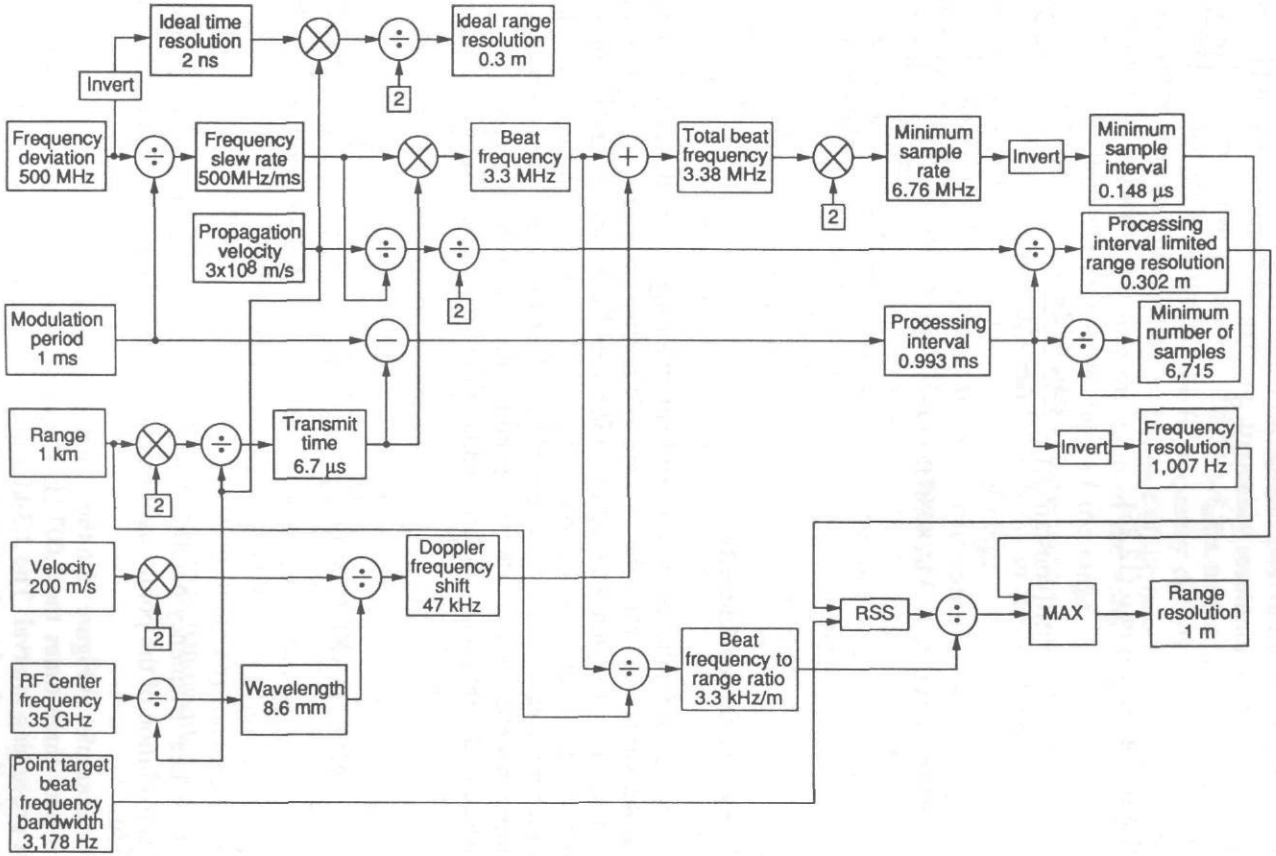

Figure 12.6 FMCW parameter interrelationships.

and rearranging (12.3):

$$T_m = \frac{\Delta F 2R}{f_b c} \tag{12.26}$$

Then substituting (12.26) into (12.25):

$$\Delta R(\text{constant } f_b) = \frac{c\Delta f_b}{2\Delta F} \frac{\Delta F 2R}{f_b c} \tag{12.27}$$

$$\Delta R(\text{constant } f_b) = \text{MAXIMUM OF}\left\{\frac{\Delta f_b}{f_b} R, \frac{c}{(2\Delta F)\left(1 - \frac{t_d}{T_m}\right)}\right\} \tag{12.28}$$

12.4.5 Frequency Sweep Linearity

The linearity of the frequency sweep also limits the range resolution. Often, even for an ideal point target, when the transmit and receive waveforms are mixed, the nonlinearities in the frequency sweep result in a beat frequency spectral width that is greater than the inverse of the coherent processing interval. In these cases the FMCW system designer will choose coarser receiver frequency resolution that is more closely matched to the expected spectral width of the target return.

Including the frequency sweep nonlinearities, the range resolution is given by:

$$\Delta R = \text{MAXIMUM OF}\left\{\frac{R}{f_b}\sqrt{B_b^2 + \Delta f_b^2}, \frac{c}{2\Delta F\left(1 - \frac{t_d}{T_m}\right)}\right\} \tag{12.29}$$

where B_b = beat frequency bandwidth of a point target. The first term accounts for the convolution of the point target bandwidth with the receiver beat frequency resolution.

For example, in Figure 12.6 the assumed point target bandwidth is 3,178 Hz, which is over three times the 1,007-Hz frequency resolution achievable with the 0.99-ms processing interval. The 3.3-kHz/m beat frequency to range ratio or scale factor results from the fact that the 3.3-MHz beat frequency corresponds to 1-km

range. The *square root of the sum of the squares* (rss) of the 3,178-kHz point target bandwidth and the 1,007-Hz receiver frequency resolution is 3.3 kHz, which corresponds to 1m range resolution. The 3,178-Hz nonlinearity bandwidth is only 6.4 ppm or 0.0006% of the 500-MHz frequency deviation. Alternatively, some investigators express linearity as a percentage of the nominal beat frequency. That convention is attractive because the ratio of the nonlinearity bandwidth to the nominal beat frequency equals the ratio of the range resolution to the nominal range. Under that convention the 3.3-kHz rss combination of nonlinearity bandwidth and receiver frequency resolution is 0.1% of the 3.3-MHz beat frequency and corresponds to range resolution 0.1% of range.

The spectrum of the product of two signals corresponds to the convolution of the spectra of the signals. For equal bandwidth gaussian spectra the convolved spectrum is wider than the individual spectra by the square root of two. Because the FMCW beat frequency spectrum results from mixing the transmit and receive signals, the bandwidth of the individual signals is broadened by approximately the square root of two. For this discussion the absolute frequency sweep nonlinearity bandwidth is defined to be the bandwidth that results from mixing the nonlinear frequency sweep with an ideally linear frequency sweep. Thus, absolute nonlinearity of 2,247 Hz is required to yield 3,178-Hz point target bandwidth. This 2.2-kHz absolute nonlinearity is only 4.5 ppm relative to the 500-MHz frequency deviation. For a typical varactor tuning sensitivity of 100 MHz/V, this corresponds to an extremely stringent 22-μV tuning voltage linearity requirement.

Closed-loop frequency sweep linearizers are needed to satisfy these stringent linearity requirements. For a Gunn diode oscillator the frequency tuning characteristic is nonlinear and sensitive to temperature and power supply variations. The closed-loop linearizer continuously compensates for these tuning errors. The linearizer may include a delay line discriminator to continuously measure the frequency slew rate and a control loop to maintain a constant rate.

Decreasing the modulation period to 0.1 ms, with the 500-MHz frequency deviation and 1-km range, increases the beat frequency to 33.3 MHz. For 1m range resolution the maximum rss combination of nonlinearity bandwidth and receiver frequency resolution increases to 33.3 kHz. The receiver filtering may be realized with analog filters for this higher center frequency and wider bandwidth.

The frequency sweep linearity will be ultimately limited by the inherent noise in the linearizer circuitry. The noise power P_n in a given bandwidth is given by:

$$P_n = kTB \tag{12.30}$$

where:

k = Boltzmann's constant,
T = temperature, and

B = noise bandwidth.

The noise voltage Vn is then given by:

$$Vn = \sqrt{P_n R_0} = \sqrt{kTBR_0} \tag{12.31}$$

where R_0 = characteristic impedance.

For a characteristic impedance of 1 kΩ (as might be expected for the linearizer output driver to the varactor tuning input), a 303K temperature, and a 1-MHz noise bandwidth, the rms noise voltage is approximately 2 μV, which is less than 10% of the 22-μV voltage tuning linearity requirement described above. The 1-MHz noise bandwidth for the linearizer avoids nonlinearities due to bandwidth limitations [2].

For short-range FMCW radar applications, good range resolution is possible with overall frequency sweep linearity somewhat worse than implied by this analysis, because of correlation between the nonlinearities in the transmit and receive waveforms. For example, a YIG-tuned oscillator with inductive tuning may offer excellent range resolution in an indoor RCS range, where the transit time is short relative to the correlation time of any nonlinearities in the frequency sweep. For Gunn diode oscillators with wide bandwidth varactor tuning and long target range, the transit time is long relative to the correlation in the nonlinearities [10], and these stringent linearity requirements must be satisfied.

Figures 12.7 and 12.8 illustrate the impact of the relationship between the transit time and the correlation time of the frequency sweep linearities. Figure 12.7 shows the transmit and receive frequency, along with the resulting beat frequency, as a function of time with sinusoidal nonlinearity with the same phase and period as the FM and 10-MHz peak amplitude. This large peak nonlinearity makes the effect more evident in the figures. The 6.7-μs transit time is short compared with the 100-μs nonlinearity period here and the beat frequency varies 4 MHz around the 33-MHz nominal value. In Figure 12.8 the nonlinearity period is decreased by a factor of 10. This 10-μs nonlinearity period is now comparable with the 6.7-μs transit time and, with the same peak nonlinearity, the resulting beat frequency varies 17 MHz around the nominal value.

As the technology for direct digital synthesis of RF waveforms advances, the present limitations of nonlinearity will be overcome. These sources offer more stability and coherence from sweep to sweep, permitting longer coherent processing intervals and finer frequency resolution. The FMCW synthesizer must step rapidly through many small frequency increments to avoid a wide beat frequency spectrum due to frequency step size. In order to achieve the 0.3m range resolution potential from a 500-MHz frequency deviation with 1-ms modulation period, the synthesizer must generate 500,000 1-kHz steps over the 1-ms period, or one step every 2 ns.

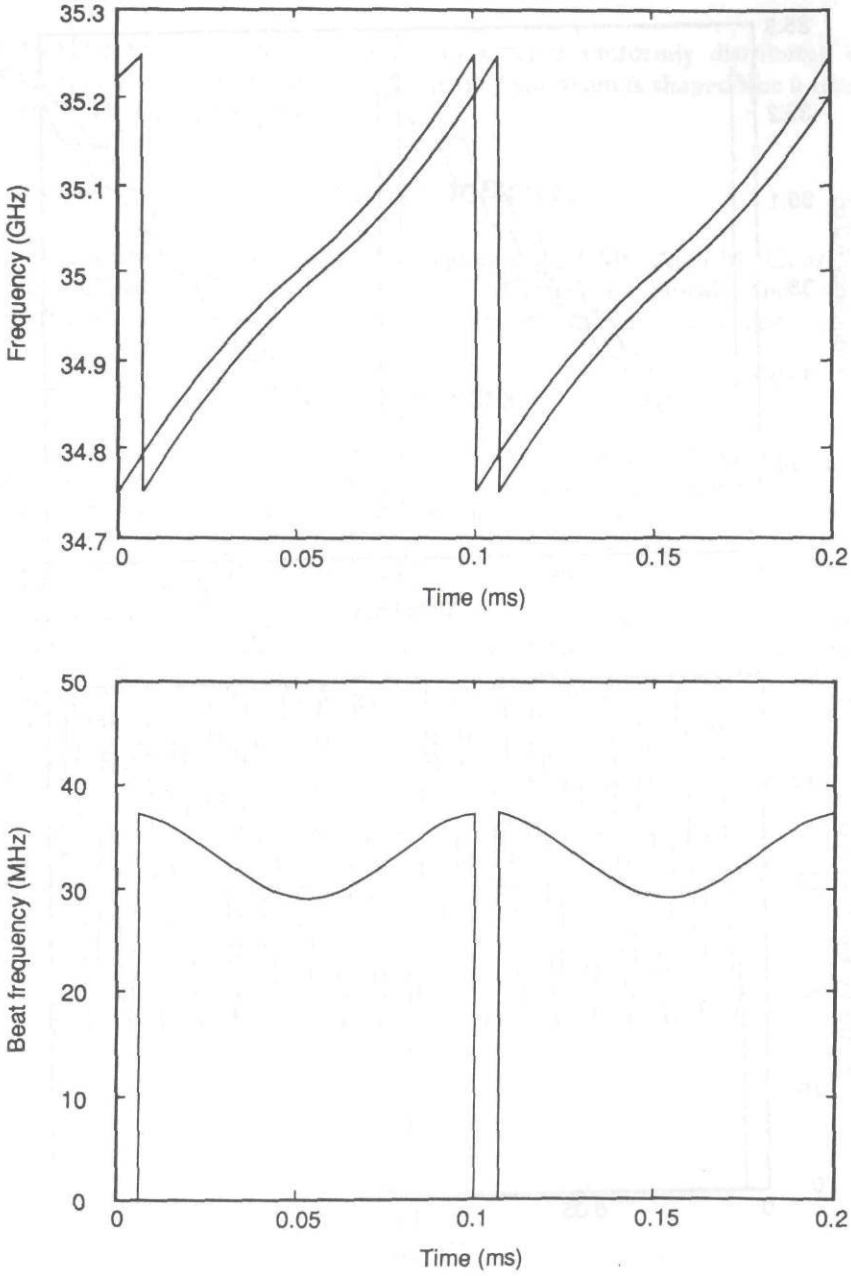

Figure 12.7 Transmit and receive frequency as a function of time with beat frequency for 0.1-ms nonlinearity period.

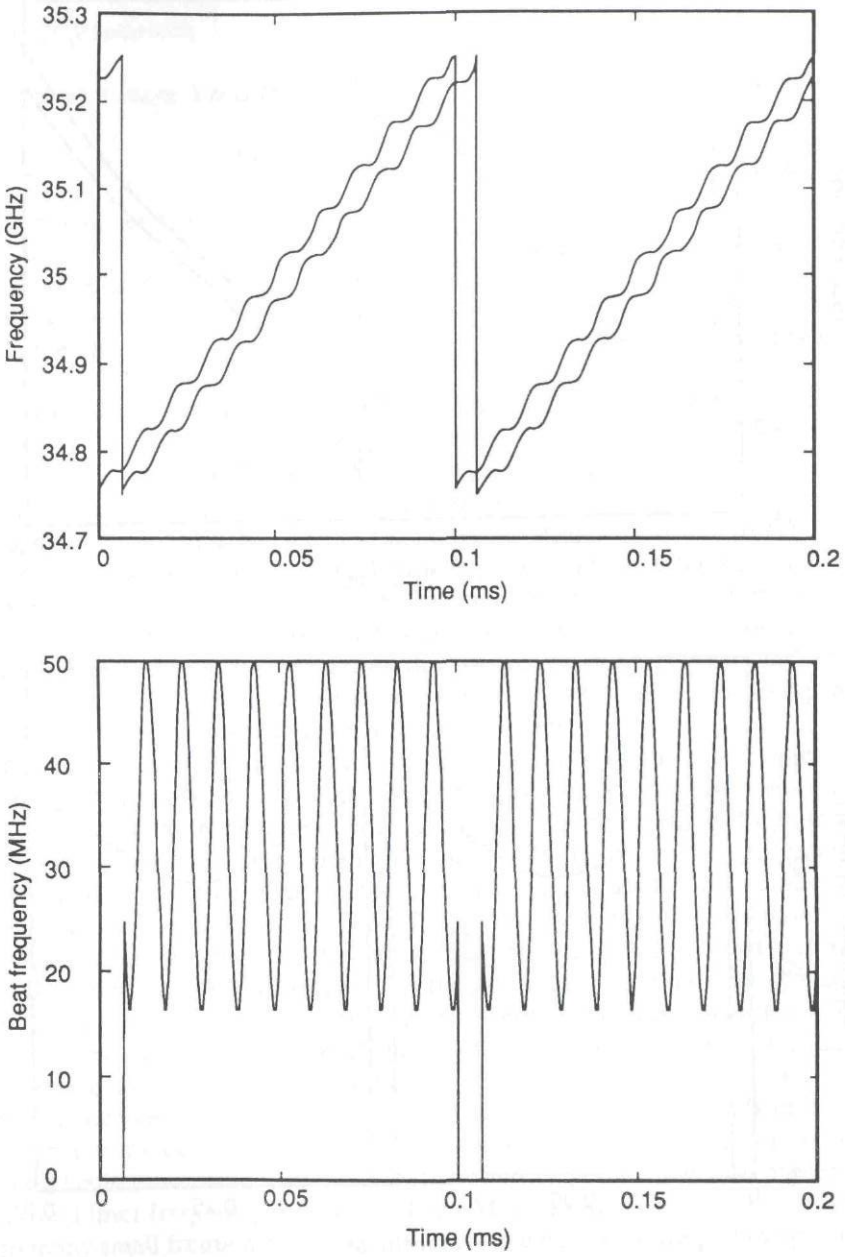

Figure 12.8 Transmit and receive frequency as a function of time with beat frequency for 0.01-ms nonlinearity period.

With 1-kHz frequency steps the frequency error is uniformly distributed over ± 0.5 kHz, and after mixing, the beat frequency spectrum is shaped like a triangle with ± 0.5-kHz halfpower points.

ACKNOWLEDGMENTS

The author wishes to acknowledge the suggestions of Mr. Alan M. Gauzens of Hercules Defense Electronics Systems, Inc., in Clearwater, Florida, and Dr. Ralston S. Robertson of Hughes Aircraft Company in Canoga Park, California.

REFERENCES

[1] Piper, S. O., "MMW Seekers," Chapter 14 in *Principles and Applications of Millimeter Wave Radar*, N. C. Currie and C. E. Brown, editors, Norwood, MA: Artech House, 1987, pp 647–692.

[2] Piper, S. O., "FMCW Linearizer Bandwidth Requirements," *Proc. 1991 IEEE National Radar Conf.*, IEEE Catalog Number 91CH2952-0, March 12–13, 1991, pp. 142–146.

[3] Saunders, W. K., "CW and FM Radar," Chapter 16 in *Radar Handbook*, M. I. Skolnik, editor, McGraw-Hill, 1970, pp. 16–26.

[4] Hughes Aircraft Company, Microwave Products Division, 1991 Millimeter-Wave Products Catalog.

[5] Barton, D. K., *Modern Radar System Analysis*, Norwood, MA: Artech House, 1988, p. 14.

[6] Saad, T. S., *Microwave Engineer's Handbook*, Norwood, MA: Artech House, 1971, p. 3.

[7] Goldman, S., "Oscillator Phase Noise Proves Important to Pulse-Doppler Radar Systems," *MSN*, February 1984, pp. 88–100.

[8] Roeder, R. S. and J. J. Teti, Jr., "Millimeter wave passive and active sensors for terrain mapping," *SPIE*, Vol 791, Millimeter Wave Technology IV and Radio Frequency Sources (1987), pp. 114–123.

[9] Robins, W. P., *Phase Noise in Signal Sources*, London: Peter Peregrinus Ltd., 1982.

[10] Piper, S. O., "FMCW Range Resolution for MMW Seeker Applications," *Proc. 1990 IEEE Southeastcon*, IEEE Catalog Number 90CH2883-7, April 1–4, 1990, pp. 156–160.

Chapter 13
Coherent Tracking

Joseph A. Bruder
Georgia Institute of Technology

13.1 REASONS FOR COHERENT TRACKING

There are a number of reasons why coherent processing is attractive for application to tracking radars. Typical noncoherent radars can provide tracking in range and in azimuth and elevation. However, most noncoherent radars fall short when trying to track a target in the presence of clutter. Coherent radars provide a fourth dimension, in that they can take advantage of the doppler frequency shifts imposed by moving targets on the radar returns and thus provide a means for clutter rejection. In addition, the processing of doppler returns provides the capability for sorting of multiple moving targets, the ability to reject interfering targets and spurious signals, and a precise means for the measurement of the target's radial velocity with respect to the radar. As a result, coherent processing using doppler information is vital to the performance of sophisticated ground-based and airborne tracking radar systems.

13.1.1 Target in Clutter Background

The radial component of motion of a target with respect to the radar will impose a doppler frequency shift on the radar returns. The doppler shift (f_d) imposed by target (t) is defined as:

$$f_d = f_t - f_c$$

where:

f_t = the center frequency of the target returns, and
f_c = the center frequency of the radar transmitter.

The doppler shift for the two-way transmission path can be shown to be [1]:

$$f_d = \frac{2v}{\lambda}$$

where:

v = radial component of target velocity, and
λ = wavelength of transmit frequency.

For a target against a clutter background, the doppler shift is detectable with a noncoherent radar because of the beating of the target return with that of the stationary clutter. Although clutter rejection can be performed by some noncoherent radars, the clutter rejection is somewhat limited, and this noncoherent clutter rejection technique will not work unless the target is in a clutter background.

One of the most important reasons for coherent tracking is that the doppler shifts imposed by moving targets on the radar returns provide a means for rejection of the relatively stationary clutter returns. An example of this is the network of aerostat radars currently being deployed along the southern border of the United States for the purpose of detecting low-flying aircraft. Because of the lookdown situation, the radar must observe the aircraft against a background of terrain clutter. There are a number of airborne radars that also need to rely upon coherent processing for the elimination of clutter. These include airborne surveillance aircraft and fighter aircraft with lookdown target tracking capability. In the case of airborne radars, the doppler frequency imposed by the motion of the clutter must be removed in order to allow tracking of the target.

13.2 EXPLOITATION OF DOPPLER SPECTRUM

The frequency spectrum of a radar is strongly dependent upon the type of radar; for example, pulsed, CW, FMCW, and *interrupted FMCW* (IFMCW). All of these types of frequency transmissions have important applications to coherent tracking.

13.2.1 Continuous Wave

This type of radar requires a separate illuminator and receiver system. Because the transmission is CW, the doppler frequency from semistationary clutter is nor-

mally quite low; however, the magnitude of the clutter and the clutter frequency sidebands can be quite large. The disadvantages with a CW radar are that (1) no range information is available on the target of interest and (2) targets provide returns continuously from all ranges, and thus, there is no means for time discrimination of the returns. The primary advantage of this type of radar is that the radar implementation is fairly simple and that long detection ranges can be achieved with moderate transmit powers.

13.2.2 Frequency-Modulated Continuous Wave

An FMCW radar typical sweeps the frequency of the radar transmission in a linear fashion, and as a result, the frequency offset of receive signals at the radar is determined by the frequency sweep rate and the range of the target from the radar. Target motion will also produce a frequency offset in addition to that due to the range separation of the target from the radar. To get around this problem, many FMCW radars employ a frequency upsweep followed by a frequency downsweep. By comparing the received frequency relative to the transmit frequency between upsweep and downsweep, the frequency shift due to range can be separated from the doppler shift due to target motion. FMCW transmit waveforms are attractive when low-power, solid-state sources are required. Interrupted FMCW is similar to FMCW, but the transmit waveform is periodically interrupted to allow for increased sensitivity on reception.

13.2.3 Pulsed Coherent Radar Systems

The transmit frequency spectrum for a pulsed coherent radar is actually composed of a series of frequency spikes separated by the PRF. An expanded view of the spectrum of the frequency returns for both high-PRF and low-PRF radars is shown in Figure 13.1. A high-PRF radar is one in which the doppler frequencies from the targets of interest are unambiguous (i.e., the highest target doppler frequency does not exceed the radar PRF), but are generally ambiguous in range. Low-PRF radars are by definition unambiguous in range (i.e., the time delay between transmit and receive pulse for the maximum range target does not exceed the interpulse period), but generally ambiguous in doppler. A medium PRF radar is ambiguous both in range and doppler, and processing techniques must be used to resolve these ambiguities. The doppler returns from three targets can be seen in Figure 13.1, showing that for the high-PRF radar, the doppler returns all appear within the PRF frequency lines of the transmit spectrum. For the low-PRF radar, the doppler returns can actually be several times the PRF, thus causing doppler frequency ambiguities.

At best, the target of interest is unambiguous in frequency, such as for target 1. Worse, the target can be aliased, such as depicted for target 2; and worse yet,

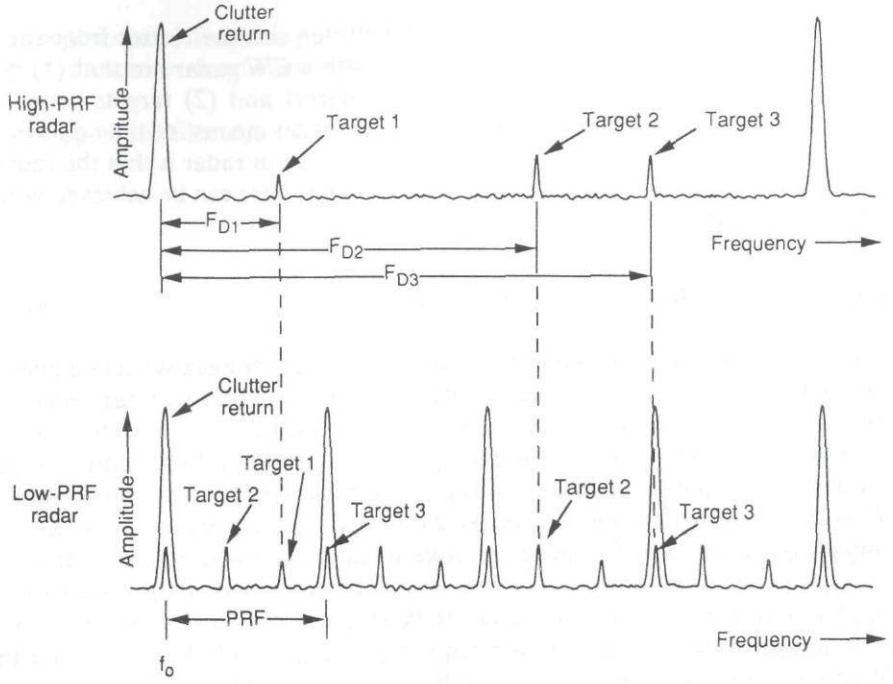

Figure 13.1 Comparison of doppler returns for high-PRF and low-PRF radars.

the target doppler frequency can be at a multiple of the PRF, and therefore masked, as target 3 is. The clutter returns cause a spread of the transmit PRF lines, and the amount of spreading is a function of the radar frequency and the internal motion of the clutter. The receive clutter spectrum for airborne radars, as described in Chapter 9, is more complex than that for ground-based radars because of the motion of the radar platform.

13.3 MOVING TARGET INDICATION RADARS

MTI radars provide clutter rejection, but in general, do not determine the actual doppler frequency of the targets of interest. Clutter returns usually have a narrow frequency spread about the transmit frequency lines and thus can be rejected by appropriate filtering of the coherent receive signals.

Doppler blind speeds occur in low- and medium-PRF radars when the doppler frequency resulting from target motion exceeds the radar PRF. This is because the transmit spectrum consists of an envelope of frequency lines separated by the PRF.

In a similar manner, blind ranges occur when the delay time between the transmit pulse and the receive signal is near a multiple of the time between pulses. In this case, the target return signal would be occurring when the radar is transmitting and thus be blind to return signals.

Blind speeds can be avoided in low-PRF radars by staggering the PRI; that is, by changing the PRI on a pulse to pulse basis. Staggered-pulse MTI radars generally use a series of transmit PRIs, which typically can be as little as 3 to as many as 20 or more distinct PRIs. An example of the MTI filter response for a radar with multiple staggered PRFs is shown in Figure 13.2. This is the MTI response for a radar with an average PRF of approximately 300 Hz, and although there is some variation in the MTI response versus doppler frequency, there are no blind speeds over the full range of expected aircraft velocities. MTI radars, which depend upon staggered PRF for blind speed avoidance, are lowPRF radars, in which the radar PRI exceeds the maximum range of target delay return time. Clutter returns whose delay times exceed that of the PRI interval would appear

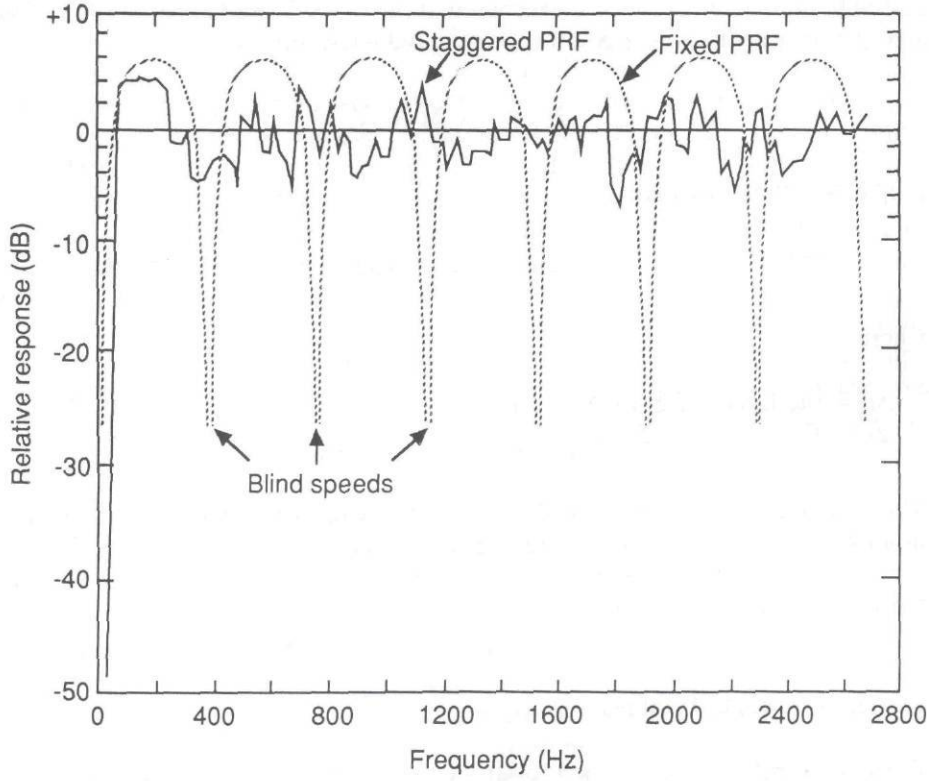

Figure 13.2 MTI filter response with fixed and staggered PRF.

to be arriving at different ranges in each PRI and thus could be passed by the MTI processing.

Tracking of targets following MTI processing for clutter rejection can be performed using either analog or digital processing. A detailed discussion of MTI filtering and processing techniques appears in Chapter 8. Most modern MTI processors use digital implementation to process *inphase* (I) and *quadrature-phase* (Q) information, and therefore, the tracking technique described in the following section is a unified tracking approach using digital MTI clutter rejection techniques.

13.3.1 MTI Range Tracking

For a digital MTI implementation, the Σ signal outputs from the MTI filter are Σ_I and Σ_Q. Although conceivably either the Σ_I or Σ_Q information could be used for range tracking, the individual components Σ_I or Σ_Q will be modulated at the doppler rate and an will result in an apparent 3-dB loss in sensitivity. Thus, the most desirable implementation uses a recombination of the I and Q components. The I and Q components can be combined using the equation:

$$\Sigma_{\text{MTI}} = \sqrt{\Sigma_I^2 + \Sigma_Q^2}$$

or can be approximated by:

$$\Sigma_{\text{MTI}} \approx \Sigma_L + 0.5\Sigma_S$$

where:

Σ_L = the larger of Σ_I or Σ_Q, and
Σ_S = the smaller of Σ_I or Σ_Q.

The resulting Σ_{MTI} signal is a wideband, clutter-canceled video signal that can be input to a conventional range tracking circuit, such as described in [2]. Once the target of interest is acquired by the range tracker, a range trigger is generated at the range of the tracked target.

13.3.2 MTI Angle Tracking

For a monopulse angle tracking radar viewing an isolated target (or a target with clutter canceled by MTI processing), the real component of the elevation angle

(β_r) to the target relative to the antenna boresight can be computed from the formula given in [3]:

$$\beta_r \approx K_m \frac{|\Delta_{EL}|}{|\Sigma|} \cos \phi_{EL}$$

where:

Δ_{EL} = difference elevation signal,
ϕ_{EL} = phase angle between Δ_{EL} and Σ, and
K_m = antenna slope constant.

The azimuth angle (θ_r) can be computed in a similar manner using the azimuth difference signal (Δ_{AZ}) and the phase angle (ϕ_{AZ}). For an isolated target, the phase angles ϕ_{AZ} and ϕ_{AZ} are normally either 0 or 180 degs, depending on which side of boresight that the target is located.

The implementation of such an MTI angle tracker is depicted in Figure 13.3. The MTI filters for the Δ_{EL} and the Δ_{AZ} channels are considerably simpler than that of the wideband Σ signal channel in that the difference signal channels only need be processed at the sampled target range. The Σ_{IS} and Σ_{QS} signals, sampled at the target range, can then be used in conjunction with the EL_I, EL_Q, AZ_I, and AZ_Q signals to compute the elevation and azimuth angles of the target from boresight. This MTI tracking could be implemented either in analog or digital circuitry, but because the MTI processing is likely to be digital, it follows that the tracking would be best be implemented with digital circuitry.

Sherman [4] indicates that additional information can be obtained by viewing the imaginary angle components as well as the real angle components. For example, with complex targets or for a target in a multipath environment, the phase angle between the sum and difference components can depart from the nominal 0 or 180 degs. The imaginary component of the elevation angle (β_i) is given as:

$$\beta_i \approx K_m \frac{|\Delta_{EL}|}{|\Sigma|} \sin \phi_{EL},$$

13.4 CW AND PULSE-DOPPLER RADAR

Chapter 9 discusses pulse-doppler radar systems in detail. The emphasis in this chapter is to summarize the aspects of doppler processing as related to tracking and to elaborate on the tracking aspects related to both CW and pulse-doppler radars.

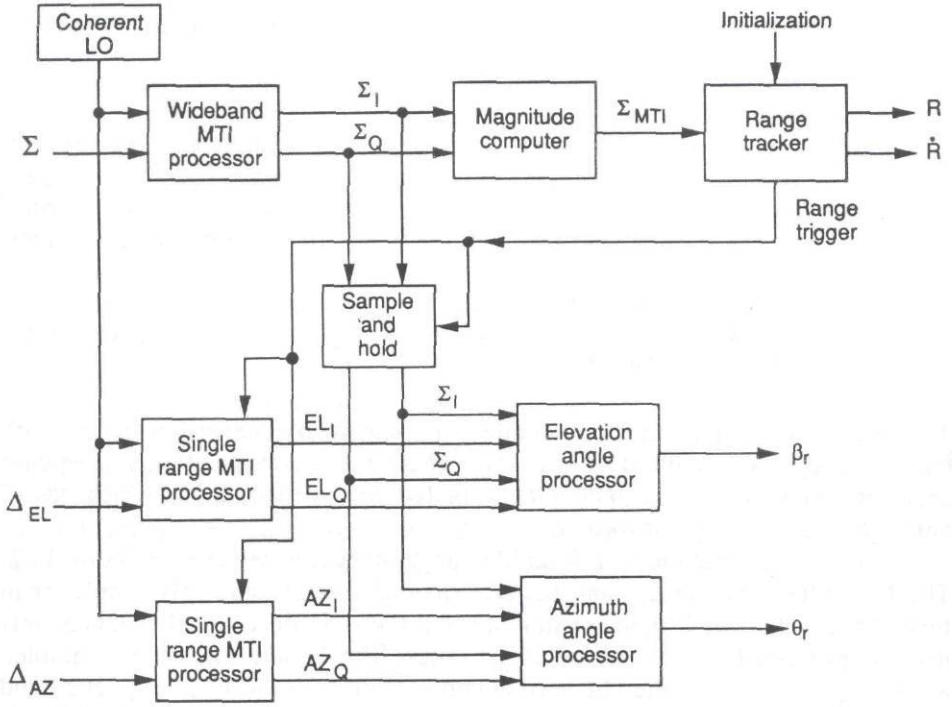

Figure 13.3 MTI range and angle tracker block diagram.

13.4.1 Doppler Tracking

CW and pulse-doppler tracking radars ideally determine the doppler frequency of the receive signal using an inherently narrowband filter. There are many different implementatios for accomplishing doppler filtering, including crystal filters, doppler tracking filters, canonical filters, correlation filters, and FFT filters.

Fine Line Filtering

A simple form of a doppler tracking filter for tracking the received central PRF line is illustrated in Figure 13.4. In this case, the input signal is mixed with the output of a *voltage-controlled oscillator* (VCO), whose frequency (assuming that the VCO frequency is above the transmit frequency) is determined by the equation:

$$f_v = f_c + f_{IF} + f_D$$

where:

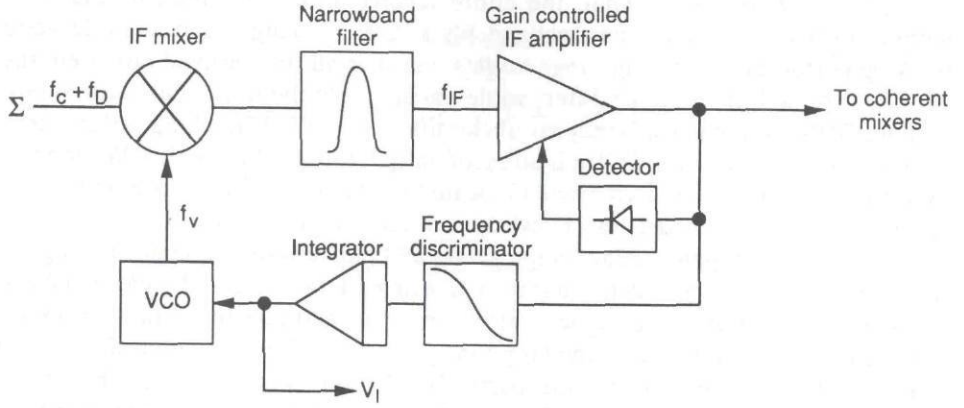

Figure 13.4 Typical pulse-doppler tracking loop.

f_v = VCO frequency,
f_c = transmitter frequency,
f_{IF} = center frequency of the narrowband filter, and
f_D = doppler frequency offset of the tracked target.

The target signal is passed through the narrowband filter and amplified. In this case the amplified signal would normally be detected and fed back to an AGC amplifier. In this manner, the signal level into the discriminator is controlled so that the voltage versus frequency offset from the discriminator is just a function of the frequency offset. The function of the discriminator is to generate an error voltage whenever the target doppler frequency changes, causing the IF to shift away from the center frequency of the narrowband filter. The discriminator error voltage causes the integrator to increase or decrease the VCO voltage, changing the VCO frequency to drive the IF frequency back to the center of the narrowband filter. Assuming that the VCO input voltage is 0V dc when the doppler frequency component is zero, then:

$$f_D = \frac{V_I}{K_v}$$

where:

V_I = VCO tuning voltage, and
K_v = frequency versus tuning voltage.

For a CW transmit signal, the entire receive spectrum would normally be within the bandpass of the narrowband filter. CW tracking radars provide good tracking performance on long-range targets, because all the received target energy is passed through the doppler filter, while passing only the noise and clutter components within the narrow bandpass of the filter. For a CW tracking radar, other means must be used for determination of target range. Although CW doppler radars can be used in a search mode to locate targets in angle, there are only about two such systems deployed, the Hawk system and one in the SA-10.

For a pulse-doppler radar, range gating and narrowband doppler filtering are normally used to approximate matched filtering of the received signals. Range gating of the received target signals prior to narrowband filtering eliminates extraneous signal and noise outside the target range interval. The frequency of the VCO is generally controlled so that the narrowband filter is centered on one of the spectral lines in the target return. Because the receive target spectrum may contain several hundred spectral lines, only a small portion of the receive signal is processed by the doppler filter. However, because the noise is limited by range gating and narrowband filtering, the SNR is preserved with this type of processing. Because only a single line of the pulsed receive waveform is processed, the signal out of the doppler filter is inherently a CW signal regardless of the type of transmit waveform. Thus, all range information is lost after the signal passes through the narrowband filter.

Phase-Locked Loop

Phase-locked loop (PLL) implementations are also commonly used for doppler tracking. PLLs can provide coherent detection superior to that achievable using conventional discriminator circuits. A simplified block diagram of a PLL circuit is shown in Figure 13.5. For a CW input signal for this circuit, the input signal is split between the inputs of two phase detectors. The VCO signal is split by a quadrature hybrid to provide the input reference signals to the I detector and Q detector. The output from the I detector (V_i) and the Q detector (V_q) are, respectively:

$$V_i = K_d \cos(\Phi_i - \Phi_o)$$

$$V_q = K_d \sin(\Phi_i - \Phi_o)$$

where:

K_d = phase detector gain factor,
Φ_i = phase of the input signal, and

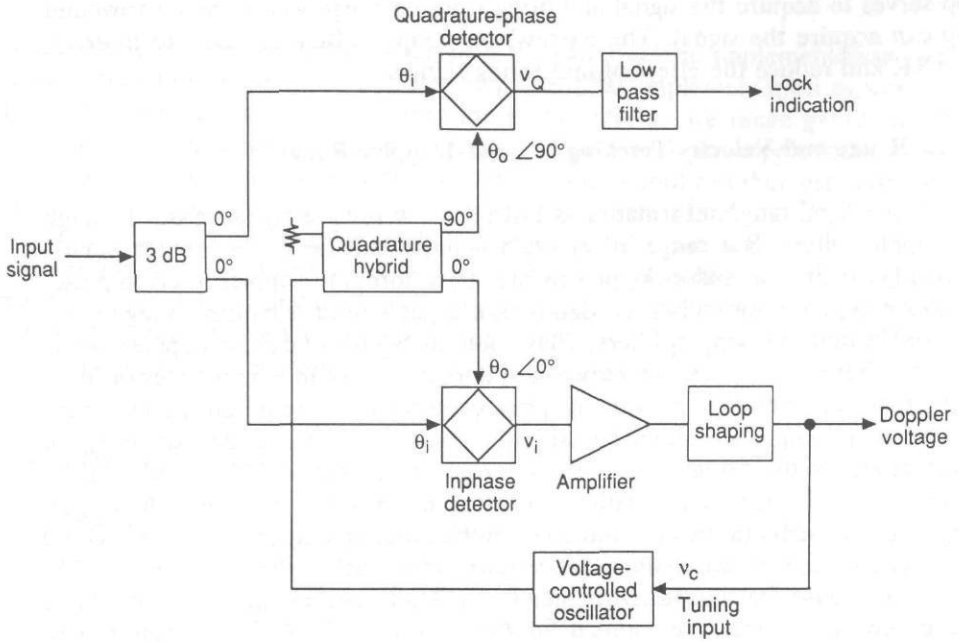

Figure 13.5 Typical PLL circuit with lock indicator.

Φ_o = phase of the VCO signal.

The loop filter transfer function is designed to drive the tuning voltage input of the VCO in such a manner that the voltage out of the I detector is maintained at nominally 0V dc. Because the output of the I detector is maintained at 0V dc, the output of the Q detector is either a maximum positive or maximum negative voltage, thus indicating the presence of the phase-locked condition. The voltage to the *phase-locked oscillator* (PLO) is then proportional to the doppler frequency. The design of the circuit and the loop transfer function is critical to the stability of the PLL, the phase-locked pull-in range, and the phase-locked servo loop noise. A recognized standard reference text for the design of PLLs is [5].

PLL circuits can also be used for coherent processing of pulsed received signals. In this case, the PLL operation must be restricted to processing of a single PRF line, either by filtering of the signal before the PLL circuit or by proper design of the loop filter. In some cases it may be necessary to have wideband PLL or

discriminator circuit followed by a narrowband PLL. In this case, the wideband loop serves to acquire the signal and bring it into a range where the narrowband loop can acquire the signal. The narrowband loop is often desirable to improve the SNR and reduce the effect of interfering signals.

13.4.2 Range and Velocity Tracking in Pulse-Doppler Radar

As indicated, all range information is lost after the receive signal passes through the doppler filters. But range information is important for pulse-doppler radars, especially for airborne pulse-doppler radars. Therefore, the doppler filters in pulse-doppler radars are normally preceded by range gates usually multiple range gates followed by multiple doppler filters. Thus, multimode airborne pulse-doppler radars feature either a rather complex network of doppler filters and range gates or high-speed digital computers to provide the processing capability required. Range tracking can be accomplished either by using the computer to track (and smooth) the target range as the target moves from range cell to range cell, or by actually implementing a range tracker with range gates that bracket and follow the target. Target velocity can also be determined from the range tracking circuitry, but could be rather coarse, particularly in a scan-to-scan range tracking implementation. The doppler response from a pulse-doppler radar is an accurate indication of range rate, except that doppler ambiguity needs to be resolved. This can be accomplished by using the range rate information from the range tracker to determine the rough range rate, which hopefully is accurate enough to enable determination of the number of multiple PRFs present in the target doppler.

13.4.3 Angle Tracking With Doppler Radar

Angle tracking with a CW or pulse-doppler radar can be accomplished by a number of means. For example, scanning of the antenna beam either mechanically or by using a phased-array antenna will provide azimuth and possibly elevation angles to the target. However, for directing weapons in airborne situations, the higher accuracy achievable with monopulse angle processing is generally required. To provide the SNR and *signal-to-clutter ratio* (SCR) required for accurate angle tracking of targets, doppler filtering of the angle data is also required. But the doppler processing of the angle data only needs be performed at the range of the target, and thus, once range track is established on the target, range gates and associated doppler filters can be set up on the elevation and azimuth difference signal channels.

13.4.4 Tracking in Doppler, Range, and Angle

Conceptually, a general configuration of a doppler tracking implementation can be as depicted in Figure 13.6. For a monopulse radar implementation as shown, the Σ, Δ_{EL}, and Δ_{AZ} components from the radar receiver are range gated either with multiple range gates or with tracking range gates prior to the doppler processor. Once the range tracker is locked onto the target, the output can then establish the target range to the angle tracking circuits. The range rate out of the range tracker can be fed back to the doppler tracker to eliminate doppler ambiguities and, in combination with the doppler frequency output, can determine the precise range rate of the target. The combination of doppler clutter rejection, target range, range rate, elevation angle, and azimuth angle can then be used for accurate tracking of the target even in a background of clutter and other extraneous signals and targets.

13.4.5 Target Detection

The target detection process is discussed in detail in [6], as well as other numerous references. For a target immersed in a clutter background, initial detection can be quite difficult without doppler filtering of the received signals to minimize the affects of clutter and other interfering signals. This is especially important when

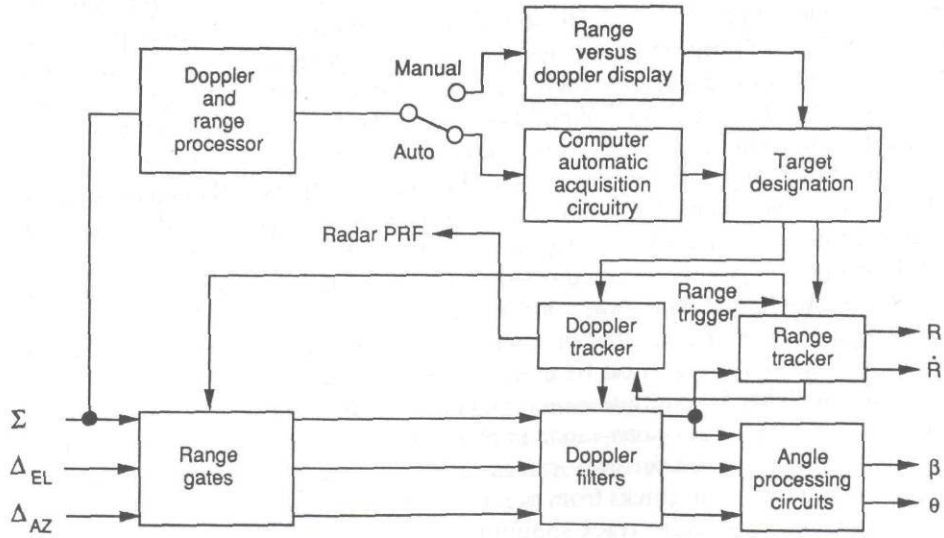

Figure 13.6 Pulse-doppler acquisition block diagram.

attempting to detect and track low-RCS targets such as projectiles. Also, there is increased emphasis on the detection of low-observable targets. Thus, doppler filtering prior to detection is essential for most pulse-doppler radar implementations. In the simplest case, the detection process could use a frequency-scanned doppler filter, and a detection would be declared when the output out of the filter exceeds a predetermined threshold. In this case, however, no range information would be available without also range gating the signals into the doppler filter. Ideally, it is desirable to have a multitude of range gates, each followed by either doppler filters or FFT processing of the range gated signals. In this manner, a mapping of range versus doppler could be generated. Ideally, some type of *constant false alarm rate* (CFAR) processing, such as that described in [6], is desired to establish the optimum levels for declaring a detection.

13.4.6 Target Acquisition

Once a target is detected, an acquisition process must be established to enable the radar to track the target in doppler, range, and angle. Acquisition, as illustrated in the block diagram for a typical pulse-doppler implementation, can be accomplished either manually or automatically.

For manual target acquisition, a number of display types could potentially be used to aid the operator in acquiring the target. One particularly useful display for this application is one that provides a map of doppler versus range, with the intensity of each doppler or range cell a function of target amplitude. Thus, all the "moving targets" would be apparent, which would enable the operator to select the target of interest. The acquisition procedure, once a target is selected, would be to first acquire the target in doppler and then in range, or first in range and then in doppler, depending upon the radar implementation. Once the target is acquired in doppler and range, the azimuth and elevation trackers could be locked onto the target.

Automatic target acquisition is somewhat more complex in that an acquisition algorithm must be established to enable the process to acquire a valid target. The decision process is somewhat analogous to that used by a manual operator. For each doppler or range cell, the circuitry must determine if the cell amplitude exceeds that of the CFAR or other threshold to determine target detections. Also, for a single target tracker, if a number of targets are present that satisfy the acquisition criteria, a decision process must be used to determine which target to acquire and track. The capability for multiple target tracking is a necessity for many applications, particularly in track-while-scan radar implementations. In this case, the tracking computer must in addition perform scan-to-scan correlations to associate the current detections with the target tracks from previous scans or, if no association is present, to determine if a new target track should be established.

13.4.7 Effect of PRF on Tracking With Pulse-Doppler Radar

For a pulse-doppler radar to track a target, the target amplitude following doppler filtering must exceed that of the clutter residual. For a ground-based radar, the PRF must be selected to keep the target doppler returns separated from the radar blind speeds. For medium- or high-PRFs, blind (eclipsed) ranges also must be considered in the implementation. High-PRFs enable unambiguous determination of doppler frequency, and the frequency regions that are clear of clutter and other interfering signals are also greater. This is especially important for the airborne radars, because of the increased frequency spread of the clutter. However, the ranges that are eclipsed by succeeding radar pulses are greater with a high-PRF radar. Thus, in many practical pulse-doppler tracking radars, the selection of PRF is usually a compromise between unambiguous doppler and unambiguous range. For this reason, medium- and sometimes low-PRFs are used for tracking radars. In the case of MTI radars with low- or medium-PRFs, the use of staggered PRF frequencies can eliminate blind speeds. However, a staggered PRF is not the most efficient means for selection of a radar PRF. With a pulse-doppler radar with a medium or high-PRF, a constant PRF must be used; otherwise, clutter exceeding the unambiguous range would appear to have doppler components and thus could not be rejected.

Because the doppler processor can determine when the target is approaching the radar blind speed or eclipsed range, the PRF can be changed to shift the target returns away from the clutter regions. To do this most efficiently, the unambiguous doppler must be determined, even though the target doppler may be several times the radar PRF. With a range tracking circuit, the rough determination of range rate can be extracted from the range tracker and, in most instances, is sufficiently accurate to enable resolution of the ambiguity. With the ambiguity resolved, doppler frequency guard bands about multiples of the PRF can be established, and when the doppler frequency approaches one of the guard bands, the computer can determine the optimum new PRF for the radar to keep the target in a clear region away from radar clutter.

13.5 FACTORS AFFECTING COHERENT TRACKING OF TARGETS

There are a number of radar-related factors affecting the tracking performance of coherent tracking systems, including radardependent errors, environmental error sources, and targetdependent errors. The purpose of this section is to enable the evaluation of the effect of these error sources on the accuracy of doppler (velocity) tracking, range tracking, and angle tracking.

13.5.1 Radar-Dependent Errors

Radar-dependent errors result from the specific implementation of the radar, and the causes and effects of these errors (as discussed in [7]) are summarized in Table 13.1. The effects of many of these systematic error sources, such as frequency instabilities, phase noise, amplitude fluctuations, and timing jitter, on coherent systems were explored in detail in previous chapters. The purpose of this section is to relate the effect of these errors on tracking performance. For random or noise-

Table 13.1
Effects of Radar-Dependent Error Sources on Coherent Tracking

Error Sources	*Doppler Tracking*	*Range Tracking*	*Angle Tracking*
Thermal noise	Increased σ_{fc}	Increased σ_r	Increased σ_{EL}, σ_{AZ}
Short term frequency stability	Increased σ_{fc}	Potential degradation due to decreased clutter cancellation	Potential degradation due to decreased clutter cancellation
Long term frequency stability	Apparent increase/ decrease in Doppler	No effect	No effect
Phase noise	Increased σ_{fc}	Potential degradation due to decreased clutter cancellation	Potential degradation due to decreased clutter cancellation
Spurious	Potential false target track	Potential false target track	Potential false target track
Timing jitter	Increased σ_{fc}, possible false target if jitter is sinusoidal	Increased σ_r	Minimal effect
Serve loop			
Noise	Increased σ_{fc}	Increased σ_r	Increased σ_{EL}, σ_{AZ}
Lag	Doppler bias errors	Range bias errors	Angle bias errors
Channel-to-channel			
Amplitude tracking errors	No effect	No effect	Affects magnitude of angle error determination
Phase tracking errors	No effect	No effect	Potential angle boresight bias

like errors that are gaussian in nature, the total standard deviation due to noise-like sources is given by:

$$\sigma_t = \sqrt{\sum_{i=1}^{n} \sigma_n^2}$$

where n = number of error sources. The bias sources, on the other hand, are directly additive contributors.

Receiver Noise and Noise Floor

Thermal noise in the receiver often is a major factor in the accuracy of determining target velocity, range, and angle. The approximate equations for the effects of the variance due to thermal noise are related for the three cases and are valid for $\text{SNR}_f \gg 1$. This is almost always the case for a coherent system, even when the SNR for a single pulse does not meet this criterion. For the case of the doppler (velocity) servo loop, the frequency servo loop noise (σ_{fc}) is given in [7] as:

$$\sigma_{fc} = \frac{B_c}{K_f \sqrt{\text{SNR}_f (B_f/\beta_{nf})}}$$

where:

B_c = bandwidth of the fine lines in the receive spectrum,
K_f = discriminator error slope,
SNR_f = signal-to-noise in the narrow bandwidth filter,
B_f = narrowband filter bandwidth, optimally $B_f \approx 1.4\ B_c$, and
β_{nf} = doppler servo loop noise bandwidth.

For the range tracker servo loop (assuming a split gate tracker), the range noise (σ_r) for high SNR is given in [7] as:

$$\sigma_r = \frac{\tau}{K_r \sqrt{\text{SNR}_f (B_f/\beta_{nr})}}$$

where:

τ = the pulse width (compressed pulse width for pulse compression systems),
K_r = range servo error slope factor, a function of the gate width and filter characteristics, and
β_{nr} = range servo loop noise bandwidth.

For the angle tracking servo loop, the angular noise (σ_t) for a monopulse tracker can be represented as:

$$\sigma_t = \frac{\theta}{K_m \sqrt{B\tau \mathrm{SNR}_f (B_f/\beta_{na})}}$$

where:

θ_t = antenna beamwidth of the Σ pattern,
K_m = monopulse antenna error slope, and
β_{na} = angle servo loop bandwidth.

Thus, it is apparent that the effects of thermal noise are similar in the velocity, range, and angle servos in the radar. The noise floor of the radar is determined by the systematic noise factors in the radar other than SNR and thus establishes the absolute limits on the accuracy of the radar. An example of the theoretical versus the measured velocity errors for an AN/FPQ-6 radar versus S/N and the noise floor is shown in [8] in Figure 13.7.

System Stability, Linearity, and Spurious Signals

There are a number of factors affecting system stability of a coherent system, including the transmitter and other elements in the radar system. The transmitter-induced errors include frequency stability of the source, phase noise, frequency spurious signals, pulse-to-pulse amplitude variations, pulse timing jitter, and pulse shape variations. Receiver error sources include the effects of frequency stability and phase noise of the COHO and other internal frequency sources, receiver A/D nonlinearity, and amplitude quantization effects. The primary effect of these error sources on a coherent tracking radar is to effectively broaden the spectrum of the target doppler response and set a lower limit on tracking system performance. Also, spurious signals can result in the detection and tracking of false targets. These items were discussed thoroughly in Chapters 1 through 6. Gray [9] provides some insight into these problems for an airborne pulse-doppler radar, as well as techniques for performing stability measurements.

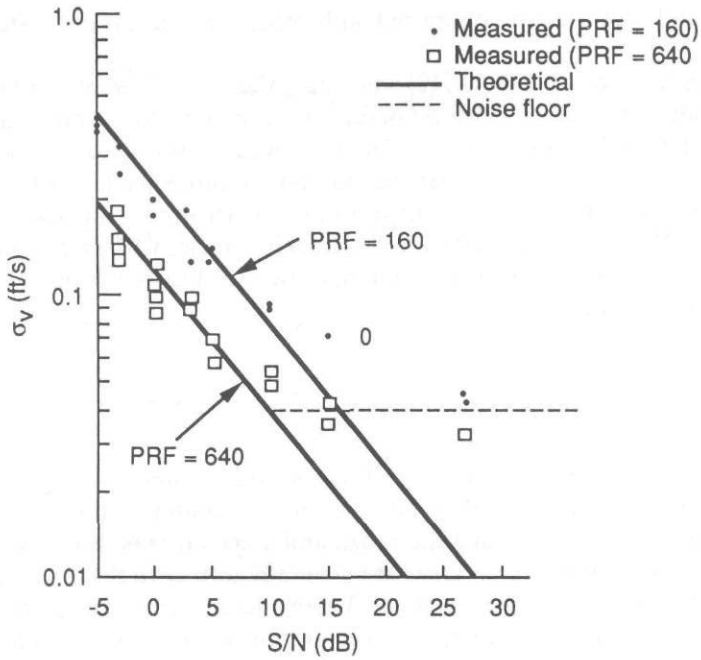

Figure 13.7 Doppler error versus SNR, AN/FPQ-6 (from [8]).

Servo Loop Effects

A coherent tracking radar may include five or more tracking loops, including a doppler tracker, range tracker, AGC circuit, azimuth angle tracker, and elevation angle tracker. The errors associated with these loops depend on the specific implementations, but in general could be characterized as a type 0, type 1, or type 2 servo loop. In a type 0 loop, the signal is fed back directly (usually low-pass filtered). Many AGC circuits use a type 0 servo loop to normalize the Σ signal to a constant level. In a type 1 servo loop, the error signal is integrated before being fed back in the tracker circuit. A type 1 servo loop is characterized as having zero error for a constant range or doppler frequency offset, but will have a lag error proportional to a constant rate of change of the input signal. A type 2 servo loop is characterized as having a second integrator following the first integrator. A type 2 servo loop will have zero lag error for a signal with a constant rate of change (such as range rate) and will have a lag error component proportional to the acceleration component of the signal. The bandwidths of the respective servo loops interact with

each other and thus must be optimized with respect to the overall system performance.

Figures 13.8 and 13.9 from [10] show the effects of different combinations of both wideband and narrowband AGC and PLL bandwidths while tracking two adjacent targets in the antenna beam. The narrowband AGC and narrowband PLL combination shows the best performance in that the influence factor (I) is affected least by increasing the interfering signal ratio (R). However, narrowband performance of the PLL, although reducing the tracking noise, will have a limited pull-in range for acquiring the target in doppler and will lose track more easily with abrupt doppler changes.

Range and Angle Tracking Error Sources

The ability of the coherent radar to perform accurate range and angle tracking of targets is generally limited by thermal noise and by clutter residual passed by the MTI or doppler filters preceding the range and angle circuits. Following the MTI or doppler filtering, the error sources are generally similar to those associated with noncoherent range and angle trackers. These include errors in gain and phase tracking over the dynamic range of the receiver, boresight and axis alignment errors,

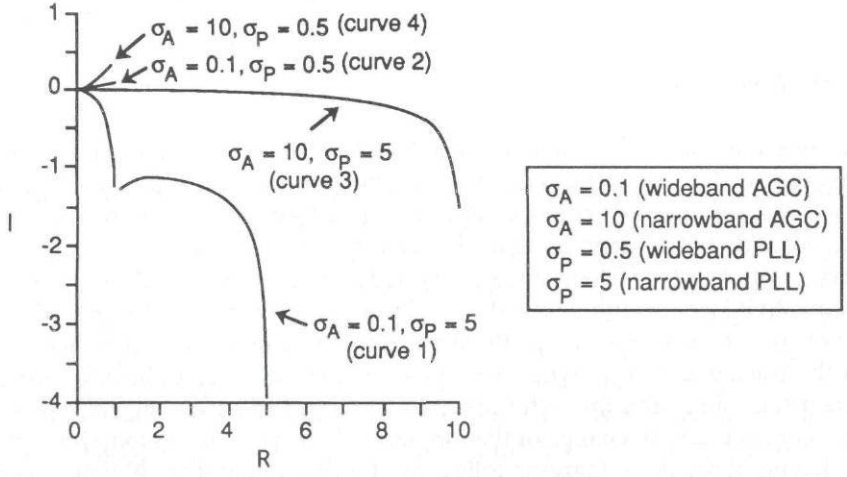

Figure 13.8 R versus I characteristics for four typical cases: narrowband and wideband AGC in combination with narrowband and wideband (from [10]).

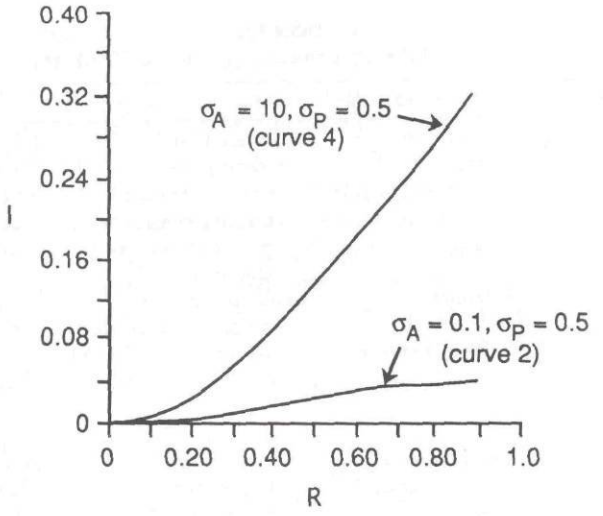

Figure 13.9 Magnified R versus I characteristics for narrowband AGC in combination with wideband PLL (curve 4) and for wideband AGC in combination with wideband PLL (curve 2) (from [10]).

angle encoder errors, bearing wobble, antenna angle crosstalk, and other factors. These error sources are described in detail in [7] and in Chapter 16 of [3].

13.5.2 Environmental Constraints on Coherent Tracking

The environmental factors that could affect target tracking, which include clutter, multipath, jamming (ECM), and propagation errors, are summarized in Table 13.2. With the increased emphasis on reduced RCS on land, air, and sea vehicles, many of the presentday radars in use for detecting and tracking targets will no longer be adequate for their tracking missions in the 21st century. Thus, the performance degradation caused by clutter, multipath, and jamming, and their effect on low-RCS targets, will cause increased emphasis on coherent tracking applications and the optimization of the radar implementation and processing techniques.

Clutter

The minimization of the effects of clutter is of prime importance to any radar that must track targets in a clutter background. For example, the aerostat tracking radars deployed along the southern border of the United States must detect and

Table 13.2
Effects of the Environment on Coherent Tracking

Error Sources	*Doppler Tracking*	*Range Tracking*	*Angle Tracking*
Clutter feed through	Increased doppler spread, decreased target detection capability	Increased range measurement errors, decreased tracking sensitivity, potential lockup on clutter return	Increased range measurement errors, decreased tracking sensitivity, potential lockup on clutter return
Multipath	Potential increased doppler spread	Potential increased range measurement errors	Induced angle errors (primarily in elevation) apparent, as angle noise with low frequency components possible
Jamming	Obscuration of target signal, possible frequency pull-off	Obscuration of target, possible range pull-off	Potential loss of target due to obscuration of target signal, possible angle pulloff if not collocated with target
Propagation effects	Possible increased doppler spread due to dispersion effects	Little effect	Possible angle errors due to diffraction of antenna beam

track low-flying aircraft of a few square meters against a background that can exceed 10^6 m^2 for mountainous clutter. Measurement of the radar's clutter rejection performance is important to ensure that the radar will be able to detect targets, while minimizing the number of false alarms due to clutter. Typically, the measurement of clutter rejection performance is accomplished using injected signals to simulate the returns from stationary clutter; however, this does not account for the effects of transmitter instabilities, spurious signals, and scanning losses. A technique for the actual measurement of clutter rejection has been accomplished using a quadrahedral-dopplerproducing target [11,12].

The performance of an MTI or doppler radar is limited by the clutter that passes through the processor. In the case of an MTI radar, the target must compete with the clutter residue in the range, azimuth, and possibly elevation cells of the target, whereas a pulse-doppler radar is affected by the clutter in the narrowband filter. For a CW or non-range-gated pulse-doppler processor, the clutter at all ranges in the narrow filter bandwidth will affect the target return. For a range-gated pulsedoppler receiver, only that clutter in the same range cell and narrow filter bandwidth will affect the tracking accuracy. Thus, the clutter rejection achievable by a pulse-doppler radar should be superior to that of an MTI radar. The

clutter rejection that can be achieved by narrowband filtering is limited by the doppler spread of the target returns. If the doppler filter bandwidth is made too narrow, it will reject some of the target returns as well. For an airborne pulse-doppler radar, the clutter rejection performance is even more critical because of the increased doppler spread of the clutter. An evaluation of airborne pulse MTI, CW doppler, and pulse-doppler radars was performed in [13] and shows that a pulse-doppler radar has superior performance for the particular example selected. The doppler spread is dependent on the type of terrain, wind speed, radar frequency, sea state for overwater measurements, and weather-related conditions such as rain. These are covered in some detail in [5] for land, sea, and weather-related clutter. Also, there is considerable interest recently with K-distributed sea clutter, as discussed in [14]. Measurements of the doppler spectra from precipitation are reported in [15].

In addition to affecting the velocity and range tracking performance of a radar, clutter also degrades the angle accuracy of tracking radar. For this reason, the angle tracking channels also need to employ either MTI or pulse-doppler filtering to reduce the clutter effects. However, the processing only need be performed at the target range, because the target is already tracked in range. Riggs [16] provides an analysis of the effect of clutter on angle tracking accuracy for a monopulse radar. In his paper he gives the standard deviation of the angle error (σ_x) as:

$$\sigma_x = \frac{1}{A_o\sqrt{\frac{2S}{C}}} \{E[G_A^2(\theta)] - E[G_A(\theta)G_B(\theta)]\}^{1/2}$$

where:

$G(\theta)$ = antenna gain of either the A or B beams of the monopulse antenna (assuming single-plane monopulse antenna), and
A_o = antenna gain on boresight.

He gives an artificial but instructive example assuming that $G(A)$ and $G(B)$ are linear and equal to A_o on boresight, then:

$$\sigma_x = \frac{A}{A_o\sqrt{\frac{2S}{C}}} \sigma(\theta)$$

And for a square transmitting beam of width β for either surface or uniform volume scattering conditions he obtains:

$$\sigma_x \approx \frac{\beta}{B\sqrt{6S/C}}$$

where B = half-power beamwidth of the radar.

Multipath

Multipath, in effect, results in both direct and indirect radar returns from the target, where the indirect returns are due to reflection of the target returns from another surface or object. Depending on the phase and amplitude of the indirect returns, they can cause amplitude fluctuations and doppler spreading of the target return. Multipath generally consists of both specular and diffuse components, depending on the surface roughness of the scattering terrain. The specular component is the reflection from a flat surface, whereas the diffuse component is the random scattering from a rough surface. From [17] the specular scattering coefficient (ρ_s) is given by:

$$\rho_s^2 = \exp\left[-\left(\frac{4\pi\sigma_h \sin\theta_s}{\lambda}\right)^2\right]$$

where:

σ_h = rms surface roughness, and
θ_s = angle between surface and multipath ray.

The phase angle between the direct path return and the multipath return is given by [18] as:

$$\Psi = \Psi_{0+}[2\pi/\lambda]\Delta r$$

where:

Ψ_0 = phase shift of the return from the reflecting surface, and
Δr = path length difference ($R_I - R_D$)

Figure 13.10 shows the doppler offset frequency of the specular component of the indirect return as a function of target height and range. For low-level targets the frequency offsets are rather small until the target is close in range. Thus, the multipath returns for low-level targets are likely to pass through the narrowband doppler filters, thus interfering with the direct returns from the target. Although

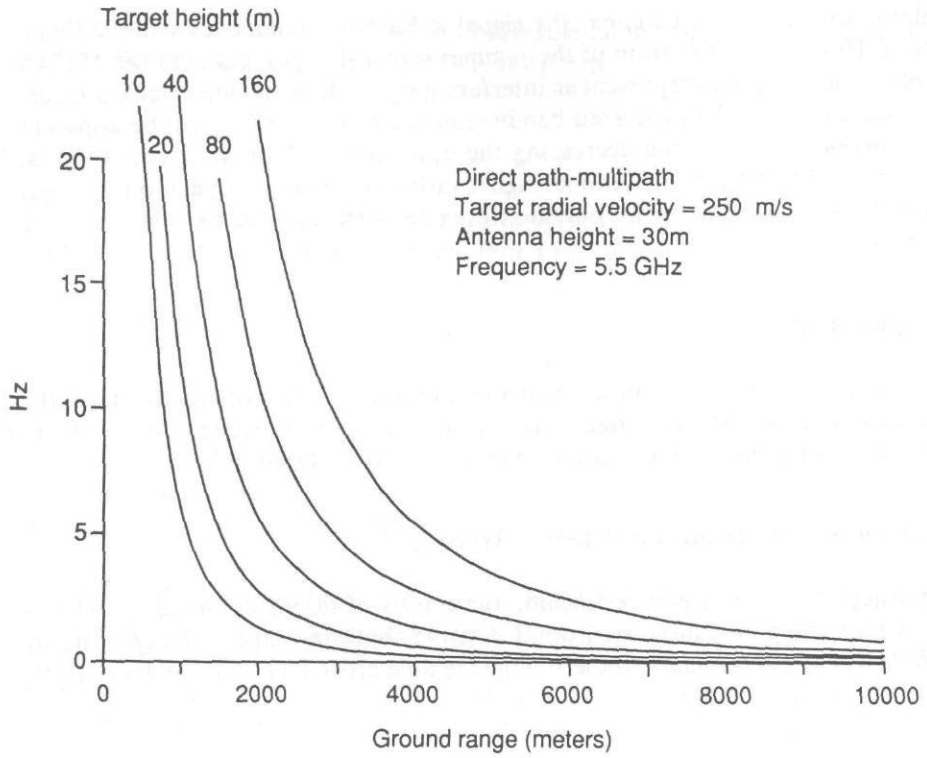

Figure 13.10 Doppler difference frequency due to multipath (from [8]).

there is likely to be some minor degradation in the velocity and range trackers because of the specular multipath component, the major effect will be in angle tracking errors (primarily elevation angle errors). The diffuse component of the multipath tends to be random in nature and, as such, may result in some spreading of the target spectrum. Both specular and diffuse multipath were analyzed to determine the errors induced by multipath for angle tracking at MMW frequencies [19].

Jamming

Intentional jamming using ECM represents additional interference to the MTI or doppler receiver. Pulse-doppler radars have the advantage over noncoherent and MTI radars in that only the portion of the jammer spectrum within the narrow filter bandwidth is processed by the radar. In addition, if the jammer is in the

sidelobes of the radar's antenna, the signal is further attenuated by the antenna pattern. However, the portion of the jammer signal that gets through the MTI or doppler processing does represent an interfering signal. If the jammer signal appears as gaussian noise in the processed bandwidth, the primary effect will be apparent as an increased noise, thus decreasing the apparent SNR of the target returns. However, if the phase of the jammer signal varies slowly with respect to the target return, the effects could be far more detrimental, particularly in the angle tracking channels.

Propagation Effects

Refraction of the radar beam through the atmosphere can potentially affect the coherence of targets at long ranges. The effects of doppler dispersion due to expansion and compression of the transmit path has been analyzed in [20].

13.5.3 Target Constraints on Coherent Tracking

Target-dependent error sources include the effects of target dynamics, as well as scintillation and glint caused by extended targets both in range and angle and by multiple targets. A summary of these target-related error sources is shown in Table

Table 13.3
Effects of Target on Coherent Tracking

Error Sources	*Doppler Tracking*	*Range Tracking*	*Angle Tracking*
Complex targets	Increased doppler spread due to phase and amplitude variations at target returns	Increased range jitter due to apparent shift in range centroid of target returns	Increased angle noise due to glint from varying amplitude and phase from target scatterers
Multiple targets (in same range and beamwidth cell)	Increased doppler spread due to phase and amplitude variations at target returns	Increased range jitter due to apparent shift in range centroid of target returns	Increased angle noise due to glint from varying amplitude and phase from target scatterers
RCS fluctuations	Potential increased doppler spread due to amplitude modulation	Increased thermal noise effects. Possible loss of target if signal disappears for extended period	Increased thermal noise effects. Possible variation of angle error if AGC slower than RCS variations

13.3. The detection and tracking of low-observable targets pose additional requirements on the performance of coherent radar systems.

Dynamics

Motion of the extended targets can result in spread of the target doppler. From [7], the expected maximum width of the target spectrum is given by:

$$B_c = f_{\max} = \frac{2\omega L}{\lambda}$$

where:

ω = angular rate of rotation, and
L = target width (normal to the radar LOS and the axis of rotation).

The result is a spreading of the target doppler spectrum due to the motion of the target. The minimum doppler bandwidth must be great enough to keep the target echo within the bandwidth or risk possible loss of target track. The minimum acceptable bandwidth to allow for radially accelerating targets (to keep the frequency change to less than $B_f/2$ within integration time $1/B_f$) is given by:

$$B_f = 2\sqrt{a_i/\lambda}$$

where a_i = target acceleration.

RCS Fluctuation

The effect of target RCS fluctuations on radar measurement accuracy on measurements of angle, range, and range rate (doppler) has been analyzed by Swerling [21]. The standard deviation σ (modified for coherent operation) for a target with a fluctuation RCS is given as:

$$\sigma = \frac{k^*}{nx},$$

where

$\rho = k^*/k$ and x = per-sample SNR,
n = number of statistically independent coherent signal-plus-noise samples entering into the measurement,
k = constant value for a nonfluctuating target, depending on the type of measurement (i.e., the waveform of the antenna beam, the type of measurement implementation, and the processing), and
k^* = value of k for a fluctuating target.

For Swerling III, the factor ρ is represented by Swerling in closed form as:

$$\rho = \frac{2}{1 + 2x_o/\bar{x}}$$

where x_o = threshold value that the signal must exceed for the target to be detectable.

And for Swerling I, ρ is given by:

$$\rho = \exp(x_o/\bar{x})E_1(x_o/\bar{x})$$

$$E_1(z) = -\gamma - \ln_z - \sum_{n=1}^{\infty} \frac{(-z)^n}{nn!}$$

where γ = Euler's constant.

Table 13.4 lists the values of ρ computed by Swerling for various threshold levels.

Range Scintillation

Range scintillation is the modulation resulting from scattering from various parts of an extended target in the range dimension. Scintillations on extended range targets can result in apparent range changes of the centroid of the target returns. This can result in an range jitter, if the frequency of the variations is less than the bandwidth of the range tracker servo.

Table 13.4
Values of $\rho = k^*/k$

x_o/x:	1.0	0.333	0.10	0.010	0.0010
Swerling I	0.77	1.1	1.4	2.0	2.5
Swerling III	0.82	1.1	1.3	1.4	1.4

Glint

Target glint is the angular scintillations resulting from different scatterers on a complex, extended-angle target adding and subtracting in phase. The result, described in [22], is that of a warped phase front, which can cause the indicated angle to the target to wander about the target and, at times, even exceed the physical bounds of the target. The typical solution for reducing the angular fluctuation caused by glint is to change the transmit frequency on a pulse-to-pulse basis, thus decorrelating the returns from successive pulses. But this is impossible for a pulse-doppler radar. However, burst-to-burst frequency agility is possible, provided that the dwell time is long enough to provide for transient recovery and filtering on a number of bursts.

Multiple Targets

Multiple targets in the same range and simultaneously in the antenna beam can result in serious angle tracking errors. The result is a classic two-target situation described in [22], in which the apparent angle to the target is determined by the amplitude and phase relations of the returns from the targets. The effect of a closely spaced target on the desired target in a coherent monopulse radar has been examined in [10]. With a pulse-doppler radar, if the velocity of the multiple targets differ by more than the narrow bandwidth filters, the returns from the multiple targets can be separated into different doppler bins and processed separately.

Track-while-scan radars are generally configured to track multiple targets. In this case, track association algorithms must be developed, such as described in [23], in order to maintain the target tracks on a scan-to-scan basis. A number of techniques are available for the multiple track target association algorithms, such as that postulated in [24]. One of the major problems associated with track-while-scan radars is the processing of false alarms, which can overload the radar processor and confuse the radar operator. Berman [25] discusses the false alarms that result from noise, clutter, and crossing targets. In addition, with the reduced-RCS targets that will have to be tracked in the future, the presence of angel clutter will have to be given greater attention. Angel clutter can often be attributed to flocks of birds or insects that have a high enough velocity to pass through the MTI filters.

REFERENCES

[1] Morris, G. V., *Airborne Pulse Doppler Radar*, Norwood, MA: Artech House, 1988.

[2] Eaves, J. L., and E. K. Reedy, *Principles of Modern Radar*, New York: Van Nostrand Reinhold, 1987.

[3] Currie, N. C., *Radar Reflectivity Measurement: Techniques & Applications*, Norwood, MA: Artech House, 1989.
[4] Sherman, S. M., *Monopulse Principles and Techniques*, Norwood, MA: Artech House.
[5] Gardner, F. M., *Phaselock Techniques*, Second Edition, New York: John Wiley & Sons, 1979.
[6] Nathanson, F. E., *Radar Design Principles*, Second Edition, New York: McGraw Hill, 1990.
[7] Barton, D. K., *Radar System Analysis*, Norwood, MA: Artech House, 1976.
[8] Mitchell, R. D., M. R. Paglee, G. M. Sparks, and G. H. Stevens, "Radar Detection and Tracking in Ground Clutter," AGARDograph No. 219 on Range Instrumentation Weapons Systems Testing and Related Techniques, AGARD-AG-219, February 1976, pp. 414–416.
[9] Gray, M., F. Hutchinson, F. Fruge, and D. Cooke, "Stability Measurement Problems and Techniques for Operational Airborne Pulse Doppler Radar," *IEEE Trans.*, AES-Vol. 5, No. 4, July 1969, pp. 632–637.
[10] Endo, T., "Analysis of Interference Effects on Monopulse Radars," *IEEE Trans.*, AES-Vol. 24, No. 6, November 1988, pp. 766–774.
[11] Bruder, J. A., "Measurement of Clutter Suppression using a Quadrahedral," *1989 Int. Symp. on Noise and Clutter Rejection in Radars and Imaging Sensors Record*, November 1989, pp. 287–292.
[12] Bruder, J. A., "Measurement of the Performance of Moving Target Indication Radars," *1990 Int. Radar Symp. Record*, May 1990, pp. 170–175.
[13] Mooney, D. and G. Ralston, "Performance in Clutter of Airborne Pulse MTI, CW Doppler, and Pulse Doppler Radar," *IRE Int. Conf. Record*, 1961, pp. 55–62.
[14] Baker, C. J., "K-Distributed Coherent Sea Clutter," *IEE Proc.-F*, Vol. 138, No. 2, April 1991, pp. 89–92.
[15] Janssen, L. H., and G. A. Van Der Spek, "The Shape of Doppler Spectra from Precipitation," *IEEE Trans.*, AES-Vol. 21, No. 2, March 1985, pp. 208–219.
[16] Riggs, R. F., "The Angular Accuracy of Monopulse Radar in the Presence of Clutter," *Proc. National Electronics Conf.*, Vol. 22, 1966, pp. 237–242.
[17] Beckmann, P., and A. Spizzichino, *The Scattering of Electromagnetic Waves From Rough Surfaces*, Norwood, MA: Artech House, 1987.
[18] Ostrovityanov, R. V., and F. A. Basalov, *Statistical Theory of Extended Radar Targets*, Norwood, MA: Artech House, 1985.
[19] Bruder, J. A., and J. A. Saffold, "Multipath Effects on Low-Angle Tracking at Millimetre-Wave Frequencies," *IEE Proc.F*, Vol. 138, No. 2, April 1991, pp. 172–184.
[20] Remley, W. R., "Doppler Dispersion Effects in Matched Filter Detection and Resolution," *IEEE Proc.*, Vol. 54, No. 1, January 1966, pp. 33–39.
[21] Swerling, P., and W. L. Peterman, "Impact of Target RCS Fluctuations on Radar Measurement Accuracy," *IEEE Trans.*, AESVol. 26, No. 4, July 1990.
[22] Howard, D. D., "Radar Target Angular Scintillation in Tracking and Guidance Systems Based on Echo Signal Phase Front Distortion," *Proc. National Electronics Conf.*, Vol. 15, 1959, pp. 840–849.
[23] Hovanssian, S. A., *Radar Detection and Tracking Systems*, Norwood, MA: Artech House, 1978.
[24] Sword, C. K., M. Simaan, and E. W. Kamen, "Multiple Target Angle Tracking Using Sensor Array Outputs," *IEEE Trans.*, AES-Vol. 26, No. 2, March 1990, pp. 367–372.
[25] Berman, A., and A Hammer, "False Alarm Effects on Estimation in Multitarget Trackers," *IEEE Trans.*, AES-Vol. 27, No. 4, July 1991.

Chapter 14
Phase Noise Testing

Tracy V. Wallace
Georgia Institute of Technology

14.1 INTRODUCTION

Previous chapters have discussed the impact of phase noise on the performance of several types of coherent radar systems (i.e., pulse compression, stepped-frequency, etc.). This chapter will address the measurement of phase noise generated by oscillators, amplifiers, and other components that are typically used in a radar. There are several methods that can be used to measure the phase noise generated by a device; the optimum method (sensitivity versus cost and complexity) depends on the operating frequency and the noise levels involved. This chapter covers several of the available methods of phase noise measurement and briefly discusses the theory behind each method and its benefits and limitations. An extensive phase noise measurement example is given at the end of this chapter that covers many of the ideas presented.

14.2 PHASE NOISE

Single-sideband phase noise is defined as the ratio of the power in one noise sideband (on a per hertz bandwidth basis) to the total signal power, or:

$$\alpha(f_m) = \frac{\text{Phase noise power in one noise sideband}}{\text{Total Signal Power}} \text{ (per Hz bandwidth)} \quad (14.1)$$

where f_m is the offset frequency from the carrier at which the measurement is made. For small modulation indexes (as is generally the case for phase noise), the following

useful, although simplistic, formula relates the phase noise density to the peak phase deviation.

$$\alpha(f_m) = 20 \log_{10}(\Delta\Phi/2) \tag{14.2}$$

where $\Delta\Phi$ = the phase deviation in radians. Therefore, measurement of the peak phase deviation of the output of a source under test relative to a noiseless source (in the real world, merely a lower noise source) yields the information needed to calculate the single-sideband phase noise.

One can readily convert from the phase modulation domain to the frequency modulation domain by using the simple formula:

$$\Delta\Phi = \Delta f/f_m \tag{14.3}$$

where:

$\Delta\Phi$ = the phase deviation in radians,
Δf = the frequency deviation in hertz, and
f_m = the modulation frequency.

Equation (14.2) can then be rewritten as:

$$\alpha(f_m) = 20 \log_{10}(\Delta f/2f_m) \tag{14.4}$$

For example, if the error frequency deviation is 1 Hz at a modulating frequency of 400 Hz, then the corresponding peak phase deviation is 1/400 or 0.0025 rad or 0.143 degs. A sinusoidal modulation of this amplitude would result in a spurious signal at a level of 20 $\log_{10}$ (0.0025/2) or -58 dB below the carrier.

14.3 PHASE NOISE MEASUREMENT TECHNIQUES

14.3.1 Direct Spectrum Measurements

Direct spectrum measurement of an oscillator's noise spectrum refers to directly connecting the output of the oscillator to the input of the spectrum analyzer. For many low-noise sources, direct measurement of the phase noise by a microwave spectrum analyzer is not practical. Superheterodyne spectrum analyzers are limited both in noise floor, which limits sensitivity, and in the minimum measurable offset frequency, which limits how close to the carrier one can measure the noise sidebands. Also, a spectrum analyzer cannot distinguish amplitude noise from phase noise, so unless the amplitude noise is much less (at least 20 dB) than the phase

noise, the measurement will be corrupted even if the analyzer has the appropriate sensitivity.

Equation (14.5) relates the power density measured on a microwave spectrum analyzer to single-sideband phase noise, assuming negligible amplitude noise and adequate analyzer sensitivity [1]:

$$\alpha(f_m) = P_m(f_m) - P_c - 10\log(B_{sa}) + P_{la} \tag{14.5}$$

where:

$P_m(f_m)$ = power level measured at the offset frequency f_m from the carrier, in decibels referred to 1 mW,
P_c = power level measured at the carrier frequency, in decibels referred to 1 mW,
B_{sa} = resolution bandwidth of the spectrum analyzer, in hertz, and
P_{la} = +2.5-dB error correction for the spectrum analyzer's logarithmic amplifier.

The first two terms of (14.5) form the basic ratio of carrier-to-noise power, and the last two terms account for bandwidth normalization (to a per hertz unit bandwidth) and the noise amplification characteristics of the analyzer's logarithmic amplifier and detector. Usage of the actual equivalent noise bandwidth instead of the resolution bandwidth of the spectrum analyzer results in a more accurate calculation, if the noise bandwidth is known. The equivalent noise bandwidth is typically about 1.2 times the 3-dB resolution bandwidth of the spectrum analyzer [1].

As an example of the limitation of a microwave spectrum analyzer's capability to directly measure the phase noise of a low-noise source, consider Figure 14.1, which is a plot of the sensitivity of the HP8566 and HP8568 spectrum analyzers, along with the typical phase noise levels of some popular microwave sources. Included on the figure is the phase noise of a low-noise 10-MHz crystal oscillator, a 1GHz synthesizer, and a 10-GHz YIG oscillator, which represent a wide range of available noise levels. As can be seen, the microwave spectrum analyzer can only directly measure the phase noise of the noisiest of sources, in this case a YIG oscillator, and even then only out to about 100kHz offset frequencies.

14.3.2 Phase Detector Measurements

Phase Detector Operation

A phase detector is implemented by using a double-balanced mixer, as in Figure 14.2. The input signals are at the same frequency and are in quadrature (90 deg

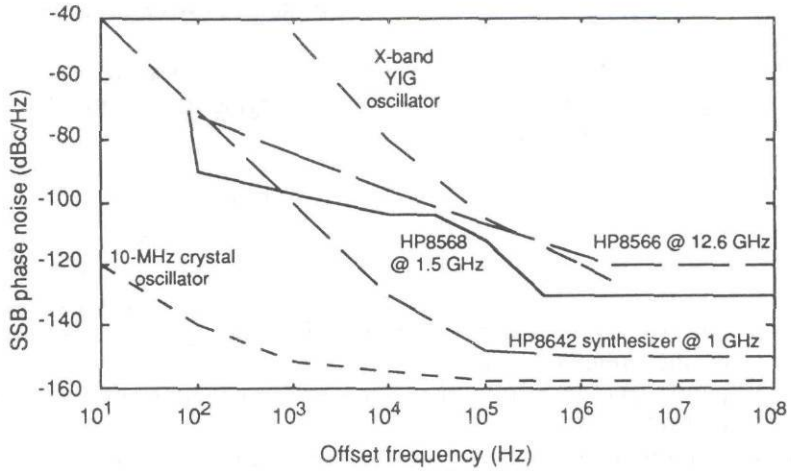

Figure 14.1 Plot of spectrum analyzer sensitivities and noise levels of some common sources.

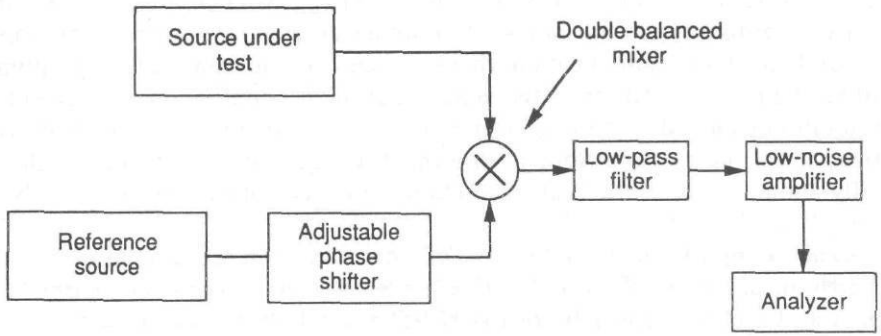

Figure 14.2 Block diagram of a phase detector measurement system.

out of phase) with respect to each other. Phase fluctuations that are not common to both inputs of the mixer result in voltage fluctuations at the mixer output. If the phase fluctuations are relatively small so that the small angle criteria holds (about less than 0.2 rad), the magnitude of these voltage fluctuations is then equal to the phase deviations (in radians) multiplied by the phase detector constant (K_m, the slope of the response of the mixer in volts/radian at quadrature). A phase detector or dc-coupled double-balanced mixer yields an output voltage that is proportional to the phase difference between two signals of the same frequency. A typical phase detector output voltage versus phase difference is shown in Figure

14.3. The output voltage is nulled to 0V when the two signals are in quadrature (90 deg out of phase). At and near quadrature, the phase detector output slope is nearly linear with phase. The lowpass filter eliminates the leakage components of the two sources and any other higher order mixing products from passing through to the *low-noise amplifier* (LNA) or spectrum analyzer. Such components can saturate the LNA or analyzer input.

The single-sideband phase noise spectrum is calculated based on the output of the phase detector by [2]:

$$\alpha(f_m) = PSD\{V(t)\}/(2K_m^2) \tag{14.6}$$

where:

$PSD\{V(t)\}$ = the power spectral density of the output voltage of the phase detector, and

K_m = the phase detector constant in volts/radian.

The factor of 2 in the denominator results from the fact that the output of the mixer is a double-sided spectrum and the single-sideband phase noise is desired.

Figure 14.2 shows a circuit comparing two different sources directly in a phase detector, in an attempt to measure the phase fluctuations of one source relative to that of a reference source. The major problem with this approach is the require-

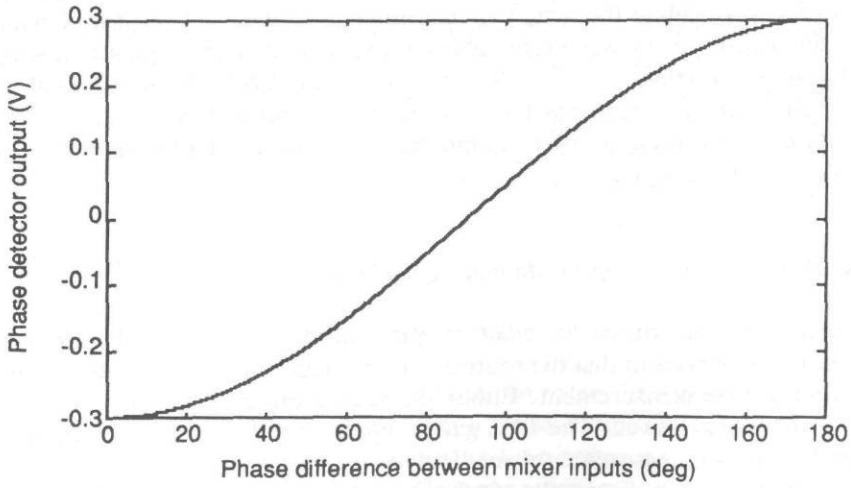

Figure 14.3 Typical output voltage of a phase detector as a function of the phase difference between input ports.

ment to maintain quadrature between the sources for the duration of the measurement, which is difficult to do by merely injecting a fixed phase shift in one arm of the circuit because of instabilities between the two sources.

This setup measures the noise from both sources, and the output of the mixer contains a folded or double-sided noise spectrum, so if each source exhibits an equal amount of noise, the single-sideband noise spectrum for either device is 6 dB lower than the measurement. If the reference source noise is known a priori and the noise measured is much greater than the reference noise, the reference noise can be neglected and the measured noise considered to be that of the source under test.

If the phase detector constant is not known, the measurement setup must be calibrated in order to reference the measured noise levels to the carrier. One method of calibration involves tuning one of the sources off frequency, which results in a pair of beat notes around the nominal carrier frequency [1]. These beat notes represent sidebands that are 6 dB below the fundamental. This level is then set to the -6 dB line on the spectrum analyzer, which references subsequent measurements in decibels below the carrier (relative to the input of the mixer, so the mixer conversion loss need not be known). If the source is retuned and quadrature established (this will have to be checked with an oscilloscope at the phase detector output), the phase noise sidebands can be measured relative to the carrier. Appropriate correction factors, as previously discussed, should be included.

For very-low-noise devices, frequency multipliers can be included in each arm of the phase detector to increase the noise level by 20 log n, where n is the multiplication ratio. This known amount of noise can be backed out of the measured data in order to calculate the actual source noise. This can increase the dynamic range of the measurement system, but also increases the carrier frequency at which the phase detector must operate. Use of a wideband LNA at the input of the spectrum analyzer also improves the dynamic range and system sensitivity. The system noise floor can be set by this amplifier if it has sufficiently high gain and sufficiently low noise figure.

Use of a Phase-Locked Loop to Maintain Quadrature

Phase-locking of one source to maintain quadrature, as shown in Figure 14.4, eliminates the requirement that the sources stay in quadrature by themselves during the duration of the measurement. Either the source under test or the reference source can be phase-locked. The PLL gain suppresses the phase noise within the loop bandwidth, so measurements are limited to offset frequencies greater than the loop bandwidth (or the results obtained within the loop bandwidth must be corrected to remove the loop gain). To minimize this effect, the loop gain should be low, which results in narrow loop bandwidth (which is proportional to loop

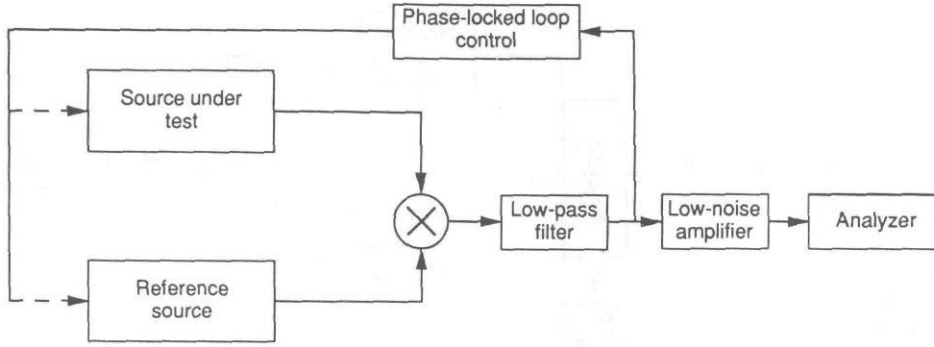

Figure 14.4 Use of a PLL to maintain quadrature between two sources in a phase detector.

gain) and relatively loose locking characteristics (i.e., the system can only tolerate small amounts of drift in the oscillator under test to maintain lock).

Pulsed Phase Noise Measurements

The phase noise of a pulsed source can be measured with the setup of Figure 14.5. The primary difference between this setup and that of Figure 14.4 is the inclusion of a pulse modulator (such as a pin switch) in line with the reference source. Synchronously pulsing the reference source and the source under test reduces the effects of phase detector dc offset and source AM noise [3]. The pulsed duty cycle sets the average power into the mixer and also the available signal power for the PLL control circuitry. Therefore, the duty cycle directly affects the phase detector sensitivity and hence the system noise floor. It should also be noted that noise measurements at offset frequencies greater than half the PRF are not necessary, because the noise spectrum repeats around each PRF line of the pulsed spectrum.

14.3.3 Discriminator Measurements

Delay Line Discriminator Operation and Sensitivity

Figure 14.6 is a diagram of a frequency discriminator. The output of the source under test is split: one path is sent through a phase shifter to one arm of the phase detector mixer, while the other is delayed in time before application to the other arm of the phase detector. This causes the noise sidebands of the source to become uncorrelated at the ports of the phase detector (the exact opposite of what is desired for a regular phase detector arrangement). Because time delay represents a linear

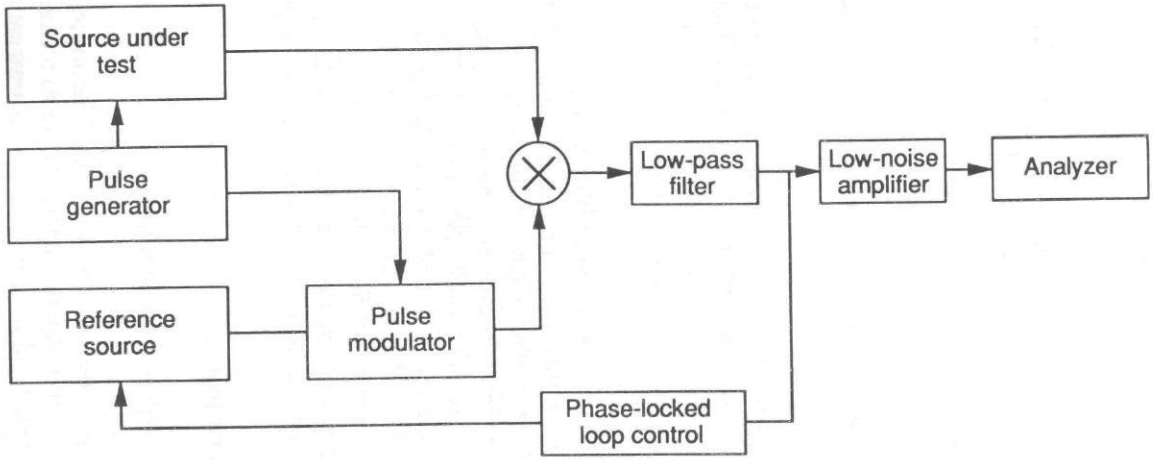

Figure 14.5 Setup to measure pulsed oscillator phase noise.

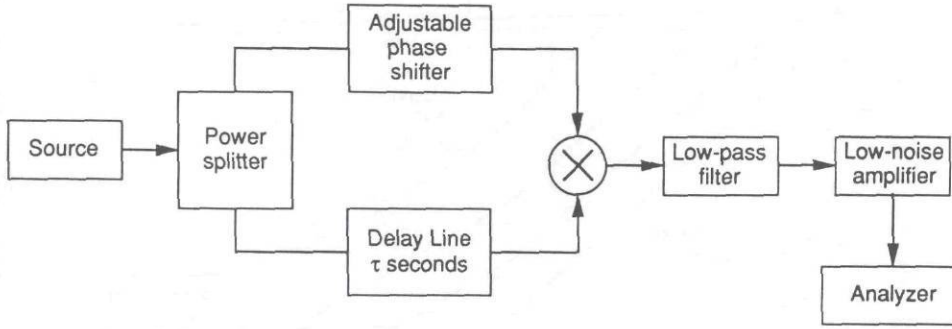

Figure 14.6 Diagram of a frequency discriminator.

phase shift with frequency, the frequency fluctuations of the source are converted to phase fluctuations at the input of the phase detector.

To characterize the response of the system, the phase detector constant must be modified by the time delay τ to form a new discriminator constant K_d given by [2]:

$$K_d(V/\text{Hz}) = K_m(V/\text{radian}) \cdot 2\pi\tau\{\sin(\pi f\tau)/\pi f\tau\}$$

or

$$K_d(V/\text{Hz}) = K_m(V/\text{radian}) \cdot 2\pi\tau \text{ for } f \leq 1/2\pi\tau \tag{14.7}$$

The single-sideband phase noise spectrum is calculated by [2]:

$$\alpha(f_m) = PSD\{V(t)\}/(2f_m^2 K_d^2) \tag{14.8}$$

The approximate sensitivity of such a measurement system is the phase detector noise floor tipped up by 20 dB/decade at an offset frequency of $1/2\pi\tau$, where τ is the time delay. Longer delays result in better sensitivity (K_d is directly proportional to τ in (14.7)) but also limit the maximum offset frequency at which a noise measurement can be made. Discriminators are valid out to offset frequencies less than about $1/2\pi\tau$.

The delay line discriminator has maximum sensitivity to FM when the inputs to the phase detector are in quadrature (which can be accomplished with the phase shifter in Figure 14.6) and when the delay τ is an integral number of odd quarter wavelengths of the carrier frequency [4].

Figure 14.7 is a plot of discriminator sensitivity for several values of delay τ for a particular phase detector noise floor. Also plotted are the phase noise of

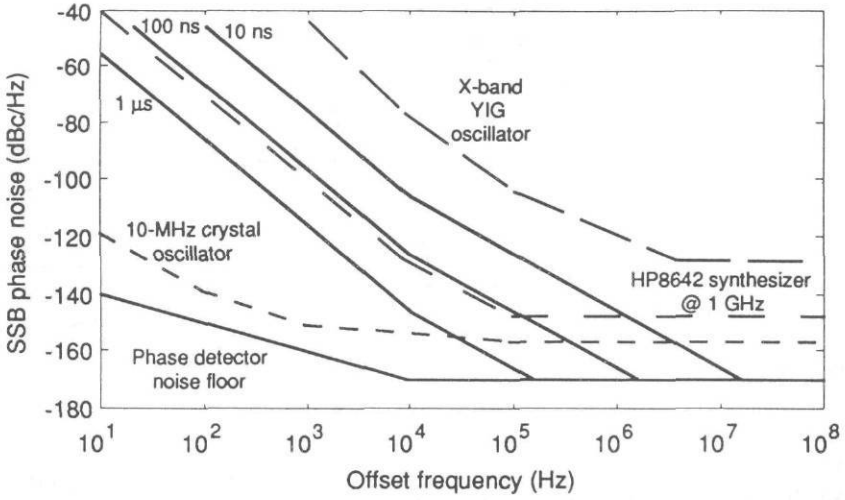

Figure 14.7 Plot of discriminator sensitivity for various delays and noise levels of some common sources.

some typical sources, which shows the relative inability of a discriminator to measure the noise of very-low-noise sources without the need for extremely long delay lines, which limit the range of offset frequencies that can be measured. Discriminators can be useful, however, in that they require no low-noise reference source.

A delay line discriminator can be calibrated by modulating a tunable source, such as a VCO, at a fixed frequency f_m, and noting the VCO output directly on a spectrum analyzer. The amplitude of the sidebands at f_m is then set to be somewhere between 30 to 40 dBc (for a low modulation index). The sideband level on the microwave spectrum analyzer is noted (let us assume 40 dB), as well as the signal on the baseband analyzer, which now corresponds to a signal that is at -40 dBc. The baseband analyzer has now been calibrated in decibels below the carrier. This general method of calibration is illustrated in the measurement example at the end of this chapter.

14.3.4 Additive or Residual Noise Measurements

The additive, or residual, noise from a device such as an amplifier can be measured as in Figure 14.8. The output of a single reference source is split; one arm is fed to the input of the device under test (dut) that drives one arm of the phase detector, while the other arm is phase shifted to set the signals at the mixer ports to be in quadrature. No PLL is needed here because only one source is involved. If the

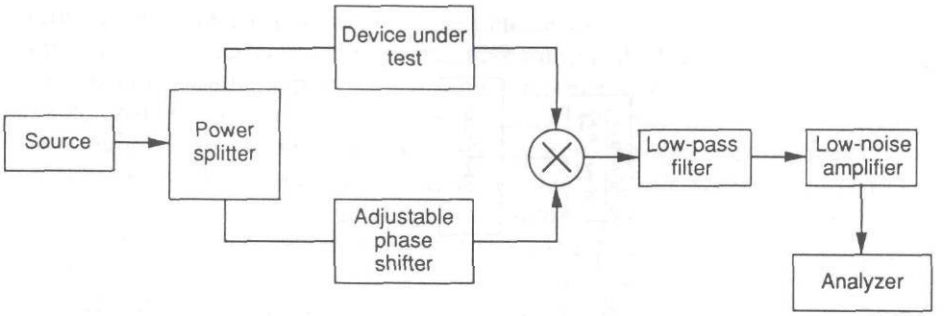

Figure 14.8 Additive or residual noise measurement setup.

time delays between the two paths are equal, the source noise will be correlated at both mixer inputs and will cancel. Any phase fluctuations due to the DUT will not correlate (because they are present only at one port of the phase detector), and hence, these fluctuations can be observed at the phase detector output. If the DUT causes frequency translation (such as a mixer or frequency multiplier), one should be inserted into each arm of the phase detector. In this case, the rms sum of the noise from both devices is measured. An assumption can be made that the noise contributions from the two (similar) devices are equal, or a three-source comparison can be made to increase the accuracy of the measurement.

Pulsed residual phase noise, such as that generated from a pulsed amplifier like a transmitter power tube, can be measured as in Figure 14.9. If the device is a high-power amplifier, the output may need to be coupled or attenuated down before application to the phase detector. As in the pulsed absolute phase noise measurement case, both sides of the phase detector should be pulsed to minimize the effects of dc offset in the mixer. The pulsed duty cycle affects the phase detector sensitivity and hence the system noise floor, but a lower duty cycle can usually be tolerated relative to the absolute noise case, because there is no requirement for a control signal for a PLL in this case. Also, as for the pulsed absolute noise case, measurements at offset frequencies greater than half the PRF are not necessary, because the noise spectrum repeats around each PRF line of the pulsed spectrum.

14.3.5 Reference Source Considerations

The phase noise of the reference source should be about 10 dB below that of the source under test (for all offset frequencies of interest) to ensure that the measurement results are not significantly degraded by reference source noise. If a reference source is not available with sufficiently low phase noise for all offset

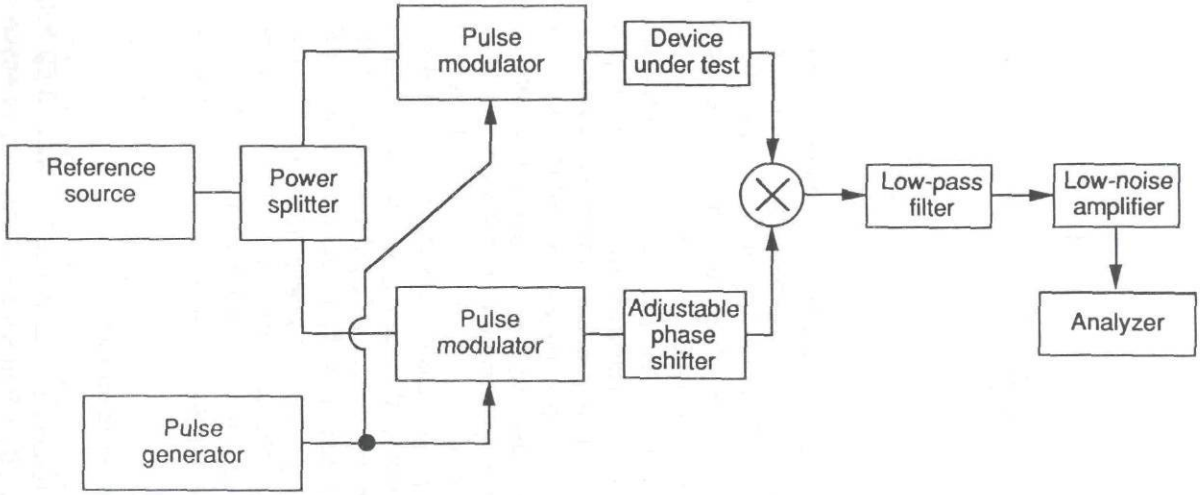

Figure 14.9 Pulsed additive or residual phase noise measurement setup.

frequencies of interest, it may be possible to use several different sources with sufficient noise characteristics at different ranges of offset frequencies. If this is not possible, another option is to use a reference source with comparable noise characteristics to the source under test and assume equal noise contributions from each source at the output of the phase detector, so that the source under test noise is estimated at 3 dB below the measured value. If three comparable sources are used and compared to each other, the resulting three dependent measurements can be used to separate the noise from each source (three equations, three unknowns).

The circuit of Figure 14.10 can be used to measure the phase noise of microwave sources that cannot be tuned and is also useful for higher frequency (especially MMW) sources [2]. The reference source is mixed with the source under test to generate an IF. Phase detection is then performed at this IF against a third oscillator that is phase-locked. One advantage of this configuration is that the high-frequency reference source is not required to be tunable and hence can be a lower noise oscillator or even a filtered multiple of the lower frequency, low-noise coherent oscillator. Also, phase detection is performed at a lower frequency, where phase detectors are available with better AM rejection.

14.4 MEASUREMENT EXAMPLE

14.4.1 Pulsed TWT Amplifier Additive Phase Noise Measurement

This section describes a technique for measuring the additive phase noise in a pulsed, MMW *TWT amplifier* (TWTA) that uses a switching HVPS. This example, therefore, covers some of the more difficult aspects of phase noise testing (i.e., pulsed versus CW and MMW versus lower microwave frequencies). CW measurements can be made without the added complication of pulsing the input to the amplifier and sampling the baseband output of the phase detector. Lower frequency microwave measurements can likely be made without the added complication of the up-conversion and downconversion scheme required in this example. This example also illustrates the effects on the additive phase noise when the transmitter high-frequency switching power supply is synchronized with the radar PRF.

Pulse-to-pulse phase jitter caused by TWT modulator and power supply voltage ripples will result in range and doppler sidebands. The amount of phase and amplitude modulation resulting from a ripple voltage waveform depends on the phase and amplitude sensitivities of the particular TWT electrode. Typical TWT cathode-to-body voltage phase sensitivity is about 30 deg for a 1% change in cathode voltage. Therefore, ripple on the cathode-to-body voltage must be kept extremely small to minimize additive phase noise.

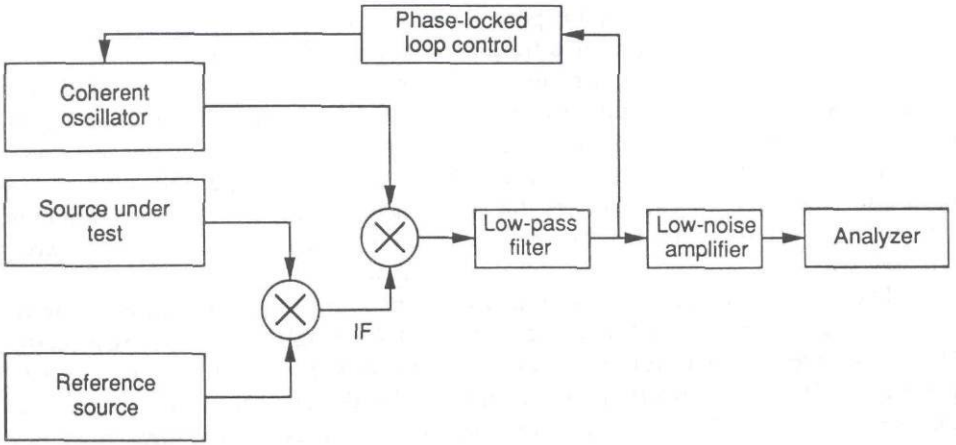

Figure 14.10 Method of measuring phase noise of high-frequency or nontunable oscillators (after [2]).

Transmitter tube phase and amplitude sensitivities can usually be provided by the tube vendor. One way to measure the phase sensitivities is to inject a known amount of ripple voltage onto the nominal value of cathode-to-body voltage within the TWT test setup and either (1) measure the spectral content of the output on a microwave spectrum analyzer and calculate the peak-to-peak phase modulation based on the sideband amplitude or (2) inject a sample of the modulated output signal into one arm of a calibrated phase detector with the other arm driven by the unmodulated drive signal. The amount of phase modulation could then be calculated using the phase detector constant and the signal displayed on a baseband analyzer.

14.4.2 Instrumentation Setup

Spectral purity measurements of pulsed sources are much more difficult to perform than for CW sources. Low-duty-cycle operation, such as in the 95-GHz TWTA described here (less than 1%), results in very-low-level spectral components of the pulsed carrier. These low-level components result in a reduction of the SNR in a microwave spectrum analyzer, limiting its dynamic range and limiting its usefulness in making the noise measurement. Instead, a phase bridge is used and the phase demodulated signal is displayed on an FFT analyzer, so that the low-frequency components can be viewed.

A phase bridge setup is used to perform additive phase noise measurements. A phase detector or double-balanced mixer (dc coupled) yields an output voltage that is proportional to the phase difference between two signals of the same frequency. At and near quadrature, the phase detector output slope is nearly linear with phase. If the electrical path lengths between the source and both sides of the phase detector are equal, the source phase noise will cancel and phase fluctuations caused by the DUT relative to the source will be sensed by the phase detector, as discussed earlier.

Figure 14.11 is a block diagram of the instrumentation setup used to measure the additive phase noise of the 95-GHz TWTA. This setup is useful in that the detected RF, intrapulse phase, and phase noise can all be measured simultaneously. This setup uses a Gunn oscillator as the W-band LO and an HP8672A synthesizer as the 2- to 4-GHz IF source for up-conversion. The output of the up-converter drives the TWTA and also one arm of the phase bridge. The signal is first gated in a pin switch so that both sides of the phase detector are pulsed. The output of the TWTA drives the other arm of the phase bridge.

Each arm of the phase bridge is down-converted with the 91-GHz LO to the 2- to 4-GHz IF. Phase detection is then performed at IF, where better phase detectors are available. This approach was followed primarily because a W-band phase detector was not readily available; it turns out that this approach is the only feasible way to view the PRF lines. The PRF lines are not distinguishable at W-band on the microwave spectrum analyzer; however, they are clearly visible at the down-converted IF of 2 to 4 GHz. In this manner, any phase noise or frequency instability inherent in the Gunn oscillator is canceled during the down-conversion process, and the stability of the synthesizer is more than adequate to allow viewing between PRF lines.

The output of the phase detector is fed to a *sample-and-hold* (S/H) circuit and then to the HP3561A dynamic signal analyzer, which is used to perform an FFT on the demodulated baseband phase deviations. Other baseband signal analyzers can be used, but they must have adequate dynamic range.

Calibration is performed similarly to that discussed for calibrating a delay line discriminator and involves looking between PRF lines of the RF carrier and injecting a known error modulation frequency that is less than the PRF/2 (and not at any known spurious signal, such as the power line frequency or any harmonics thereof). For instance, if the PRF is 10 kHz, an error modulation frequency of 3 kHz is acceptable. The error modulation signal is added to the cathode HVPS through its feedback circuit, phase modulating the TWT output signal by exploiting the phase sensitivity of the TWT cathode voltage. While viewing the pulsed carrier on the HP8562A microwave spectrum analyzer, the error modulation amplitude is increased to some measurable level below a PRF line (-35 dBc in this example). Then, when the output of the S/H is displayed on the FFT analyzer, the phase

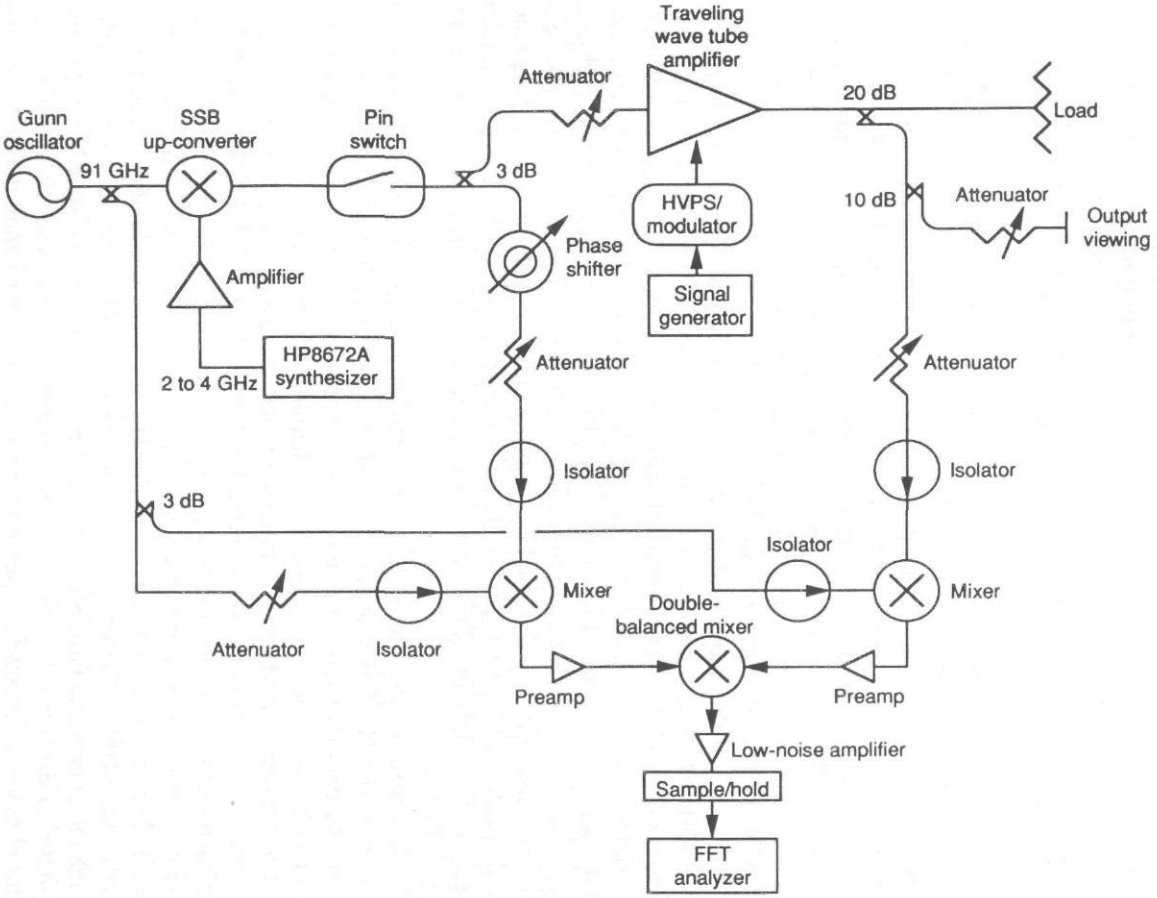

Figure 14.11 Instrumentation setup for measuring 95-GHz pulsed TWTA additive phase noise.

noise level can be referenced to the error modulation level in decibels below the carrier.

An additional calibration step is required in order to characterize the noise floor of the measurement setup. The TWT is removed from the waveguide system and replaced with WR-10 waveguide. The resulting phase noise measurement represents the noise floor (limit of the minimum detectable signal level) of the system. Measured data on the amplifier are then compared to the noise floor to ensure that the measurements are not noise floor limited.

14.4.3 Example Phase Noise Test Results

Phase noise was measured at various PRFs, both synchronized and unsynchronized with the HVPS switching frequency. For continuity between measurements, all phase noise levels quoted in the text are taken from the plots at an offset frequency of the PRF/4. Phase noise data above the PRF/2 point are merely a mirror image of that below the PRF/2 point, but attenuated by a S/H sinc magnitude function. The S/H correction factor given as [5]:

$$A(f) = 20 \log|\sin \pi f/\text{prf})/(\pi f/\text{prf})| \tag{14.9}$$

has a maximum value of -3.92 dB at the PRF/2. The value of this correction factor at the PRF/4 point is less than 1 dB and is therefore ignored for the rest of this discussion. Bandwidth normalization is also used to convert the FFT outputs to decibels below the carrier in a 1-Hz bandwidth. The actual noise level in decibels below carrier in a 1-Hz bandwidth is 10 log(BW/Hz) below the value read off of the plot, where BW is the resolution bandwidth of the HP3561A, which is noted at the top of each plot.

Figure 14.12 is the spectrum analyzer display showing a PRF line at 10-kHz PRF at the IF frequency of 3 GHz. This signal is taken from the output of the IF amplifier on the output side of the TWT phase bridge. At the 10-kHz span (1 kHz per horizontal division) the error modulation (calibration) signal at 3 kHz is easily distinguishable at 35 dB below the PRF line. This error signal is used to calibrate all baseband phase noise results in decibels below the carrier.

For example, Figure 14.13 shows the baseband data (from the HP3561A) at 10-kHz PRF with the calibration signal at 3 kHz and -35 dBc; Figure 14.14 is the same test case with the calibration signal removed, but showing the -35-dBc calibration level. At 10-kHz PRF synchronized with the HVPS switching frequency, the additive phase noise level appears to be below -70 dBc (in a 119-Hz bandwidth) or -90 dBc/Hz. From Figure 14.15, when the PRF is not synchronous with the power supply, the noise level rises about 5 dB to -85 dBc/Hz.

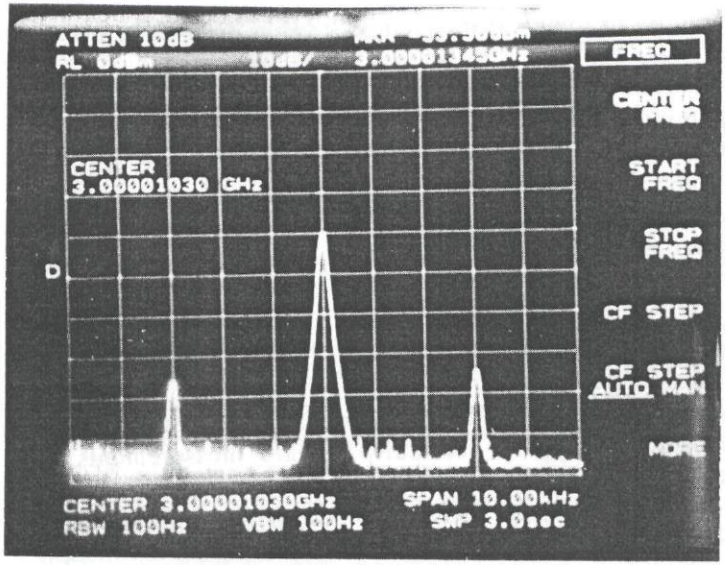

Figure 14.12 Microwave spectrum analyzer display showing a PRF line at 10 kHz and the error calibration signal 3 kHz away at −35 dBc.

Figures 14.16 and 14.17 are test results at 20-kHz PRF. Figure 14.16 shows the phase noise when the PRF is synchronized with the HVPS. The phase noise level is about −92 dBc/Hz, and a significant spur exists at −40 dBc at 10 kHz. Figure 14.17 shows the same case, except that the TWT trigger pulse has been time delayed an optimal amount (2.8 μs in this case) relative to the HVPS synchronizing pulse train. The phase noise level is about −96 dBc/Hz; also note the absence of the spur at 10 kHz. This spur occurs when the transmitter pulses at odd integer multiples of 10 μs (HVPS sync period), because the HVPS ripple waveform is a triangular waveform at 50 kHz. At 20-kHz PRF or 50-μs period, the transmitter pulses alternately during the up and down slopes of the HVPS ripple voltage. This suggests that proper placement (delay) of the TWT trigger pulse relative to the power supply synchronization signal might greatly reduce pulse-to-pulse jitter at PRFs such as 20 kHz by equalizing the voltage at both phases of the power supply ripple waveform. Figure 14.17 confirms this suggestion.

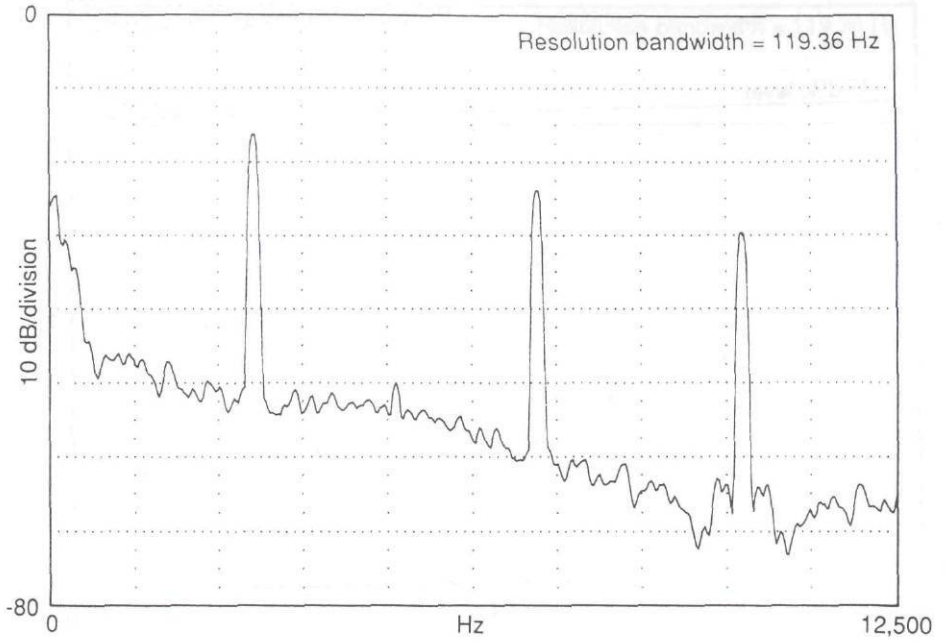

Figure 14.13 FFT display at 10-kHz PRF (synchronized) showing 3-kHz error calibration signal at −35 dBc.

14.4.4 Noise Floor Measurement

The TWT was removed from the setup and replaced with a piece of WR-10 waveguide. Figure 14.18 is a plot of the FFT display of the noise floor at 20-kHz PRF. Similar data was obtained at 10-kHz PRF. The noise floor appears to be about 10 dB below the measured TWTA additive phase noise data, so the measurements are not noise floor limited. To further reduce the noise floor, a higher quality S/H circuit would be needed or possibly more careful layout of the W-band waveguide runs to equalize electrical path lengths to both sides of the phase detector. This latter consideration was not very practical in this setup, so the path lengths are not matched, and therefore, some Gunn oscillator phase noise may be contaminating the measurement.

14.5 GENERAL COMMENTS ON PHASE NOISE MEASUREMENTS

Each method of phase noise measurement has its own peculiarities, but some general comments can be made that are applicable to all of the methods.

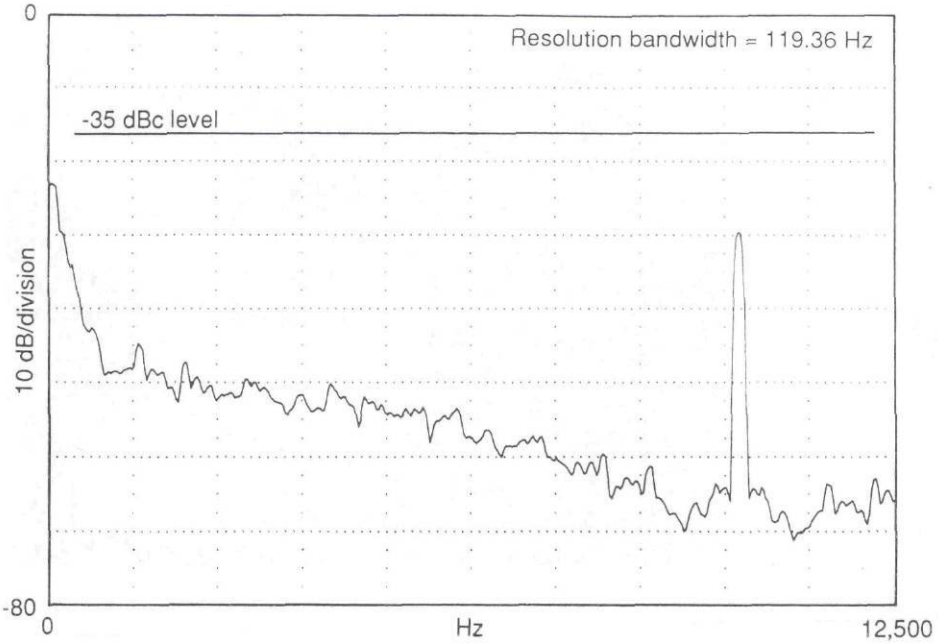

Figure 14.14 FFT display at 10-kHz PRF (synchronized) showing −35 dBc calibration level.

1. For phase noise measurements to be accurate, the spectrum or baseband analyzer resolution bandwidth should be much less than (≤5%) the offset frequency at which the measurement is being made.
2. All phase noise measurements are very sensitive measurements and are subject to contamination from external noise sources (i.e., vibration, signals generated in the lab next door, etc.). Appropriate grounding, shielding, and other noise reduction techniques need to be applied to make accurate low-noise measurements.
3. It is desirable to use more than one method to measure the phase noise of a device so that the results can be compared. If vastly different results are obtained, then it is probable that an error was made during at least one of the tests, and the test(s) should be rerun.

14.6 SUMMARY

This chapter has covered some of the more prevalent methods of phase noise measurement. The optimum choice of a measurement system depends on the phase

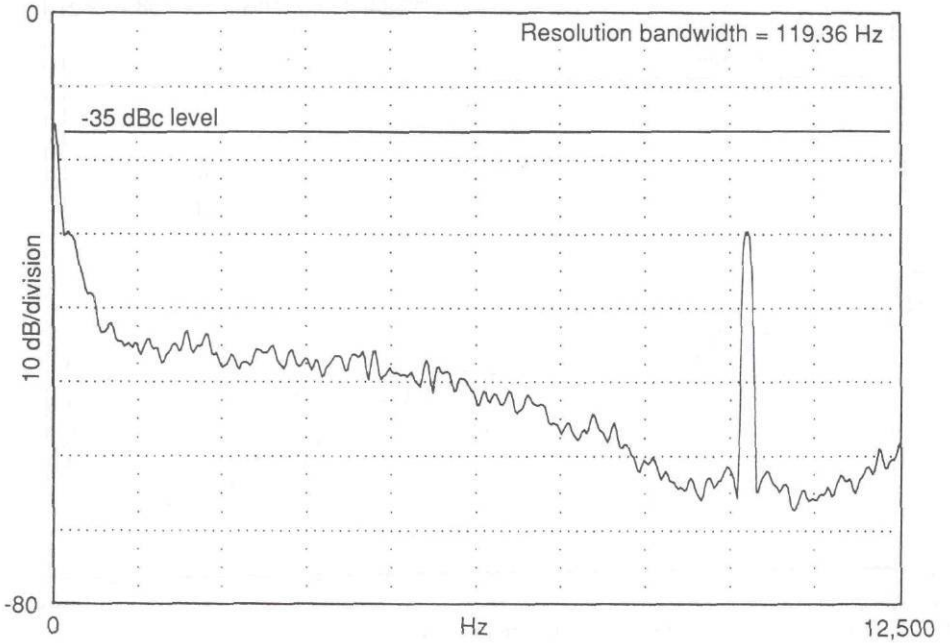

Figure 14.15 FFT display at 10-kHz PRF (not synchronized).

noise level of the device to be tested (which sets the sensitivity requirements) and its operating frequency (which may limit the utility of certain methods). Direct measurement of phase noise with a spectrum analyzer is generally not practical because of a lack of sensitivity, although spectrum analyzers are extremely useful (e.g., in obtaining a quicklook measurement of an oscillator's output spectrum). Various other methods that suppress the carrier frequency, so that a baseband or lower frequency spectrum analyzer with greater sensitivity can be used to display the demodulated noise sidebands, are more desirable and provide more accurate measurements. Such methods also tend to eliminate or greatly reduce amplitude noise and therefore only display the actual phase noise.

Two carrier suppression methods were discussed: the phase detector and the delay line discriminator. The phase detector is the most sensitive technique, but is more complicated to implement than the discriminator, as it commonly requires a low-noise reference oscillator and a PLL. Discriminator sensitivity improves with increasing delay line length, but longer delays also limit the maximum offset frequency at which the noise can be accurately measured.

This chapter has presented an extensive example that illustrated the measurement of the additive phase noise from a pulsed, 95-GHz TWTA. The mea-

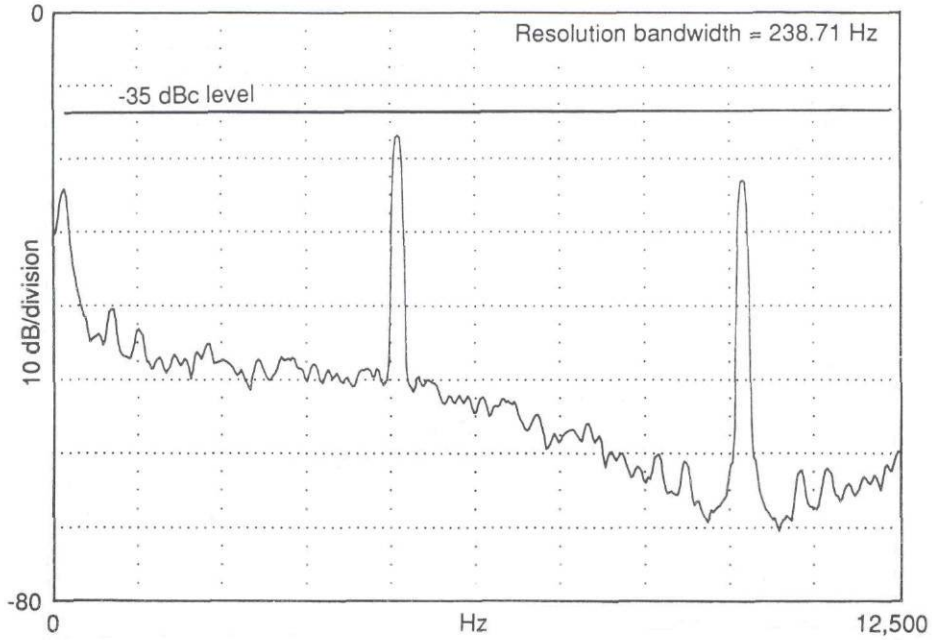

Figure 14.16 FFT display at 20-kHz PRF (synchronized).

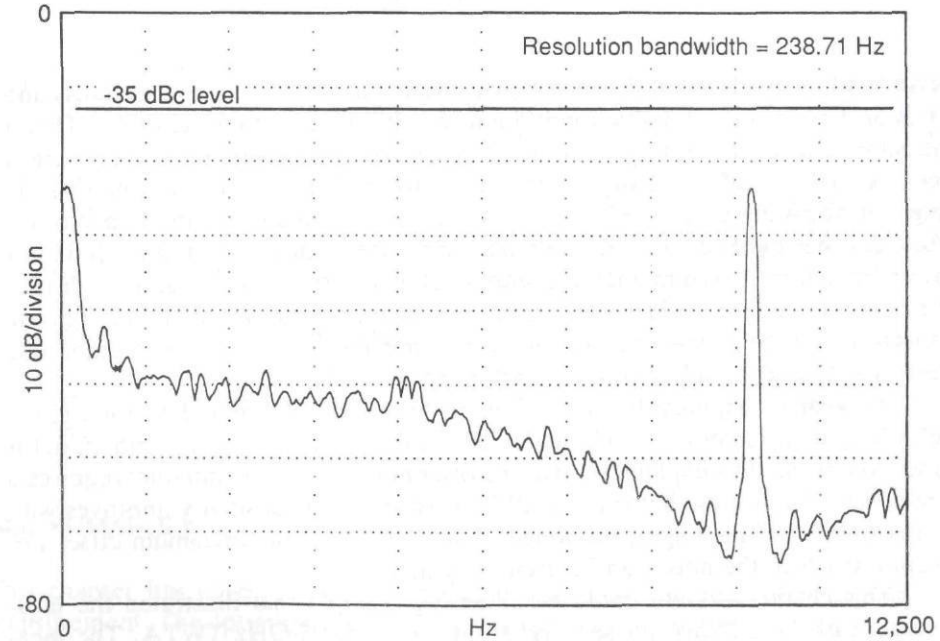

Figure 14.17 FFT display at 20-kHz PRF with optimal time delay (synchronized).

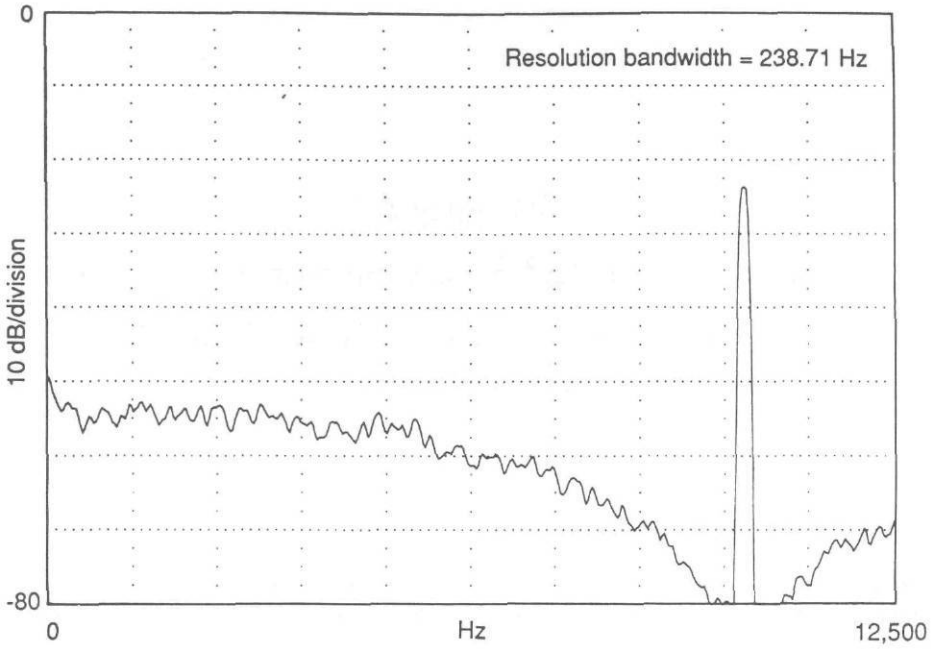

Figure 14.18 Noise floor measurement at 20-kHz PRF.

surement setup used a phase detector, with some additional hardware required for frequency conversion. Calibration of the test results in decibels below the carrier and the effects of the high voltage switching power supply on the phase noise measurements were discussed.

REFERENCES

[1] "Spectrum Analysis—Noise Measurements," Hewlett Packard Application Note 150-4, April, 1974.

[2] Decker, T., and B. Temple, "Choosing a Phase Noise Measurement Technique; Concepts and Implementation," *Hewlett-Packard RF and Microwave Measurement Symp.*, 1983.

[3] "Analysis and Simulation Techniques for Modern Radar," Short Course Notes, Hewlett-Packard, Palo Alto, CA, 1988.

[4] Manassewitsch, V., *Frequency Synthesizers; Theory and Design*, New York: John Wiley & Sons, 1980.

[5] Nocella, P., "Practical Spectral Purity Measurement of Pulse Doppler Radar Transmitter Amplifiers," *17th Power Modulator Symp.*, 1986.

Chapter 15
Radar Component and Subsystem Tests

James L. Kurtz and Robert G. Pauley
Scientific Research Corporation and
Georgia Institute of Technology

15.1 APPROACH AND EMPHASIS

In this chapter we will discuss coherent radar component and subsystem tests. Important test considerations for radar components are reviewed and specific test techniques applicable to coherent radar components are discussed in more detail. Basic testing of transmitter and receiver components is addressed only briefly here, because such information may be found in various texts, whereas special emphasis is placed on the testing of components critical to coherent radar performance (e.g., quadrature detectors and A/D converters).

Table 15.1 lists some of the major test considerations for components and subsystems within the coherent radar shown in Figure 15.1. Although these are not all of the important component and subsystem test considerations, each is usually important to coherent radar operation.

To ensure proper coherent radar performance at the system level, the various components and subsystems should first be individually evaluated. After it has been determined that test specifications are met at this level, system-level performance tests may be performed. The following discussion, referring to Table 15.1, describes component and subsystem tests that should be considered before system level tests are initiated. System-level performance tests are discussed in Chapter 16.

15.2 TRANSMITTER/EXCITER TESTING

Waveforms generated in the radar exciter must exhibit stability to ensure good coherent radar performance. The radar pulse widths and PRFs need to be accurately

Table 15.1
Coherent Radar Testing Component and Subsystem Test Considerations

Component/Subsystem	*Component Level Test Considerations*
Transmitter/exciter	Peak Power Pulse width Modulation type(s) Phase noise Frequency agility Pulse jitter
LNA(s) and IF amplifier(s)	Noise figure Sensitivity Gain Dynamic range/linearity Automatic gain control Bandwidth Gain compression Spurious and intermodulation products Sensitivity time control Phase response versus frequency
Mixers and mixer preamps	Noise figure Sensitivity Conversion loss/gain Dynamic range linearity Spurious and intermodulation products Phase response versus frequency
Filters	Loss Bandwidth Amplitude response versus frequency Phase response versus frequency
Quadrature detectors	Quadrature phase error Gain imbalance DC offset Image rejection Dynamic range
A/D converters	Linearity, resolution, bandwidth, aliasing
Digital signal processor(s)	Signal sampling and aliasing Quantization errors Dynamic range Functional and algorithmic tests

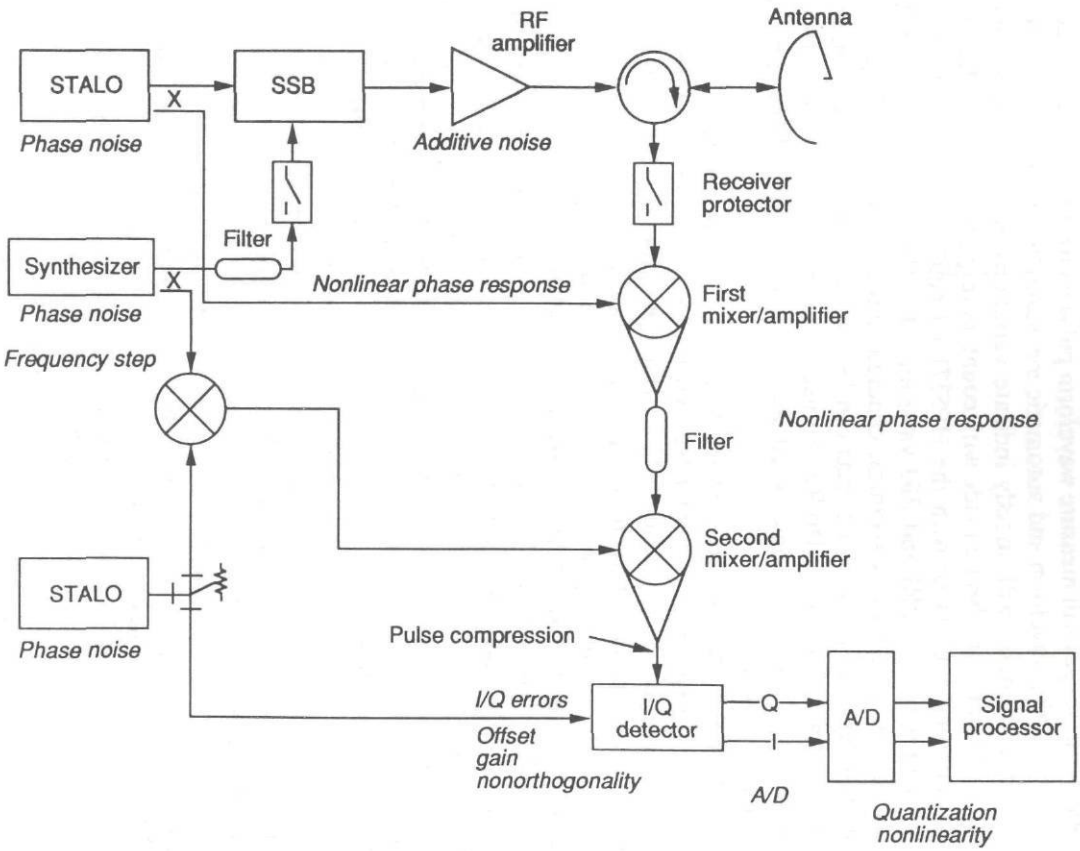

Figure 15.1 Coherent radar system block diagram.

generated and maintained to ensure coherent detection. Pulse width, PRF, and pulse jitter are usually measured in the time domain (i.e., with an oscilloscope). Pulse waveforms at video or IFs (a few hundred megahertz or less) can be measured directly on an oscilloscope, provided the oscilloscope has sufficient bandwidth. Many digital oscilloscopes will measure waveform pulse width and period by placement of cursors on the waveform and automatic measurement of time differences. Some of these instruments will directly indicate variations in pulse width. Time interval measurements can also be made with counters (e.g., the Hewlett-Packard HP5360A computing counter or with the HP5371A frequency and time interval analyzer) to determine the PRI and PRI variations. If either pulse width or PRI jitter exists on the radar pulse waveform, coherent integration and MTI performance can be degraded; these two effects can be measured in the time domain. Once the waveform is up-converted to RF, it is usually necessary to either envelope-detect the waveform for display on an oscilloscope or measure the characteristics in the frequency domain.

A spectrum analyzer can be used for frequency domain measurements of pulse waveform characteristics at higher frequencies. A CW pulse waveform will have the characteristics shown in Figure 15.2. Thus, the pulse width and PRF (1/PRI) can be readily measured at the carrier frequency of the waveform [1], as shown in Figure 15.2. The requirement for observing the pulse spectrum is that the spectrum analyzer IF bandwidth, B, exceeds the PRF ($B_{IF} > B_{PRF}$). In order to observe the PRF line spectrum (i.e., individual lines at the PRF), it is necessary to reduce the spectrum analyzer bandwidth to less than the PRF line spacing. Most spectrum analyzers have the capability to envelope-detect RF pulses as well (this is often referred to as the "zero span mode" in a spectrum analyzer). With envelope-detection, the pulse waveform time domain characteristics can be measured.

Transmitter/exciter modulation characteristics often can be verified in the frequency domain (i.e., spectrum analyzer measurements). However, it is sometimes difficult to isolate or separate unintentional amplitude and phase errors from those that are related to the desired modulation. Measurement of waveform errors in the frequency domain requires a priori knowledge of the spectral characteristics of an error-free waveform and some insight into the effects of different errors on the waveform. For example, a rectangular RF pulse with amplitude droop across the pulse will raise frequency spectrum sidelobes; however, FM within the pulse will cause the same or similar effects (see Chaps. 6 and 11). Thus, the effects of amplitude and FM on the pulse are difficult to differentiate when observing the spectrum. Amplitude and phase demodulator instrumentation can be used to measure the amplitude and phase characteristics of a waveform in the time domain. This type of equipment can be especially useful to analyze chirp or phase-coded waveforms. By demodulating the transmitter/exciter waveform with a COHO and displaying the *inphase* (I) and *quadrature-phase* (Q) components in time, it is possible to detect amplitude and phase errors in coded waveforms.

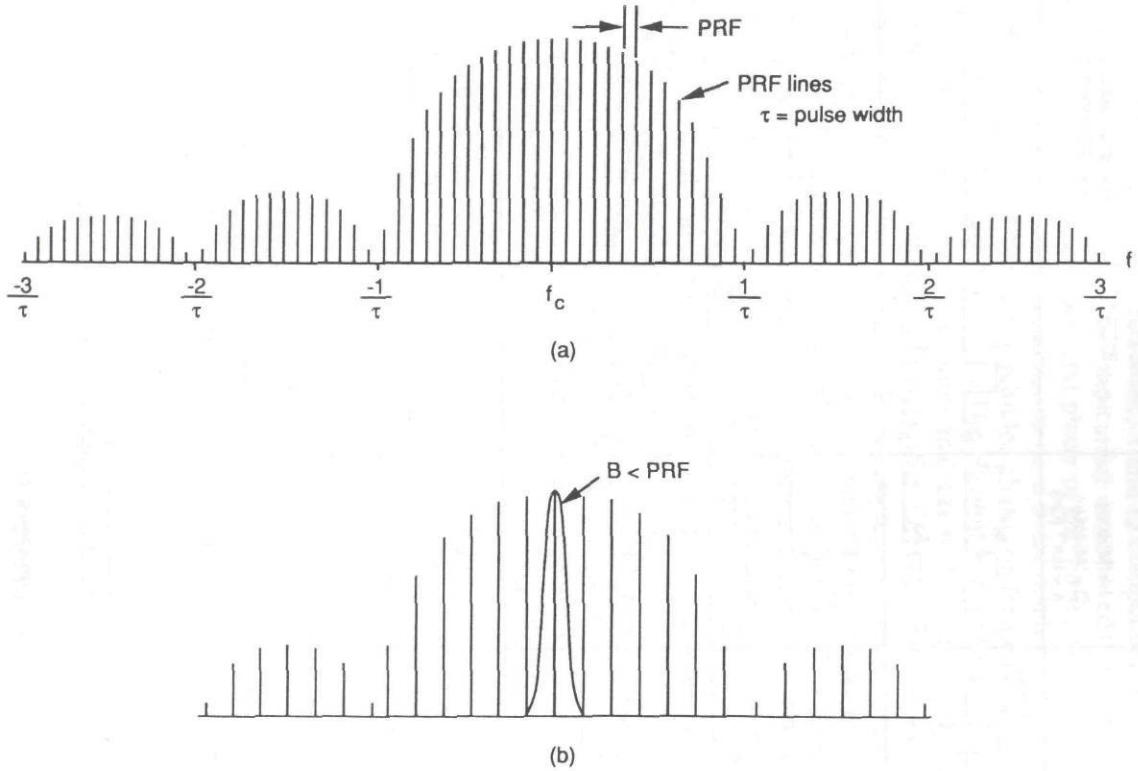

Figure 15.2 (a) Spectrum of a carrier amplitude modulated with a rectangular pulse; (b) pulse spectrum IF bandwidth smaller than PRF.

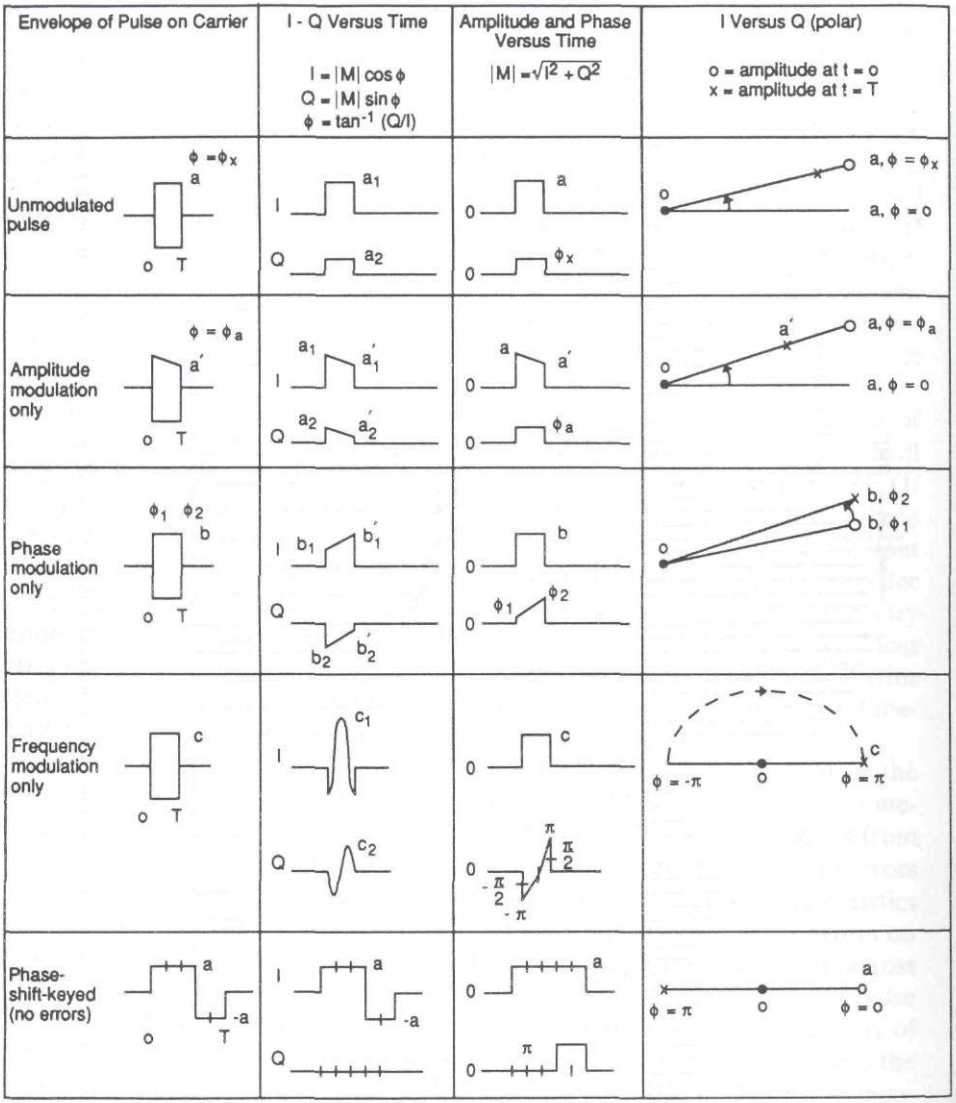

Figure 15.3 Time domain waveform examples.

Figure 15.3 shows examples of time domain waveforms, as they would appear in several different types of time displays. The first column of Figure 15.3 shows the envelope of the waveform as it would appear on a carrier (at RF or IF). The second column of Figure 15.3 shows the I and Q components versus time, if the pulse is coherently detected (i.e., the carrier is removed). The third column of Figure 15.3 shows the amplitude and phase of the pulse, and the fourth column shows a plot of the I and Q components on a polar display. As shown in Figure 15.3, different types of errors (amplitude, phase, or frequency) are more easily detected in different display formats. The Hewlett-Packard HP8980A vector analyzer and HP8981A vector modulation analyzer will coherently demodulate and display waveforms such as those in Figure 15.3. Other instrumentation can be used to measure chirp waveform linearity. For example, a calibrated delay line discriminator will provide an output voltage proportional to frequency for measuring coarse linearity. Special purpose instrumentation (such as the HP5371A) will provide very accurate plots of frequency versus time or statistical averages (means and variances) of chirp waveforms versus time functions. Residual amplitude and phase modulation on signal sources can also degrade coherent radar performance. Techniques for measuring signal source phase noise and for differentiating amplitude and phase modulation are discussed in Chapter 14.

Transmitter power level directly affects the radar's detection performance (according to the radar range equation). Power meters allow the measurement of average power at RFs or IFs, and some power meters will measure pulse power (e.g., the Hewlett-Packard HP8990A with the appropriate power sensors). Pulse power can also be measured using a spectrum analyzer [1]. For a rectangular pulse, the pulse power may be measured from the peak pulse spectrum response (i.e., power level on a spectrum analyzer) and corrected by adding a desensitization factor, α_p, where:

$$\alpha_p[dB] = 20 \log(\tau_{eff} \cdot K \cdot B) \tag{15.1}$$

and τ_{eff} is the pulse width, B is the analyzer 3-dB IF bandwidth ($B >$ PRF), and K is a constant, usually $K \approx 1.5$. Alternatively, the power level may be determined from the peak power level plus 20 log (PRI/τ_{eff}), where PRI is the pulse repetition interval, when $B <$ PRF.

15.3 AMPLIFIER, MIXER, AND FILTER TESTING

Many of the specifications and requirements for amplifiers, mixers, and filters are similar when employed as coherent radar components. Some of the salient performance specifications of these components and techniques for measuring them will be discussed.

Noise figure relates to the amount of noise a component adds to the subsystem or system, in addition to the existing thermal noise, when measured in a particular bandwidth and at a particular temperature. The noise figure can be expressed as the SNR at the input to a component (or system) divided by the SNR at the output and is generally greater than unity (i.e., almost all components or systems add thermal noise). Techniques exist for measurement of noise figure using spectrum analyzers, and the specifics of those techniques can be found in manuals for the analyzer or in application notes [2]. However, specially designed equipment is also available for measurement of noise figure. These instruments usually inject a known amount of added or "excess noise" to the input of the component and measure the total noise at the component's output under these conditions. Additional noise (over that injected) at the component's input is a measure of the component's noise figure [3, 4]. Noise figure will directly relate to the component's, and the radar receiver's, sensitivity or ability to detect small signals; that is, an increased noise figure reduces the radar system sensitivity directly.

Gain (or loss), dynamic range, bandwidth, and spurious characteristics and specifications can all be measured in the frequency domain on a spectrum analyzer, using a well-controlled signal generator, under matched impedance conditions. These measurements involve injection of the test signal at the component's input at known (or measured) signal levels and measurement of the component's output under these conditions. Gain or loss is measured by the relative increase or decrease, respectively, of the signal level, as compared with the input level. Dynamic range is usually taken as the difference between the lowest level (or noise-limited level) at which a component operates and the maximum level (or saturated level) at which the component will operate. Dynamic range can be measured by lowering the input signal to the lowest level discernible at the component's output and increasing the input signal until the output level saturates or begins to compress. The difference in the input level for these two conditions is the component's dynamic range. A linear operation region (input to output) will usually be contained within the limits of the component's dynamic range.

Spurious responses within a coherent radar component can degrade the radar's performance by resulting in false detections or in unwanted interference with normal target detections. Spurious performance is measured in the frequency domain (using a spectrum analyzer), as unwanted frequency components will be readily apparent. A single frequency can cause spurious frequencies to be generated if a component has a nonlinear input to output response characteristic. These spurious responses will be observable in the frequency domain as harmonics of the input signal frequency. It is desirable to keep spurious responses far below (in amplitude) the desired or main response. Intermodulation distortion can also occur in a component if more than one frequency is input to the component. To measure intermodulation distortion, two frequency tones at frequencies f_1 and f_2 are input to the component (usually tones from two stable frequency sources are employed). In

general, the two tones will result in intermodulation products at the component's output at frequencies $mf_1 + nf_2$, where m and n are integers. The level of the intermodulation products will relate to the component's compression (or saturation) point. Spectral measurements will allow direct measurement of those levels, and from those levels, maximum spurious free input signal levels may be inferred.

Quite often it is necessary or desirable to measure a component's gain and phase characteristics across a range of frequencies (rather than at just a single frequency). Flat amplitude or linear phase characteristics are generally required for correct radar receiver performance. Swept frequency measurements can be made with instruments such as network analyzers, which operate over broad frequency ranges (i.e., 10 MHz to 26 GHz) and at specific MMW bands with the appropriate accessories. The Hewlett-Packard HP8510B/C network analyzer is an example of the type of instrument suitable for these measurements. The instrument can be calibrated to precisely measure a component's swept frequency gain and loss, phase response, time delay, and impedance characteristics. It is possible to calibrate such equipment to remove some of the effects of impedance mismatch and accurately measure system amplitude and phase errors. Measurements to within 0.1 dB amplitude and 1 deg phase are readily achievable, after calibration. Swept frequency amplitude and phase measurement equipment also allows a component's bandwidth to be measured (bandwidth is usually defined as the point where the relative power level drops to one-half or 3 dB lower than the midband power level).

15.4 QUADRATURE DETECTOR TESTS

Most modern coherent radars use quadrature detectors to provide a baseband representation of the complex radar return. It is a critical function, and errors introduced can limit dynamic range, create false targets, and degrade ISAR images. Testing of this subsystem is important for diagnosing system problems and measuring quantities that are part of an overall system error budget. Some radar systems will have BIT capabilities for this important subsystem, whereas others will require modification or removal of the I/Q detector for testing. The outcome of these tests forms part of an error budget to determine target detection performance or RCS measurement accuracy, for example.

15.4.1 Quadrature Detector Operation

The I/Q detector is usually structured similar to the circuit shown in Figure 15.4. The diagram shows one IF receiver channel that is applied to the input power splitter of the I/Q detector. The I outputs of the splitter are applied to two mixers whose LO signals are obtained from a quadrature hybrid. The quadrature hybrid

is usually placed in the radar's COHO path. This is done because the COHO is a fixed frequency, and the quadrature splitter can be optimized for that frequency. The outputs of the mixers are low-pass filtered to provide baseband outputs. A test port is often included for injecting a test signal.

Before discussing tests of quadrature detectors, we will analyze this method of detecting a received bandpass signal. Assume the receive waveform $x(t)$ is a bandpass signal of the form:

$$x(t) = r(t)\cos(\omega_o t + \phi(t)) \tag{15.2}$$

where ω_o may represent the carrier frequency or an IF, $r(t)$ and $\phi(t)$ are the amplitude and phase modulation functions, respectively, associated with $x(t)$. By a bandpass signal we mean that all the spectral components of $x(t)$ are in a band $\omega_o - \Delta\omega/2 \leq \omega \leq \omega_o + \Delta\omega/2$, where $\Delta\omega$ is the bandwidth. Expanding (15.2), we obtain:

$$x(t) = x_I(t)\cos(\omega_o t) + x_Q(t)\sin(\omega_o t) \tag{15.3}$$

where $x_I(t)$ and $x_Q(t)$ are the I and Q components, respectively, given by:

$$x_I(t) = r(t)\cos(\phi(t)) \tag{15.4}$$

$$x_Q(t) = -r(t)\sin(\phi(t)) \tag{15.5}$$

The I and Q components are band-limited to the band $|\omega| \leq \Delta\omega/2$ [5]. The circuit of Figure 15.4 develops the Q components of $x(t)$. Lowpass filters at the I and Q outputs are used to remove spectral components at $2\,\omega_o$, while passing the band

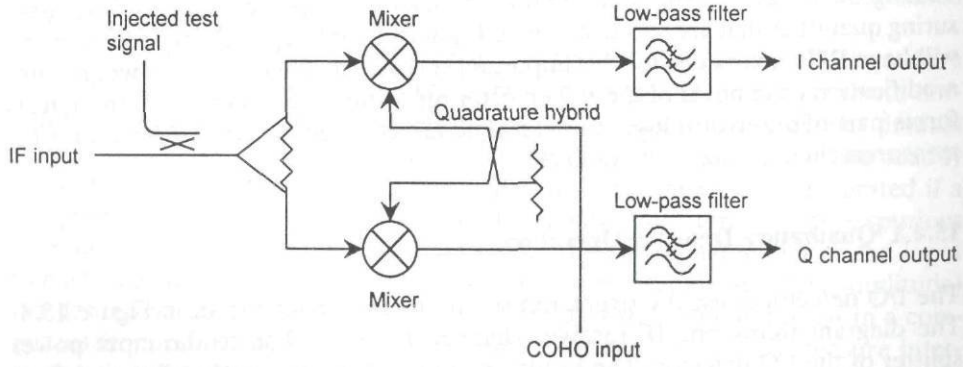

Figure 15.4 Quadrature detector block diagram.

$-\Delta\omega/2 \leq \omega \leq \Delta\omega/2$. The Q components contain relatively low frequencies compared to the carrier or LO frequency. Note that the I and Q components contain the important waveform information that has been removed from the received carrier. These components are referred to as the baseband components of the received signal.

The advantages of the I/Q detector are clear: components (mixers and hybrid couplers) are readily available, the baseband output is easily interfaced to data storage and processing systems, and the bandwidth of each output is only half of the input bandwidth (the total bandwidth for the two outputs remains the same as the input). The main disadvantages of the I/Q detector are a result of the use of two baseband channels (real signals) to represent a complex signal. DC offsets produce a false response at zero frequency in doppler processing. Imbalances between the I and Q channels lead to images of the received signal resulting in false targets, extra sidelobes for beam-forming systems, and degraded performance in pulse compression systems. These errors can be reduced by manual trimming or through software error correction as discussed below.

15.4.2 Model of Quadrature Detector Errors

The I/Q detector errors can be modeled in several ways. They are often lumped together into one channel as shown in Figure 15.5. Here, the I channel is assumed to be perfect, whereas the Q channel has a gain error, k, an offset error, a, and a phase shift error, $\delta\phi$. In reality, the errors are the net error as compared to two balanced channels.

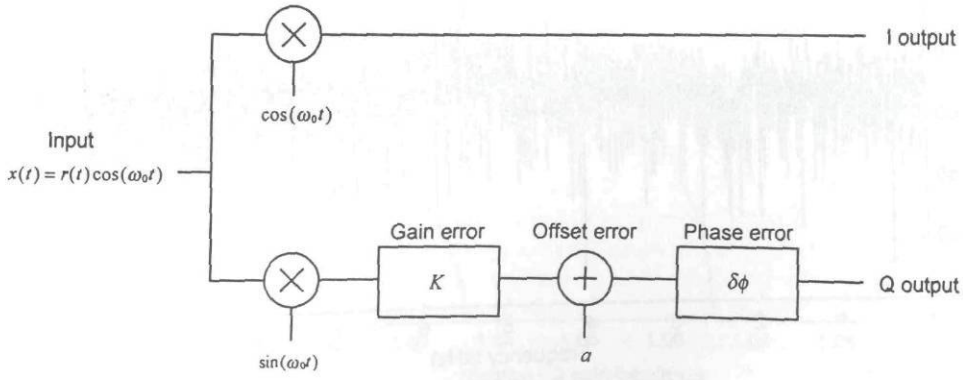

Figure 15.5 Model of quadrature detector errors.

Detector errors are most easily seen in the spectrum for a single input frequency that is offset from the COHO. This would be the case for a single radar return with a fixed doppler frequency. In this case, the dc offset errors show up as terms at zero frequency, whereas the input signal is the term at the doppler frequency. Gain and phase errors show up as an image term at the negative, or image, of the doppler frequency. Figure 15.6 shows an example of the spectrum of the Q detector output. The signal has an apparent doppler frequency of 5,500 Hz. The actual doppler frequency is not known because the signal was sampled at some frequency, f_s, and there was no antialiasing filter ahead of the sampler (see Sec. 15.6 for discussion of sampling requirements). The term at zero frequency is 37 dB below the signal and the image term (4,500 Hz) is 38 dB down. The frequency axis has a range of 0 to 10 kHz, where the segment from 5 to 10 kHz is sometimes referred to as negative frequencies. (Again, the actual doppler frequency of the image is not known because there was a possibility of aliasing.)

The image rejection that a given I/Q detector can achieve is a function of the gain balance and quadrature relationship between the two channels of the detector.

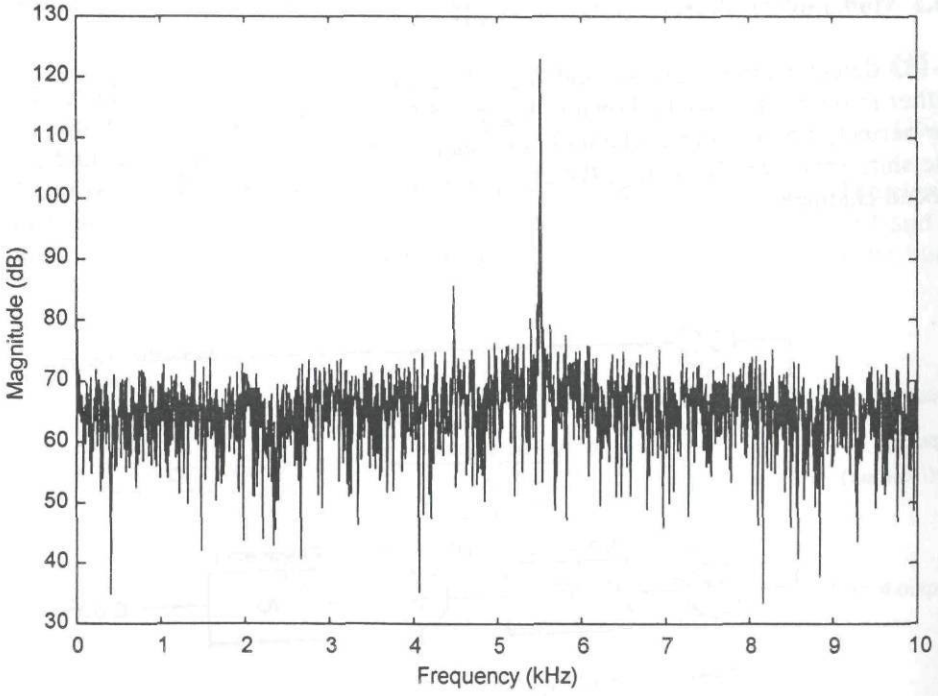

Figure 15.6 Output spectrum of a quadrature detector.

This relationship can be expressed in analytical terms [6]. The image rejection, R, is given by:

$$IR = \frac{1 + 2k \cos \delta\phi + k^2}{1 - 2k \cos \delta\phi + k^2} \tag{15.6}$$

where k is the ratio of the gain of the one channel to the other channel so that the ratio is greater than one, and $\delta\phi$ is the error from a quadrature relationship between the two channels.

The image rejection, as determined by the equation above, is plotted in Figure 15.7. The plot shows contours of constant image rejection as a function of k and $\delta\phi$. Based on this information and a measured value of image rejection, it is clear what the range of gain and phase errors can be. This information is also useful from a design standpoint, where components must be selected and decisions made concerning manual phase and gain adjustment.

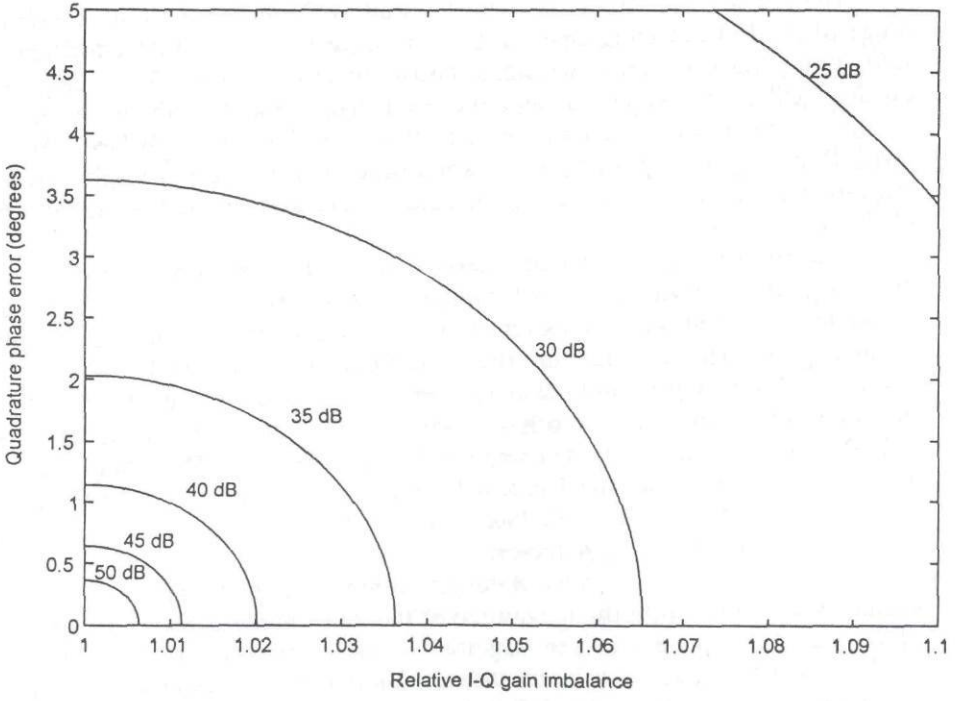

Figure 15.7 Contours of constant image rejection.

15.4.3 Quadrature Detector Tests

The I/Q detector errors described by the model in the previous section lead to effects that can be seen in both the time and frequency domains. These effects can be seen with standard test equipment or in computer displays of the output data.

Perhaps the simplest display consists of an oscilloscope whose x channel is the I voltage and y channel is the Q voltage. If the x and y gains of the oscilloscope are equal and the zero points are set to some reference point, then a sinusoidal test signal should produce a circle centered about the reference point. Deviations from the circular pattern are a result of errors in the I/Q detector. A rough adjustment of the detector can be done at this stage. With no input, the offsets of the I and Q channels are adjusted to zero. With an injected signal offset in frequency from the COHO, an ellipse is seen on the oscilloscope. First, the quadrature adjustment is made to move the major axis of the ellipse to coincide with the x or y axis of the oscilloscope. Then, the gain of one or both channels can be adjusted until the ellipse becomes a circle. (This assumes that the oscilloscope channels are matched in gain, which is easily verified by exchanging the input cables and again observing a circle.) This method of adjusting by eye usually yields image rejection ratios of 30 to 35 dB.

The oscilloscope display can also be used to characterize the input dynamic range of the I/Q detector. Operation of the mixers in the I/Q detector near the saturation point can lead to harmonic distortion of the signal. This is easily seen on the oscilloscope x-y display as a diamond shape. For most diode mixers, this condition begins when the input level to the mixer is 7 to 10 dB below the LO level. Reducing the input amplitude while observing this output display gives an indication of the dynamic range of the detector, but may be limited by the sensitivity of the oscilloscope.

Measurement of the detector characteristics in the frequency domain is usually more sensitive than the previous technique. The spectrum of the detected signal is usually generated on a computer after the I/Q detector outputs are converted to digital data. This requires that the I and Q channels be sampled at some frequency, f_s. Individual I and Q channels can be observed on a spectrum analyzer, but the display from $f_s/2$ to f_s will be a mirror image of the display from zero to $f_s/2$. The FFT performed on the computer is a complex FFT. The input is complex and is formed by taking the I channel sample and adding $j \times$ (the Q channel sample). The output of this FFT has no images from zero to f_s (or $-f_s/2$ to $f_s/2$), except for errors in the I/Q detector.

For an input signal with fixed doppler frequency, an alternative to FFT processing is a calculation of the magnitude of the input to the detector as a function of the detected signal angle. The magnitude is the square root of the sum of I^2 and Q^2. For a constant magnitude input, the calculated magnitude will show some ripple depending on the errors in the I/Q detector. The ripple in the magnitude plot is

due to detector imbalance or, in the frequency domain interpretation, the presence of an image term.

15.4.4 Error Correction

The error correction process that will be described here is a modified approach from that described in [7]. The referenced approach uses a doppler input that is synchronized to a submultiple of the sampling frequency (the PRF). This eliminates any spectral leakage (discussed in [8] and Sec. 15.5). The approach described here does not require synchronization, but relies on more data samples and a weighting window to reduce spectral leakage. This has the advantage of using a free-running oscillator for the test source, instead of an oscillator that is phase-locked to the COHO and PRF.

A block diagram of the test setup is shown in Figure 15.8. The coherent detector has a local oscillator (COHO) and an injected signal that is offset from the COHO. In this case, the COHO is at 240 MHz and the sampling frequency is 100 kHz. The offset frequency for the injected signal is not critical, but there are some general guidelines. The output frequency of the detector should be approximately one-third or two-thirds of the sampling frequency. This can be seen by examining Figure 15.9. This computer simulation shows a plot of the spectrum obtained from the complex output of a I/Q detector. The terms that must be resolved are the term at 0 Hz (dc offset), the desired output, and the image. To reduce the effects of spectral leakage, it is best to separate these three terms as widely as possible. This occurs when the desired output is at one-third or two-thirds the sampling frequency and the image is at two-thirds or one-third, respectively.

The weighting window applied to the data can be triangular, Hanning, or any commonly used window. The window can even be rectangular (no window) if enough samples of the data are taken. The real requirement is that the spectral leakage from one of the frequency terms does not interfere significantly with another frequency term. If the desired result is error correction to obtain -50 dB image and dc terms, then the spectral leakage from the largest amplitude frequency component should have sidelobes that are below -60 dBc at the image frequency and zero frequency.

Once we ensure that the three terms are not interfering with each other, it is a fairly simple process to find the error correction terms and apply the correction algorithm. Table 15.2 summarizes the necessary steps for this procedure. A weighting window is applied to the I and Q data, and a complex FFT produces the spectrum. The dc offset errors are calculated from the zero-frequency term of the spectrum. The complex values at the signal frequency and its image frequency determine the remaining error terms, E and P.

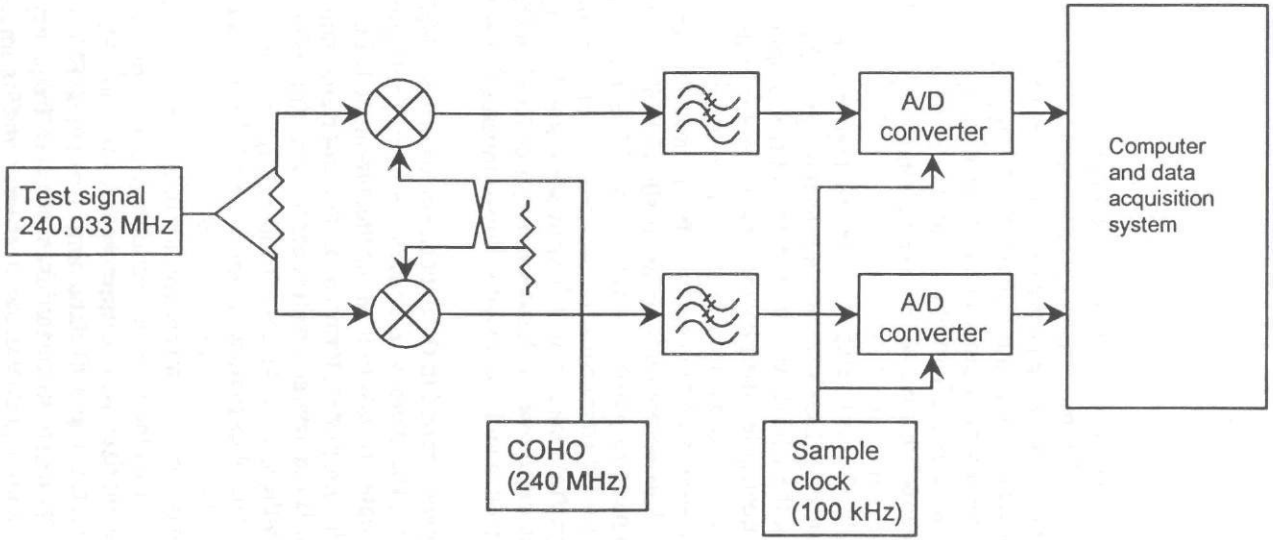

Figure 15.8 Test configuration for Q detector correction.

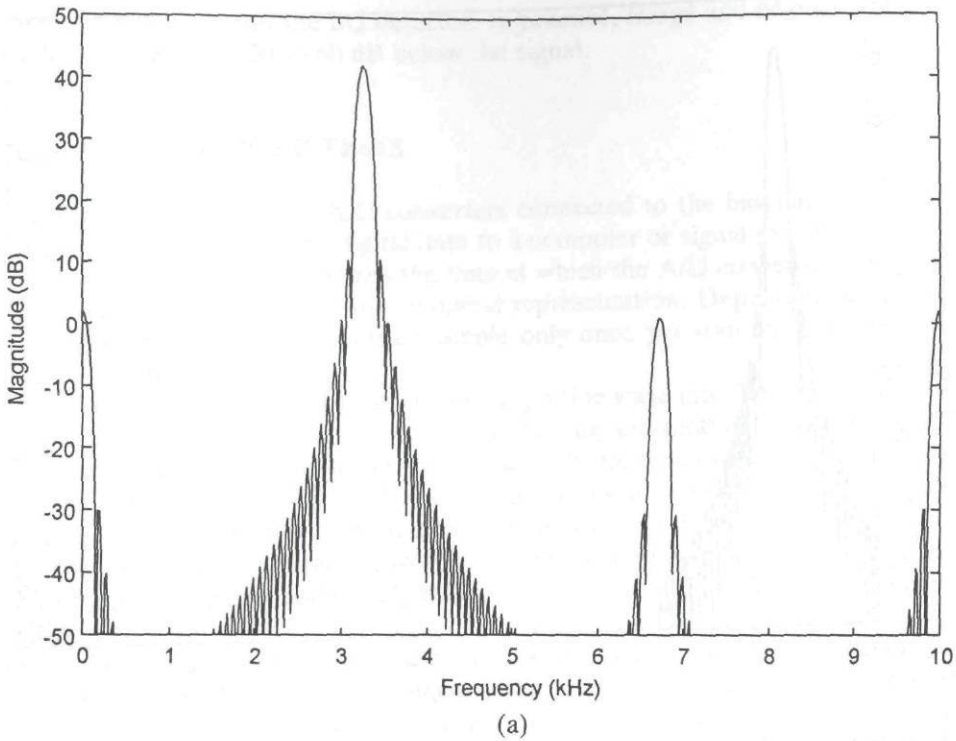

Figure 15.9 Output spectrum of Q detector (a) with no correction and (b) after correction.

Several subtle points must be considered in this approach. E and P, determined from the gain and Q errors, are ratios of the signal and image terms, whereas the dc term, Xdc, is not. The weighting window has a coherent gain less than one, and the FFT results in scalloping loss if the signal does not fall exactly on a point in the frequency domain. The ratio (for E and P) cancels these losses for the gain and Q error terms, but not for the dc term. There is no scalloping loss for the dc term, because the dc offset of the I/Q detector falls exactly on the zero frequency point of the FFT. We do, however, need to correct for the coherent gain of the window . The coherent gain can be calculated or found in [8]. For a Hanning window, for example, the coherent gain is 0.5. The dc error term must be divided by the coherent gain to obtain the offset errors of the I/Q detector.

Figure 15.9 also shows the spectrum after correction. The correction process is a simple matter. Two linear equations operate on the received I and Q data [7] to produce corrected data as shown in Table 15.2. The operation could be done by a computer for a measurement radar or by the signal processing subsystem for a realtime radar system. The result of the correction process is a reduction in the

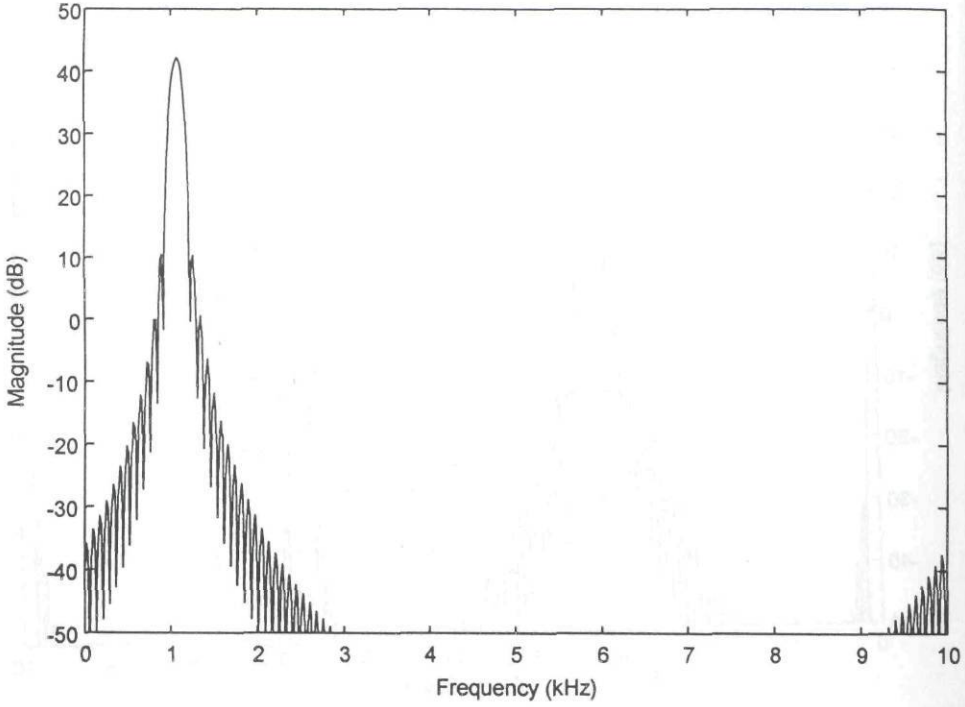

(b)

Figure 15.9 (Contd.)

Table 15.2
Summary of Quadrature Detector Correction Algorithm

Correction Coefficient Derivation
• Test signal on, sample N data points: $x(n) = I(n) + jQ(n)$, $n = 1, 2, \ldots, N$
• Multiply by weighting window: $w(n)$ with coherent gain G_w.
• N-point FFT: $X(k) = FFT[x(n)w(n)]$, $k = 1, 2, \ldots N$
• Calculate offset: $Xdc = X(0)/[NG_w]$
• Find peak signal response: $Xs = X(a)$
• Find image of peak: $Xi = X(N - a + 2)$
• Calculate coefficients: $E = -Re[2Xi/(Xs^* + Xi)]$
$P = -Im[2Xi/(Xs^* + Xi)]$
Correction Process
• Sample I and Q data.
• Calculate corrected I and Q values: $Icor = (E + 1)(Isamp - Real\ (\text{Xdc}))$
$Qcor = P[Isamp - Real\ (Xdc)] + [Qsamp - Imag(Xdc)]$

image and dc offset for the I/Q detector. In practice, image and dc outputs can be reduced to levels of 50 to 60 dB below the signal.

15.5 A/D CONVERTER TESTS

Most coherent radars use A/D converters connected to the baseband outputs of the I/Q detector to provide digital data to a computer or signal processing subsystem. A sample clock determines the time at which the A/D converter will sample the input signal and convert it to a digital representation. Depending on the type of radar, the A/D converters may sample only once per transmit pulse or many times per transmit pulse.

A/D testing usually consists of injecting a sine wave into the input and storing a record of digital data for subsequent processing and plotting. Most of the A/D converters suitable for radar use have bandwidths that are in the megahertz range, so the most readily available, clean test signal is a sine wave. Multiple frequencies may be injected to observe intermodulation products as described in Section 15.3, or the input may be terminated to observe the inherent noise in the unit. The tests can be quite extensive and usually require a dedicated setup utilizing several pieces of precision test equipment.

The tests can be divided into dynamic and static tests. The dynamic tests quantify the performance of the unit under actual operating conditions (an HF input signal), and the static tests characterize the dc performance. The dynamic tests are the most stringent tests and are often the hardest to perform accurately. The static specifications for an A/D converter describe the input voltage range of the device, the offset error and drift, the output levels, and so forth. These specifications are generally required for determining basic circuit operation and have little impact on the performance of the device for a radar application.

The most important dynamic specifications are SNR, spurious-free dynamic range, and harmonic distortion. The SNR is the ratio of the signal to total noise amplitude in the output spectrum. The spurious-free dynamic range is the ratio of the signal amplitude to the highest spurious amplitude in the output spectrum. Harmonic distortion is often specified as total harmonic distortion, which is the ratio of the signal amplitude to the sum of all the identified harmonic outputs. Some data sheets will also specify a signal-to-total-error ratio or signal-to-noise and distortion.

The input bandwidth specification usually refers to the input frequency for which the output spectrum shows a 3-dB decrease in signal amplitude. This specification is sometimes much higher than the maximum sampling rate of the A/D converter. The dynamic specifications are usually not specified to this high a frequency, because they are significantly worse than at lower input frequencies. Most

manufacturers give dynamic specifications up to one-half of the maximum sampling rate.

Many A/D converters have a specification for the "effective number of bits" at a given sampling rate and input frequency. This number is calculated from the SNR or the spurious-free dynamic range and represents the number of bits an ideal A/D converter would have in order to match the performance of the tested unit. The calculation is based on the theoretical performance of an A/D converter with a sine wave input. Following the development in [9], the input signal is large, traversing many states of the A/D converter, and the distribution of the quantization error can be approximated as uniform from $-\Delta/2$ to $\Delta/2$, where Δ is the input voltage corresponding to the difference between adjacent digital output codes. The variance of the quantization error, σ_e^2, is found to be:

$$\sigma_e^2 = \frac{\Delta^2}{12} \tag{15.7}$$

and the variance of a full-scale sine wave, is:

$$\sigma_x^2 = \left(\frac{2^b\Delta}{2\sqrt{2}}\right)^2 \tag{15.8}$$

where b is the number of bits of the A/D converter. The ratio of the signal and error variances is the *SNR*, which can be expressed in decibel form as:

$$\text{SNR(dB)} = 6.02b + 1.76 \tag{15.9}$$

Rearranging this gives the expression for effective number of bits, *ENB*:

$$\text{ENB} = \frac{\text{SNR(dB)} - 1.76}{6.02} \tag{15.10}$$

A 12-bit converter, for example, with a measured *SNR* of 65 dB would have an *ENB* of 10.5.

15.5.1 Test Considerations

The testing of A/D converters can prove to be a significant effort, especially for high-resolution or high-speed devices. The same can be said about specifying A/D converters, because not all manufacturers use the same definitions for the quantities involved. The following paragraphs define several important parameters

and describe some of the common problems encountered when testing (and specifying) A/D converters.

The signals used in the dynamic tests can greatly affect the results of the tests. The signals must be very stable and clean or the measured performance will be worse than the actual performance. Problems with signal generators include harmonics, spurious outputs, and phase noise (or jitter). Note that these problems are important for the sample signal, as well as for the input signal. Harmonics and spurious outputs can show up directly in the spectrum obtained from the output data. Harmonics, for example, are often specified to be only -40 dBc for an RF signal generator. Harmonics with this relative amplitude can obscure the harmonics generated by a high-resolution A/D converter (greater than 8 bits) and filtering of the signal generator output may be necessary. Phase noise or jitter on the input signal or sample clock will usually show up as a higher noise level than expected. For a sinusoidal input with frequency f, the maximum SNR that can be realized, SNR_{MAX}, is given by the relationship:

$$SNR_{\mathrm{MAX}} = 20 \text{ LOG } \left| \frac{1}{2\pi f Jitter_{RMS}} \right| \tag{15.11}$$

where $Jitter_{RMS}$ is the total rms jitter between the input and the sample clock.

The signal processing techniques used to analyze the output data from the A/D converter can also affect the measured performance (see the following section on digital signal processor tests). The main problems are due to the discrete time samples and the finite length of the time sample record. Transforming to the frequency domain with an FFT (one implementation of the DFT) results in spectral leakage and scalloping loss. Given a single input frequency, spectral leakage is the apparent output at other frequencies in the FFT output. This is due to the finite length of the time sample record and the periodic assumption of the FFT. Weighting windows applied to the time domain data reduce the spectral leakage, but degrade the resolution in the frequency domain. Scalloping loss occurs when the frequency does not fall exactly on one of the output frequencies of the FFT. This results in an apparent loss in signal level, and the maximum value of this loss depends on the weighting window used [8].

The problems associated with spectral leakage and the use of weighting windows can be eliminated if the sampling signal is phaselocked to the input signal. If this is true, then the outputs of the FFT fall only on the sample points in the frequency domain and there is no spectral leakage or scalloping loss. This can be accomplished in the laboratory by phase-locking the signal generators that produce the sampling and input signals for A/D converter testing. The generators are then setup up so that the input frequency, f_{in}, is given by the following relationship:

$$f_{in} = mf_s/N \tag{15.12}$$

where f_s is the sample frequency, N is number of points in the FFT, and m is an integer.

Electromagnetic interference (EMI) can be a problem with highspeed and high-resolution A/D converters. For a 12-bit converter with 2V peak-to-peak input range, for example, one *least significant bit* (LSB) is equal to 488 μV. Digital signals with fast transitions can easily couple into the sensitive input circuit and degrade performance. Interference from discrete digital clock frequencies can sometimes be recognized by examining the interfering frequency in the output data. Varying the sample clock frequency and examining the movement of the spurious signal may link the interference to a known clock frequency. Interference from digital data buses and other pseudorandom digital signals will appear as extra noise in the A/D converter's output. Reducing such interference usually requires shielding, rerouting interconnections, or isolating power supply connections. In a dedicated laboratory setup, it is usually possible to eliminate these sources of interference.

15.5.2 A/D Dynamic Tests

A/D converter testing requires collecting data from the unit under test and then analyzing the data. The analysis is most commonly done in the frequency domain, but can also be done in the time domain. Frequency domain analysis is probably more practical from a radar application standpoint, because the data are usually transformed into the frequency domain for normal operation. Doppler information, high-range resolution profiles, and ISAR images are all obtained from the frequency domain data.

Time domain characterization of A/D converter performance can be useful for diagnosing some causes of A/D converter problems. The input of the converter is driven by a full-scale sine wave and output data are collected. A plot of the time series is useful, but can be augmented by another plot showing errors from a perfect sine wave. In this case, a sine wave is fitted to the output data to have the least error in a mean squared sense. To do this, a sine wave of the approximate frequency, amplitude, and phase is adjusted in terms of these three parameters until the rms value of the difference from the time series has been minimized. The error as a function of time can then be overlaid on a plot of the time series as shown in Figure 15.10. One difficulty with this technique is ensuring that the fitting technique converges to the correct answer. This technique can be very useful in finding errors that are due to glitches or nonmonotonicity of the A/D converter [10].

Some A/D converters exhibit missing states; there is one (or more) digital output code that does not occur even with the input signal traversing the full input range. This phenomenon usually occurs only for HF inputs and is not seen during dc testing. One method of testing for this is to inject an HF input signal that is just slightly offset from some multiple of the sampling frequency. For example, a

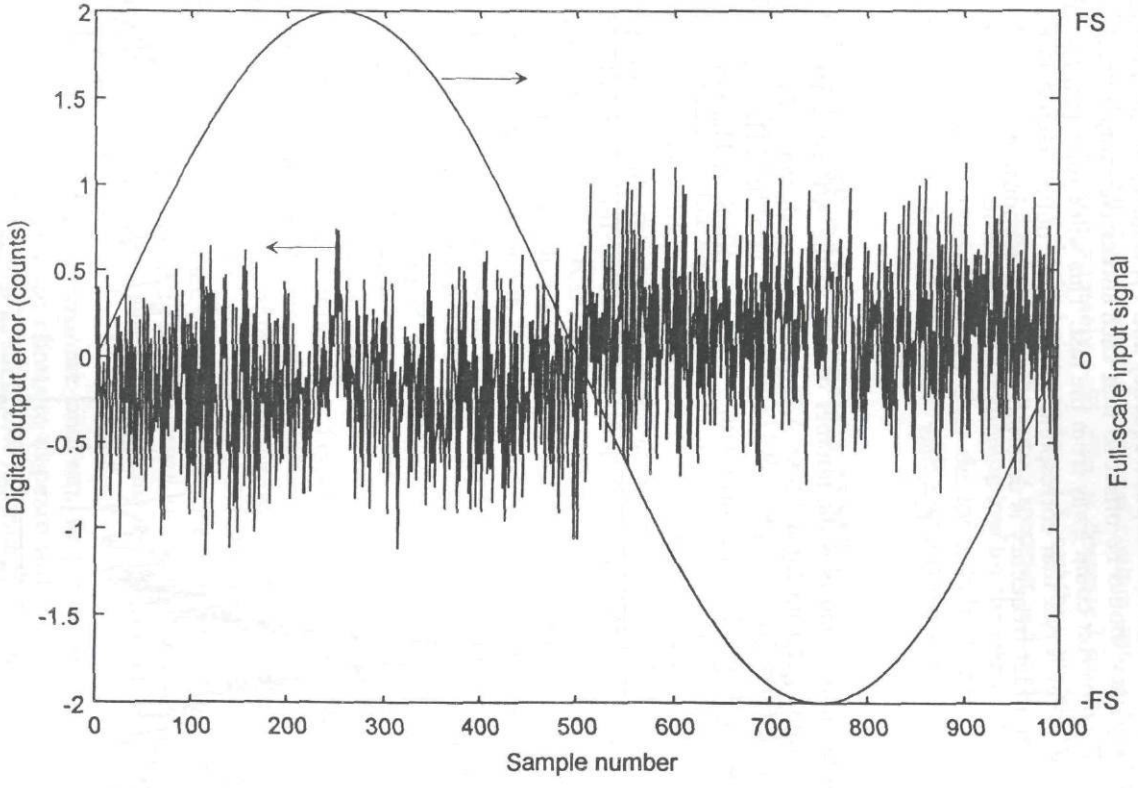

Figure 15.10 Plot of time domain errors for an A/D converter.

system with a single range gate may sample at 100 kHz and input frequency components may extend beyond 5 MHz. The maximum slew rate for the input sine wave is $\pi f_{in} V_{FS}$, where f_{in} is the input frequency and V_{FS} is the full-scale input range. The input frequency should be offset so that each successive sample value is less than one A/D converter count away from the last. This will ensure that the analog input is sampled at levels that correspond to all digital output codes. For a full-scale input, the input frequency is determined by the relationship:

$$f_{in} = mf_s \pm \frac{f_s}{\pi 2^N} \tag{15.13}$$

where m is an integer and N is the number of bits for the A/D converter.

The output spectrum for a 12-bit A/D converter is shown in Figure 15.11. The data record was composed of 256 samples taken at a 100-kHz sample rate. The input was a 4.10-MHz sine wave with a level −1 dBFS. A Hanning window

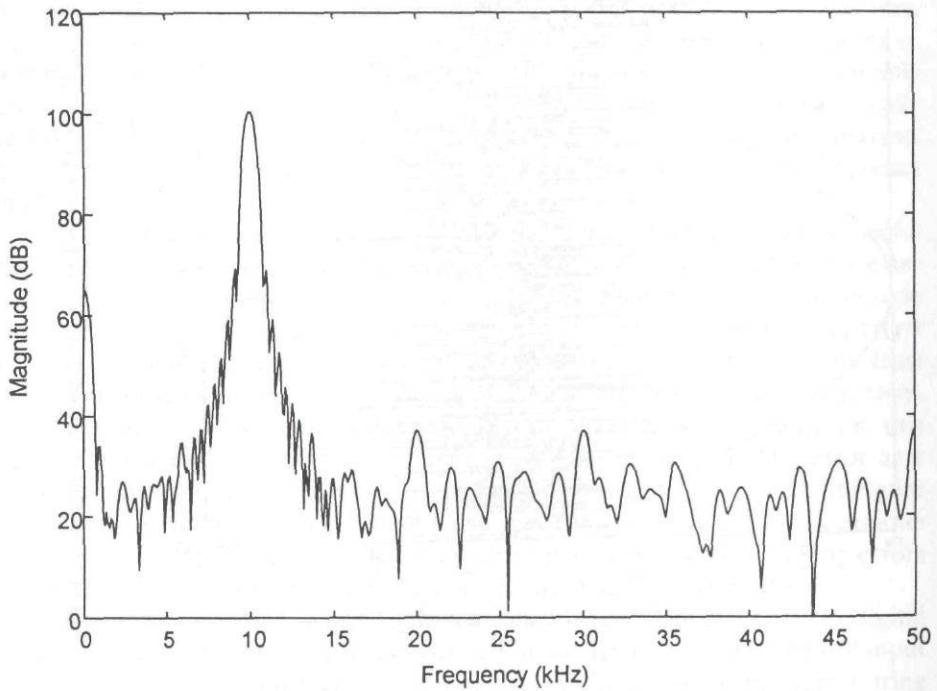

Figure 15.11 Example output spectrum for a 12-bit A/D converter.

was applied to the time domain data. The spectrum contains the fundamental aliased to 10 kHz and several harmonics of the input signal. The average noise level can be found by averaging the points that do not contain any discrete components. This noise level, approximately −85 dBc, is decreased by the *equivalent noise bandwidth* (ENBW) of the Hanning window, 1.5, and then multiplied by the number of data samples. The total noise in the output spectrum is found to be −65 dBc and this is the *SNR*. In order to avoid scalloping loss for the signal, the FFT was zero-filled to a record length of 2,048. Only the lower half of the spectrum was used for the calculation, because the upper half contains the same information.

15.6 DIGITAL SIGNAL PROCESSOR TESTS

15.6.1 Digital Signal Processor Waveform Sampling Considerations

Modern radars utilize *digital signal processors* (DSP) to perform various functions within the radar. Often, the received signal is converted to a lower IF, I and Q components of the received signal are developed with an I/Q detector, as shown in Figure 15.4, and the I/Q detector outputs are digitized with an A/D converter. The sample rate of the A/D converter and the rate at which data are clocked into the signal processor will depend on the bandwidth of the received waveform and the processing performed in the signal processor. If an I/Q detector and low-pass filters are employed as discussed in Section 15.4.1, the I and Q components of the signal $x_I(t)$ and $x_Q(t)$ are limited to the frequency band $|\omega| \leq \Delta\omega/2$. Each of the signals $x_I(t)$ and $x_Q(t)$ may be sampled at a rate of $\Delta\omega/2\pi$ samples per second (the Nyquist rate) and the signal reconstructed.

Often, a sampling rate consistent with sampling the signal bandwidth is not required for radar signal processing. For example, for range-doppler processing, a range gate may be developed and the A/D converter strobed to sample each detected pulse at the PRI of the radar. The phase of each detected pulse will vary, in the case of a moving target, creating a doppler frequency. If sampling is at the PRF (PRF = 1/PRI), then doppler frequencies of one-half the PRF can be reconstructed. The PRF sampling rate, however, is usually much less than that required to sample the signal bandwidth. Range-doppler processing is discussed in more detail below.

As the frequency response and sampling rates of A/D converters have improved, there have been efforts to dispense with the I/Q detector and directly sample the received signal at some low IF, usually below 50 MHz. A single A/D is used to sample the signal at a rate that is greater than twice the bandwidth of the signal. If the center frequency is chosen correctly in relation to the sampling frequency, then this is all that is necessary to accurately represent the signal. The output is a series of real integers that can be processed digitally to yield a complex

spectrum [11]. Digital signal processing is used to develop the I and Q components, either by proper waveform sampling and filtering (averaging) or using algorithms that implement the Hilbert transform.

The advantage of this approach is the absence of the imbalance errors that occur in a I/Q detector. The leakage term at zero frequency and the images seen in a I/Q detector are greatly reduced, because there is only one analog channel and one A/D converter. Thus, excellent performance can be obtained without extensive manual trimming or software error correction.

The main disadvantage of the direct sampling approach is the stringent requirements placed on the A/D converter. The sampling rate must be twice as high as the sampling rate for one A/D with the I/Q detector. The bandwidth of the signal applied to the A/D is also at least twice that of the baseband signals output by the I/Q detector. This reduces the SNR and distortion characteristics of the A/D, because it samples with a finite aperture time, instead of an ideal impulse. The higher signal bandwidth results in higher slew rates of the voltage applied to the A/D input, thus creating larger errors when sampled with a finite aperture A/D converter.

The sampling rates and processing functions performed in radar DSPs varies considerably. For example, the DSP may perform digital pulse compression; in this case, the data input to the DSP must adequately sample the pulse compression waveform bandwidth, and the processing rates must be consistent with those sample rates. Other functions performed in the DSP may include multichannel digital beamforming and adaptive processing, detection thresholding, digital MTI, or *electronic counter-countermeasure* (ECCM) processing. Each of these types of processing has unique processing and sampling requirements.

15.6.2 DSP Testing Considerations

Often signal processors are most efficiently and thoroughly tested at the system level, where targets, interference, and noise effects can be realistically reproduced. For system-level tests, signals are input to the radar by space excitation or injected at RF, although sometimes they are injected as digital data directly at the DSP. Such system-level-test techniques are discussed in Chapter 16. In some cases, it is desired to perform functional or performance tests on the signal processor alone. This will require insertion of digital data into the signal processor in the format and at the data rates used by the A/D converters. If the digital signal processor performs DFT or FFT processing, it is desirable to generate digital data that are synchronous with the A/D clock (to minimize leakage or scalloping loss effects as described above for A/D tests).

The types of tests that should be considered for the digital signal processor, before beginning more complex system tests, include verification of adequate signal

sampling for the type of input data, evaluation of quantization noise, evaluation of signal level capability and dynamic range, and a verification of functional or algorithmic operation (filtering, weighting functions, etc.)

Adequate signal sampling in the DSP is a concern, just as in the A/D converter. One way to verify the proper sampling rate within the signal processor is to input the expected type(s) of digital data into the DSP and observe the DSP output in either the time or frequency domain. As described for the A/D tests, the digital data should be representative of stable and spurious-free analog signals and should be synchronous with the DSP clocks. Frequency domain evaluation of the output is often the most informative, as the signal will occur at the correct frequency, with no "foldovers" or frequency domain aliases if the signal is adequately sampled. To observe the DSP output in the frequency domain in real time usually requires that the data be converted to an analog voltage for display on a spectrum analyzer. This can be achieved by using a *digital-to-analog* (D/A) converter at the output of the signal processor. The D/A converter should have resolution (number of bits) and sample rate capabilities that match the data output from the DSP. An alternative way to examine the DSP output data is to collect the data with digital storage devices (for example, a digital computer) or digital recorders and analyze the data afterwards to determine the frequency spectrum characteristics. This approach eliminates the need for a D/A converter and errors that it might introduce.

Quantization noise will often be present in the output of a digital signal processor. The level of the quantization noise will be affected by the number of bits employed in the DSP (and the A/D prior to the DSP) and the type of arithmetic (i.e., fixed-point or floating-point arithmetic). Many DSPs employ hardware that uses fixed-point arithmetic, although newer systems are utilizing floating-point arithmetic. Quantization noise usually becomes more significant in those processors that use fixed-point arithmetic, because computations (such as the results of multiplications) in the DSP are usually either truncated or rounded. Often these effects are lumped together and termed "roundoff noise" [12]. If a D/A converter is used to examine the DSP output, the number of bits in the D/A converter may affect the resultant quantization noise as well (especially if the number of bits is fewer that those used in the DSP). The quantization noise in the DSP sets the lowest discernible level at the DSP output, much as thermal noise limits analog components. Usually, the quantization noise is uncorrelated with the signal input, especially for relatively large inputs. Therefore, it is advisable to measure the amount of quantization noise to quantify the minimum discernible signal at the DSP output. This can be done in the frequency domain, as discussed in Section 15.5, by inserting a known signal and measuring the noise level at the DSP output relative to the known signal level. Usually a sine wave or other narrowband signal is useful for such a test. The peak level of the signal at the DSP output (in the frequency domain) can be compared to the quiescent noise level, and the noise level may be determined by the relative magnitude of the two outputs. Signal levels at or below

the noise level will not be reliably displayed by the DSP. Dynamic range of the DSP can be evaluated by increasing the input level of the narrowband test signal until full-scale output of the DSP is obtained and comparing that output level to the quantization noise level.

Quantization or roundoff effects may cause other deleterious effects in the DSP, besides limiting the noise level or SNR. Roundoff errors can cause the desired digital filter transfer functions not to be properly realized. Such errors may cause passband ripples or other errors in the filter transfer function. These errors, if they occur, can be determined by observing the DSP output in the frequency domain, as described above.

Digital signal processors can perform many different functions or algorithms. Common DSP functions include DFT (or FFT) processing to develop range-doppler maps, followed by constant false alarm processing or thresholding, and so forth. Functional (or performance) tests of the DSP will depend significantly on the functions performed in that processor. With pulse radar waveforms (whether CW pulses or coded pulses) it is typical that timing signals will be developed as A/D strobes to sample the I/Q detector outputs at each PRI. By delaying the sample strobe, relative to the transmit pulse, target returns at a particular delay (range) are sampled; thus, a range gate is formed. With digitized I/Q data at each PRI (i.e., with a sample strobe at the same delay relative to the transmit pulse), a measure of the rate of change of phase (i.e., doppler frequency) may be obtained. If this data is processed by a DFT or FFT processor, the doppler frequency can be determined.

A common functional or performance test in a pulsed coherent radar involves the injection of I/Q data corresponding to a linear increasing change in phase (at a sample rate corresponding to the PRI sample times); such data represent those which would be obtained with a constant doppler. It is important that the functional change of the I/Q data be synchronous to the A/D clock; for example, if the data vary as a sine function, the period of the variation should be synchronous to the A/D clock. If a DFT or FFT processor is used, then the data are usually generated with a change of 360 deg in phase (or multiples of 360 deg) in 2^n pulses, where n is an integer and 2^n the number of points in the FFT. The amplitude level of the injected data signal (percentage of full scale) can be adjusted to test the DSP's dynamic range or response to different level signals. Randomized noise data, representative of white noise or thermal noise, may be superimposed on the data representing the doppler data, simulating a received signal with a particular SNR. The amplitude of the doppler signal data may be weighted according to range (to a target), antenna gain, target RCS, path loss, and so forth to simulate other effects. By properly modeling the received waveform and generating test data for different cases, DSP tests can become comprehensive simulations of radar performance under different conditions [13]. These types of tests, however, are usually to eval-

uate the system-level performance of the radar and the DSP and are discussed in more detail in Chapter 16.

REFERENCES

[1] Hewlett-Packard Application Note AN-150-2, "Spectrum Analysis... Pulsed RF Measurements," Hewlett-Packard, November 1971.

[2] Hewlett-Packard Application Note AN-150-4, "Spectrum Analysis Noise Measurements," Hewlett-Packard, April 1974.

[3] Hewlett-Packard Application Note AN-57-1, "Fundamentals of RF and Microwave Noise Measurement," Hewlett-Packard, July 1983.

[4] Hewlett-Packard Application Note AN-150-9, "Spectrum Analysis-Noise Figure Measurement," Hewlett-Packard, April 1976.

[5] Peebles, Jr., P. Z., *Digital Communication Systems*, Englewood Cliffs, NJ: Prentice-Hall, 1987, pp. 33–39.

[6] Monzingo, R. A., and S. P. Au, "Evaluation of Image Response Signal Power Resulting from I-Q Channel Imbalance," *IEEE Trans. on Aerospace and Electronic Systems*, Vol. AES-23, No. 2, March 1987.

[7] Churchill, F. E., G. W. Ogar, and B. J. Thompson, "The Correction of I and Q Errors in a Coherent Processor," *IEEE Trans. on Aerospace and Electronic Systems*, Vol. AES-17, No. 1, January 1981.

[8] Harris, F. J., "On the Use of Windows for Harmonic Analysis with the Discrete Fourier Transform," *IEEE Proc.*, Vol. 66, No. 1, January 1978.

[9] Oppenheim, A. V., and R. W. Schafer, *Digital Signal Processing*, Englewood Cliffs, NJ: Prentice-Hall, 1975, pp 413–417.

[10] Demler, M. J., "Time-domain techniques enhance testing of high-speed ADCs," *Electronic Design News*, March 30, 1992.

[11] Liu, H., A. Ghafoor, and P. H. Stockmann, "A New Quadrature Sampling and Processing Approach," *IEEE Trans. on Aerospace and Electronic Systems*, Vol. AES-25, No. 5, September 1989.

[12] Jackson, L. B., *Digital Filters and Signal Processing*, Chapter 11, "Quantization Effects," Norwell, MA: Kluwer Academic Publishers, 1986.

[13] Mitchell, R. L., *Radar Signal Simulation*, Chapters 2, 3, 4, and 5, Norwood, MA: Artech House, 1976.

Chapter 16

Coherent Radar System Tests: Techniques, Considerations, and Equipment

James L. Kurtz
Scientific Research Corporation

16.1 RADAR SYSTEM TESTS INTRODUCTION

Errors within either the exciter/transmitter or the receiver/signal processor of a coherent radar will affect radar performance. Test techniques for evaluating some coherent radar component and subsystem errors have been addressed in Chapter 15. The primary emphasis in this chapter will be on test techniques and considerations related to radar system performance measurements of the coherent radar receiver, from the antenna to the receiver/signal processor, as shown in Figure 15.1. A motivation for emphasizing receiver testing is that it will allow us to evaluate error effects that may occur in the transmitter/exciter waveforms, in the transmission and target environment, and in the receiver chain components. Ultimately, errors in any of these areas will be measurable by reduced performance in the receiver/signal processor. Often, reduced radar performance can be measured by tests of the radar receiver/signal processor, with the appropriate simulated waveforms, representing target or interference as might be generated by return signals from the transmitter. The appropriate waveform parameter variations are often employed to simulate error effects and to evaluate reduced performance. Reduced performance may take several forms; for example, reduced or degraded target detection at the radar output(s), inaccuracies in target measurement in range, doppler, or angle, or other reductions in performance. It is our objective to consider testing techniques that will allow us to evaluate radar system-level performance. These test techniques will also allow us to simulate the effects of various types of errors and evaluate the effects of those errors on radar system performance.

16.2 LEVELS OF TESTING: REQUIREMENTS AND CONSIDERATIONS

The testing requirements for performance tests of a coherent radar are, in general, more severe that those required for a noncoherent radar. At the outset, system-level performance tests usually require that coherence of test signals be maintained (i.e., frequency and phase coherence with the oscillators within the radar). Figure 16.1 shows three types of tests that allow radar testing with coherent test signals. Each type of test may have advantages, depending on the objectives of the test and available test equipment and resources. Table 16.1 shows some of the types of system-level performance tests that are typically performed.

16.2.1 Space Excitation Testing

Figure 16.1(a) shows a technique for space excitation testing. The transmitter/exciter can be used to radiate signals for reception by the receiver, either directly or after reflection from targets or the background environment (or clutter). This approach allows operation and testing of the radar under conditions that closely approximate the actual operation of the radar, including the effects of the antennas. In order to simulate received targets, a known calibrated target can be illuminated by the transmitter antenna with the radar waveform and, after reflection, received by the receive antenna. By using calibrated reflectors, with known RCS properties, the radar receiver may be calibrated in terms of sensitivity and dynamic range. Antenna characteristics such as gain, beamwidth, and pattern responses can be evaluated by space excitation with appropriate positioning of the illuminating source. Using reflectors with known polarization characteristics also allows the polarization characteristics of the radar to be measured. Quite often, dihedral (or diplane) and trihedral corner reflectors are employed to perform system-level tests of this type. Table 16.2 shows the response of diplane and trihedral reflectors to different transmitted polarizations, for different rotational angles of the reflectors.

Space excitation allows the measurement of the radar up through the signal processor. Therefore, signal processor performance can be evaluated if the proper target and background environment is used for the test. For example, multiple target tests require the use of multiple reflectors. Doppler tests and varying phase tests are not easily implemented in space excitation tests (unless targets are actually moving). However, researchers at Georgia Institute of Technology have employed rotating diplanes (spaced by one-eighth wavelength) in space excitation tests to simulate a moving target of known RCS. If the target (or targets) is placed in a clutter environment approximating the actual operating environment, space excitation tests can be very realistic and provide measures of performance in that clutter environment. Thus, radar MTI and clutter rejection capabilities can be assessed.

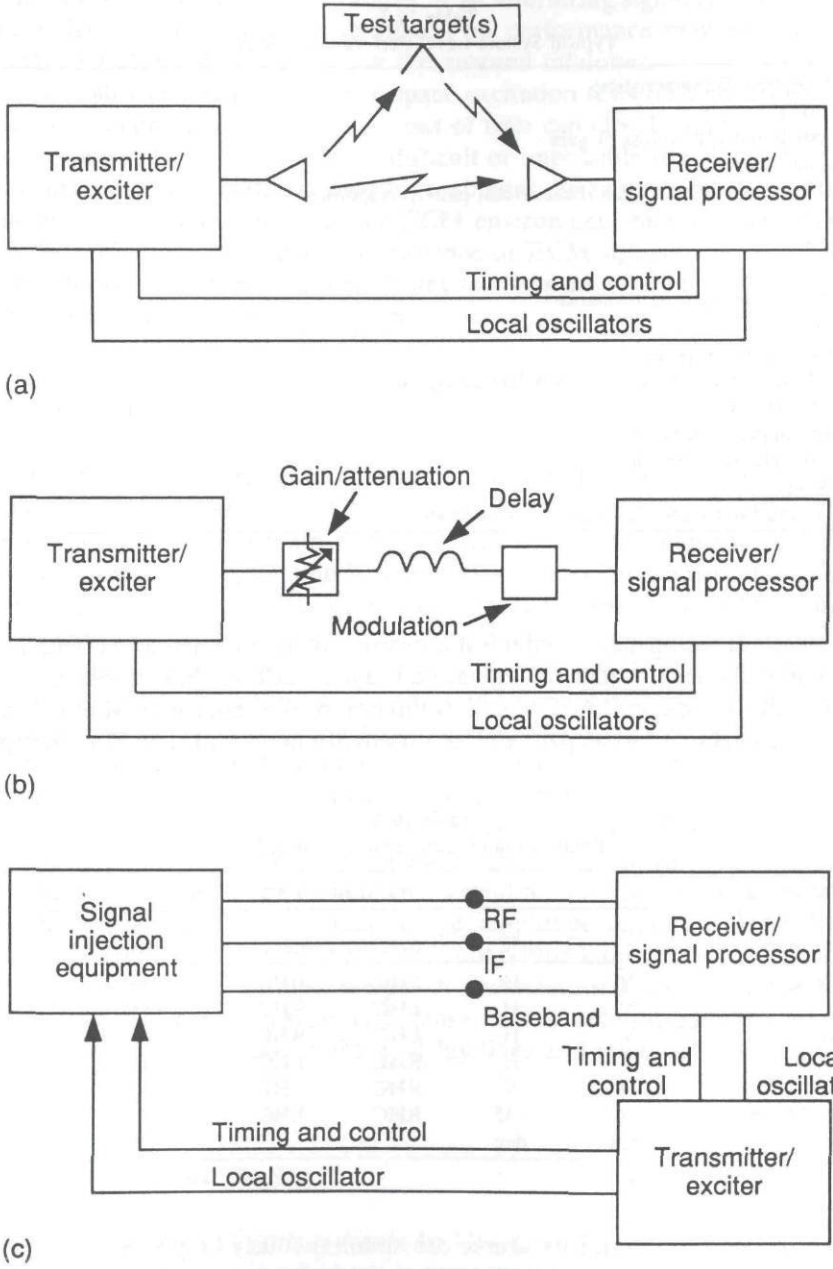

Figure 16.1 Levels of radar testing: (a) Space excitation testing; (b) "Closed loop" radar testing; (c) Signal injection testing.

Table 16.1
Typical System-Level Performance Tests

Radar Reception Characteristics:
Sensitivity
Subsystem and system loss or gain
Dynamic range
Antenna characteristics: gain, beamwidth, pattern responses
Calibration:
Amplitude
Phase
Quadrature detector performance
Polarization:
Polarization responses
Polarization isolation (to cross polarized signals)
Processor Performance:
Range-doppler processing
MTI and clutter rejection
Tracking
Interference and ECM and ECCM performance

Similarly, for tracking measurements it is possible to use moving targets with known RCS characteristics in order to evaluate a radar's tracking characteristics.

A radar's response to ECM and evaluation of the radar ECCM effectiveness can also be evaluated in a space excitation environment and test. For example, a

Table 16.2
Polarization of Echoes from Reflectors

Relfector and Polarization of echo from:	*Illuminated Polarization*					
	V	*H*	*RHC*	*LHC*	*+45°*	*−45°*
Flat Plate	V	H	LHC	RHC	+45°	−45°
Sphere	V	H	LHC	RHC	+45°	−45°
Trihedral	V	H	LHC	RHC	+45°	−45°
Diplane (V)	V	H	RHC	LHC	−45°	+45°
Diplane (45 deg)	H	V	RHC	LHC	+45°	−45°
Diplane (22.5 deg)	+45 deg	−45 deg	RHC	LHC	V	H

target reflector and interfering source can simultaneously be placed in the field of view of the radar's antenna to evaluate degradation of performance in such an environment. This type of testing has the advantage of allowing the effects of the

antennas to be determined. For example, if an interfering signal is in the mainlobe of the radar's receiver antenna, its effects on performance may be significantly different than if the interference is in the antenna sidelobes.

It is highly desirable to perform space excitation tests on a coherent radar if test resources permit, because these types of tests can closely approximate actual radar operation. However, it may be difficult or impossible to create a target and background environment that closely approximates the actual conditions. Also, the resources to test a radar in a realistic ECM environment may be unavailable, or it may be undesirable to radiate interference or ECM signals that are known to have deleterious effects on radar performance (transmission of these signals may interfere with other radars, for example).

16.2.2 Closed-Loop Radar Testing

Even in those cases where space excitation tests are planned and are necessary, it is often desirable to test some of the radar's coherent performance characteristics without a space excitation setup. Figure 16.1(b) shows a technique for performing closed-loop radar testing, suitable for use in a laboratory. In concept, this technique is quite straightforward; it requires injection of the transmitter signal back into the radar receiver by using an appropriate length of RF delay, representing target delay. This technique can be used to inject coherent signals into the receiver that simulate a point target response and works well for simulating returns at reasonably close delays. Although testing long delays can be achieved, a straightforward implementation with cabling or delay lines becomes cumbersome because of attenuation and physical size. By using a modulator in the path of the return signal, it is possible to coherently phase or frequency shift the return waveforms. Using this technique, it is possible to simulate doppler frequency shift on the return signal.

The closed-loop testing technique is useful for testing certain types of radar performance (i.e., sensitivity, dynamic range, amplitude and phase calibration, and phase noise) (see Chap. 14). However, it is not particularly well suited to tests that require multiple targets, multiple doppler frequencies, or similar tests that exercise the signal processor target capacity, because the test setup usually becomes cumbersome (i.e., multiple cable paths or delay lines and many RF components are required).

16.2.3 Signal Injection Testing

Signal injection testing, shown in Figure 16.1(c), provides some specific advantages for coherent radar testing in a laboratory environment. As shown in Figure 16.1(c), coherent radar receiver testing can be performed as long as the injected signals

are in phase and frequency coherence and time synchronization with the receiver's LOs and timing and control signals, respectively.

The accuracy required for coherent radar tests places stringent demands on the equipment and techniques used for those tests, particularly for signal injection tests. Consider those components and subsystems in the receiver chain of Figure 15.1. Some of the signal generation requirements for testing these components and subsystems are summarized in Table 16.3. These requirements are by no means all inclusive, but each is important for coherent radar testing; therefore, we will concentrate on these requirements. ([Note: Hewlett Packard offers a seminar [1] in the area of radar simulation and waveform generation. Many signal injection concepts and specialized techniques are presented in more detail in that seminar.)

One of the first observations we can make regarding radar receiver signal injection testing is the need to generate complex waveforms and modulations (i.e., chirps, phase codes, or other modulations) and insert those waveforms into the radar receiver at either RF, IF, baseband frequencies (i.e., at the appropriate points in the receiver chain), or at the signal processor in digital format. Complex waveform signal generation is usually more difficult to implement at the front end of the radar receiver, where the radar signal carrier frequency may range from low frequency VHF to the MMW region. Generating complex radar modulation waveforms at these frequencies may require expensive or specially designed test equipment. Radar IFs typically are in the tens of megahertz to hundreds of megahertz region. Although signal generators at these frequencies are generally less expensive and more available than the required equipment at RF, the requirements to generate complex waveforms may again necessitate special signal generators. Regardless of whether RF or IF test signals are injected, they should be coherent with the receiver's COHO(s). Baseband waveforms, such as those at the I/Q detector output, contain the required signal information, but are not on a carrier frequency; therefore, many laboratory signal generators will generate these waveforms. Finally, to test the radar signal processor (alone) requires the injection of digital data. Depending on the testing requirements, it may be desirable to test only a

Table 16.3
Coherent Radar Receiver Performance Testing Signal Generation Requirements and Considerations

Complex waveform modulation and injection at:
Radio frequencies
Intermediate frequencies
Baseband frequencies
Phase coherence and waveform synchronization
Frequency stability, accuracy, and resolution
Spurious-free signal generation (i.e., high spectral purity test waveforms)
Complex target and interference injection tests

portion of the radar receiver. For example, once the front-end components (amplifiers, filters, etc.) have been characterized, it may be simpler and more desirable to inject test signals at the IF, or at baseband frequencies, or as digital data at the signal processor(s). In some cases the test signals will need to be inserted at multiple points in the radar receiver. For example, if the radar is a monopulse system or has an array of antennas, then the signals may need to be injected at more than one port. In this case, maintaining the proper time, phase, and amplitude relationships between the injected signals will be important. This again may require special signal sources or distribution networks to route the test signals into the radar at the appropriate points with the correct relative time, phase, and amplitude.

In those cases where it is desired to accurately assess coherent radar performance, phase and frequency coherence and synchronization of the test signals or waveforms with the radar transmitter/exciter and COHO(s) are especially important considerations. The receiver/signal processor will only duplicate actual performance if the injected test signal has a precise time and phase relationship to the transmitter/exciter and LO signals. Coherence of the test signal can be achieved either by extracting (for example, by coupling) a sample of the transmitter/exciter waveform, or generating a coherent replica of the waveform, and injecting the waveform with the appropriate delay or modulation into the receiver as described above. Because the requirement for coherence is one of the most demanding for testing, techniques for achieving coherence will be discussed in more detail in subsequent sections.

Test waveform frequency stability and phase noise, accuracy, and resolution are also important considerations for coherent radar testing. Phase noise relates to the short-term source stability, although long-term frequency source stability and accuracy are also important. Phase noise on the test signal must be kept sufficiently low so that the test signal will not introduce unwanted errors or other effects, which cannot easily be differentiated from other effects such as clutter. Often, the test signal must be adjustable in frequency and phase (in a time varying fashion) to simulate the effects of doppler or frequency errors. The frequency resolution of the test signal source must be sufficient to test the minimum doppler or frequency error. The injected test waveforms for testing must also be inserted into the receiver with high spectral purity and free of spurious signals and harmonics. Spurious signals and harmonics will have the effect of giving false detections or interfering with target detections.

It should be noted that the test techniques of Figure 16.1 overlap one another and can be combined to achieve test objectives. For example, closed-loop testing can be realized with signal injection equipment that injects synchronous coherent signals into the radar (rather than using the transmitter). Also, coherent signals can be used with antennas for space excitation tests.

16.3 SIGNAL GENERATION EQUIPMENT FOR INJECTION AND OTHER TESTING TECHNIQUES

16.3.1 Radar Waveform Generation and Simulation Techniques

Upon consideration of Tables 16.1 and 16.3, it is clear that a major requirement for testing coherent radar performance is the ability to generate and inject precisely controlled and stable waveforms into the receiver/signal processor. Moreover, it is important that these waveforms can be injected with phase and frequency coherence in the radar under test. Because waveform generation is an important part of coherent radar system testing, we will specifically address techniques for waveform generation that are applicable to coherent radar testing.

To begin, we will consider the specifications of a high-quality signal generator, the Hewlett-Packard HP8780A vector signal generator, and how that generator may be applied to coherent radar testing. The HP8780A is a synthesized signal generator capable of generating waveforms at frequencies between 10 MHz and 3 GHz, with exceptionally wide FM, AM, and pulse modulation bandwidths. The vector modulation capability is implemented by using a very stable coherent carrier and modulating the carrier with the appropriate signals in a single-sideband modulator. The two mixers, 90-deg phase shifter, and summer in Figure 16.2 make up a single-sideband modulator, and this modulator achieves "vector modulation" of the carrier with the signals $X_I(t)$ and $X_Q(t)$. In the HP8780A, the modulating signals may be input in analog form (with up to 350 MHz bandwidth on each input), or the modulation can be applied with an internal digitally controlled modulator. The carrier signal frequency of the HP8780A may also be changed by direct frequency modulation of the synthesized source. The configuration of the HP8780A is especially advantageous for coherent radar testing, in which it is necessary to precisely adjust the amplitude and phase of complex waveforms. The salient specifications of the HP8780A are listed in Table 16.4 [2, 3].

With the capabilities listed in Table 16.4, the HP8780A can be used to generate and inject precisely controlled waveforms into the IF or RF inputs of a radar receiver. With proper inputs to the I and Q inputs, a variety of complex waveforms can be generated with the HP8780A. Coherence of the HP8780A signals and a radar receiver can be achieved by frequency- and phase-locking the synthesized source to the radar LOs, specifically the COHO of the radar.

Quadrature Waveform Generation

The circuit in Figure 16.2 can be used for generating an IF (or RF) signal using the I and Q baseband signals and a reference oscillator. The I and Q input signals are defined in Section 15.4 and are referred to here as $x_I(t)$ and $x_Q(t)$. It is assumed

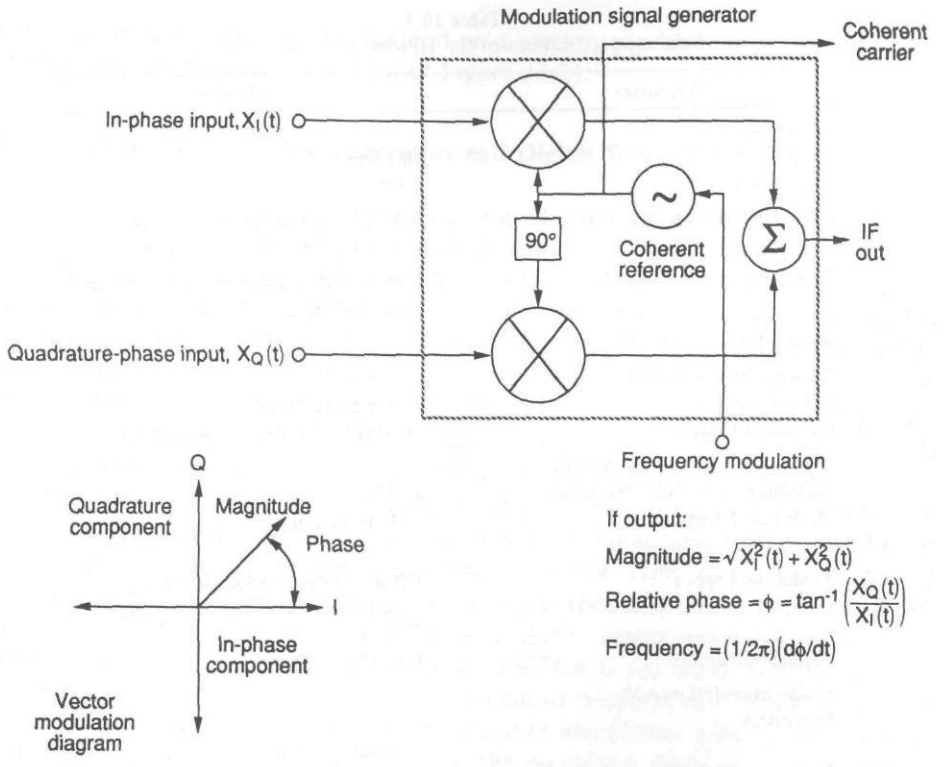

Figure 16.2 A single-sideband modulator used for vector modulation.

that the resultant signal is band-limited to $\Delta\omega$ rad/s, so the baseband I and Q signals are band limited to $\Delta\omega/2$ rad/s. The mixers in Figure 16.2 are essentially product devices so that the products of $x_I(t)$ and $x_Q(t)$ with the quadrature components of the reference (carrier) frequency are obtained and summed to obtain the final output. The resulting bandlimited signal is centered (in frequency) on the reference or carrier frequency. The magnitude of the output, M, is determined by the quadrature signals as:

$$M = \sqrt{X_I^2(t) + X_Q^2(t)} \tag{16.1}$$

and the phase, ϕ (relative to a coherent carrier), is:

$$\phi = \tan^{-1}(X_Q(t)/X_I(t)) \tag{16.2}$$

Table 16.4
Salient Specifications of the HP8780A (from [2, 3]) *

Parameter	*Specification*
Frequency:	
Range	10 MHz to 3 GHz
Resolution	1 Hz
RF output level range	+10 to −100 dBm < 2.5 GHz +4 to −100 dBm ≥ 2.5 GHz
Coherent carrier output	Unmodulated coherent carrier except for FM mode
Modulation capabilities:	
AC-coupled frequency modulation:	
Rates (3 dB)	20 Hz to 12 MHz
Deviation ranges	50 kHz to 50 MHz peak-to-peak
DC-coupled frequency modulation:	
Maximum rate (3dB frequency)	10 kHz
Deviation ranges	150 Hz to 150 kHz
Digital Modulation:	
Modulation types	BPSK, QPSK, 8PSK, 16QAM, Arbitrary two state, burst, plus others
Parallel data rates	0 to 150 MHz clocked
Scalar modulation/AM:	
Sensitivity	0V to +1V for 0 to full-scale envelope mod
Vector modulation	Frequency response: dc to 350 MHz (−3 dB) Vector accuracy: <1.5% full scale (typical)
Internal reference oscillator	Aging rate: $< 5 \times 10^{-10}$/day Temperature effects: 1×10^{-10}C/deg Line voltage: $< 5\ 10^{-10}$/(+5% to −10%)
Spectral purity	Phase noise: −110 dBc at 100 kHz Harmonics: < −35 dBc Nonharmonics: < −55 dBc

*These are abbreviated specifications for descriptive purposes only; for full specifications see the references.

The frequency can be changed by varying the rate of change of phase; that is:

$$f = \left(\frac{1}{2\pi}\right)\frac{d\phi}{dt} \tag{16.3}$$

Thus, the output signal, while centered on a carrier, can be changed in amplitude or phase (as in the phaser diagram of Figure 16.2).

16.3.2 Arbitrary Waveform Generators and Digital Waveform Generation

Several techniques exist for digital generation of radar target signal replicas, interference (clutter as well as ECM), and other simulated radar waveform conditions and effects (i.e., antenna scan modulation effects). One such technique employs digital arbitrary waveform generation to create the required waveforms at low IFs (or baseband frequencies) and subsequently up-convert those waveforms to RF; an example instrumentation system is the Hewlett-Packard *vector arbitrary waveform synthesizer* (VAWS) [2 (pp. 453–455), 4]. In this system the I component ($X_I(t)$) and Q component ($X_Q(t)$) of the desired waveforms are stored as data points in a digital random access memory (12 bits resolution and 512 KB) in the HP8770A arbitrary waveform synthesizers ($X_I(t)$ and $X_Q(t)$ are each stored in separate synthesizers). These waveforms can be generated from equations or reproduced from measured data and downloaded into memory in the HP8770As. To produce a waveform, the waveform data are read out synchronously into a D/A converter, filtered, and then input into the HP8780A vector signal generator modulation inputs. The maximum readout rate of the HP8770A is 125 MHz, but the data are filtered with output low-pass filters having a cutoff frequency of 50 MHz. Because I and Q data are used, the system can generate waveforms with up to 100 MHz bandwidth. The data points representing the waveform must be at time sample points that satisfy Nyquist sampling criteria for the I and Q signals, as discussed in Section 15.6. The resultant waveform generated by the HP8780A can be centered on a carrier frequency between 10 MHz and 3 GHz. Although this output can be used directly for radar IF testing, the output must be up-converted to the radar operating frequency for higher frequency RF testing.

After generating a waveform with an arbitrary waveform generator system, external modulation can be applied to the waveform at the output. For example, target-doppler effects can be realized externally with a modulator as in Figure 16.1(b). Although the arbitrary waveform generator can introduce the effects of doppler offsets as well, externally applied doppler offsets allow conservation of data memory and also allow for more flexibility in doppler offset generation. Other external modulations (amplitude, phase, or frequency) can be impressed on the waveform externally as well. To maintain coherence, the COHO from the radar exciter can be used to generate a frequency reference for the arbitrary waveform generator system and the other radar LOs can be used to up-convert the waveform to the radar RF frequency. In this way, the arbitrary waveform generation system can generate waveforms that are coherent with the radar. Both coherent target signal and delayed target signal waveforms can be generated. Delays can be

achieved by reading out the waveform data from memory after a time delay representing a target delay.

It is possible to combine multiple waveforms in the arbitrary waveform generators (for example, target signals and noise), even in those cases in which the waveforms overlap in time, because waveform superposition techniques can be used. Additionally, waveforms can be combined (added) externally at the RF output. Thus, for example, target signals can be generated by the arbitrary waveform generator system and noise or other interference generated at RF and added to output. This approach can have advantages, because the signal amplitude and other characteristics of the digitally generated waveform and the externally generated waveform can easily be independently modified, without modifying the waveform stored in memory. Waveforms can be created for the arbitrary waveform generators by defining the desired time or spectral characteristics and using (forward or inverse) FFT techniques to generate the time samples of the waveform, which are downloaded to waveform memory. Alternatively, it is possible to store actual measured waveform data points into the waveform memory.

Once an RF waveform is generated, it can either be applied directly to the input of the radar by means of coaxial cable or waveguide (i.e., signal injection), or alternatively, the signal can be applied to an antenna for space excitation. If multiple signals from different directions (angles-of-arrival) are desired, it is convenient to use antennas and space excitation. This may necessitate two channels of independent arbitrary waveform generators, depending on the time synchronization of the waveforms required at the two antennas. On the other hand, direct injection of the test waveforms can often be employed and allows for controlled and repeatable tests and test conditions.

Several manufacturers build laboratory arbitrary waveform generator systems. For example, Hewlett-Packard, LeCroy, and Analogic build such systems. Additionally, "board-level" arbitrary waveform generators are available from other manufacturers. These signal generators may installed in personal computers or external card cages. In general, board-level arbitrary waveform generators are much less expensive than the laboratory generators, but with somewhat reduced performance. Memory sample rates of up to several hundred megahertz, with 8- or 12-bit resolution, and 512 KB of memory are available for laboratory waveform generator systems. Board-level systems operate up to about 25 MHz with 8-bit resolution and onboard memory of typically 16 KB. Although board-level systems are slower and have less memory than laboratory systems, they are often adequate for the generation of many radar waveforms. There are other tradeoffs to consider in the selection of laboratory versus board-level arbitrary waveform generator systems. For example, most laboratory systems are programmable through the IEEE-488 bus, a standard instrumentation interface bus; board-level systems are often programmed with digital data and control words, with specific handshaking to transfer the data. The result is that more programming "overhead" is sometimes

required to program board-level arbitrary waveform generator systems. However, this burden can be offset by a substantial savings in test system cost. Recently, manufacturers have begun to develop board-level arbitrary waveform generators that are compatible with the *VMEbus extensions for instrumentation* (VXI) bus. The VXI bus is a derivative of the *Versa Module Eurocard* (VME) standard, which uses standard board configurations and a standard bus configuration. The control and programming of these boards also utilizes standard protocol.

16.3.3 Direct Digital Synthesis Test Techniques

Although the concept of DDS has existed for some time, significant developments in DDS hardware and test systems in the last several years have made the technique more viable as a test tool. Waveforms generated by DDS techniques can be made coherent with (i.e., frequency- and phase-locked to) LOs within a radar and can be used as test signals to evaluate either benign radar performance or performance in the presence of errors. Figure 16.3 shows a block diagram of a typical DDS system architecture. With the architecture of Figure 16.3 it is possible to generate waveforms defined as $A \sin(\omega t + \phi)$, where ω (radian frequency), ϕ (phase), and A (amplitude) are digitally generated and control the output waveform. A key feature of the DDS architecture is a means for generating a waveform, on a point-by-point basis, using a sine or cosine lookup table, where the address inputs of the lookup table are derived from the instantaneous phase of the desired waveform and the amplitude of the waveform at each point is the data (for each address) in the lookup table. In order to obtain the total instantaneous phase, it is necessary to integrate the instantaneous frequency. Thus, as shown in Figure 16.3, the digital frequency word ω (center frequency) and $\Delta\omega$ (frequency modulation) are input to a digital adder to accumulate the total instantaneous phase. Other changes in waveform phase (i.e., phase modulation) are added to the phase word due to frequency before inputting to the address port of the lookup table. After the waveform has been digitally generated in the lookup table, it can be amplitude-modulated with a digital multiplier and then converted to an analog signal by a D/A converter. Finally, to remove or reduce the effects of sampling and quantization, the alias filter removes spurious, while passing the desired fundamental waveform.

The DDS architecture has several advantages over analog waveform generation techniques and in some cases is even superior to other digital waveform generation techniques. Table 16.5 summarizes some of the potential DDS waveform generation advantages [5].

The DDS architecture allows the generation of coherent test signals by using a DDS clock that is phase-locked to a master reference oscillator and subsequent heterodyne up conversion to RF with oscillators that are locked to the reference oscillator (such as the radar COHO). The DDS clock frequency must satisfy Nyquist

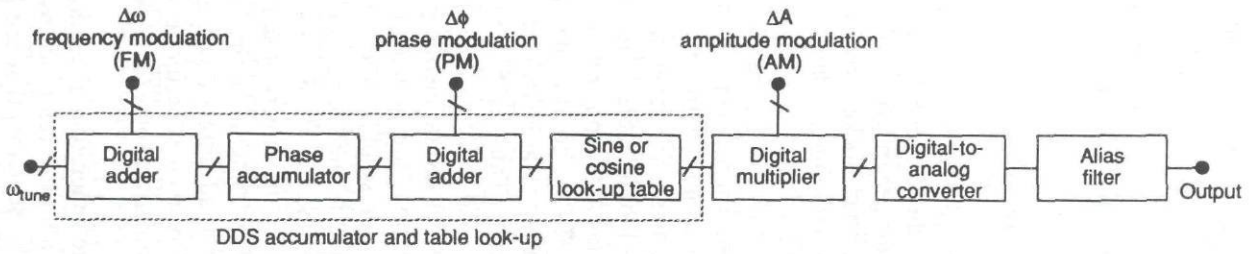

Figure 16.3 Direct digital synthesis system architecture.

Table 16.5
DDS Waveform Generation Advantages (from [5])

Fast frequency change settling time (usually $< 1\ \mu s$)
Multioctave operation possible
Very-fine-frequency resolution possible (10^{-6} Hz)
Phase coherent frequency changes
Exceptionally linear sweep (16 bits typical)
Quadrature waveform generation over several octaves possible

criteria for sampling the bandwidth of the generated waveform. The fast frequency settling time of direct digital synthesizers allows their use in system tests of frequency agile systems. Moreover, DDS devices can be used to generate extremely linear chirps or well-controlled phase codes. It is not unusual for DDS hardware to use 12- to 16-bit words to control frequency and phase information, resulting in very precise frequency and phase control. The number of bits input to the D/A controls the amplitude and is therefore determined by the number of bits in the lookup table data. The number of bits employed in the D/A converter can be fewer than the number of frequency or phase bits; usually 8 or 10 bits are sufficient.

Laboratory instrumentation systems and board-level integrated circuit DDS systems are currently available to support radar testing. The Hewlett-Packard HP8791 frequency agile signal simulator (FASS) is an example of a laboratory system now available. The salient specifications of the HP8791 are listed in Table 16.6 [6]. Stanford Telecom, Sciteq, and other companies make several different types of board-level and integrated circuit DDS components with frequency ranges of several megahertz, typical switching speeds of 1 μs, and typical spurious of < -50 dBc.

Once a coherent waveform is generated with the DDS, either space excitation or signal injection testing can be performed, as with arbitrary waveform generators. A DDS might be chosen over an arbitrary waveform generator because of the characteristics noted in Table 16.5. They are especially useful for generation of extremely linear chirps, for phase-coded waveforms, and for fast-switching and frequency-agile waveforms.

16.4 DIGITAL RF MEMORIES

The arbitrary waveform generator or DDS systems discussed above can be a cost-effective solution to radar test and evaluation in a variety of simulated waveform conditions. However, as noted above, to generate waveforms that are coherent with the radar under test, it is necessary to use direct interfaces to the radar LOs. If the radar LO signals are available, these approaches can be viable solutions for

Table 16.6
Salient Specifications for the Hewlett-Packard HP8791 Frequency Agile Signal Simulator (from [6])**

Parameter	*Specification*
Output Frequency:	
Range	10 to 3,000 MHz
Resolution	0.125 Hz
Switching time	<250 ns
Switching delay	2.63 μs after trigger
RF Output:	
Power range	+10 to −107 dBm
Attenuator	0 to 70 dB, 10 dB steps
Accuracy	0.2 dB
Spectral Purity:	
Spurious outputs	< −50 dBm clock related < −50 dBc nonharmonic < −50 dBc harmonic
SSB phase noise	−85 dBc at 100 Hz offset −120 dBc at 10 kHz offset −125 dBc at 1 MHz offset
Instantaneous bandwidth	40 MHz peak to peak
Amplitude Modulation:	
Range	0% to 100%
Rate	0 to 20 MHz bandwidth
Accuracy	1%
Phase Modulation:	
Deviation	−180 deg to 180 deg, 0.88 deg steps
Accuracy	0.1 deg typical
Rate	0 to 10 MHz
Frequency Modulation:	
Deviation	0 to 20 MHz (40 MHz peak to peak)
Maximum chirp rate	40 MHz/ms
Rate	0 to 2 MHz (approx.)
Pulse Modulation:	
PRF	< 0.01 Hz to < 10 MHz
Minimum rise time	< 20 ns
Minimum fall time	< 20 ns
On/off ratio	> 80 dB
Frequency Standards:	
Internal	+ 10 MHz, aging < 5×10^{-9}/day
Internal (locked to external)	5 or 10 MHz
Programmability	IEEE-488 bus

**These are abbreviated specifications for descriptive purposes only; for full specifications see the reference.

radar testing. However, if the LO signals are not available, or if it is desired to perform coherent signal testing without hardwired connections to the radar under test, alternative techniques must be employed to capture and regenerate the radar signal. *Digital RF memory* (DRFM) techniques allow for the capture of a transmitted radar waveform and the coherent retransmission of that waveform with different delays, doppler shifts, and other modulation superimposed on the waveform. DRFMs can be used for both space excitation testing and signal injection testing of coherent radars.

In DRFMs the received RF signal is mixed down to an IF or baseband by an internal LO that has been tuned to place the received signal frequency within the DRFM's instantaneous bandwidth. The resultant IF (or baseband) signal is digitized, sampled, and stored in digital memory in real time. In the case of a pulsed radar system, the continuous high-speed sampling and storage process preserves the intrapulse phase history and provides a coherent pulse history in digital memory. When an output replica of the pulse is desired, phase history is nondestructively recalled from memory at IF (or baseband), processed, and up-converted back to the original frequency by the same LO (see [7]). Figure 16.4 is a block diagram of a basic digital RF memory.

Some of the key parameters to consider in selecting a DRFM are instantaneous bandwidth, resolution (number of bits), tuning frequency range, sensitivity, signal storage capacity (memory size), spurious outputs, special modulation capabilities, and control modes on input and output. The instantaneous bandwidth of DRFMs is limited by sampling speed of the internal digitizing devices; currently 8-bit devices with more than 500 MHz instantaneous bandwidth are available, although the sampling speed decreases with more resolution. The tuning frequency range required depends on the variation in frequency of input signals. For example, if the center frequency varies over a large range from pulse to pulse, then a large tuning range is required.

Most DRFMs begin the conversion and storage process when the received signal exceeds a certain threshold level. Therefore, the sensitivity of the DRFM may be important, depending on the received SNR. If the received SNR is maintained relatively high (>13 dB), the waveform will generally exceed the threshold and be captured with minimal degradation.

Signal storage capacity or memory size is one of the more critical parameters to be specified for a DRFM, because it has direct bearing on the length of waveform, in time, that can be stored in memory. DRFMs with tens to hundreds of microseconds of memory capacity are available with sampling speeds in the hundreds of megahertz. This is typically sufficient to capture and reproduce the longest pulses in most radar systems. However, it may not be sufficient to capture an entire PRI of radar data. Noise or other background signals may be added to the reproduced pulse to create an entire PRI of the transmit waveform.

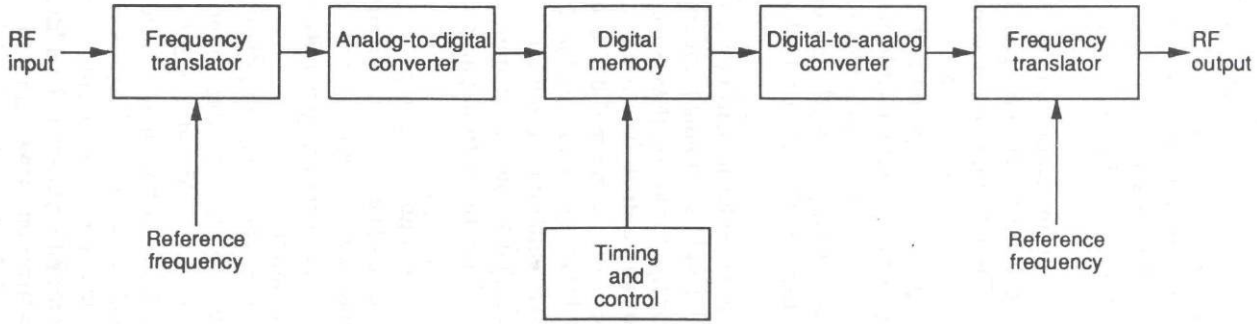

Figure 16.4 Digital RF memory block diagram.

Spurious outputs in the DRFM are primarily dependent on the number of bits of resolution employed. A single-bit conversion will result in spurious about 9 dB below the desired waveform. However, for many waveforms, such as chirp pulses, only a few bits (usually no more than 6 bits) of resolution are required, because it is primarily the phase history that must be adequately reproduced, and undesired spurious can be easily filtered from the DRFM output.

Specialized modulations can be applied to the stored waveforms with the DRFM. There are different techniques, for example, to create doppler offsets and to effect frequency translations within the DRFM. Some DRFMs employ digital techniques to slightly modify the regenerated signal frequency, whereas others employ slight variations in the LO frequency for regeneration.

The mode controls for both reading waveform data into memory and reading the data back out of memory are also important considerations for DRFMs. For example, read-in controls can "window" or bracket the incoming pulse, based on anticipated pulse arrival time. Similarly, readout mode controls can play out one pulse (or several pulses) after a delay (depending on a delay instruction).

By combining special DRFM features, many types of interference waveforms can be created with DRFMs. For example, a specialized DRFM modulation feature may allow simulated ECM, such as velocity gate pulloff effects, to be realized. Similarly, the proper readout controls may allow range-gate pulloffs to be achieved.

16.5 TAPE RECORDERS AND TAPE PLAYBACK

Recording and playback of radar data are important aspects of radar testing. Although low-frequency IF or video radar signals can be recorded as analog voltages on analog tape, it is more common that digitized radar outputs (i.e., the A/D converter outputs) are recorded. In a coherent radar, for example, it is common to record the I and Q data after digitizing. Often time codes, such as *interrange instrumentation group* (IRIG) timing or other timing information is recorded simultaneously with the radar data, so that other events can be correlated with the recorded data. Additionally, other information, such as position and velocity of the host radar vehicle (e.g., an aircraft), may be recorded. Radar performance can be assessed by posttest processing and analysis of the recorded data (e.g., to develop range-doppler maps of target areas and to evaluate MTI performance). For testing purposes, recorded I and Q data can be injected into the radar (e.g., at the signal processor to evaluate performance of the radar processor under previously measured conditions).

Important considerations and parameters for radar data recorders are dynamic range and resolution, the formatting of data, data recording rate, and the data storage capacity of the tape recorder. The number of recorded bits will need to accommodate the dynamic range of the data. A rule of thumb is about 6 dB/bit;

thus, 8-bit recorders can a handle data with up to about 48 dB dynamic range, whereas 12-bit recorders can handle almost 72 dB dynamic range. Similarly, the number of bits determines the resolution or amplitude granularity; 8-bit and 12-bit data correspond respectively to approximately 0.5-dB and 0.03dB amplitude granularity for linear data. Recorded data formats can be either serial or parallel, and generally, a recorder will pack the data on the tape in a format suitable for later playback by a companion unit that recognizes the recorded format. Many tape recorders require external devices for formatting the data. Usually, there are multiple tracks on the tape, which allows the recording of multiple channels of data and correlation of data on those channels in time.

Data rates and data storage are often two of the more important characteristics of the data recorder and playback system. Typically, data are recorded each PRI. Suppose, for example, there is one 8-bit I and Q channel (i.e., 2 bytes) of data to be recorded at 10 kHz PRF, which is equivalent to a 100-μs PRI. Further assume that 10 range gates are developed for each PRI. To record these data requires a recording rate of 200 KB/s (2 bytes 10 range gates 10 kHz). This is not a particularly demanding data storage rate, but suppose the PRF is increased by a factor of 10 or the number of range gates is increased by 10, then the data rate increases to 2 MB/s, which is significant. To record data for 60 sec at 2 MB/s requires a data storage capacity of 120 MB, again not particularly stressing for most recorders. However, if the recording time were to increase to 10 min at 2 MB/s, the data storage requirements would increase to 1.2 GB. Many data recorders will handle data storage of several gigabytes. Table 16.7 shows some data recording devices, with gigabyte storage capacity.

16.5.1 Playback

Radar data can be reinserted into the radar for test purposes in several ways. For example, once data are recorded, along with the appropriate timing information, they can be synchronized to the radar receiver A/D converter clock and played back into a radar signal processor. This can be quite useful as a test technique, because data runs corresponding to actual scenarios (e.g., radar flights over actual targets and terrain) can be reevaluated in postprocessing tests. Similarly, the digital data can be converted to analog format using D/A converters for insertion into the radar at baseband, or alternatively, the signals can be up-converted to IF or RF using the radar LOs and reinserted at the appropriate points in the radar chain. A potential advantage of digital recorders and playback systems for radar testing is that long test scenarios (corresponding to relatively long times and significant amounts of data) can be run using tape recorder test techniques, as compared with digital waveform generation techniques that store the waveforms in memory. On the other hand, each new test scenario must be recorded on tape before playback

Table 16.7
Data Recording Devices*

Manufacturer	*Model*	*Number of Tracks*	*Storage (GB)*
Honeywell	HD 101E	14	12.5
Honeywell	VLDS	2	5.2
Fairchild	85	28	7.4
Thorn EMI	SE 7000 MW	14	3.6
Kodak	M14-LR	28	4.3

*Parameters shown are for descriptive purposes only; for detailed specifications consult the manufacturers.

into the radar, and thus, utilization of tape recorders for testing is not always as versatile as digital waveform generation techniques, where the waveform data can be quickly changed.

16.6 SUMMARY

This chapter has described some of the more common test techniques and equipment available for and employed in coherent radar system testing. Several types of testing (i.e., space excitation, closed-loop, and signal injection testing) have been described. Equipment and techniques for generating coherent radar waveforms at RF, IF, and baseband frequencies have been described, along with techniques for generating and storing digital data that are typically available at the radar (signal processor) output.

The utilization of the equipment and techniques described in this chapter will vary considerably depending on the types of radar testing to be performed. For example, space excitation of the radar may be desirable for full end-to-end testing, whereas digital data injection testing of the radar signal processor may suffice for other tests.

REFERENCES

[1] "Analysis and Simulation Techniques for Modern Radar," Seminar Notes, Hewlett-Packard, Palo Alto, CA, 1988.

[2] Hewlett-Packard 1992 Test and Measurement Catalog, the HP8780A Vector Signal Generator, Hewlett-Packard Company 1991, Santa Clara, CA, pg. 460.

[3] Hewlett-Packard Product Note 8780A-1, "Introductory Operating Guide to the HP8780A Vector Signal Generator," HewlettPackard, November 1, 1986.

[4] "Hewlett-Packard HP8770S Signal Simulator System dc-50 MHz Technical Data," Hewlett-Packard, July 1987.
[5] Stanford Telecom Application Note 10, "Introduction to Direct Digital Synthesis," Stanford Telecom, Santa Clara, CA, March 1990.
[6] "Hewlett-Packard Model 10, Frequency Agile Signal Simulator (FASS) Technical Data," Publication 5953-2336 0400, Hewlett-Packard, March 1990.
[7] "Whittaker Electronic Systems Digital RF Memory (DRFM's) Experience, Resources and Product Specifications," Whittaker Electronic Systems, September 1987.

Glossary

Term/Symbol	Definition
A	amplitude (of signal)
a	arbitrary coefficient; quadrature channel amplitude offset error
$A(f)$	amplitude versus frequency function
$A(t)$	signal (function of time)
A/D	analog-to-digital
$a[n]$	amplitude error (discrete function)
a_1	first harmonic Fourier coefficient of amplitude response
A_c	cosine component amplitude
ADC	analog-to-digital
AGC	automatic gain control
a_i	target acceleration
$A_i(t)$	amplitude as a function of time or i^{th} sample of amplitude function
AM	amplitude modulation
AM to PM	amplitude modulation to phase modulation
a_n	amplitude of error modulation (for n cycles of error)
A_o	amplitude of sine or cosine; antenna gain on boresight
a_o	direct current (dc) Fourier coefficient of amplitude response
A_s	sine component amplitude
ATR	automatic target recognition
AZ_I	inphase component of the elevation signal
AZ_Q	quadrature-phase component of the elevation signal
b	arbitrary coefficient; number of bits
B	bandwidth; measurement frequency band; total stepped frequency bandwidth coded pulse bandwidth (pulse compression); bandwidth of noise

B_c	expected maximum width of target spectrum
B_f	minimum acceptable bandwidth
b_1	first harmonic Fourier coefficient of phase response
B_{IF}	spectrum analyzer IF bandwidth
BIT	built-in test
b_o	direct current (dc) Fourier coefficient of phase response
B_p	effective bandwidth of pulse
B_{PRF}	frequency separation of PRF lines
BPSK	bi-phase shift keyed waveform
B_r	bandwidth of fine lines in receive spectrum
B_{sa}	resolution bandwidth of spectrum analyzer
BT	bandwidth-time product (in pulse compression)
C	clutter
°*C*	degrees centigrade
c	propagation velocity of light
CA	clutter attenuation
CA_N	clutter attenuation divided by ratio of noise powers (N_i/N_o)
CFAR	constant false alarm rate
C_i	clutter input level
cm	centimeter
C_o	clutter output level
COHO	coherent oscillator
CPI	coherent processing interval
CW	continuous wave
D	transmit duty cycle
D/A	digital-to-analog
dB	decibel
dBc	decibels below carrier
dBc/Hz	decibels below carrier in 1-Hz bandwidth
dBFS	decibels below full scale
dBHz	decibels relative to one Hertz
dBK	decibels relative to one degree Kelvin
dBm	decibels relative to one milliwatt
DBM	double-balanced mixer
DBS	doppler beam sharpening
dc	direct current
DC	first doppler bin in FFT or DFT
DDS	direct digital synthesis; direct digital synthesizer
deg	degree (angular)
df/dv	voltage pushing (in an oscillator)
DFT	discrete Fourier transform
DRFM	digital RF memory

DRO	dielectric resonator oscillator
DSP	digital signal processor
DTFT	discrete time Fourier transform
DUT	device under test
dx/dt	velocity
E	maximum target extent; coefficient for I/Q detector correction
E_ϕ	peak phase ripple in paired echo analysis
$E(f)$	envelope of spectral lines; spectral amplitude envelope
$E(N, f)$	envelope amplitude
$e(t)$	received signal time function
ECCM	electronic counter-countermeasure
ECM	electronic countermeasure
E_k	deviation from ideal frequency at kth frequency step (step frequency)
EL_I	inphase component of the elevation signal
EL_Q	quadrature-phase component of the elevation signal
EMI	electromagnetic interference
ENB	effective number of bits
ENBW	equivalent noise bandwidth
E_o	least significant bit (voltage)
E_{pp}	peak-to-peak signal voltage
F	frequency (transmitted); system noise factor or noise figure
$\dot{F}$	time derivative of frequency
f	frequency; frequency of a signal; radar frequency; transmitter frequency
$F(f)$	frequency function
f_1, f_2	frequencies of tones for intermodulation tests
f_a	frequency limit (arbitrary): analog frequency
f_b	frequency limit (arbitrary); beat frequency (FMCW)
$f_{b(\text{sawtooth})}$	beat frequency for sawtooth waveform (FMCW)
$f_{b(\text{triangle, upsweep})}$	beat frequency for triangle waveform (FMCW) on upsweep
$f_{b(\text{triangle, downsweep})}$	beat frequency for triangle waveform (FMCW) on downsweep
$f_{b(\text{triangle})}$	beat frequency for triangle waveform (FMCW)
f_c	center frequency
$\dot{f}_c$	time change in carrier frequency
f_{c_i}	final output frequency at i^{th} sample
f_{coho}	coho frequency
f_D	doppler frequency
f_d	doppler frequency
$f_{d(\max)}$	highest expected doppler frequency
f_{da}	apparent ambiguous doppler
FET	field effect transistor

FFT	fast Fourier transform
f_{IF}	center frequency of narrow-band IF filter
f_i	frequency of i^{th} step (step frequency)
f_{in}	input frequency
f_{ips}	frequency due to induced phase shift
f_k	k^{th} frequency transmitted (ideal) (step frequency)
FM	frequency modulation
f_m	modulation frequency (FMCW, etc.)
FMCW	frequency-modulated continuous wave
f_o	nominal reference frequency; resonant frequency; output frequency; normalized frequency; center of frequency band
f_r	pulse repetition frequency; voltage controlled oscillator frequency; center of frequency band
f_s	sampling frequency
f_{stab}	stable local oscillator frequency
f_{syn}	synthesizer frequency
f_{syn_i}	synthesizer frequency at i^{th} sample
f_t	radar frequency of operation; frequency shift
F_t	transmitter noise figure
G	antenna gain
$G_A(\theta)$, $G_B(\theta)$	antenna gains of beams of monopulse antenna
g	gravity force
$G(\phi)$	antenna gain as a function of ϕ
$G(f)$	frequency response function
$g(t)$	time domain signal
GB	gigabyte
GB/s	gigabyte per second
GHz	gigahertz
G_m	arbitrary matched filter gain constant
G_{mf}	maximum filter gain
G_p	IF gain of receiver
GPS	global positioning system
H	horizontal polarization
$H(f)$	receiver frequency response; matched filter frequency response (pulse compression)
$h(t)$	matched filter time response
HF	high frequency
HPRF	high-PRF
HRR	high-range resolution; high resolution radar
HVPS	high-voltage power supply
Hz	Hertz

i	an integer
I	inphase component of a waveform; clutter improvement; interference
IDFT	inverse discrete Fourier transform
IF(t)	intermediate frequency time function
IFMCW	intermittent frequency-modulated continuous wave
I_1, I_2, I_3	individual clutter improvement limits
I_2	improvement factor for two-delay canceller
$I_i(t)$	inphase signal as a function of time at i^{th} sample
IM	intermodulation
IMU	inertial measurement unit
INS	inertial navigation system
IPRW	impulse response width (time)
IPS	induced phase shift
I_q	quantized noise clutter improvement limit
IR	image rejection
IRIG	interrange instrumentation group
I_S	system clutter improvement limit
ISAR	inverse synthetic aperture radar
ISL	integrated sidelobe level
$J_0(\delta)$, $J_1(\delta)$ $J_0(\delta)$, $J_3(\delta)$	Bessel function coefficients of the first kind
$\text{Jitter}_{\text{rms}}$	total rms jitter
J_m	Bessel function of first kind and order m
k	quadrature channel amplitude imbalance; Boltzmann's constant; saturation to rms signal level ratio; broadening factor due to weighting; constants for non-fluctuating targets
k^*	constants for fluctuating targets
KB	kilobytes
k_c	wind velocity coefficient
K_d	discriminator constant (volts per Hertz)
k_d	phase detector gain factor
k_f	discriminator error slope
kg	kilogram
kHz	kilohertz
km	kilometer; slope of mixer/phase detector; monopulse antenna error slope
k_r	range servo slope
k^2	phase noise correlation factor
L	number of FFT bins shifted due to radial velocity; target length
L_{fill}	loss due to polarization
LFM	linear frequency modulation

LHC	left hand circular polarization
$L(f)$	single-sideband noise to carrier power ratio
LNA	low-noise amplifier
LO	local oscillator
LO(t)	local oscillator time function
LOS	line of sight
LPRF	low-pulse repetition frequency
L_s	system losses
LSB	least significant bit
L_T	receiver losses
M	number of range profiles (in ISAR); number of points in measurement; number of bits; number of pulses processed for cross range resolution; magnitude of signal (time signal); number of points in DFT or FFT; number of range profiles (in ISAR)
m	modulation coefficient, meter
m/s	meters per second
m/s^2	meters per second squared (acceleration)
mA	milliampere
M_{eff}	effective number of bits
MHz	megahertz
MHz/μs	megahertz per microsecond
MLC	mainlobe clutter
mm	millimeter
MMW	millimeter wave
MOPA	master-oscillator-power-amplifier
MPRF	medium-pulse repetition frequency
ms	milliseconds
MTI	moving target indication
$M(t)$	signal time function
mw	milliwatt
N	excess noise constant; number of FFT or DFT points; number of steps in step frequency waveform; number of pulses in sequence; noise; number of subpulses in phase shift keyed waveform; number of spectral lines
n	number of pulses; number of sequence points; multiplication ratio in a frequency multiplier (an integer); number of statistically independent samples of signal and noise power
N_c	number of cross-range cells moved in coherent integration time
N_d	number of doppler ambiguities
N_{fft}	number of points in FFT
N_i	noise input; integration gain
NLFM	nonlinear frequency modulation waveform

N_m	number of range cells migrated
N_o	noise output
N_{oi}	transmitter input noise level
N_{pc}	number of pulses coherently processed
ns	nanoseconds
N_t	number of range cells shifted
Ω	resistance unit
p	location of point in y-z earth plane; normalized target "range walk"; coefficient for I/Q detector correction
p-p	peak-to-peak
P/P_c	sideband power to carrier power ratio
P_c	carrier power level
P_{ci}	average clutter power return from i^{th} range ambiguity
P_d	probability of detection
PDR	phase-derived range
P_{fa}	probability of false alarm
PGA	phase gradient algorithm
P_i	incident power
P_{in}	transmitter power
P_{la}	error correction for spectrum analyzer logarithmic amplifier characteristic
PLL	phase-locked loop
PLO	phase-locked oscillator
PM	phase modulation
$P_m(f_m)$	power level measured at the offset frequency f_m
P_n	noise power
PN	pseudorandom
P_{out}	output power vector
P_{nom}	nominal output power vector
P_r	received power
P_{ref}	reflected power vector
PRF	pulse repetition frequency
PRF'	effective PRF
PRI	pulse repetition interval
PS	peak shift
PSD	power spectral density
PSD$\{v(t)\}$	power spectral density of phase detector voltage
PSK	phase shift keyed
PSL	first peak sidelobe to mainlobe peak ratio or peak sidelobe level
P_t	peak transmitted power; target power
PUL$(f\tau)$	Fourier transform of envelope of pulse
P_uM	pulse modulation

Q	quadrature-phase (component of a waveform); quality factor of resonant circuit
$q_{er}(t)$	receiver chain exciter time function
$q_{et}(t)$	transmitter chain exciter time function
$Q_i(t)$	quadrature-phase signal as a function of time at i^{th} sample
Q_L	loaded quality factor of a circuit or network
QPSK	quadra-phase shift keyed (waveform)
$q_t(t)$	transmitter time function
R	range; slant range
$\dot{R}$	time derivative of range
$r(t)$	amplitude response as function of time
$R(t)$	range as a function of time; cross correlation
R_1, R_2, R_3, R_4	voltage reflection coefficients
RBE	range bin error
r_c	cross range; scatterer distance from center of target
$r_{c(\max)}$	maximum cross range dimension
RCS	radar cross section
RCS_v	relative radar cross section
RDP	radar data processor
resFM	residual frequency modulation
RF	radio frequency
RHC	right hand circular
R_L	load resistance
RLC	resistor, inductor, capacitor (circuit components)
$R_{\max}$	maximum range
rms	root mean square
R_o	characteristic impedance; initial slant range; reference range
R_r	range resolution
RRI	ramp repetition interval
rss	square root of the sum of the squares
Rt	range to target
R_u	unambiguous range
S	signal; waveguide length (between mismatches)
$S_{\Delta\theta}$	internal phase noise
$S_{\Delta\phi(f)}$	spectral density of phase noise
$S_{\Delta f(f)}$	spectral density of frequency variations
$S(f)$	frequency spectrum of a signal; normalized signal source power density spectrum
S/C	signal-to-clutter ratio
S/C_{mlc}	signal-to-clutter for mainline clutter ratio
S/C_{rqd}	signal-to-clutter required ratio
S/H	sample-and-hold

S/N	signal-to-noise ratio
$(S/N)_f$	signal-to-noise ratio in a narrorw band filter
$S/(N+C)$	signal-to-noise plus clutter ratio
SAR	synthetic aperture radar
SAW	surface acoustic wave
SBP_i	sideband power of i^{th} sideband
SFWF	stepped-frequency waveform
S_i	input signal power
SIR	signal-to-interference ratio
$(S/N)_o$	output signal-to-noise ratio
SNR	signal-to-noise ratio
SNR_{max}	maximum realizable signal-to-noise ratio
SNR_N	signal-to-noise ratio for coherent integration of N pulses
(S/N)sp	single pulse signal-to-noise ratio
S_o	output signal power
$S_R(f)$	received signal spectrum
ssb	single-sideband
$S_T(f)$	normalized phase noise power density spectrum
STALO	stable local oscillator
STC	sensitivity time control
T	pulse repetition period or inverse of pulse repetition frequency; pulse width (of expanded pulse in pulse compression) system temperature; absolute noise temperature; aperture time; coherent processing interval time; MTI canceller delay; rectangular pulse width (time)
t	time
T_{ad}	analog-to-digital converter timing jitter
T_c	clock timing jitter; chip pulse width in PSK waveform
t_d	time delay of maximum matched filter output; transmit delay time
t_{di}	two-way range time delay to clutter in the i^{th} ambiguity
T_{dwell}	length of coherent processing interval fill time
T_e	envelope time length of PSK waveform
T_{fill}	time of pulse fill-in
T_i	integration time or coherent integration time
TMR	target motion resolution
T_o	modulation period; standard temperature; duration of coherent processing interval
t_o	time delay
T_p	pulse forming network timing jitter
t_P	pulse width; CW pulse width
t_r	antenna reflection delay

T_{tr}	transmit delay jitter
T_W	pulse compression chirp pulse length
TWT	traveling wave tube
TWTA	traveling wave tube amplifier
v	velocity due to angular rotation
V	volt; vertical polarization
$v(t)$	velocity as a function of time
V_1, V_2, V_3, V_4, V_5, V_6, V_7	forward and reflected voltages at output of TWT
v_1, v_2	velocity of scatterers at distances r_1 and r_2
V_a	aircraft velocity
VAWS	vector arbitrary waveform synthesizer
V_b	blind velocity
V_c	doppler velocity
VCO	voltage-controlled oscillator
VHF	very high frequency
VME	Versa Module Eurocard
v_o, $v(0)$	intial velocity
$V_{p\text{-}p}$	volts peak-to-peak
V_Q/V_I	ratio of quadrature-phase voltage to inphase voltage
v_r	radial velocity
V_R	relative velocity
V_s	surface wave velocity
VSWR	voltage standing wave ratio
V_t	target velocity
V_u	total closing velocity; unambiguous velocity
VXI	VMEbus extension for instrumentation
$W(fT_o)$	Fourier transform
W_c	cross range window (in ISAR)
x, y, z	directions or axes in three-dimensional space
x	distance; per sample signal-to-noise ratio
$X(f)$	transmit voltage spectrum
$x(f)$	waveform frequency function or spectrum
$x(t)$	continuous time signal; transmit voltage time waveform; a voltage versus time function
X-band	fequency region
$x[n]$, $x(nT)$	discrete time signal, where T = sampling interval
X_{dc}	dc error in I/Q detector
$X_I(t)$	inphase waveform component as function of time
x_o	peak amplitude (distance)
$X_Q(t)$	quadrature-phase waveform component as function of time
x_r, y_r, z_r	radar coordinates in x, y, z space

$x_r(t)$	time domain response of matched filter or of received waveform
x_t, y_t, z_t	target coordinates in x, y, z space
$x_t(t)$	time domain waveform of chirp (pulse compression waveform)
y_i	fractional frequency variation of the i^{th} measurement (Allan variance)
YIG	yttrium indium garnet (oscillator)
z	measure of clutter spreading
Z	voltage standing wave ratio in transmitter
z_g	impedance of waveguide

Greek Symbols Used

α	an exponent on f_m; quadratic phase constant in linear FM pulse compression; linear phase shift; arbitrary angle
α_p	pulse desensitization factor
$\alpha(fm)$	phase noise in one noise sideband (per Hertz)/total signal power at frequency f_m
β	ripple frequency due to paired echo distortions
β_f	narrow band filter bandwidth
β_i	imaginary component of elevation angle
β_{na}	angle servo loop noise bandwidth
β_{nf}	doppler servo loop noise bandwidth
β_{nr}	range servo loop noise bandwidth
β_r	real component of elevation angle
$\chi(\tau, f_d)$	cross correlation function in variables τ and fd
γ	amplitude of ripple in dB due to paired echo distortions; magnitude of clutter; PRI ratio; Euler's constant
δ	an angle in x, y, z space
δ_{f_i}	frequency stability over one PRI
δ_{f_s}	required frequency stability
δR	change in range during processing time; processed range resolution
δ_t	timing jitter
δ_A	amplitude variation
δ_ϕ	quadrature channel phase shift error
Δ	voltage difference corresponding to digital codes
Δ_{AZ}	azimuth difference signal
Δ_{EL}	elevation difference signal
Δf	frequency over an interval; change in frequency
Δf_b	beat frequency resolution

Δf_d	doppler difference or resolution
ΔF	chirp pulse bandwidth in pulse compression; frequency deviation
$\Delta F'$	effective processed bandwidth (FMCW)
Δf_s	stepped-frequency step size (frequency)
Δf_{rms}	rms frequency variation
$\Delta \Omega_i$	angle moved during coherent integration time
$\Delta \omega$	radian frequency bandwidth
$\Delta \phi$	phase change or deviation; null-to-null antenna beamwidth
$\Delta \phi / \Delta F$	ratio of phase shift to frequency shift
$\Delta \phi(t)$	phase variation in signal (function of time)
ΔR	change in range; processed range resolution
ΔR_w	range walk (part of range migration)
Δr	path length difference
Δr_{sf}	stepped-frequency resolution (range)
Δr_c	cross range resolution; separation of scatterers in cross range
ΔR_c	range curvature (part of range migration)
Δr_d	down-range resolution
ΔR_p	range curvature (part of range migration); range resolution of pulse
ΔR_o	ideal range resolution
Δt	time separation between main pulse and time sidelobes (pulse compression)
$\Delta t/t$	relative change in delay
ΔT	change in temperature; time resolution
$\Delta \theta$	antenna beamwidth
$\epsilon(t)$	amplitude variations (signal)
ϵ	depression angle to clutter; fractional amplitude imbalance in I/Q system
λ	RF wavelength
λ_g	waveguide wavelength
λ_s	wavelength of surface wave
μ	$\Delta f/f$ or $\Delta \phi$ for frequency or phase modulations respectively
μs	microseconds
μV	microvolts
$\phi(t)$	phase time function
ϕ	instantaneous waveform phase; absolute phase; an angle in z, y, z space; phase deviation due to VSWR changes; fractional phase error; phase response due to range; angle to velocity vector
ϕ_{AZ}	phase angle between azimuth difference and sum channel
ϕ_{EL}	phase angle between elevation difference and sum channel

ϕ_e	phase error
ϕ_{error}	quadratic phase error in pulse compression
ϕ_i	phase of i^{th} echo; phase of input signal
ϕ_o	phase of VCO signal
$d\phi/dt$	time derivative of phase
$\phi_{\max}$	maximum phase error
ϕ_{peak}	relative phase angle due to reflections in TWT
$\phi[n]$	phase error (discrete function)
ϕ_o	phase of VCO signal
$\dot{\phi}$	derivative of phase with respect to time
ϕ_{SAR}	phase of impulse response of SAR processor
π	constant 3.14159
ψ	fractional phase imbalance in I/Q system; angle in x, y, z space; radar depression angle
ρ	desired sidelobe level
σ	radar cross section; net standard deviation of clutter
σ_c	power density spectrum of clutter; radar cross section of clutter
σ_{fc}	frequency servo loop noise
σ_i	total standard deviation due to noise factors
σ^o	clutter backscatter coefficient
σ_n	standard deviation or noise of error source n; rms surface roughness
σ_ϵ	standard deviation of pulse leading edge
σ_e^2	variance of quantization error
σ_g	standard deviation of pulse duration time error
σ_ϕ	rms phase noise
σ_r	range noise of error source n
$\sigma_{\text{std dev } y(t)}$	standard deviation of $\sigma_{y(\tau)\text{k}}$
σ_t	angular noise for monopulse tracker, rms value of timing jitter
σ_v	clutter velocity spectrum
$\sigma_y(\tau)$	Allan variance
σ_x	standard deviation of angle error
$\sigma_{1,\,2,\,3}$	clutter standard deviations due to different factors
σ_{ad}^2	variance due to analog-to-digital converter timing jitter
σ_c^2	variance due to clock timing jitter
σ_p^2	variance due to pulse forming network delay jitter
σ_t^2	variance due to timing jitter
σ_{tr}^2	variance due to transmit delay jitter
θ_g	phasing length
θ_n	angle between surface and multipath rays
θ_t	antenna beamwidth

$\theta_\theta(\tau)$	correlation function
τ	range delay or time delay; measurement interval (Allan variance); pulse width or pulse duration (time); sampling interval; range delay
τ_e	time shift error in pulse compression
τ_{eff}	effective pulse width
ω	radian frequency; target angular rotation rate
Ω	resistance unit (ohm)
ω_o	carrier radian frequency

Index

The Artech House Radar Library

David K. Barton, Series Editor

Active Radar Electronic Countermeasures, Edward J. Chrzanowski

Adaptive Signal Processing for Radar, Ramon Nitzberg

Airborne Early Warning System Concepts, Maurice Long, et al.

Airborne Pulsed Doppler Radar, Guy V. Morris

AIRCOVER: Airborne Radar Vertical Coverage Calculation Software and User's Manual, William A. Skillman

Analog Automatic Control Loops in Radar and EW, Richard S. Hughes

Aspects of Modern Radar, Eli Brookner, et al.

Aspects of Radar Signal Processing, Bernard Lewis, Frank Kretschmer, and Wesley Shelton

Bistatic Radar, Nicholas J. Willis

CARPET (Computer-Aided Radar Performance Evaluation Tool): Radar Performance Analysis Software and User's Manual, developed at the TNO Physics and Electronic Laboratory by Albert G. Huizing and Arne Theil

Cryptology Yesterday, Today, and Tomorrow, Cipher Deavours et al.

Cryptology: Machines, History, and Methods, Cipher Deavours et al.

DETPROB: Probability of Detection Calculation Software and User's Manual, William A. Skillman

Designing Automatic Control Systems, W.L. Rubin

Detectability of Spread-Spectrum Signals, Robin A. Dillard and George M. Dillard

Electronic Countermeasure Systems Design, Richard Wiegand

Electronic Homing Systems, M.V. Maksimov and G.I. Gorgonov

Electronic Intelligence: The Analysis of Radar Signals, Richard G. Wiley

Electronic Intelligence: The Interception of Radar Signals, Richard Wiley

Electronic Warfare Receiving Systems, Dennis D. Vaccaro

Engineer's Refractive Effects Prediction Systems–EREPS, Herbert Hitney

EREPS: Engineer's Refractive Effects Prediction System Software and User's Manual, developed by NOSC

High Resolution Radar, Donald R. Wehner

High Resolution Radar Cross-Section Imaging, Dean Mensa

Interference Suppression Techniques for Microwave Antennas and Transmitters, Ernest R. Freeman

Introduction to Electronic Defense Systems, Fillippo Neri

Introduction to Electronic Warfare, D. Curtis Schleher

Introduction to Sensor Systems, S.A. Hovanessian

IONOPROP: Ionospheric Propagation Assessment Software and Documentation, Herbert Hitney

Kalman-Bucy Filters, Karl Brammer

Laser Radar Systems, Albert V. Jelalian

Lidar in Turbulent Atmosphere, V.A. Banakh and V.L. Mironov

Logarithmic Amplification, Richard Smith Hughes

Machine Cryptography and Modern Cryptanalysis, Cipher A. Deavours and Louis Kruh

Millimeter-Wave Radar Clutter, Nicholas Currie, Robert Hayes, and Robert Trebits

Modern Radar System Analysis, David K. Barton

Modern Radar System Analysis Software and User's Manual, David K. Barton and William F. Barton

Monopulse Radar, A.I. Leonov and K.I. Fomichev

MTI and Pulsed Doppler Radar, D. Curtis Schleher

Multifunction Array Radar Design, Dale R. Billetter

Multisensor Data Fusion, Edward L. Waltz and James Llinas

Multiple-Target Tracking with Radar Applications, Samuel S. Blackman

Multitarget-Multisensor Tracking: Advanced Applications, Volume I, Yaakov Bar-Shalom, ed.

Multitarget-Multisensor Tracking: Advanced Applications, Volume II, Yaakov Bar-Shalom, ed.

Over-The-Horizon Radar, A.A. Kolosov, et al.

Principles and Applications of Millimeter-Wave Radar, Charles E. Brown and Nicholas C. Currie, eds.

Pulse Train Analysis Using Personal Computers, Richard G. Wiley and Michael B. Szymanski

Radar and the Atmopshere, Alfred J. Bogush, Jr.

Radar Anti-Jamming Techniques, M.V. Maksimov, et al.

Radar Cross Section Analysis and Control, A.K. Bhattacharyya and D.L. Sengupta

Radar Cross Section, Second Edition, Eugene F. Knott, et al.

Radar Electronic Countermeasures System Design, Richard J. Wiegand

Radar Engineer's Sourcebook, William Morchin

Radar Evaluation Handbook, David K. Barton, et al.

Radar Meteorology, Henri Sauvageot

Radar Polarimetry for Geoscience Applicatons, Fawwaz Ulaby

Radar Propagation at Low Altitudes, M.L. Meeks

Radar Reflectivity Measurement: Techniques and Applications, Nicholas C. Currie, ed.

Radar System Design and Analysis, S.A. Hovanessian

Radar Technology, Eli Brookner, ed.

Radar Vulnerability to Jamming, Robert N. Lothes, Michael B. Szymanski, and Richard G. Wiley

RGCALC: Radar Range Detection Software and User's Manual, John E. Fieldng and Gary D. Reynolds

SACALC: Signal Analysis Software and User's Guide, William T. Hardy

Signal Detection and Estimation, Mourad Barkat

Small-Aperture Radio Direction Finding, Herndon Jenkins

Solid-State Radar Transmitters, Edward D. Ostroff, et al.

Space-Based Radar Handbook, Leopold J. Cantafio, ed.

Spaceborne Weather Radar, Robert M. Meneghini and Toshiaki Kozu

Statistical Signal Characterization, Herbert Hirsch

Statistical Signal Characterization: Algorithms and Analysis Programs Software and User's Manual, Herbert Hirsch

Statistical Theory of Extended Radar Targets, R.V. Ostrovityanov and F.A. Basalov

Surface-Based Air Defense System Analysis, Robert Macfadzean

Surface-Based Air Defense System Analysis Software and User's Manual, Robert Macfadzean and James M. Johnson

Synthetic-Aperture Radar and Electronic Warfare, Walter W. Goj

VCCALC: Vertical Coverage Plotting Software and User's Manual, John E. Fielding and Gary D. Reynolds

For further information on these and other Artech House titles, contact:

Artech House
685 Canton Street
Norwood, MA 01602
(617) 769-9750
Fax:(617) 762-9230
Telex: 951-659

Artech House
6 Buckingham Gate
London SW1E6JP England
+44(0)71 630-0166
+44(0)71 630-0166
Telex-951-659